Modeling Thermal-Hydraulic-Mechanical-Chemical Processes in Rocks and Seals for Deep Geological Disposal

Final Report

No. RSP 413.7

for Canadian Nuclear Safety Commission

BY

Zhenze Li, PhD

May 19, 2017

Executive Summary

Decades of continuous development and utilization of nuclear power generation in Canada, like in many other countries in the world, have resulted in a substantial amount of radioactive wastes. Geological disposal is believed to be one of the best options for the long-term management of the wastes, making use of multi-barrier safety functions in order to retard the potential migration of contaminants towards the biosphere. The Canadian Nuclear Safety Commission has either actively participated in international research projects or initiated cutting-edge studies in close collaboration with Canadian and international partners to improve understanding of safety issues related to deep geological repositories. This report summarizes a series of comprehensive investigations into the multiphysics coupling of mechanical, hydraulic, thermal and chemical factors that influence the short-term and long-term behaviours of the clay seals and host rocks for radioactive waste disposal.

HM Scoping Assessment

A preliminary scoping study of the short-term and long-term behaviours of a DGR for low and intermediate level waste (LILW) is conducted. The numerical simulation is based on hydraulic-mechanical coupled governing equations, with consideration of geoscientific site investigation results for various overburden geological formations. The short-term assessment mainly addresses the excavation induced poroelastic response of the host rock. The long-term assessment discusses the impact of glacial cycles on the stability of host rocks, vertical shaft, and horizontal waste caverns. All simulations are conducted with conservative scenarios that represent the worst situation under most likely circumstances. It is found that the excavation induced damage zone (EDZ) extends from the cavern floor into the underlying Sherman Fall layer. The overall extent of the EDZ is approximately 2 times of the tunnel height in the vertical direction and in the horizontal direction is over 1 m into the 13 m thick pillars. As for the vertical shaft, the EDZ radial extent into the walls is limited between 1-2 times of the shaft diameter, even in the weakest formation such as the Blue Mountain formation. Under glaciation cycles, the whole geological repository is mechanically stable throughout the 120,000 years of post-closure period. The resulted gas pressure from radioactive wastes decomposition causes hydrogeological perturbation to the regions around the vertical shaft which is more permeable to other rocks. Tracer transport modelling reveals that diffusion is the dominant mechanism in the host rock and cap rocks, despite the very high hydraulic gradients induced by the combined effects of the overpressure in and above the Cambrian, and higher permeability of the repository and the shafts.

THM Assessment for Seals and Host Rocks

A modelling investigation of the HE-E heater experiment, performed at the Mont Terri underground research laboratory (URL) in Switzerland is conducted. The THM coupled models proposed by Nguyen et al. (2013) was applied to study the lab and field experimental observations of various physical parameters. The model was first calibrated with laboratory scale small column heating tests. Nonlinear vapour diffusivity and engineered barrier system (EBS) compressibility are found critical to the estimation of temperature and relative humidity evolution in the clay barriers. A staged numerical

simulation was developed to account for the excavation, backfilling and heating steps of the field experiment. The model reproduces very well most of the temperature profile, moisture movement, and pore pressure fluctuation at some locations of the repository. The excavation induced damage zone (EDZ) with higher permeability and lower air entry value than the intact host rock, proves to be beneficial to EBS desaturation within a short period of time under thermal gradient, but turns out to be an obstacle to bentonite resaturation in the long run. The impacts of nonlinearity in vapour diffusion coefficient and matrix compressibility are found to be critical to the success in numerical modelling and are in good agreement with experimental observations.

Visco-elastoplastic Model for Anisotropic Shale

Argillaceous rocks are candidate host and or cap formations for the geological disposal of nuclear wastes in many countries, including Canada, France and Switzerland. The understanding of the long term mechanical behaviour of such rocks is an essential requirement for the assessment of its performance as a barrier against radionuclide transport. Using the data from creep tests, monotonic and cyclic triaxial tests performed at the Canmet Laboratories, we developed constitutive relationships for the mechanical behaviour of the Tournemire shale. The model is based on the theory of plasticity, and takes into consideration the inherent anisotropy due to the existence of bedding planes, hardening behaviour before the peak strength, and viscosity. The constitutive relationships were implemented in finite element model to simulate the excavation damage zone around the century-old tunnel at the Tournemire URL. The influences of porewater pressure, desaturation and the fault that crosses the tunnel are examined. It was shown that desiccation must be taken into account in order to reproduce the shape of the excavation damage zone around the tunnel.

HM Assessment of Cobourg Limestone

The OPG proposes to place LILWs in the Ordovician-aged argillaceous limestone of the 28 m thick Cobourg Formation. The HM coupled behaviour of Cobourg limestone was studied in detail, including the governing equations, material properties, the damaged permeability, the long-term mechanical and rheological strength as well as the numerical schemes. Through a systematic review of poroelasticity of sedimentary rocks, the Biot's coefficient is found to vary closely with porosity. We found that low permeable rocks with low porosity always have extremely low Biot's coefficient. The weak HM coupling or poroelastic response of Cobourg limestone is found to pose limited impact to the propagation of the EDZ. This also ensures validity of the pulse decay permeability test method to be applied even under complex stress and loading conditions for granite, shale, marble and argillaceous clay rocks. Biot's coefficient is recommended to be derived from the experimental data on Skempton's B value, due to the fact that the bulk modulus of the solid skeleton varies with effective mean stress and mineral constituents. Time dependent failure of rocks under shear stress beyond the crack initiation threshold may involve rheological damage to the overall strength. A visco-elastoplastic model can well reproduce the relaxation test data on an argillite limestone. The progressive time-dependent failure of Cobourg limestone is further implemented in a numerical study of the long-term safety assessment of the waste cavern in repository.

Characterizing Bentonite Seals with DDL Theory

Characterization of the fundamental properties of expansive soil always involves different experimental strategies and methods. In this study, a unified theoretical framework was developed to address the uniqueness of various fundamental parameters behind the discrepancy in characterizing techniques. The classical Poisson-Boltzmann (PB) equation for diffuse double layer (DDL) was modified by taking into account the mass balance principle in order to reproduce the experimental results. The swelling pressure, suction and permeability of expansive soil (i.e. MX-80) were separately analyzed, discussed and calibrated against test data with the PB equation based models. Influences of dry density of soil and salinity of pore fluid on the swelling pressure, water retention curve, compression curve and permeability of bentonite clay were all successfully modelled. For unsaturated expansive soil, the air/water interface (meniscus) which was discovered to possess positive electric potential is believed in this study to be attracted by the negatively charged clay surface. This electrostatic attractive pressure in unsaturated porous media, which was discussed for the first time, was comparable to the experimentally observed matric suction. Using analytical approximate solution of the attractive pressure between asymmetrically charged planes, the water retention curve of bentonite was linearized and modelled with excellent agreement. On the other hand, flow in DDL predominant pore space of saturated bentonite was found to be governed by both viscosity and electro-osmosis, coupling of which results in electro-viscous retardation to the pressure driven flow. Using PB equation and the governing equation for electrokinetic flow, the permeability of compacted bentonite at various dry densities and salinities were numerically evaluated and compared against the reported test data with satisfying agreement. It is shown that the DDL dominates many aspects of bentonite's hydraulic-mechanical behaviour and the versatile DDL theories are sufficient to model these behaviours.

HM Assessment of Sand-bentonite Mixed Soil

Based on diffuse double layer (DDL) theory of expansive clay, the swelling behaviour of MX-80 bentonite was predicted before relevant experimental results were available. A new constitutive model for unsaturated expansive soil was proposed in this study. The new model considers the well-known Bishop's effective stress principle, and assumes a unique equilibrium state line coincident with the virgin compression curve. The rebound strain due to unloading in terms of effective stress is assumed to be elastic. Wetting of unsaturated soil induces reduction in effective stress and the correspondent rebound swelling strain. However, this is not sufficient to represent the overall swelling when the soil is subject to wetting, as intensely discussed in the literature. Therefore an extra component of the total swelling strain that is designated to the DDL expansion due to suction variation is defined in the classical e-log(σ') graph by invoking an equilibrium state line for the final swollen state. The suction-relevant swelling strain addresses the concerns on the limit of Bishop's effective stress from the advocators for bimodal stress state variables.

Besides, for expansive soils the saturation degree based water retention curve is insufficient to address the large strain induced saturation degree change. An alternative relationship based on gravimetric

water content is adopted to model the WRC of highly expansive soil. The governing equation for the unsaturated hydraulic flow is rewritten in accordance with the w-log(S_u) relationship.

Based on the new constitutive model, a series of hydraulic-mechanical coupled modelling was undertaken to predict the variation of the swelling pressure of a gradually saturated sand-bentonite mixture at designated initial density and left with technical void and fixed total volume. The modelling predicts the wetting-induced softening in swelling pressure and a subsequent hardening behaviour. A number of factors that influence the swelling performance were also examined by parametric investigations. It is found that the mock-up test will be equilibrated within days of brine infiltration.

HMC Assessment of MX-80 Bentonite Seals

The DGRs for nuclear wastes are commonly faced with potential risks on the long-term behaviors of engineered barrier system (EBS) imposed by the interaction with moderate to highly concentrated brine water present in the geological formations on site. The bentonite-based EBS is expected to be compacted to a target density at optimum water content that is adjusted with non-saline water. When this expansive soil is exposed to the in-situ saline groundwater, transient mass transport (hydraulic flow and solute transport) will take place right after. This process will involve time-dependent Hydraulic-Mechanical-Chemical (HMC) couplings and appear to be different from our previous predictions based on the equilibrium state principle. The laboratory experiments conducted at Queens' University have already indicated some "odds", e.g. the swelling pressure of MX-80 bentonite inundated with brine shows a big and instant pulse at early stage of flooding but diminishes gradually afterwards. In order to fully understand the underlying mechanism for these experimental observations, a comprehensive HMC coupled model has to be developed.

A dual-porosity conceptual model was proposed in this study to reflect the transient variation of swelling pressure observed in MX-80 bentonite, when flooded with highly concentrated brine water representative of the geological groundwater at Bruce DGR site. In order to describe the fully coupled HMC influences on expansive soils, governing equations for HMC processes were developed by adopting a dual-porosity framework and some hypothesis of microstructure-water content dependence and WRC-chemistry correlation. The dependence of hydraulic and mechanical properties on factors including porosity, salinity, and water content was discussed in detail. The proposed models were successfully implemented into a general-purpose mutiphysics-coupled FEM software COMSOL (Ver 5.2a), and were further calibrated with experimental results on the swelling pressure of compacted MX-80 bentonite flooded with brine model water (from Queens'U), and infiltration of bentonite column with clean water (from POSIVA). The observed temporal evolution of water content, suction and swelling pressure of compacted MX-80 can be well reproduced by our model.

The elastic moduli, permeability, WRC parameters were predetermined experimentally, while the chemo-osmosis semipermeable coefficient, suction toe, fluid exchange rate, mass exchange rate were optimized by best-fitting the swelling pressure evolution curves through numerical simulation. A number of unique relationships are developed for MX-80, i.e. permeability of micropore at various void ratios, WRC of micro- and macro-pores, constitutive relations of micropore dependence on water content, and the diffusion coefficients at various porosities. These constitutive relations are physically sound,

verifiable by experiments, and unique to MX-80. It can thus be applied to analyzing complicated HMC couplings of the engineered barrier system for waste disposal in both short-term and long-term risk assessments.

HM Scoping Assessment – Updated

A second round of scoping study is conducted about the repository host rock and bentonite seals, by incorporating the recently acquired knowledge from the to-be-completed project. Assumptions were reviewed, parameters were updated, and the scenarios were reassessed. We basically confirm most of the assumptions and parameters adopted in the original model. No major discrepancy in conclusions and findings is noticed in this study. The conservative scenario is confirmed to be justifiable. The excavation induced damage zone (EDZ) extends across the Cobourg Formation into the underlying Sherman Fall formation. The EDZ appears to be limited within 1-2 diameters into the sidewall of the shaft, preferential in perpendicular to the major principal stress. The tunnel pressure resulting from waste gases causes perturbation to the regions around the vertical shaft which is more permeable to other rocks. Glacial cycle would not impact the mechanical stability of all formations under consideration.

Contents

Chapter 1 Scoping study of geological repository by hydro-mechanical coupled modelling

Summary

This chapter deals with a preliminary scoping study of the short-term and long-term behaviours of radioactive waste repository. The numerical simulation is based on hydraulic-mechanical coupled governing equations, with consideration of geotechnical site investigation results for various overburden geological formations. The short-term assessment mainly addresses the excavation induced poroelastic response of the host rocks. The long-term assessment discusses the impact of glacial cycles on the stability of host rocks, vertical shaft, and horizontal waste caverns. All simulations are conducted with conservative scenarios that represent the worst situation under most likely circumstances. It is found that the excavation induced damage zone (EDZ) extends cavern floor into the underlying Sherman Fall layer. The overall scope of the EDZ is approximately 2 times of the tunnel height and is horizontally over 1 m into the 13 m thick pillars. As for the vertical shaft, the EDZ appears to be limited within 1-2 times of diameters even in the weakest formation such as the Blue Mountain formation. Under glaciation cycles, the whole geological repository is mechanically stable throughout the 120,000 years of postclosure period. The resulted gas pressure from radioactive wastes decomposition causes hydrogeological perturbation to the regions around the vertical shaft which is more permeable to other rocks. Tracer transportation modelling reveals that diffusion is the dominant mechanism in host rocks, despite the very high hydraulic gradients induced by the combined effects of the overpressure in and above the Cambrian, and higher permeability of the repository and the shafts.

1. Introduction

The author under contract to Canadian Nuclear Safety Commission (CNSC), has undertaken numerical simulation work for the hydraulic-mechanical (HM) behaviour of a Deep Geological Repository (DGR) for Low and Intermediate Wastes proposed by Ontario Power Genweration (OPG) at the Bruce nuclear site located in Kincardine, Ontario, Canada. The purpose of this numerical study is to assess the short-term and long-term performance of the DGR, focusing on the stability of the waste placement rooms as well as the vertical shafts that are viewed as the potential route for the upward migration of waste gases and pollutants.

This report summarizes the results of the HM coupled modeling study for typical rooms and shafts completed as part of the first research task in the period November 2014 to December 2014. Conceptual models were constructed in accordance with the preliminary design parameters as proposed by OPG. Geoscientific data used in this study were collected from various available technical reports published by the Nuclear Waste management Organization (Geofirma and Quintessa, 2011; Itasca, 2011; Intera, 2011; NWMO, 2011; Quintessa, 2011).

This report provides a summary description, assessment and interpretation of numerical simulations carried out in terms of a series of modeling efforts which cover the theoretical background, conceptual model, model parameters, modeling scenarios, evolution of pore pressure and effective stress after excavation and post-closure, change in the factor of safety, displacement and strain etc. The modeling is completed with the COMSOL multiphysics simulation platform (gradually updated versions from Ver 4.3 to Ver 5.3).

2. Theoretical framework for HM coupled modeling

2.1 Mathematical model

According to Dr. Son Nguyen's work (1995) on THM coupled models for porous media, the following reduced form of the hydraulic-mechanical coupled model can be obtained:

$$G\frac{\partial^2 u}{\partial {x_i}^2} + (G+\lambda)\frac{\partial^2 u}{\partial x_i \partial x_j} + \alpha\frac{\partial p}{\partial x_i} + F_i = 0$$

$$\alpha\frac{\partial}{\partial t}\left(\frac{\partial u}{\partial x_i}\right) - C_e\frac{\partial p}{\partial t} + \frac{\partial}{\partial x_i}\left(\frac{k_{ij}}{\mu}\left(\frac{\partial p}{\partial x_j} + \rho_f g_j\right)\right) = 0$$

where the shear modulus G=E/2(1+v); $\lambda = vE/(1+v)(1-2v)$; Biot-Williams coefficient $\alpha = 1 - K_D/K_S$; body force F_i; fluid density ρ_f; parameter $C_e = \frac{n}{K_f} - \frac{n}{K_S} + \frac{\alpha}{K_S}$; k is permeability and μ is viscosity of pore fluid; n is porosity; u is strain and p is pore pressure.

2.2 Implementation of models in COMSOL

With the HM coupled models in consideration, COMSOL provides the option to solve the above partial differential equations. In this study, the Solid Mechanics and Darcy's Flow modules were used to accomplish the coupling purpose.

The COMSOL software solves the following equation of equilibrium of the porous medium

$$-\nabla\sigma = F_V$$

While the equations for Darcy's flow is

$$\mathbf{u} = -\frac{k}{\mu}(\nabla p + \rho g \nabla D)$$

The water mass conservation equation is written as

$$\frac{\partial}{\partial t}(\rho\varepsilon_p) + \nabla(\rho\mathbf{u}) = Q_m$$

Accordingly the body load F_V is actually the coupling term from the pore pressure. As pore pressure represents a countering balance toward the overall total stress, the sign of this variable should be minus in the equation. It can thus be written as

$$F_V = -\alpha \frac{\partial p}{\partial x} - \rho g$$

The mass source for the flow equation reads

$$Q_m = -\rho\alpha \frac{\partial \varepsilon_V}{\partial t} + \rho C_e \frac{\partial p}{\partial t}$$

where ε_V is the volumetric strain.

In COMSOL we can turn to the storage equation to represent the second term in the above equation that addresses the compressibility of both pore fluid and solid skeleton.

$$C_e = n\chi_f + (1-n)\chi_p$$

where χ_f is compressibility of fluid and χ_p is compressibility of solid particles. This equation equals to the definition of C_e if $\alpha = 1$.

Along with appropriate boundary conditions, the HM coupled excavation problems both in the Cobourg Lower formation and across multilayers along the vertical shaft can be numerically analyzed.

Table 1.1 Geophysical parameters of interested formations for the room and shaft modeling scenarios

Top vertical depth	Formation	Hydraulic Conductivity		Porosity	Mechanical parameters			Rock density			Formation pressure		α**
		kh	kh:kv	%	E	v	σ_{1C} *	wet bulk	dry bulk	grain	Top	Bottom	
m		m/s			Gpa		Mpa	g/cm3	g/cm3	g/cm3	Mpa	Mpa	$1-K_D/K_S$
447.7	Queenston	3.00E-14	10	7.05	15	0.31	48	2.65	2.59	2.76	4.76	3.24	0.7
518	Gorgian Bay	3.00E-14	10	7.1	12	0.23	32	2.65	2.59	2.76	3.24	3.31	0.76
608.9	Blue Moutain	3.00E-14	10	7.35	5	0.1	21	2.65	2.59	2.76	3.31	3.95	0.9
651.6	Collingwood Member	2.00E-14	10	2.1	30	0.27	107	2.69	2.66	2.71	5.54	5.54	0.4
659.5	Cobourg Lower member	1.00E-14	10	1.8	39	0.3	113	2.69	2.66	2.71	5.54	6.36	0.22
688.1	Sherman Fall	9.00E-15	10	1.72	23	0.22	49	2.69	2.66	2.71	6.36	6.11	0.54
716.1	kirkfield	4.00E-15	10	1.95	26	0.2	64	2.69	2.66	2.71	6.11	7.54	0.48
762	Coboconk	2.00E-11	10-1000	0.75	68	0.33	118	2.69	2.66	2.71	7.54	8.71	0
785	Gull River	2.00E-12	10-1000	1.95	56	0.27	132	2.69	2.66	2.71	8.71	10.64	0
838.6	Shadow Lake	1.00E-09	10	1.95	23	0.33	72	2.6	2.54	2.72	10.64	10.64	0.54
843.8	Cambrian	3.00E-06	1	8.9	23	0.33	72	2.6	2.54	2.72	10.64	10.64	0.54
860.7	Precambrian	1.00E-10	1	3.8	68	0.33	118	2.6	2.54	2.72	10.64	10.64	0
Reference	Table 3.1 in DGSM	Table 4.19 in DGSM		Fig. 4.2 in DGSM	Table 3.14 in Geosynthesis			Table 4.1 in DGSM			Fig. 5.2 in Geosynthesis		

Note:

*: The uniaxial compressive strength is obtained from lab test within limited time duration and thus represents the peak strength of intact rock. For the sake of safety, σ_{1C} needs to be reduced to 65% for the calculation of FS.

**: The modulus of solid skeleton is assumed as 5GPa for the calculation of this parameter.

2.3 Mechanical and hydrological parameters

Table 1.1 lists the complete dataset showing the stratigraphic, mechanical and hydrological information that are required for the numerical simulations. The heterogeneity in permeability is not considered in this study. Instead, an isotropic permeability is assumed for the whole analysis domain. The formation pressure that is regarded as the initial mechanical stress is interpolated with depth and is assigned onto the whole domain. Parameter α is calculated from the relative stiffness, whereas the negative value is taken as 0.0 in the simulation to indicate that the HM coupling could be negligible due to the extremely high value in Young's modulus of the host rock.

3. Conceptual model

3.1 Geometry of the conceptual models for room and shaft excavation

Figures 1.1a-1.1b shows the geometry of conceptual models for both emplacement room and shaft. A typical room is considered as a plain strain problem while the shaft is axisymmetric. Size of the room is 7 m high and 4.3 m in half width. The left boundary at x=0 indicates a symmetric center in width. The right boundary indicates the centerline between two adjacent rooms (distant from each other with an interval of 17.2 m). For the shaft model, the radius of the excavated shaft is at 6.5 m. The preliminary design of the DGR considers the excavation of two shafts, one for room access and one for ventilation purposes, with a system of access galleries and rooms around the shafts. The real problem is in fact three dimensional, however in these scoping calculations we simplify the model into an axisymmetric one, with one central shaft which has an equivalent volume of two shafts, The far end of the FEM zone extends to 500 m away from the axis.

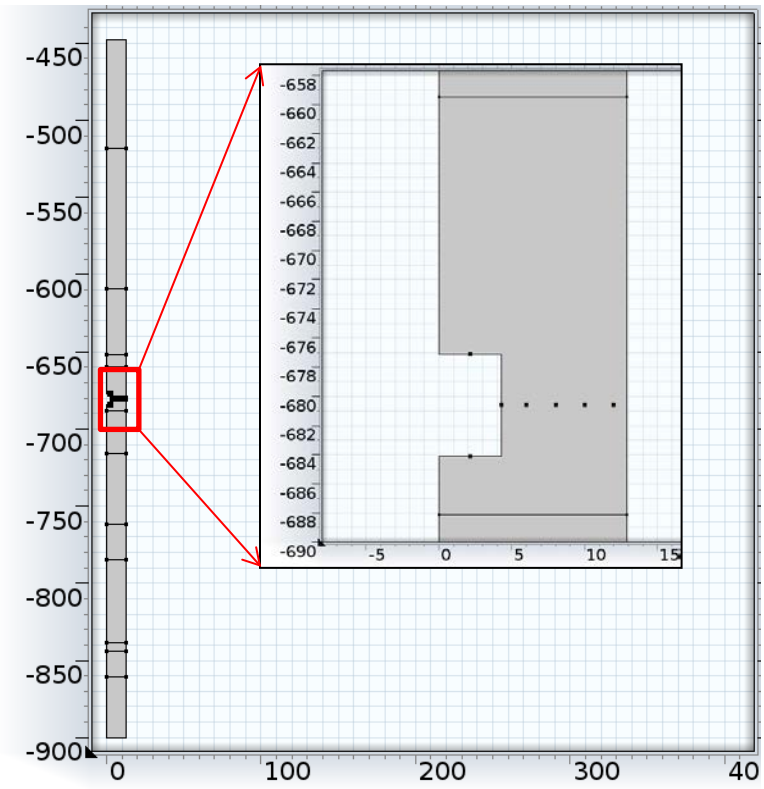

(a)

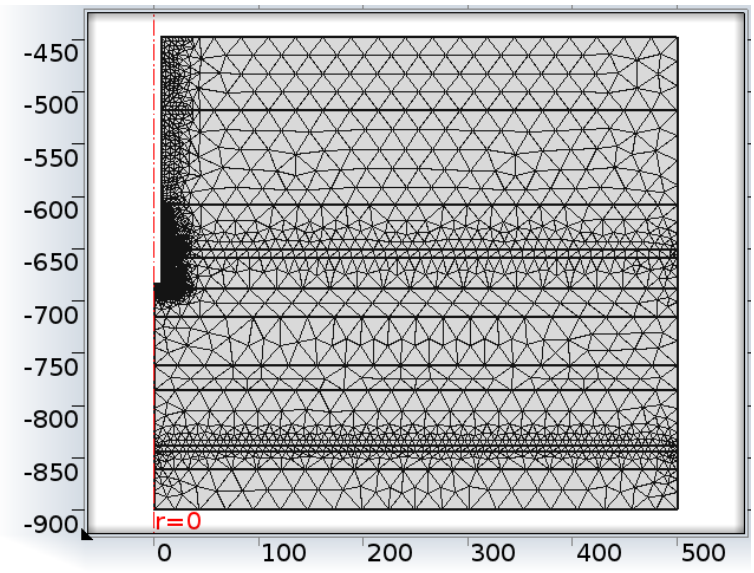

(b)

Fig. 1.1 Geometry of the conceptual models for (a) a typical room and (b) the vertical shaft

Fig. 1.2 shows the geological stratigraphy of each formation considered in this study. The upper boundary is at the top layer of the Queenston, while the bottom boundary is fixed into the Precambrian formation. The depth as adopted in the simulation is referenced from the ground surface. The repository rooms are located in the Cobourg lower member formation.

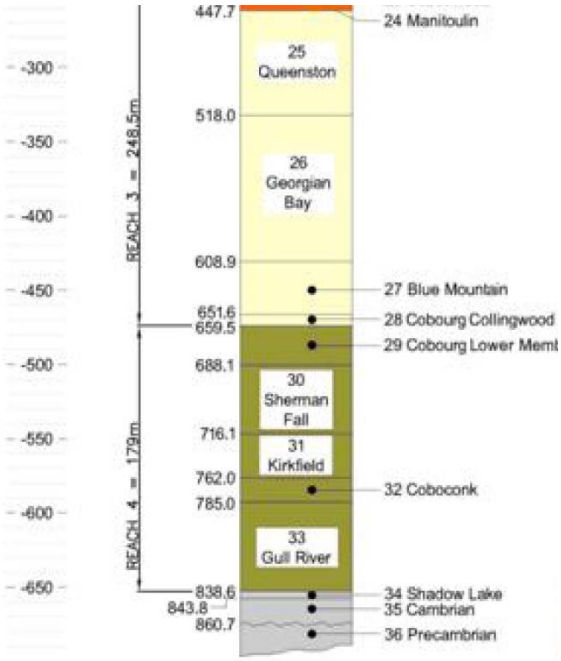

Fig. 1.2 The stratigraphic sequence of the interest geological profile

3.2 Porosity profile

Fig. 1.3 shows the distribution of porosity with depth as determined from well loggings. The solid line indicates the average value of test data and is adopted as the input parameter in this study.

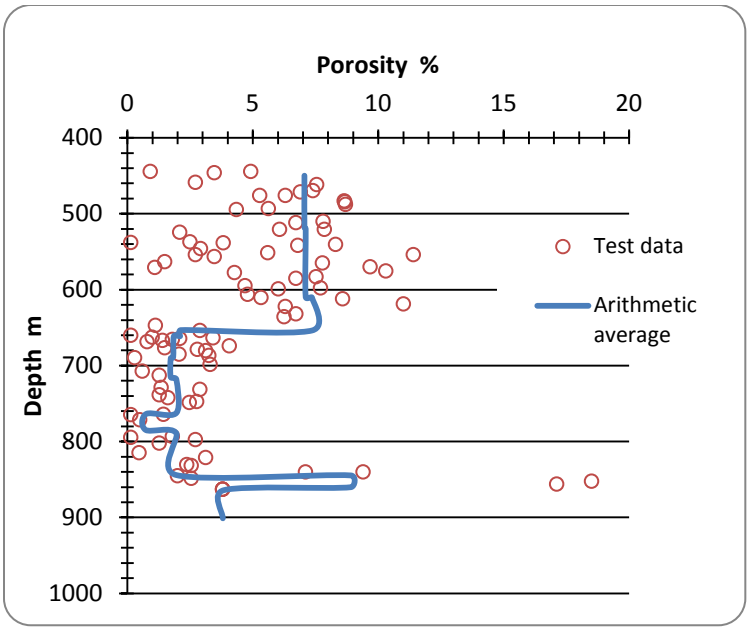

Fig. 1.3 Porosity profile vs depth as determined from DGR core

3.3 Boundary conditions

The room excavation model is hypothesized as symmetric across the center of adjacent rooms. Therefore the left and right boundaries are treated as rollers, allowing only vertical displacement. The bottom boundary is fixed, and the top boundary is free.

The room boundary is prescribed with initial ground stress for the initialization computation. Pore pressure and stress loading at the room boundary are gradually removed to mimic the time-dependent excavation stage.

Subsequent simulation is also carried out after the excavation is finished, in order to evaluate the long-term HM evolution of the surrounding rocks.

Roller boundary is applied to left, top, right and bottom boundaries, except for the excavation front which is treated as a boundary load in terms of the following expression,

$$F_b = (-\rho g h + p) * \mathrm{exc}(t)$$

where exc(t) is a stepwise reducing function ranging from 1.0 to 0.0 with increasing time that models the excavation stage.

3.4 Excavation duration

The excavation is supposed to finish within a limited time span. It can be achieved within days to dig through the room front. In this study we assume a 2-D plane strain model. For this purpose, we may

need to consider a conceptualized room model with a certain length, for instance 50 m. Then a somewhat extended period may be reasonable to attain a complete excavation. We consider here an excavation period of 30 days during which the boundary loading upon the surrounding rock is gradually removed in a smoothly declining manner. Fig. 1.4 shows the time-dependent excavation function exc(t).

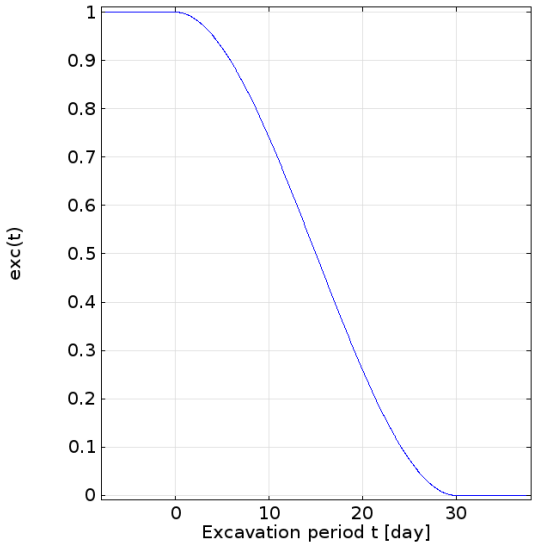

Fig. 1.4 Excavation time-dependent function exc(t)

3.5 Initial conditions

Regional data for in-situ stress indicate that horizontal stresses are larger than the vertical stress, with a maximum ratio of 2.0. To be on the conservative side, it is assumed in this study that the initial horizontal stress is twice the vertical static stress. The initial pore pressure is taken from the Geosynthesis report as well as the DGSM report. Underpressure in the target formations is commonly observed. Averaged value in pore pressure is adopted in this study. The depth profile of pressure is shown as following.

The horizontal stress reads:

$$\sigma_x = 2\rho g h$$

And the vertical stress is written as:

$$\sigma_y = \rho g h$$

The pore pressure distribution follows the observed pattern of the field data. Underpressure in a number of formation layers, in particular in the host and overlying cap rocks, is considered. Overpressure is present in deeper regions such as the Gull River, Cambrian and Precambrian formations. The pore pressure and environmental head distribution with depth are shown in the following graphs (Fig. 1.5-1.6).

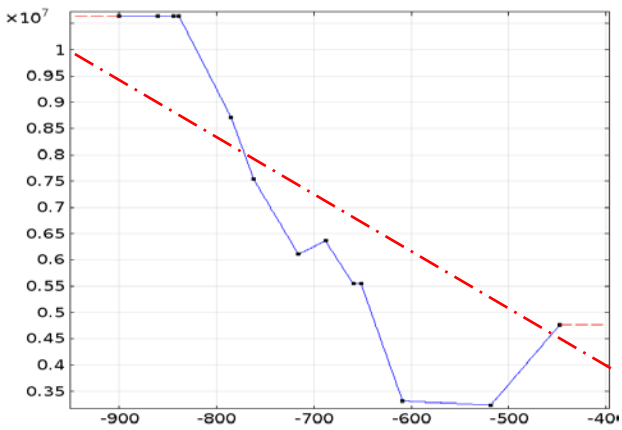

Fig. 1.5 Pore pressure (MPa) vs depth (m) (The dashed line indicates the hydrostatic pore pressure.)

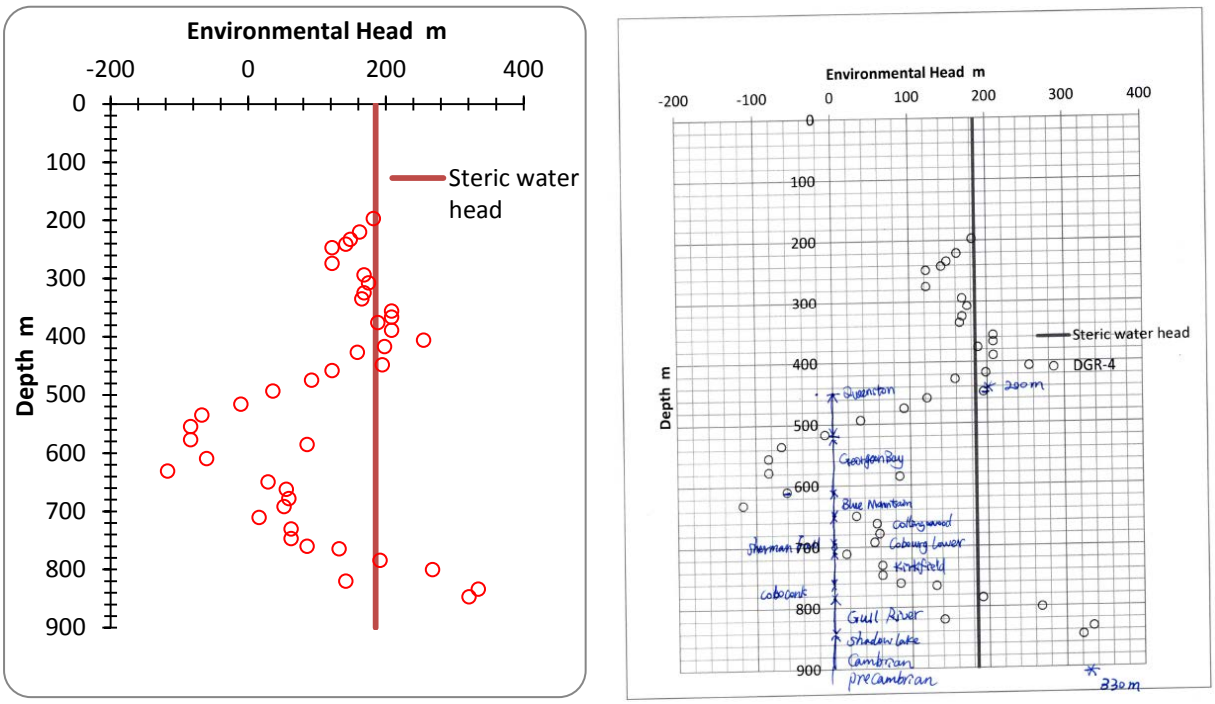

Fig. 1.6 Stratigraphy vs formation pore pressure expressed in environmental head (m)

3.6 Factor of safety

The classic Hoek-Brown failure criterion is used for the calculation of the safety factor. The Hoek-Brown criterion is written as

$$\sigma'_{1f} = \sigma'_3 + \sigma_{1C}(m_b \frac{\sigma'_3}{\sigma_{1C}} + S)^a$$

where σ'_{1f} is the major effective principal stress at failure; σ'_3 is the minor effective principal stress; σ_{1C} is the uniaxial compressive strength (UCS) of the intact rock material; m_b is a reduced value (for the rock mass) of the material constant for the intact rock; S and a are constants which depend upon the characteristics of the rock mass.

Then the factor of safety is defined as:

$$\mathrm{FS} = \frac{\sigma'_{1f}}{\sigma'_1}$$

where σ'_1 is the actual major principal stress.

It is noteworthy that the strength of intact rock needs to be reduced to a certain percentage in order to be representative of the rock-mass mechanical behavior that associates with the scale effect and the effect of rock mass jointing (Long term Geomechanical Stability Analysis Report, 2011, P 13). According to the Itasca Consulting Group's parametric input, the Hoek-Brown strength criterion for the Sherman Fall limestone includes the following three values,

m_b=3.438, s=0.0205, a=0.502.

And the shale formations, e.g. Blue Mountain formation etc., have the following Hoek-Brown criterion:

m_b=2.740, s=0.0357, a=0.501.

These parameters were obtained by using GSI=75, m_i=8 and damage factor D=0 as a starting point to develop properties for mechanical analysis. The choice of the above set of parameters has been detailed in the Long-term Geomechanical Stability Analysis report (Page 26, NWMO DGR-TR-2011-17).

Furthermore, the value of σ'_{1C} obtained from laboratory uniaxial compressive stress are reduced to 65%, in order to account for long term strength degradation.

It may not be justifiable to apply the above set of parameters on the whole domains, however, this can be regarded as a conservative case study especially in view of the comparative strengths of various types of rock mass. Rocscience has compiled a collection of Hoek-Brown strength criteria for different rocks. According to literature (Rocscience), a massive weak rock has the following model constants: m_b=6.675, s=0.062, a=0.501. It is also noted that shale typically has a constant m_b=6$\pm$2. Therefore, the choice of the model constants for Hoek-Brown criterion can be representative of the needed conservative scenario.

4. Results and discussion

4.1 Results for room

Figures 1.7-1.9 show the contour of variables of primary interest, such as the FS, pore pressure and mean stress. In this report, the convention of positive in tension is adopted for stress and strain. The mean stress is however positive in compression.

Plots are representative of increased elapsed time from 15 days to 8 years. In Fig. 1.7, it is shown that the excavation induced damage zone (EDZ) extends across the Cobourg formation into the underlying Sherman Fall formation. Horizontally the EDZ extends by 1.4 m into the pillar as confirmed by the distribution of FS in Fig. 1.7. In case of FS<0, tensile failure would be expected to occur. A compressive type of damage is expected when 0<FS<1, and no damage is expected when FS>1. From the contour of FS we can see that EDZ tends to elongate vertically in the direction of the minimum principal stress. Localization of EDZ near the upper and lower right corners are observed, which is closely related to the stress localization as shown in Fig. 1.9.

Fig. 1.8 shows the parts surrounding the room section with both increase and decrease in pressure. The evolution of the pore pressure is consistent with the evolution of the mean stress shown in Figure 1.9. Increased pressure is found in zones where the mean stress increases, resulting in a pore volume compression, and decreased pressure is found in zones where the mean stress decreases resulting in pore volume expansion. However, due to drainage, both increased and decreased pressures gradually dissipate with time. It is noteworthy that the some zones even experience negative presure, suggesting an over-expanded phenomenon with pore fluid unable to fill in the gap in volumetric change. This "suction" gives rise to the effective stress and acts as a stabilizing counter balance, which further leads to an increase in FS. In regions on the right side of the room sidewall the FS is absent before 1 year, and turns out to be unstable afterwards when the "suction" disappears (see Fig. 1.8).

Factor of safety after excavation

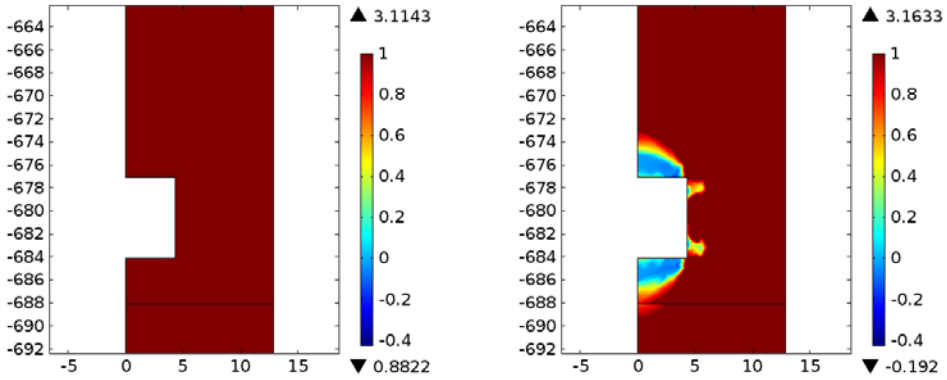

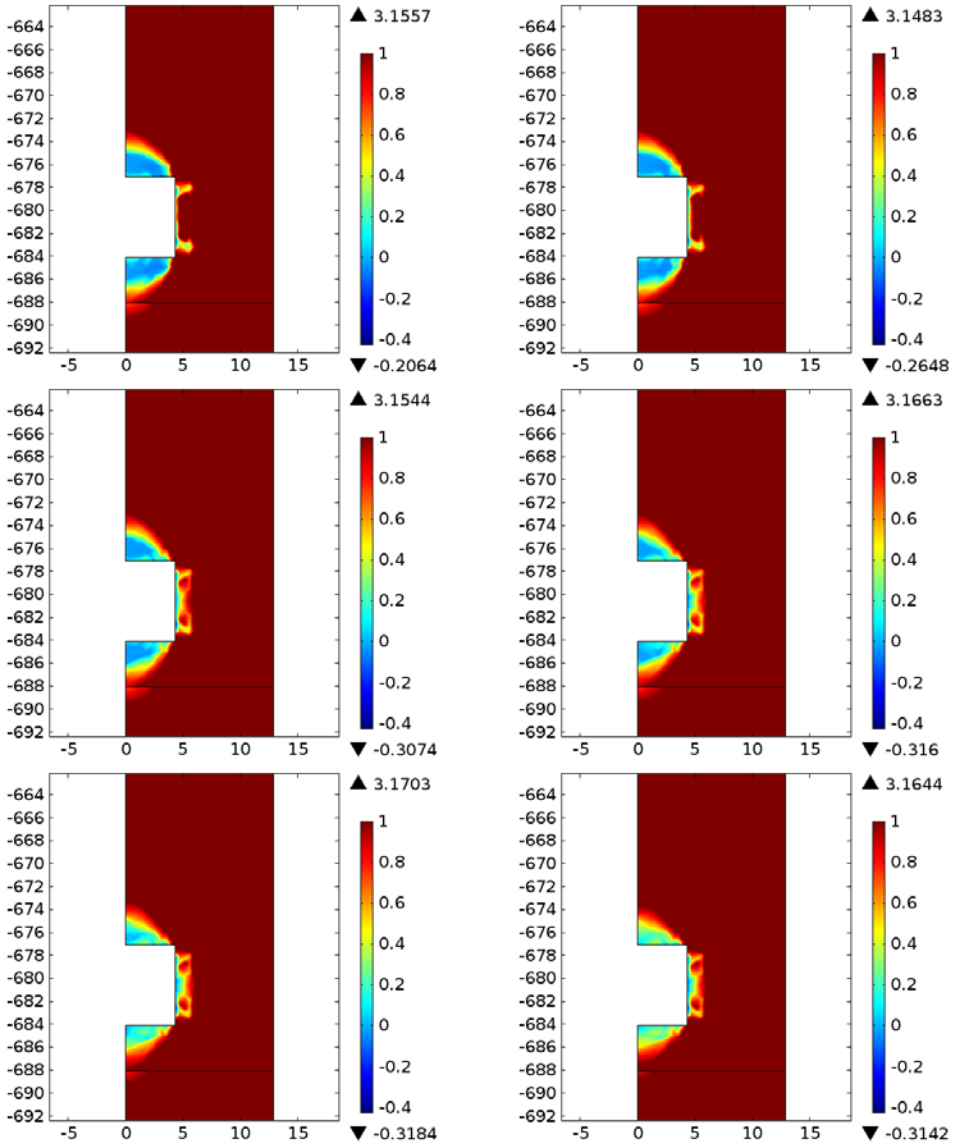

Fig. 1.7 Contour plots of the factor of safety with increasing elapsed excavation time (a-h: 15 day, 30 day, 60 day, 120 day, 1 a, 2 a, 4 a, 8a)

Pore pressure evolution

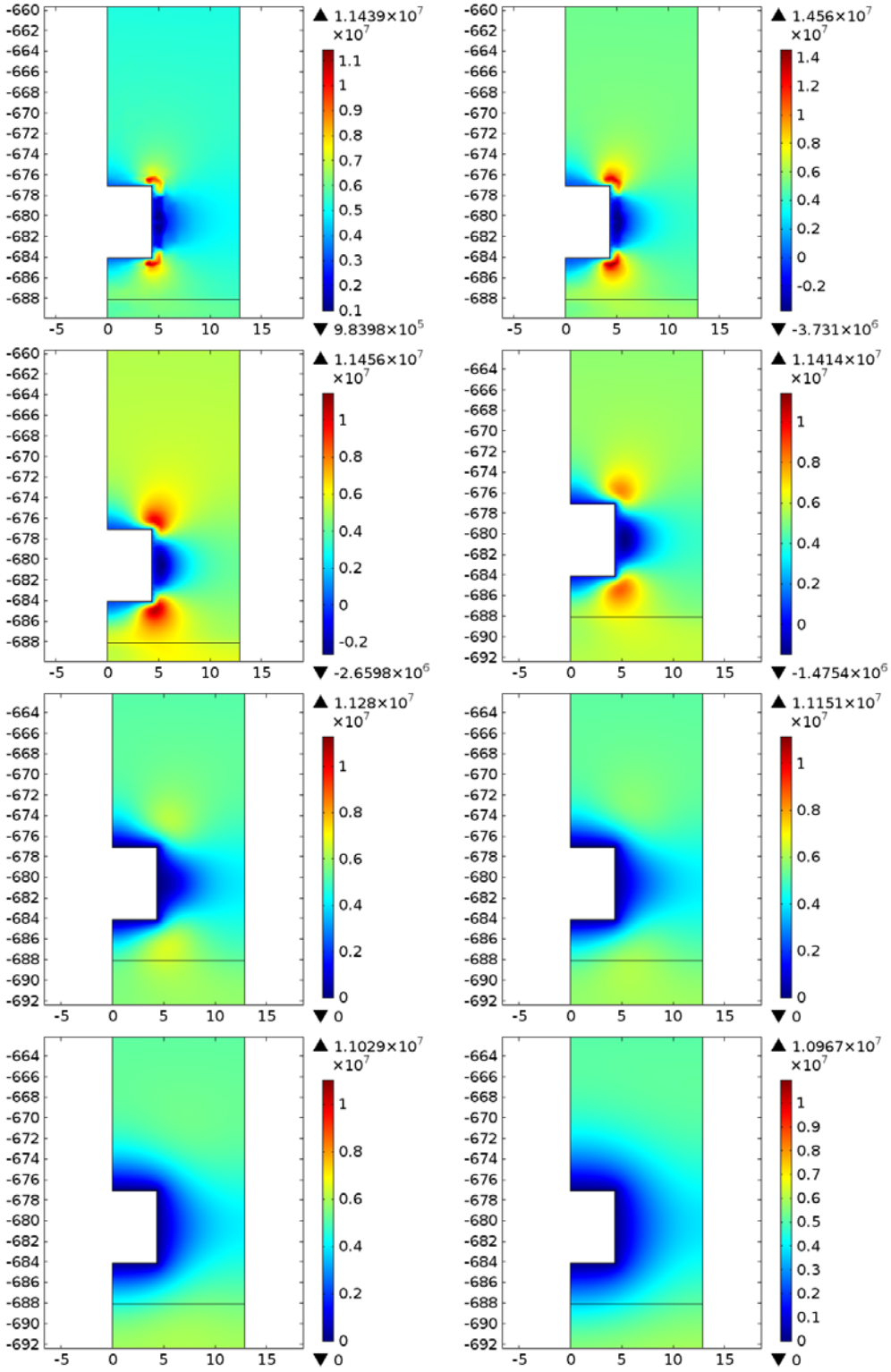

Fig. 1.8 Contour plots of the pore pressure with increasing elapsed excavation time (a-h: 15 day, 30 day, 60 day, 120 day, 1 a, 2 a, 4 a, 8a)

Mean stress

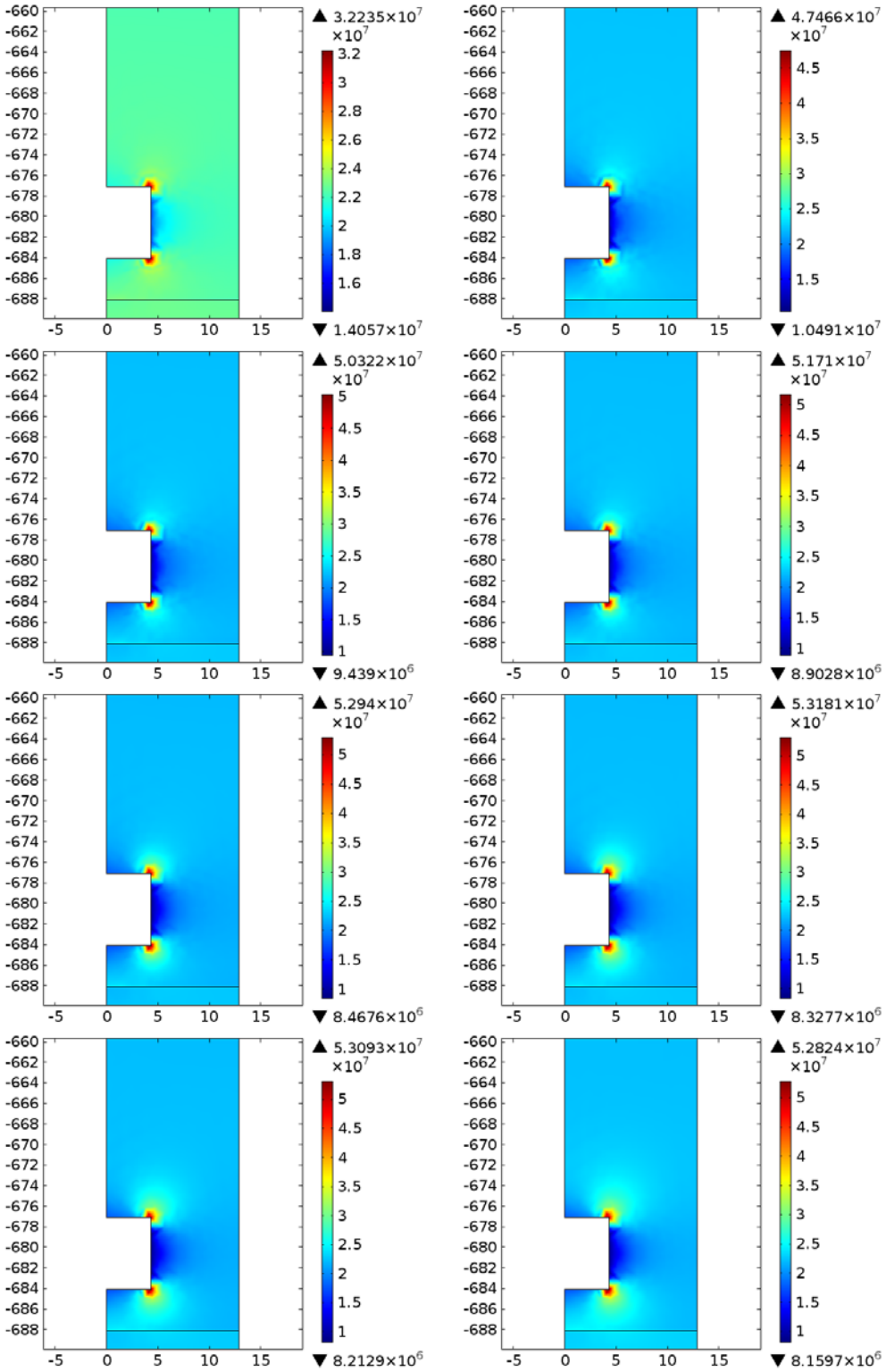

Fig. 1.9 Contour plots of the mean stress with increasing elapsed excavation time (a-h: 15 day, 30 day, 60 day, 120 day, 1 a, 2 a, 4 a, 8a)

HM evolution at selected critical points

Monitoring points are picked around the room inner surface and along the horizontal center line through the center of sidewall as shown in Fig. 1.10. Figs. 11-16 show the results of various variables.

As shown in Figure 1.11, all points in the vicinity of the room experience damage (FS<1). The pillar however remains essentially undamaged as shown from points 22, 23 and 24. Fig. 1.12 shows the pore pressure evolution. All points show the combined effects of drainage to the room and poroelastic effects. In particular, point 21 experiences a sharp decrease of the pore pressure to negative values due to volumetric expansion induced by stress relief. Fig. 1.13 shows the volumetric strain along the horizontal cut line at different elapsed time. The volumetric strain is found to change all the time, with gradual increase in values and rapid decline along the distance inward the sidewall. From volumetric strain it is shown that the whole region between two adjacent rooms is susceptible to excavation induced disturbance. But the extent of disturbance does not accumulate to the degree that can threaten the stability of the overall surrounding rock mass. FS calculation indicates that the EDZ is limited and localized in space irrespective of the time effect.

The points on the inner room surface are prone to excavation damage right after the removal of confining loading. The edge points #18 and #20 have the largest mean stress as shown in Fig. 1.14.

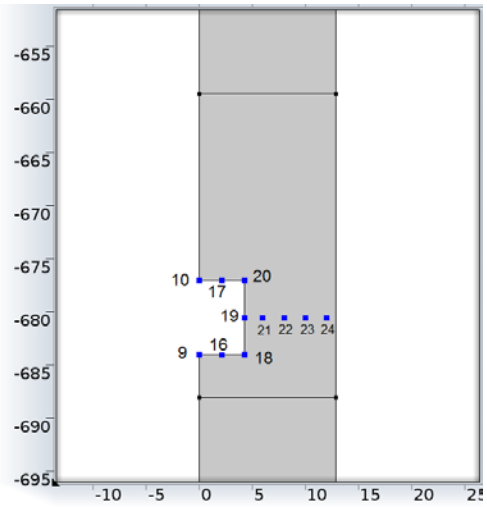

Fig. 1.10 Geometric location of selected points for plotting of time-dependent variables

Factor of safety

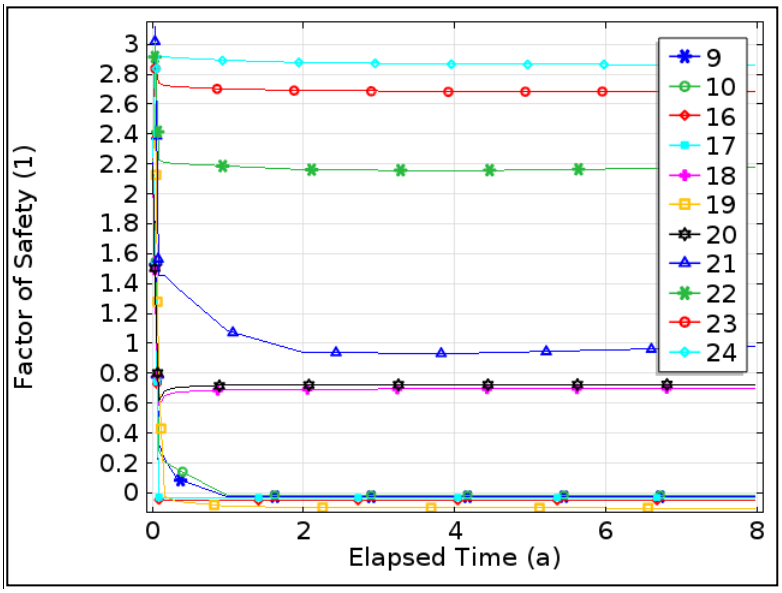

Fig. 1.11 Variation of FS with elapsed time for selective monitoring points

Pore pressure

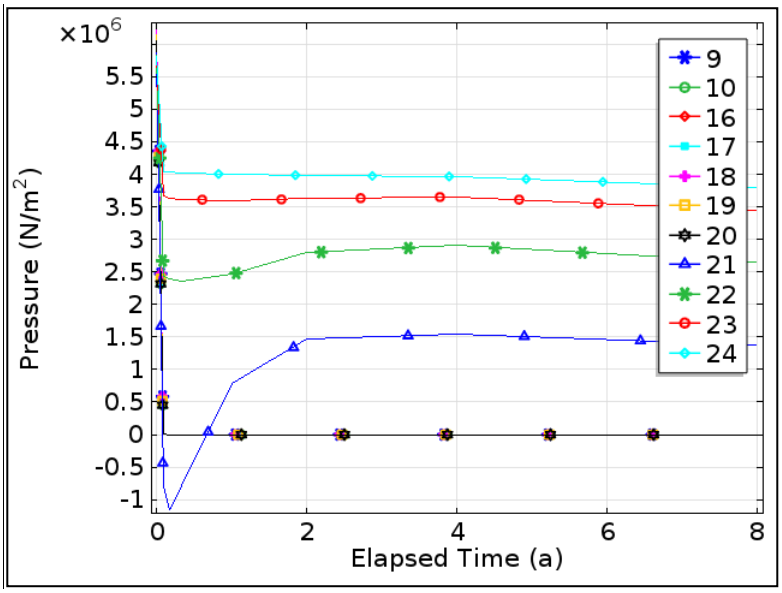

Fig. 1.12 Variation of pore pressure with elapsed time for selective monitoring points

Volumetric strain

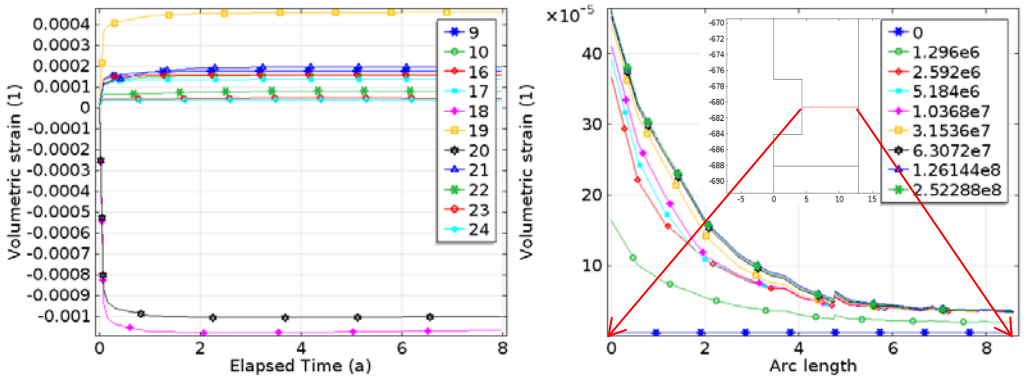

Fig. 1.13 Variation of volumetric strain (a) with elapsed time for selective monitoring points and (b) with arc length along the horizontal cut line through center of sidewall. Note: expansion is positive

Mean stress

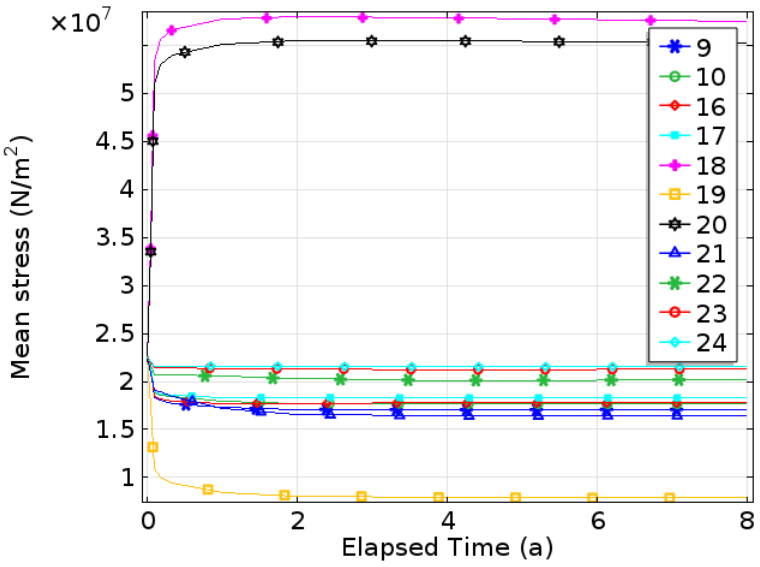

Fig. 1.14 Variation of mean stress with elapsed time for selective monitoring points. Note: compression is positive

Principal stresses

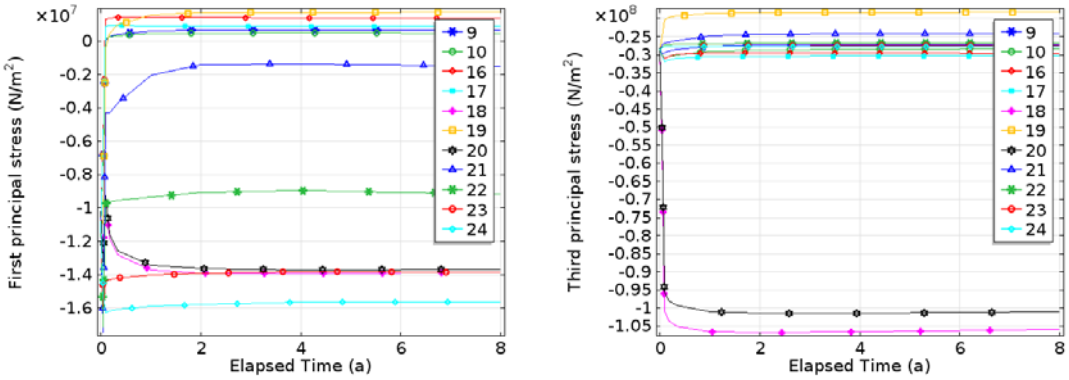

Fig. 1.15 Variation of principal stresses with elapsed time for selective monitoring points. Note: tension is positive.

Displacement in horizontal and vertical directions

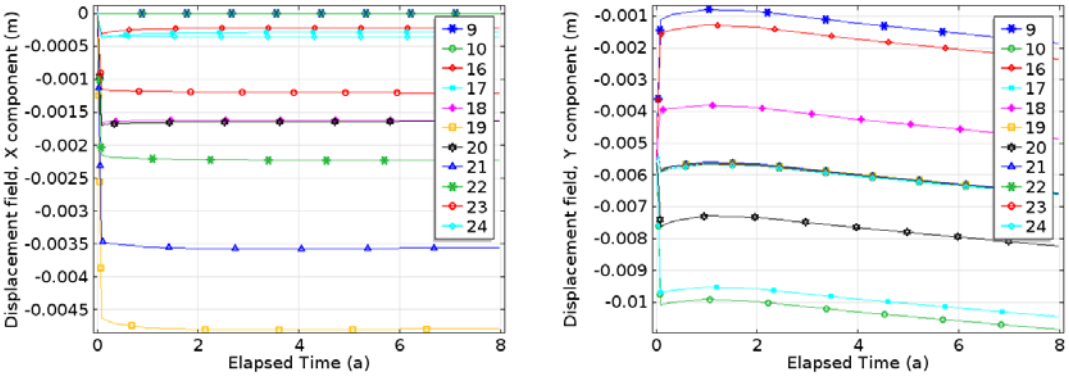

Fig. 1.16 Variation of directional displacement with elapsed time for selective monitoring points

4.2 Results for shaft case

4.2.1 Contour plotting

Figures 1.17-1.19 show the contours of FS, pore pressure and mean stress for the zones of interest near the vertical shaft. The EDZ appears to be limited to within 1-2 diameters into the sidewall in the weakest formation, the Blue Mountain formation. The EDZ at the bottom of the shaft does not penetrate through the Cobourg formation. Pore pressure dissipation develops as expected, due to the combined effects of poroelasticity and drainage towards the shaft. Stress localization and concentration are observed near the right bottom edge of the shaft and interface between formations with great difference in material properties.

Factor of safety

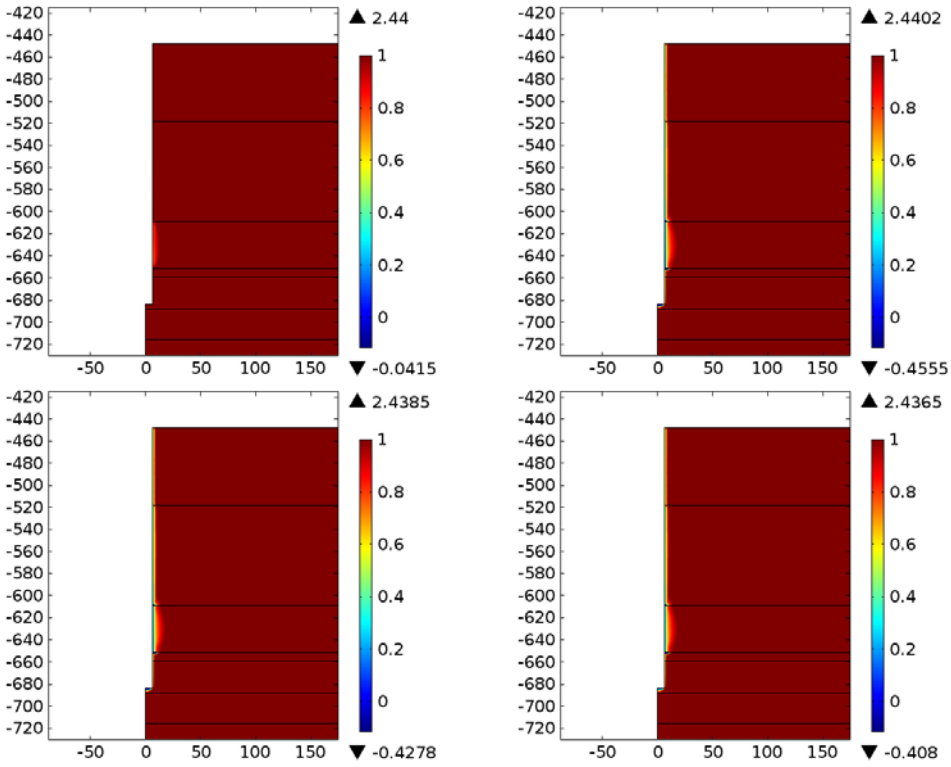

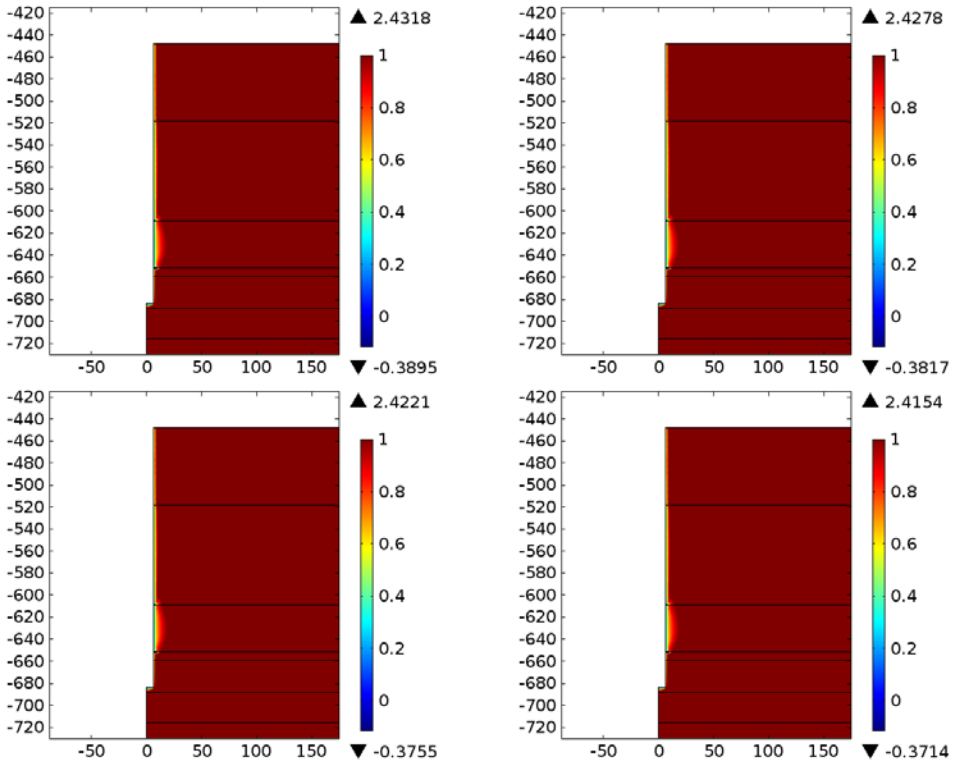

Fig. 1.17 Contour plots of FS for shaft with increasing elapsed excavation time (a-h: 15 day, 30 day, 60 day, 120 day, 1 a, 2 a, 4 a, 8a)

Pore pressure

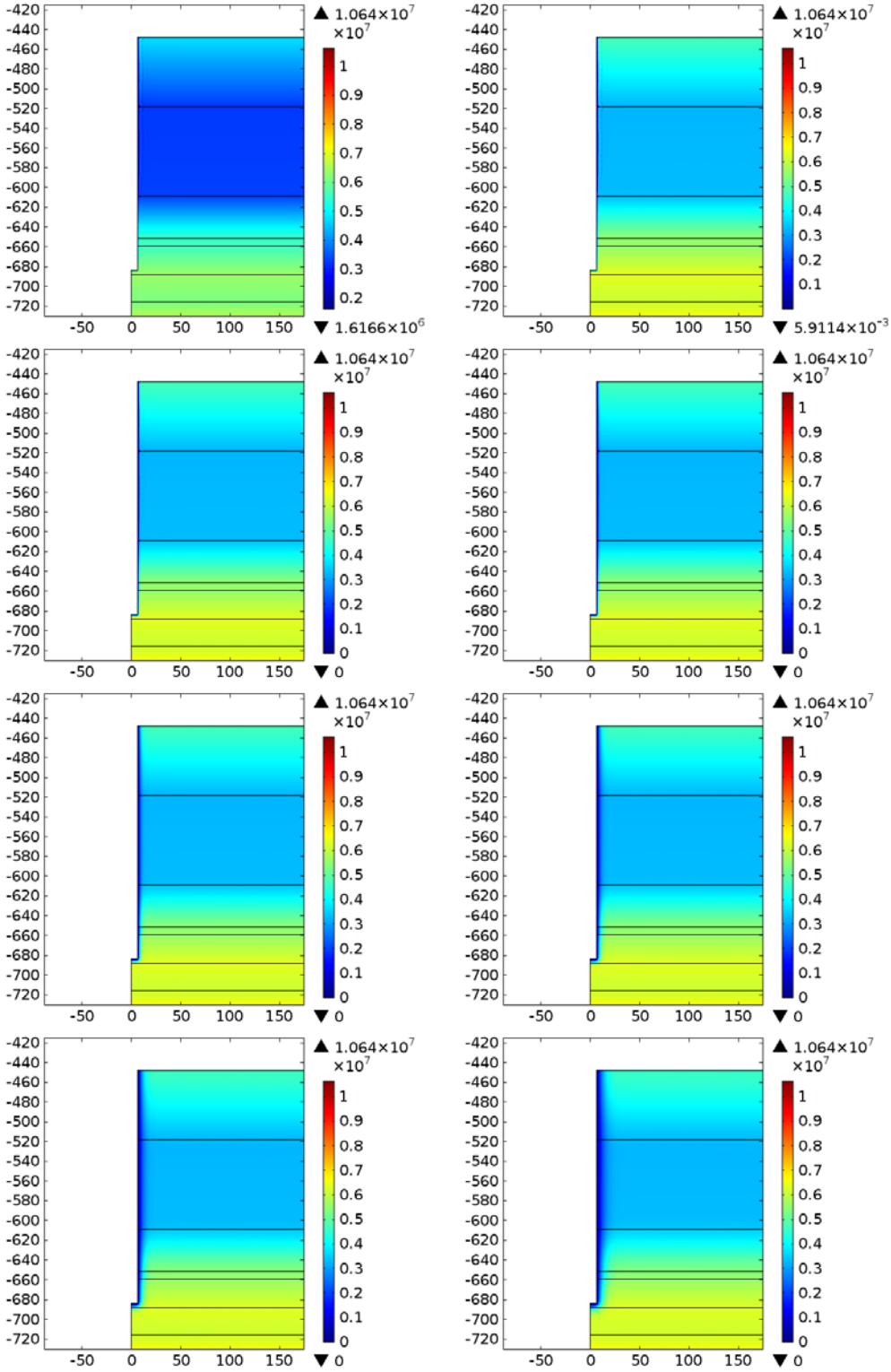

Fig. 1.18 Contour plots of pore pressure for shaft with increasing elapsed excavation time (a-h: 15 day, 30 day, 60 day, 120 day, 1 a, 2 a, 4 a, 8a)

Mean stress

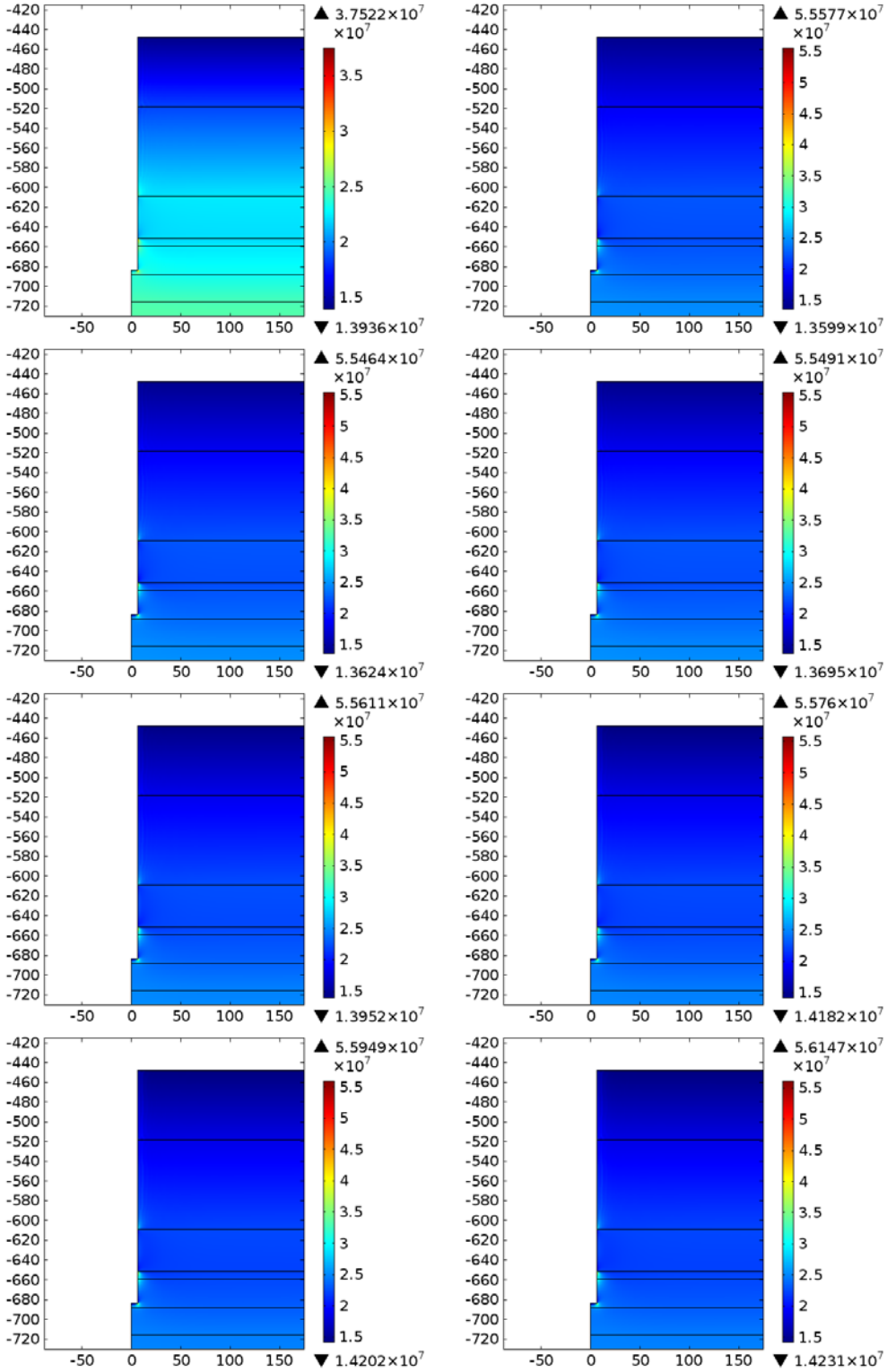

Fig. 1.19 Contour plots of mean stress for shaft with increasing elapsed excavation time (a-h: 15 day, 30 day, 60 day, 120 day, 1 a, 2 a, 4 a, 8a)

4.2.2 Monitoring results along cut-lines

Two cut-lines are made, as shown in Fig. 1.20, to monitor the simulation results for discussion. L1 is along the axis in vertical direction, and is located at r=0.5 m. L2 is in radial direction, extending from shaft sidewall to r=50 m, at the middle of the Blue Mountain formation that displays the most extensive EDZ. Figures 1.21-1.25 show the results on cut-line L1. Figures 1.26-1.30 show the results on cut-line L2.

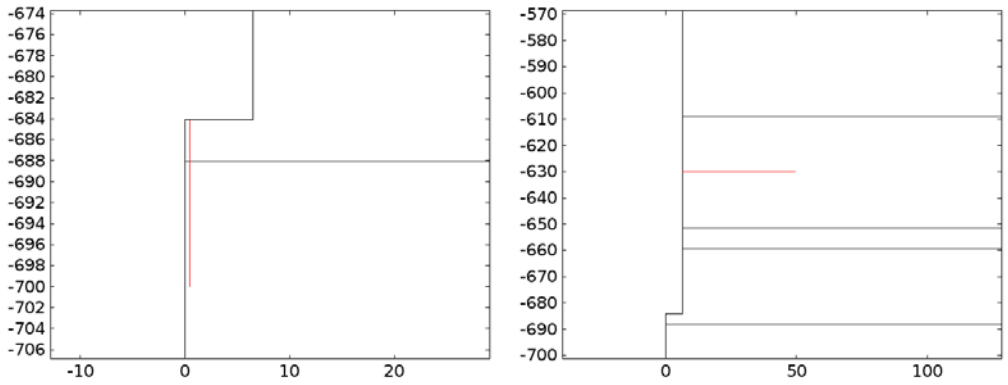

Fig. 1.20 Cut-lines for results visualization (a) L1 close to axis at r=0.5 m and (b) L2 at minimum FS at z=-630 m.

4.2.2.1 HM evolution along cut line L1

The EDZ does not propagate deeply into the Sherman Fall formation as shown from Fig. 1.21. Excavation leads to rapid unloading in the vertical direction (Fig. 1.22b) and thus results in a quick reduction in FS. Such impact is observed even in deeper regions 10 m underneath the shaft bottom; however the “damaged” zone, with FS less than 1, is restricted to a depth of 5m. Fig. 1.22a demonstrates the re-equilibration and reorientation of stress. The resulting mean stress and volumetric strain experience fluctuations, e.g. the mean stress in Cobourg formation reduces (swelling in volume as shown in Fig. 1.25b) in regions within 2 m under the shaft bottom, and increases (compression in volume in Fig. 1.25b) by 4 MPa below 2 m under the bottom.

Factor of safety

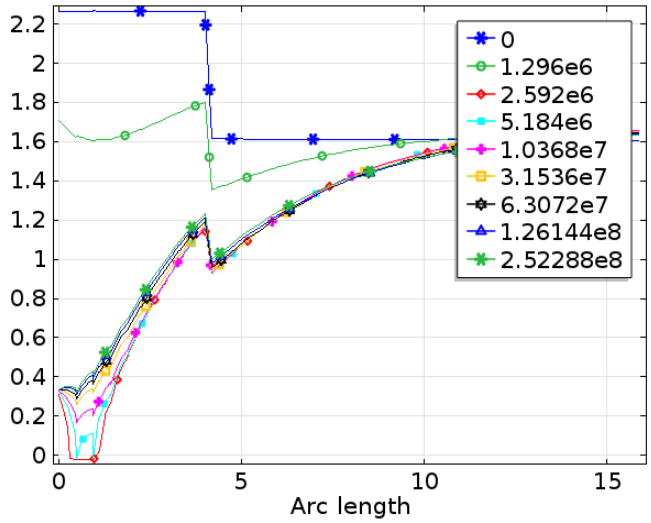

Fig. 1.21 Variation of FS along the downward cut line L1

Directional stresses

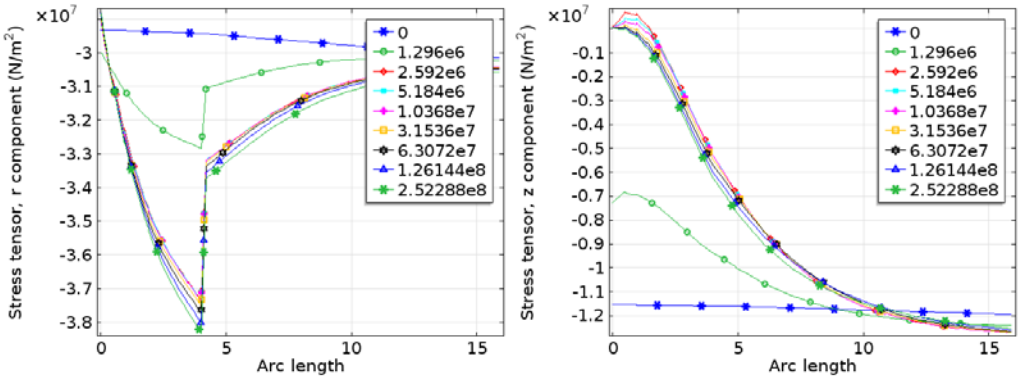

Fig. 1.22 Variation of radial and vertical stress along the downward cut line L1 at times of 0, 15, 30, 60, 120 days and 1, 2, 4 and 8 years – Tension is positive

Pore pressure

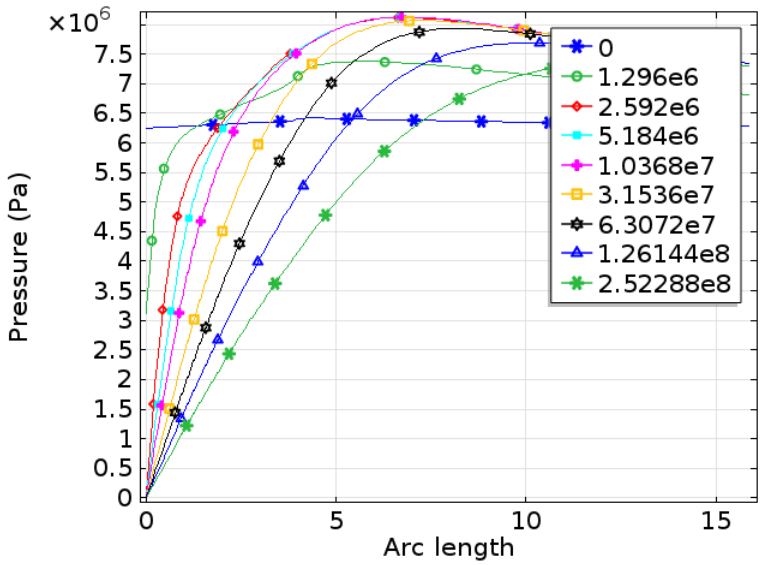

Fig. 1.23 Variation of pore pressure along the downward cut line L1 at times of 0, 15, 30, 60, 120 days and 1, 2, 4 and 8 years – Tension is positive

Mean stress

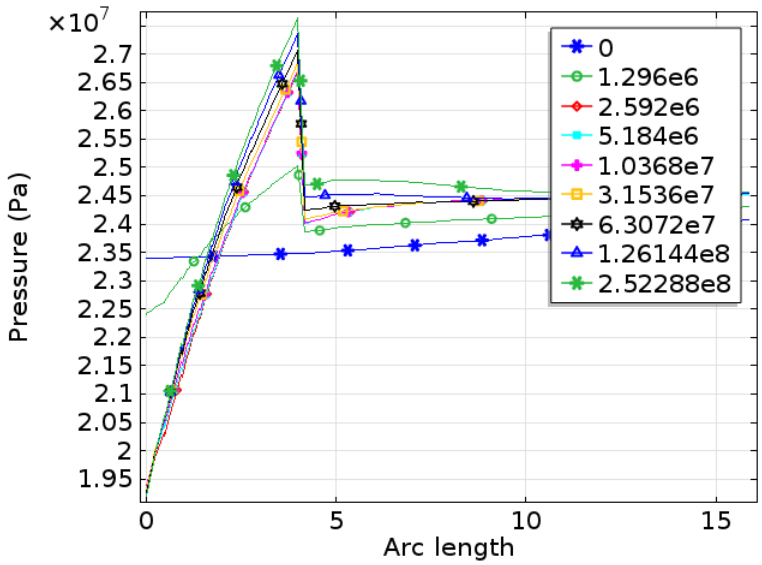

Fig. 1.24 Variation of mean stress along the downward cut line L1 at times of 0, 15, 30, 60, 120 days and 1, 2, 4 and 8 years – Tension is positive

Displacement and volumetric strain

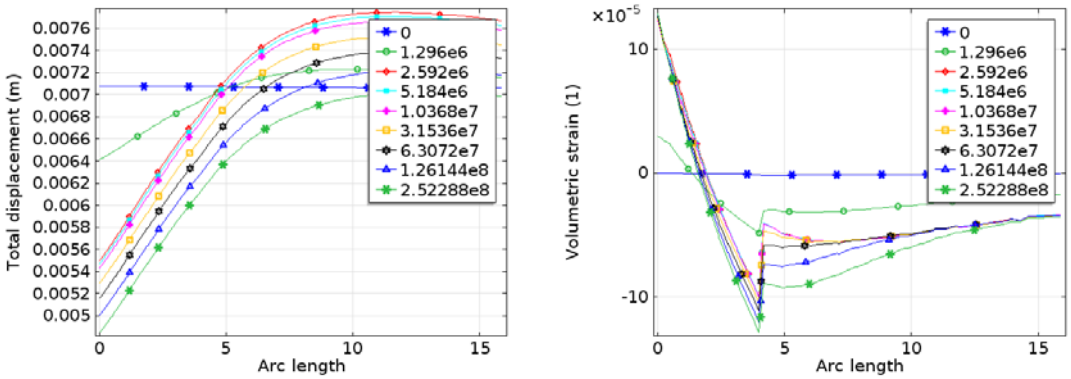

Fig. 1.25 Variation of displacement and volumetric strain along the downward cut line L1 at times of 0, 15, 30, 60, 120 days and 1, 2, 4 and 8 years – Tension is positive

4.2.2.2 HM evolution along cut line L2

It is shown in Fig. 1.26 that the factor of safety (FS) for the Blue Mountain shale formation is about 1.15 at the beginning of the simulation, indicating the weakest layer amongst the different formations. With elapsed time the FS reduces to the minimum immediately at the end of excavation (30 days) and then stabilizes without obvious change afterwards. The oscillation in pore pressure and mean stress is likely caused by the size of mesh and gridding. Further refinement of the size of mesh may help eliminate this phenomenon.

Fig 27 shows the redistribution of pore pressure that is mainly governed by drainage towards the shaft. Fig 28 shows the re-distribution of the horizontal and vertical stress due to excavation of the shaft, while Figs 29 and 30 show the evolution of mean stress, displacement and volumetric strain.

Factor of safety

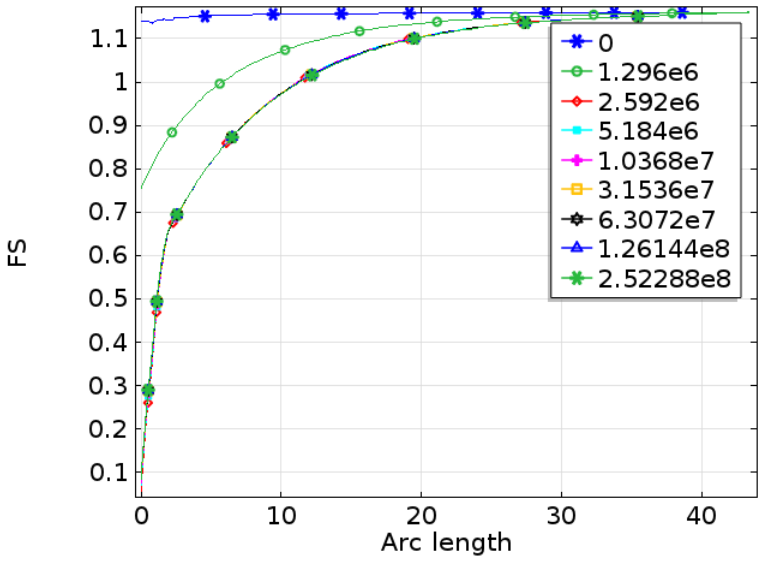

Fig. 1.26 Variation of FS along the rightward cut line L2

Pore pressure

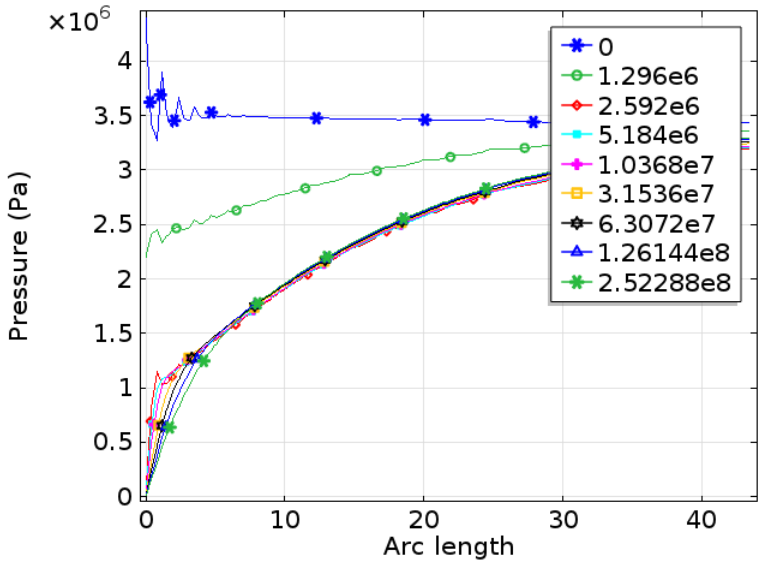

Fig. 1.27 Variation of pore pressure along the rightward cut line L2

Directional stress

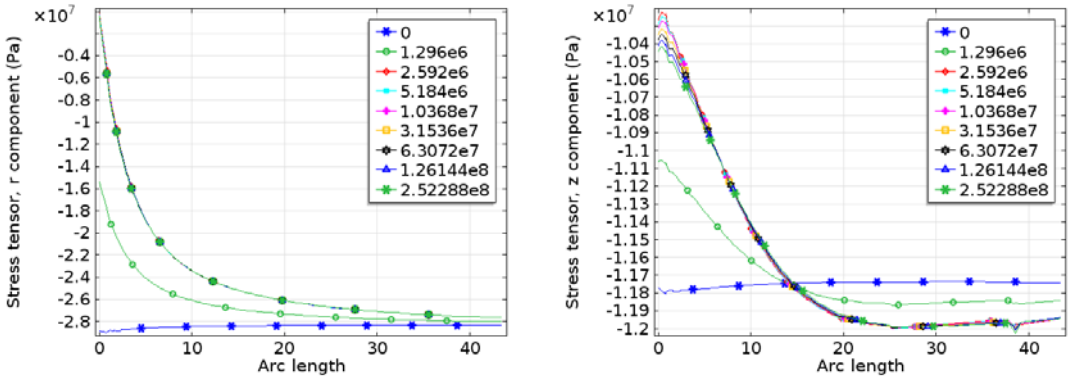

Fig. 1.28 Variation of the radial and vertical stress along the rightward cut line L2 at times of 0, 15, 30, 60, 120 days and 1, 2, 4 and 8 years – Tension is positive

Mean stress

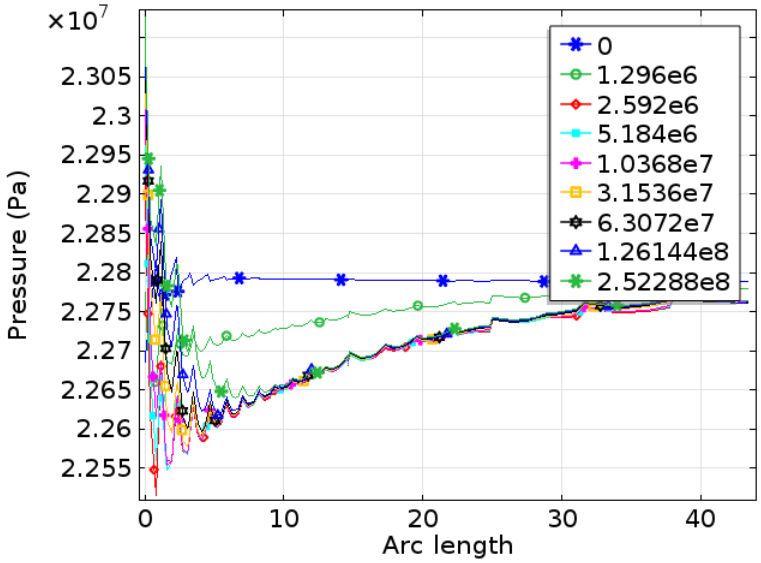

Fig. 1.29 Variation of the mean stress along the rightward cut line L2

Displacement and volumetric strain

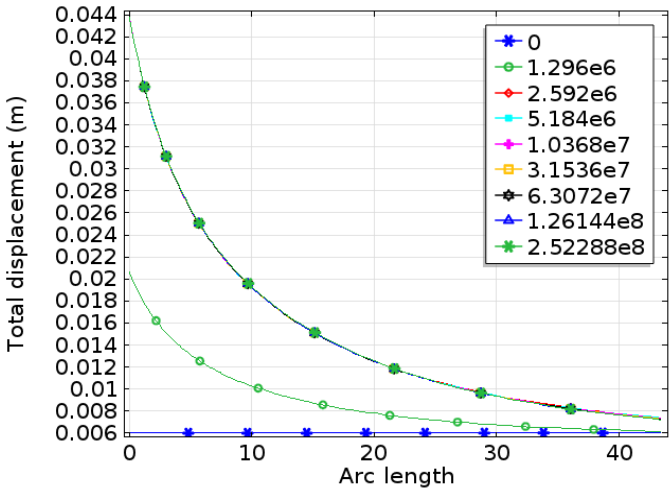

Fig. 1.30 Variation of displacement and the volumetric strain along the rightward cut line L2

5. Large scale scale long-term evolution scenarios

5.1 Large scale repository model

In this simulation case, the shallow geological formations are included in the FEM analysis zones. Fig. 1.31 shows the plan view of the designed repository rooms, monolith, and the vertical shafts. The repository is located in Cobourg formation at 680 m underneath the ground surface. There are two panels of emplacement rooms, 8.6m wide and 7 m high, with total volume at 420,000 m^3. The emplacement rooms are separated by 17.2 m wide pillars to support roof loading. There are two shafts, one is the main shaft (r=6.5 m) and the other acts as ventilation (r=5.0 m). Access tunnels with various lengths are also included in the design.

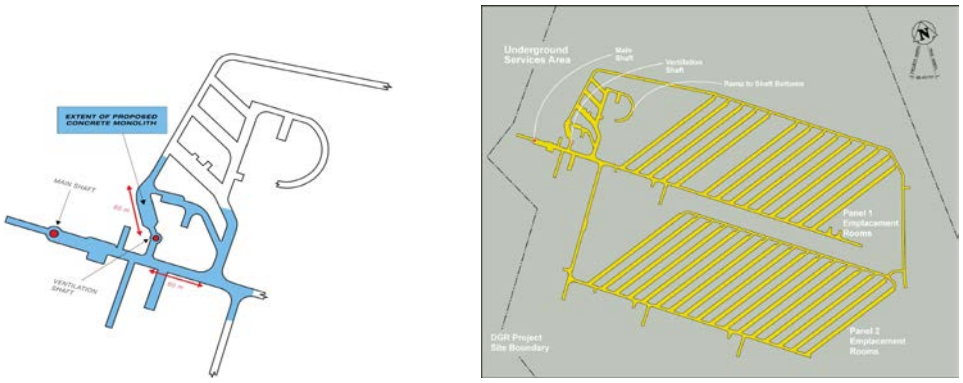

Fig. 1.31 The design sketch for the extent of the proposed monolith (left) and base case layout showing the access tunnel length measured at 250 m from the main shaft (OPG letter, 2012)

5.1.1 Conceptual model

Fig. 1.32 shows the conceptual model for the field conditions. The vertical shafts are simplified into a single shaft with equivalent radius at 5.9 m, and acts as the axis of the axisymmetric model. The access tunnel is omitted here to conceptualize the most important feature of the repository. The length and volume of the repository are calculated to reflect the total equivalence of the designed volume. The damage zone around the repository rooms is shown to be approximately 2 times the room height in the previous simulation case. For the long term analysis, we assume that the damaged zone would fall into the rooms in the form of rock debris that would swell and fill the rooms. The total volume of the enlarged rooms filled with debris is then assumed to be two times of the volume of the original rooms.

The initial conditions include both the mechanical and hydrogeological conditions. The initial pore pressure of the rock mass follows the distribution shown in Fig. 1.5. As for the shaft and repository, the initial pore pressure is assumed to be at atmospheric pressure. In order to avoid the potential difficulty in numerical computations for the weak sediments near the ground surface, the upper boundary of our analysis domain is confined at z=100 m depth.

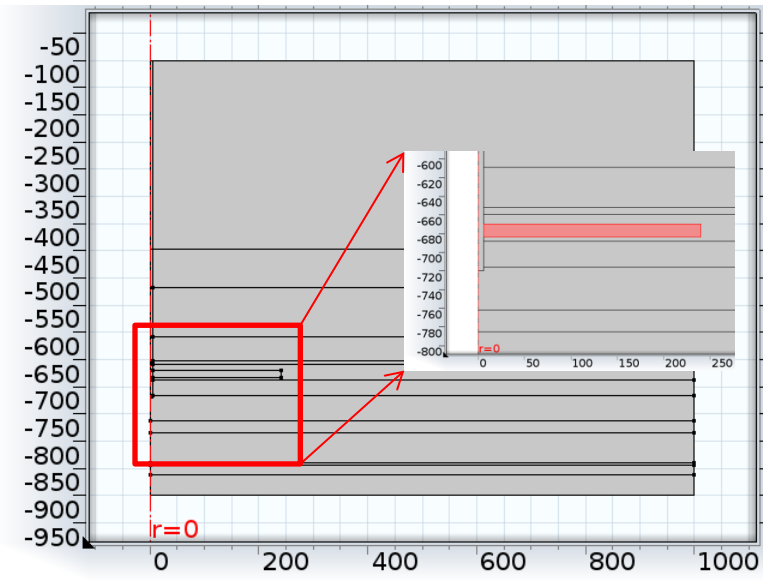

Fig. 1.32 Conceptual model of the large scale HM analysis case

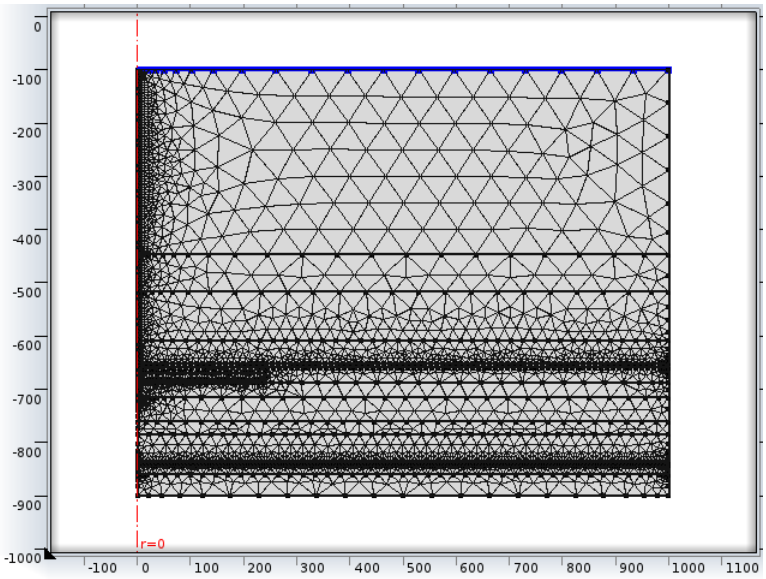

Fig. 1.33 Meshing of the FEM domains

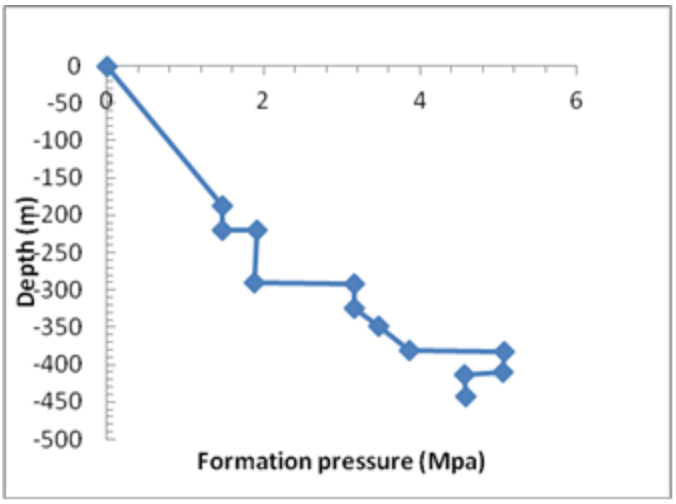

Fig. 1.34 Formation pressure in shallow sedimentary rocks

5.1.2 Properties of the shallow formations

Shallow formations above the Queenston formation include several aquifers and interlayered stiff and soft rocks. The fundamental properties of these rock masses are obtained from the DGSM report and shown in Table 1.2. The porosity and permeability profiles are plotted in Fig. 1.35.

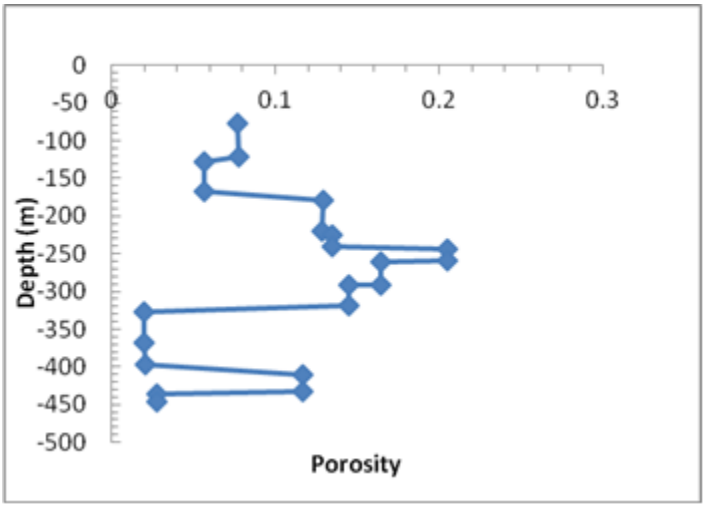

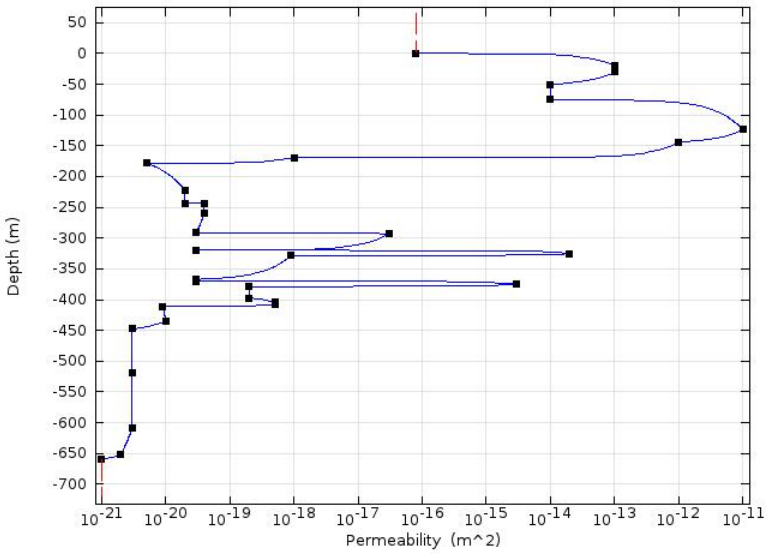

Fig. 1.35 Porosity profile (upper) and permeability profile (bottom) with depth for shallow sedimentary rocks

Table 1.2 Properties of shallow formations above the Queenston formation

Top depth (m)	Formation	E	v	σ_{1c}	α	C_e
		Gpa		Mpa	$1-K_D/K_S$	
20	Lucas	-	-	-	-	-
30.4	Amherstburg	43	0.21	98	0.14	2.80E-12
75	Bois Blanc	37	0.18	94	0.26	5.20E-12
124	Bass Islands	19	0.23	43	0.62	1.24E-11
178.6	Salina F	12	0.21	31	0.76	1.52E-11
244.6	Slina C	9	0.17	20	0.82	1.64E-11
260.3	Slina B	3	0.4	8	0.94	1.88E-11
293.1	Salina A2	19	0.11	48	0.62	1.24E-11
325.5	Salina A1	41	0.23	143.1	0.18	3.60E-12
370.5	Salina A0	63	0.43	197.6	0	0
374.5	Guelph	28	0.32	60	0.44	8.80E-12
378.6	Goat Island	37	0.37	148	0.26	5.20E-12
411	Cabot Head	4	0.38	13	0.92	1.84E-11
434.8	Manitoulin	23	0.24	66	0.54	1.08E-11
-	Shaft	Varies with depth	0.34	10	0	0
Reference	Table 3.1 in DGSM	Table 3.14 in Geosynthesis				

5.1.3 Equivalent repository material

The repository rooms are spaced from each other and separated with pillars. In this 2D-axisymmetric model, the repository is treated as an equivalent homogeneous domain with equivalent properties. For example, the equivalent elastic modulus is calculated by force balance equation that considers the relative cross section area of the rooms and pillars,

$$E_{eq} = \frac{2}{3}E_0$$

$$\sigma_{1C\_eq} = \frac{2}{3}\sigma_{1C}$$

The permeability of the repository is assumed to be very high, with a value of 1.7e-10 m^2.

5.1.4 Shaft material

Elasticity of porous medium depends on porosity, confining pressure and volumetric compressivity. The constrained elastic modulus (E_k) of solid skeleton of a porous medium is reported to have the following relationship with compression coefficient C_c (Jorgensen, 1980):

$$E_k = \frac{(1+e_0)\sigma_c}{0.434C_c}$$

where e_0 is the initial pore ratio and σ_c is the confining pressure.

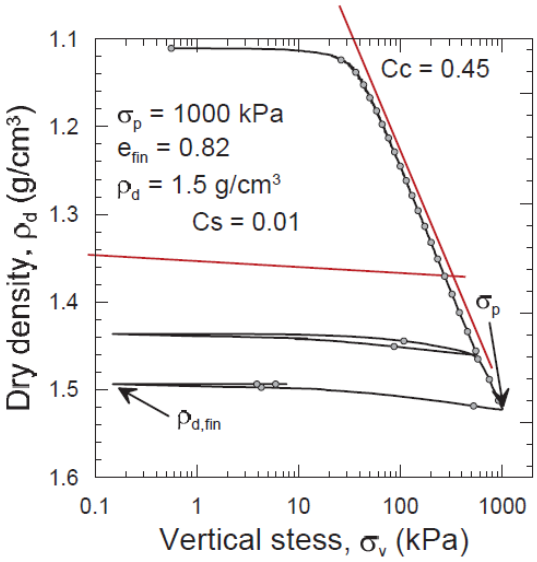

Fig. 1.36 Evolution of the specimen dry density with the applied vertical stress during the specimen compaction (FORGE report 2013, quartz sand and MX-80 Bentonite mixed at 80/20 in mass ratio, dry density at 1.5 g/cm^3)

Rueedi et al. (2013) reported a series of experimental studies on sand-bentonite mixture. Fig. 1.36 shows the compression curve as appeared in the FORGE project final report. The compression

coefficient C_c is estimated at 0.45 for 80/20 sand-bentonite mixture at 1.5 g/cm^3. Blatz et al. (2003) reported the modulus of a different sand-bentonite mixture at 50/50 ratio as 0.14 (wetter) and 0.09 (drier) with dry density at 1.7 g/cm3 and saturation of about 85% (the matric suction ranges from 3.7-4.5 MPa).

Using the above shown equation for elastic modulus, E_k can be obtained for the results of Rueedi (2013) and Blatz (2003) respectively as 9.3 MPa and 102 MPa. Putting the estimated E_k for Blatz (2003) in the following graph gives a good agreement with the experimental results of Tang (1999).

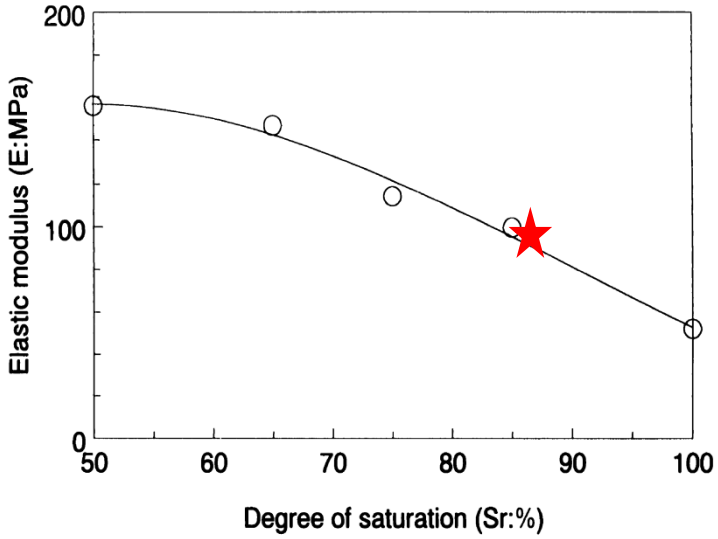

Fig. 1.37 Elastic modulus vs saturation as reported by Tang (1999) (ρ_d=1.75 g/cm3, Sr=85%, mass ratio at 50/50. Star shows the estimated Ek based on the result of Blatz (2003).)

As a convenient treatment, the elastic modulus of buffer material is hypothesised to vary linearly with depth with a scaling parameter *R*:

$$E = (1 + Rz)E_k$$

where E_k is the laboratory result of sand-bentonite mixture on elasticity, z is depth (m). In this study it is taken as R=0.0125. At 700 m depth the elasticity of the buffer material is assumed to be 0.975 GPa, which is still much softer than the surrounding rock (E>5 GPa).

5.1.5 Glacial stress loading

During the last million years, it is estimated that the Northern Hemisphere was subjected to 9 glacial cycles, each one lasting approximately 120,000 years. It is estimated that in another 60,000 years another glacial cycle similar to past ones will occur. Fig. 1.38 shows the calculated vertical stress resulting from the glacial impact that is used for dry case where at the base of the glacier, free draining conditions are assumed, and the water is assumed to be at atmospheric pressure. In the wet case situation, the phreatic table is assumed to be at the top surface of the glacier; therefore, no mechanical load is transmitted to the rock formations, however the glacier will impose a hydraulic pressure,

equivalent to the weight of the glacier, which would increase the stresses and also induce water infiltration into the formations. The dry case is studied and discussed in detail in the following sections. The wet case, although likely to happen in certain circumstances, is not included in the current study.

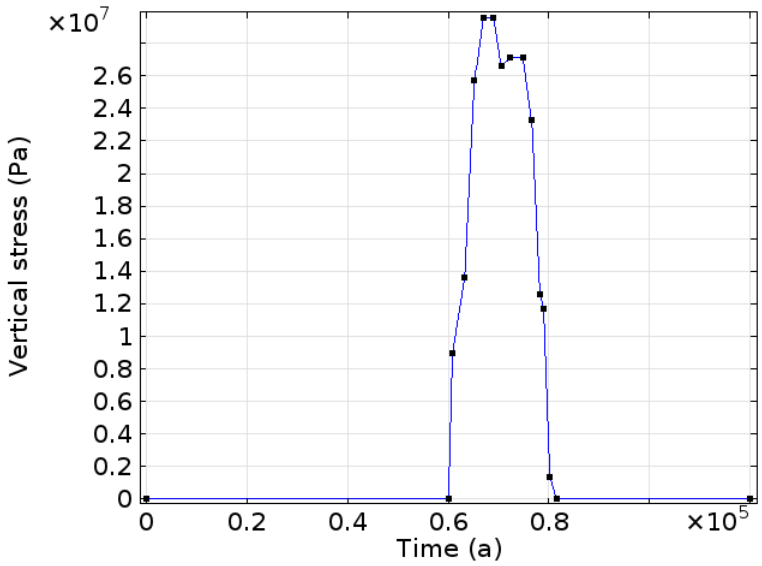

Fig. 1.38 Simulated evolution of ice sheet load during single glacial event as assumed in the longterm scoping analysis

5.1.6 Gas pressure in the rooms

The repository rooms would become gradually filled with waste gases produced by corrosion and biological activities in the long run. Fig. 1.39 shows the evolution of room gas pressure with increasing elapsed time in the postclosure period up to 1Ma. These data are from the gas modeling results of NWMO report (AECOM, 2011) and were further adopted in the long-term geomechanical stability analysis of DGR as conducted by Itasca Consulting Group Inc. It contains both an extreme scenario and a base scenario that represent different probability of potential risk posed on the room safety. This study considers both cases in the numerical simulation, however, in this report only the results corresponding to the extreme scenario are shown in the following section.

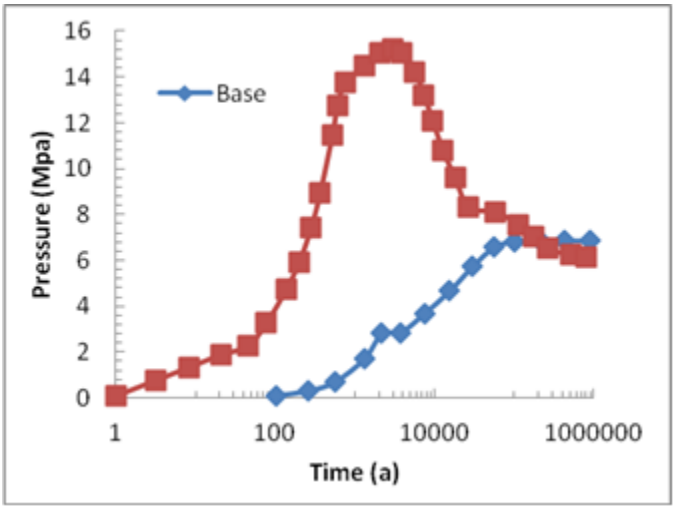

Fig. 1.39 Pressure inside the room vs postclosure time

5.1.7 Monitoring points and cut lines for data postprocessing

Figures 1.40-1.41 show the selected points and cut lines for results visualization and analysis. They are all located in regions of interest for the stability and pore pressure change when exposed to glacial stress loading. Fig. 1.42 shows the sampling time for contour plotting of key variables like *p*, mean stress and factor of safety.

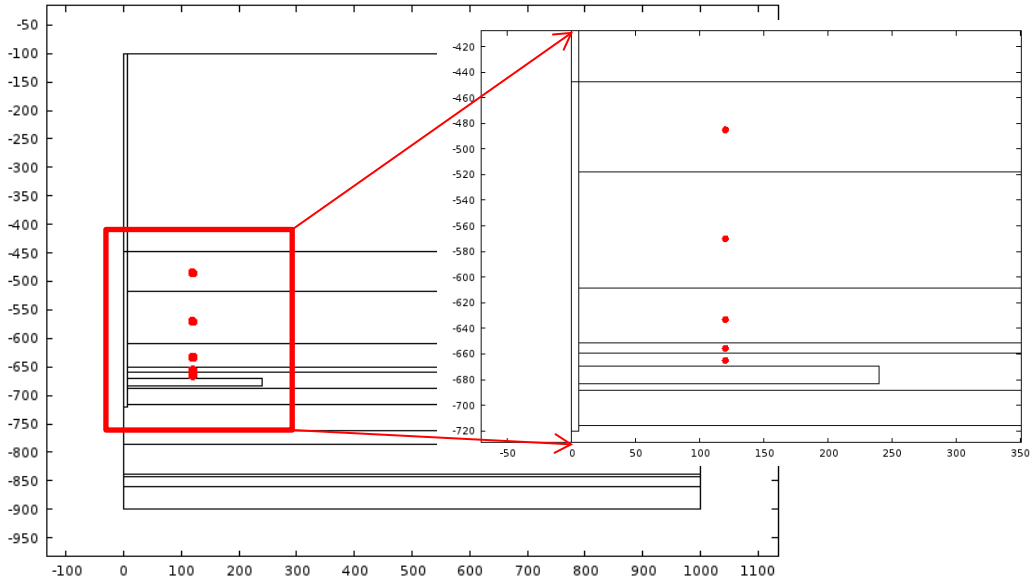

Fig. 1.40 Monitoring points (P1-P5) along the vertical center line above the tunnel

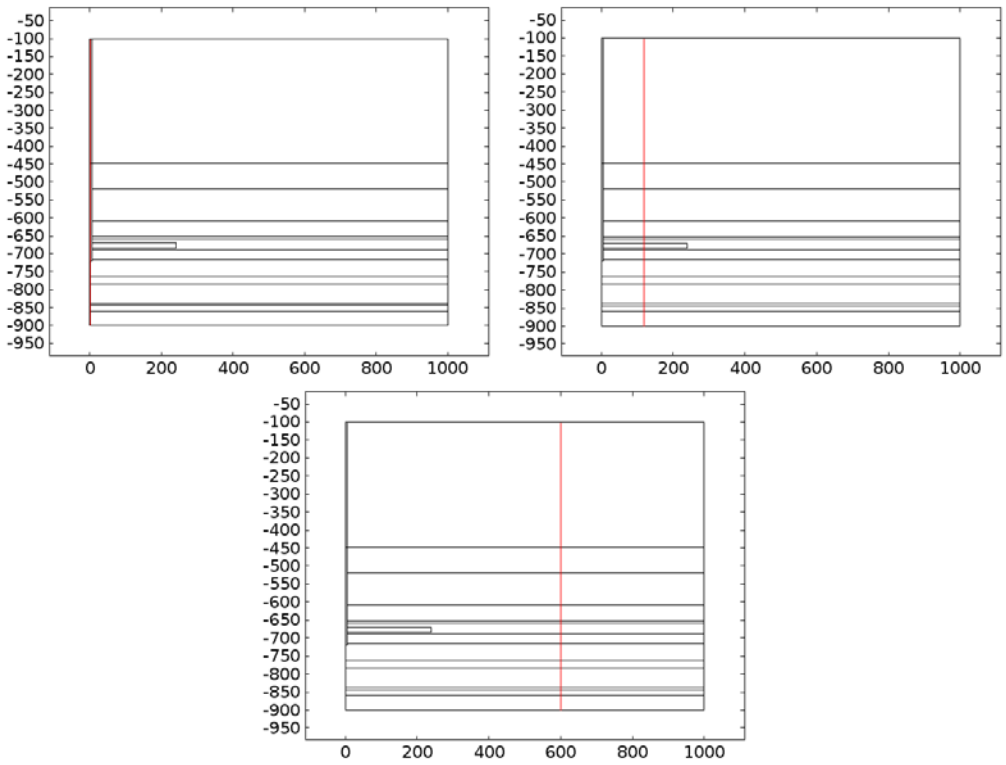

Fig. 1.41 Cut lines in shaft and across tunnel for data visualization with time (a, L1; b, L2; c, L3)

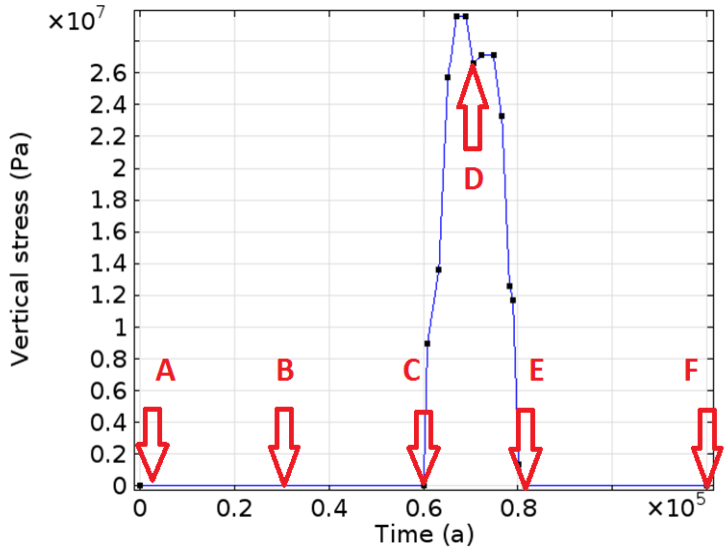

Fig. 1.42 Sampling time for the plotting of contours

5.1.8 Key Simulation Parameters

Table 1.3 shows the simulation case—dry-extreme—undertaken in the long term HM assessment. Critical parameters e.g. shaft permeability and upper boundary loading type are also given in this table. Since the permeability of the shaft material may significantly influence the pore pressure evolution in the shaft and surrounding regions, a conservatively high permeability is used to investigate the long term impact. The design permeability of the engineered barrier material in shaft is 1E-19 m^2. For the dry case, we assumed that the permeability increases by a factor of 10.

Table 1.3 Simulation cases and the key parameters used in the analysis

Case type	Dry
Room pressure type	Extreme
Room permeability (m^2)	1.7E-10
Shaft permeability (m^2)	1.2E-18
Upper boundary loading	Stress

1.1.9 Tracer chemical migration

In order to verify how the glacial cycle affects the groundwater flow in regions near the repository and the underlying highly permeable Cambrian formation, we simulate the movement of a conservative tracer originating from the repository and the Cambrian formation, by solving the transport equation:

$$\frac{\partial C}{\partial t} = D_e \nabla^2 C + v\left(\frac{\partial C}{\partial x} + \frac{\partial C}{\partial y}\right)$$

where C is the tracer concentration, D_e is the effective diffusion coefficient, and v is the groundwater velocity. The diffusion coefficient D_e is taken as 1E-11 m^2/s, which is at a medium level of the reported value in multiple formation layers (Quintessa, 2011). The groundwater velocity *v* is calculated from Darcy's flow module.

The boundary conditions are shown in the following graph Fig. 1.43. Chemical concentration C=1.0 is assigned onto the tunnel outer boundary and the upper boundary of the underlying Cambrian formation. The tracers seeded in the repository will help assess the potential impact of gas pressure and glaciation on the hydraulic regime in the vicinity of the repository. The tracer seeded in the Cambrian will help assess the magnitude of upward flow induced by the overpressure in that formation. Initial concentration C=0 is assumed for the whole analysis domain while C=1.0 for the repository tunnel.

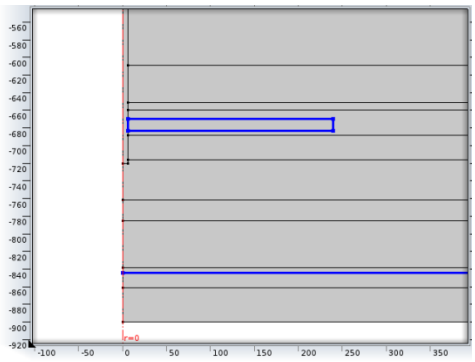

Fig. 1.43 Boundary conditions for tracer migration simulation

1.2 Results and discussion

The calculated FS indicates that the whole domain is mechanically stable throughout the 120,000 years of simulation period. The mechanical stress seems to be responsive to both tunnel pressure and overburden loading. The tunnel pressure reaches peak within 10,000 years, causing perturbations to the regions around the vertical shaft which is more permeable than other rocks. The distribution of pore pressure changes in pattern with elapsed time. The shaft acts as a permeable interlayer connection that facilitates the flow of pore water in regions near the shaft between 400 to 650 m in depth. Glacial loading induces extra pore pressure uprising especially for the thick layers between 40 and 750 m in depth. This perturbation rapidly disappears once the vertical glacial loading is removed.

Factor of safety

At Z=630 m, FS turns to be near 1.0 for most of the postclosure period. This domain represents the Blue Mountain formation, which is a weak shale layer and has been found to be damaged due to excavation in the shaft simulation case. This stage of damage corresponds to the peak in tunnel pressure as shown in Fig. 1.48(B). Therefore the damage is thought to be caused by the overpressure of the waste gases in the repository tunnel. Other parameters appear to be normal with respect to the overburden glacial stress. For the whole analysis domain, FS turns to be increased by the glacial loading. This phenomenon will be discussed in detail by the stress patch approach in the following section.

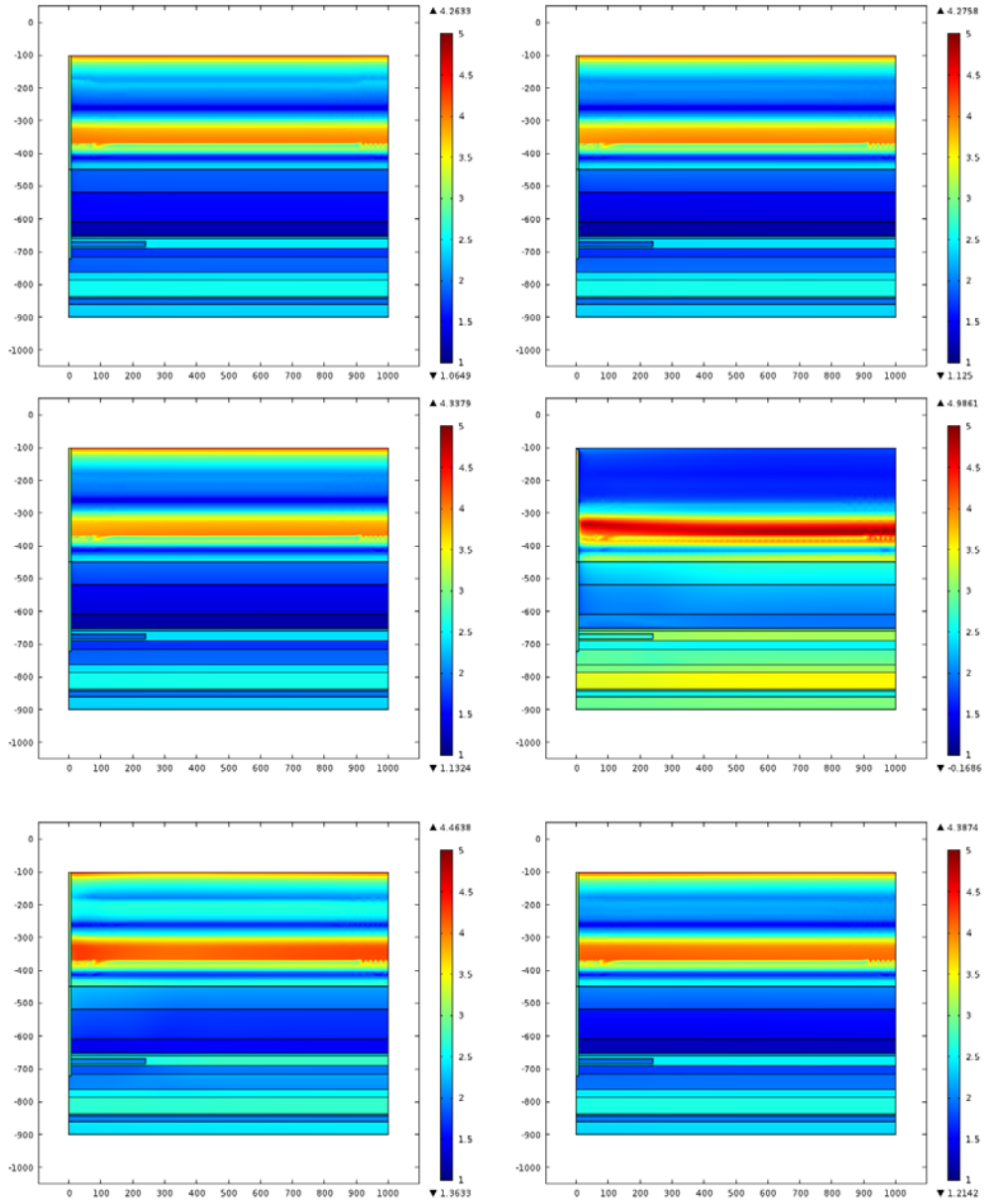

Fig. 1.44 Spatial distribution of the factor of safety at different postclosure time corresponding to sampling points A-F

Pore pressure

The pore pressure evolution is shown in Fig. 1.45. The tunnel pressure follows the assigned boundary condition. In Fig. 1.45b-1.45c, regions near the vertical shaft in Queenston and Gorgian Bay seem to have smaller pore pressure than the normal level of the formation pressure. This phenomenon results from the higher permeability of the shaft that contributes to the pore pressure dissipation in these two formations with limited influence from the repository tunnel. Corresponding to the peak of glacial loading in Fig. 1.45d, the pore pressure increases within formations between Queenston and Sherman Fall with a maximum pressure of 26 MPa. At the end of glacial loading, the pressure in this region

sharply decreases to levels lower than the ones prior to glacial loading (Fig. 1.45e) due to the HM coupling effect, and gradually regains the equilibrium state (Fig. 1.45f).

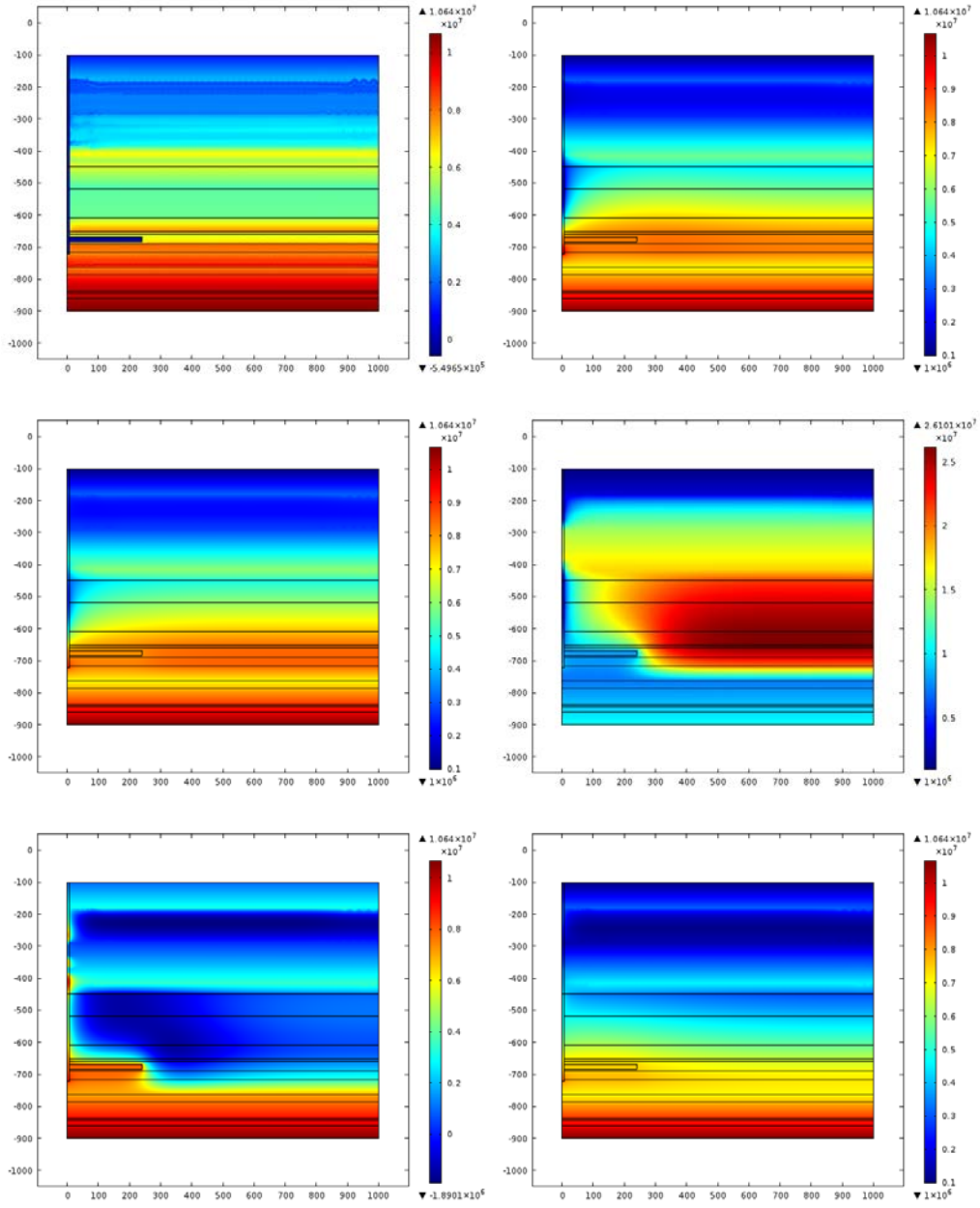

Fig. 1.45 Spatial distribution of the pore pressure at different postclosure time corresponding to sampling points A-F

Maximum principal stress

The maximum principal stress (Fig. 1.46) is increased by the glacial loading for the host rock near the repository. The minimum principal stress (Fig. 1.47) increased due to the glacial loading at time D, and then decreased by the unloading at time E in the repository and its surrounding regions. There is no stress localization throughout the whole analysis domain.

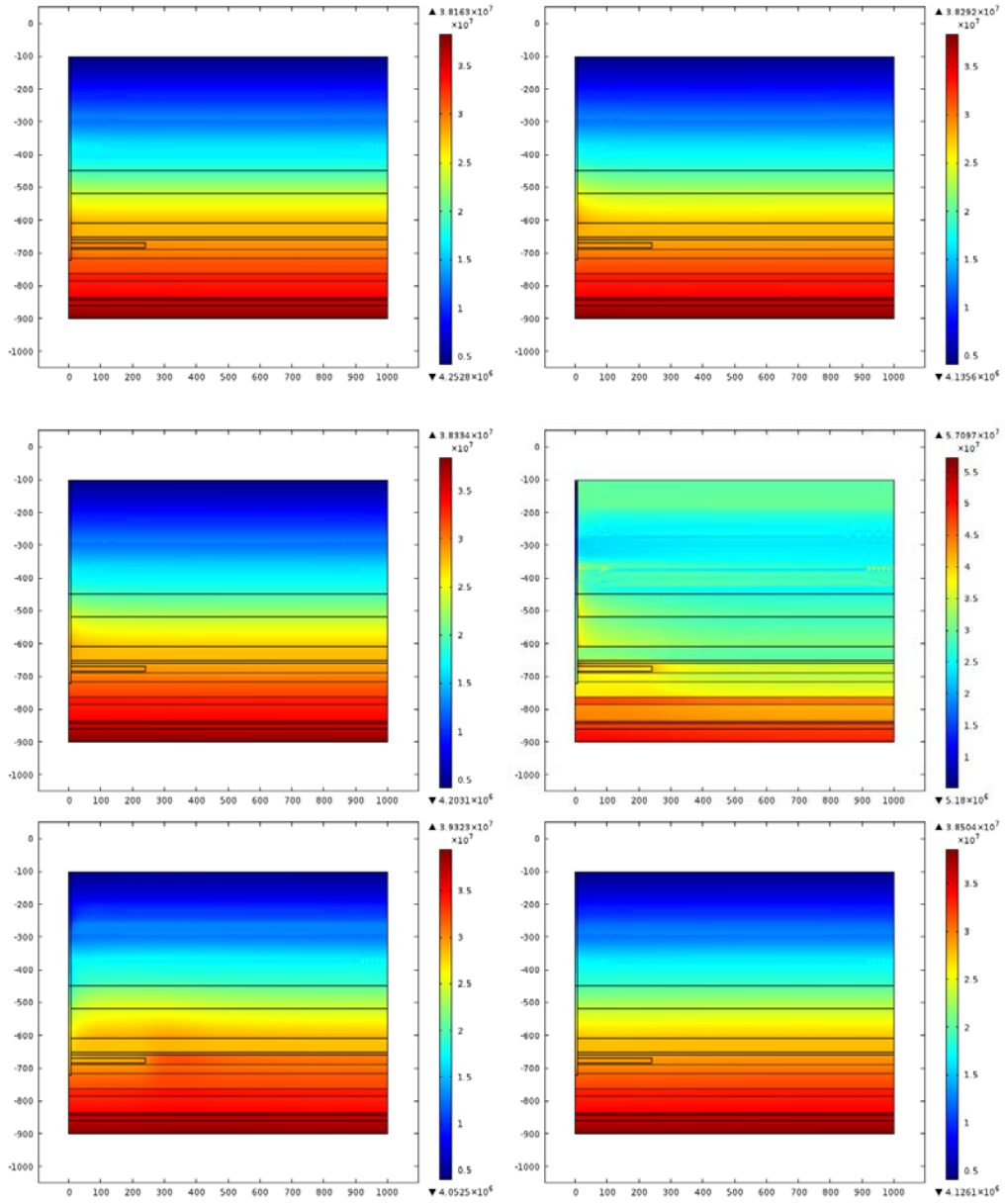

Fig. 1.46 Contour plotting of principal stress Sig1 at different postclosure time corresponding to sampling points A-F

Minimum principal stress

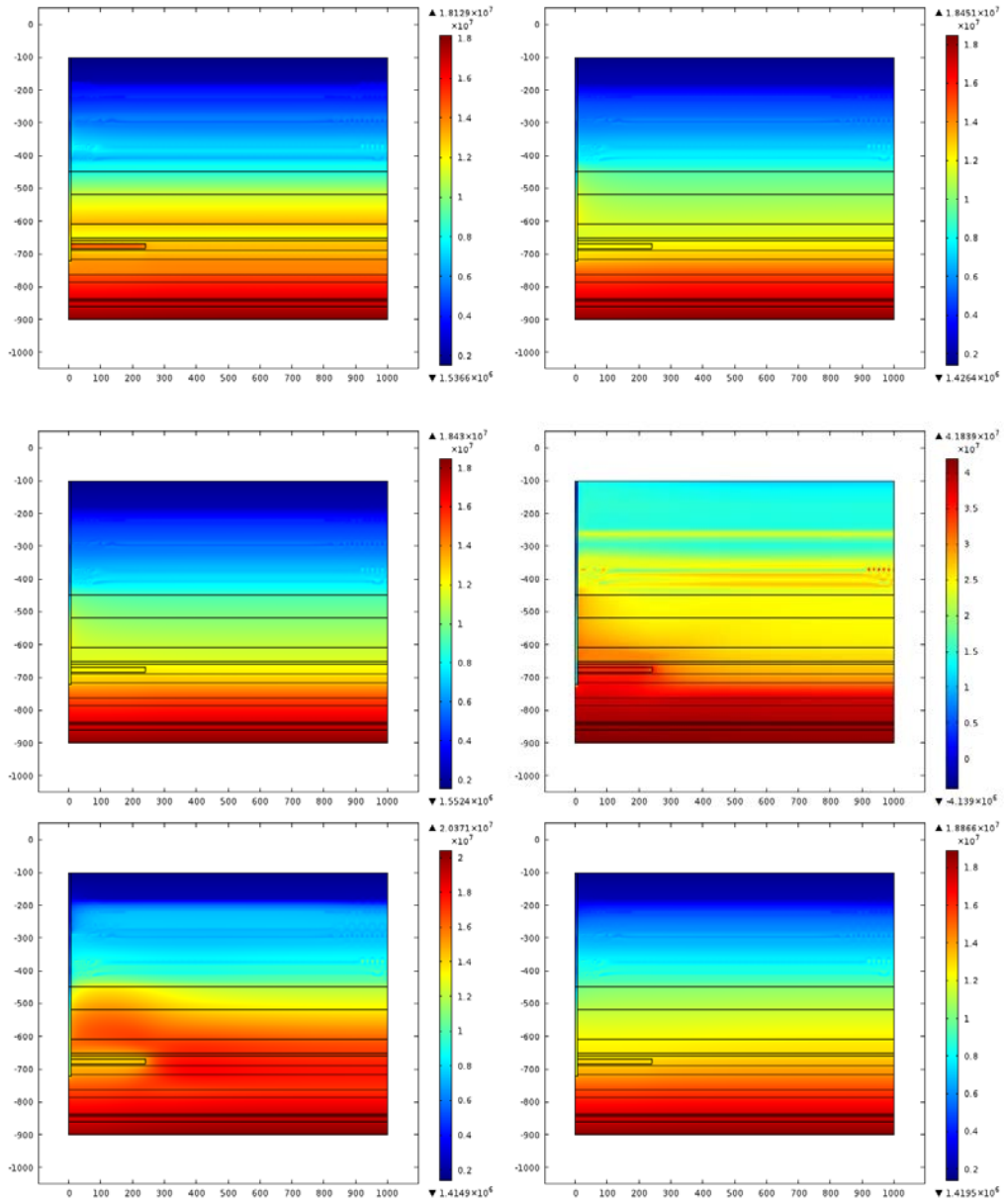

Fig. 1.47 Contour plotting of principal stress Sig3 at different postclosure time corresponding to sampling points A-F

Results on cut points P1-P5

Figs. 48 show the time-dependent results of FS, pore pressure and principal stresses on interested monitoring points P1-P5. It is clearly demonstrated that the FS increases by 60-70 % during the glacial

loading period, during which time the pore pressure also increases. For the peak of pore pressure as observed before t=10 ka, it is believed to be the result of gas pressure accumulation inside the repository tunnel. The principal stresses show more vertical stress growth compared to the horizontal stress variation as caused by the overlying glacial loading.

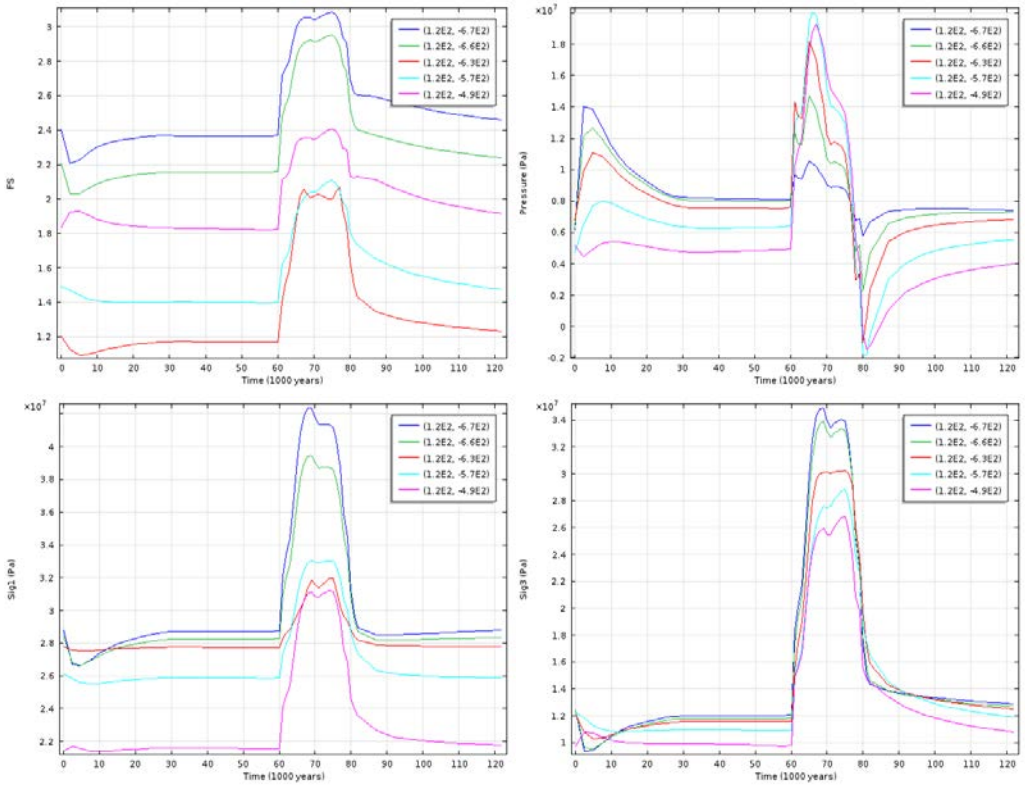

Fig. 1.48 Variation of parameters at cut points with elapsed time in postclosure period

Stress path of cut points P1-P5

Figs. 1.49(a-f) show the stress path of five monitoring points P1-P5 above the repository tunnel and located in the middle depth of relevant geological formations. The formation-specific Hoek-Brown strength envelopes are also plotted in the graph in order for the understanding of the variation of Factor of Safety in the postclosure period. Data are selected corresponding to the interested critical time point A-F, whereas at time D the glacial loading reaches the peak level. The initial geological stress is 2 times of overburden weight in the horizontal direction. The vertical loading due to glacial cycles contributes to the vertical stress, which is actually the minimum principal stress (σ_3). Therefore the stress path of monitoring points P1-P5 all moves to the right hand side and away from the HB strength envelope. Hence the calculated factor of safety FS turns to increase by glacial loading as shown in Fig. 1.48.

Fig. 1.49d shows the results of monitoring point located in Blue Mountain formation. The Hoek-Brown strength envelope is the closest the in-situ stress level amongst all the monitoring points. It is because this formation has the least strength compared to other formations. Previous simulation on vertical shaft as shown in Fig. 1.17 confirms that Blue Mountain has the most excavation damage zone.

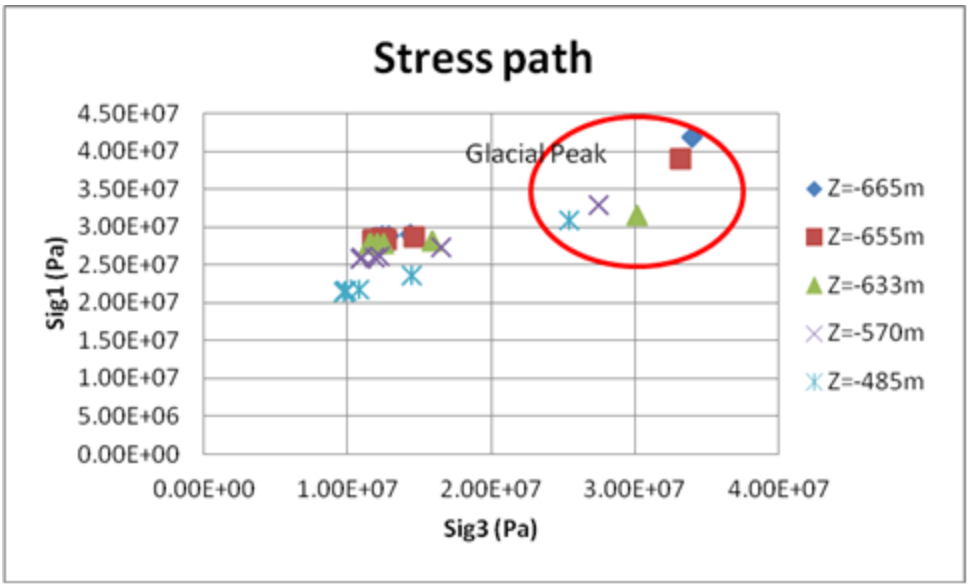

(a) Overall variation of principal stresses at postclosure time A-F for monitoring points P1-P5

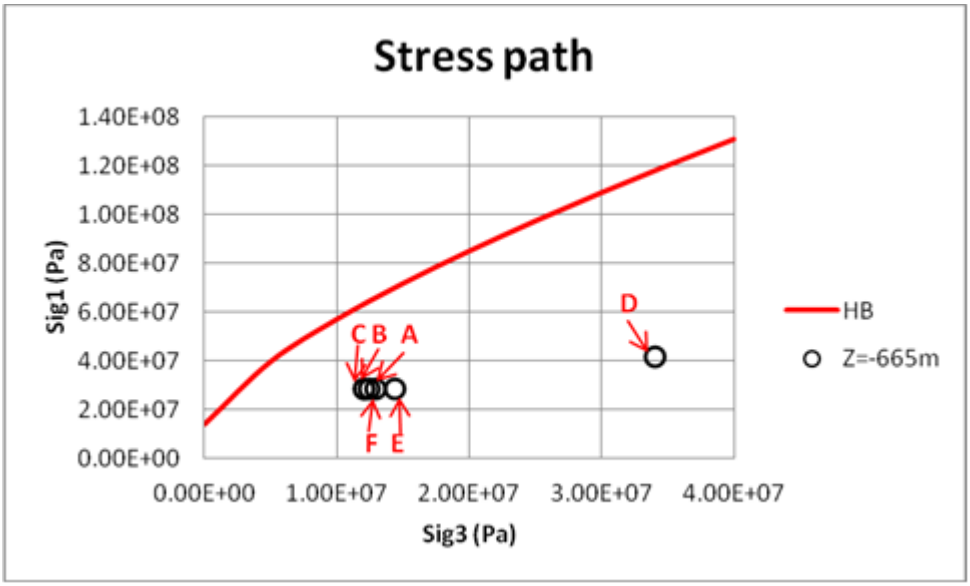

(b) Variation of principal stresses at postclosure time A-F for monitoring points P1

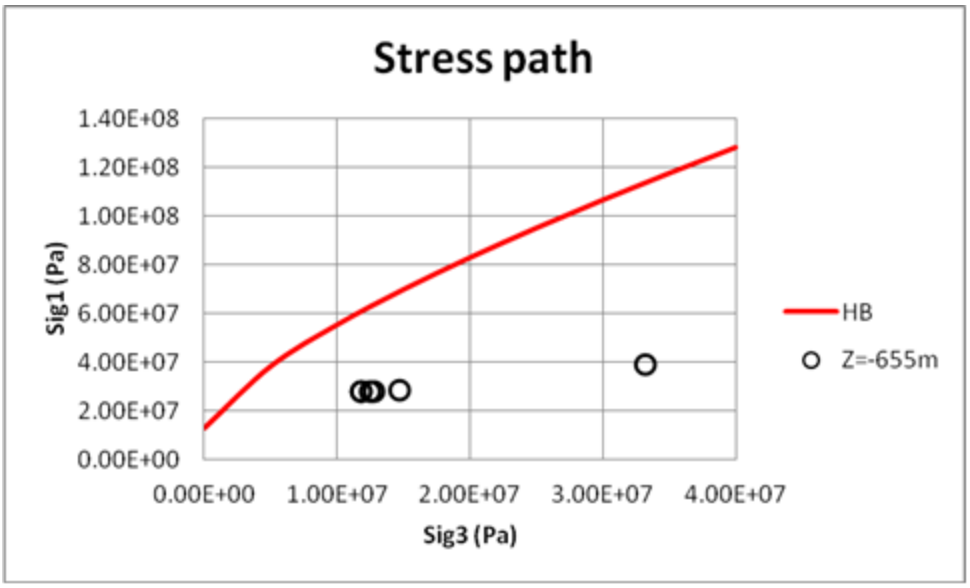

(c) Variation of principal stresses at postclosure time A-F for monitoring points P2

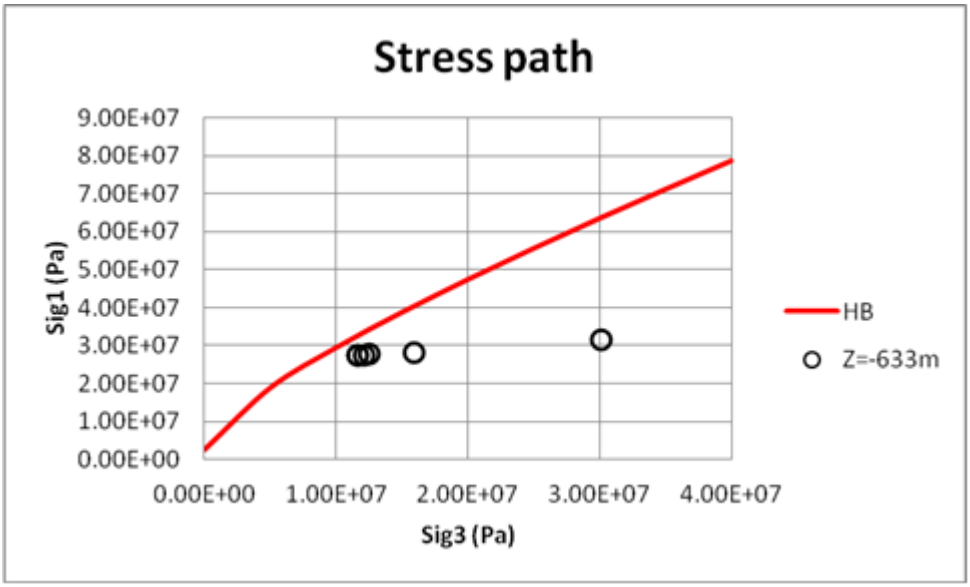

(d) Variation of principal stresses at postclosure time A-F for monitoring points P3

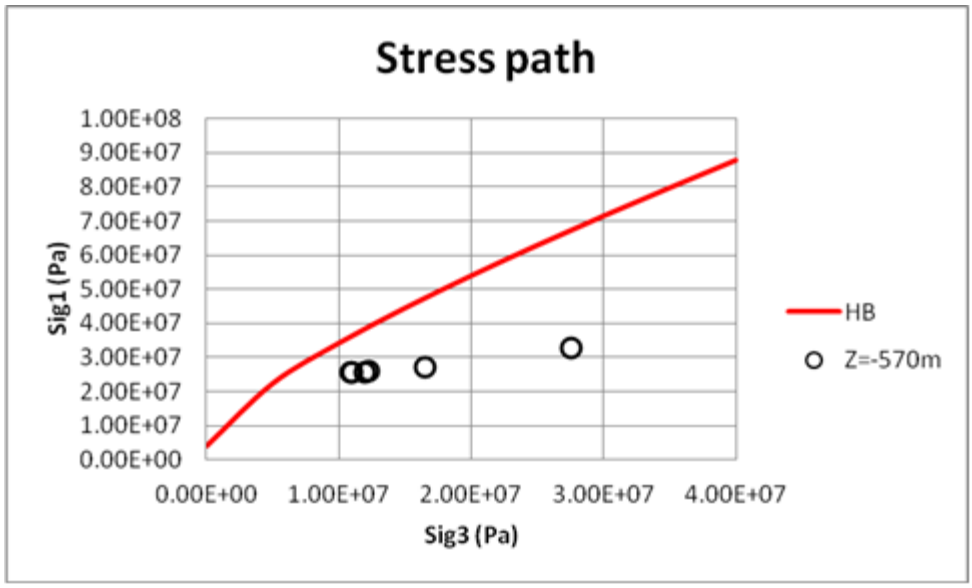

(e) Variation of principal stresses at postclosure time A-F for monitoring points P4

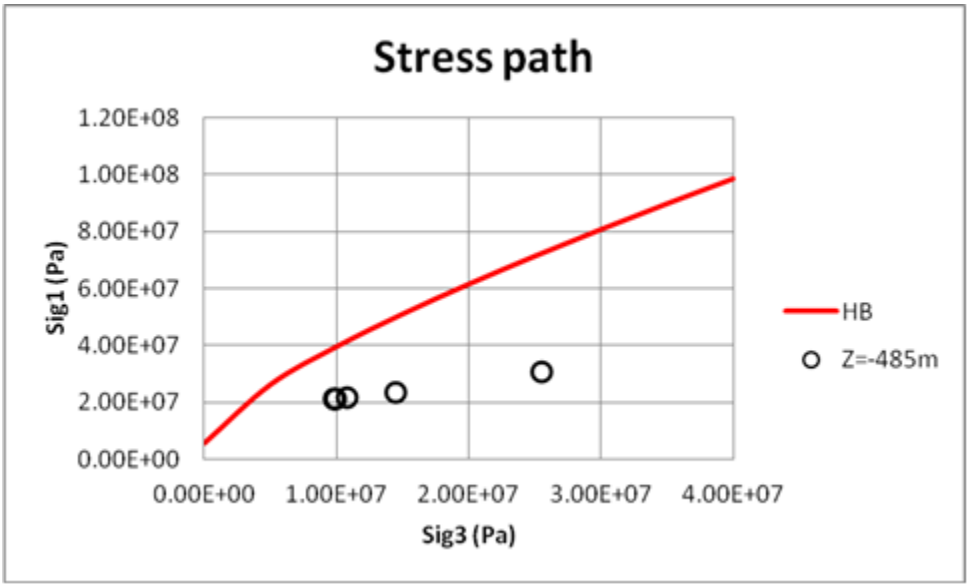

(f) Variation of principal stresses at postclosure time A-F for monitoring points P5

Fig. 1.49 Stress paths of monitoring points (P1-P5) at different locations above the center of the repository tunnel (Solid line indicates the relevant Hoek-Brown strength envelope)

Results on Cut lines L1-L3

Figs. 50-52 show the historical results of FS, pore pressure and principal stresses along the vertical cut lines L1-L3. The factor of safety FS in the shaft ($z<720$ m) is higher than 2.7 throughout the glacial cycle except for the vicinity of ground surface at peak of glacial loading (FS>1.6). In the context of the

assumed scenario for this simulation case, the bentonite-filled shaft seems to be stable and not likely to fail under the glacial loading/unloading cycles. Pore pressure p is found to rise from 0.0 to 1-5 MPa at z<600 m after 60 ka. At z>600m, the pressure in shaft is controlled by the tunnel boundary condition that is reliant on the gas production. At time D, the peak of glacier appears to enhance the pore pressure growth for the shaft, which is mainly restricted in zones at depth 200<z<450 m.

The shallow region (z<200 m) has comparatively high permeability than the rest, therefore displays better performance in pore pressure dissipation, and thus has no pressure accumulation as shown in Fig. 1.51(b). Deeper zones (z>700 m) underlying the repository tunnel are not obviously affected by glacier cycle due to the absence of hydraulic-mechanical coupling because these host rocks are extremely stiff, take on most of the overburden and thus outweigh the extra effective stress that may transmitted by the pressure of pore fluid.

The host rocks have FS>1.2 for most of the analysis domains as shown in Fig. 1.52(a). The zones with least FS are found to be the Blue Mountain formation at 608<z<651 m, which is in good agreement with the previous simulation case for the vertical shaft (as shown in Fig. 1.17). Pore pressure is concentrated at regions 200<z<750 m at the peak of glaciers. Subsequent unloading results in volumetric bounce that is accompanied with pore pressure decrease that even reaches a negative value.

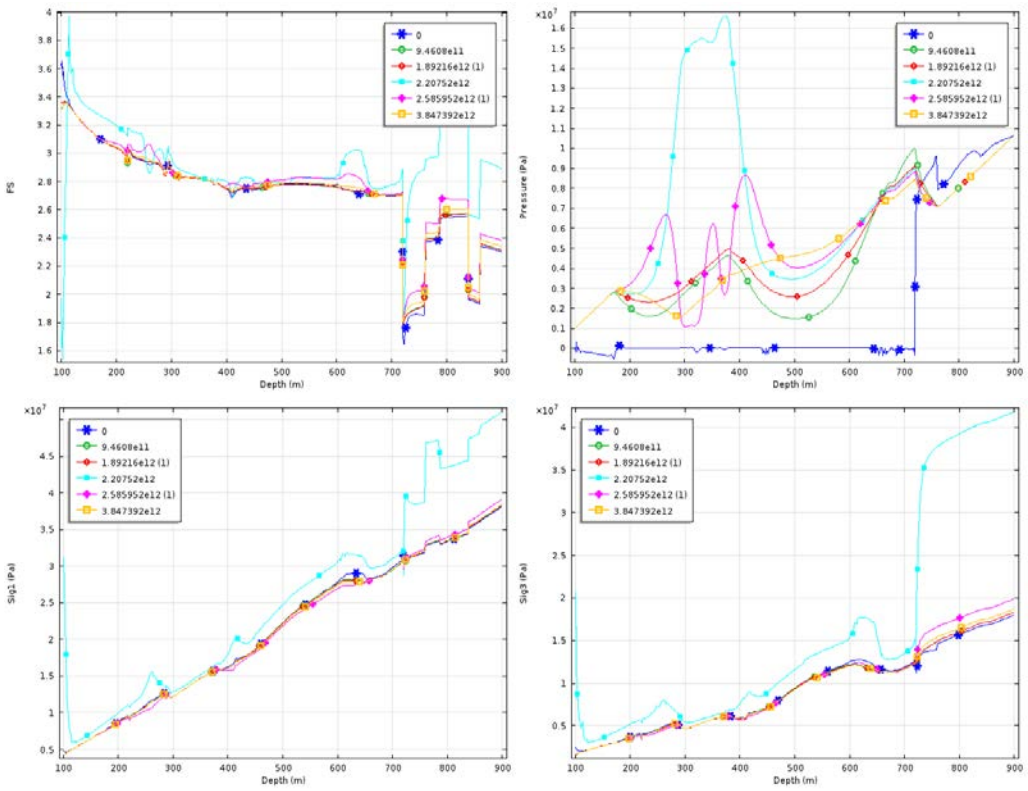

Fig. 1.50 Variation of parameters along cut line L1 with elapsed time in postclosure period

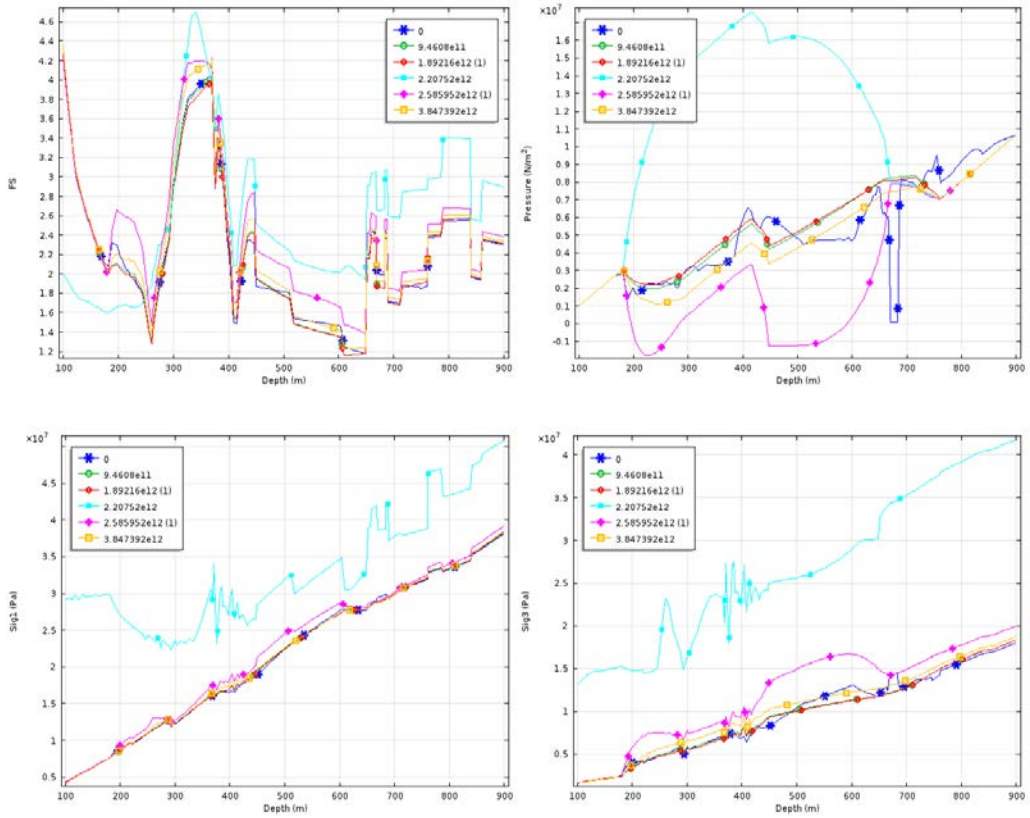

Fig. 1.51 Variation of parameters along cut line L2 with elapsed time in postclosure period

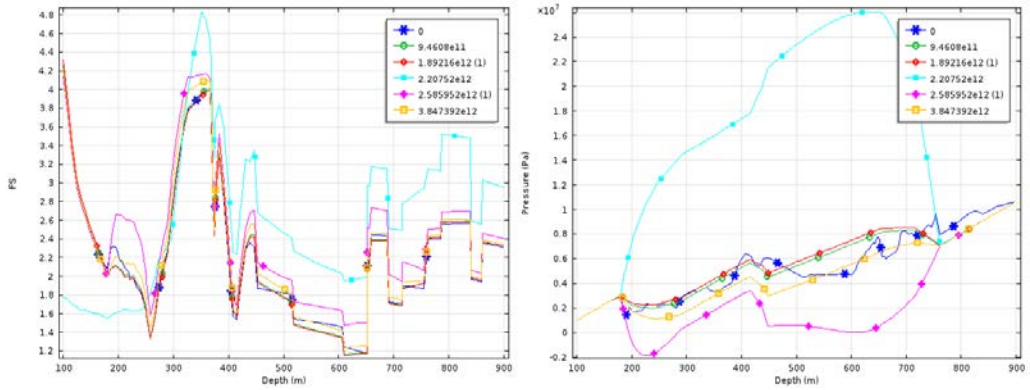

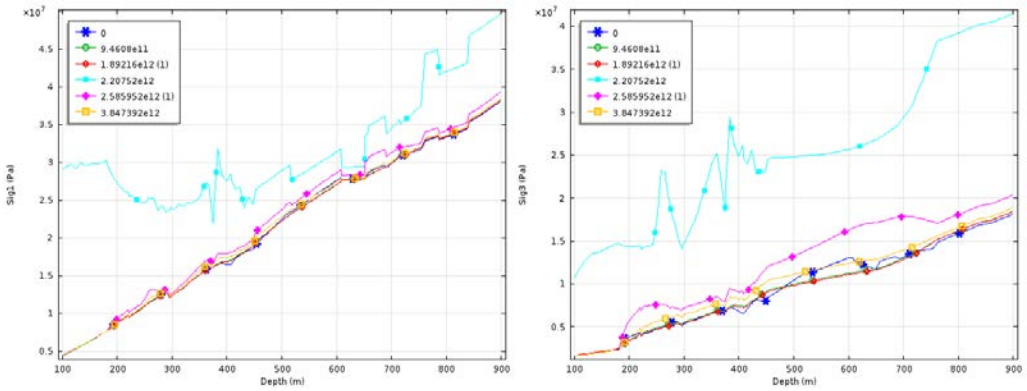

Fig. 1.52 Variation of parameters along cut line L3 with elapsed time in postclosure period

Distribution of trace chemical

Figs. 1.53-1.54 show the tracer concentration at different times. In host rocks, diffusion is shown to be the the dominant mechanism for solute transport. Even in case of significant stress disturbance from the glacial cycle, no obvious change is observed in the pattern of tracer distribution. For the vertical shaft, the tracer is found to move upward from the repository as far as to -600m underground. The deeper permeable formation, Cambrian, appears to be stable throughout the whole glacial cycle in terms of tracer movement. Fig. 1.51 shows the contour of tracer concentrations at C<0.01M. The tracer moves to the furthest depth at -560m via the shaft. In host rocks, the tracer extends homogeneously from z=-730 to z=-630m after 120,000 a. Due to the very low permeability of the host and cap rocks, the glacial loading and unloading cycle seems to have negligible impact on the groundwater flow and tracer migration in the vicinity of repository. Furthermore, the overpressure that currently exists around the Cambrian formation does not induce any substantial groundwater flow towards the repository, during the 120,000 years simulation period.

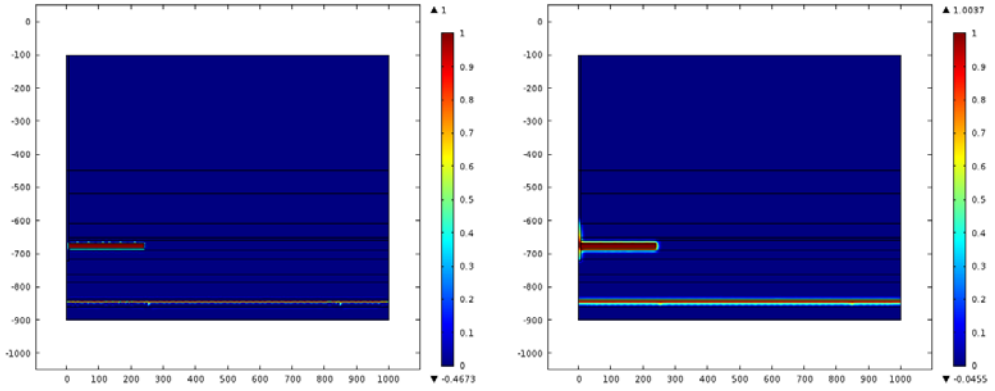

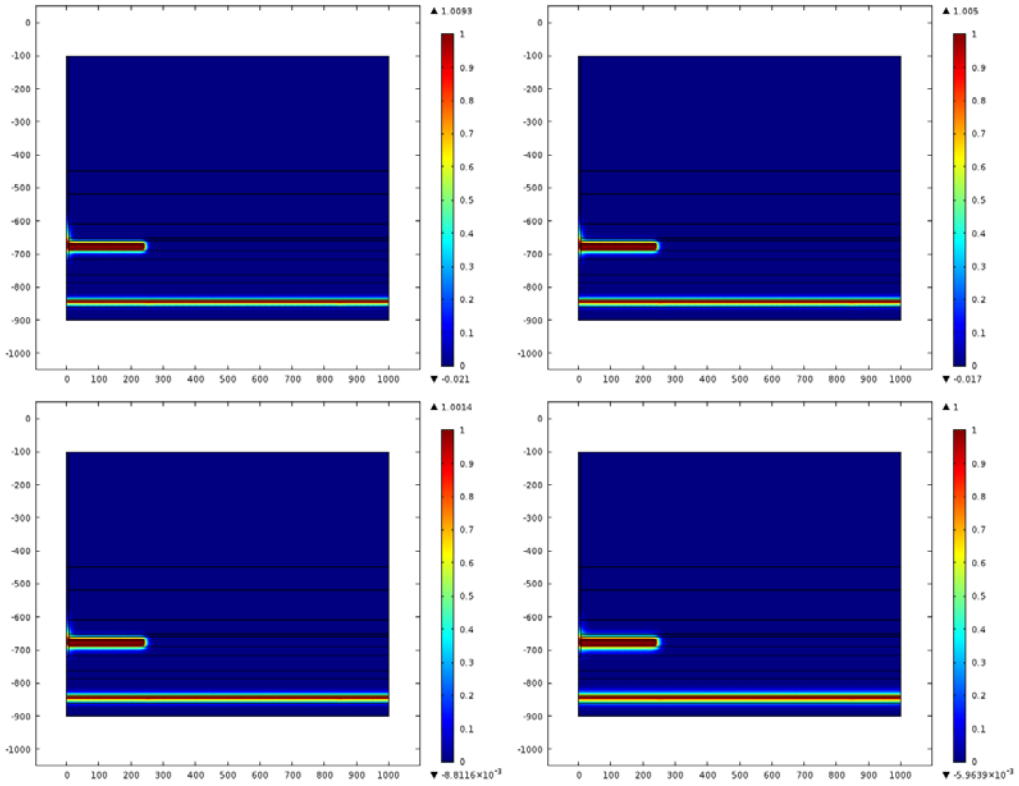

Fig. 1.53 Contour plotting of the trace chemical concentration at different postclosure time corresponding to sampling points A-F

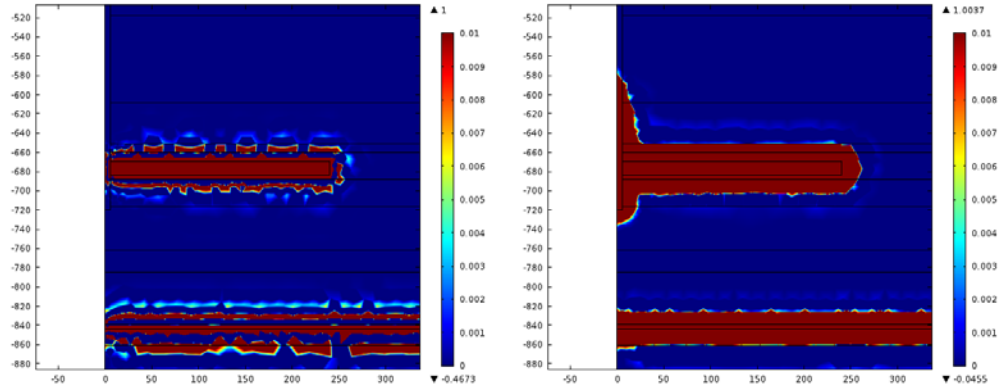

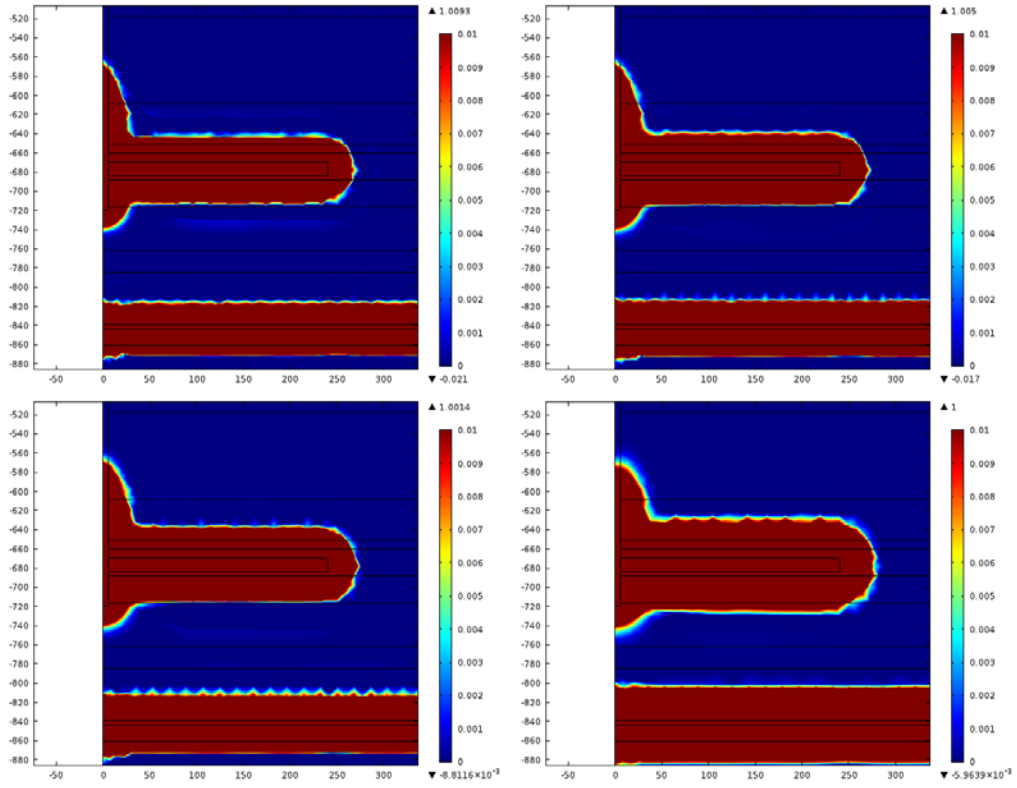

Fig. 1.54 Enlarged and rescaled (C<0.01 M) contour plotting of the trace chemical concentration at different postclosure time corresponding to sampling points A-F

6. Conclusions

The numerical analyses reported here consider conservative assumptions in order to assess the potential HM changes to the surrounding rock mass as well as the long-term evolution of the whole geological formations in view of the glacial cycles. The excavation damage zone (EDZ) is investigated for the tunnel and shaft. The long-term hydraulic-mechanical coupled modeling study for the large scale repository system takes into consideration the ice load on the surface due to a future glacial cycle and gas pressure generated in the repository. The movement of tracers numerically seeded in the repository and above the Cambrian was assessed in order to better visualize the changes in the hydraulic regimes induced by excavation, gas generation and future glaciation.

The model parameters are carefully selected from published technical reports previously carried out on the Bruce nuclear site. For the calculation of factor of safety (FS), special attention was given to long term strength degradation behavior of the rock mass under in situ stress conditions. We assume a 65 % of the peak UCS to represent the long term strength parameter. Internal boundary conditions for the emplacement tunnel are also considered in the simulations. For the present scoping analysis, only 1

cycle of glacial influence is included in the analysis. The conclusions from this study are summarized as below.

- The excavation induced damage zone (EDZ) extends across the Cobourg formation into the underlying Sherman Fall formation. The overall scope of the damage zone is approximately 2 times of the tunnel height and penetrates marginally over 1 m into the 13 m thick pillars.
- The EDZ appears to be limited within 1-2 diameters into the sidewall of the shaft even in the weakest formations such as the Blue Mountain formation. Such impact is observed even in deeper regions 10 m underneath the shaft bottom.
- The whole domain is mechanically stable throughout the 120,000 years of postclosure period. The mechanical stress seems to be responsive to both tunnel pressure and overburden loading.
- The tunnel pressure resulting from waste gases causes perturbation to the regions around the vertical shaft which is more permeable to other rocks.
- Stress path of monitoring points in the host and cap rock formations suggest that the principal stresses move to the right hand side and away from the Hoek-Brown strength envelope by the glacial loading, and thus the FS increases during glaciation.
- Diffusion is the dominant mechanism for chemical transportation in host rocks, despite the very high hydraulic gradients induced by the combined effects of the overpressure in and above the Cambrian, gas pressure in the repository, and future glacial loading, in addition to higher permeability of the repository and the shafts.

Reference

Blatz, J. A. & Graham, J. (2003) Elastic-plastic modelling of unsaturated soil using results from a new triaxial test with controlled suction. Geotechnique. 53, No. 1, 113–122.

Geofirma Engineering Ltd. And Quintessa Ltd. (2011) Postclosure Safety Assessment: Gas Modelling. NWMO DGR-TR-2011-31

Itasca Consulting Group Inc. (2011) Long-Term Geomechanical Stability Analysis. NWMO DGR-TR-2011-17.

Intera Engineering Ltd. (2011) Descriptive Geosphere Site Model. NWMO DGR-TR-2011-24.

Jorgensen, Donald G. Relationships between Basic Soils-Engineering Equations and Basic Ground-Water Flow Equations. Geological Survey Water-Supply Paper 2064. United States Government Printing Office, Washington: 1980.

Nguyen, Son (1995) Computational modeling of thermal-hydrological-mechanical processes in geological media. PhD Thesis. McGill University, Montreal, Quebec, Canada.

NWMO: Nuclear Waste Management Organization (2011) Geosynthesis. NWMO DGR-TR-2011-11

OPG letter (2012) Albert Sweetnam to JRP Chair, “Updated Information in Support of OPG’s Licence Application for a Deep Geologic Repository for Low and Intermediate Level Waste”. CD# 00216-00531-00101.

Quintessa Ltd. (2011) Postclosure Safety Assessment: Analysis of the Normal Evolution Scenario. NWMO DGR-TR-2011-26

Rocscience. Rock mass properties.
http://www.rocscience.com/hoek/corner/11_Rock_mass_properties.pdf

Tang, Gary Xiangmin (1999) Suction Characteristics and Elastic-Plastic Modeling of Unsaturated Sand-Bentonite Mixture. Thesis. Department of Civil and Geological Engineering, University of Manitoba, Winnipeg, Manitoba.

Chapter 2 THM coupled modelling of HE-E heating test

Summary

This chapter reports a modelling investigation into the international collaborative field test of HE-E heating experiment. The THM coupled models proposed by Nguyen et al. (2013) was applied to study the lab and field experimental observations of various physical parameters. The model was first calibrated with laboratory scale small column heating tests. We discovered nonlinearity in vapour diffusivity and EBS compressibility that are critical to the temperature and relative humidity evolution in the EBS materials. A staged numerical simulation was developed to account for the excavation, backfilling and heating steps as happened to the field experiment. The model reproduces very well most of the temperature profile, moisture movement, and pore pressure fluctuation at some locations of the repository. With the consideration of the excavation induced damage zone (EDZ) with higher permeability and lower air entry value than the intact host rock, it is beneficial to EBS desaturation within a short period of time under thermal gradient, but turns out to be an obstacle to bentonite resaturation in the long run. The impacts of nonlinearity in vapour diffusion coefficient and matrix compressibility are found to be critical to the success in numerical modelling and are in good agreement with experimental observations.

1. Introduction

We have undertaken numerical simulations of the thermal-hydraulic-mechanical (THM) coupled behaviour of the engineered barrier system (EBS) and its interaction with the host rock (Opalinus clay rock) in a field heating test, i.e. DECOVALEX HE-E project, at Mount Terri. The purpose of this numerical study is (1) to assess the short-term performance of the EBS, focusing on the THM coupled behaviour and (2) to calibrate the THM coupled models that have been continuously developed at the CNSC with laboratory experimental results of heating tests on small column and finally (3) to apply the models and parameters to simulate the in-situ heating test at the Mont Terri Underground Research Facility (URF).

Conceptual models were constructed in accordance with the field experimental design parameters as reported by Nagra (Gaus et al. 2014). Geoscientific data used in this study were collected from various available technical reports (Villar et al. 2012; Nguyen and Barnichon, 2013) published by the DECOVALEX project participants. The model parameters for bentonite and sand/bentonite mixture are obtained by calibrating laboratory test data with numerical modelling. The parametric input that give the best fitting with test data are regarded as representative of the characteristics of the EBS materials and are used in the simulation of the field test.

Field experimental results are provided by Nagra, Switzerland. Due to the fact that the field conditions may deviate from those occurring in the laboratory scale test, fine tuning of the modelling parameters were carried out to better reflect the field test data.

This report provides a summary description of the theoretical background, the conceptual model, the model parameters and modelling scenarios. Modelling results for the evolution of pore pressure, relative humidity and temperature after tunnel excavation, EBS emplacement and subsequent heating are presented and compared with the experimental measurements. The modelling tool is the COMSOL multiphysics (Ver. 4.3b) commercial software package.

2. Theories on THM coupled models

Coupled governing equations

The theoretical framework for the THM coupled models has been well documented in the literature and previously reported by Nguyen et al. (2013) among others. The fundamental principle that is invoked in order to develop the governing equations of coupled THM processes is the principle of conservation of mass, energy and momentum. In addition, the following main assumptions are made:

1) The geological medium is conceptualized as a porous medium;

2) Only heat is considered in the energy balance equation. Thermal equilibrium is assumed between the solid and liquid phases. Furthermore, heat transfer occurs only by conduction;

3) The porewater can exist either in a liquid or gaseous (vapour) state. The flow of liquid water is by advection and is assumed to follow Darcy's law, while the vapour flow is by diffusion;

4) A modified Biot's effective stress principle is assumed:

$$\sigma = \sigma' + \chi p$$

where σ is the total stress, σ' is the effective stress, p is pore pressure and

$$\chi = \begin{cases} \alpha, \text{if } p \geq 0 \\ 0, \text{if } p < 0 \end{cases}$$

where α is the Biot's coefficient.

The resulting governing equations are as follows:

$\rho_s C \frac{\partial T}{\partial t} = \nabla(\mathbf{k_T} \nabla T) + Q$

$\rho_l \left(\frac{C_m}{\rho_l g} + S_e S\right) \frac{\partial p}{\partial t} + \nabla \frac{\rho_l \mathbf{k}}{\mu} \nabla p = \alpha \rho_l S_e \frac{\partial \varepsilon_v}{\partial t} + \rho_l S_e [\beta(1-\alpha) - n\beta_w - (1-n)\beta_s] \frac{\partial T}{\partial t}$ (for partially saturated host rock)

$\rho_l \left(\frac{C_m}{\rho_l g} + S_e S\right) \frac{\partial p}{\partial t} + \nabla \frac{\rho_l \mathbf{k}}{\mu} \nabla p + \nabla \rho_l (D_{pv} \nabla p + D_{Tv} \nabla T) = \alpha \rho_l S_e \frac{\partial \varepsilon_v}{\partial t}$ (for unsaturated EBS materials with vapour migration)

$\mathbf{C}: \nabla(\boldsymbol{\varepsilon} - \beta \mathrm{d}T\mathbf{I}) + \alpha \nabla p = 0$ (for saturated host rock)

$\mathbf{C}: \nabla(\boldsymbol{\varepsilon} - \beta \mathrm{d}T\mathbf{I}) = 0$ (for unsaturated EBS)

where ρ_l is fluid density; ρ_s is solid density; C is the specific heat capacity for the bulk material; T is temperature (K); t is time (S); $\mathbf{k_T}$ is heat conductivity and Q is heat source term; S_e is effective water saturation; S is storage term ($S = n\chi_f + (1-n)\chi_s$) χ_f is the compressibility of the porewater, χ_s is the compressibility of the solid particles; C_m is the specific moisture capacity that describes the slope of moisture variation with pressure change and can be determined by the soil water characteristic curve (SWCC); p is pore pressure (Pa); **k** is the permeability tensor; μ is the dynamic viscosity of pore fluid; β is the thermal induced volumetric expansion coefficient for the solid skeleton; β_w is the thermal expansivity of pore fluid; β_s is the thermal expansivity of the grains; ε_v is the volumetric strain; D_{pv} and D_{Tv} are the thermal diffusivities for water vapour; **C** is the stiffness matrix for the porous media and **ε** is the strain tensor.

As for the mechanical model, both host rock and EBS are assumed to follow Hooke's law of elasticity. Anisotropic properties of the host rock in terms of permeability and elasticity matrix are taken into account in the THM coupled modelling.

Relative humidity

Relative humidity was measured throughout the heating test in the HE-E project. Therefore it is an important indicator of moisture migration and the THM coupling influences. The relative humidity in the pore space is related to matric suction and temperature in the form of the Kelvin's equation,

$$RH = e^{\frac{P_c m^w}{\rho_w RT}}$$

where P_c is the matric suction, ρ_w is water density, R is atmospheric constant (R=8.314), m^w is the molecular weight of water (18E-3 kg/mol) and T is absolute temperature (K).

$$P_c = \rho_w R_v T \ln(RH)$$

In case of RH=0.95 for the boundary condition of the tunnel-air interface and neglecting the chemical potential, the pore pressure can be obtained as

$$p = -P_c = -6.82 \text{ MPa}$$

Theory of moisture movement in porous media

Vapour diffusion in porous media has been proposed to be written as (Philip and Vries, 1957)

$$q_v = -D_v \nabla \rho_v$$

with the vapour diffusion coefficient D_v written as

$$D_v = -D_{atm} \tau n (1 - S_e)$$

where τ is the tortuosity factor, n is porosity, S_e is effective liquid saturation degree, and D_{atm} is the free diffusion coefficient of water vapour in atmospheric pressure.

The density of vapour (ρ_v) at a certain suction and temperature is then related to RH by definition as (see e.g. Charlaix and Ciccotti, 2010)

$$\rho_v = \rho_{vs} * RH$$

where ρ_{vs} is the saturated vapour density. It is assumed in this study that the vapour is at atmospheric pressure, then ρ_{vs} is a unique function of T and can be calculated with the following empirical relationship

$$\rho_{vs} = 1.4 * 10^{-6}T^3 - 1.2305 * 10^{-3}T^2 + 3.724 * 10^{-1}T - 37.584$$

The above two equations determine a single value of vapour density for a given state (p_c, T). When the state changes, the amount of vapour in the pore space, as given by ρ_v, would either decrease by evaporation or increase by condensation. Therefore, by using Kelvin's equation in our modelling approach, the condensation/evaporation process is implicitly taken into account

Differentiating the vapour density function, we obtain two components that are respectively dependent on pore pressure and temperature

$$\nabla\rho_v = \nabla\left(\rho_{vs} * e^{\frac{P_c}{\rho_l R_v T}}\right) = D_p\nabla p + D_T\nabla \mathrm{T}$$

Because the saturated vapour density only depends on temperature, then

$$D_p = \frac{d\rho_v}{dp} = \rho_{vs} * e^{\frac{P_c}{\rho_l R_v T}}\frac{-1}{\rho_l R_v T}$$

which can be further written as

$$D_p = \frac{-\rho_v}{\rho_l R_v T}$$

and

$$D_T = \frac{d\rho_v}{dT} = \rho_{vs}\frac{de^{\frac{P_c}{\rho_l R_v T}}}{dT} + e^{\frac{P_c}{\rho_l R_v T}}\frac{d\rho_{vs}}{dT}$$

Expanding the above equation yields

$$D_T = \frac{d\rho_v}{dT} = \rho_{vs} * e^{\frac{P_c}{\rho_l R_v T}} * \frac{-P_c}{\rho_l R_v T^2} + e^{\frac{P_c}{\rho_l R_v T}}\frac{d\rho_{vs}}{dT}$$

which can also be expressed as

$$D_T = RH\frac{d\rho_{vs}}{dT} - \frac{P_c\rho_v}{\rho_l R_v T^2}$$

Philip and Vries (1957) expressed vapour flux in the form of

$$q_v = -\rho_l(D_{pv}\nabla p + D_{Tv}\nabla T)$$

where the diffusivity components D_{pv} and D_{Tv} are related to the vapour density components D_p and D_T by the vapour diffusion coefficient D_v

$$D_{pv} = \frac{D_p D_v}{\rho_l}$$

$$D_{Tv} = \frac{D_T D_v}{\rho_l}$$

which leads to the isothermal vapour diffusivity

$$D_{pv} = \frac{D_v \rho_v}{\rho_l^2 R_v T}$$

and the thermal vapour diffusivity

$$D_{Tv} = \frac{f_{Tv} D_v}{\rho_l}\left(RH\frac{d\rho_{vs}}{dT} - \frac{P_c \rho_v}{\rho_l R_v T^2}\right)$$

where f_{Tv} is a thermal enhancing factor for vapour diffusion according to Rutqvist et al. (2001) and will be discussed later in this report.

Citing an empirical formula for the atmospheric vapour diffusivity,

$$D_{atm} = 2.416 \times 10^{-5}\left(\frac{T}{273.15}\right)^{1.8}$$

then the vapour diffusivity in porous media can be determined by the following function (Lee and Wilke, 1954)

$$D_v = D_{atm}\tau n(1 - S_e) = 2.416 \times 10^{-5}\tau n(1 - S_e)\left(\frac{T}{273.15}\right)^{1.8}$$

Enhanced vapour diffusion in porous media

Experimental data have repeatedly proven the significant enhancement of diffusion in porous media for condensable gases such as water vapour. The enhancing effect can lead to vapour migration coefficient as large as the free diffusion coefficient. Philip and de Vries (1957) and others (e.g. Ho and Webb, 1996) explains the enhancing effect by two main arguments. First, “liquid islands” can exist in a porous network. Vapour that reaches one island condenses at one end and evaporates at the other, creating thus a direct vapour migration path through the island, instead of going around to other pores which are “island” free. Therefore, the tortuosity is substantially reduced. The second reason for the enhanced vapour movement is that at the local scale of air-filled pores the temperature gradient may be

significantly greater than the average temperature gradient in a representative elemental volume of the porous medium. The enhancement is expressed by a parameter (η) in the form of

$$D_v = \eta\tau n(1 - S_e)D_0$$

Or

$$D_v = \beta D_0$$

The enhancement factor η is reported to range from 1 to 15 for various types of soils (Cass et al., 1984). Parameter β can be in the order of 1.0 which means that the vapour diffusivity in pore space is comparable to its free diffusivity, and is not influenced by porosity, saturation and tortuosity at all. However, this enhancing effect is restrained within a certain range of saturation degrees, i.e. sandy soil has a sharp increase in value of η from 1 to 15 within S_e=0.1-0.2, while silt loam has a similar trend (1-10) within S_e=0.2-0.4.

This thermal enhancement on vapour diffusion has been systematically investigated by peers in UC Berkeley with TOUGH software. Rutqvist et al. (2001) has proposed a thermal enhancement factor f_{Tv} in the THM coupled models for porous media, which is in good agreement with these experimental observation and theoretical speculations. It is worth emphasizing here that, for thermal induced vapour diffusion,

$$f_{Tv} = \eta$$

and accordingly f_{Tv} is supposed to vary with the degree of saturation degree. In our previous simulations, f_{Tv} is generally treated as a constant rather than a dependent variable. Particularly to the model calibration using the laboratory scale small column test, the degree of saturation degree of the whole system was within a limited range of variation, which did not permit a thorough examination of such a hypothesis with regards to thermal enhancement factor. In the field HE-E heating test the dependence of f_{Tv} with the effective saturation of the EBS materials was taken into account.

Retention curves

Brooks-Corey model

The effective degree of saturation S_e is written as an equation of matric suction

$$S_e = (\alpha P_c)^{-n}$$

For cases with

$$P_c \geq \frac{1}{\alpha}, S_e = 1$$

where P_c is matric suction written in the form of water head (m H_2O).

In this study, the Brooks-Corey model was applied to the EBS materials for both the calibration of the column test and the simulation of the field case.

van Genuchten model

The effective degree of saturation using the van Genuchten model takes the following form,

$$S_e = [1 + (\alpha P_c)^n]^{-m}$$

where $m = 1 - 1/n$.

For

$P_c \geq 0, S_e = 1$

Due to the fact that van Genuchten model is able to more accurately describe the suction characteristics near full saturation , the van Genuchten rather than the Brooks-Corey model was used for the host rock which is expected to experience some desaturation during the excavation and heating stages.

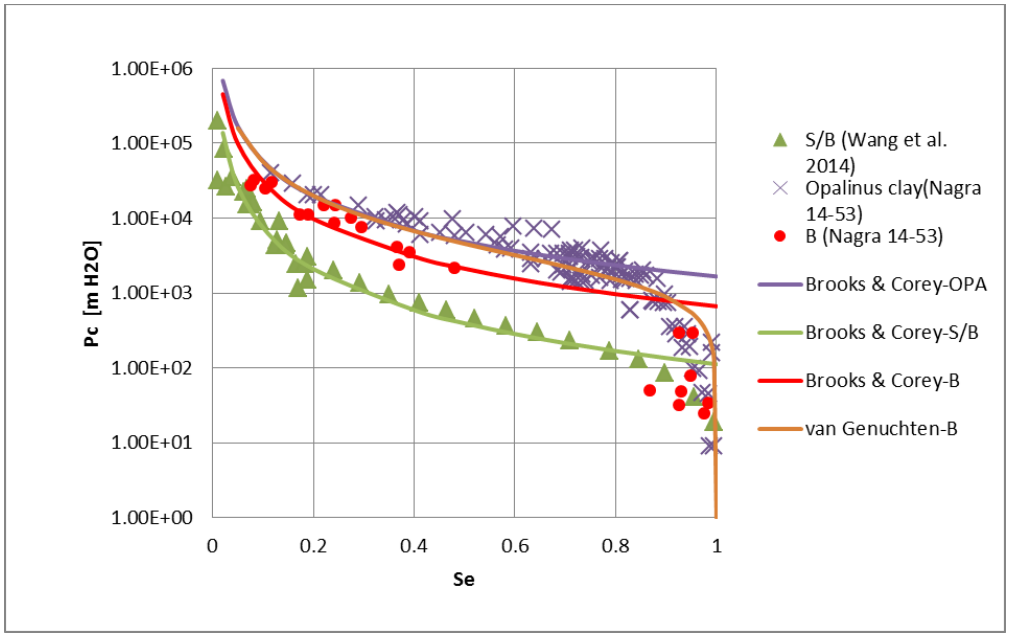

Figure 2.1 Fitting of SWCC for Opalinus clay rock, MX-80 Bentonite and Sand/Bentonite mixture (1.5 dry density) with Brooks-Corey and van Genuchten models

Relative permeability

From the van Genuchten model, the relative permeability is given by

$$k_r = (S_e)^{\lambda}\left[1 - \left(1 - {S_e}^{1/m}\right)^m\right]^2$$

where m=1-1/n, which is identical to the one used in retention curve function; l is model parameter that determines the shape of relative permeability. The classical van Genuchten model assumes the model constant λ to be 0.5 (Nowamooz et al. 2009), which has been adopted in the CIMNE model (Gaus et al. 2014). In COMSOL, λ is an adjustable parameter and is calibrated in the following numerical simulations.

From the Brooks-Corey model, the relative permeability takes the following form

$$k_r = (S_e)^{\lambda}$$

λ is reported to be 9 and 10 for Bentonite pellets and Sand/Bentonite mixture, respectively by Gaus et al. (2014). In COMSOL, $\lambda = \frac{2}{n} + l + 2$.

Thermal expansivity of water

The thermal expansion coefficient of liquid water varies with temperature. The following empirical correlation is used (Otero et al., 2002)

$$\beta_w = \left(A + \frac{B}{C + \pi}\right) * 10^{-4} \ (\mathrm{K}^{-1})$$

where model constants A, B and C vary with temperature and pressure in terms of

$$A = 47.8506 - 8.12847 * 10^{-2}T + 8.49849 * 10^{-5}T^2$$

$$B = 5.56047 * 10^5 - 3.76355 * 10^3 T + 5.56395 * T^2 + 5.59382 * 10^{-3} T\pi - 27.6522\pi$$

$$C = -4.28067 * 10^3 - 33.915T + 0.365873T^2 - 5.89617 * 10^{-4}T^3$$

$$\pi = P + 3.28892 * 10^{-4}P^2 - 2.65933 * 10^{-8}P^3$$

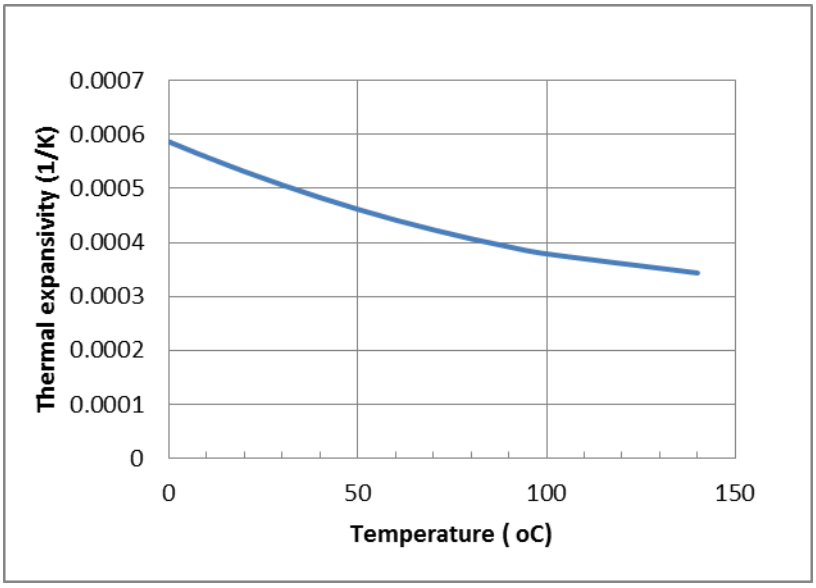

Figure 2.2 Variation of thermal expansion coefficient for water with increasing temperature

Dynamic viscosity of water at various temperatures

The hydraulic conductivity that governs porewater flow in a porous medium is inversely proportional to the dynamic viscosity of the porewater. Figure 2.3 shows the adopted relationship between μ and T that is experimentally determined for water. It is found that the viscosity decreased from 0.0018 to 0.0002 when temperature increases from 0.0 to 140 ^{o}C, resulting in a significant increase in the hydraulic conductivity and consequently in the Darcian flow rate. Such a big change has to be accounted in the simulations.

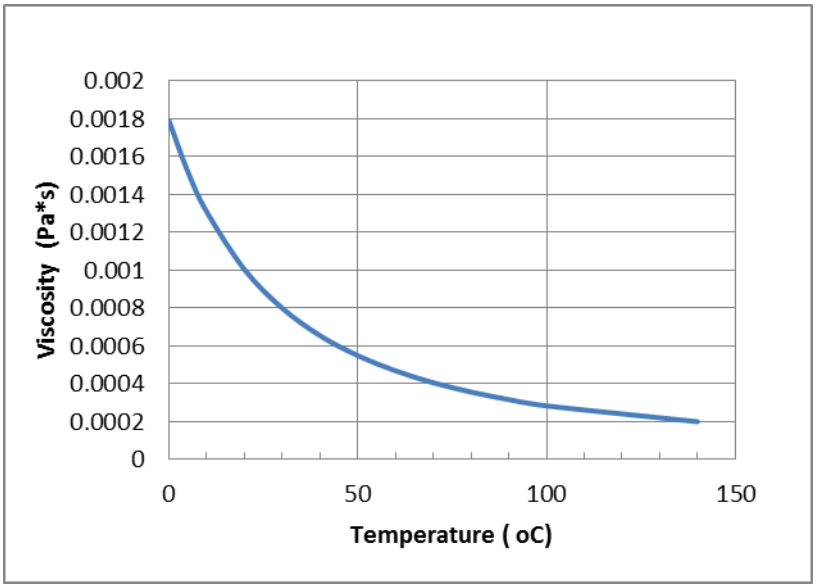

Figure 2.3 Variation of dynamic viscosity for water with increasing temperature

3. Model calibration for Sand/Bentonite (S/B)

The HE-E test involves a series of laboratory scale column heating tests on both types of engineered barrier system (EBS) materials, e.g. the sand-bentonite mixture (S/B) and bentonite pellet (B). These experimental results are designed to calibrate the input parameters of THM coupled models for the specific EBS materials. Dr. Nguyen has previously conducted excellent calibration works for bentonite pellet. This research task (#2) includes the calibration works for S/B as obtained from the laboratory scale heating experiment.

The experiment was reportedly (Villar et al., 2012) carried out in such a way that the top boundary allowed a little leakage of water into the column during the initial equilibration period by accident. This disturbance introduced redundant moisture movement downward from the top layer, and thus caused difficulty in numerical modelling to reflect the evolution of relative humidity for regions close to the top boundary. The RH evolution curve for the sensor #1 could not be satisfyingly calibrated by numerical simulation because of the lack of information about the mass flux and leaking duration. Therefore the focus of our calibration was placed on the other two sensors located closer to the heater.

Experimental set up for THM cells

THM cell tests for EBS materials are schematically shown in Fig. 2.4. The inner size of the column is D*L=7*50 cm^2. EBS materials are filled into the column and are gently compacted to the required density (1.45-1.47 g/cm^3). Three sensors for measurement of relative humidity were installed to different depths. Heating was supplied at the bottom boundary. The upper boundary is connected to the hydration system which can permit water permeation towards the EBS material.

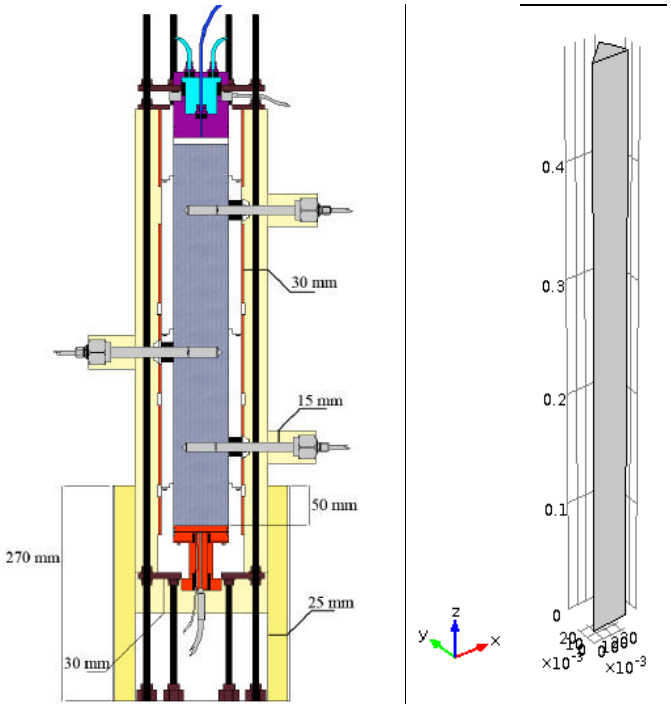

Figure 2.4 Sketch of the laboratory scale heating cell test column (Villar et al., 2012) (left) and numerical model (right)

Boundary conditions

Heating source

The column test was modelled by setting the bottom of EBS column quickly to the target temperature in two stages as shown in Figure 2.5, consistently with the measured temperature at the heater/column interface.

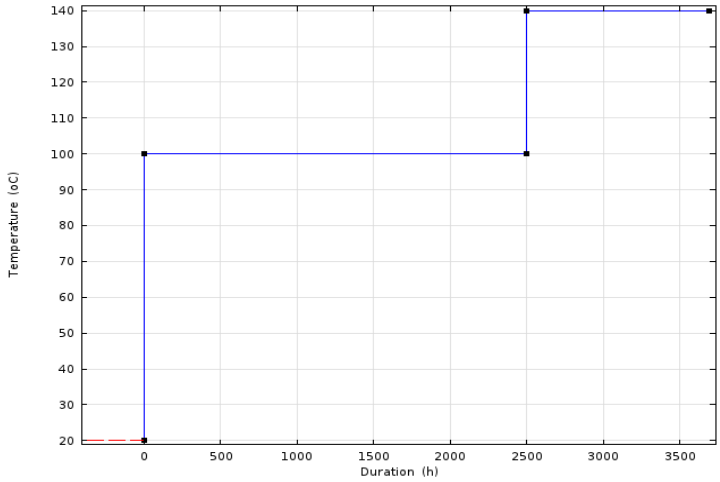

Figure 2.5 Temperature of heater

Heat leakage rate on the side boundary

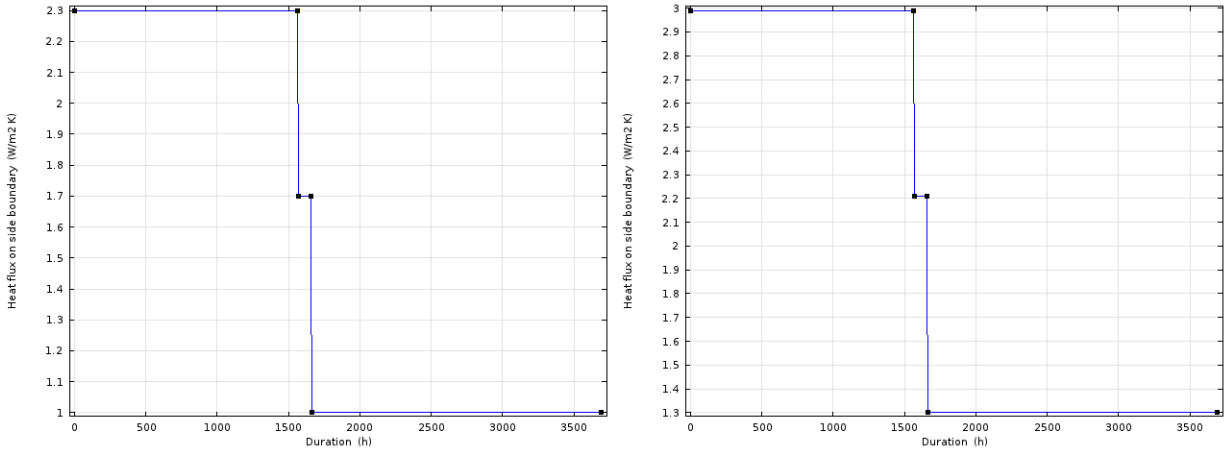

Figure 2.6 Heat leakage rate on the side boundary for zones (a) z>0.2 m and (b) z<=0.2m

Despite the insulation on the side boundary, a certain amount of heat from the heater at the bottom boundary would leak out by conduction and convection. Our simulation attempted to estimate the heat leakage rate and the best results were obtained by applying the heat flux onto the side outer boundary as shown in Fig. 2.6. The sharp reduction in heat leakage rate after 1600 h mimicked the upgrading the insulator material that was conducted at that time. For zones closer to the heater, a higher rate of heat leakage is expected to occur due to the larger value in heat gradient. Therefore an enhanced leakage rate was assumed for the bottom zones in proximity to the heater.

Monitoring results

Figure 2.7 shows the temperature history at three monitoring points. The sensor that is located closest to the heater shows higher value in temperature, and more obvious variation due to temperature change near the heating source. The relative humidity profiles for the three monitoring points are shown in Figure 2.8.

The locations of the 3 sensors are respectively at 10, 22 and 40 mm from the heater. It is shown that a quick increase in heating source leads to an immediate response of RH spike for sensor #3, and a gradually declining tail. As for the other two sensors located farther from the heater, the monitored RH values are consistently climbing until an equilibrium value at about 80%. This indicates that the humidity is driven by heat and moving towards the cold end with time, which is consistent with the physical mechanism.

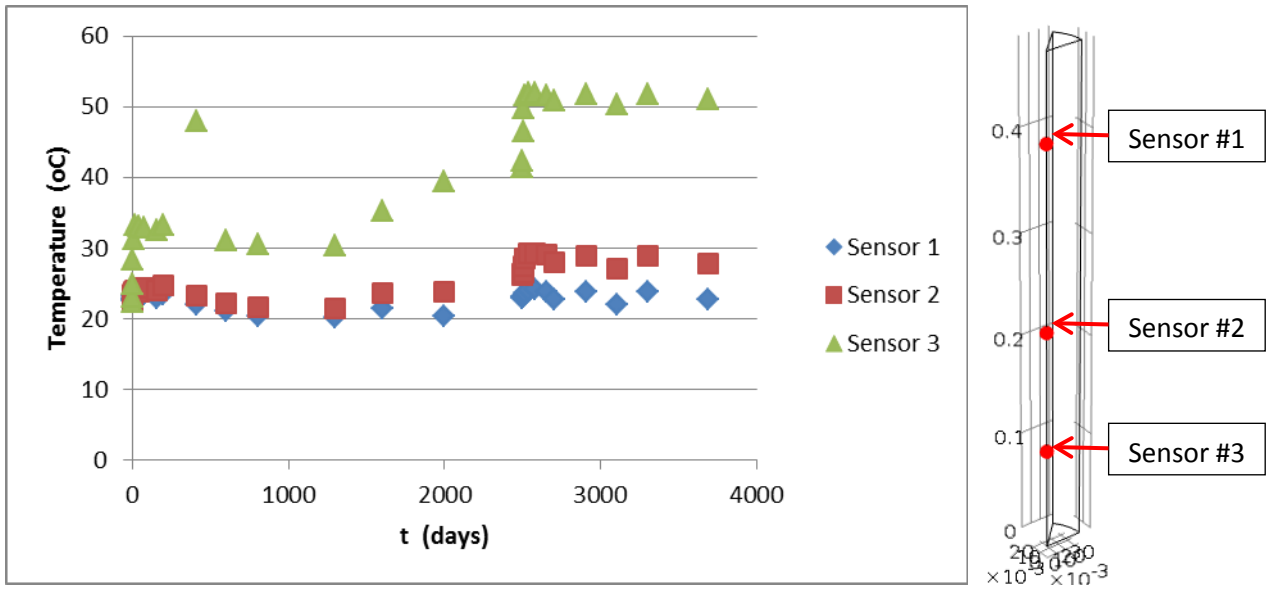

Figure 2.7 Monitored temperature evolution at different locations

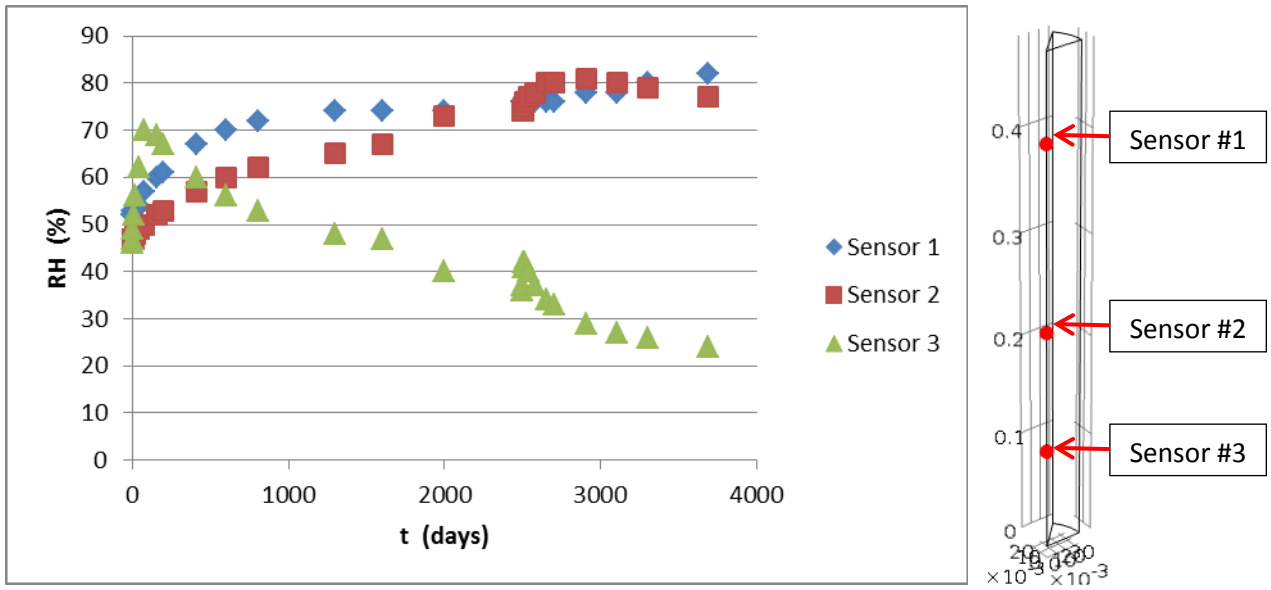

Figure 2.8 Monitored relative humidity evolution at different locations

Modelling approach and results

An axisymmetric model was established with COMSOL multiphysics (ver 4.3b) as shown in Fig. 2.4b. Initial conditions and boundary conditions are consistent with those in the experiments that were detailed by Villar et al. (2012). The focus of model calibration is to find the best-fitted parameters for pore compressibility and retention curve. After a number of trial simulations we obtained a set of model parameters that are representative of the EBS material and are able to reproduce the experimental results.

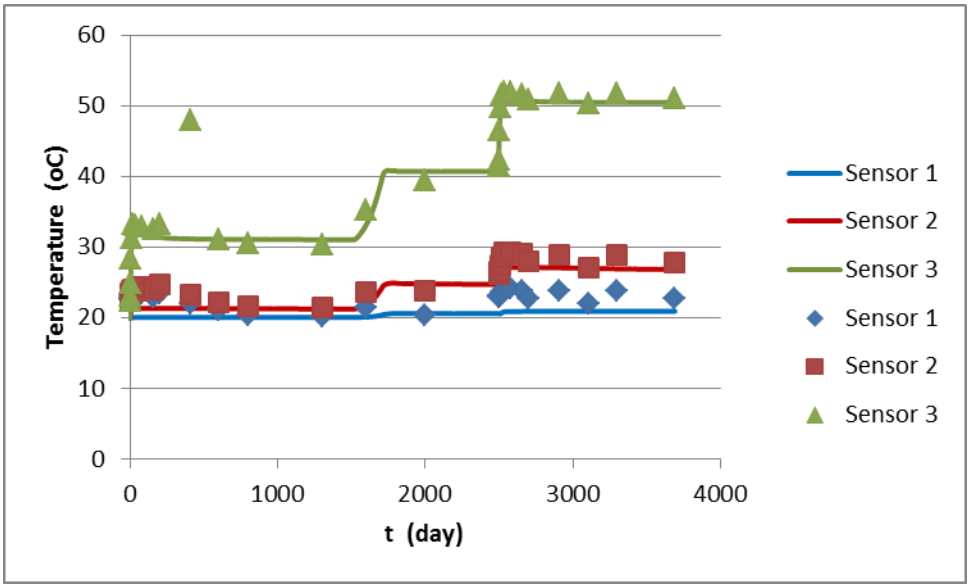

Figure 2.9 Comparison of modeled and test results of temperature (Scattered dot is test data and the solid line is modelling results.)

Table 1 lists all the necessary parameters for the numerical simulations. The calibrated model parameters are in good agreement with others (Gaus et al. 2014). Figures 9-10 show the comparison between test data and modelling results with respect to temperature and relative humidity. The good agreement with each other indicates a satisfying calibration has been achieved in this study.

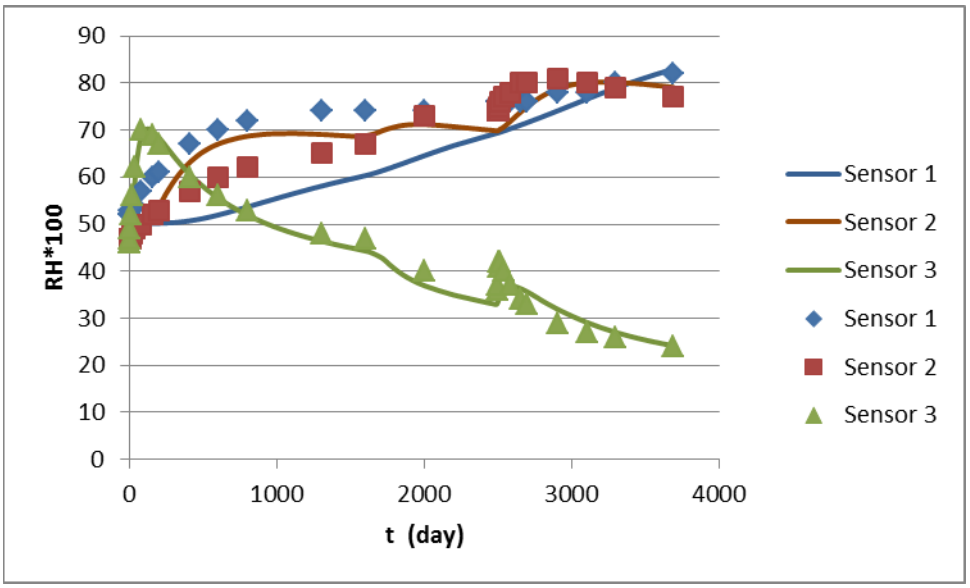

Figure 2.10 Comparison of modeled and test results of RH (Scattered dot is test data and the solid line is modelling results.)

Table 2.1 Calibrated model parameters for S/B

Parameter	**S/B**	**B**
Diffusivity		
F_{Tv}	4.3	3.0
τ	0.5	0.5
D_v	4.64E-6 – 1.04E-4	3.96E-6 – 9.04E-6
D_{pv}	7.86E-21 – 3.48E-17	1.03E-18 – 2.53E-17
D_{Tv}	2.86E-13 – 2.5E-10	1.64E-11 – 1.33E-10
Porosity	0.47	0.45
ρ_{vs}	1.13-4.99	1.13 – 4.99
ρ_v	1.45E-4 – 1.00	0.02 – 0.85
Water retention capacity (Brooks-Corey)		
α (1/m H_2O)	8.92E-3	1.5E-3
n	0.55	0.50
l	3.37	3.66
Thermal properties		
Expansivity (1/K)	2.5E-5	2.5E-5
Conductivity (W/m K)	0.35 – 1.30	0.35 – 1.30
Specific heat (J/kg C)	800 - 1500	800 - 1500

Hydration of EBS column and vapour migration

The column tests were subject to hydration at the end of heating test. Hydration from the top boundary led to a sharp front of pore pressure gradient with negligible temperature gradient. This situation provides a unique and good ground for the discussion of the vapour diffusion coefficients D_{pv} and D_{Tv}. Because of the small thermal gradient, the contribution of thermal diffusion to the overall vapour flux is negligible compared to the pressure driven diffusion, then the governing equation can be shown, as detailed in section 5, to simplify to:

$$\left(\frac{C_m}{\rho_l g} + S_e S\right)\frac{\partial p}{\partial t} + \nabla\left(\frac{k}{\mu} + \nabla D_{pv}\right)\nabla p = 0$$

For unsaturated bentonite, the unsaturated permeability is much smaller than the saturated permeability k_0=1E-21 m^2. In this case the vapour diffusion dominates the water transport process. But when soil approaches saturation, the relative permeability gradually raises to 1.0, which makes water permeation comparable to the level of vapour diffusion.

In this case, effective compressibility of soil (χ_p^e) plays an important role in estimating the vapor movement. As C_m is normally of the order of 10^{-5}-10^{-6}, making the term of $C_m/\rho g$ negligible in contrast to the term of $S_e S$ in the order of 10^{-7} for soils. Therefore, the above equation can be further simplified into the following form (more details see section 5)

$$S_e(1-n)\chi_p{}^e\frac{\partial p}{\partial t} + \nabla\left(\frac{k}{\mu} + \nabla D_{pv}\right)\nabla p = 0$$

The effective compressibility of a porous media that takes into account the volumetric strain can be regarded as the reverse of its bulk modulus $\chi_p{}^e = \frac{1}{K}$. The bulk modulus of clay soils are normally varied with saturation degree, with the higher value in correspondence to the drier state (Tisato and Marelli, 2013). Assuming a growing polynomial function for effective compressibility, we were able to better model the fluid flow and vapour movement in the vicinity of the saturated state.

4. HE-E heating test—Field case

This section describes the modelling efforts on THM coupled processes taking place in the HE-E heating test at Mont Terri. It is divided into several subsections that specifically deal with the geometry, input parameters, initial and boundary conditions, modelling strategy, results and discussion.

4.1 Geometry of the analysis zone

Figure 2.11a shows the location and adjacent tunnel infrastructures at the test site. The configuration of the heating test is shown in Fig. 2.11b. Two sections 4m in length are constructed in a micro-tunnel. S/B was emplaced in one section and B in the other. Concrete plugs separate the two sections, and were also emplaced at the two ends in order to separate the test area from the rest of the micro-tunnel. Heating tubes are placed within the EBS and supported by bentonite block base (Figure 2.12.a). Sensors are installed in the EBS, host rock and their interfaces at selected points to monitor temperature, relative humidity and pore pressure.

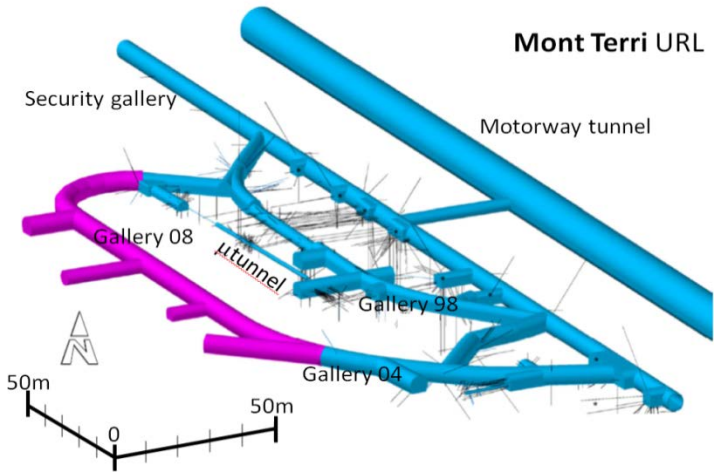

(a)

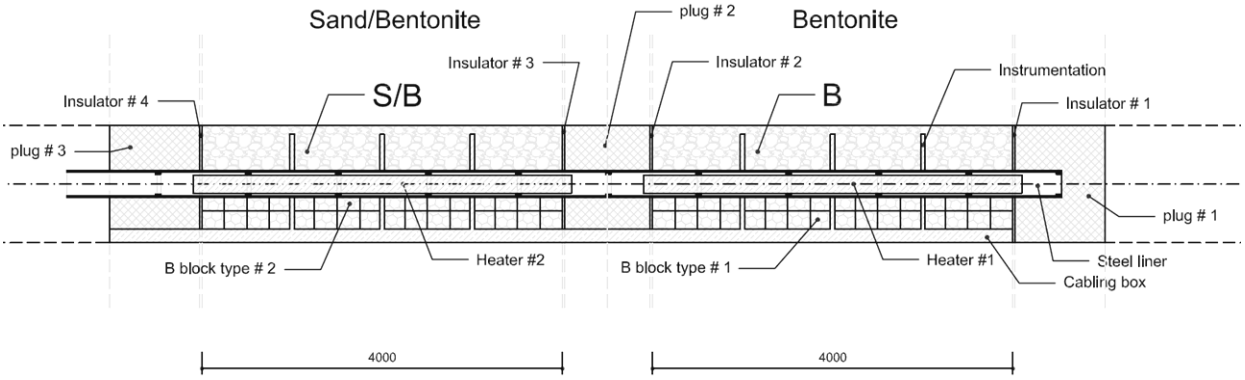

(b)

Figure 2.11 Layout of the test location-the micro tunnel (a) and the design of the heating upon EBS components (b)

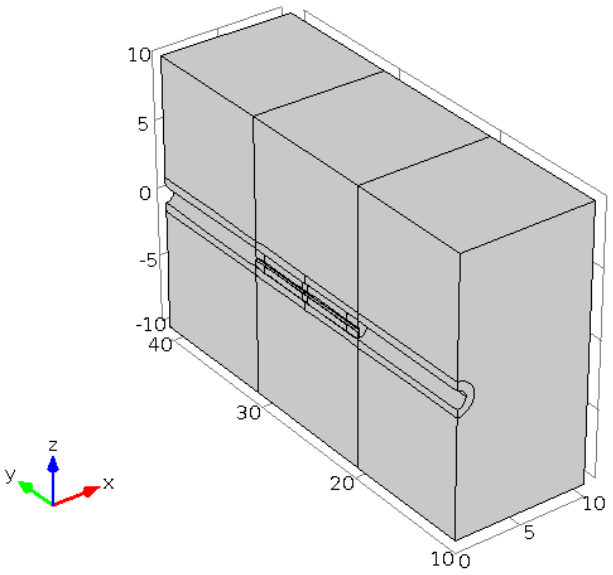

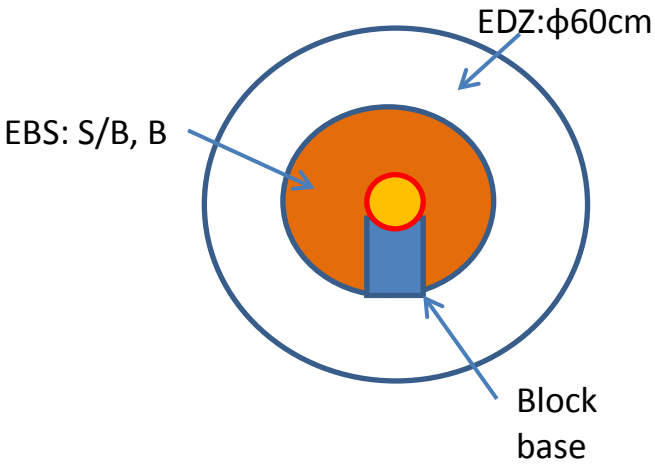

(a)

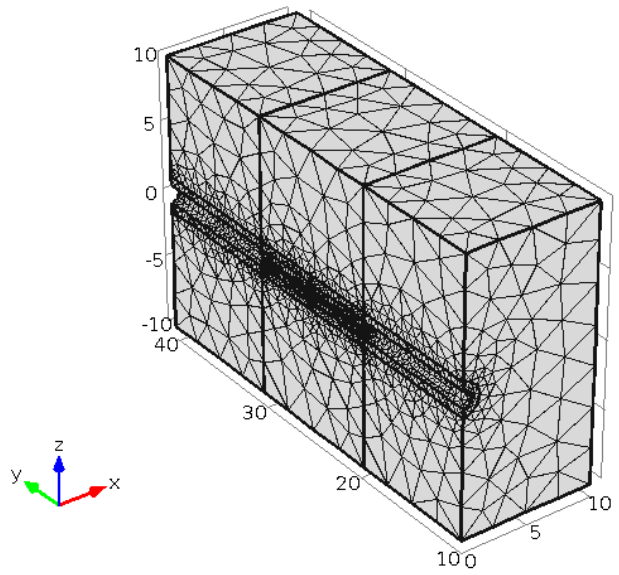

(b)

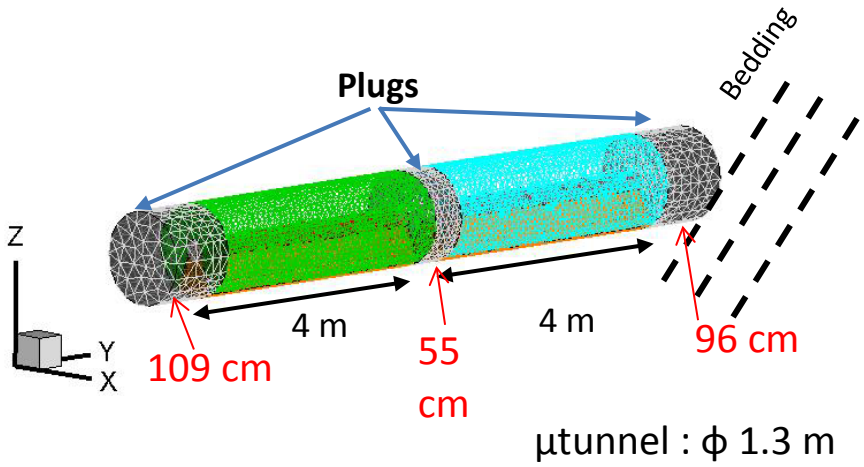

(c)

Figure 2.12 Schematic diagram showing the geometry and components for the numerical modelling of HE-E field test (a) and meshing of the analysis domains (b) and the micro tunnel (c)

Figure 2.12 shows the numerical model; symmetry is assumed along the centre vertical plane parallel to the axis of the micro-tunnel. Therefore only half of the geometry is represented in the finite element mesh (Figure 2.12-b). The cross sectional view of the filled tunnel is shown in Fig. 2.12c. The tube-like feature surrounding the EBS is a thin layer of excavation induced damage zone (EDZ) with a radical thickness of 30 cm. OPA is anisotropic in nature with the bedding plane inclined at 40 degrees towards the tunnel axis (Fig. 2.12d). The initial ground stress is in the level of

$$\sigma_x = -2.2\text{MPa}$$

$$\sigma_y = -4.3\text{MPa}$$
$$\sigma_z = -6.5\text{MPa}$$

4.2 Parametric settings for the analysis

Table 2.2 Fundamental parameters for the numerical simulation

Parameter	S/B	B	Opalinus clay	Bentonite block	Plug
Physical properties					
Grain density	2546	2700	2700	2700	2650
Dry density	1.383	1.513	2.33	1.806	-
Porosity	0.47	0.45	0.12	0.33	0.15
Initial Saturation	0.11	0.2	1	0.63	0.04
Mechanical properties					
E [Mpa]	18	18	8000/3000*	24	3.30E+04
v	0.35	0.35	0.33/0.29*	0.2	0.3
Diffusivity					
f_{Tv}	Figure 2.40-a	Figure 2.40-b	3	3	3
τ	0.5	0.5	0.5	0.5	0.5
χ_p^e	Figure 2.42-a	Figure 2.42-b	1.00E-09	7.50E-08	6.00E-10
k_s [m^2]	1.00E-19	1.00E-21	2.50E-20	2.50E-21	1.00E-20
Brooks & Corey					
α [1/m]	8.92E-03	5.00E-03			
n	5.50E-01	3.60E-01			
l	-1.370	5.500			
van Genuchten					
α [1/m]			5.5E-4	5.0E-3	6.0E-4
n			1.67	1.67	1.67
l			2	2	2
Thermal properties					
Thermal expansion Tx [1/K]	2.50E-05	2.50E-05	1.70E-05	1.70E-05	1.50E-05
Thermal conductivity wet [W/mK]	1.30	1.30	1.77/0.98*	1.9	1.4
Thermal conductivity dry [W/mK]	0.35	0.35	1.3	1.3	0.5
Specific heat [J/kg ^oC]	800-1500	800-1500	946.5	995	1000
Initial conditions					
Initial pore pressure [Pa]	-9.3E7	-1.25E8	1E6	-9.3E7	-9.3E7

Note:

*: Anisotropic parameter in horizontal direction over that in vertical direction with respect to the bedding plane k_h/k_v.

Table 2 shows all the parametric values of different materials that are necessary as input for the numerical modelling. The EDZ domain is assumed to have similar properties to the intact rock, except for the intrinsic permeability k=5.0E-20 m^2 and air entry value (5 MPa, α=0.002).

Thermal conductivity of EBS

Figure 2.13 shows the reported thermal conductivities of Bentonite block, Bentonite pellets and Sand-Bentonite mixture (Gaus et al., 2014). With the increase in saturation degree, the thermal conductivity of these clayey soils will grow accordingly. The regressed fitting curves are shown in Fig. 2.13b, which are used as model input parameters in the following simulations.

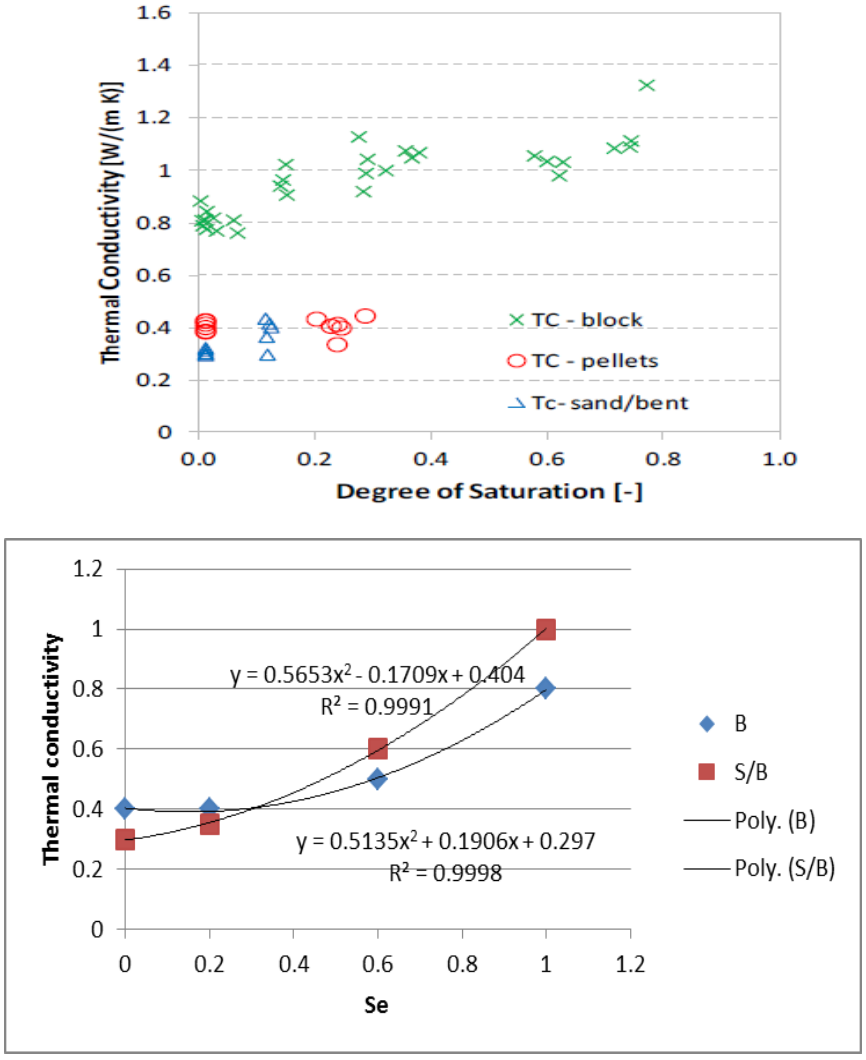

Figure 2.13 Thermal conductivity of EBS materials: the experimental results (a) and regressed functions for parametric input (b)

4.3 Boundary conditions for field case simulation

Heating source

The heater for the HE-E test was powered by electric devices, which was controlled by power for the first 365 days, and then controlled by temperature targeted at 140 ^{o}C on the heater surface for the remaining time. Figure 2.13 displays the recorded power evolution with heating duration for both sections. Figure 2.14 shows the recorded temperature evolution on heater surface for S/B section. It is noted that non-uniform temperature is observed on the surface of the heaters. For example Figure 2.14 shows the range of temperature observed on the surface of the heater in the S/B section. The maximum value is observed at the bottom while the minimum value is observed at the top. This is due to the fact that the bentonite block at the bottom of the heater has a lower thermal conductivity than the one of the S/B.

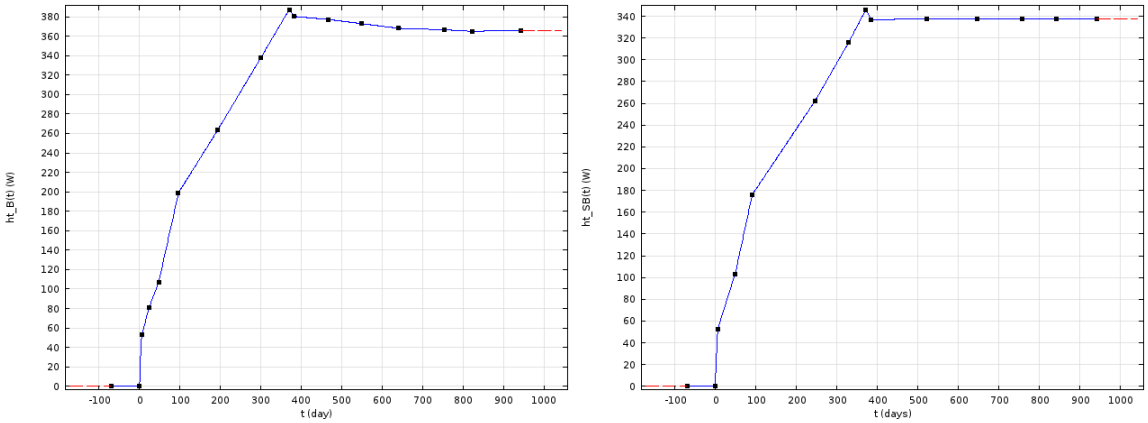

Figure 2.14a Heating power as recorded during the test for Bentonite (left) and Sand-Bentonite mixture (right)

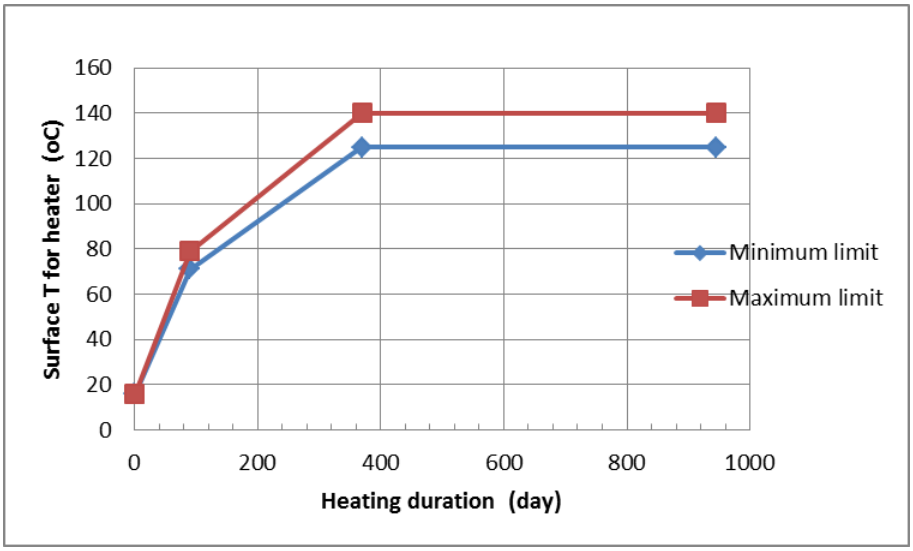

Figure 2.14b Temperature historical profile of the heater surface for the S/B section

4.4 Modelling strategy

Three steps representative of corresponding engineering measures are taken into account in our modelling works, i.e. excavation followed by partial de-saturation (10 years), emplacement (70 days) and heating (3 years). The following parts are illustrated in the same sequences in consistence with the experimental steps.

- Excavation and partial de-saturation: The boundary load on the tunnel surface was gradually removed in terms of a time-dependent loading function. Pore pressure on the tunnel surface was assumed to be the initial pore pressure for the whole analysis zone, and then gradually reduced to the value equivalent to RH=95%.
- Emplacement: The elements for EBS materials were activated in this step to simulate the emplacement inside the tunnel. Fine meshes were made to improve numerical convergence and precision. Initial conditions for the EBS materials involve the matric suction estimation and coupling scheme (e.g. volumetric strain is excluded from coupling for the unsaturated EBS, but compressibility of porous matrix is adjusted to reflect the coupling effect.). Thermal field is not considered in this step due to the isothermal condition.
- Heating: In this stage, the thermal field is activated for consideration. The fluid flux equation for the EBS material is modified to show the thermal diffusion process. The boundary condition for the heater-EBS interface is described by thermal flux in terms of power input. The evolution of key variables like relative humidity, temperature, and pressure are recorded with elapsed time at monitoring points. The heating lasted for 960 days until January 2014.
- The simulation was also extended into long-term re-saturation (11,000 years). The heating power is hypothesized to be shut down after a certain period of time (8 years in this study). The long-term evolution of moisture and temperature during the cooling period was predicted up to the time when full resaturation is achieved.

Table 2.3 Initial conditions for the excavation of OPA host rock

Variable	Value	Unit
Initial conditions for OPA host rock		
T	15.75	^{o}C
RH	100	%
p	1.0	MPa
$\sigma_x\sigma_y\sigma_z$	-2.2, -4.3, -6.5	MPa
Retention curve-Van Genuchten		
α	5.0E-4	1/m
n	1.67	
l	2	
Boundary conditions for tunnel excavation		
RH	99.5	%
p (in pore space)	-0.668	MPa
p (in open space)	0.10	MPa

Table 3 shows the initial and boundary conditions for the excavation of micro tunnel in OPA host rock at the Mont Terri site. The diameter of the micro tunnel is controlled at 0.65 m. Relative humidity (RH) was maintained at a level of RH≥0.995 for the post-excavation period up to 10 years in length. The humidity sensors installed in several monitoring sections show nearly saturated state with stable pore pressure distribution in the host rock (Nagra NAB 14-53).

4.5 Results and Discussions

Excavation induced desaturation

Figure 2.15 shows the distribution of pore pressure after 10 years after tunnel excavation. The enlarged graph shows the anisotropic pattern of the pore pressure distribution. This is due to the anisotropic permeability of the OPA host rock with respect to the existence of the inclined bedding plane.

Figure 2.16 shows results of effective saturation 10 years after the excavation. It is found that the unsaturated zone is mainly restrained in the thin layer of EDZ, due to its higher permeability and lower air entry value. The EDZ actually serves as a buffer zone to prevent the OPA pressure from being dissipated quickly to get equilibrated with the pressure in the EBS. Figure 2.17 clearly demonstrates the above effect. As shown in Fig. 2.17(b), the pore pressure profile seems much steeper in EDZ than that in the host rock. The same phenomenon applies to the effective saturation as shown in Fig. 2.17(c), where S_e varies from 0.99 on the EDZ-OPA interface rapidly to a low value at 0.60 on the tunnel surface.

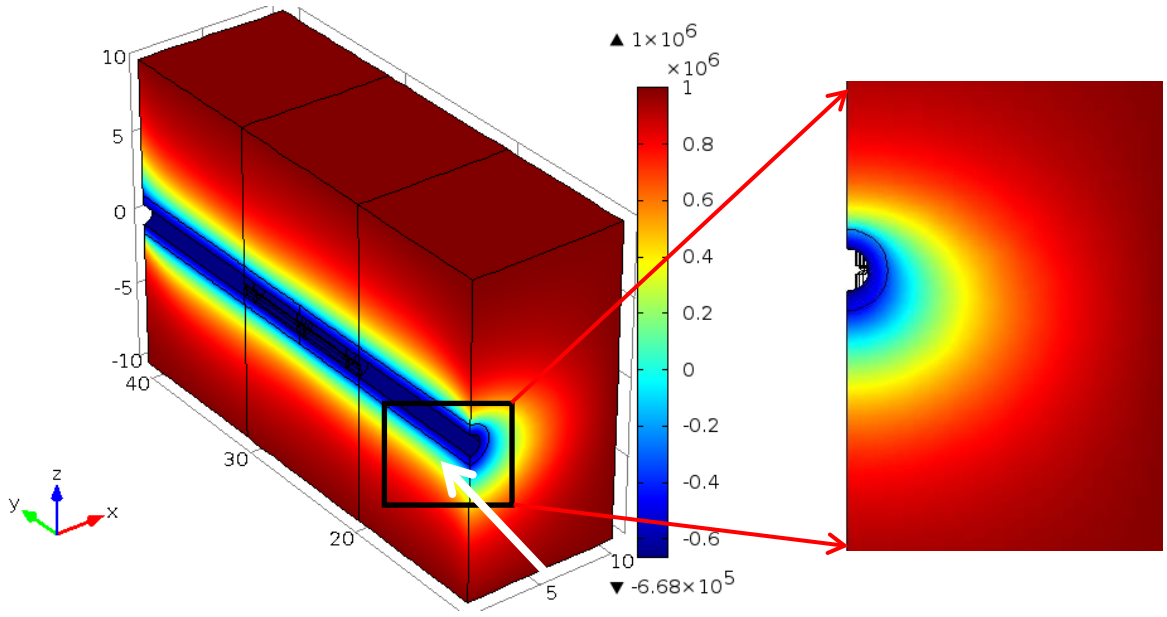

Figure 2.15 Contour plotting of pore pressure 10 years after excavation

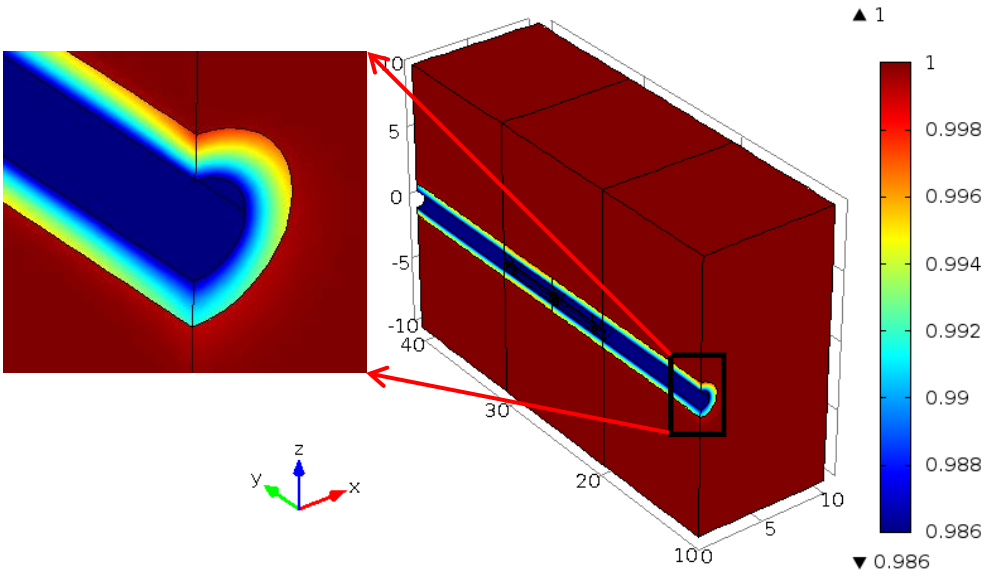

Figure 2.16 Contour plotting of effective saturation degree (Se) 10 years after excavation

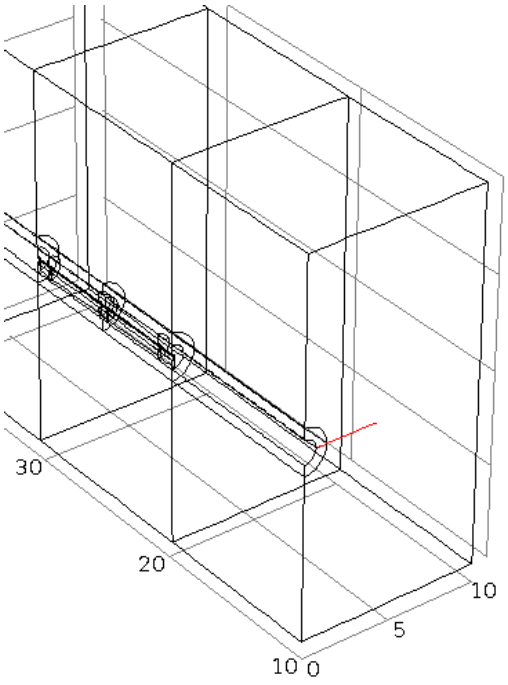

(a)

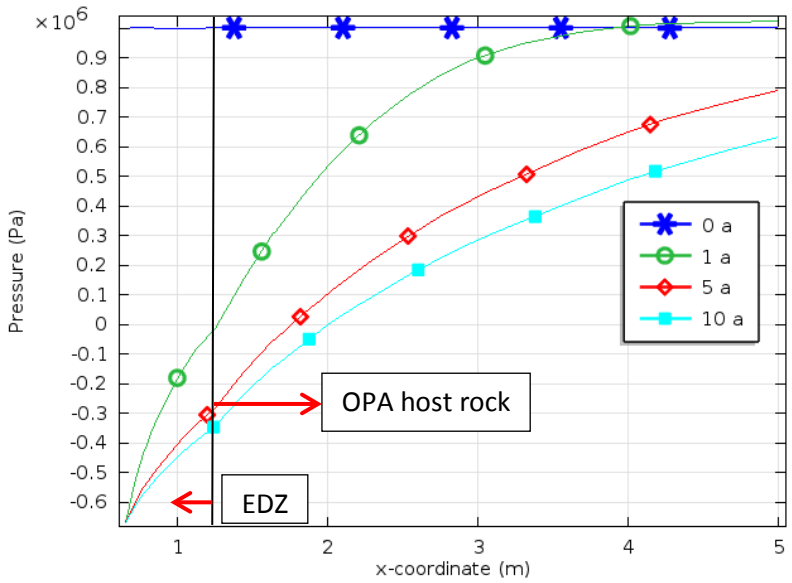

(b)

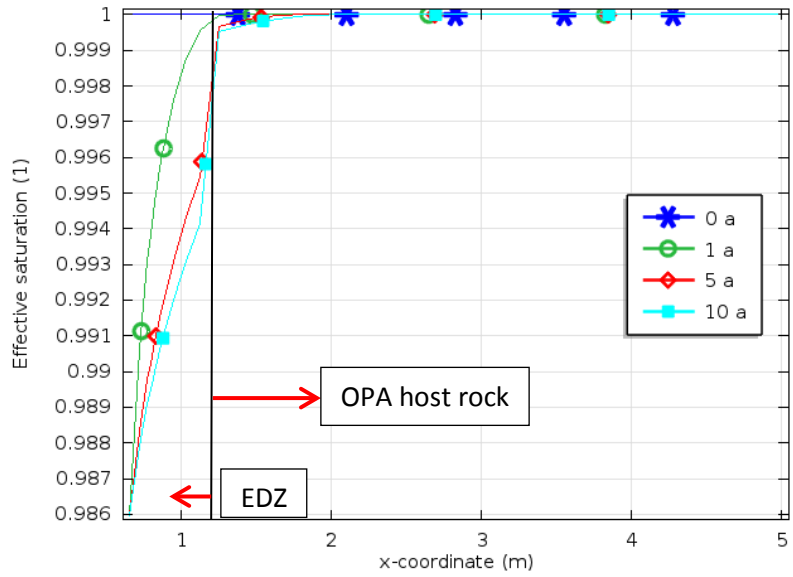

(c)

Figure 2.17 Evolution of variables along the X-axis cut line at Z=0 (a) location of the cutline, (b) pore pressure profile, (c) effective saturation profile

Emplacement of EBS induced re-equilibration in saturation

Emplacing EBS materials in situ takes a short period of time. It was reported (Villar et al., 2012) that no or very limited effort in compaction was needed for the installation. A number of sensors for temperature, relative humidity and pore pressure were installed in the pre-drilled monitoring holes in

the host rock and within the EBS. During this period of time, no results are available for model calibration. We briefly present here the behavior of some parameters obtained in our modelling.

Two cut-lines are created across the EDZ and the intact host rock in the X-axis direction at Z=0 m as shown in Fig. 2.18. The evolutions of effective saturation and pore pressure near the B and S/B sections are shown in Fig. 2.19 and Fig. 2.20, respectively. Throughout the emplacement time, no obvious change in these parameters is observed, suggesting that hydraulic-mechanical interactions are not obvious between the EBS and the host rock under the isothermal experimental conditions. The modelling of this step provides a stable and equilibrium state for the subsequent heating test.

Traces of difference between B and S/B are observed in terms of RH profile inside the EBS zone. Comparing Fig. 2.19(a) and Fig. 2.20(a) it is found that the S_e inside Sand/Bentonite mixed soil is not evenly distributed as that inside Bentonite pellets. The S/B EBS seems to have a uniform RH value for regions R<0.65 m, but turns out to show a very sharp increase in value for regions at R=0.65m. This un-equilibrated initialization in the EDZ domain may influence the RH evolution for the later heating stage.

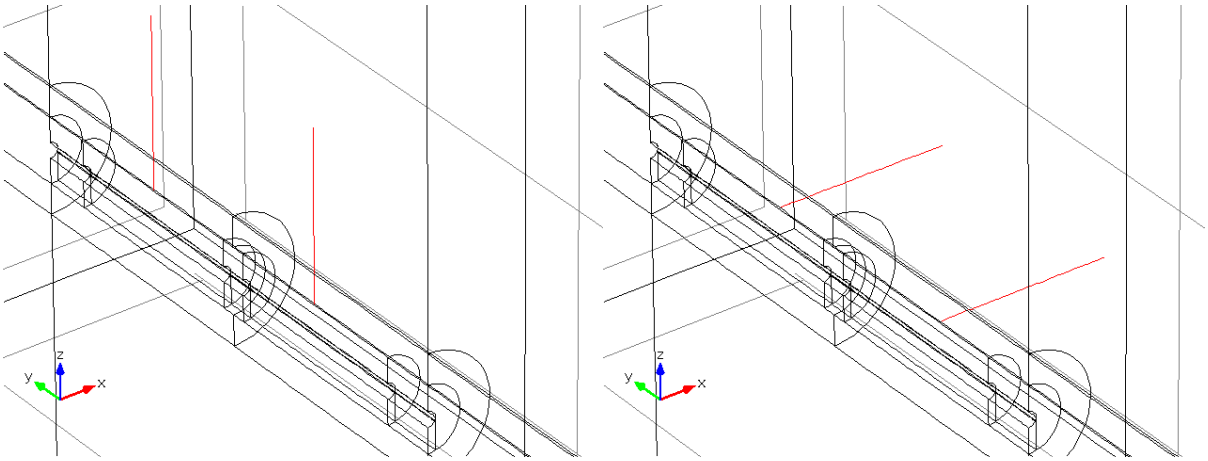

Figure 2.18 Location of the vertical (left) and horizontal (right) cutlines for results plotting about the host rock after emplacing EBS in the µtunnel

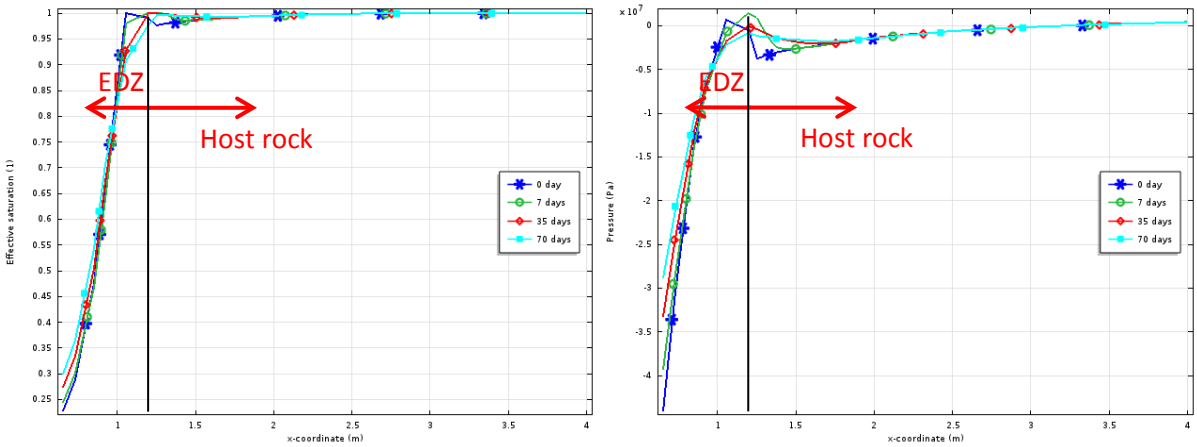

Figure 2.19 Evolution of effective saturation (left) and pore pressure(right) for B after 70 days of emplacement of EBS

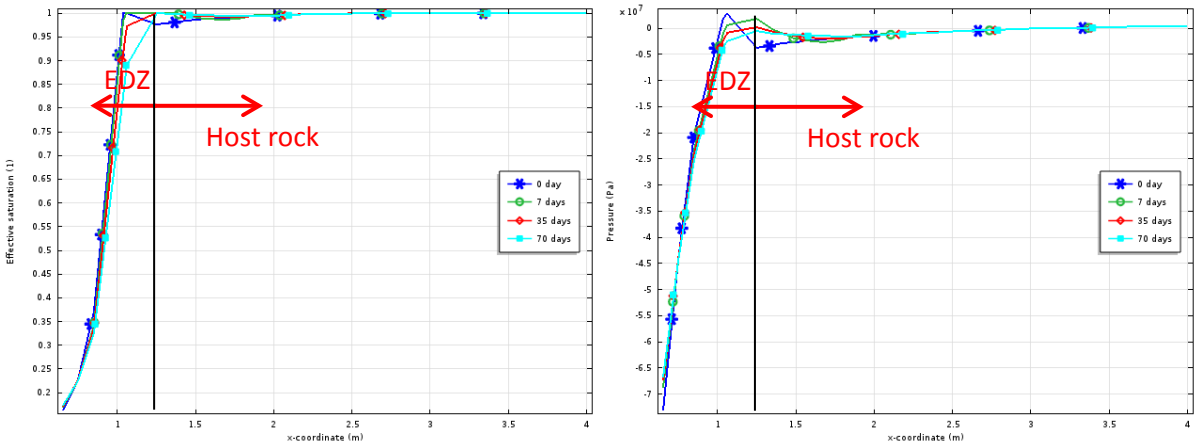

Figure 2.20 Evolution of effective saturation (left) and pore pressure(right) for S/B after 70 days of emplacement of EBS

Heating induced THM coupling phenomena

Figure 2.21 shows two typical sections of host rock with monitoring sensors that are respectively located at the middle point of each EBS section. Parameters including pore pressure and temperature are continuously recorded since the heating was started. Figure 2.22 shows the nomenclature and spatial location of sensors inside the engineered barrier. In the EBS relative humidity and temperature are monitored throughout the course of the experiment. As the model is symmetric across the vertical plane along the axis of the tunnel, the data of points at 9 o'clock will be represented by those at 3 o'clock. These experimental data will be used in the following comparative studies with our modelling work.

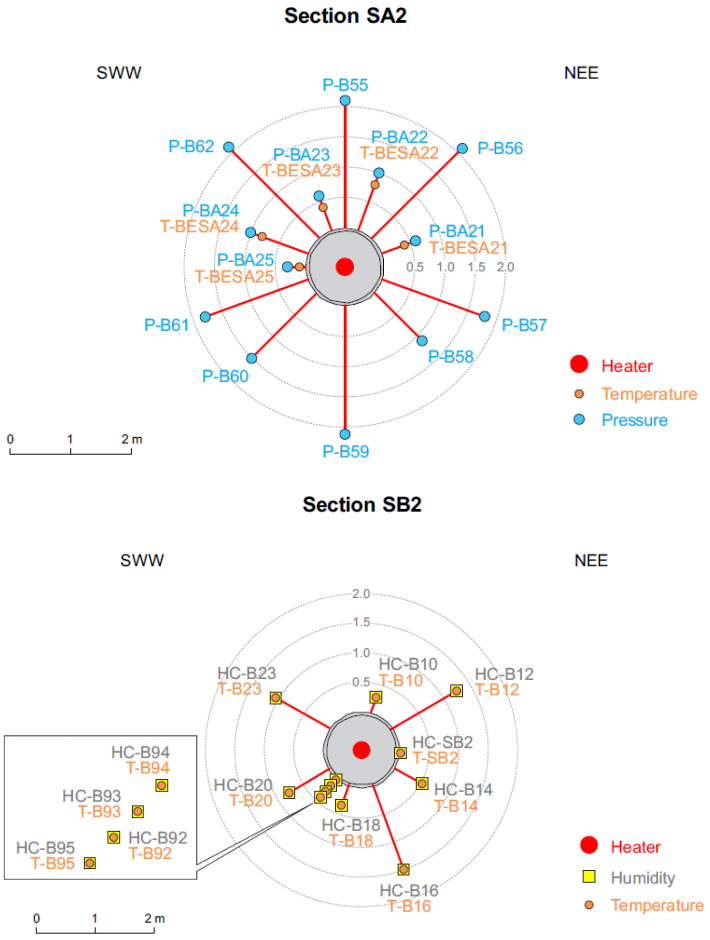

Figure 2.21 Sensor types and locations in Section SA2 and SB2 (distances from the microtunnel wall)

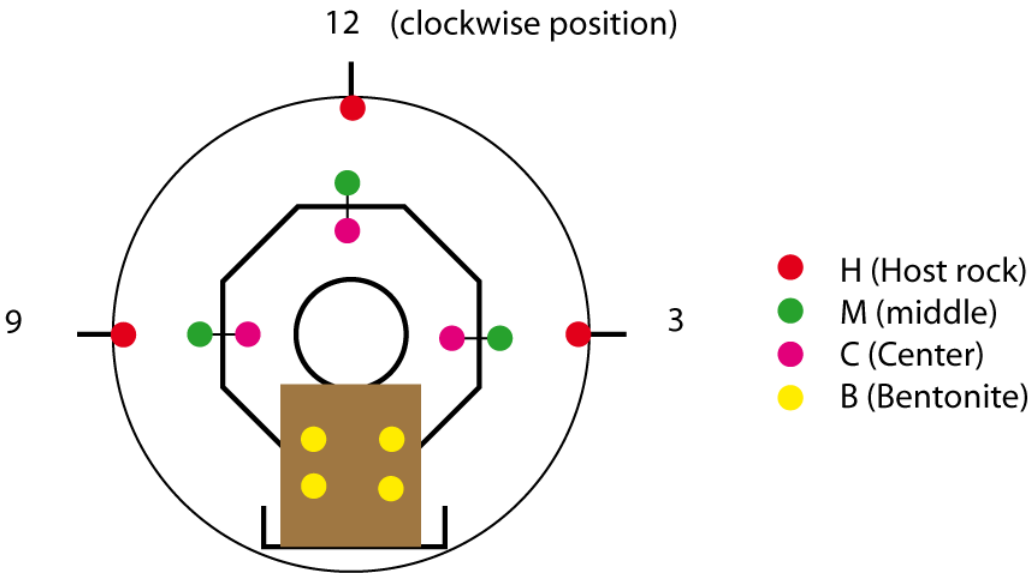

Figure 2.22 Location of temperature and relative humidity sensors installed inside EBS body

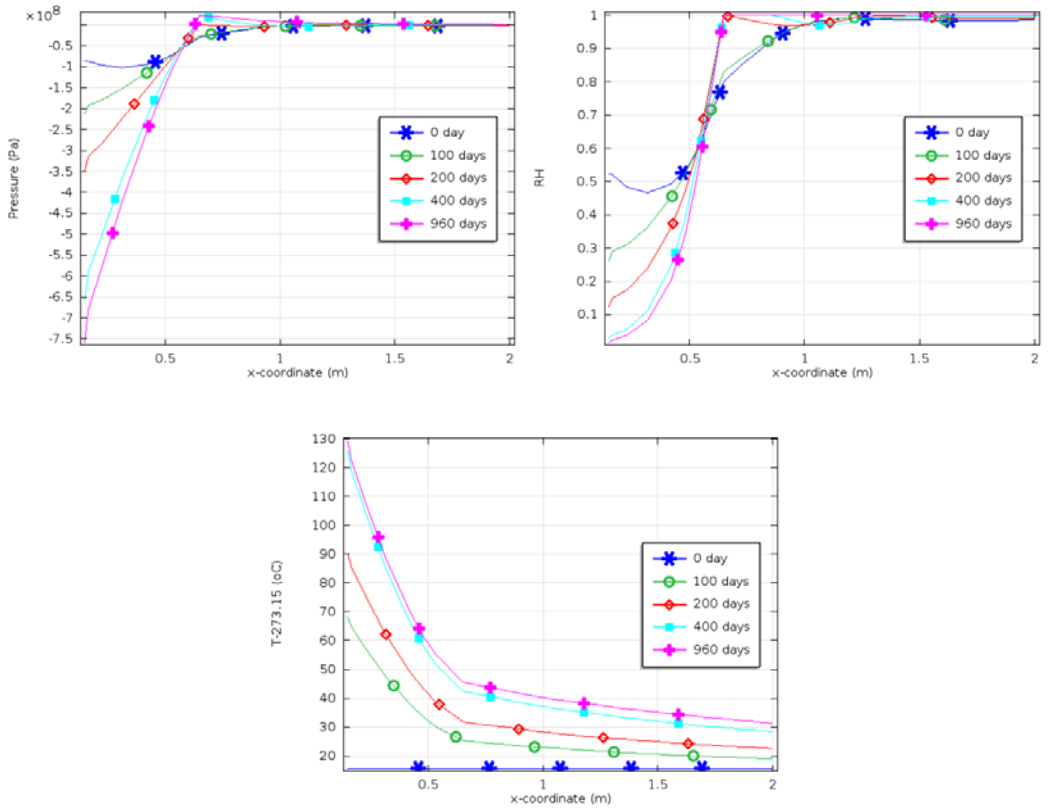

Figure 2.23 Distribution of various variables along the horizontal cut line across S/B section

Figures 23-26 show the time-dependent variation of various variables(e.g. pore pressure, RH and temperature) along the representative cut lines across the tunnel axis. It is shown that heating desiccates the EBS from the vicinity of the heater surface, causing pore pressure to decrease to -750 – -850 MPa, corresponding to RH of S/B at 0.05. Heating effects are most pronounced within 400 days; afterwards, all variables become stable with elapsing time. The temperature rise in the surrounding host rock is limited to less than 46 ^{o}C. Comparing the temperature profiles in the horizontal with that in the vertical direction, it is found that temperature is a bit higher in former at the same radial distance from the tunnel center. This is due to the effect of bedding in the host rock.

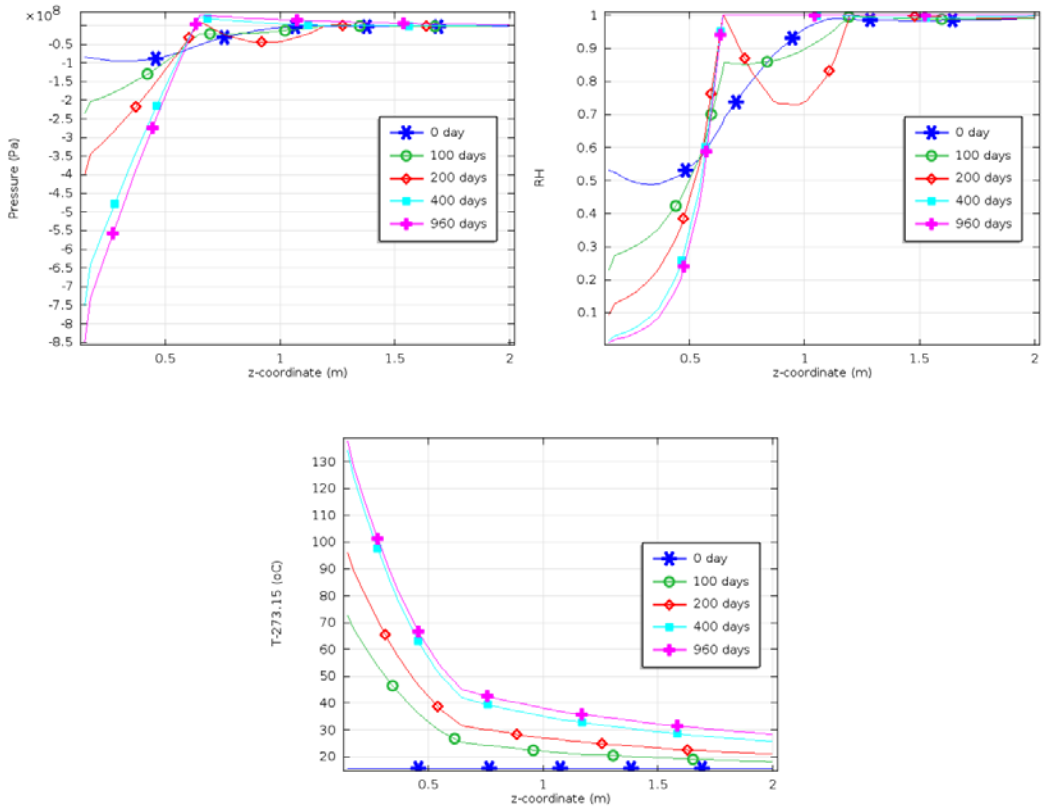

Figure 2.24 Distribution of various variables along the vertical cut line across S/B section

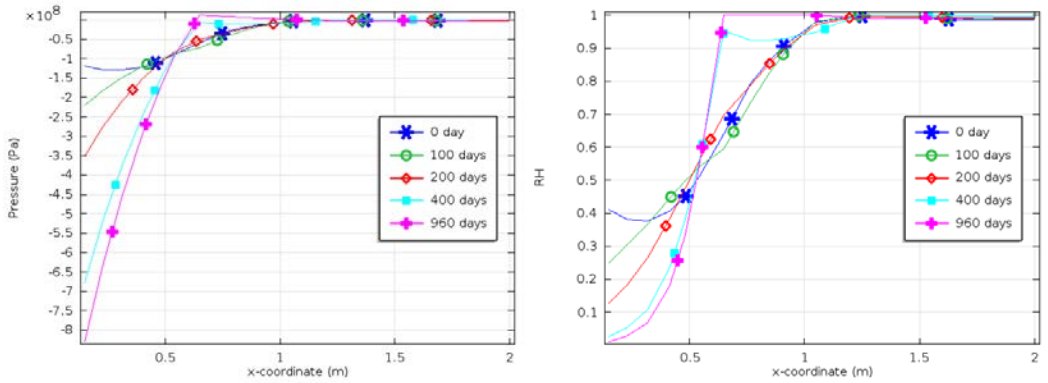

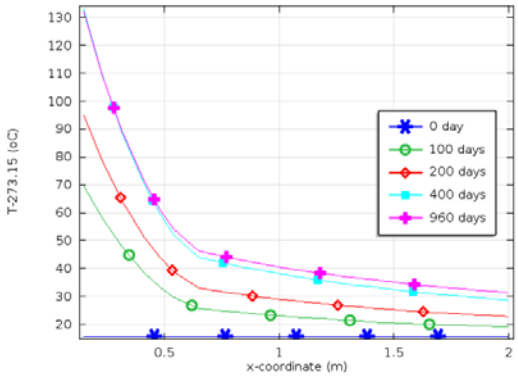

Figure 2.25 Distribution of various variables along the horizontal cut line across B section

Figures 25-26 show the modelling results for p, RH and T for the B section. The minimum pore pressure in EBS reaches as low as -800 – -950 MPa near the heater. Other parameters are similar in trend to those of S/B section. Temperature declines quickly from the heater surface to the EBS/OPA interface, and turns to change much more gradually in the host rock. More detailed data comparison and analysis will be provided next.

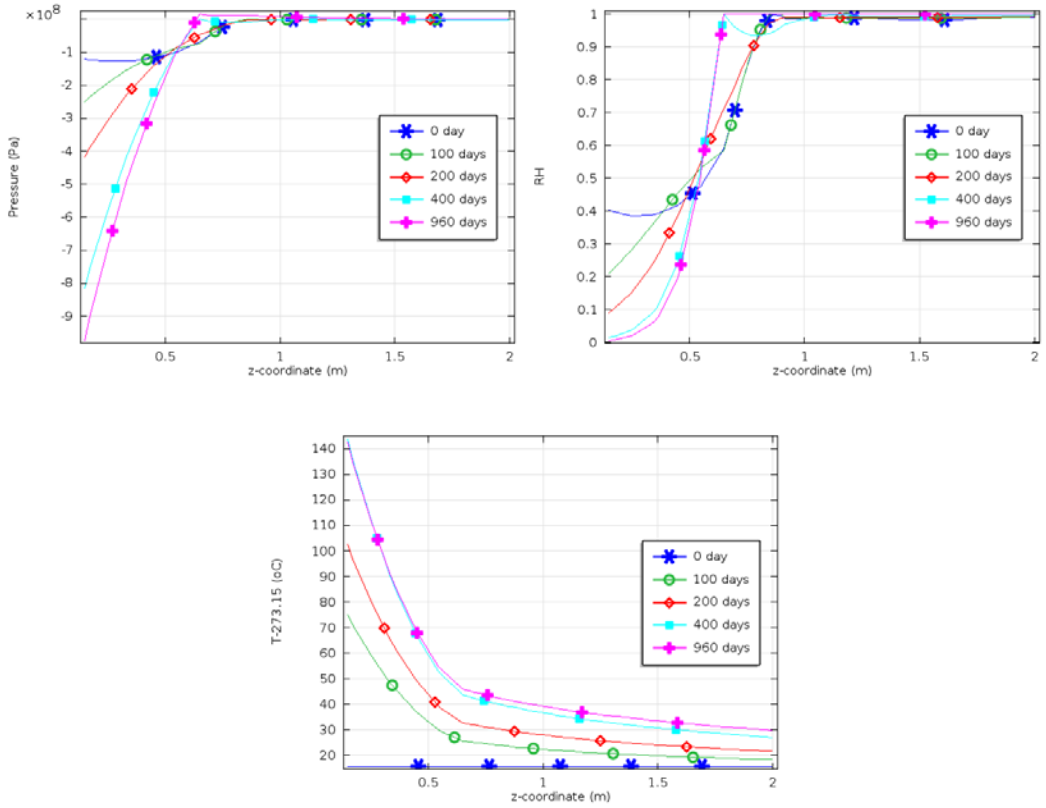

Figure 2.26 Distribution of various variables along the vertical cut line across B section

Plotting of isosurface for effective saturation

Figure 2.27 shows the isosurface plotting for the effective saturation S_e at the end of the heating test. It is shown that the EBS materials have the smallest S_e at about 0.10 while the Bentonite block and concrete plug have similar values in S_e to the initial condition. This is due to the fact that the model neglects the process of vapour transport in the B block and plugs. The S_e value in the EDZ are found to be mostly higher than 0.9, and only a thin layer of EDZ in proximity of the EBS shows a sign of desaturation with S_e<0.9. The two EBS materials, i.e. the S and S/B section, show increase in S_e in the outward radial direction. This phenomenon can be explained by thermally induced vapour migration from the heater followed by condensation at cooler temperature, combined with water migration from the host rock.

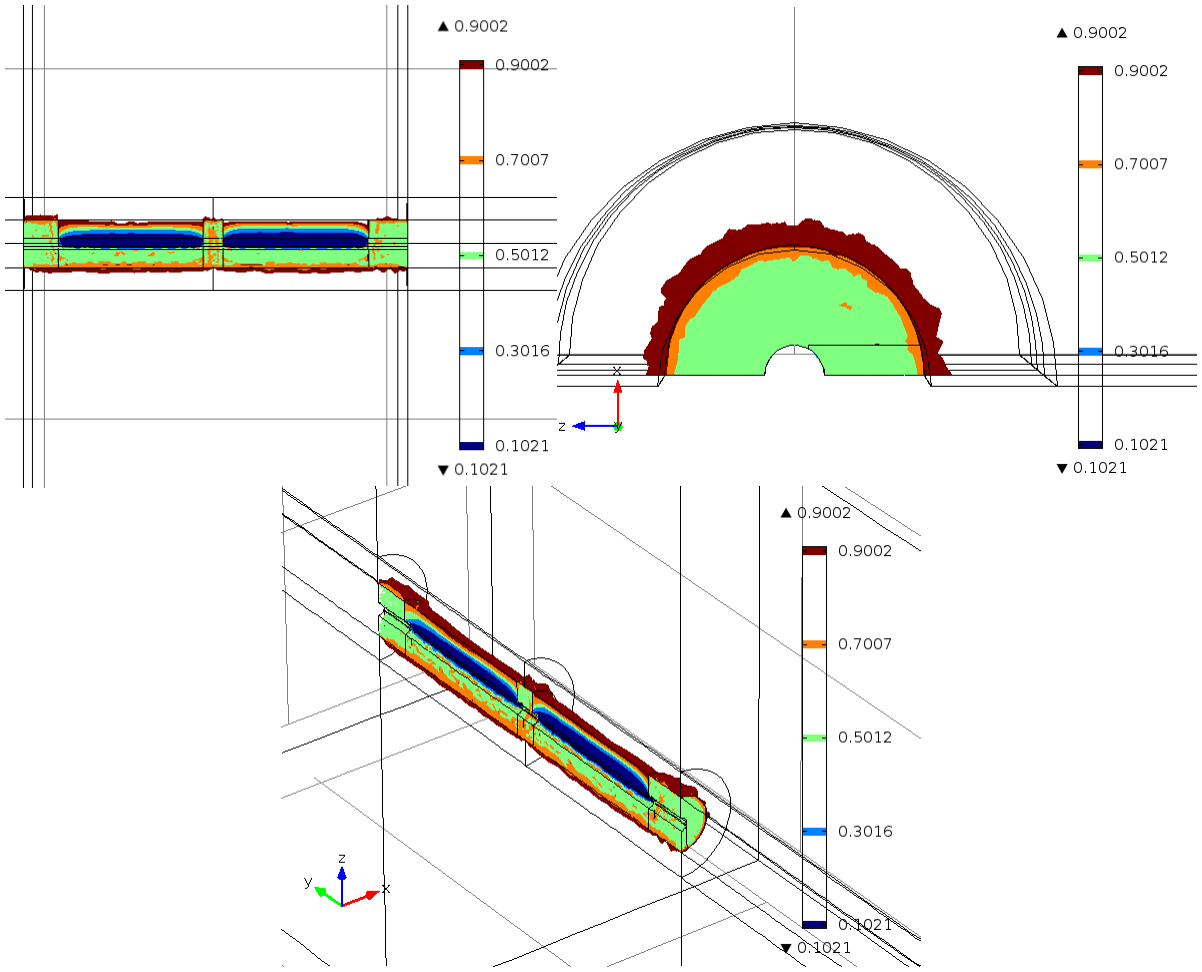

Figure 2.27 Isosurface plotting of effective saturation at the end of heating test

Contour plotting for temperature

Figure 2.28 shows the contour plotting of temperature that shows the effects of anisotropy in the host rock due to bedding. Inside the EBS material, temperature mainly concentrates near the heater, and declines quickly to an average level of less than 45 ^{o}C. This comes from the difference in thermal conductivity between EBS and host rock. The EBS is less thermally conductive compared to the intact

clay rock, and acts as a heat insulator resulting in higher temperature distribution in EBS. The disturbance on in situ temperature field reaches 6-7 meters in the radial direction. In the direction of the tunnel axis, the temperature perturbation appears to be restrained within 1.5 m from the ends of the heaters.

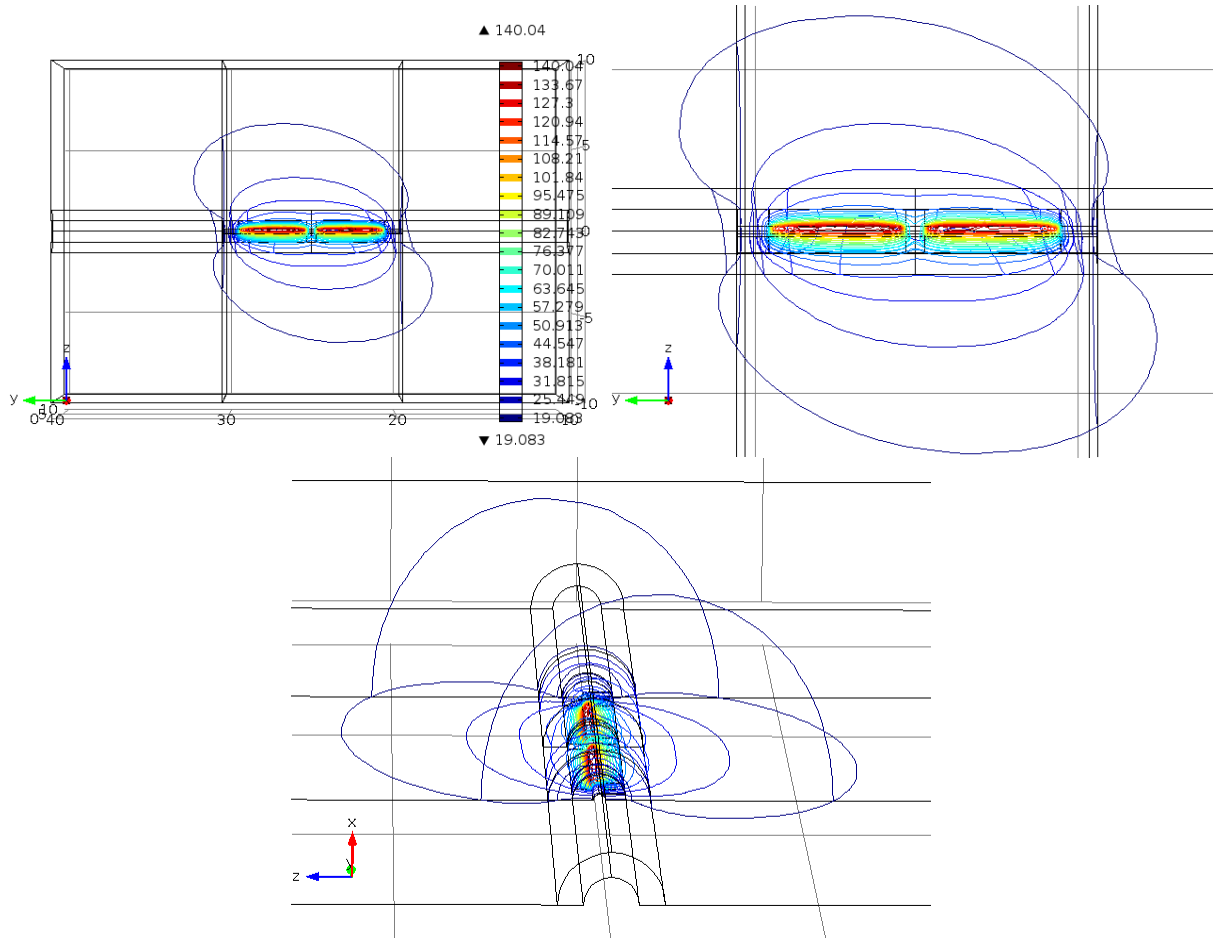

Figure 2.28 Contour plotting of temperature at the end of the heating test

Surface plotting for relative humidity and temperature

Figure 2.29 shows the vertical surface plotting of variables including relative humidity and temperature across the tunnel axis. The current simulation does not consider vapour transport in Bentonite blocks and concrete plugs, therefore no variation of RH in these components is observed in Fig. 2.29a. The RH in EBS increases from extremely dry state (RH=0.2%) on the heater surface to nearly saturated value (RH≈1.0) on the EBS-host rock interface. Figure 2.29b shows the temperature profile on the same cross section as Fig. 2.29a. Maximum temperature is found to be on the Bentonite-heater interface rather than Bentonite block-heater interface, which is attributed to the higher thermal conductivity of the latter. Temperature is found to quickly decline to about 40 ^{o}C in the host rock, suggesting a rapid thermal dissipation in OPA.

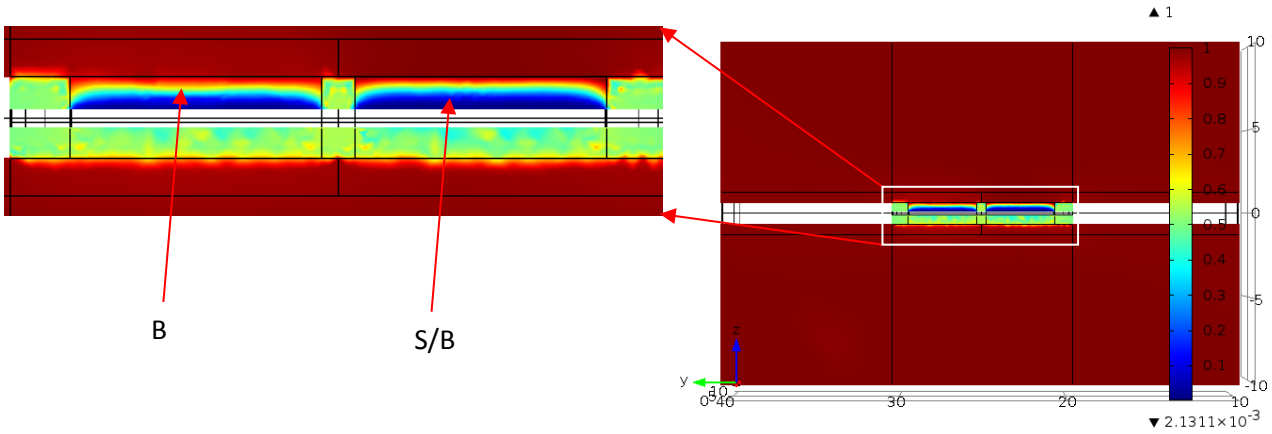

(a)

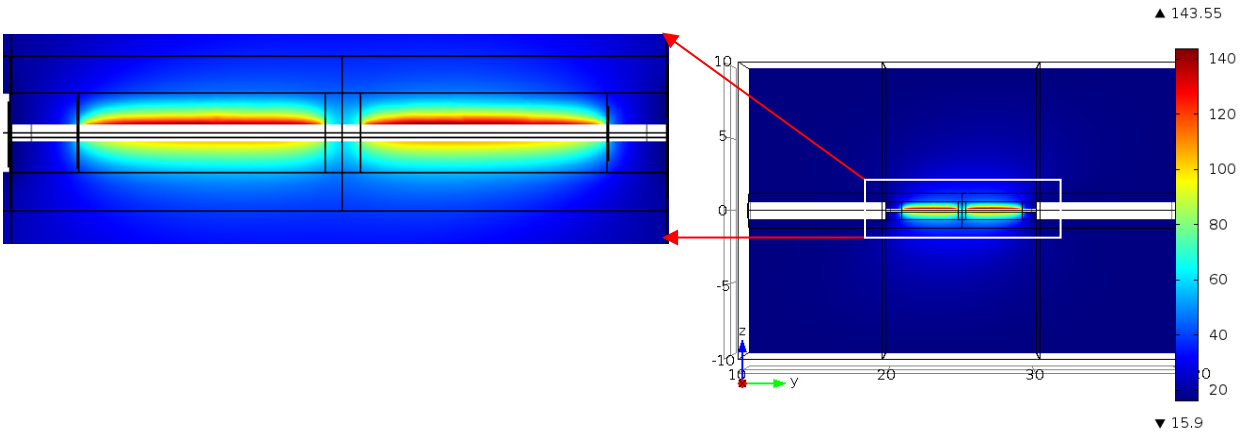

(b)

Figure 2.29 Surface plotting of RH (a) and T (b) for the Y-Z plane across the tunnel axis at the end of the heating test

Comparason with test data

Temperature data for S/B

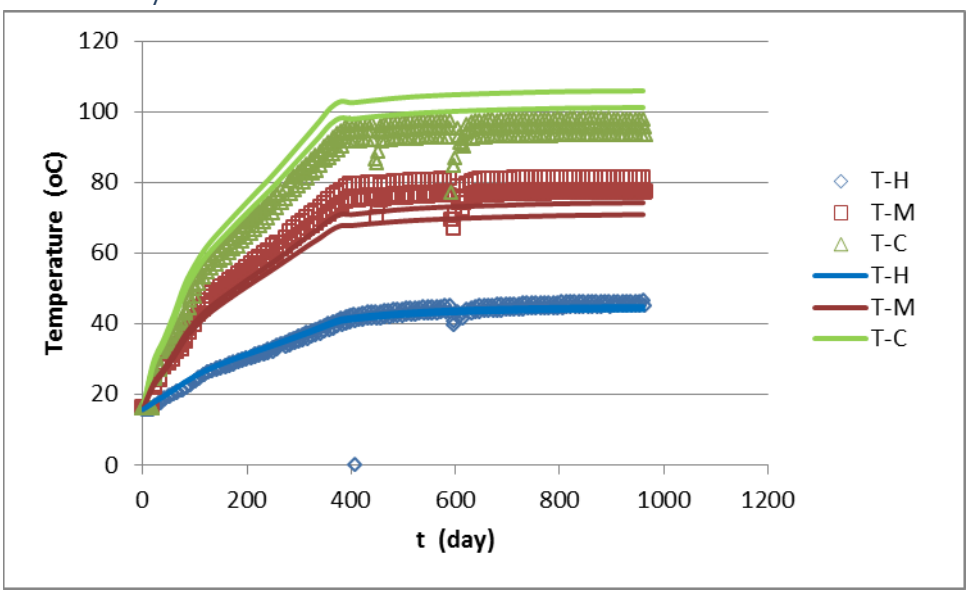

Figure 2.30 Temperature evolution for monitoring points inside EBS at S/B section

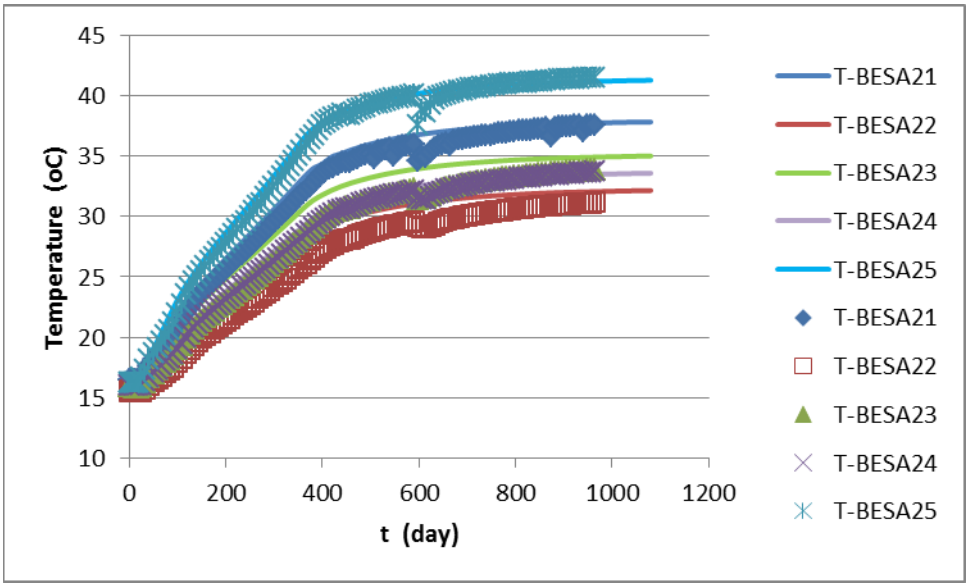

Figure 2.31 Temperature evolution for monitoring points in host rock (T-SA2) at S/B section

Figure 2.30 shows the evolution of temperature at the monitoring sensors inside the S/B EBS. The experimental results are well reproduced by our modelling, particularly with respect to the points at the central position (T-C) and at the interface (T-H) between EBS and host rock. Figure 2.31 shows the comparison between modelling and test data for the monitoring sensors located in the host rock at S/B

section. The good agreement between modelling and test data provides confidence that the THM coupled models as well as the parametric sets are representative of S/B material.

Relative humidity data for S/B

Figure 2.32 shows the RH comparison between test data and modelling results for EBS in S/B section with elapsing time. The simulated results are in good agreement with the experimental data for monitoring points at EBS-host rock interface, middle, and the central position of the EBS. The residual RH values are well reproduced by our modelling, which suggests the viability of the vapour diffusion parameters as applied in the modelling. With the consideration of the EDZ surrounding the EBS, the RH at the interface (H) can be well reproduced by the modelling. The EDZ has higher air entry value compared to the intact host rock, which allows a reasonably high level of RH (83-92.5%) to develop in the OPL rock. Simulation cases without EDZ were found to give discrepancy in RH against the test data, which can be improved either by adjusting SWCC function for host rock or by supplementing the highly permeable EDZ between EBS and host rock. Since the excavation induced damage zone is normally encountered in tunnelling of rocks, the hypothesis of its existence in our modelling is justifiable.

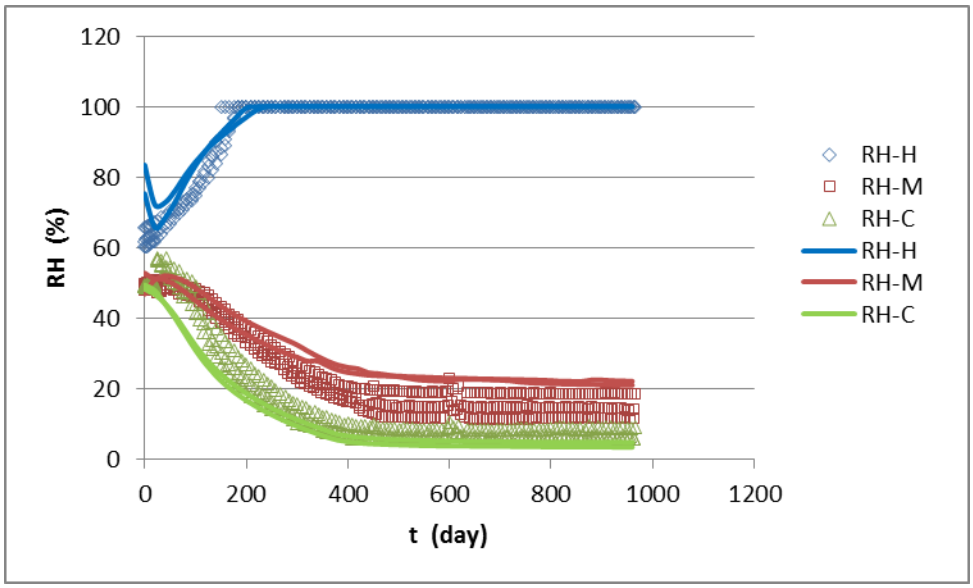

Figure 2.32 RH comparison for EBS material in S/B section

Temperature data for B

Figure 2.33 shows the modelling results of temperature vs test data. The modelling results are consistent with the monitoring results in most of the cases, particularly for the host rock-EBS interface. Results at the center (C) and middle (M) points are somewhat different from the test data. The temperature diffusion is closely coupled with the moisture transport. Therefore the success in reproducing the moisture profile lays a solid foundation for the fitting of the temperature profile. The authors referred to the Nagra report on the HE-E heating test and found that the modelling peers have the similar problem in best fitting the temperature at center and middle points.

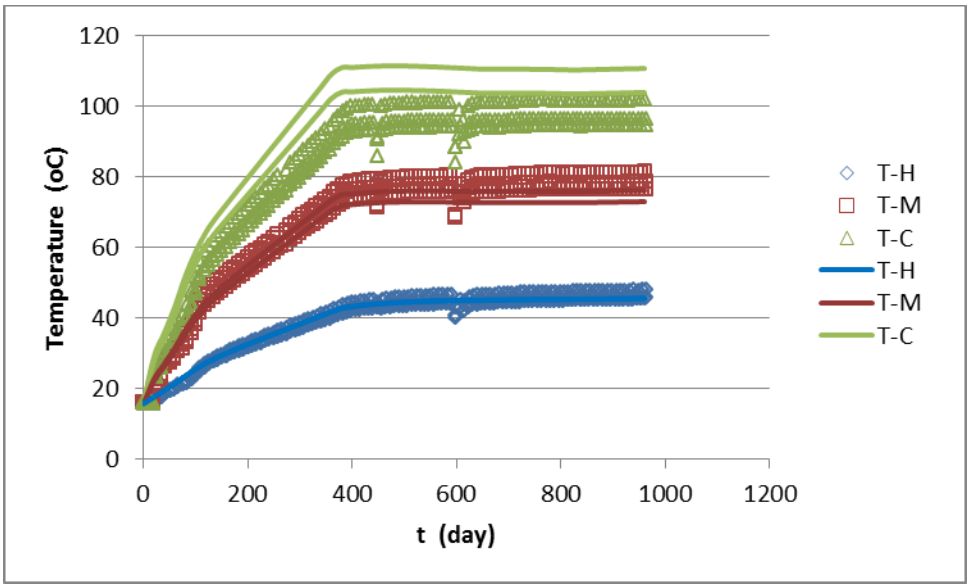

Figure 2.33 Temperature comparison for EBS material in B section

Figure 2.34 shows the temperature evolution curves for the B section in the host rock that has been intensively monitored in the field studies. The modelling results agree reasonably well with the experimental data. With the prolonged heating the temperature in the host rock changes accordingly. After being heated for 400 days, the source temperature was maintained at a stable level of 140 ^{o}C, which resulted in levelling off for the temperature evolution curve for all the monitoring points. Despite the good agreement for some points, e.g. T-B10 and T-B11, some discrepancy between the modelling and the test data is observed in Fig. 2.34b. Temperature profile appears to be consistent inside the EBS domain, except for the far field host rock domain. The thermal conductivity of the host rock as used in the simulation seems to overestimate the temperature value, and thus needs to be increased somewhat for a better agreement of the T profile.

Our modelling results generally overestimate the temperature profile for the host rock, except for the sensors at T-B92 -- T-B95 that are installed in the regions that are within 0.5 m from the tunnel surface, i.e. inside the EDZ zone (r=0.65 m as assumed in this study). At these locations the modelling results underestimate the temperature for most of the time. This may suggest that in the EDZ domain, thermal transport behaviour may differ from that in the intact host rock, and has to be addressed in the following simulating efforts in a certain forms that can reflect the variation in parameters.

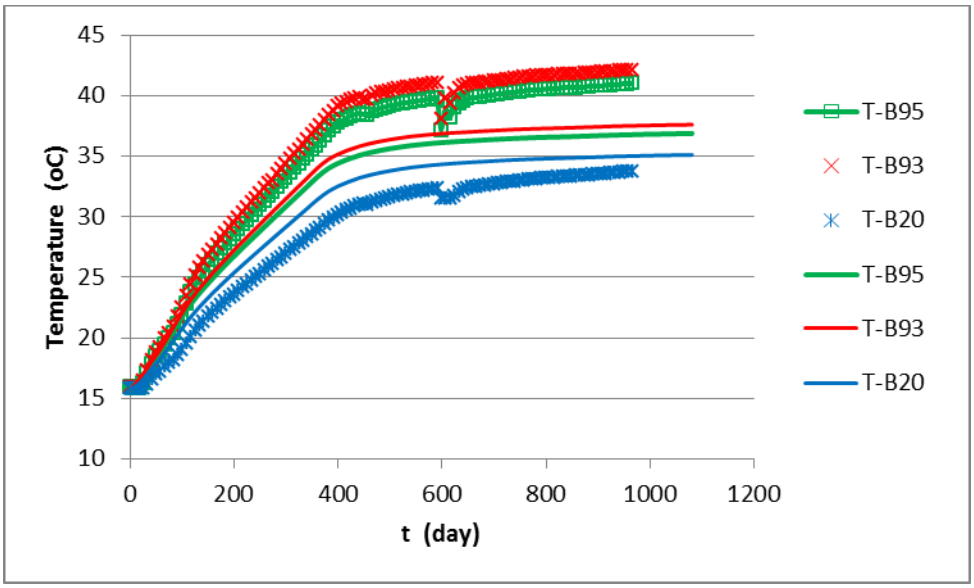

(a)

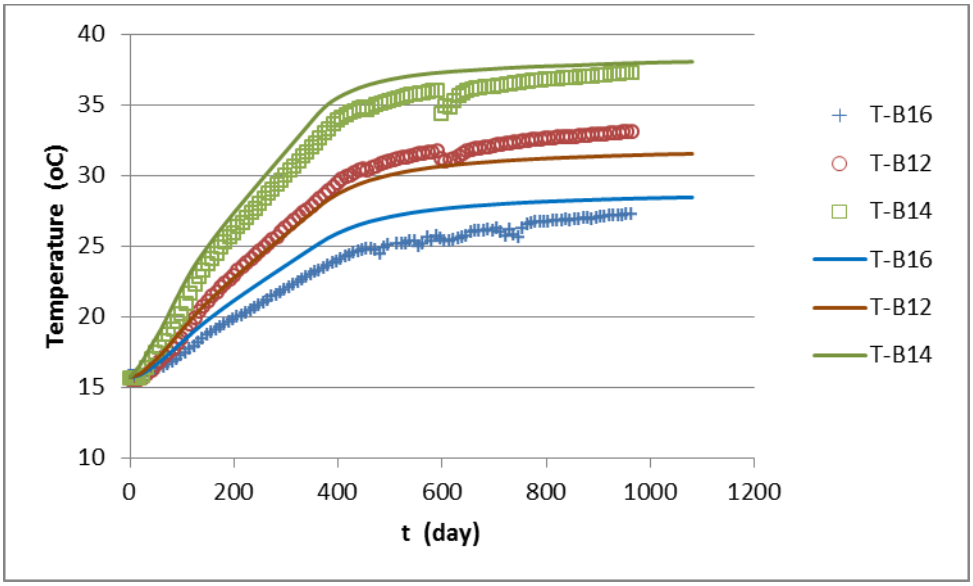

(b)

Figure 2.34 Results comparison for temperature sensors in host rock at T-SB2 profile around B section

Relative humidity data for B

Figure 2.35 shows the evolution of RH with time for both the modelling results and the test data. Similar to the case for S/B, good agreement is found for points at H, M and C locations. As compared to the S/B section, the RH at H increases much more slowly in the B section. Note that the resaturation of Bentonite at EBS-rock interface is governed by two factors, one is from vapour diffusions from EBS and the other is from fluid infiltration from the surrounding host rock. Therefore the permeability of EBS and host rock significantly influences the rate of resaturation. Bentonite pellets have a permeability value at

1E-21 m^2, 2 orders of magnitude less than S/B. Because the host rock has the same permeability for both B and S/B sections, therefore the diffusivity of vapours inside EBS dominates the resaturation process.

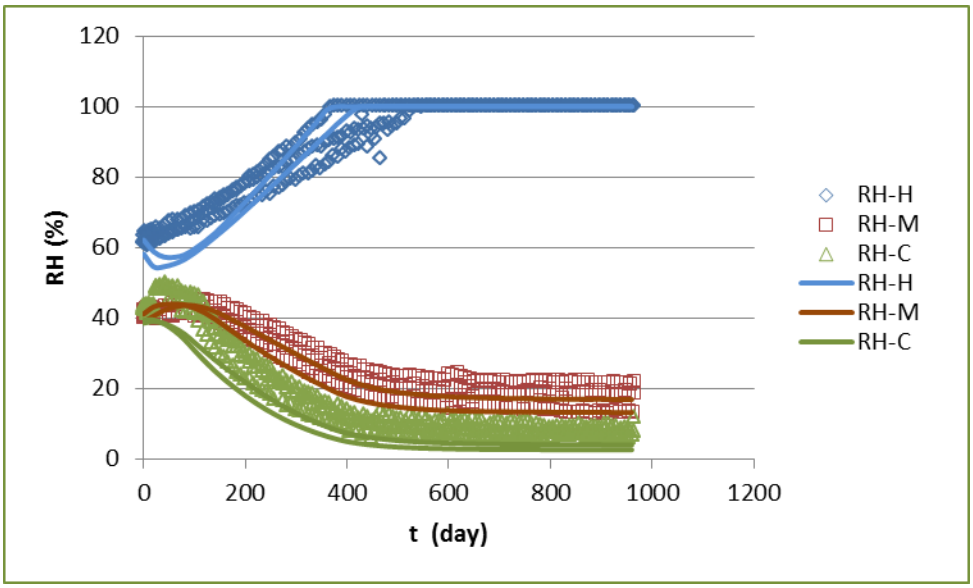

Figure 2.35 RH comparison for EBS material in B section

Pore pressure data

Figures 36 (a-b) show the thermal induced pore pressure response in the host rock for the S/B section. The monitoring points at P-B55, P-B56 and P-B62 are amongst the most sensitive positions that have the most obvious, swift and strong THM coupling behavior. These three monitoring points are located at 2.0 m away from the tunnel surface, and are all located vertically above the heater. For sensors P-B60 and P-B61 that are below the heater in vertical direction, although they are closer to the heater compared to the rest three sensors, no pressure increase was observed before 600 days, and only very limited amount of pressure enhancement effect appears after about 800 days of heating. The difference in pore pressure response is most likely attributable to the anisotropic nature of the host rock that is related to the presence of bedding planes.

Our modelling results confirm the gradually increasing trend of pore pressure accumulation during the early stage of heating. As for points at P-B55, P-B56 and P-B62, the modelling results of pore pressure are amongst the top three in magnitude, which is in good agreement with the experimental observation. The increment is about 500 kPa for these three monitoring points, which is consistent with the observed range of increment between 600 and 900 kPa. Gradual increases in pore pressure for the remaining two points are also demonstrated clearly in the first 600 days.

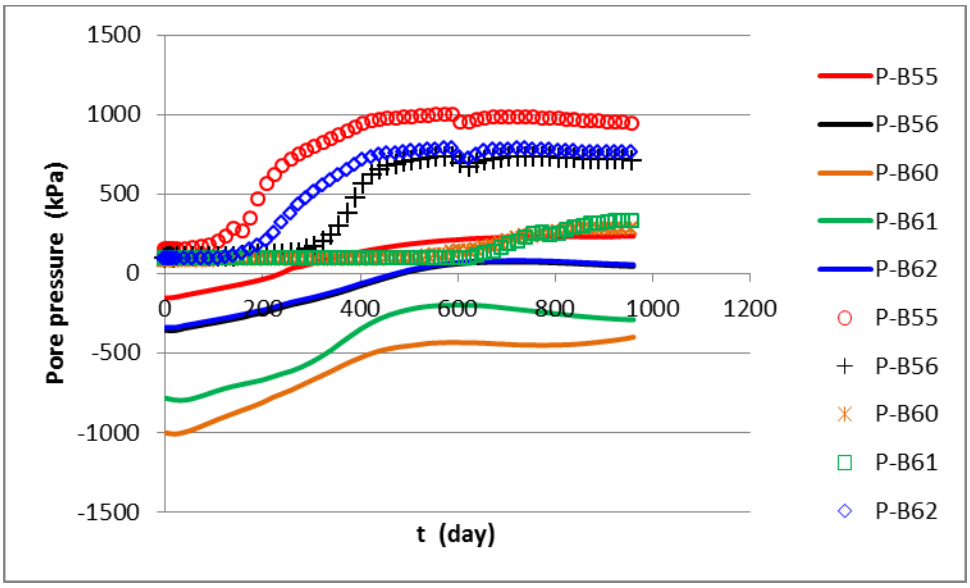
1500
1000
500
0
-500
-1000
-1500
0
200
400
600
800
1000
1200
Pore pressure (kPa)
t (day)
P-B55
P-B56
P-B60
P-B61
P-B62
P-B55
P-B56
P-B60
P-B61
P-B62

(a)

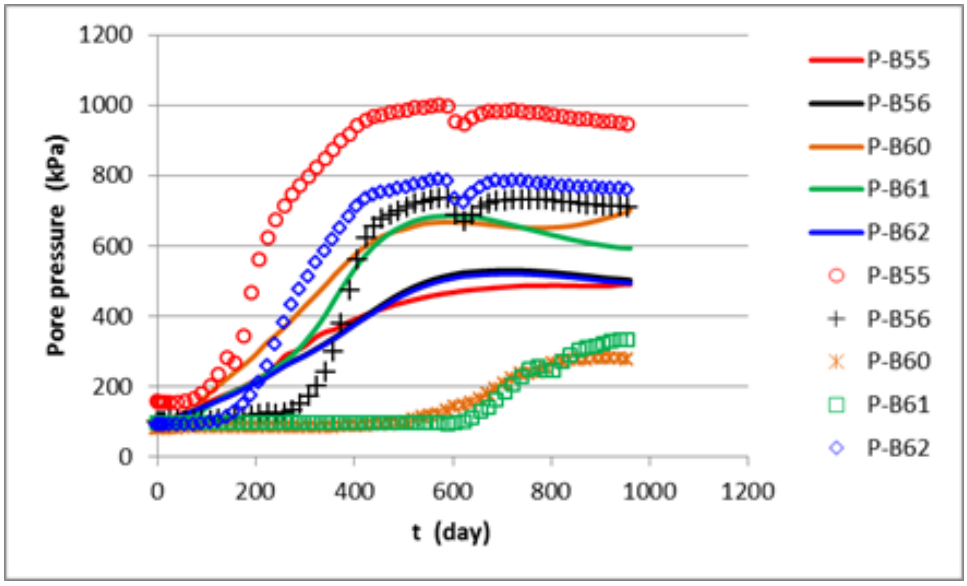
1200
1000
800
600
400
200
0
0
200
400
600
800
1000
1200
Pore pressure (kPa)
t (day)
P-B55
P-B56
P-B60
P-B61
P-B62
P-B55
P-B56
P-B60
P-B61
P-B62

(b)

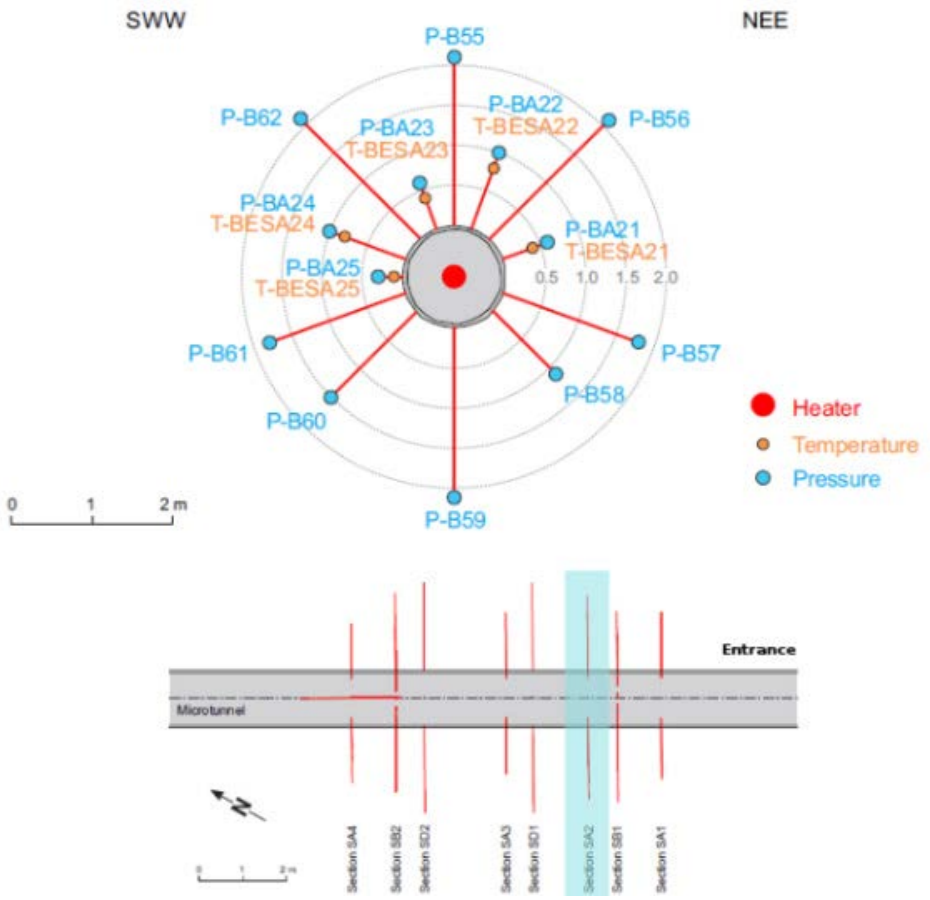

(c)

Figure 2.36 Pore pressure evolution (a), net increment of pore pressure (b) and locations (c) for monitoring points P55-P62 surrounding S/B section (scattered points are test data and solid lines are modelling results)

Relative humidity data for EDZ at S/B section

Figure 2.37 shows the evolution of relative humidity for sensors located in the EDZ domain. The modelling results agree with the test data in most of the ranges, clearly demonstrating the gradual increase of RH due to the re-saturation process with elapsing time. The time required for RH to reach fully saturated state ranges from 300 to 500 days for the modelling results, which seem to be a bit faster than the actual time of 400 to 550 days. By considering the enhancement in thermal-driven vapour diffusion, saturation of the EDZ and proximate host rock appear to be dominated by the water vapour coming from the EBS. Pore pressure evolution in the host rock increases steadily throughout the heating period, suggesting that there is a continuous source of water supply. This seems to originate from the heated EBS. Our previous modelling with constant value in thermal diffusivity does not result in steady increase in pore pressure, but rather in a sharp increase followed by a rapid decline when the temperature gradient stabilizes in the host rock. An elevated thermal diffusion coefficient can thus be related to the changing pattern of the pore pressure in the host rock.

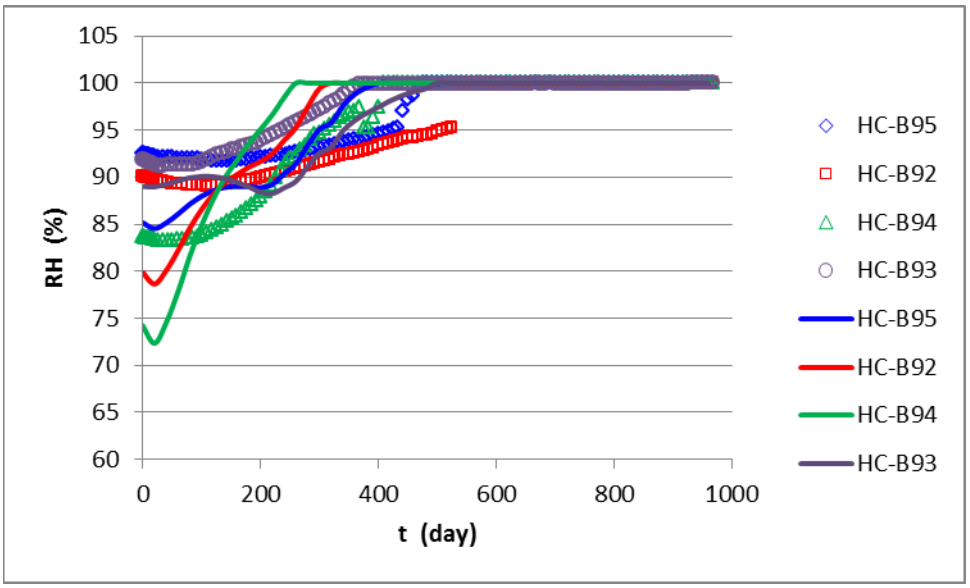

(a)

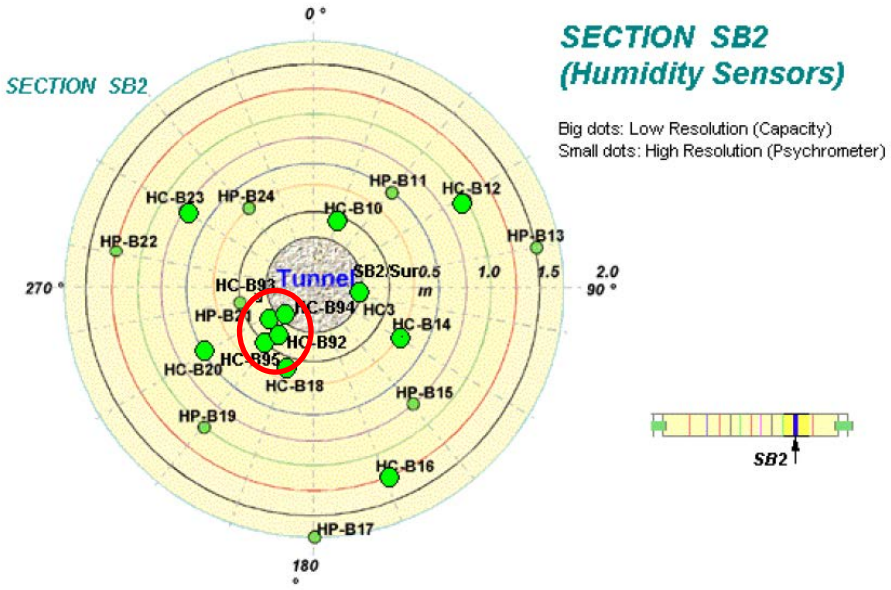

(b)

Figure 2.37 Relative humidity evolution in EDZ domain (a) and sensor locations (b) (Open symbols are test data and solid lines are modelling results)

Long-term resaturation estimation

Figures 14a and 14b show the modelling results of the long-term resaturation process that follows immediately the shutdown of heating source at 7.9 years. It is shown clearly that the temperature profile in the EBS declines rapidly to the background level at 15.75 °C. The moisture level quickly becomes equilibrated at RH=41% within 20 years of post-closure. Since the temperature gradient

diminishes, moisture migration may only be dominated by the pressure gradient. The resaturation is governed by the host rock as the source of pore fluid in the long-term period. The model predicts that complete saturation (>99.99%) of the EBS would be achieved in 11,000 years.

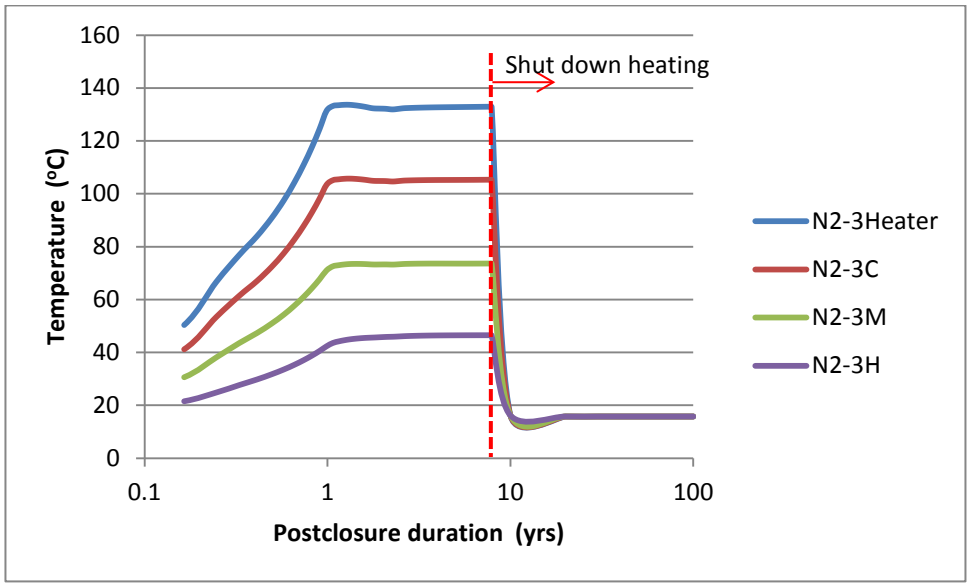

(a)

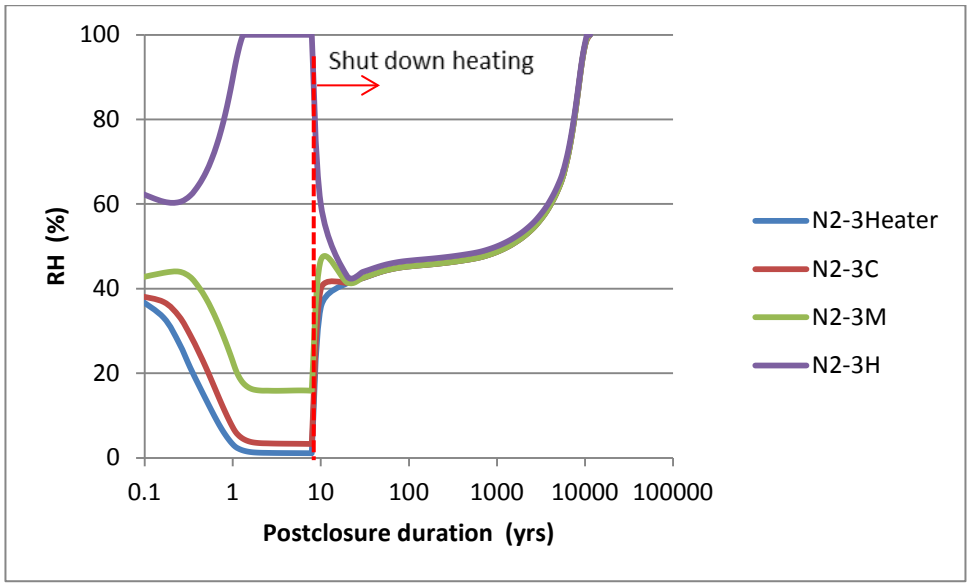

(b)

Figure 2.38 Evolution of (a) temperature and (b) relative humidity in the long-term period along radial direction for section N2 at 3.00 o'clock location

5. Discussion

From the simulation of the HE-E test, we found that the following points, related to thermoplasticity of OPA, nonlinear thermal diffusivity and effective compressibility need some more detailed discussion.

5.1 Thermoplasticity of Opalinus clay

Elevated temperature induces thermal strain to the rock mass and might lead to thermoplastic behavior under certain circumstances. Yu et al. (2014) reported the experimental results on volumetric strain of Opalinus clay rock under cyclic thermal loadings from 25 to 84 ^{o}C as shown in Fig. 2.39. Thermal expansion was observed at the beginning of heating test, and then the plastic contraction occurred at a threshold temperature around 70 ^{o}C. It is believed that the historical maximum temperature as experienced by the Opalinus clay during geological history is estimated around 70 ^{o}C, corresponding to the threshold value for the turning trend in volumetric strain. A second heating cycle exhibits the similar behavior. Such thermoplasticity of sedimentary rock actually resulted from the coupled THM influences. It could be ascribed to the weakening of stiffness and strength as a result of thermal loading onto the matrix. Some researchers explain this behavior by creep theories (Xiong et al. 2014).

This thermal-induced stiffness decline phenomenon for the Oalinus clay rock is important for a better calibration of the HE-E heating test. Due to the limitation of the linear elastic assumption, the lasting tail of thermal-induced pore pressure, which even exists when rock mass reaches a steady-state temperature, cannot be reproduced by this model. Therefore a modified THM coupled model may be necessary to take into account the thermoplastic behavior by decreasing the stiffness of the clay rock in terms of a function of time or temperature. In such a way the modelling results about pore pressure could be better fitted with the test data.

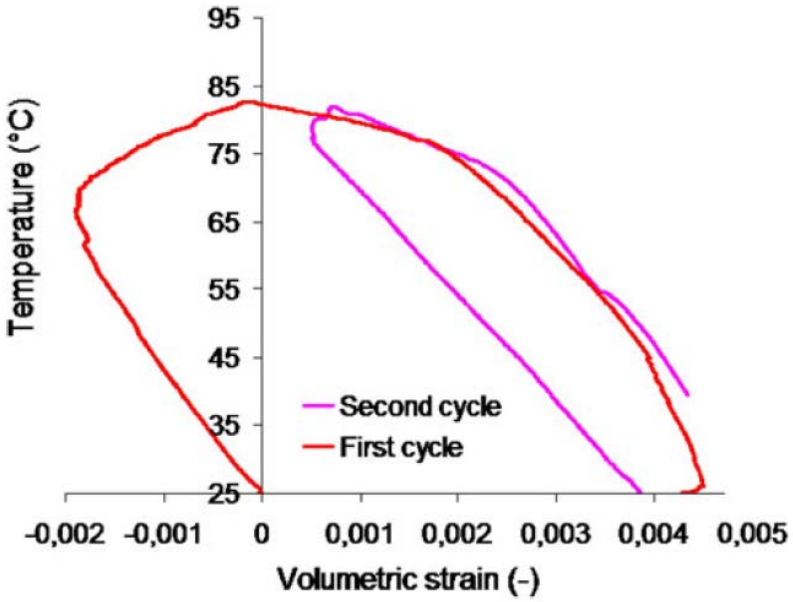

Figure 2.39 Drained heating test on Opalinus clay under in situ stress (Yu et al. 2014)

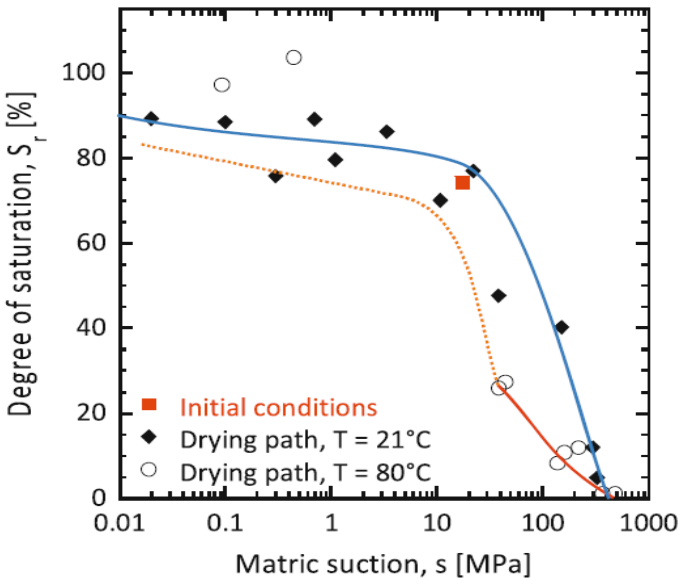

Figure 2.40 (a) Water retention curves of the Opalinus clay at two different temperatures (Yu et al. 2014)

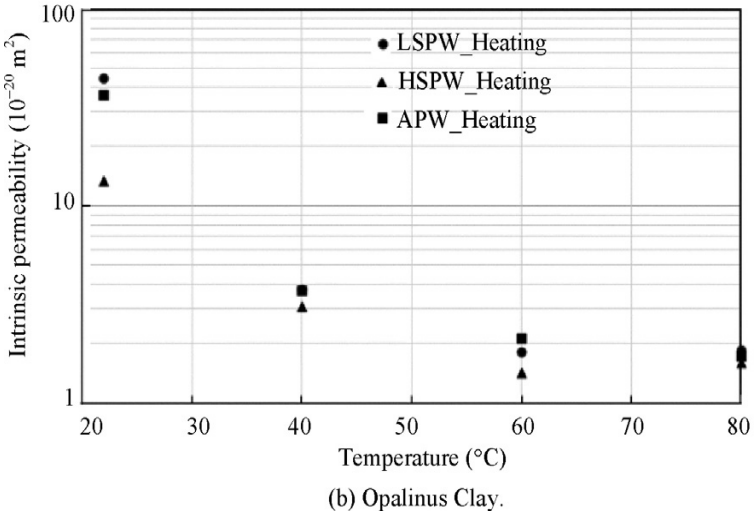

(b) Opalinus Clay.

Figure 2.40(b) Variation of the intrinsic permeability with temperature for Opalinus Clay (Li 2013)

Increased temperature influences the hydraulic properties of rocks. Figure 2.40 shows the variation of water retention characteristics and permeability of Opalinus clay rock with elevated temperature. The air entry value of OPA was found to decrease at higher temperature, and the overall water characteristic curve moves to the left-hand side. Permeability of OPA seems to decline from 15-40E-20 m^2 at 22 ^oC to about 2E-20 m^2 at 80 ^oC. Others have reported a nonlinear increase in thermal conductivity with increasing temperature for jointed rock mass (Baroni et al. 2014), which is, although not applicable to this study, informative to indicate the significant coupling influence on various aspects of the rock mass

from thermal effect. We have not included the influence of thermal effects on the hydraulic properties of rock, and it would be interesting to do so in future studies.

5.2 Nonlinear vapour diffusivity enhancement factor

In order to improve the consistency between modelling results and test data, we carried out extensive trial simulations that take into account the nonlinear behaviors of vapour diffusivity and effective grain compressibility for the unsaturated engineered barrier system (EBS). The results that we showed are the best results we have obtained so far. The parametric information is explained and analyzed as followings.

Figure 2.41 shows the best-fitted nonlinear parameters for the thermal enhancement factor f_{Tv} of vapour diffusivity. As discussed earlier, experimental proof of such enhanced evaporation has been widely reported in the literature. Figure 2.42 shows a series of typical experimental results on thermal enhancement factor η (η=f_{Tv} in this study). It is suggested that this enhancement ranges from 1 to 15 with increasing saturation from 0 to 0.2-0.4. The inflection point differs from the type of soil. Sandy soil has a less pronounced inflection point than clayey soils, which might be attributable to the difference in matric suctions of these soil types. In this sense, our fitted parameters are generally located inside the reasonable range and thus appear to be justifiable.

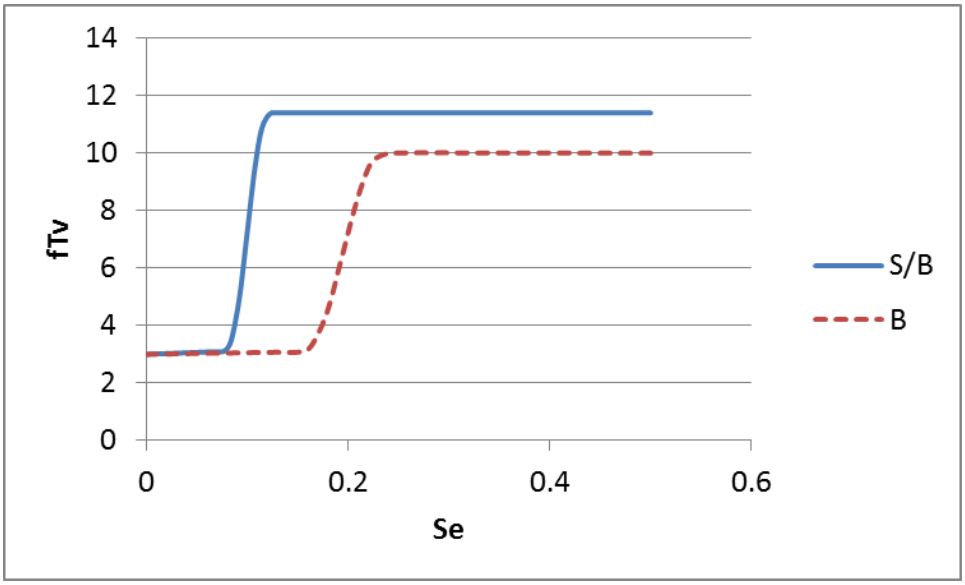

Figure 2.41 Dependence of diffusivity enhancement factor f_{Tv} with saturation degree for S/B and B

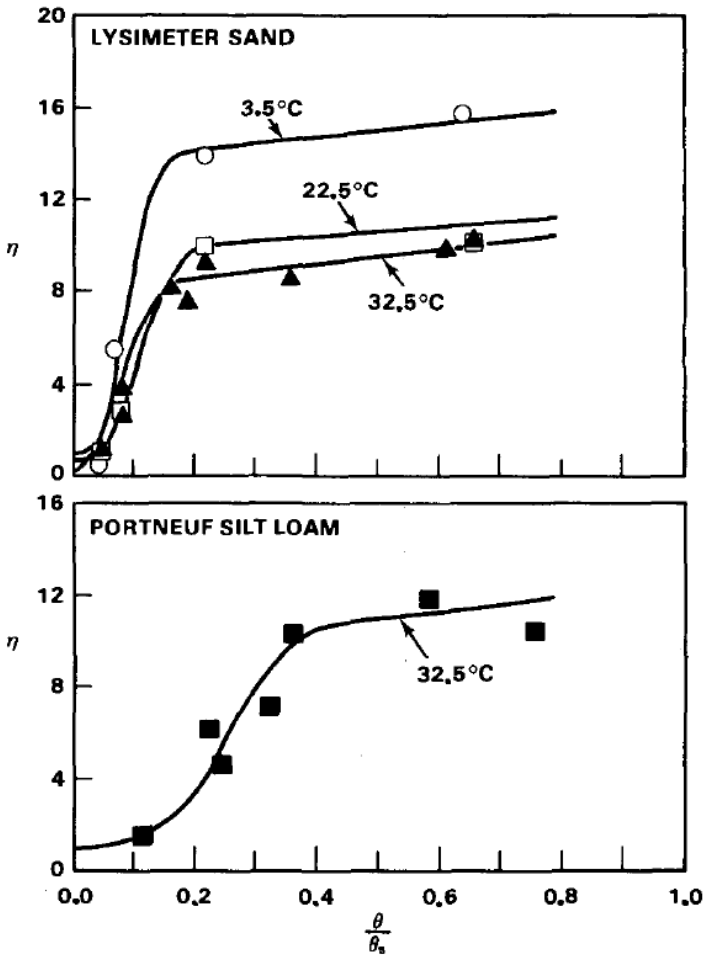

Figure 2.42 Mechanistic enhancement factor η as a function of saturation and temperature T (Cass et al., 1984)

5.3 Nonlinear compressibility of unsaturated soil

Theoretical framework

Different from rock, soil is known for its strong strain-hardening or softening behavior, which is related to saturation, dry density and confining pressure. Relationships exist between stiffness, soil suction, and net stress while other factors such as the degree of compaction and material properties are also important to soil behavior. For unsaturated clayey soils, field experiments showed an increasing stiffness with an increasing dry unit weight (Curd, 2013). For soils compacted at similar densities, soil fabric is not the main determinant of the behavior of soil stiffness. Instead, the stiffness increases proportionally with matric suction, and appears to depend primarily on the soil's state of stress. Tests showed that the moisture content of a cohesive soil had a substantial impact on stiffness (Curd, 2013). Zhan et al. (2014) studied the wetting-induced softening behavior of unsaturated expansive soils. It was found that the wetting-induced swelling of the soil included a significant component of plastic strain and its magnitude decreased with the net confining stress. When a soil specimen was subjected to wetting at a constant deviator stress, a threshold value of soil suction was identified after which the axial strain increased

greatly. Rojas and Chavez (2013) proposed a constitutive elastoplastic model to address the suction-induced volumetric strain of unsaturated expansive soil. That model was based on the effective stress principle and the semi-logarithmic e-log(p) relationship for isotropic compression.

To derive the dependence of effective compressibility (χ_p^e) with matric suction, we can rewrite the governing equation for the unsaturated EBS by considering the following relationships:

$$\rho_l \left(\frac{C_m}{\rho_l g} + S_e S\right)\frac{\partial p}{\partial t} + \nabla\frac{\rho_l k}{\mu}\nabla p + \nabla\rho_l(D_{pv}\nabla p + D_{Tv}\nabla T) = \alpha\rho_l S_e\frac{\partial \varepsilon_v}{\partial t}$$

Assuming the convention of volumetric strain as plus for swelling and minus for compression, we obtain for one-dimensional and pseudo three-dimensional consolidation:

$$\frac{\partial \varepsilon_v}{\partial t} = -m_v\frac{\partial p}{\partial t} = -\frac{1}{K}\frac{\partial p}{\partial t}$$

where m_v is the bulk compressibility and K is bulk modulus that follows Terzaghi's consolidation theory. The bulk modulus can be calculated by

$$-\frac{1}{K} = \frac{d\varepsilon_v}{dp}$$

The governing equation reduces then to

$$\rho_l \left(\frac{C_m}{\rho_l g} + S_e S'\right)\frac{\partial p}{\partial t} + \nabla\frac{\rho_l k}{\mu}\nabla p + \nabla\rho_l(D_{pv}\nabla p + D_{Tv}\nabla T) = 0$$

where storage term S' accounts for the volumetric strain in terms of an effective compressibility for the porous media matrix ($\chi_p{}^e$)

$$S' = n\chi_l + (1-n)\chi_p{}^e$$

Then we can obtain the following expression for the effective compressibility of solid matrix

$$\chi_p{}^e = (1-n)\chi_s + \frac{\alpha}{K}$$

where α is Biot's coefficient. As for soft soils, this parameter is usually treated as α=1.0.

Because the compressibility of the solid particles is of the order of 10^{-11} Pa^{-1} and is much larger than 1/K,

$$\chi_p{}^e \approx \frac{1}{K}$$

According to Rojas and Chavez (2013), the volumetric strain of unsaturated soil has the following relationship,

$$\frac{d\varepsilon_v}{dp'} = \frac{-\lambda_v}{p'V} = -\frac{\lambda_v}{V}\frac{1}{\bar{p} + \chi s}$$

where λ_v is the compressive index as determined from e-logp curve; V is the volume and $\bar{p}$ is the mean stress, χ is the Bishop coefficient and *s* is the matric suction.

Replacing matric suction with Brooks-Corey equation leads to another formula

$$\chi_p{}^e = -\frac{\lambda_v}{V}\frac{\alpha}{\alpha\bar{p} + \chi S_e{}^{-1/n}}$$

For confined strain and fixed stress loading cases, it can be further simplified into

$$\chi_p{}^e = \frac{a}{1 + bS_e{}^{-1/n}}$$

where *a* and *b* are model constants and *n* is the parameter from Brooks-Corey relationship. It is clearly shown that the effective compressibility of soil increases nonlinearly with the saturation degree. Note that this discussion is rather qualitative and does not consider the influence of compaction effect or pre-consolidation history of the unsaturated soil. It is also suitable for description of the wetting path-related stiffness estimation, while the influences of drying from the original water content on elasticity of the unsaturated soil might be biased by the above equation.

Parameterization for the EBS materials

Figure 2.43 shows the nonlinear effective compressibility for both S/B and B that were best-fitted in our numerical studies. The shape of these curves are based on physical mechanisms that involve drying and wetting induced volumetric strain as well as the influence of initial saturation. It is noted that the effective compressibility for both soils as shown in Fig. 2.43 start to rise near the initial saturation degree (S_{e0}) as prepared on site, i.e. S_{e0}=0.09 for S/B and S_{e0}=0.16 for B (as seen from Figures 2.19-2.20). Desiccating the compacted clay from the original state (i.e. the pre-consolidation state) will lead to a flat unloading stress path that yields very limited change in volumetric stiffness (see Fig. 2.44), which means the elasticity of the unsaturated soil with S_e<S_{e0} can be treated as a constant.

Experimental studies on expansive soil have revealed that the compression curve appears to be linear when suction is less than a certain threshold value (s_t), e.g. s_t=1.0 MPa for Boom clay and Bentonite-kaolin mixed soil (Wheeler et al., 2003). Dueck and Nilsson (2010) have investigated the volume change of unsaturated MX-80 Bentonite specimens by compression tests and swelling/shrinkage tests. Measured stresses, deformation are presented versus each other in Figure 2.45. It is clearly shown that the threshold value for MX-80 Bentonite s_t=30.0 MPa (Dueck and Nilsson, 2010). MX-80 Bentonite is exactly the EBS materials used in HE-E test, therefore such a threshold value in suction may be reflected in the expression of effective compressibility. Referring back to the water retention curves of S/B and B as shown in Figure 2.46, this threshold value s_t=30 MPa corresponds approximately to effective saturation S_e=0.12 (S/B) and S_e=0.24 (B). Further wetting of these EBS materials from the threshold suction value s_t will result in a constant elasticity, which suggests a constant value in the effective compressibility as shown in Figure 2.43.

The stiffness of the unsaturated soil in the region between the threshold suction value S_t and initial saturation S_{e0} is controlled by the e-log(p) relationship as described in the prior section. The sharp

increase trend between the two plateaus as shown in Figure 2.43 can be best fitted with the relevant function.

It is noted that with the application of these nonlinear parameters for the vapour transport equations, we can best reproduce the experimental results by our modelling. The choice of these nonlinear parameters is explained either with experimental proof, or with theoretical basis, and is physically justifiable.

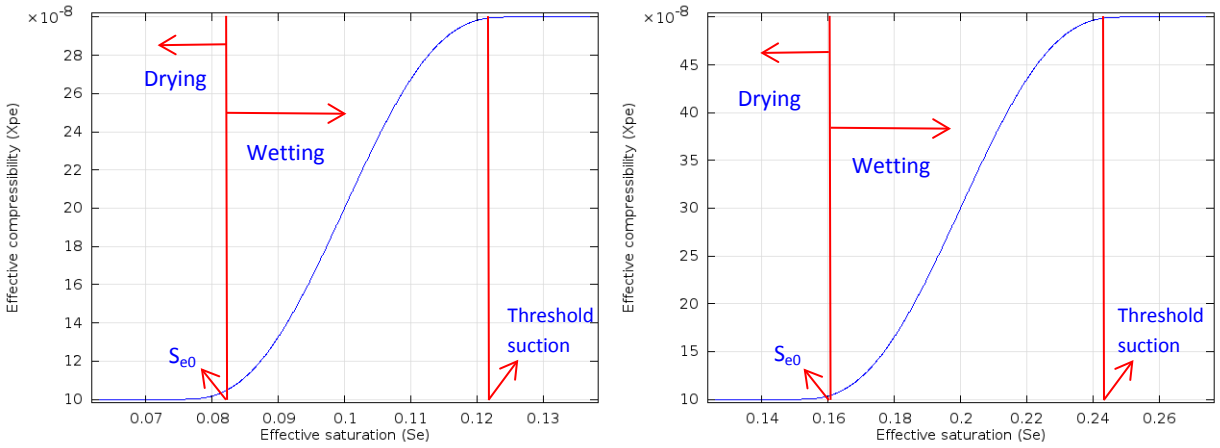

Figure 2.43 Dependence of effective compressibility (χ_p^e) with saturation degree for S/B (a) and B (b)

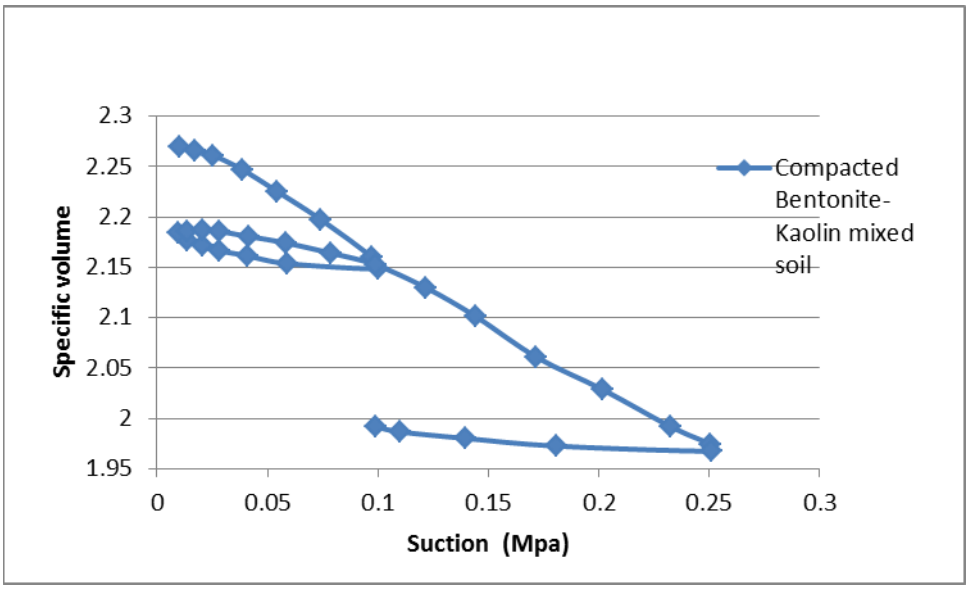

Figure 2.44 Suction induced compression curve for compacted Bentonite-Kaolin mixed soil (Wheeler et al., 2003)

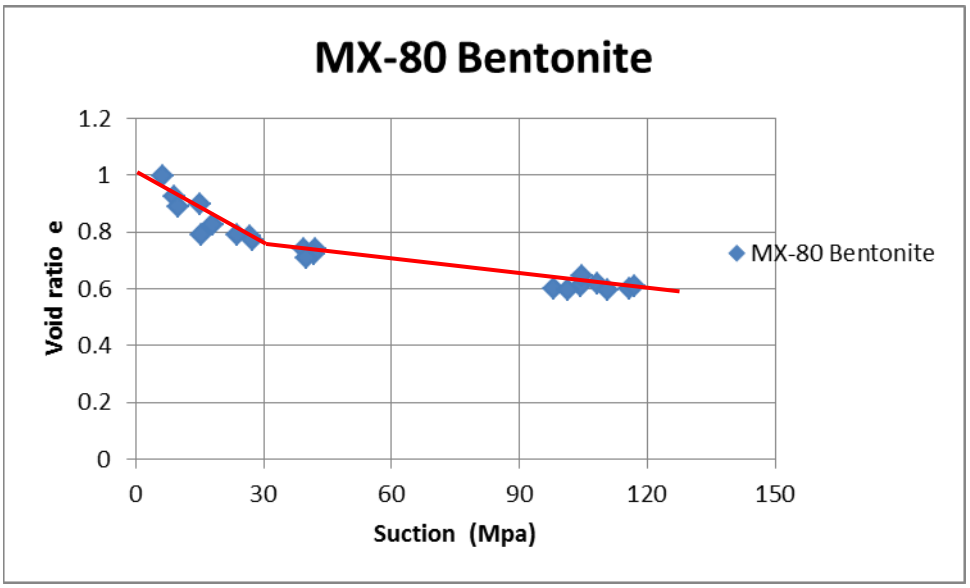

Figure 2.45 Variation of void ratio of compacted MX-80 Bentonite with matric suction (Dueck and Nilsson, 2010)

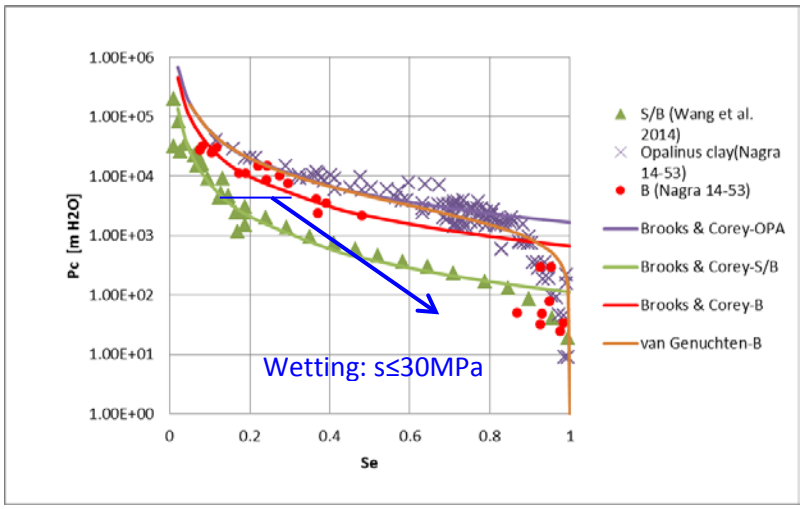

Figure 2.46 Indication of the threshold suction value of the EBS materials for the wetting path

6. Conclusions

Through the modelling investigations as carried out in this research task, we offer the following conclusions.

- The THM coupled models proposed by Nguyen et al. (2013) satisfyingly reproduced the field experimental observations from HE-E heating test.

- Laboratory scale small column heating tests allowed calibration of the modelling input parameters for the EBS, and provide confidence in the validity of the assumed THM processes in unsaturated bentonite-based materials.
- Nonlinearity in vapour diffusivity and EBS compressibility are critical to the temperature and relative humidity evolution in the EBS materials. The experimental results can be successfully reproduced by accounting for the nonlinear enhanced vapour diffusivity and compressibility of specific EBS materials.
- The EBS materials in the HE-E test have lower heat conductivity compared to the surrounding host rock, and thus act as thick layers of thermal insulation that, during the duration of the experiment, largely confine the heat inside the EBS material and limit the temperature increase in the host rock.
- The initialization of field conditions needs more data support from further in-depth field surveys. Pore pressure is generally assumed to be at the level of 1.0 MPa for numerical modelling. However, monitoring sensors give pressure readings different from this initial condition. Uneven pore pressure distribution exists before heating was initiated, e.g. readings of sensors located above the tunnel are generally higher than those below the tunnel, and are more prone to the heating disturbance.
- The excavation induced damage zone (EDZ) has higher permeability and lower air entry value than the intact host rock, and are beneficial to EBS resaturation within a short period of time. Sensors H indicate full saturation within 180 days for S/B and 500 days for B, respectively.
- Slow dissipation of thermally induced pore pressure response in the host rock is believed to be due to plasticity or even creep which is part of the intrinsic properties of OPA clay rock. Our THM models only address the poroelastic constitutive relationships, and thus are not sufficient to fully reflect the gradual change of the in situ monitoring results. The subsequent research task will be specifically oriented to this technical issue, and will hopefully be able to answer those aspects.
- Resaturation of the EBS is estimated to take at least 11,000 years before reaching full saturation (>99%) in a shutdown of the heating source following 8 years of maintaining a constant temperature of 140 ^{o}C on the heater-EBS interface. Should such a long re-saturation time be found to be associated with a geological disposal system, the implications on the repository performance should be assessed.

References

C. Y. Lee and C. R. Wilke (1954) Measurements of Vapor Diffusion Coefficient. Industrial Engineering Chemistry. (11): 2381-2387

J. R. Philip, D. A. De Vries (1957). Moisture movement in porous materials under temperature gradients. Eos, Transactions American Geophysical Union. 38(2): 222–232

E. Charlaix and M. Ciccotti (2010). Capillary Condensation in Confined Media. Handbook of Nanophysics - Volume 1. Edited by Klaus Sattler. CRC Press

C. Baroni et al. (2014) Thermomechanical stress–strain numerical modelling of deglaciation since the Last Glacial Maximum in the Adamello Group (Rhaetian Alps, Italy). Geomorphology 226: 278–299

A. Cass, G. S. Campbell, and T. L. Jones (1984) Enhancement of Thermal Water Vapor Diffusion in Soil. Soil Sci. Soc. Am. J. 48(1): 25-32

T.S. Nguyen, J.D. Barnichon (2013) Modelling the Mont Terri HD-E experiment for the Thermo-Hydro-Mechanical response of bedded Opalinus clay to heating, DECOVALEX 2013 progress.

I. Gaus, B. Garitte, R. Senger (2014) The HE-E Experiment: Lay-out, Interpretation and THM Modelling. Technical Report: Nagra NAB 14-5

Clifford K. Ho and Stephen W. Webb (1996) A Review of Porous Media Enhanced Vapor-Phase Diffusion Mechanisms, Models, and Data-Does Enhanced Vapor-Phase Diffusion Exist? Technical Report: SAND96-1198

X. Li (2013) TIMODAZ: A successful international cooperation project to investigate thethermal impact on the EDZ around a radioactive waste disposal in clay host rocks. Journal of Rock Mechanics and Geotechnical Engineering. 5: 231–242

H. Nowamooz, M. Mrad, A. Abdallah, and F. Masrouri (2009) Experimental and numerical studies of the hydromechanical behaviour of a natural unsaturated swelling soil. Can. Geotech. J. 46: 393–410

L. Otero, A. D. Molina-García & P. D. Sanz (2002) Some Interrelated Thermophysical Properties of Liquid Water and Ice. I. A User-Friendly Modelling Review for Food High-Pressure Processing, Critical Reviews in Food Science and Nutrition, 42(4): 339-352

J. Rutqvista, L. BoÈ rgesson, M. Chijimatsu, A. Kobayashi, L. Jing, T.S. Nguyen, J. Noorishad, C.-F. Tsang (2001) Thermohydromechanics of partially saturated geological media: governing equations and formulation of finite element models. International Journal of Rock Mechanics & Mining Sciences. 38: 105-127

N. Tisato and S. Marelli (2013) Laboratory measurements of the longitudinal and transverse wave velocities of compacted bentonite as a function of water content, temperature, and confining pressure. Journal of Geophysical Research: Solid Earth. 118: 3380–3393

L. Yu, E. Weetjens et al. (2014) Consequences of the Thermal Transient on the Evolution of the Damaged Zone Around a Repository for Heat-Emitting High-Level Radioactive Waste in a Clay Formation: a Performance Assessment Perspective. Rock Mech Rock Eng. 47:3–19

Y.L. Xiong, S. Zhang, G.L. Ye, F. Zhang (2014) Modification of thermo-elasto-viscoplastic model for soft rock and its application to THM analysis of heating tests. Soils and Foundations. 54(2):176–196

M.V. Villar, P.L. Martín, R. Gómez-Espina, F.J. Romero, J.M. Barcala (2012) Long-term THM tests reports: THM cells for the HE-E test: setup and first results. CIEMAT Technical Report CIEMAT/DMA/2G210/03

Jason M. Curd (2013). Unsaturated Soil Parameters From Field Stiffness Measurements. Theses and Dissertations--Civil Engineering. University of Kentucky.

T. Zhan, R. Chen, C. Ng (2014). Wetting-induced softening behavior of an unsaturated expansive clay Landslides. 11(6), 11(6) 1051-1061

E. Rojas and O. Chavez (2013). Volumetric behavior of unsaturated soils. Can. Geotech. J. 50: 209‑222

Ann Dueck and Ulf Nilsson (2010). Thermo-Hydro-Mechanical properties of MX-80: Results from advanced laboratory tests. Technical Report: SKB TR-10-55

S. J. Wheeler, R.J. Sharma, & M.S.R. Buisson (2003) Coupling of hydraulic hysteresis and stress–strain behaviour in unsaturated soils. Geotechnique. 53(1) 41–54

Chapter 3 Development of A Stress-Strain Constitutive Model For Anisotropic Sedimentary Rocks

Summary

This chapter reports a preliminary development of elastoplastic model for progressive failure of stiff anisotropic argillite claystone. The elastoplastic model is based on Mohr-Coulomb plasticity, modified with a concept of mobilized hardening prior to the peak strength and a softening damage in the post-peak. The model is first applied to analyse the triaxial test data about Tournemire shale. The Young's modulus is found to decrease exponentially with the increasing plastic strain, regardless of the direction with respect to the bedding plane. A microstructure tensor approach is also implemented to describe the oriented strength parameters. The laboratory testdata are well reproduced by the above model regarding the stress-strain relationship, and cyclic loading-unloading behaviours. A second study is about the hydro-mechanical coupling of Cobourg limestone. Our model can simulate the crack damage in terms of plastic strain and correlate it with the measured permeability values. All the modellings in this chapter dealt only with elasto-plasticity, and are not final. The model will be revised and updated in the following stage of this research project.

1. Introduction

Deep geological disposal is being proposed for the long term management of nuclear waste in many countries, including Canada. Sedimentary rock formations are one of the host medium being considered. In Southern France, the IRSN operated an underground research laboratory in Tournemire located in an argillaceous sedimentary rock, the Tournemire argillite that is found in a Mesozoic marine basin (Abdi et al. 2015). The Tournemire argillite possesses strong anisotropy in stiffness, deformation and permeability. Anisotropy of geomaterials always involves the compositional layered structures, i.e. bedding, layering, and foliation. Loading history, mineral constituents, deposition intervals are all reponsible for the formation of anisotropy. Considering the potential risk of preferential leakage route associated with the excavation induced damage zone for radiative contaminants, it is thus required to thoroughly understand the anisotropic behavior of the sedimentary rocks of interest.

Experiments on sedimentary rocks have indicated that the general trend of compressive strength varies with the loading angle. The weakest plane exists between 30-60^{o} of loading angle against the bedding plane, while the maximum strength is found parrallel or perpendicular to the bedding plane. Besides the strength properties, elasticity of these mateirals also indicate significant dependence on the orientation. In order to characterize the mechanical behaviour of the the sedimentary rocks, triaxial tests were carried out to investigate the different effects of confining pressure, loading angle and loading rate. The anisotropy in mechanical properties of sedimentary rocks leads to challenges in the numerical modelling

of various underground geotechnical engineering problems within the framework of the classical homogeneous elastoplastic theories.

Numerous efforts have been devoted to the development of appropriate constitutive models for anisotropic geomaterials. Amongst them, the microstructural tensor approach, which was originally developed by Pietruszczak (2001) and later extended by Nguyen and Le (2015) and Le and Nguyen (2015), proved to be robust, viable, straight-forward and easy to use for the characterization and modelling of the constitutive behaviour of materials with transverse isotropy.

This study is mainly based on the microstructural tensor approach to develop a constitutive model for sedimentary rocks like Argillite clay and Cobourg limestone. We analysed the triaxial experimental data of the rocks with varying confining pressures and loading angles in order to conceptualize the constitutive models. Before reaching the peak strength, a strain-hardening is commonly found to occur after the initial elastic yielding, at which point the volumetric dilatancy appears to be initiated. Mohr-Coulomb strength parameters (c, ϕ) were correlated with both the loading angle in terms of microstructural tensor and the plastic strain in terms of a mobilized hardening law that spans from initial yielding to the peak failure. Accordingly, an elastoplastic mobilized hardening model was developed in this study to simulate the above mentioned experimental phenomena. Three series of test data with β=0, 45 and 90 ^{o}, respectively, were analyzed to estimate the model constants. The proposed constitutive equations were then implemented in COMSOL (Ver 5.1) to get validated by reproducing the triaxial experimental data.

The Cobourg limestone, which is the proposed repository formation for Ontario Power Group's (OPG) low and intermediate level nuclear waste at the Bruce site, Ontario, is being experimentally investigated with regard to the hydraulic-mechanical coupled behaviour by colleagues at the University of Toronto. The experimental program consists of tri-axial compression tests with the determination of the evolution of the hydraulic conductivity and acoustic velocity. Some preliminary experimental results have been available for us to simulate. Therefore another part of this report will be devoted to the modelling of these data currently in hand. Due to the nature of the sampled Cobourg limestone, anisotropy is not as obvious as the Argillite clay. The strain-hardening stage seems absent from the stress-strain curves as well. A simplified version of the proposed Elasto-Plastic model was used for the data calibration. It is noteworthy that the hydraulic-mechanical coupling was taken into account to derive the permeability change in the damaged rocks. Some empirical relationships for hydraulic properties are achieved by correlating the damage index (dependent on the effective plastic strain) and permeability.

2. Theories and Equations

The following is devoted to the development of an anisotropic elasto-plastic theory for the Tournemire argillite as tested in an earlier study (Abdi et al. 2015). The geometry of the samples tested in triaxial cells is represented in Figure 3.1. The load angle β is the angle between bedding plane and the

horizontal direction. The convention of load angle in this study may vary in expression with specific purposes, whereas β is the default symbol except otherwise indicated.

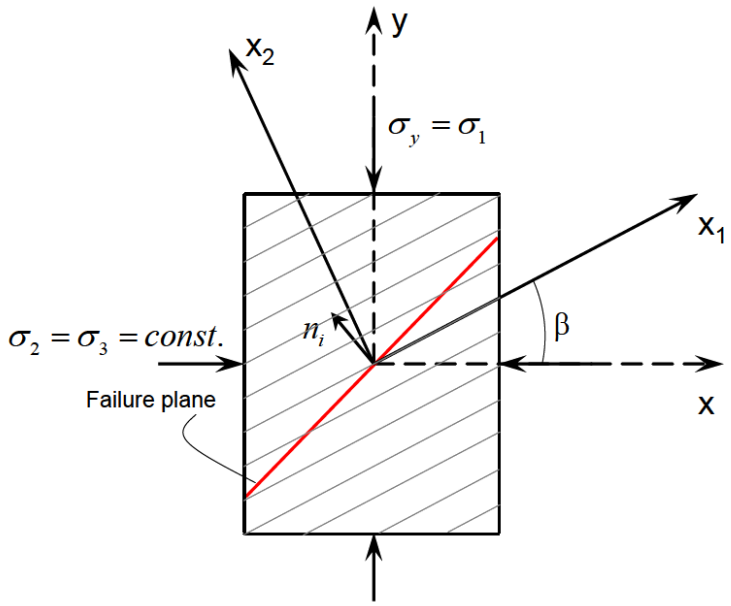

Figure 3.1 Geometry of the Tournemire sample in triaxial tests

2.1 Anisotropic stiffness

Due to the convenience of use of an empirical stiffness parameter E_{50}, the difficulty in extracting the Young's modulus of a sample at early stage of triaxial shear test may be largely avoided (Schanz et al., 1999). This approach has been used in an earlier constitutive study of anisotropic rocks by Nguyen and Le (2015). This study relies on the tangent modulus as determined by cyclic loading-unloading experimental data. As for anisotropic rock mass, the effect of load angle on its elasticity cannot be overlooked from the consideration. According to orthotropic composite mechanics, the following relationship can be deduced,

$$\frac{1}{E_\beta} = \frac{sin^4\beta}{E_L} + \frac{cos^4\beta}{E_T} + (-2\frac{v_{LT}}{E_L} + \frac{1}{G_{LT}})sin^2\beta cos^2\beta \qquad (1)$$

where E_β is the elasticity at load angle β; E_L and E_T are in plane and transverse moduli, respectively; v_{LT} is the transverse Poison ratio; G_{LT} is the transverse shear modulus.

Provided that stiffness is known for a series of load angle, as is the case in this study, the transverse Poisson ratio and shear modulus can be estimated by curve fitting using the above equation as shown in the following graph(where?). It is noteworthy that the estimated material properties, i.e. the transverse Poison ratio v_{LT} and the transverse shear modulus ratio G_{LT}/E_{LT} are all consistent with each other for test conditions under different confining pressures.

Table 3.1 shows the obtained parameters for the anisotropic elasticity of the Argillite clay. The in plane Poisson's ratio is found to be dependent on the confining pressure in terms of an exponential equation.

In order to estimate the in plane Poisson's ratio, the bulk modulus K was first calculated by plotting the mean stress ($p = (\sigma_1 + \sigma_3)/2$) against the volumetric strain (ε_v). The curve was fitted with linear equations to get the slope which is the required bulk modulus (K). Using the stiffness formula between K and E, the Poisson ratio can be computed ($\nu_{\parallel} = 1 - \frac{E}{3K} - \nu_{\perp}$). Detailed data are shown in the following parameterization section.

In this study the tangent modulus (E_t) was considered as representative of the material stiffness. Through extensive data analysis, a unified relationship between tangent modulus and the effective plastic strain is found to be

$$E_t = E_i * f(\gamma^p) \tag{2a}$$

$$f(\gamma^p) = e^{-(\gamma^p)^{\frac{1}{2}}} \tag{2b}$$

where E_t is tangent modulus, E_i is the initial modulus, and γ^p is the effective plastic strain. The above equation excludes the influence of confining pressure on elastic modulus, which is found to be valid for Argillite clay as determined by cyclic shear test. The influence of effective plastic strain has a unique correlation with the tangent modulus in terms of $f(\gamma^p)$, which greatly simplifies the parametrization works. The correlation function $f(\gamma^p)$ is found to be an exponential equation as shown in Eq. (2b).

Table 3.1 Model constants for the characterization of anisotropic Argillite

Variables	Value	Unit
$E_{\perp}$	11.2	GPa
$E_{\parallel}$	20.9	GPa
$\nu_{\perp}$	0.15	
$\nu_{\parallel}$	0.253	
$G_{\perp}/E_{\perp}$	0.19	
$G_{\parallel}$	$E_{\parallel}/2(1+\nu_{\parallel})$	GPa

Note: // is for the in plane stiffness and ⊥ is for the transverse stiffness.

2.2 Elasto-plastic modeling

2.2.1 Mohr-Coulomb model

The Mohr-Coulomb yield criterion can be written in the following form (COMSOL user manual),

$$F = \frac{I_1 sin\phi}{3} + \sqrt{\frac{J_2}{3}}\left((1+sin\phi)cos\theta - (1-sin\phi)cos\left(\theta + \frac{2\pi}{3}\right)\right) - c * cos\phi = 0 \tag{3}$$

where I_1 is the first invariant of stress tensor, J_2 is the second invariant of deviatoric stress tensor, θ is the Lode angle, c is cohesion, and ϕ is frictional angle.

or in a more compact manner,

$$F = \sqrt{J_2}m(\theta) + \alpha I_1 - k = 0 \quad (4)$$

$$m(\theta) = \cos\left(\theta - \frac{\pi}{6}\right) - \sqrt{1/3}\, sin\phi \sin(\theta - \frac{\pi}{6}) \quad (5)$$

$$\alpha = sin\phi/3 \quad (6)$$

$$k = c * cos\phi \quad (7)$$

where θ is Lode angle in the range of (0, π/3).

According to classical theory of plasticity, loading induces a total strain consisting of two components, the elastic strain and the plastic strain.

$$\varepsilon_{ij} = \varepsilon_{ij}^{e} + \varepsilon_{ij}^{p} \quad (8)$$

The elastic strain reads

$$\varepsilon_{ij}^{e} = C_{ijkl}\sigma_{ij} \quad (9)$$

where C_{ijkl} is the compliance tensor.

The plastic strain on the other hand is derived from a separate plastic potential equation, i.e. Drucker-Prager criterion in terms of nonassociative flow rule, which has a similar functional form as the yield function (COMSOL user mannual):

$$G = \sqrt{J_2} + \frac{2}{\sqrt{3}}\frac{sin\phi}{3-sin\phi} I_1 - \frac{2\sqrt{3}cos\phi}{3-sin\phi} = 0 \quad (10)$$

which matches Mohr-Coulomb strength criterion at compressive meridian, suggesting a relatively less value in dilatancy angle.

In this regard, the plastic strain rate takes the form of

$$\dot{\varepsilon}_{ij}^{p} = \lambda \frac{\partial G}{\partial \sigma_{ij}} \quad (11)$$

where λ is the consistency parameter that can be determined by classical elasto-plastic theory with appropriate rearrangement of the differentiated form of the yield function (Simo, Hughes, 1998).

2.2.2 Modified Mohr-Coulomb model by hardening law – A review

With the hardening factor H taken into account, the above Mohr-Coulomb yield function turns into (Haghighat & Pietruszczak, 2015)

$$\sqrt{J_2} + \left(\frac{\alpha I_1}{m(\theta)} - \frac{k}{m(\theta)}\right)\beta = 0 \tag{12}$$

$$H = 1 + \frac{\gamma^p}{A + B\gamma^p} \tag{13}$$

where γ^p is plastic strain, A and B are model constants. It is obvious that two scenarios are achievable by adjusting the hardening factor: 1) hardening when 0<H<1; 2) softening when H>1 and 3) ideal plastic when H=1. The plastic strain is the effective plastic strain defined as:

The plastic strain can be defined as (Hashiguchi, 2014; COMSOL user mannual)

$$\gamma^p = \int \dot{\gamma}^p dt = \int \sqrt{\frac{2}{3}\dot{\varepsilon}_{ij}^{p\prime}\dot{\varepsilon}_{ij}^{p\prime}}\, dt = \int \sqrt{\frac{2}{3}\left(\dot{\varepsilon}_{ij}^{p} - \frac{1}{3}\dot{\varepsilon}_{v}^{p}\mathbf{I}\right)\left(\dot{\varepsilon}_{ij}^{p} - \frac{1}{3}\dot{\varepsilon}_{v}^{p}\mathbf{I}\right)}\, dt \tag{14}$$

In triaxial compression experimental conditions, the above formula can be expressed in another form,

$$\gamma^p = \sqrt{\frac{2}{3}\left[\left(\varepsilon_1^p - \frac{1}{3}\varepsilon_v^p\right)^2 + 2\left(\varepsilon_r^p - \frac{1}{3}\varepsilon_v^p\right)^2\right]} \tag{15}$$

where ε_1^p is accumulative axial plastic strain, $\varepsilon_r^p = \nu\varepsilon_1^p$ is the accumulative radial plastic strain, and ε_v^p is the volumetric plastic strain.

The above Mohr-Coulomb equation can be rewritten to be consistent with the classical Mohr-Coulomb Elasto-Plastic theory as adopted in COMSOL. The equation reads

$$\sqrt{J_2} + \frac{\bar{\alpha} I_1}{\bar{m}(\theta)} - \frac{\bar{k}}{\bar{m}(\theta)} = 0 \tag{16}$$

where $\bar{\alpha}$, $\bar{k}$ and $\bar{m}(\theta)$ are the required COMSOL input parameters that are consistent with the modified Mohr-Coulomb Elasto-Plastic theory that takes into account the hardening factor H.

Rearranging the equations leads to the following relationship,

$$\bar{c} = \frac{c * tan\bar{\phi}}{tan\phi} \tag{17}$$

$$\bar{\phi} = arcsin\frac{sin\phi\cos(\theta - \frac{\pi}{6})}{\beta\cos\left(\theta - \frac{\pi}{6}\right) - \frac{\beta - 1}{\sqrt{3}}sin\phi sin(\theta - \frac{\pi}{6})} \tag{18}$$

In case of ideal plasticity, hardening factor H=1 and the above formula gives the identical parameters between modified and classical MC model ($\bar{c} = c;\ \bar{\phi} = \phi$).

Therefore, the nonlinear elasto-plastic behaviour can be modelled with the appropriate selection of model parameters i.e. A and B.

Strain softening is common for compression failure of brittle rocks. If the concept of mechanical damage is introduced to the modification parameter, then we may be able to simulate the sharp reduction in shear stress. The hardening factor can be further extended into the following form (Chen et al. 2010),

$$H = (1-\omega)\left(1+\frac{\gamma^p}{A+B\gamma^p}\right) \tag{19}$$

where ω=f(γ_p) is the damage factor induced by plastic strain which will be expanded and discussed later.

2.2.3 Development of a mobilized hardening/softening elasto-plastic model

2.2.3.1 Initial yielding

For brittle rocks, it is usually accepted that there exists a crack initialization strength that is about 30-60% of the peak strength (see e.g. Martin, 1993). When the stress level surpasses the crack initialization strength, micro-cracks are expected to be initiated and grow in intensity with increasing shear stress until the nucleation of numerous cracks that eventually lead to shear failure (Ghazvinian et al., 2013).

Here we hypothesize that the plastic strain starts at a certain percent of the peak strength (σ_{1p}), say $\varpi\%$, and the elastic modulus decays gradually throughout the elasto-plastic transition stage due to the crack damage effect. This is consistent with the mechanism of crack initialization strength. Some researchers regard this stage of strength evolution as the crack damage (Martin, 1993), while others further distinguish them from each other by accounting for the acoustic emission phenomenon (Popp et al., 2001).

Then we obtain the initial yielding stress

$$\sigma_1^0 = \varpi\sigma_{1p} \tag{20}$$

where σ_1^0 is the initial yielding stress; σ_{1p} is the peak value of major principal stress.

In case of stress level over the crack initialization threshold value, plastic strain in principal stress direction starts to grow with respect to the crack initialization threshold value ϖ

$$\varepsilon_i^p = \begin{cases} 0, & \sigma_1 < \varpi\sigma_{1p} \\ \varepsilon_i - \frac{\sigma_1-\sigma_3}{E_t}, & \sigma_1 \geq \varpi\sigma_{1p} \end{cases} \tag{21}$$

where ε_i^p is the plastic strain in principal direction; ε_i is the strain in principal direction; ε_i^{ϖ} is the strain corresponding to crack initialization.

2.2.3.2 Hardening law – A normalized hardening model

A normalized hardening-softening yield surface based on Mohr-Coulomb criterion is proposed here along with the parameterization approaches and selection criterion for the evolution of yield in triaxial shear test.

Normalized damage

We first define a normalized damage parameter in terms of ω as an important variable contributing to the strain hardening process. It relates the effective plastic strain to the maximum plastic strain and gets it transformed into a unified range between (0, 1). Similar processing of plastic strain has been carried out by Martin (1993) in the analysis of strength of Lac du Bonnet granite.

$$\omega = \frac{\gamma^p}{\varepsilon_{epe}}, \quad 0 \leq \omega \leq 1.0 \tag{22}$$

where ε_{epe} is the plastic strain corresponding to the peak strength that marks the end of strain hardening and the starting of softening. For the Tournemire argillite, a linear relationship is found to exist between the maximum plastic strain and the confining pressure, as shown in Fig. 3.2.

$$\varepsilon_{epe} = C + D\sigma_3 \tag{23}$$

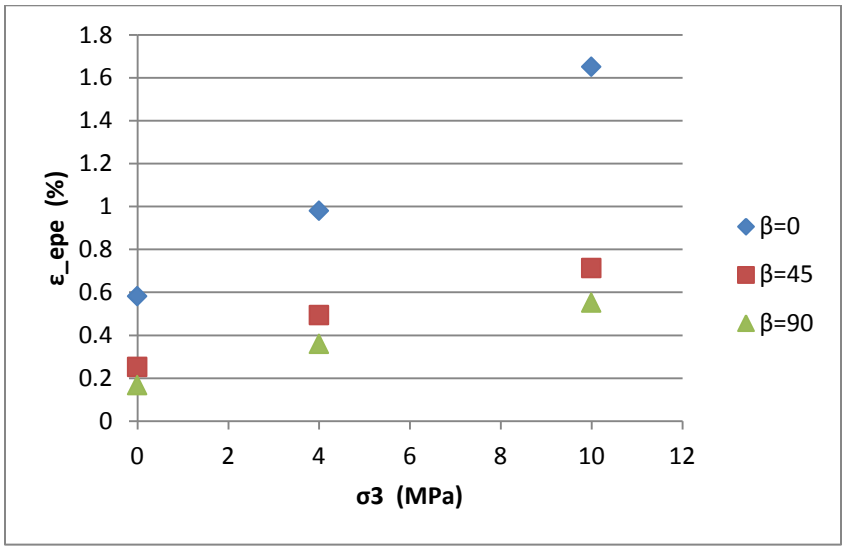

Figure 3.2 Peak plastic strain vs confining pressure for Tournemire Argillite at different orientations

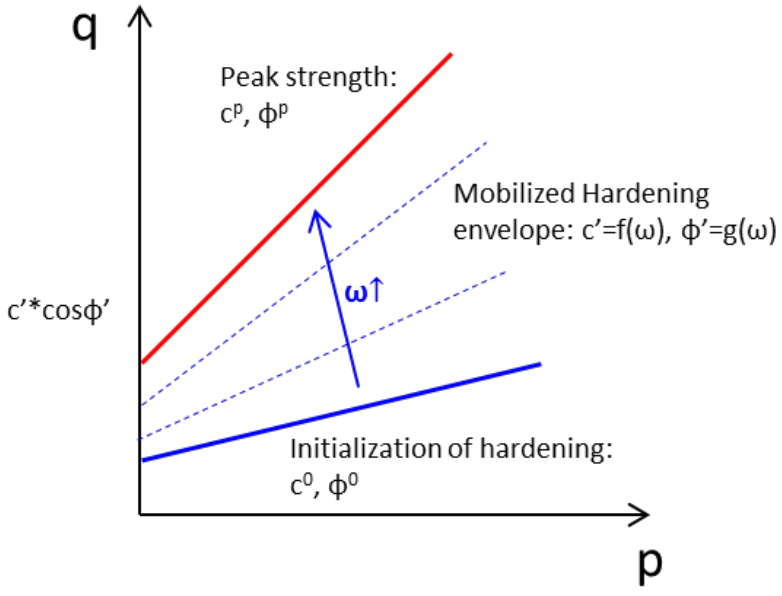

Figure 3.3 Diagram showing the evolution of hardening plastic flow from the initial yielding to the peak failure with varying value of the normalized damage

Mohr-Coulomb strength in the hardening stage

As shown in Fig. 3.3, there exists a gap between the initial yielding and the peak failure in p-q space, which can be attributed to the strain-hardening stage. The following part will discuss the development of analytical formulas for the hardening law.

In the plastic hardening stage, the major principal stress can be derived into such a linear form as the following equation

$$\sigma_1 = \alpha\omega + \sigma_1^0 \tag{24}$$

where σ_1^0 is the stress level corresponding to the initialization of plastic strain, and parameter α is a model constant to be determined by experimental data as shown in Fig. 3.4.

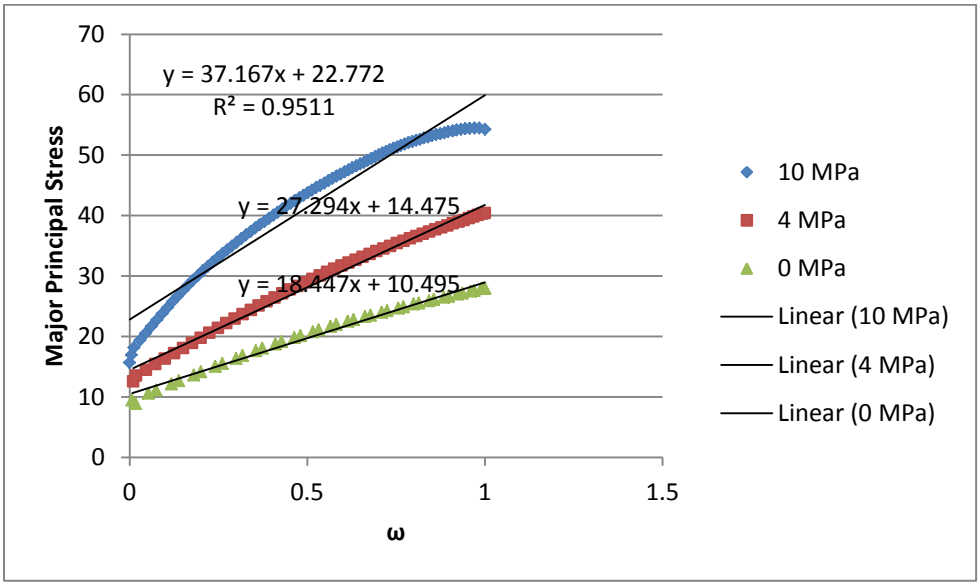

Figure 3.4 Variation of σ_1 with normalized damage factor ω for various confining pressures (β=0°)

Actually σ_1^0 determines the crack initialization strength by Mohr-Coulomb criterion representative of the initial yielding, e.g. the transition of deformation from elasticity to plasticity. Instead of focusing on the peak strength, the elasto-plastic transition stress state has to be identified in this study to calculate the strength parameters.

$$\sigma_1^0 = h + l\sigma_3 \tag{25}$$

Test with three confining pressures have been conducted about Argillite clay. This can lead to the estimation of a set of Mohr-Coulomb parameters that are noted as c^0 and ϕ^0.

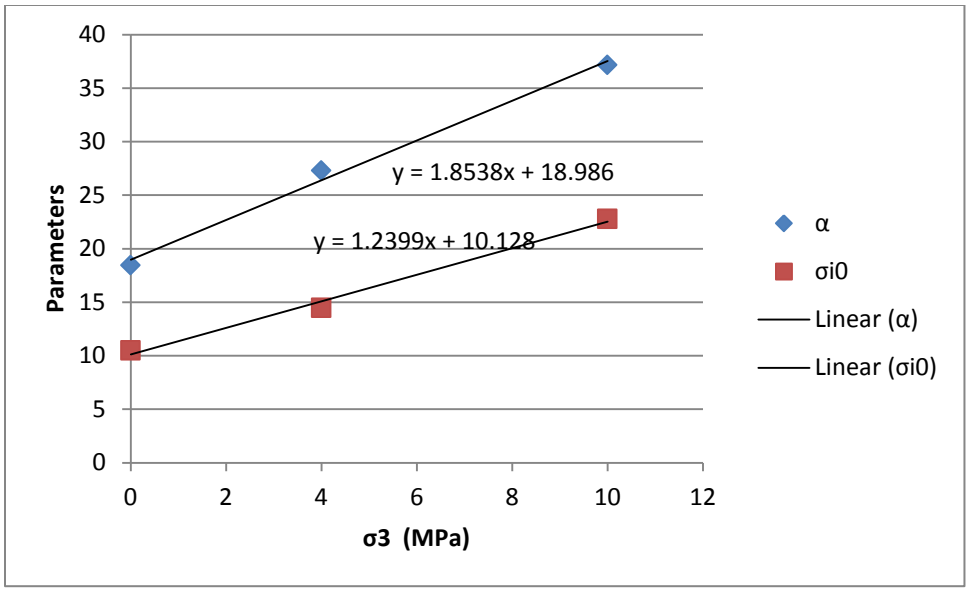

Figure 3.5 Dependence of hardening parameters α and σ_i^0 on confining pressure ($\beta=0^o$)

By analyzing the test data, an empirical linear function of confining pressure is found to be valid for the parameter α in such a form as

$$\alpha = k + m\sigma_3 \tag{26}$$

where model constants of *k* and *m* can be determined by fitting the experimental data for the hardening stage. As shown in Fig. 3.5, a good linearized form of the test data can be obtained by this equation. The slope and intercept are simultaneously determined. This model takes into account both of the initial yielding and the peak failure by a normalized damage parameter ω. Let us look at the two extreme cases with ω=0 and 1 representing the initial yielding and the peak failure, respectively.

$$\sigma_1 = \begin{cases} \sigma_1^0 = h + l\sigma_3, & \omega = 0 \\ \alpha + \sigma_1^0 = (h+k) + (l+m)\sigma_3, & \omega = 1 \end{cases} \tag{27}$$

The transition between the initial yielding and the peak failure can be modeled smoothly and seamlessly with a series of varying value of ω. The evolution of the Mohr-Coulomb envelope from initial yielding to the peak failure can also be reflected with the proposed hardening model as shown in Fig. 3.3.

This enables the derivation of the following function

$$\sigma_1 = (k\omega + h) + (m\omega + l)\sigma_3 \tag{28}$$

Then can we write out the analytical expression for its strength parameters according to Mohr-Coulomb strength criterion,

$$\frac{\sigma_1 - \sigma_3}{2} = c * cos\phi + \frac{\sigma_1 + \sigma_3}{2}\sin\phi \tag{29}$$

where c and ϕ are Mohr-Coulomb strength parameters for the hardening stage that are dependent on the normalized damage factor ω.

Rearranging the above formula leads to

$$\sigma_1 - \sigma_3 = 2c * cos\phi + (\sigma_1 + \sigma_3)\sin\phi \quad (30)$$

$$\sigma_1(1 - sin\phi) = 2c * cos\phi + (1 + sin\phi)\sigma_3 \quad (31)$$

$$\sigma_1 = \frac{2c*cos\phi}{1-sin\phi} + \frac{1+sin\phi}{1-sin\phi}\sigma_3 \quad (32)$$

Referring back to the hardening law results in

$$k\omega + h = \frac{2c*cos\phi}{1-sin\phi} \quad (33)$$

$$m\omega + l = \frac{1+sin\phi}{1-sin\phi} \quad (34)$$

Solving the above functions may bring about the required Mohr-Coulomb strength parameters for the hardening model

$$\phi = \mathrm{asin}(\frac{m\omega+l-1}{m\omega+l+1}) \quad (35)$$

$$cos\phi = \frac{2\sqrt{m\omega+l}}{m\omega+l+1} \quad (36)$$

$$c = \frac{k\omega+h}{m\omega+l+1}cos\phi = \frac{k\omega+h}{2\sqrt{m\omega+l}} \quad (37)$$

It is easy to conclude that when ω=0, $c=c^0$, $\phi=\phi^0$; and when ω=1, $c=c^p$, $\phi=\phi^p$.

Table 3.2 Orientation dependent hardening parameters determined from curve fitting on test data

	β=0	β=45	β=90	Unit
ϖ	0.3	0.3	0.3	1
C	0.14	0.08	0.015	
D	0.005	0.004	0.004	
k	21.2	12.29	21.85	MPa
m	1.72	1.83	2.58	
h	8.6	4.99	9.04	MPa
l	0.78	0.72	0.84	
ξ^*	0.5	0.5	0.65	

Note: * ξ is a reduction factor used for adjusting the initial Young's modulus E_i. This parameter is discussed in detail as shown in Eq. (63).

Discussion on parameters

Model constants of *k* and *h* can be related to crack initialization threshold value ϖ in such a way as

$$k = \frac{h}{\varpi}(1 - \varpi) \tag{38}$$

$$m = \frac{l}{\varpi}(1 - \varpi) \tag{39}$$

To deduce the above relationships, two cases of initial yielding and peak failure have to be recited:

$$\sigma_1^0 = h + l\sigma_3, \qquad \omega = 0 \tag{40}$$

$$\sigma_1^p = \alpha + \sigma_1^0 = (h + k) + (l + m)\sigma_3, \quad \omega = 1 \tag{41}$$

$$\sigma_1^0 = \varpi\sigma_1^p \tag{42}$$

Assigning a specific condition of unconfined shear test, i.e. σ_3=0, leads to a following expression

$$h = (k + h)\varpi \tag{43}$$

while maintaining a certain level of confining pressure will gives the following expression

$$l\sigma_3 = (l + m)\varpi\sigma_3 \tag{44}$$

which can be simplified into

$$l = (l + m)\varpi \tag{45}$$

In this regard model constants can further be reduced by half in quantity from 4 to 2. When ϖ is taken as 50 %, we can get the following relationship between model constants:

$$\begin{cases} k = h \\ m = l \end{cases} ; \quad \varpi = 50\% \tag{46}$$

2.2.3.3 Softening Model

Once the peak strength is reached, the corresponding plastic strain γ_t^p has to be output as a measure to reset the mode of stress-strain behavior from the hardening to the softening stage. This definition infers that

$$\gamma_t^p = \varepsilon_{epe} \tag{47}$$

The subsequent propagation of plastic deformation needs to be recalculated and hypothesized to start from γ_t^p, then the post-failure softening Mohr-Coulomb criterion (c_{ptf}) takes the form of

$$c_{ptf} = c^r + (c^p - c^r)\exp[-E(\gamma^p - \gamma_t^p)] \tag{48}$$

where c^r and c^p are respectively the residual and the peak Mohr-Coulomb cohesions; E is the model constant determining the dropping rate of the post-failure cohesion with plastic strain.

The above softening model still needs to be adjusted into the framework of the mobilized hardening/softening strength envelope, which involves a constantly evolving friction angle throughout the plastic deformation processes. In this manner, it is derived that

$$\phi_{ptf} = \phi^r + (\phi^p - \phi^r)\exp[-E(\gamma^p - \gamma_t^p)] \quad (49)$$

where ϕ_{ptf} is the post-failure softening friction angle; ϕ^p is the equivalent residual cohesion for the mobilized model; ϕ^r is the residual Mohr-Coulomb friction angle determined by experiment.

2.3 Microstructural tensor approach for strengths modeling

The anisotropy of strength can be modeled with the so called microstructural tensor, which correlates the stress loading in the geometrical space with that in the material coordinate (structural coordinate) by rotation matrixes. For transversely isotropic materials with bedding orientation as shown in Fig. 3.1, the extent of rotation depends on the loading angle β, which can be characterized by the loading unit vector l_i,

$$l_1^2 = \frac{\sigma_x^2 cos^2\beta + \sigma_y^2 sin^2\beta}{\sigma_x^2 + \sigma_y^2 + \sigma_z^2} \quad (50)$$

$$l_2^2 = \frac{\sigma_x^2 sin^2\beta + \sigma_y^2 cos^2\beta}{\sigma_x^2 + \sigma_y^2 + \sigma_z^2} \quad (51)$$

$$l_3^2 = \frac{\sigma_z^2}{\sigma_x^2 + \sigma_y^2 + \sigma_z^2} \quad (52)$$

According to Nguyen and Le (2015), the Mohr-Coulomb strength parameters, e.g. c and ϕ, can be expressed into a tensor function of the microstructural tensor,

$$\eta = \eta_0[1 + A_{ij} l_i l_j] \quad (53)$$

where η is the symbol for strength parameter and can be written as a tensor form of microstructural tensor a_{ij}

$$\eta = a_{ij} l_i l_j \quad (54)$$

$$A_{ij} = \frac{\mathrm{dev}(a_{ij})}{\eta_0} \quad (55)$$

which can be further expanded into polynomial equation of the loading unit vector as

$$\eta = \eta_0[1 + \sum b_i (A_1(1 - 3l_2^2))^i] \quad (56)$$

where b_i and A are model constants adjustable for best-fitting of test data; l_2 is component of the loading unit vector in the direction perpendicular to bedding (Y axis in this case).

The crack initialization, peak and residual strengths of the studied Argillite clay at different loading angles are shown in the following graphs (Figs. 6-7). These parameters are based on ideal elasto-plastic theory of the Mohr-Coulomb model. In order to be able to use in the proposed mobilized hardening/softening elasto-plastic model, these parameters can be transformed into compatible parameters by the relevant formulas as discussed earlier in this report, which will eventually formulate a unified microstructural-tensor based elasto-plastic model capable of taking into account conditions with all loading angles and confining pressures.

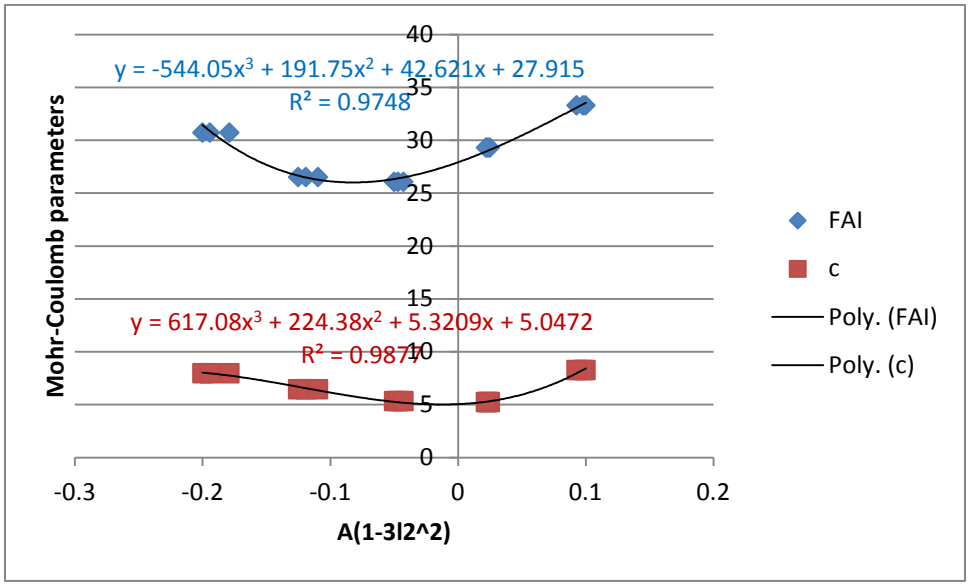

(a)

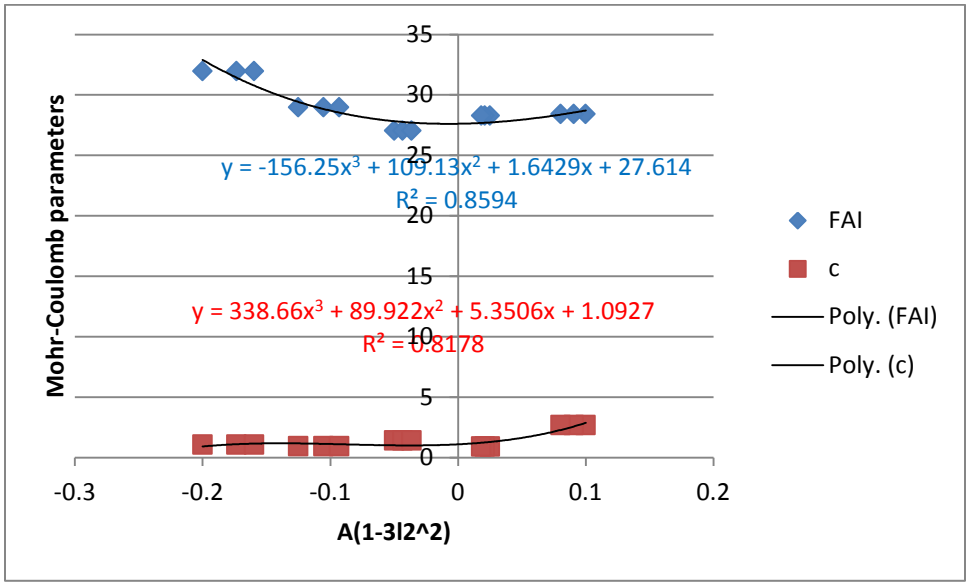

(b)

Figure 3.6 Dependence of Mohr-Coulomb strength parameters on the loading orientation parameter (a) the peak strength and (b) the residual strength

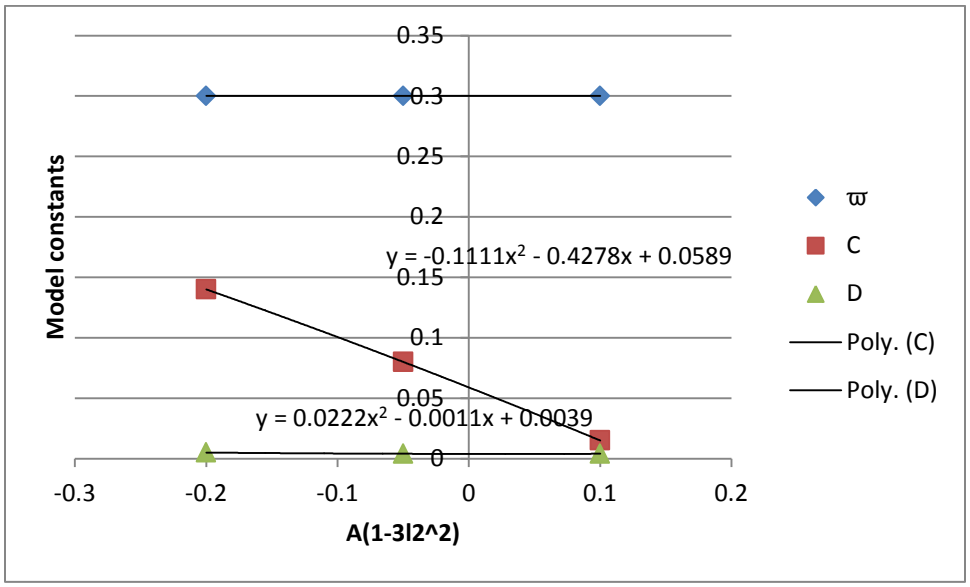

(a)

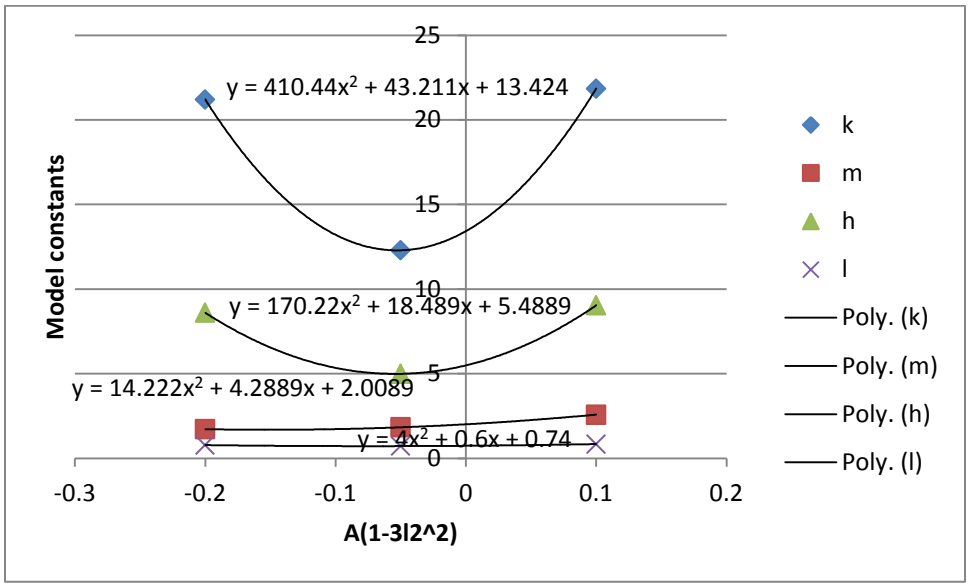

(b)

Figure 3.7 Dependence of model constants for peak plastic strain on the microstructural tensor

2.4 Tsai-Hill anisotropic peak strength model

Following Mohr-Coulomb strength criterion, both the in-plane and transverse shear strength can be separately evaluated, giving different sets of model parameters that need further analysis to set up an internally coherent relationship. The Tsai-Hill strength criterion can be used to reflect the curved evolution of the shear strength of an anisotropic rock.

$$\frac{cos^4\theta}{\sigma_{LU}^2} - \frac{cos^2\theta sin^2\theta}{\sigma_{LU}^2} + \frac{sin^4\theta}{\sigma_{TU}^2} + \frac{cos^2\theta sin^2\theta}{\tau_{LTU}^2} = \frac{1}{\sigma_\theta} \quad (57)$$

where σ_{LU} and σ_{TU} are ultimate compressive strength at longitude and transverse direction, respectively; and τ_{LTU} is the ultimate transverse shear strength; σ_θ is the principal stress loading on the specimen with load angle equals to θ, which is equivalent to σ_1 in this study. Figure 3.10 shows the directional strength of glass epoxy as predicted by Tsai-hill strength criterion. It is shown that the varying trend of the failure strength with load angle against the bedding plane can be reproduced with very smooth curve and good agreement.

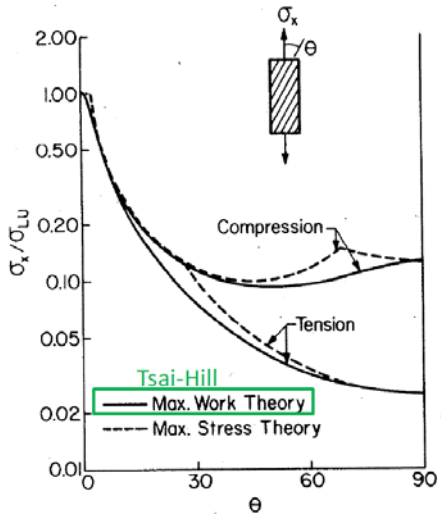

Figure 3.8 Anisotropic strength vs load angle using Tsai-Hill criterion for glass-epoxy composite (The load angle used in this case is valid for θ+β=90°)

(http://scmero.ulb.ac.be/Teaching/Courses/MECA-H-406/H-406-4-Failure.pdf)

Classical Hill strength does not consider the influence of confining pressure on the enhancement of ultimate strength. This behavior has been observed in some recent studies. For instance, Davila et al. (2005) proposed a series of failure criteria for fiber reinforced polymer considering the Mohr-Coulomb effective stresses. Sun et al. (1996) modified another composite strength criterion to account for the increase in shear strength due to compressive intermediate stress. However, there still is not a modified Tsai-Hill criterion taking into account the mean stresses. In this study, Mohr-Coulomb theory was integrated into the above shown Tsai-Hill theory to demonstrate the enhancement of confining pressure upon the shear strength.

A modified composite strength criterion can be proposed in such a form as,

$$\sigma_{LU} = a + b\sigma_3$$

$$\sigma_{TU} = c + d\sigma_3 \quad (58)$$

$$\tau_{LTU} = e + f\sigma_3$$

After a series of deduction, the following formulas are obtained:

$$C_\theta = \frac{A}{2\sqrt{B}} \quad (59)$$

$$\phi_\theta = arcsin\frac{B-1}{B+1} \quad (60)$$

where C_θ and ϕ_θ are anisotropic cohesion and internal friction angle within the framework of Mohr-Coulomb strength criterion, respectively, depending on load angle θ and three strength envelops, i.e. in plane peak strength, transverse peak strength and shear strength; A and B are model constants that can be derived from the following equations,

$$A = \left(\frac{cos^2\theta cos2\theta}{a^2} + \frac{sin^4\theta}{c^2} + \frac{sin^2\theta cos^2\theta}{e^2}\right)^{-\frac{1}{2}} \quad (61)$$

$$B = \left[b\frac{cos^2\theta cos2\theta}{(a+b\sigma_3)^3} + d\frac{sin^4\theta}{(c+d\sigma_3)^3} + f\frac{cos^2\theta sin^2\theta}{(e+f\sigma_3)^3}\right] * \left[\frac{cos^2\theta cos2\theta}{(a+b\sigma_3)^2} + \frac{sin^4\theta}{(c+d\sigma_3)^2} + \frac{cos^2\theta sin^2\theta}{(e+f\sigma_3)^2}\right]^{-\frac{3}{2}} \quad (62)$$

Figure 3.9 shows the curve fitting with regard to the experimental data by the above Tsai-Hill/Mohr-Coulomb strength criterion. Good agreement is observed between test data and theoretical estimations, suggesting the validity of this strength criterion for the studied anisotropic sedimentary rock. In order to validate the above equation, we take the case with load angle $\theta=0^o$ for instance, whereas the MC strength parameters can be estimated from above equations to be c=8.25 MPa and $\phi=33.3^o$, which are exactly the same values as estimated from traditional Mohr circle method.

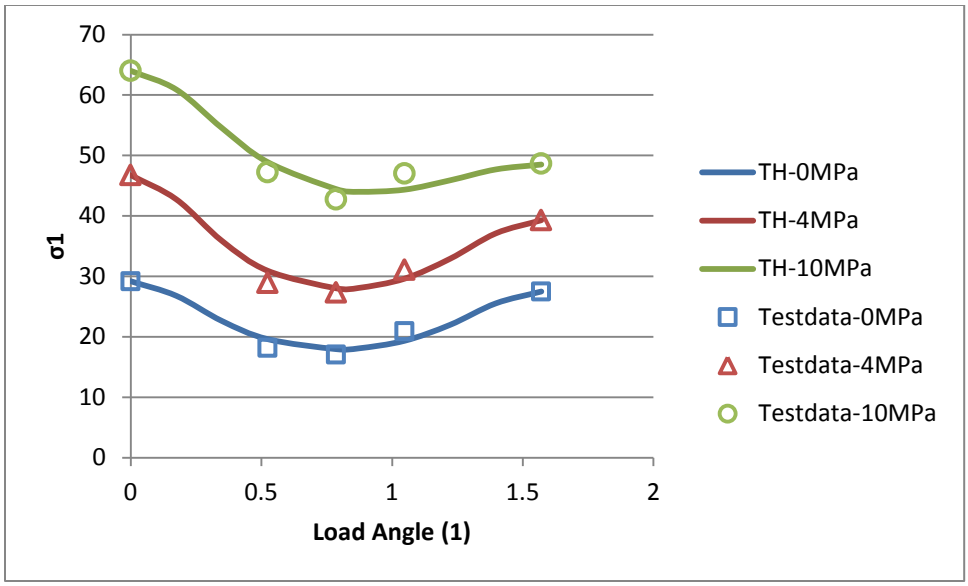

Figure 3.9 Peak strength of anisotropic Argillite vs load angle under various confining pressures

3. Experimental results

3.1 Argillite clay

Tiaxial test

Abdi et al. (2015) reported the uniaxial and triaxial compression test data on Argillite clay. The original experimental results are plotted in the following part and are re-analysed in this study for the validation of our models. The deviatoric stress and the volumetric strain are plotted against the axial strain to reflect the dilatancy and yield of the specimen. Hardening is present in all the tested rock samples. After the peak strength, a rapid reduction in strength instantly follows. Such behaviors indicate the occurrence of strain localization, which cannot be modelled within the capacity of the FEM programs like COMSOL. This study is mainly confined to the framework of continuum mechanics. The post-failure behavior is modelled, however, not to the extent of reflecting the cracking propagation and reconciliation that can be simulated by extended FEM or other damage models.

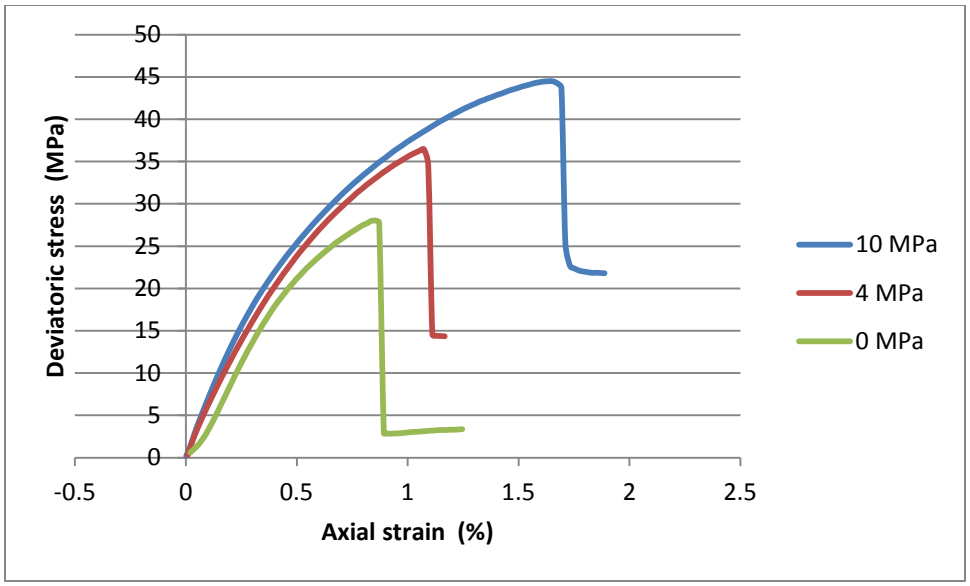
Deviatoric stress (MPa)
50
45
40
35
30
25
20
15
10
5
0
-0.5
0
0.5
1
1.5
2
2.5
Axial strain (%)
10 MPa
4 MPa
0 MPa

(a)

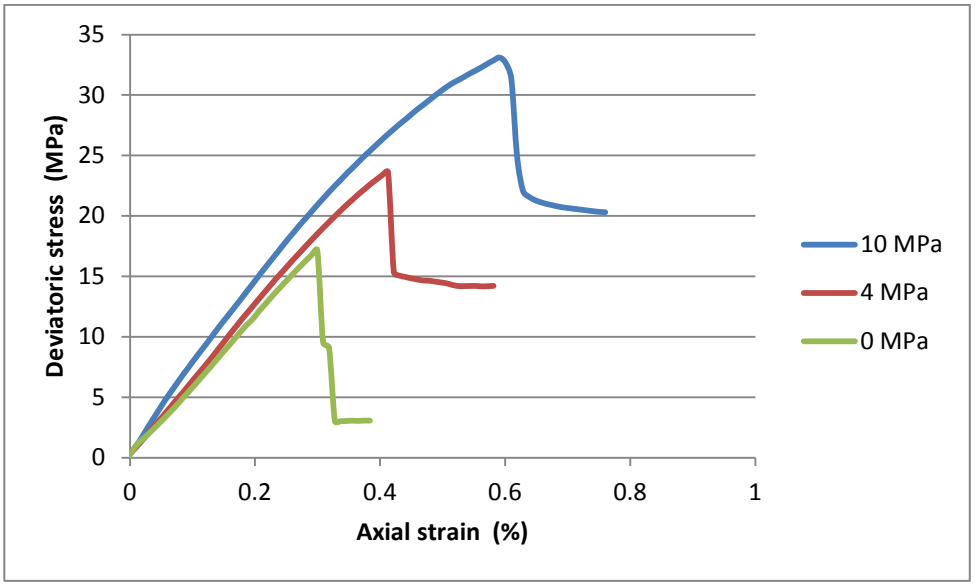
Deviatoric stress (MPa)
35
30
25
20
15
10
5
0
0
0.2
0.4
0.6
0.8
1
Axial strain (%)
10 MPa
4 MPa
0 MPa

(b)

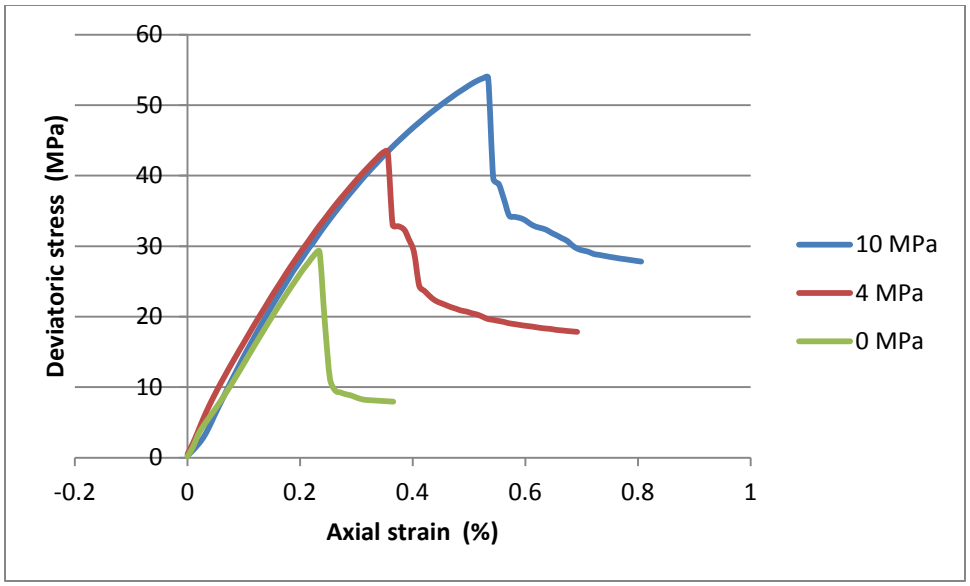

(c)

Figure 3.10 Stress strain relationship for Argillite clay under three confining pressures (0, 4 and 10 MPa): A) β=0°; B)) β=45°; C)) β=90°

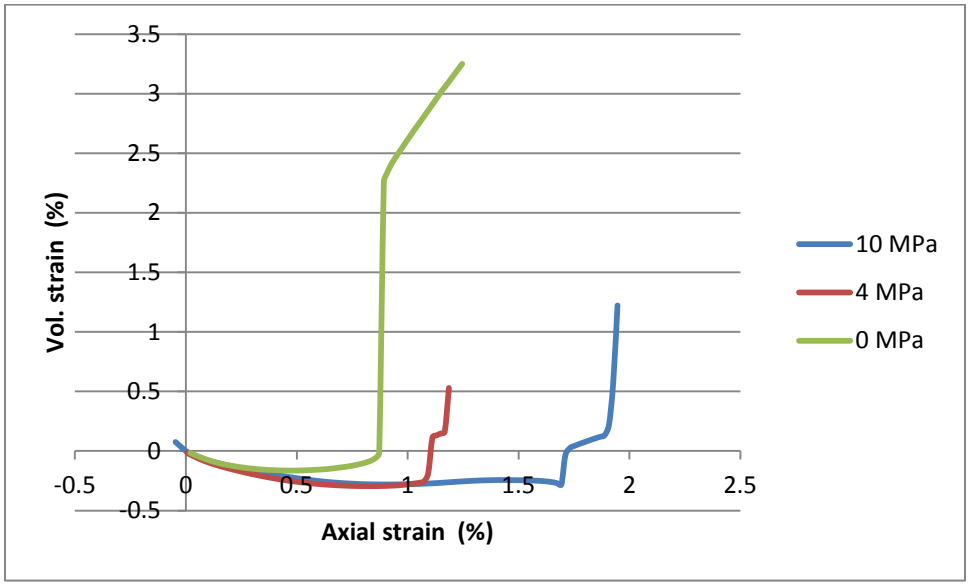

(a)

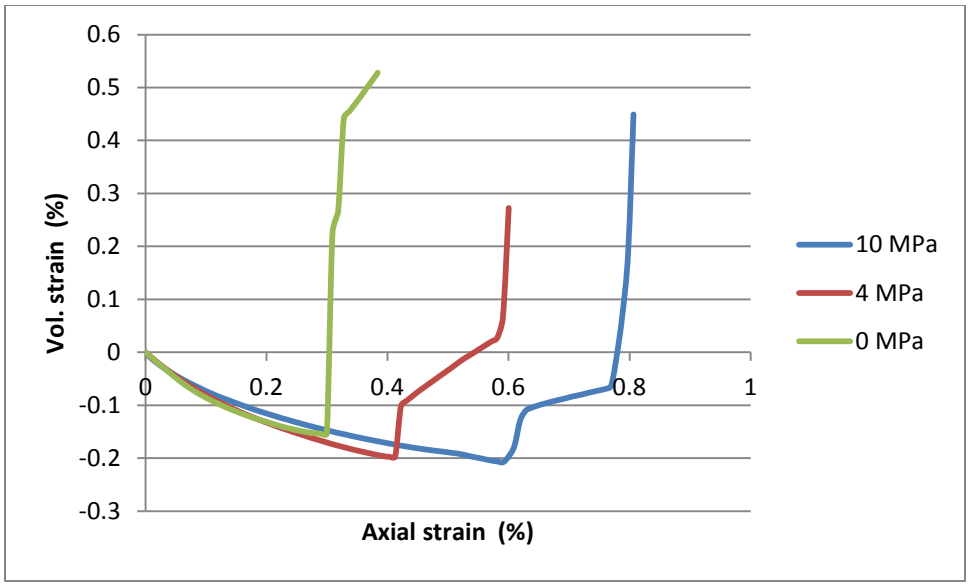

(b)

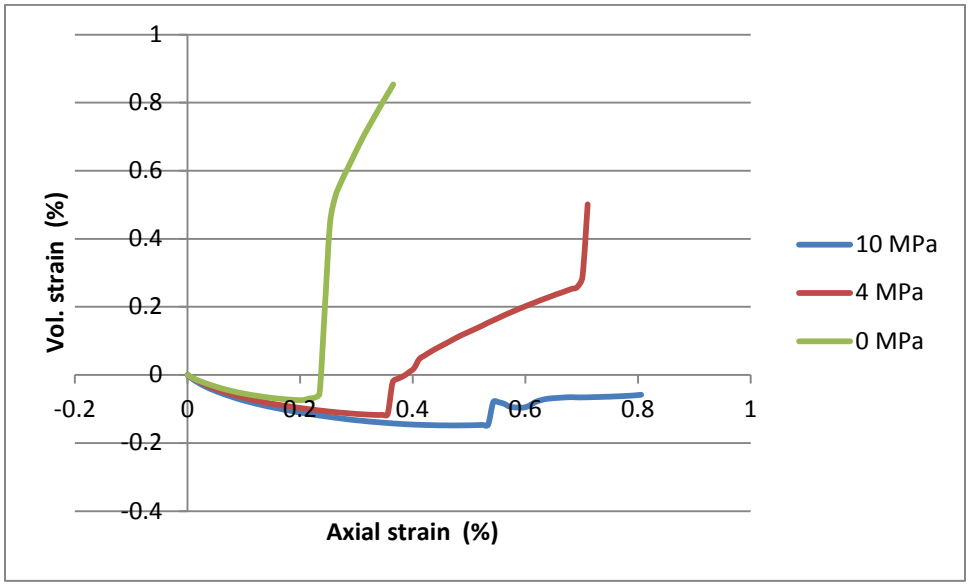

(c)

Figure 3.11 Volumetric strain and axial strain relationship for Argillite clay under three confining pressures (0, 4 and 10 MPa): A) β=0°; B)) β=45°; C)) β=90°

Cyclic triaxial shear test

Figures 3.12-3.13 show the stress-strain and volumetric variation behaviours of Argillite under cyclic loading test. These data enable the calculation of various critical model constants, i.e. tangent modulus, Poisson's ratio and the degradation of stiffness with plastic strain. It is noted that the crack initialization

originates at about 30 % of the peak strength. In this regard, the plastic strain was calculated based on the strain variation at the point where stress level was reversed to the lowest level. The Young's modulus of the test sample was determined by calculated the slope of the cycle of stress reversal. The evolution of Young's modulus with changing plastic strain was also investigated in our analysis. These parameters were further correlated with the loading angle in order to establish a generalized microstructural tensor-based elasto-plastic model.

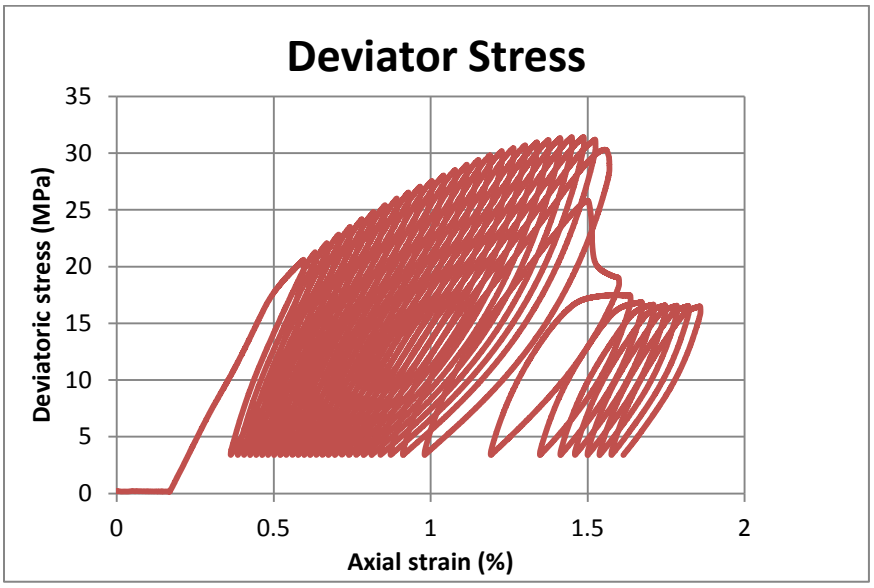

(a)

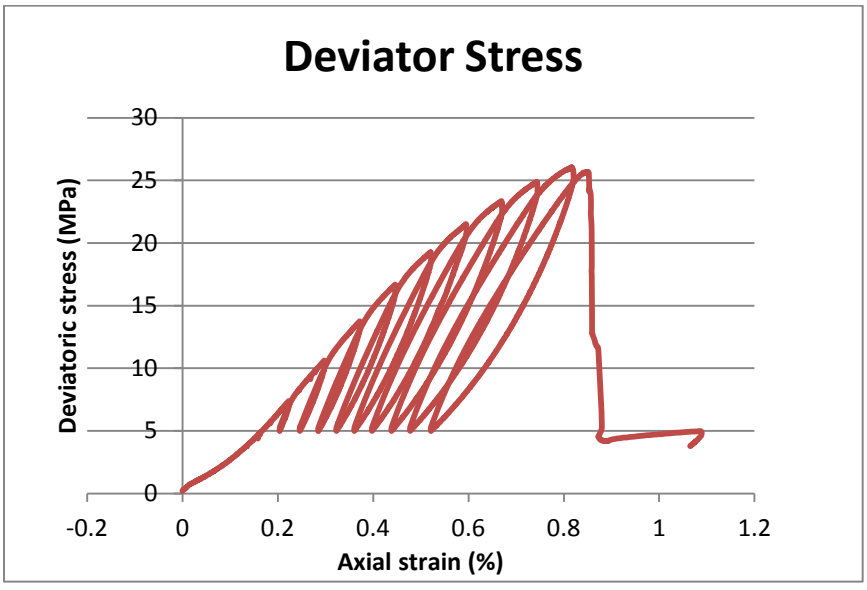

(b)

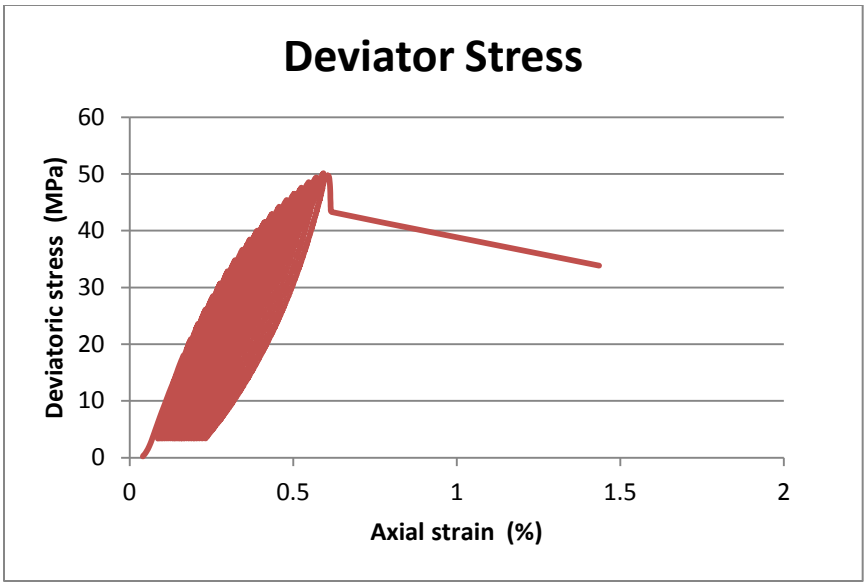

(c)

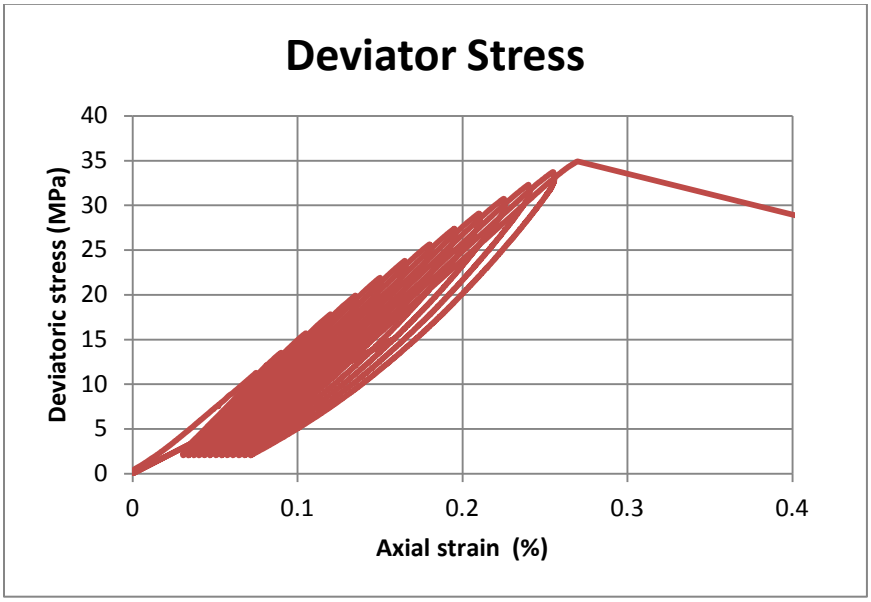

(d)

Figure 3.12 Deviatoric stress vs axial strain for cyclic triaxial test under various conditions (a) β=0; σ_3=10 MPa (b) β =0; σ_3=0 MPa (c) β =90; σ_3=10 MPa (d) β =90; σ_3=0 MPa

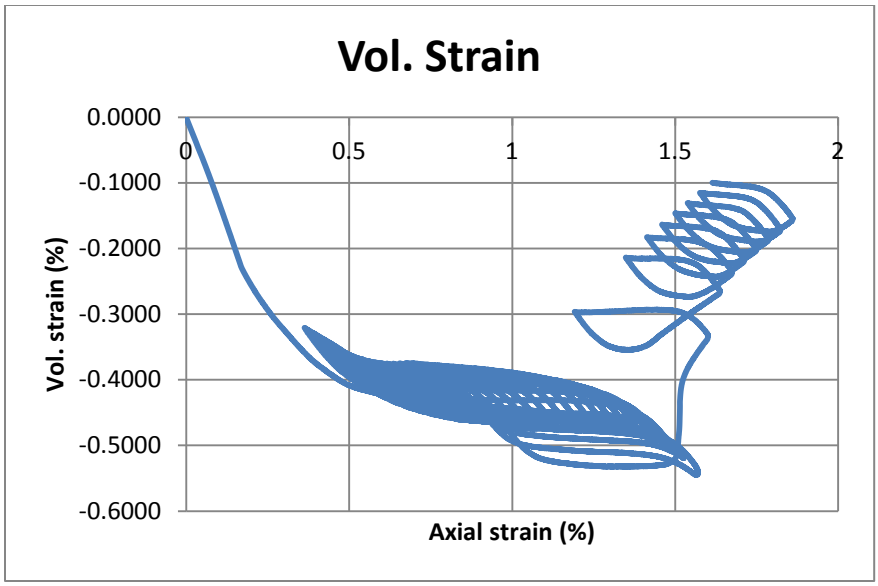
Vol. Strain
0.0000
-0.1000
-0.2000
-0.3000
-0.4000
-0.5000
-0.6000
0
0.5
1
1.5
2
Vol. strain (%)
Axial strain (%)

(a)

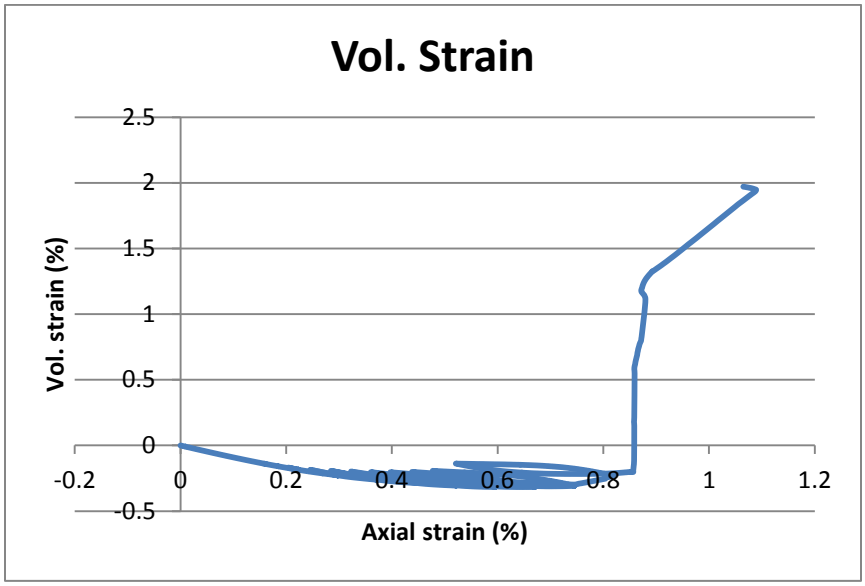
Vol. Strain
2.5
2
1.5
1
0.5
0
-0.5
-0.2
0
0.2
0.4
0.6
0.8
1
1.2
Vol. strain (%)
Axial strain (%)

(b)

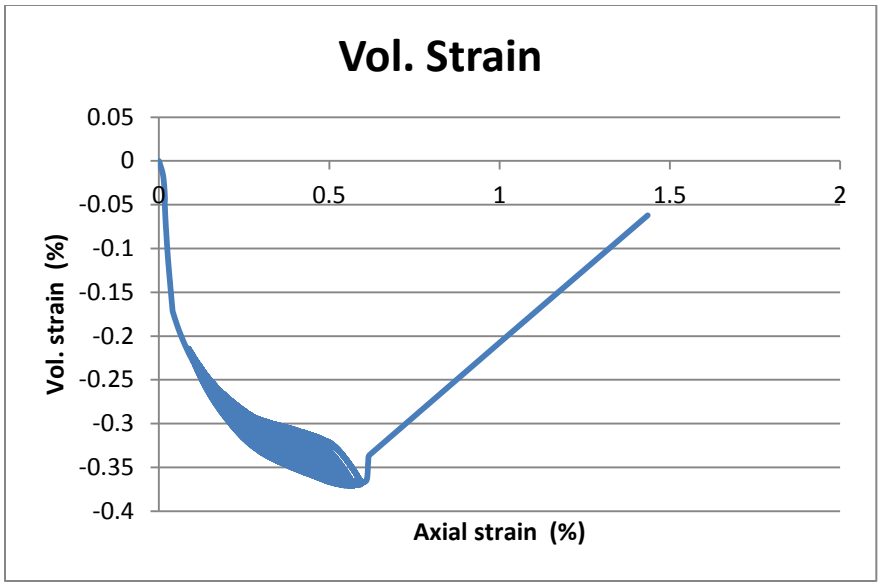

(c)

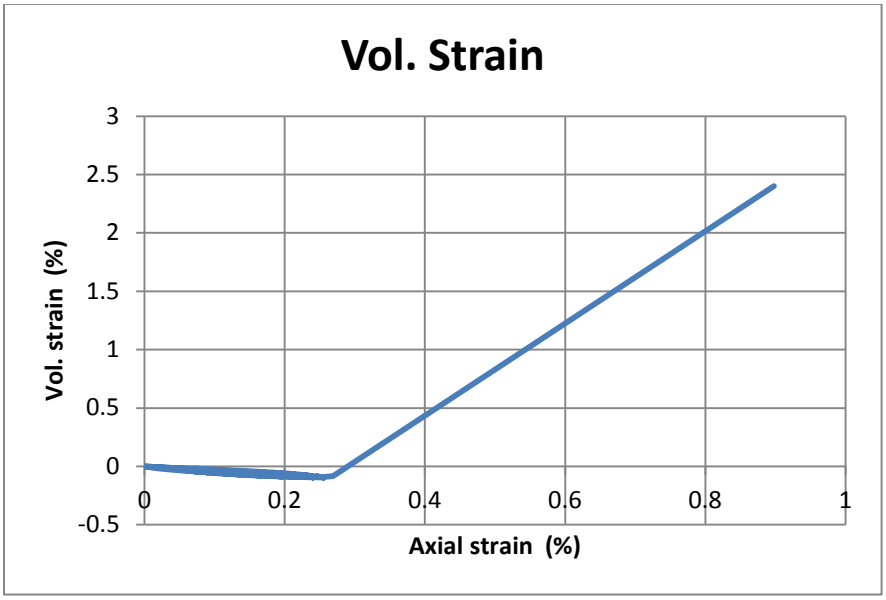

(d)

Figure 3.13 Volumetric strain vs axial strain for cyclic triaxial test under various conditions (a) β=0; σ_3=10 MPa (b) β =0; σ_3=0 MPa (c) β =90; σ_3=10 MPa (d) β =90; σ_3=0 MPa

3.2 Cobourg limestone

Figures 3.14 show the triaxial test results for Cobourg limestone. The rock specimens were sampled from a quarry near the Bruce site. Experiments were carried out in University of Toronto. So far only part of the proposed tests has been finished. Many important information and parameters about the

Cobourg limestone are still missing at present. Two hydraulic-mechanical coupled compression tests under 5 MPa confining pressure and 3 MPa pore pressure are screened as qualified for the validation against our models. The test data are shown as following.

The first specimen parallel to bedding failed at 103 MPa of axial stress with a maximum axial strain of 0.45% and a radial strain of 0.18%. The triaxial compressional strength of the other specimen tested perpendicular to foliation plane is lower than the ones tested parallel to foliation plane. The specimen perpendicular to bedding plane failed at 47 MPa of axial stress with a maximum axial strain of 0.3% and a radial strain of 0.3%.

Table 3.3 lists the estimated elasticity and Poisson's ratios for the anisotropic Cobourg limestone. It is noted that the transverse shear modulus is unavailable for the current study, of which the estimation has to address the cases with load angle other than 0 and 90 ^{o}.

Figures 3.14C-14D show the correlation between the volumetric and axial strains. The linear relationship between axial and radial strains suggests a constant value of Poisson's ratio, preceding the peak strength. Dilatancy mainly occurs to the post-failure stage that involves a significant percentage of plastic strain. The peak strength was estimated from the experimental data along with the reported value of friction angle at 31 ^{o} (Damjanac, 2008). Ghazvinian et al. (2013) reported the anisotropic strength properties of Cobourg limestone and showed that its peak strength has a friction angle ranging from 36.9 to 45.6 ^{o} and the crack initialization strength has a friction angle ranging from 23.6 to 30 ^{o}. For safety purpose, a medium value (as adopted by ITASCA for mechanical modeling of DGR, φ= 31 ^{o}) was taken into account in this study. It is also hypothesized that ϕ=31 ^{o} is valid for both cases with different load angles. Then can we calculate the cohesion as shown in Table 3.3.

Note that the objective of this numerical study is not to derive a generalized strength envelope or constitutive model for Cobourg limestone that is valid for all loading conditions (β, σ3 etc.). Instead, we are aiming at 1) understanding the hydraulic-mechanical coupling behavior and the permeability evolution mechanism and formulas, and 2) validating our proposed mobilized hardening/softening model against another set of experimental results. To the end of this study, it seems sufficient to get these objectives fulfilled by the completed numerical simulations.

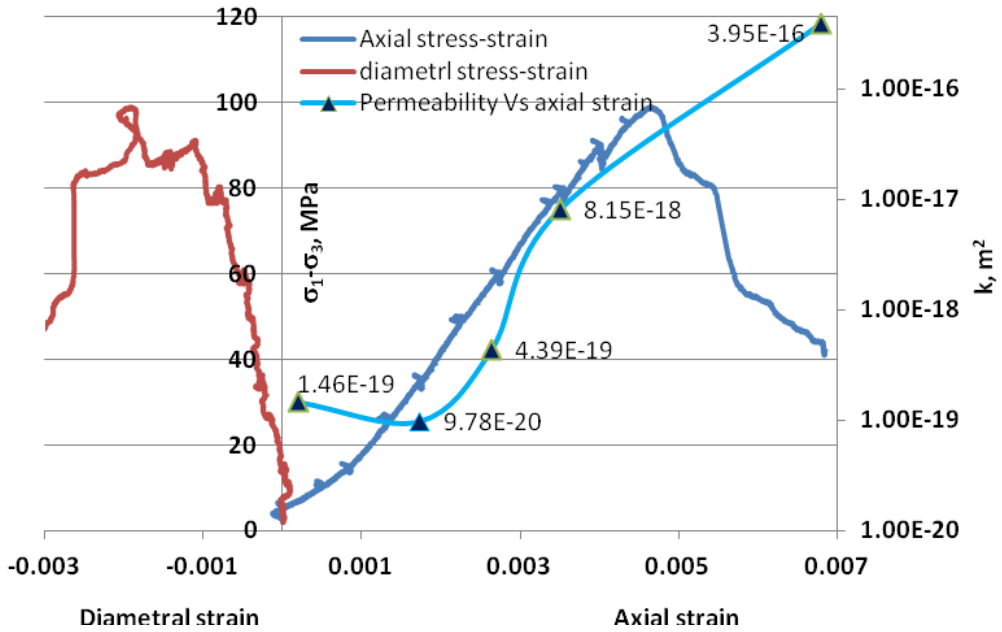

Figure 3.14A Variation of axial and radial strains with differential stresses for specimen CLH-1-U tested at 5 MPa and 3 MPa of confining and pore pressures respectively. k vs axial strain is shown in the second vertical axis. β=90°

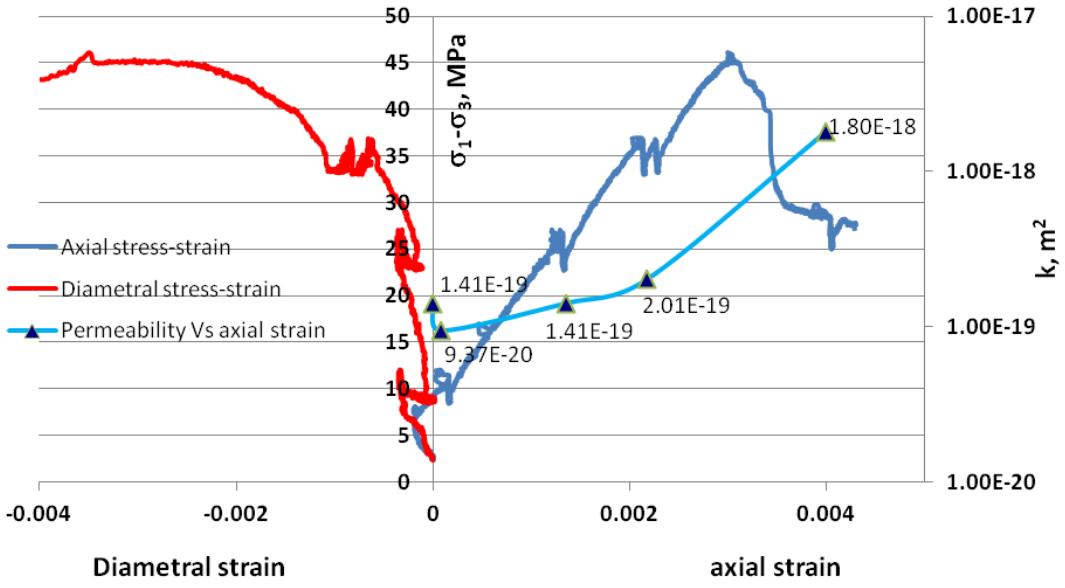

Figure 3.14B Variation of axial and radial strains with differential stresses for specimen CLV-3-T tested at 5 MPa and 3 MPa of confining and pore pressures respectively. β=0°

Table 3.3 Stiffness and strength parameters for Cobourg limestone (From limited data available at present)

Variables	Value	Unit/note
Stiffness		
$E_{\perp}$	12.3	GPa
$E_{\parallel}$	21.5	GPa
$v_{\perp}$	0.200	
$v_{\parallel}$	0.252	
$G_{\perp}/E_{\perp}$	NA	
$G_{\parallel}$	$E_{\parallel}/2(1+v_{\parallel})$	GPa
Strength		
ϕ	31	deg
$c_{\perp}$	9.73	MPa
$c_{\parallel}$	24.72	MPa
Yielding		
ϖ	0.30	
Post-failure		
E	100	β=0°
E	60	β=90°

The size of the test specimen was measured at L*D=12.5*5.4 cm*cm. According to studies of Ghazvinian et al. (2013) on the same rock, the crack initialization and crack damage values are 30, 60 % of the peak strength, respectively. This suggests potential links between permeability and early stage of plastic hardening, e.g. equivalent to the hypothesis of crack initialization in our mobilized hardening/softening model. In this study, we took 30% as the onset of crack initialization threshold value. This value is also justified by the variation of acoustic velocity as tested on Cobourg limestone by Nasseri and Young (2015).

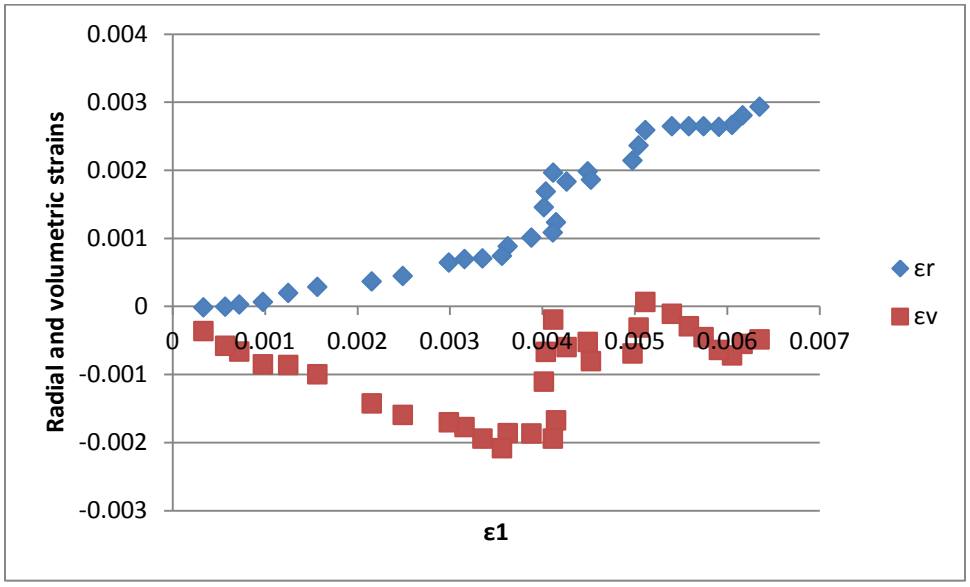

Figure 3.14C Volumetric strain and radial strain vs axial strain for Cobourg limestone. β=90°;

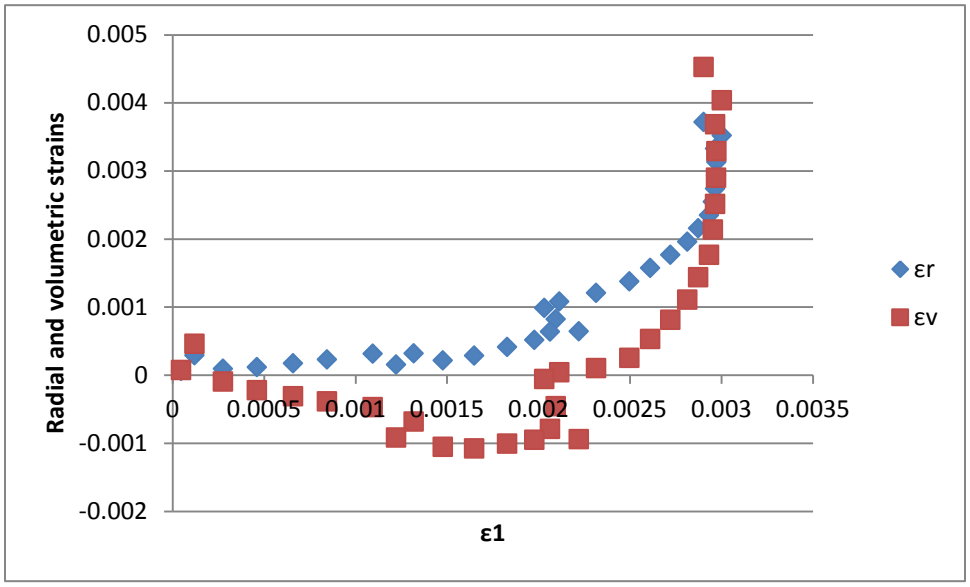

(b)

Figure 3.14D Volumetric strain and radial strain vs axial strain for Cobourg limestone. β=0°

4. FEM model

A 3-D cylinder-shaped FEM model for the triaxial shear test was developed with COMSOL (Ver 5.1). The dimension of the test cell is at H*R=133*35 mm*mm. The geometric sketch and FEM mesh of the model are shown in Fig. 3.15a. The bottom plane was assigned with confined strain while the side surfaces with confining pressure Pc. The upper boundary was assigned with prescribed displacement in vertical direction. The evolution of vertical stress was monitored throughout the simulation for comparison with test data. A stationary problem was assumed valid for all the simulation studies. A modified Mohr-Coulomb elasto-plastic theory as described above was implemented into COMSOL. Three cases with different confining pressure Pc=0, 4 and 10 MPa, were numerically investigated in the following parts.

As for the FEM model for Cobourg limestone, the specimen measures at H*R=12.5*2.7 cm*cm. Figure 3.15b shows the meshing of the triaxial test cell. The confining pressure assigned at the side surface is maintained at 5 MPa. Except for the model constants that are different, other settings are kept identical to the above models for Argillite clay.

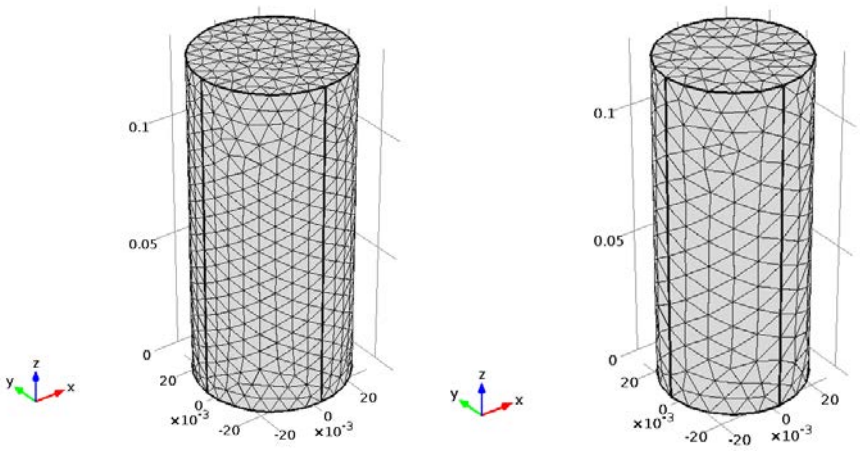

(a) (b)

Figure 3.15 Meshing of the FEM model for triaxial compression test on (a) Argillite and (b) Cobourg limestone

5. Results and discussion

5.1 Tournemire argillite

5.1.1 Stress-strain behaviour

Figures 3.16a-3.16c show the modelling results of stress-strain curves and the comparison with test data. Good agreement between modeling and testdata can be observed for most of the test cases, except for the sample under confining pressure of 10 MPa at β=45°, which shows some discrepancy in the strain-hardening process prior to the peak strength. The linear hardening law with which the model parameters were determined seems sufficient to reflect the gradually curved growth of axial stress with increasing axial strain. The peak strength fits well with the estimated Mohr-Coulomb strength envelope.

The Young's moduli applied in our modeling were originally derived from the cyclic shearing test. It is noticed that this parameter cannot be used directly for the calibration purpose because it turns out to universally overestimate the stress level in elastic stage. This discrepancy can be attributed to the difference between tangent modulus and secant modulus, whereas the latter is regarded to be 1/3-1/2 of the former. Viscoplasticity may play a role in this system as well, which can explain the comparatively higher value in reversed tangent modulus than the observed Young's modulus. In this study, a slightly reduced value of tangent moduli were used to give the best modeling results with respect to the test data, as following

$$E_i = \xi E_t \tag{63}$$

where ξ is a reduction factor; E_i is the adopted initial modulus for modelling and E_t is the experimentally determined tangent modulus. The best-fitted reduction factors are shown in Table 3.2 for reference.

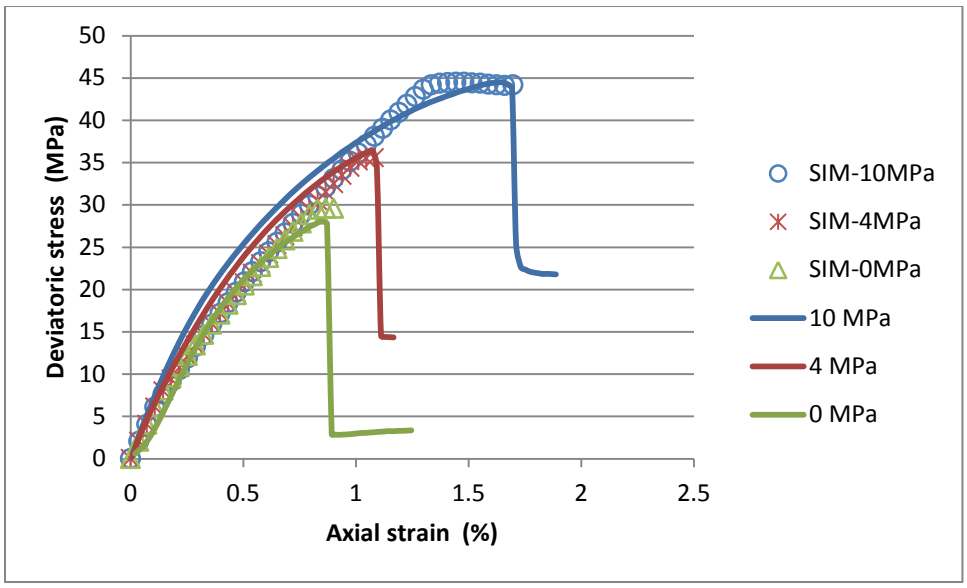

(a)

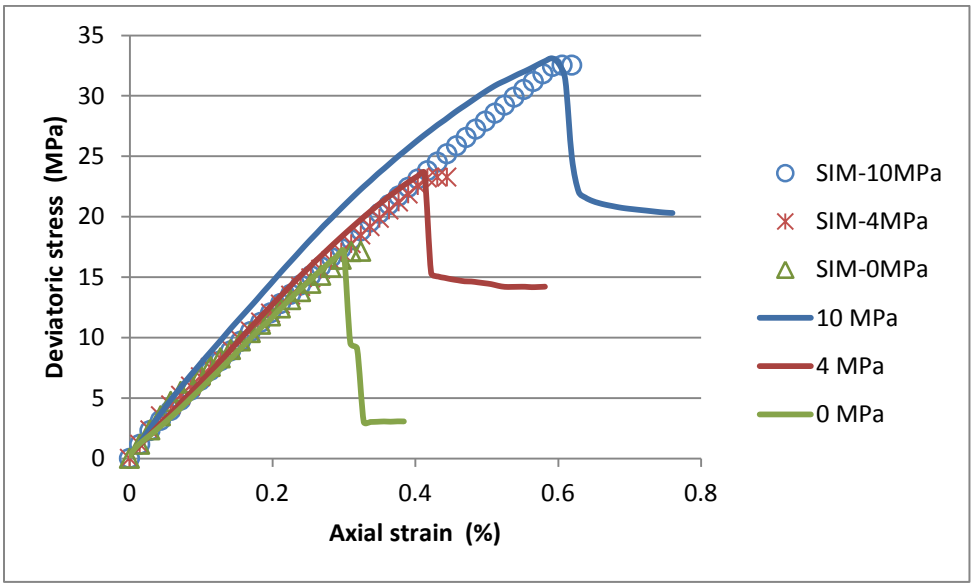

(b)

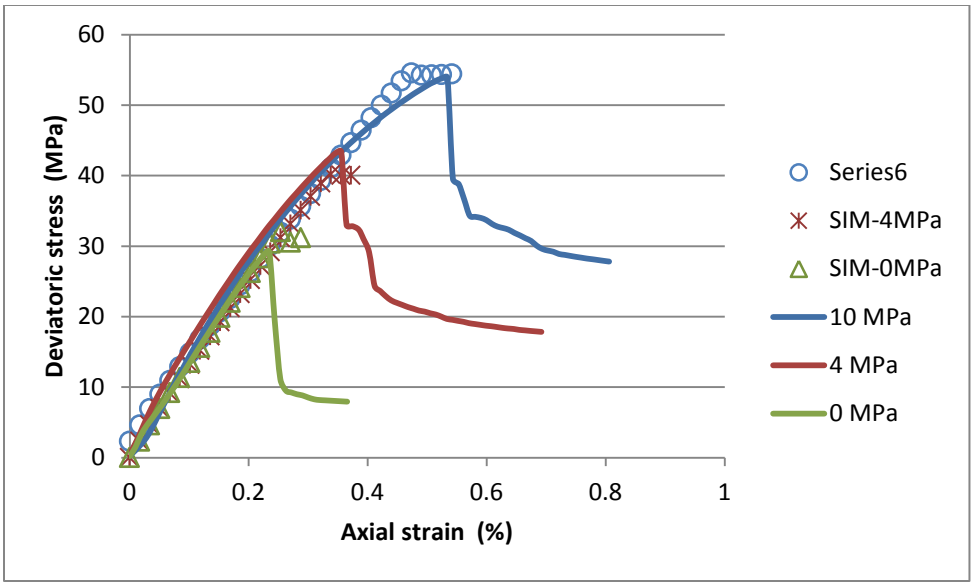

(c)

Figure 3.16(a-c) Stress strain curves for specimens with load angle at β=0, 45 and 90^{o} (solid curves are test data and open symbols are simulation results)

5.1.2 Volumetric strain vs axial strain

Figures 3.17a-3.17c show the predicted volumetric strain and its comparison with the test data. The overall volumetric strains are well reproduced by our model, particularly for test cases with load angle at 45 and 90 ^{o}. It is found that the hardening stage turns out to behave differently for cases with various load angles in terms of the volumetric strain. For test conditions with β=90 and 45 ^{o}, the hardening stage sticks to a mode showing obvious plastic flow pattern without significant dilatancy or volumetric shrinkage. The specimens with β=0 ^{o} show a similar pattern in volumetric change as determined by experiment, however, experience moderate dilatancy in the hardening stage in the experiment. Higher confining pressure always induces faster dilatancy in the strain hardening stage such as those with loading orientation at β=0 and 45 ^{o} under σ_3=10 MPa. This discrepancy may suggest a different mechanism that controls the plastic strain during the hardening process.

The post-failure pattern of stress strain curves was not simulated for the Tournemire argillite. This is because of the lack of information about hydraulic-mechanical coupling that has to be related to effective plastic strain. As for the Tournemire argillite, there were no experiments on the damage induced permeability enhancement available to this study. Therefore it appears to be unnecessary to investigate the post-failure softening behaviour, especially considering the inability of our continuum mechanics-based elasto-plastic model to model the phenomenon with significant strain localization. The next series of experiment about Cobourg limestone will see the modelling of post-failure softening behavior.

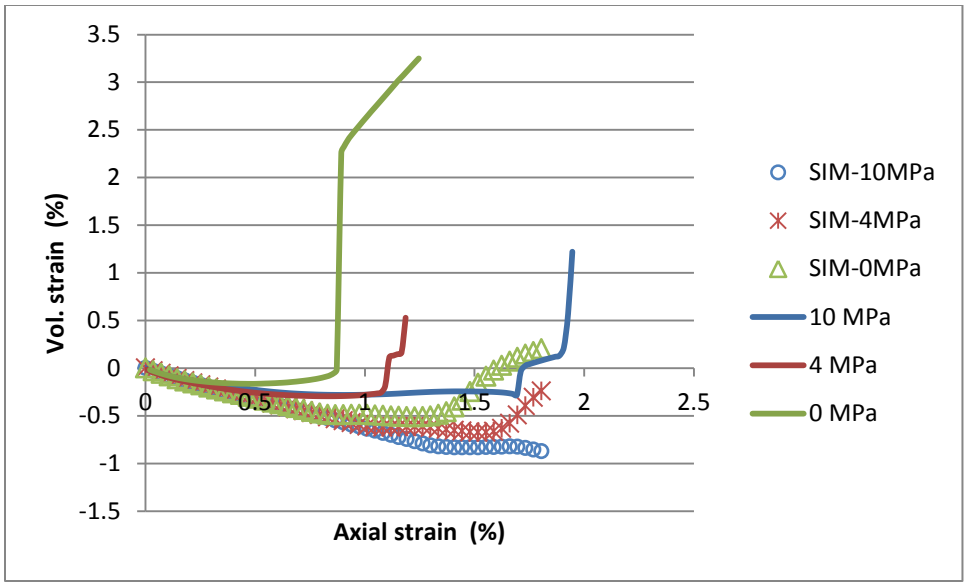
3.5
3
2.5
2
1.5
1
0.5
0
-0.5
-1
-1.5
0
0.5
1
1.5
2
2.5
Vol. strain (%)
Axial strain (%)
SIM-10MPa
SIM-4MPa
SIM-0MPa
10 MPa
4 MPa
0 MPa

(a)

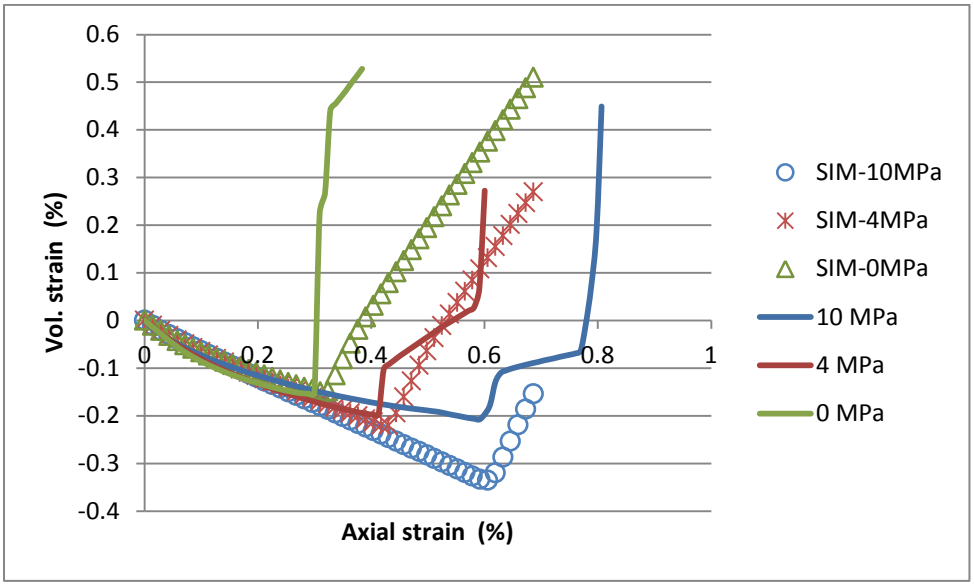
0.6
0.5
0.4
0.3
0.2
0.1
0
-0.1
-0.2
-0.3
-0.4
0
0.2
0.4
0.6
0.8
1
Vol. strain (%)
Axial strain (%)
SIM-10MPa
SIM-4MPa
SIM-0MPa
10 MPa
4 MPa
0 MPa

(b)

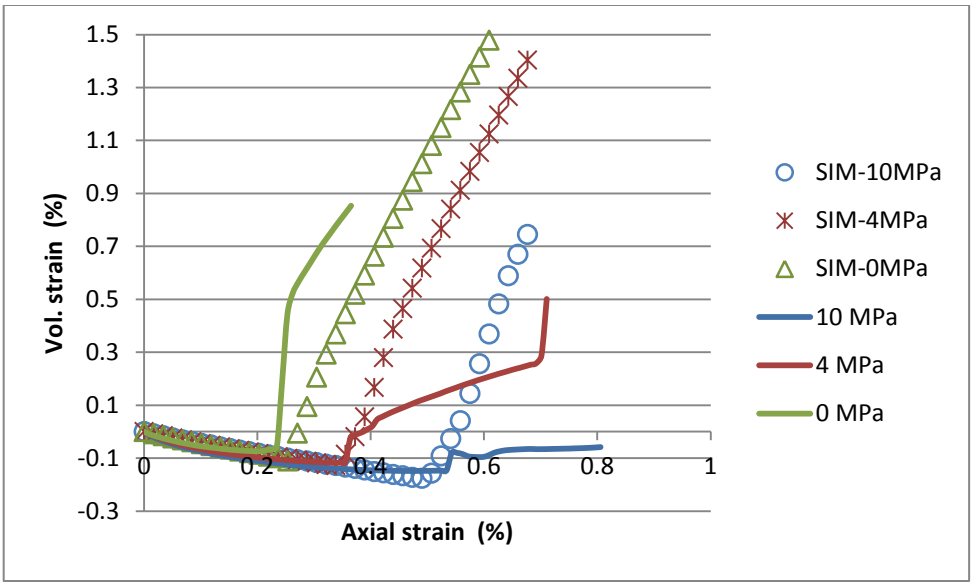

(c)

Figure 3.17(a-c) Volumetric strains for specimens with load angle at β=0, 45 and 90° (solid curves are test data and open symbols are simulation results)

5.2 Cobourg limestone

5.2.1 Stress-strain behaviors and volumetric strains

Figure 3.18 shows the reproduced stress-strain curves for Cobourg limestone using the proposed model. Good agreement with the experimental data is well demonstrated. The modeled stiffness and peak strength are both consistent with the test data. As for the post-failure softening behaviour, our modeling results differ somewhat from the test data. This is mainly attributed to the choice of model constant *E*. The declining trend could be much steeper when employing a larger *E*. But this will cause significant problem to the numerical convergence of COMSOL. The presented results are amongst the best that we can get within the capacity of the simulation platform.

Figure 3.19 shows the evolution of volumetric strain. For the first sample at β=0°, the dilatancy after crack initialization is so significant that the volumetric strain heads upward rapidly to be plus before reaching the peak strength. The other sample shows moderate dilatancy after the crack initialization strength is exceeded with the volumetric strain remaining in the minus side even at the peak strength. The test data is well reproduced for the perpendicularly loaded sample (β=90°).

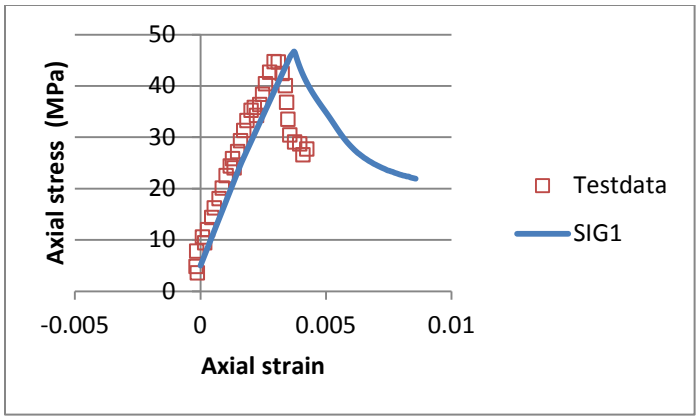

(a)

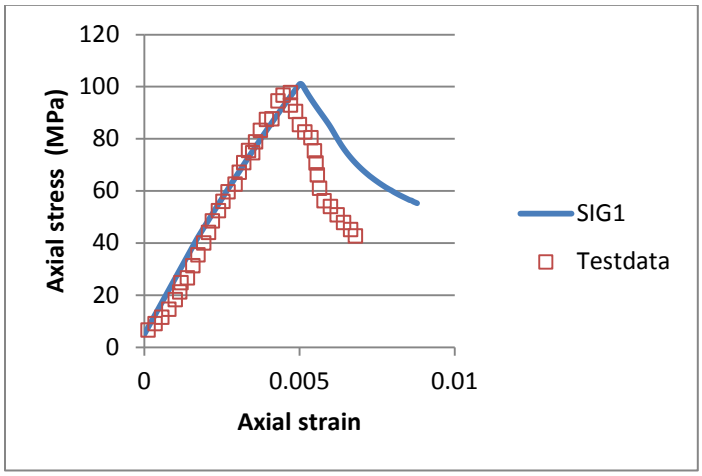

(b)

Figure 3.18 Modeling results of stress strain curves for Cobourg limestone at two load angles (a) β=0^{o} and (b) β=90^{o}

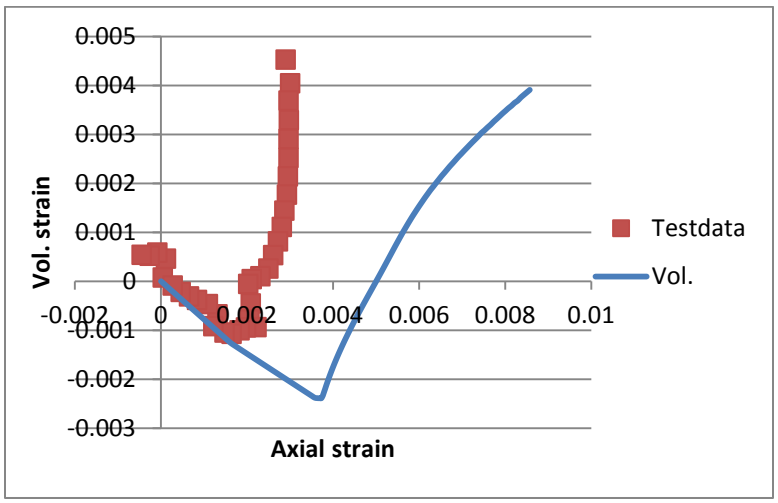

(a)

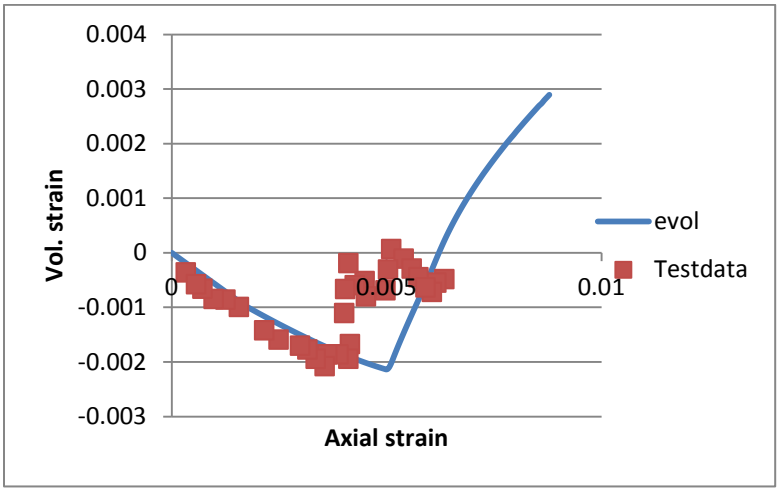

(b)

Figure 3.19 Modeling results of volumetric strain for Cobourg limestone at two load angles (a) β=0° and (b) β=90°

5.2.2 Permeability versus effective plastic strain

Figure 3.20 shows the dependence of permeability of Cobourg limestone on plastic strain. A threshold value of plastic strain was observed to dominate the variation of permeability. When Υ^p is less than the threshold value of 5E-5, the rock sample maintains a stable level of permeability at 1E-19 m^2. A rapid increase of permeability takes place when Υ^p>5E-5. Fitting these limited testdata results in an expression of the following relationship

$$k = \begin{cases} 6 * 10^{-19} e^{1410 * \gamma^p}, & \gamma^p > 5 * 10^{-5} \\ 10^{-19}, & \gamma^p \leq 5 * 10^{-5} \end{cases} \quad (64)$$

where k is permeability, γ^p is plastic strain, the correlation coefficient R^2=0.81.

The above formula resembles the recognized logarithmic relationship for the permeability of damaged geomaterials, which reads (Poulet et al., 2012; Rutqvist et al., 2009)

$$log \frac{k}{k_0} = \kappa' \gamma^p \quad (65)$$

where k is the damaged permeability and k_0 is the intact permeability; κ' is the model constant.

This equation can be applied to the modelling of hydraulic-mechanical coupled problems encountered in the Canadian DGR for nuclear waste. Since this is just a preliminary modeling study of Cobourg limestone, we do not have sufficient experimental data to formulate a more reliable and confident empirical equation for the permeability evolution of the damaged rocks. This issue can only be resolved

in future studies when the planned experiments on Cobourg limestone are completed and made available to analysis.

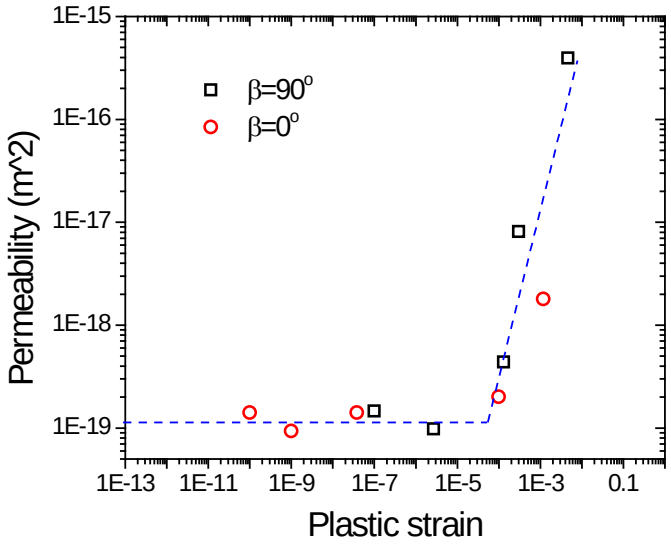

Figure 3.20 Evolution of permeability with computed plastic strain

5.2.3 Failure mode and experimental proof

Figure 3.21 shows the plotting of the simulated plastic strain at the end of compression test. It is obvious that shear bands are formed in both cases in the middle portion of the specimen. Figure 3.21 show the zones of plastic strain calculated with the finite element code COMSOL. The code does not have the capability to model localization, however it is instructive to examine the extent and shape of the calculated plastic zones and compare them to the real failure patterns. The maximum plastic strain is higher in samples with $\beta=90^{o}$ than that with $\beta=0^{o}$. The inclination of the former is also larger than the latter in the slope angle towards the vertical direction. These features are comparable to the experimentally observed pattern of the shear failure planes as shown in Fig. 3.22. The general shape of the calculated plastic zones is consistent with the factual failure pattern. The simulated plastic zone is concentrated within a limited space, which suggests the nucleation of microcracks resulted from former stage of compression, i.e. the crack initialization stage. This pattern appears near the peak strength and gets intensified in the post-failure stage in our modeling, which is consistent with the concept of crack nucleation and propagation that occurs immediately prior to the peak strength (Martin, 1993).

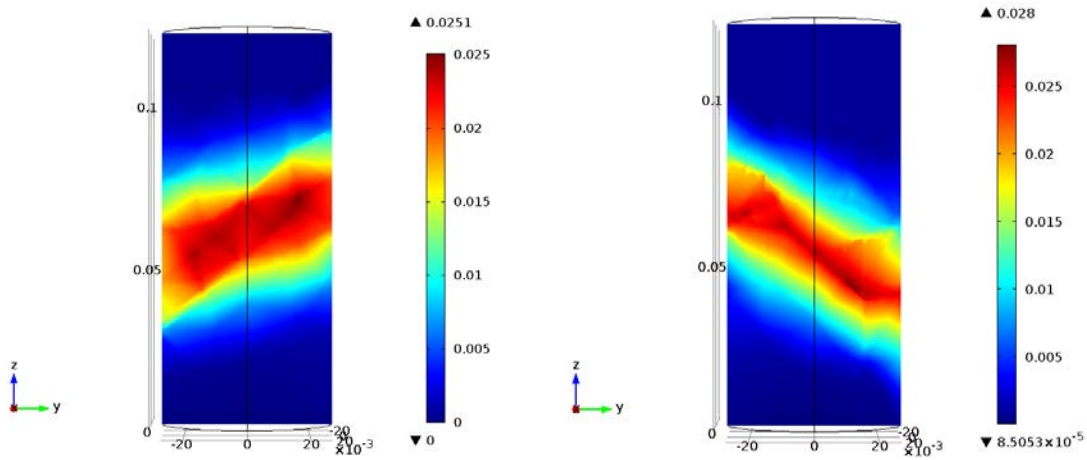

(a) (b)

Figure 3.21 Simulated failure mode of Cobourg limestone under triaxial compression conditions (a) β=0° and (b) β=90°

(a) (b)

Figure 3.22 Observed failure mode of Cobourg limestone under triaxial compression conditions (a) β=0° and (b) β=90° (Nasseri and Young, 2015)

5.3 Discussions on parameterization of Argillite clay

5.3.1 Residual and tensile strengths

For brittle rocks, the residual strength always indicates a large portion of frictional effect. Figure 3.23a indicates that the strength envelop can be modelled by the Mohr-Coulomb theory with good correlation. The test data on Argillite shows that the load angle affects the residual strength only in the parallel direction, other than which, there seems no difference in the residual strength for different load angles.

The tensile strength of the anisotropic Argillite clay rock appears to be varying with different load angles as shown in Fig. 3.23b. However, the scope of the variation of the determined tensile strength is so limited that it just consists of 20% of the mean strength. This value is also relatively small compared to the unconfined compressive strength. Therefore it is valid to assume a constant value for tensile strength can in the modelling.

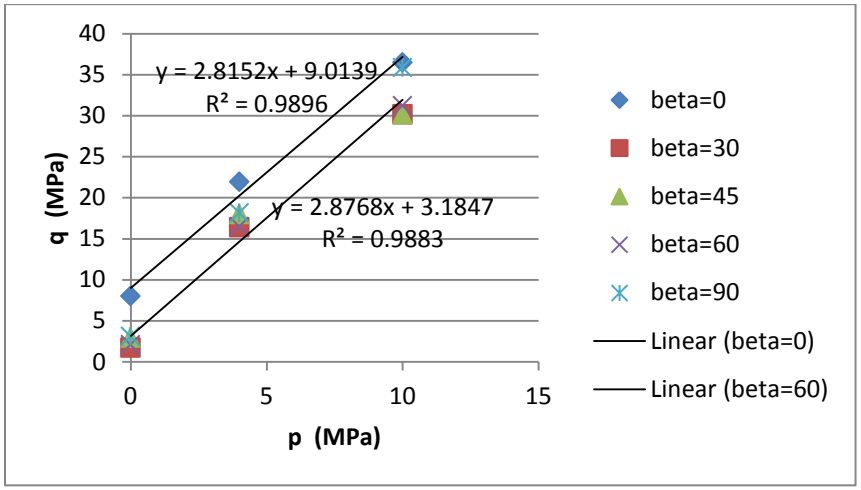

(a)

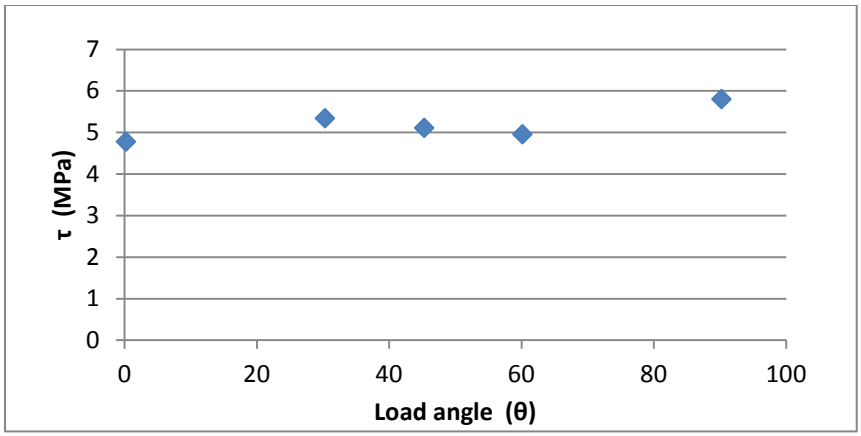

(b)

Figure 3.23 Residual (a) and tensile (b) strengths of Argillite at different load angles

5.3.2 Parameterization of the elasticity

Figure 3.24 shows the nonlinear variation of anisotropic stiffness of Argillite clay with the confining pressure. The elasticity of E_i is considered for the modelling of the initial elastic stage prior to reaching the crack initialization. It is found that confining pressure exerts conversely different influence on the change of stiffness when loaded in different angles. A general trend of declining Young's modulus can be found with increasing loading angle. Due to the narrow distribution of initial elasticity E_i, the average value was taken as the required parameter for the modelling purpose.

According to the cyclic shear test results, for most of the test scenarios the plastic strain is a weakening factor for the change of stiffness, which can be normalized into a unified curve as shown in Figure 3.25. This behavior is bound to the hardening stage where crack initiation strength has been passed. The strength appears to be growing with plastic strain, however, the stiffness as a sensitive indicator of the crack damage starts to decline. The good agreement between the fitting curve and test data attest the reliability of the fitting equations. For simplicity purpose Eq. (2b) was used in the modelling studies.

Figure 3.26 shows the best-fitted anisotropic elasticity with the alternative model derived from the anisotropic elastic mechanics. The only unknown parameter for this model is the transverse shear modulus G_{LT}, which can be estimated by trial-and-error method for all these sets of data under different confining pressures. It turns out to be identical to each other for the estimated shear modulus even under different confining pressures.

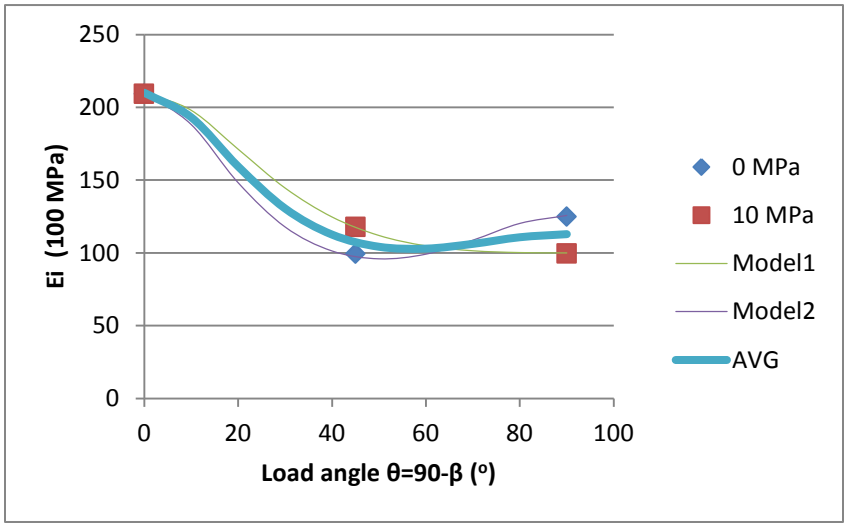

Figure 3.24 Stiffness of anisotropic Argillite clay rock vs confining pressure and load angle (Symbols are test data and curves are estimated by Eq. (1). The averaged stiffness was used in the simulations with the fitted parameters for AVG as v_{LT}=0.15; G_{LT}/E_{LT}=0.19. The shear modulus G_{LT}/E_{LT} is estimated to be 0.16 and 0.23, respectively for cases with σ_3=0 and 10 MPa)

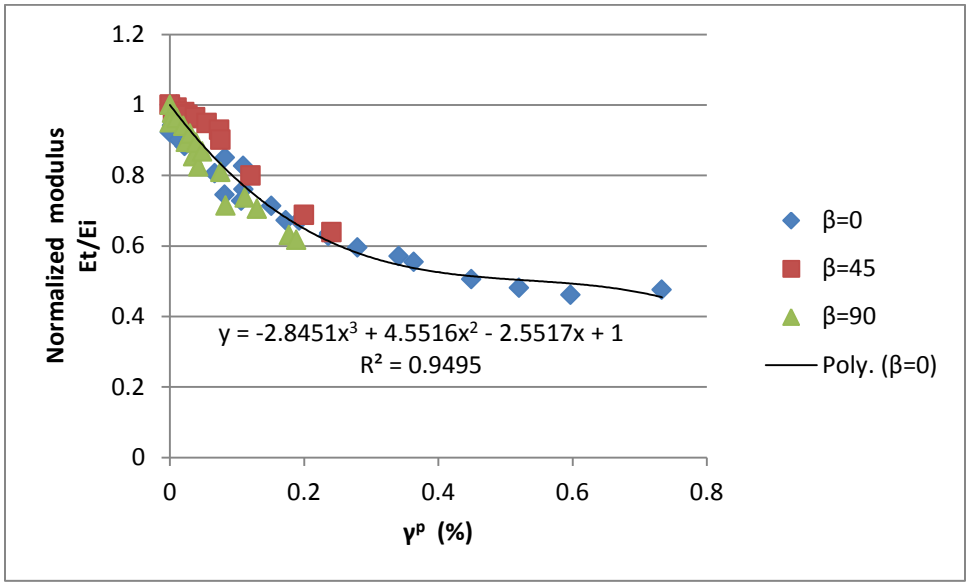

(a)

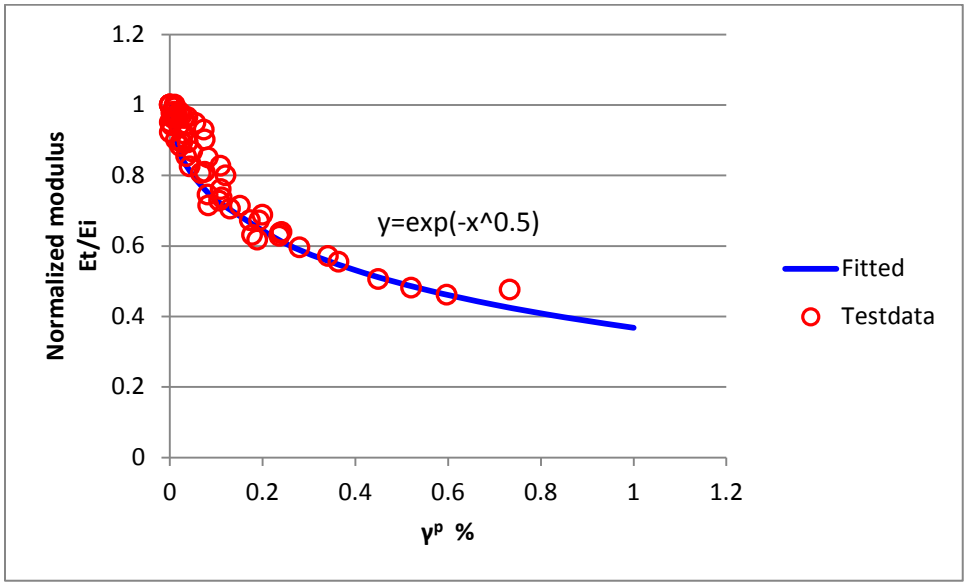

(b)

Figure 3.25 Tangent stiffness of anisotropic Argillite varying with effective plastic strain can be normalized into consistent relationship in a single formula of (a) a polynomial equation and (b) an exponential equation

5.3.3 Determination of bulk modulus and Poisson ratio (β=90°)

Figure 3.26 shows the relationship between mean stress and volumetric strain of Argillite clay with load angle at 90°. This graph exemplifies the procedure to estimate the bulk modulus in the elastic domain.

Bulk modulus is not only a necessary input data for the modeling, but also an important intermediate for the estimation of Poisson's ratio.

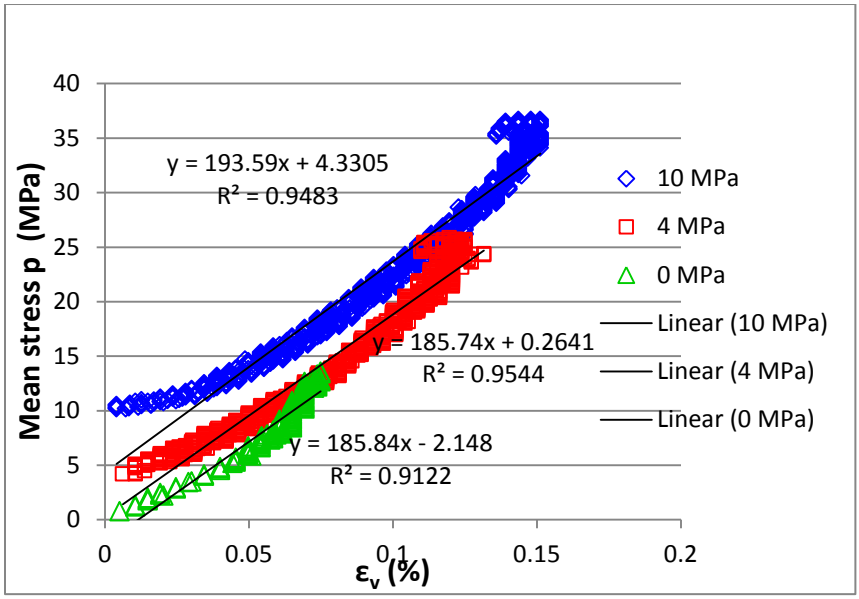

Figure 3.26 Bulk modulus of Argillite clay under various confining pressures with load angle β=90°

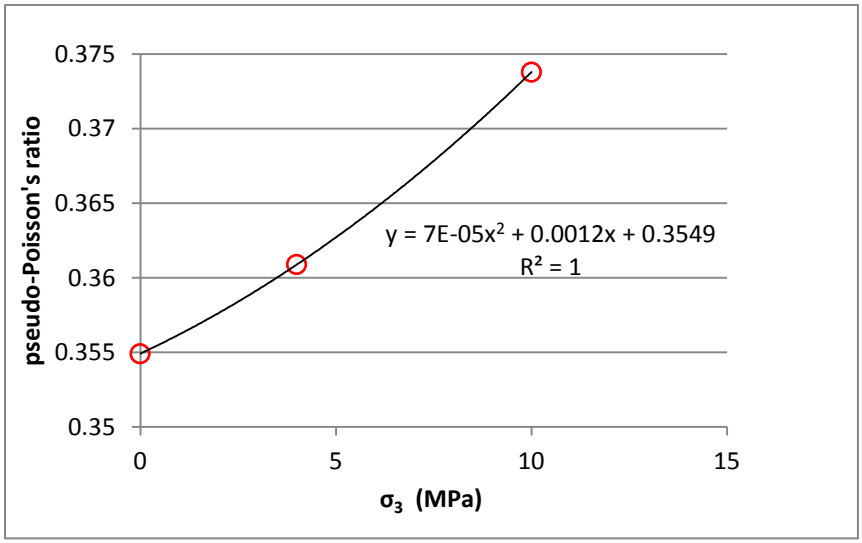

Figure 3.27 The variation of pseudo-Poisson ratio with confining pressure for parallel loading (β=90°)

Figure 3.27 shows the results of pseudo-Poisson's ratio that is calculated by using the total strains in terms of $\varepsilon_r{}^t/\varepsilon_a{}^t$ and seems dependent on the confining pressure. This behavior has been widely observed in the shearing test of various types of rocks (Islam and Skalle, 2013; Martin, 1993). The upper boundary for Poisson's ratio of an anisotropic rock may be higher than 1.0. Besides, this parameter also changes in magnitude during the shearing process. For brittle Lac du Bonnet Granite the Poisson's ratio was shown to increase with crack damage from about 0.1 to the equilibrium value of 0.8 when failure damage occurs (Martin, 1993). It is noted that the above discussed pseudo-Poisson's ratio was not

applied in the modelling, instead, the initial linear portion of the volumetric-axial strain relationship was used for the estimation of Poisson's ratio, which is 0.253 for the in plane elastic material properties as shown in Table 3.1. Comparing the pseudo-Poisson's ratio with the initial Poisson's ratio in the elastic domain it is found that the former is larger in value, indicating a certain dilatancy has been accumulated in hardening.

5.3.4 Application of Tsai-Hill anisotropic strength criterion for Argillite

From the Tsai-Hill strength criterion modified with Mohr-Coulomb model we can calculate the nonlinear Mohr-Coulomb strength envelop on the basis of the load angle and confining pressure. For Argillite, all parameters are available to us as shown in Table 3.4, e.g. σ_{LU}, σ_{TU}, τ_{LTU}, and the nonlinear elasticity (E_{50}), enabling us to reproduce the triaxial shear testdata as shown in Figures 28-29. This model can be an alternative to the microstructural tensor as adopted in this study.

Table 3.4 Tsai-Hill/Mohr-Coulomb strength parameters

Variables	Value	Unit
a	30.62	MPa
b	3.43	
c	28.83	MPa
d	2.06	
e	9.22	MPa
f	1.56	

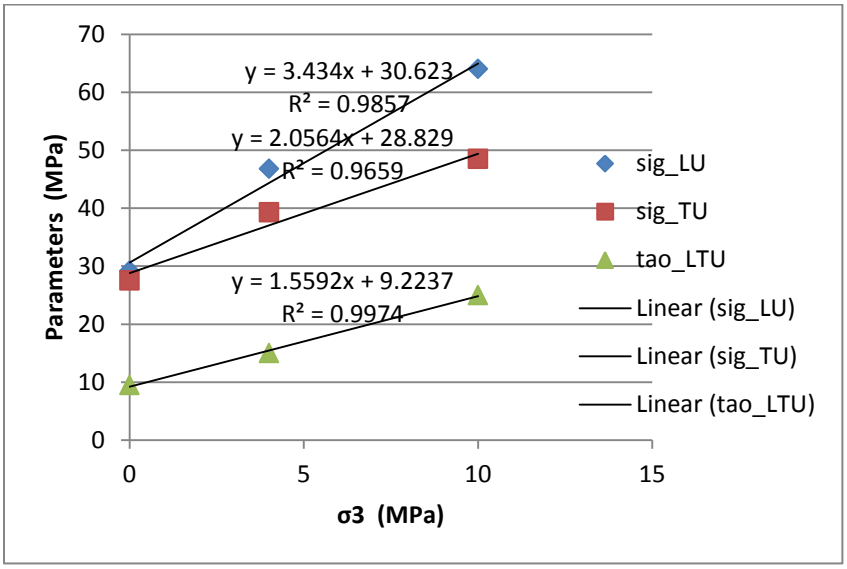

Figure 3.28 Tsai-Hill/Mohr-Coulomb strength parameters vs confining pressure

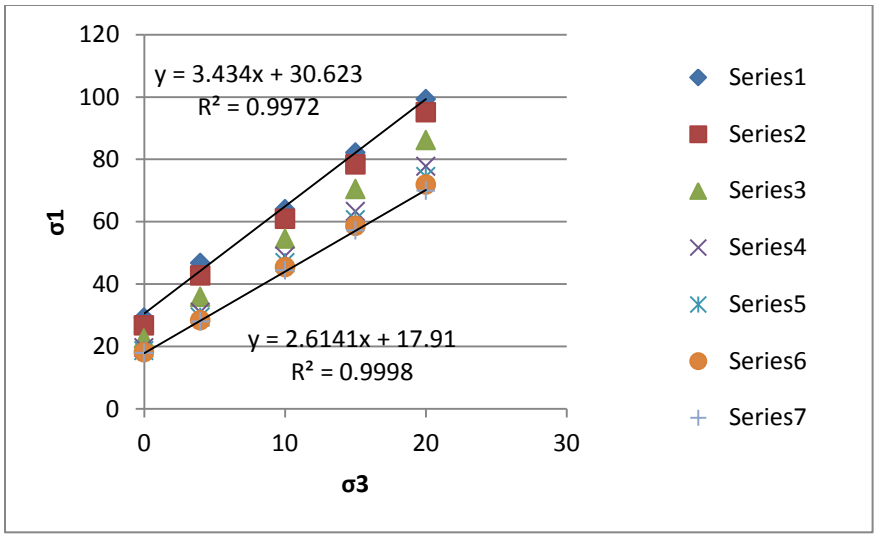

Figure 3.29 Estimated peak strengths vs confining pressure under different load angles

5.4 Further discussion on dilatancy

5.4.1 Volumetric strain and dilatancy angle in the shearing stage

Associative flow rule, which is originated from the study of metals, is known to overestimate the plastic volumetric strain for geomaterials. The plastic potential function is always modified to reflect the realistic plastic strain, which is termed as the non-associative flow rule. In COMSOL, this goal can be realized by defining the dilatancy angle ψ and making it different from the internal friction angle. The dilatancy angle can be estimated from the triaxial compression test by the following equation (Bolton, 1986),

$$sin\psi = -\frac{\frac{\dot{\varepsilon}_v}{\dot{\varepsilon}_1}}{2-\frac{\dot{\varepsilon}_v}{\dot{\varepsilon}_1}} \tag{66}$$

where $\dot{\varepsilon}_v$ and $\dot{\varepsilon}_1$ are both plastic strain rate, and are volumetric and axial strain, respectively. Figure 3.30 shows the definition of the dilatancy angle.

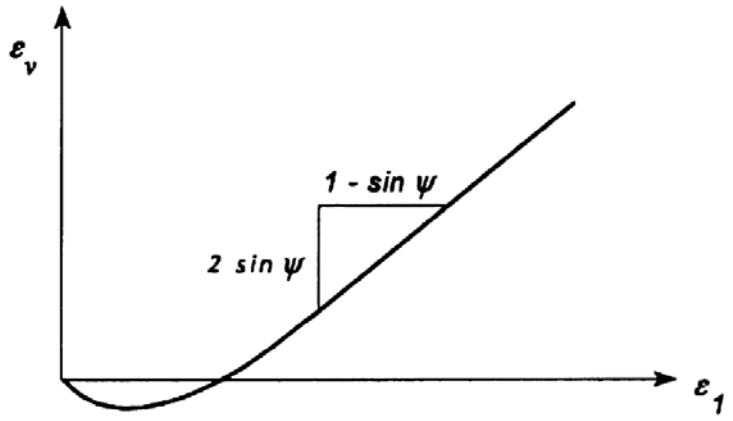

Figure 3.30 Volumetric strain vs axial strain and the relevant dilatancy angle (Modified after Schanz et al. (1999))

For brittle rock masses, the dilatancy angles are reported to be dependent on various factors including the confining pressure, plastic axial strain, rock type etc. (Zhao and Cai, 2010). The dilatation process is observed to be divided into several consecutive evolving stages involving the initialization and prorogation of microcracks and the strain localization. Dilatation of rock mass starts from the pre-failure conditions and is gradually transformed into the post-failure mode. A critical state may be applicable for some geomaterials that have an eventual equilibrium state in volumetric strain (Bolton, 1986). It was also indicated that dilation increases significantly for heavily constrained geotechnical problems (Houlsly, 1991), and gradually decreases with increasing hydrostatic pressure.

Anisotropy of rock has been experimentally observed to affect its dilatation behavior. Initialization of dilation is reported to mark the onset of dependence of volumetric strain on anisotropy (Hatzor and Heyman, 1997). Tournemire argillite although demonstrating strong anisotropy in mechanical properties, shows no obvious difference in the dilatant pattern (see Fig. 3.17). In the crack damage stage, the volumetric strain remains constant for all the samples until peak failure happens. Cobourg limestone, which is comparatively more brittle than Argillite clay, has the above mentioned crack damage induced dilatancy as early as passing the crack initialization strength (see Fig. 3.19).

5.4.2 Dilatancy yield locus

Dilatancy of rock has long been known to relate to the microscale crack damage. Shear-dilatancy is identified as an integral part of elastic and post-elastic deformation of solid isotropic media; it is not, as is widely believed, the result of cracking, but the cause of crack initiation (Freudenthal, 1975). Vajdova et al. (2004) illustrated the significance of dilatancy and brittle-ductile transition in strength evolution of limestones. The brittle-ductile transition is associated with a broad spectrum of highly complex deformation and failure mechanisms. With increase of shear stress, the net mean stress increases accordingly in the tri-axial compression test. Under high confining pressure conditions, the specimen experiences normal hydrostatic compaction, enhanced compaction and dilation consecutively. Coming

back to the mobilized hardening constitutive model that has been developed in this study, the initial yielding that defines the brittle-ductile transition can be regarded as an indicator of the beginning of dilatancy. The initial yielding somewhat coincides with the yield locus in p-q stress space as discussed in the followings.

Dilatancy is universally observed prior to the inception of shear localization. Extensive experimental proofs confirmed the dilatancy yield surface as shown in Figs. 31-32 (Popp et al., 2001; Vajdova et al., 2004; Martin 1993). Shear-enhanced compaction was observed to evolve to dilatant cataclasis in tri-axial shear tests. The transition from compactive to dilatant flow involves the propagation of separate and nucleated cracks and accumulative volumetric dilation that exceed the concomitant compaction due to pore collapse. Vajdova et al. (2004)'s perspective on the shear failure of carbonate rocks clearly suggests the existence of compaction yield surface in the stress space. This compaction yield surface is defined by the onset of shear enhanced strain. Shear-enhanced compaction was found to be appreciable in magnitude even for a relatively compact rock (Baud et al., 2000). Argillite clay rock is also observed to have such enhanced compaction under high confining stress (σ_3=10 MPa) when loading perpendicular to the bedding plane.

Further increasing the differential stress beyond the compaction yield surface will lead to deviation of volumetric strain from the hydrostatic compaction curve, and approaching to the dilatancy threshold plane, which marks the rapid and sudden turning of volumetric strain trend towards dilatancy (Baud et al., 2000; Vajdova et al., 2004).

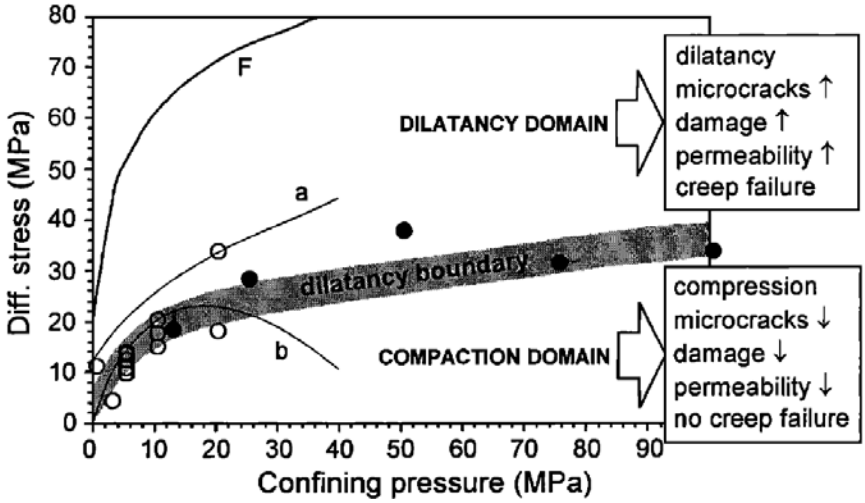

Figure 3.31 Dilatancy boundary for rock salt separating the domain where rock salt behaves compactible from the domain where rock behaves dilatant compression (F is failure surface. Graph after Popp et al. (2001))

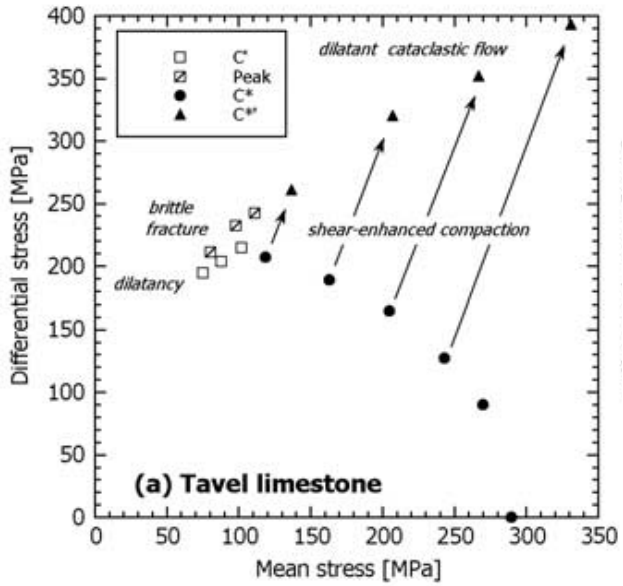

Figure 3.32 Stress space of failure mode for Tavel limestone (Vajdova et al., 2004). Three regimes of inelastic failure can be identified: brittle fracture, dilatant cataclastic flow, and shear-enhanced compaction.

5.4.3 Dilatancy affects mechanical properties

Brace et al. (1966) reported experimental study of dilatancy of brittle rocks in triaxial compression and found that the stress-volumetric strain behavior is qualitatively the same for these rocks and appear to be purely elastic at low stress. The rocks become dilitant as the maximum stress becomes one-third to two-thirds the fracture stress. The magnitude of the dilatancy, which is not markedly affected by pressure, ranges from 0.2 to 2.0 times the maximum elastic volume changes that would have occurred before dilitancy took place. And the brittle-ductile-transition flow is commonly observed to be a transient phenomenon, in that the failure mode evolves with increasing strain to dilatant cataclastic flow and ultimately shear localization (Baud et al., 2000).

Dilatancy is closely bounded with crack damage and its evolution. Martin (1993) quantitatively investigated the dilatancy yield locus of Lac du Bonnet Granite and noticed gradual loss of stiffness with Young's modulus decreasing from 50 GPa to 25 GPa in the crack damage phase under compression involving the progressively changing failure mechanisms from axial cracking to sliding. For granite, the dilatancy yield stress was also strongly strain-rate dependent; the higher the loading rate the higher the stress. Even for crystalline materials, slower strain rate was reported to induce creep or ductile behavior (Renshaw & Schulson, 2001), which is consistent with the observations of Brace et al. (1966) and the behavior of Argillite in this study.

Dilatancy affects permeability. Our study on Cobourg limestone clearly suggests permeability enhancement due to crack damage and dilatancy. Popp et al. (2001) observed dramatic increase of permeability with increasing progressive dilatancy, which was followed by a constant permeability during strain hardening stage. It is also believed that microcrack nucleation contributes to the

permeability change both in magnitude and in directional anisotropy. Such characteristics of hydraulic-mechanical coupling of the anisotropic dilatant shear of rock mass have to be taken into account in the coupled modelling in the future.

Because ideal plastic flow does not involve any volumetric change, which means that ideal Elasto-Plastic theory cannot predict the dilatant volume change. Our modelling uses a non-associative flow rule, i.e. the Drucker-Prager criterion, to compute the plastic strains. In spite of good agreement between modelling and testdata for most of the orientations, some discrepancies are still existent. Therefore, specific care has to be devoted to the development of an empirical formula for the dilatancy angle. It appears to be necessary to invoke Cap EP model to take into account the dilatancy yield behavior. However, the experimental results on limestone show that this behavior is valid only for higher confining pressures. In case of modeling the deep geological repositories for nuclear wastes in field conditions, large in-situ ground stress will be inevitably concomitant with large value in depth. Then it has to be investigated experimentally for the determination of the dilatancy yield locus. In this study, however, the Argillite clay rock samples were tested in low confining pressure conditions ($\sigma_3 \leq 10$ MPa), which may not involve large amount of shear-enhanced compaction in the pre-peak strength stage. In this regard, the dilatancy yield condition can be simplified and treated as the same to the critical yield condition as defined by Mohr-Coulomb failure plane.

6. Conclusions

A mobilized hardening/softening elastoplastic model was proposed in this study for the modeling of anisotropic sedimentary rocks. Anisotropy in stiffness, crack initialization strength, peak strength and hardening parameters that are all dependent on load angle can be modeled with the microstructural tensor approach.

The proposed model gets validated successfully with two sets of triaxial compression test data, i.e. Argillite clay and Cobourg limestone. The former is complete in test conditions while the latter is still ongoing in laboratory tests. As to Argillite clay, the hardening behavior and dilatancy in crack damage stage can be well reproduced by the new model. Focus of study on Cobourg limestone is about the hydraulic-mechanical coupling and resulted permeability variation. Our model can simulate the crack damage in terms of plastic strain and correlate it with the measured permeability values. Such modeling leads to an empirical formula for permeability-plastic strain dependence, which appears to be another achievement of this study and can be applied to future studies of similar objectives.

Controlling factors for the dilatancy remains to be explored with regard to Cobourg limestone which involves a hypothesis of fast mobilized hardening model to reproduce the apparently elastic deformation after the crack initialization. The Poisson's ratio is expected to increase with evolution of crack damage, which can give rise to the volumetric strain prior to the peak strength. More efforts are required on this respect provided adequate resources are allocated in the future.

Reference

T. Schanz, P.A. Vermeer, P.G. Bonnier (1999). The hardening soil model: Formulation and verification. Beyond 2000 in Computational Geotechnics-10 Years of PLAXIS. Balkema, Rotterdam.

C.G. Dvila, P.P. Camanho, C. Rose (2005). Failure Criteria for FRP Laminates. Journal of Composite Materials. 39 (4) 323-345.

J.C. Simo, T.J.R. Hughes (1998). Computational Inelasticity. Springer-Verlag New York, Inc.

C.T. Sun, B.J. Quinn and D.W. Oplinger (1996). Comparative Evaluation of Failure Analysis Methods for Composite Laminates. DOT/FAA/AR-95/109.

X.G. Zhao, M. Cai (2010). A mobilized dilation angle model for rocks. International Journal of Rock Mechanics and Mining Sciences. Volume 47, Issue 3, April, Pages 368–384

L. Chen, J.F. Shao, H.W. Huang (2010). Coupled elastoplastic damage modeling of anisotropic rocks. Computers and Geotechnics. 37: 187–194

M.D. Bolton (1986). The strength and dilatancy of sands. Geotechnique 36 (1) 65-78

G.T. Houlsly (1991). How the dilatancy of soils affects their behaviour. Tenth European Conference on Soil Mechanics and Foundation Engineering. Florence, Italy, 28th May, 1991.

Y.H. Hatzor and E.P. Heyman (1997). Dilation of anisotropic rock salt: Evidence from Mount Sedom diaper. Journal of Geophysical Research, VOL. 102, NO. B7, 853-14,868

X.G. Zhao, M.F. Cai, M. Cai (2010). Considerations of rock dilation on modeling failure and deformation of hard rocks—a case study of the mine-by test tunnel in Canada. Journal of Rock Mechanics and Geotechnical Engineering., 2(4): 338–349

K. Hashiguchi (2014). Elastoplasticity Theory, Second Edition. Springer-Verlag Berlin Heidelberg.

T.S. Nguyen and A.D. Le (2015). Development of a Constitutive Model for a Bedded Argillaceous Rock from Triaxial and True Triaxial Tests. Canadian Geotechnical Journal.

R.R. Gottschalk, A.K. Kronenberg, J.E. Russell, J. Handin (1990). Mechanical anisotropy of gneiss: Failure criterion and textural sources of directional behavior. J. Geophys. Res. 95, 21613-21634.

V. Vajdova, P. Baud, .F. Wong. (2004) Compaction, dilatancy, and failure in porous carbonate rocks. Journal of Geophysical Research, VOL. 109, B05204-219

W. F. Brace, B.W. Paulding, and C. Scholz (1966). Dilatancy in the Fracture of Crystalline Rocks. Journal of Geophysical Research. 71(16) 3939-3953

C. E. Renshaw and E.M. Schulson. (2001). Universal behaviour in compressive failure of brittle materials. Nature 412, 897-900

P. Baud, A. Schubnel, T.F. Wong (2000). Dilatancy, compaction, and failure mode in Solnhofen limestone. Journal of Geophysical Research. Volume 105(B8) 19289–19303

A.M. Freudenthal. (1975). Shear dilatancy in rock and precursory changes in seismic velocities. Geophysical Research Letters. 2(11). 517-520

David A. Lockner, James D. Byerlee (1994). Dilatancy in hydraulically isolated faults and the suppression of instability. Geophysical Research Letters, VOL. 21, NO. 22, PAGES 2353-2356

T. Popp, H. Kern, O. Schulze (2001). Evolution of dilatancy and permeability in rock salt during hydrostatic compaction and triaxial deformation. JOURNAL OF GEOPHYSICAL RESEARCH, VOL. 106, NO. B3, PAGES 4061-4078

M.A. Islam, P. Skalle (2013). An Experimental Investigation of Shale Mechanical Properties Through Drained and Undrained Test Mechanisms. Rock Mech Rock Eng (2013) 46:1391–1413

S. Pietruszczak, Z. Mroz (2001). On failure criteria for anisotropic cohesive-frictional materials. Intern. Journ. Num. Anal. Meth. Geomech., vol.25, pp. 509-524.

H. Abdi, D. Labrie, T.S. Nguyen, J.D. Barnichon, G. Su, E. Evgin, R. Simon, and M. Fall (2015). Laboratory investigation on the mechanical behaviour of Tournemire argillite. Can. Geotech. J. 52: 268‑282

E. Haghighat, S. Pietruszczak (2015). Constitutive modelling of Tournemire shale: Final Report. Canadian Nuclear Safety Commission.
B. Damjanac (2008). Phase I Long-term Cavern Stability. OPG Technical Report. No. OPG 00216-REP-01300-00005-R00.
M.H.B. Nasseri, R.P. Young (2015). Coupled Hydro-mechanical properties of Cobourg limestone and Tournemire shale with special reference to the Excavation Damage Zone. Canadian Nuclear Safety Commission. Internal Report. Report No. RFDF_CNSC_01.
C. D. Martin (1993). The Strength of Massive Lac du Bonnet Granite Around Underground Openings. PhD Thesis. University of Manitoba. Winnipeg, Manitoba.
J. Rutqvist, L. Borgesson, M. Chijimatsu, J. Hernelind, L.R. Jing, A. Kobayashi, and S. Nguyen (2009). Modeling of damage, permeability changes and pressure responses during excavation of the TSX tunnel in granitic rock at URL, Canada. Environmental Geology 57, 1263-1274.
T. Poulet, A. Karrech, K. Regenauer-Lieb, L. Fisher, and P. Schaubs (2012). Thermal- hydraulicmechanical-chemical coupling with damage mechanics using ESCRIPTRT and ABAQUS. Tectonophysics 526, 124-132.
E. Ghazvinian, M. Perras, C. Langford, M. Diederichs. (2013) A comprehensive investigation of crack damage anisotropy in Cobourg limestone and its effect on the failure envelope. GeoMontreal 2013.
COMSOL user manual. COMSOL Multiphysics (Ver 5.1). COMSOL Inc. 2015.

Chapter 4 Development of a visco-elastoplastic model for anisotropic sedimentary rocks and its application to the old tunnel at Tournemire site

Summary

Argillaceous rocks are candidate host and/or cap formations for the geological disposal of nuclear wastes in many countries, including Canada, France and Switzerland. The understanding of the long term mechanical behaviour of such rocks is an essential requirement for the assessment of its performance as a barrier against radionuclide transport. The Institut de Radioprotection et de Sûreté Nucléaire (IRSN) operates an Underground Research Laboratory (URL) in Tournemire, France, in such a rock formation known as the Tournemire shale. Many types of experiments are conducted at the Tournemire URL in order to better understand the physical and chemical behaviour of the shale and its interaction with seal materials intended to be used in the geological disposal of radioactive wastes. The Canadian Nuclear Safety Commission (CNSC) collaborates with the IRSN and Canmet Laboratories to perform experimental and theoretical research on the mechanical behaviour of the Tournemire argillite. Using the data from creep tests, monotonic and cyclic triaxial tests performed at the Canmet Laboratories, we developed constitutive relationships for the mechanical behaviour of the Tournemire shale. The model is based on the theory of plasticity, and takes into consideration the inherent anisotropy due to the existence of bedding planes, hardening behaviour before the peak strength, and viscosity. The constitutive relationships were implemented in finite element model to simulate the excavation damage zone around the century-old tunnel at the Tournemire URL. The influences of pore water pressure, desaturation and the fault that crosses the tunnel are examined. It was shown that desiccation must be taken into account in order to reproduce the shape of the excavation damage zone around the tunnel.

1. Introduction

Deep geological disposal is being proposed for the long term management of nuclear wastes in many countries, including Canada, France and Switzerland. Sedimentary rock formations are one of the host medium being considered. In Southern France, the IRSN operated an underground research laboratory in Tournemire located in an argillaceous sedimentary rock, the Tournemire shale that is found in a Mesozoic marine basin (Rejeb and Stephansson, 2007). The Tournemire shale possesses strong anisotropy in stiffness, deformation and permeability (Niandou et al. 1997; Zhang et al. 2002; Zhang et al. 2004). Anisotropy of geomaterials always involves the compositional layered structures, i.e. bedding, layering, and foliation. Loading history, mineral constituents, deposition intervals are all reponsible for

the formation of anisotropy. Considering the potential risk of preferential leakage route associated with the excavation induced damage zone for radiative contaminants, it is thus required to thoroughly understand the anisotropic behaviour of the sedimentary rocks of interest.

Experiments on sedimentary rocks have indicated that the general trend of compressive strength varies with the loading angle (Rejeb 1999). The weakest plane exists between 30-60^{o} of loading angle against the bedding plane, while the maximum strength is found parrallel or perpendicular to the bedding plane. Besides the strength properties, elasticity of these materials also indicate significant dependence on the orientation. In order to characterize the mechanical behaviour of the the sedimentary rocks, triaxial tests were carried out to investigate the different effects of confining pressure, loading angle and loading rate. The anisotropy in mechanical properties of sedimentary rocks leads to challenges in the numerical modelling of various underground geotechnical engineering problems within the framework of the classical homogeneous elastoplastic theories. Numerous efforts have been devoted to the development of appropriate constitutive models for anisotropic geomaterials. Amongst them, the microstructure tensor approach developed by Pietruszczak (2001) proved to be robust and relatively easy to use for the characterization and modelling of the constitutive behaviour of materials with transverse isotropy. The microstructure tensor approach was later applied by Nguyen and Le (2015a) and Le and Nguyen (2015) to model the behaviour of Opalinus clay during the excavation of a micro-tunnel, followed by water and gas injection in the tunnel.

The mechanical behaviour of brittle rocks due to increased loading involves consecutive processes of crack initiation and propagation, which could be characterized and evidenced by acoustic incidence (Martin 1993; Popp et al., 2001; Vajdova et al., 2004; Ghazvinian et al. 2013). Argillaceous rocks formed from sedimentation are however considered to be semi-brittle and experimental data from laboratory testing (e.g. Abdi et al. 2015) indicate several distinctive features, as compared to brittle rocks, mainly the inherent anisotropy due to sedimentation, but also strong time-dependency (Wang et al. 2012; Sun et al. 2014; Chauveau and Kaminski, 2008; Zhang and Rothfuchs, 2004; Fabre and Pellet, 2006; Gunzburger and Cornet, 2007; among others), among other factors.

Time dependent behaviour is so important to the long term stability of geomaterials that it cannot be overlooked in view of the potential risks that may be introduced by neglecting it. Therefore, much effort was spent by many researchers in developing constitutive models to take the time-dependency into account, within the theoretical framework of viscoelasticity, or elasto-viscoplasticity (Simo, 1987; Fafard et al. 2001; Rouabhi et al. 2007 ; Pellet et al. 2009; Xiong et al. 2014; and Zhang and Zhang ,2009; among others).

The purpose of the present study is to develop a constitutive model that can capture the most important physical processes that prevail in the mechanical behaviour of argillaceous rocks, such as the Tournemire shale. The model should however be simple enough to be readily implemented in numerical models to simulate coupled Thermal (T) - Hydrological (H) - Mechanical (M) processes that occur in underground facilities, such as deep geological repositories (DGR) for the disposal of radioactive wastes. The model was developed and calibrated using experimental data on Tournemire shale, obtained from a comprehensive program of triaxial tests performed at the Canmet Laboratories in Ottawa. The proposed

constitutive equations were then implemented in commercial finite element software, COMSOL Multiphysics (Ver 5.1) in order to simulate the evolution of the HM coupled processes following the excavation of a century old tunnel at the Tournemire Underground Research Laboratory (URL) in Aveyron, France.

2. Laboratory triaxial tests of mechanical behaviour of Tournemire shale

A brief review of the behaviour of brittle rock in laboratory triaxial tests

Since the 1960s, the deformation and strength characteristics of brittle rocks have been studied by many researchers (Brace, 1964; Bieniawski, 1967; Wawersik and Fairhurst, 1970; Martin and Chandler, 1994, just to name a few). These studies come to a general consensus that with increased loading, the mechanical behaviour of brittle rocks is governed by the initiation, propagation and coalescence of cracks. During a triaxial or uniaxial test, a brittle rock would go through five phases (Figure 4.1). In phase I, the applied stress results in a closure of pre-existing cracks in the sample. This is followed by phase II of essentially linear elastic behaviour. The onset of microfracturing starts at the beginning of phase III. In phase III, crack growth is stable, meaning that crack propagation would stop if the load is removed. The microcracks are mostly intragranular, and oriented in the direction of the major principal stress. In phase IV, unstable crack growth would start. This phase is marked by the onset of dilatancy. In Figure 4.1, the volumetric strain curve starts to show negative slopes at the onset of phase IV, indicating dilatant incremental volumetric strain. In addition to intragranular cracks parallel to the direction of the applied load, transgranular inclined cracks are formed. In the post-peak phase (phase V), macrocracks develops and eventually lead to the collapse of the sample.

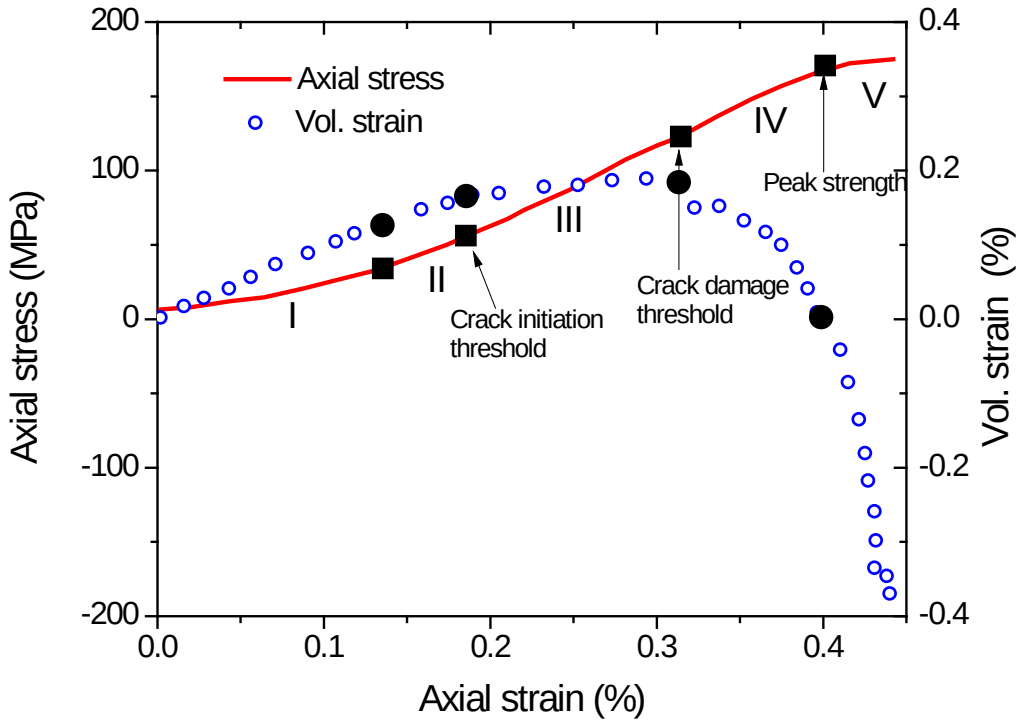

Figure 4.1 The five phases of the mechanical behaviour of brittle rock in triaxial tests

The quantitative delimitation of the above regions is not straightforward, and could be rather subjective. Martin (1993) subtracted a theoretical elastic volumetric strain to the total measured volumetric strain in order to obtain what he defines as the crack volumetric strain. Using the latter value, he determined that the onset of phase III starts at approximately 40% of the peak axial stress; he calls that the crack initiation stress. The onset of region IV starts at what he calls the crack damage stress, at approximately 80% of the peak stress. The method proposed by Martin requires the determination of the elastic constants, determined in region II; this determination could be subjective. Eberhardt et al. (1998) used a combination of strain gauge analysis and acoustic emission (AE) monitoring techniques in order to refine Martin's method for determining crack initiation and crack damage thresholds.

As cracks develop, grow and coalesce with increased loading, permanent changes in mechanical and hydraulic properties occur in the rock sample. Figure 4.2 shows the complete stress-strain behaviour of the same test illustrated in Figure 4.1, with a few stress reversal cycles at different loading stages. It could be seen that with increased loading, the magnitude of permanent strain increases. The reversal cycles shows hysteretic behaviour, indicating energy dissipation. The mean slope of these cycles decreases as the accumulated permanent strain increases, indicating a degradation in the stiffness of the rock. Martin (1993) defined a measure of accumulated damage as the sum of permanent volumetric strain at a given load level. He showed that with increasing damage, the stiffness and the strength of the granite decreases. The degradation of strength parameters can be explained conceptually at the scale of

microcracks (Figure 4.3). In phase III, cohesion is gradually deteriorating by the formation and growth of intragranular cracks. At the end of region III, beginning of region IV, inclined micro-shears become more dominant and slippage along these micro-shears starts, and thus friction is gradually mobilized. Following Griffith (1921), Berry (1960) and Cook (1965) the failure conditions in brittle rock can be considered as being initiated by tensile stress concentration at the tips of sub-microscopic elliptical flaws in the rock sample. Using energy considerations, Cook (1965) proposed a strength criterion which depends on the size of these elliptical flaws, and their surface energy, and also the friction coefficient across the crack faces. The Cook criterion can be written in the same form as the Mohr-Coulomb criterion and the empirical cohesion c is shown to depend on the size of the cracks or flaws and the surface energy, while the friction angle is directly related to the friction coefficient. Martin (1993) shows that the cohesion c degrades with accumulated damage, while the mobilized friction angle ϕ grows to a maximum value that includes interlocking effects, before decreasing to a residual value ϕ_r when the interlocking disappears due to asperity damage along the microcrack faces (Figure 4.3).

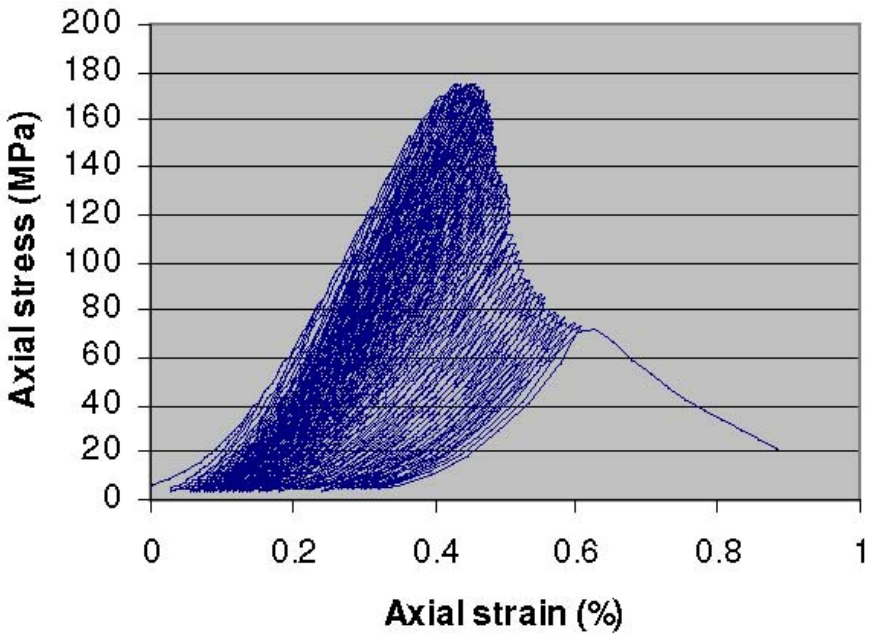

Figure 4.2 Cyclic triaxial test on Lac du Bonnet granite

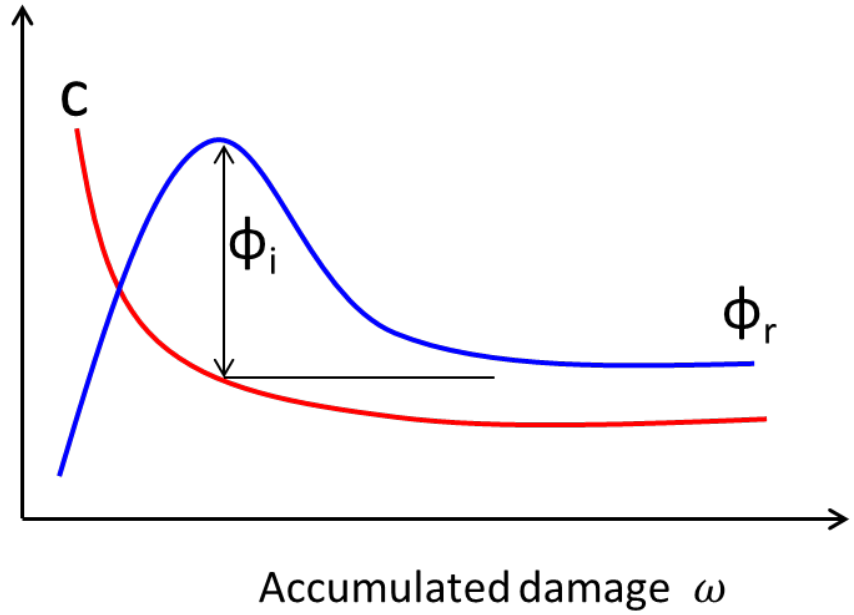

Figure 4.3 Evolution of cohesion and friction during the different phases of crack initiation, propagation and coalescence in brittle rocks (adapted from Martin (1993))

The behaviour of Tournemire shale in laboratory triaxial tests

The current study is concerned with argillaceous rocks, specifically the Tournemire shale. Such types of rocks are semi-brittle. Although the stress-strain curves obtained from laboratory triaxial tests generally exhibit the five phases as summarized above for brittle rocks, there are some marked differences, as noticed by Nguyen and Le (2015a). The main differences reside in the inherent anisotropy due to bedding, the pronounced time-dependent effects, the apparent lower density of pre-existing cracks or microcracks, and also the possibility that crack propagation and coalescence only starts very near the peak load. At the Canmet Laboratories in Ottawa, an experimental program consisting of monotonic triaxial, cyclic triaxial and creep tests was performed using samples of Tournemire shale at different bedding orientation with respect to the axial load. The experimental results were reported by Abdi et al. (2015), and the main features are discussed here in order to provide a conceptual basis for the ensuing development of a constitutive model. The geometry of the samples being tested is represented in Figure 4.4. The load angle β is the angle between bedding planes and the horizontal direction. The convention of load angle in this study may vary in expression with specific purposes, whereas β is the default symbol except otherwise indicated.

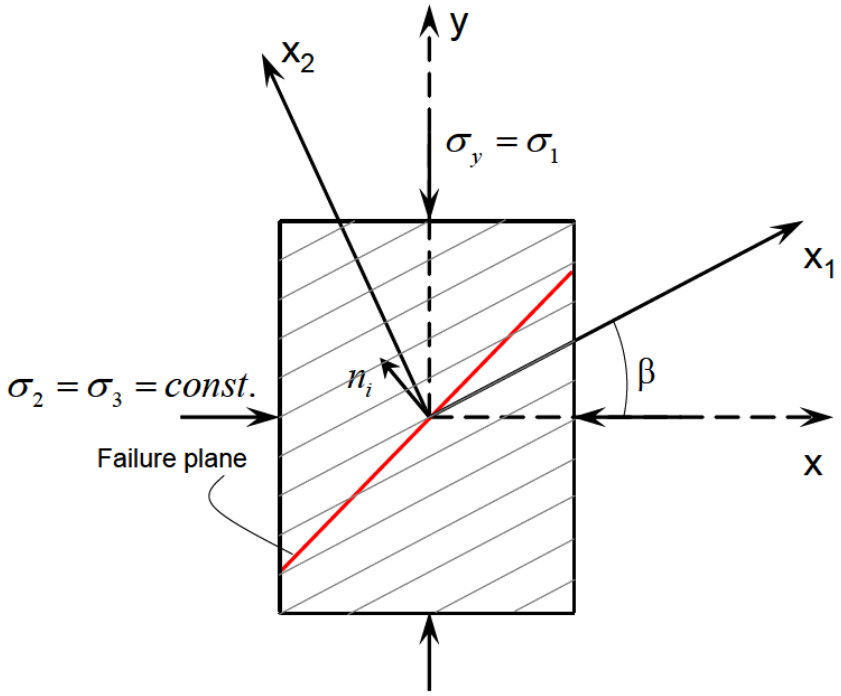

Figure 4.4 Geometry of the Tournemire sample in triaxial tests

Monotonic triaxial tests on Tournemire shale

A typical plot of the deviatoric stress and the volumetric strain versus the axial strain is shown in Figure 4.5. Compared to Figure 4.1 for brittle rocks, there are some differences:

- The crack closure phase is absent for this particular test, suggesting that for the Tournemire shale, any initial cracks that exist in the sample are either inexistent or healed. Evidence of a crack closure phase is

only found for unconfined tests with horizontal bedding planes. This suggests that for those tests, the crack closure phase would actually be due to closure of the bedding planes.

- The crack damage phase seems to start at more than 95% of the peak. This is corroborated by the acoustic emission record, as reported by Abdi et al. (2015).

Apart from the above differences, similarly to brittle rocks, there is a linear portion of both the deviatoric stress and volumetric deformation curves up to approximately 30% of the peak. At that point crack initiation and propagation are inferred up to the peak, resulting in nonlinearity of the curves. After the peak, collapse of the material is found, with the localization of strain along narrow failure bands.

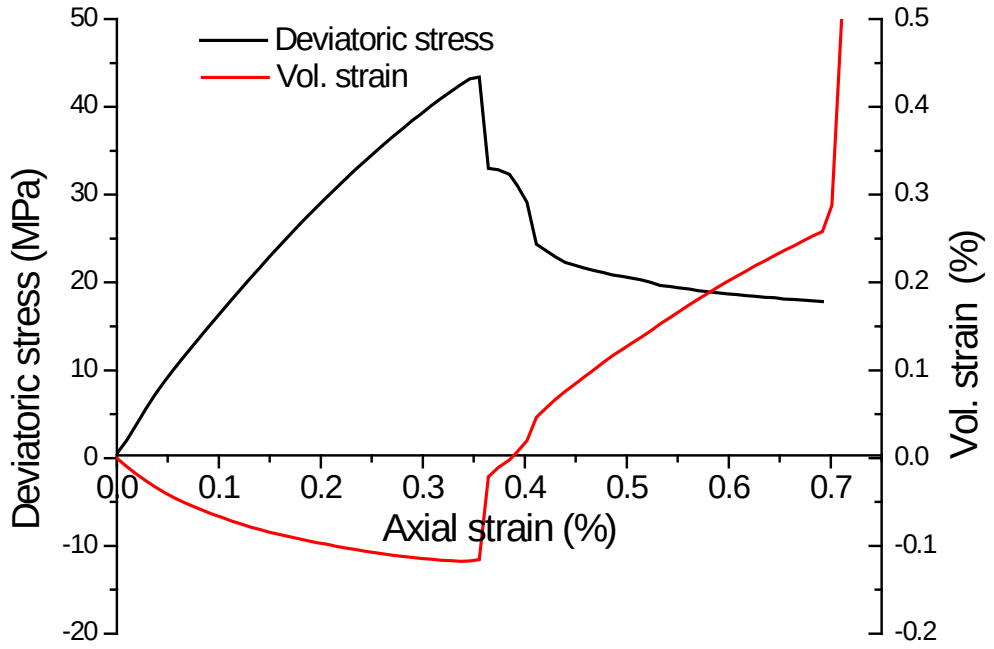

Figure 4.5 Variation of deviatoric stress and volumetric strain with axial strain for specimen at $\beta=90^{o}$, $\sigma_3=4$ MPa

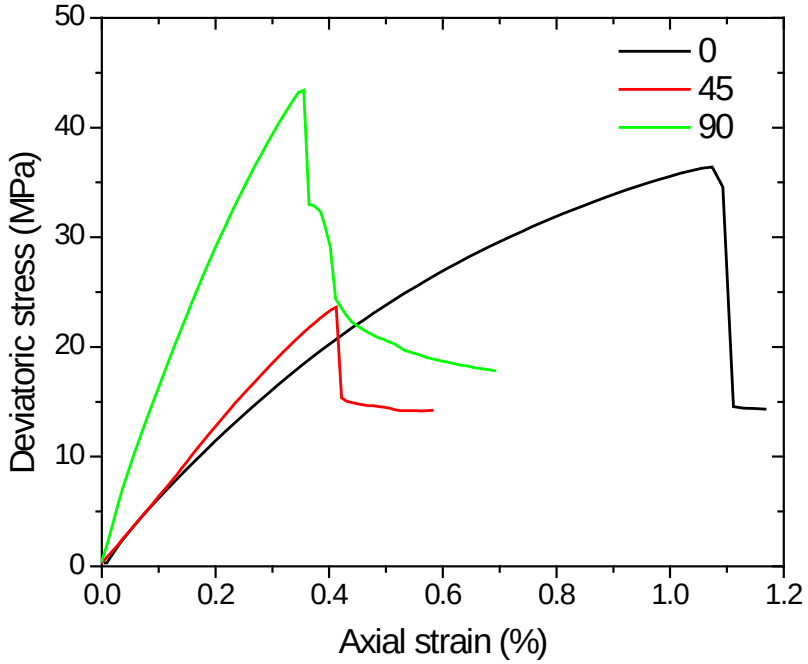
Deviatoric stress (MPa)
Axial strain (%)
0
45
90
0
10
20
30
40
50
0.0
0.2
0.4
0.6
0.8
1.0
1.2

(a)

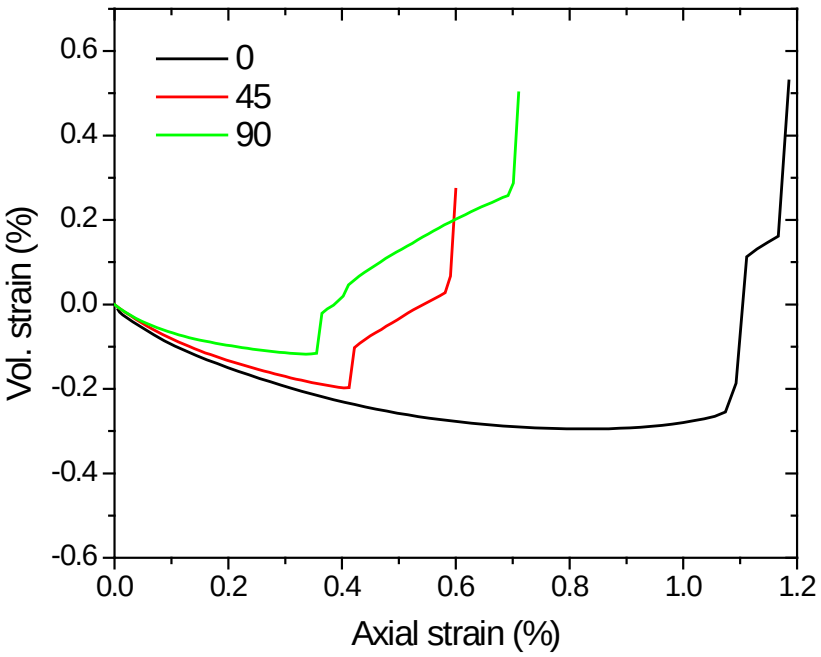
Vol. strain (%)
Axial strain (%)
0
45
90
0.6
0.4
0.2
0.0
-0.2
-0.4
-0.6
0.0
0.2
0.4
0.6
0.8
1.0
1.2

(b)

Figure 4.6 Variation of deviatoric stress (a) and volumetric strain (b) with axial strain for specimen at β=0, 45 and 90°, respectively, with σ_3=4 MPa

Figure 4.6 shows the strong influence of bedding plane orientations on the stress-strain and dilatancy behaviour of Tournemire shale. This influence is reflected in the stiffness and peak strength of the material. The Tournemire shale is found to be stiffer and stronger when loading is parallel to the bedding planes (β=90°).

Cyclic triaxial test

Figure 4.7 shows the stress-strain and volumetric variations of the Tournemire shale for a typical cyclic triaxial test. It could be seen that similarly to the behaviour of brittle rocks shown in Figure 4.2, hysteretic loops are formed from unloading-reloading sequences. The slope of the loops decreases with the loading level, indicating a degradation of the stiffness of the rock as for the case of brittle rocks. However, as compared to brittle rocks, argillaceous rocks such as the Tournemire shale exhibit larger energy dissipation as evidenced by the larger areas of the hysteretic loops. Furthermore, the areas of the loops increase with the stress level. This phenomenon is characteristic of a material where viscosity might play an important role in its stress-strain behaviour.

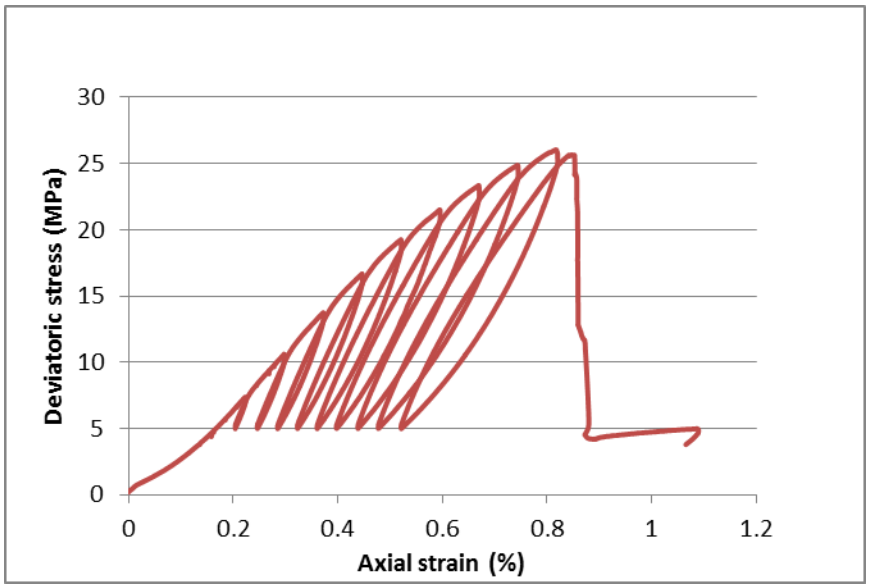

Figure 4.7 Deviatoric stress vs axial strain for cyclic triaxial test β =0; σ_3=0 MPa

3. A constitutive model for the Tournemire shale

The comprehensive test data that we obtained from the laboratory test program summarized above allows us to formulate a constitutive model that would capture the main physical features that were found during those tests:

- the existence of three regions of the stress-strain curves as described above

- the directional dependence of the loads with respect to the bedding orientation

- time dependent behaviour that is evidenced from creep tests and the existence of important energy dissipation found in cyclic triaxial tests.

Similarly to Haghighat and Pietruszczak (2015) and Nguyen and Le (2015a) the model is developed within the framework of elastoplasticity, using the Mohr-Coulomb yield criterion that is formulated in such a way to include directional dependence, and strain-hardening of the yield parameters. Before yielding starts, the material is assumed to be visco-elastic.

The constitutive relationship predicts the response of a material to a solicitation. If the solicitation is an imposed stress increment, the relationship predicts the strain increment and vice versa. Mathematically, the relationship can be written in matrix notation as follows:

$$\mathrm{d}\boldsymbol{\sigma} = \mathbf{D}(\mathrm{d}\boldsymbol{\varepsilon} - \mathrm{d}\boldsymbol{\varepsilon^p} - \mathrm{d}\boldsymbol{\gamma}) \quad (1)$$

where d**σ** is the increment of the stress tensor (written as a vector); d**ε** is the increment of total strain tensor (written as a vector); d$\boldsymbol{\varepsilon^p}$ is the increment of the plastic strain tensor (written as a vector); d**γ** is the increment of the viscous strain tensor (written as a vector) and **D** is the elastic stiffness tensor (written as a matrix).

In the following sections we describe how **D**, d$\boldsymbol{\varepsilon_p}$ and d**γ** are derived in order to fully define the proposed constitutive model.

Determination of the elastic parameters of the stiffness tensor D

The secant modulus E_{50}, determined from a secant line between the beginning of loading to 50% of the peak load in a triaxial test, is used in this study to estimate the initial Young's modulus. That modulus varies with the direction of the bedding plane β. For a transversely isotropic material, the following relationship describes that variation:

$$\frac{1}{E_\beta} = \frac{sin^4\beta}{E_L} + \frac{cos^4\beta}{E_T} + (-2\frac{\nu_{LT}}{E_L} + \frac{1}{G_{LT}})sin^2\beta cos^2\beta \quad (2)$$

where E_β is the modulus at load angle β; E_L and E_T are in plane and transverse moduli, respectively; ν_{LT} is the transverse Poison ratio; G_{LT} is the transverse shear modulus.

Provided that stiffness is known for a series of load angle, as is the case in this study, the transverse Poisson ratio and shear modulus can be estimated by curve fitting using the above equation. Figure 4.8

shows the best-fit curves using equation (2). Due to the small difference in values for different confining stress, the average value was taken as the required parameter for the modelling purpose.

The cyclic triaxial test results show that the stiffness degrades with increasing loads. Similarly to Martin (1993), we found that this decrease could be expressed as a function of the cumulative irreversible deformation. Using the secant slopes of the stress reversal loops, a normalized curve (Fig. 4.9) of stiffness degradation versus the effective plastic strain γ^p is derived. The effective plastic strain is used as a measure of cumulative irrecoverable deformation, as detailed in section 3.3. The experimental data in Fig. 4.9 shows very little disparity between different loading angles, and thus one unique exponential function can be fitted to the experimental points.

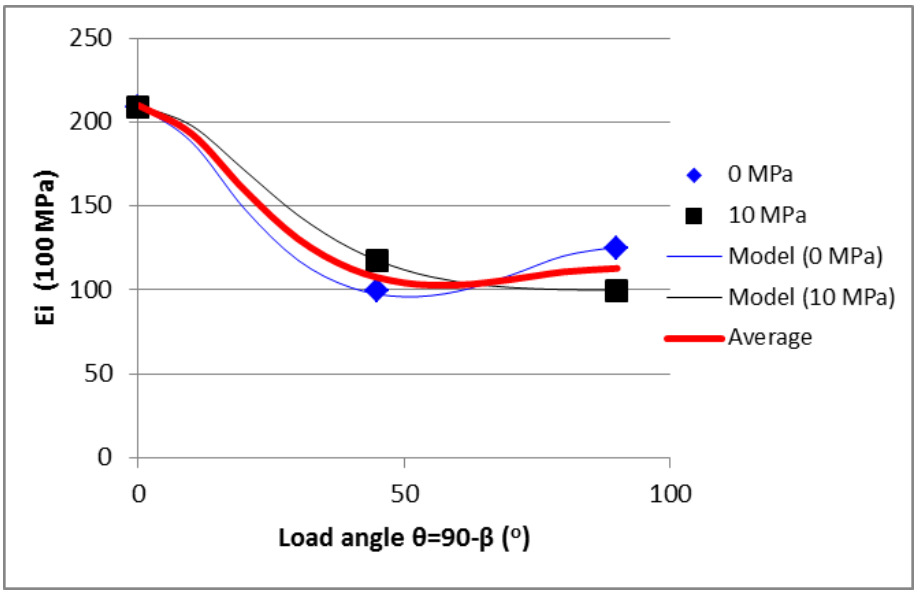

Figure 4.8 Initial Young's modulus as a function of the load angle

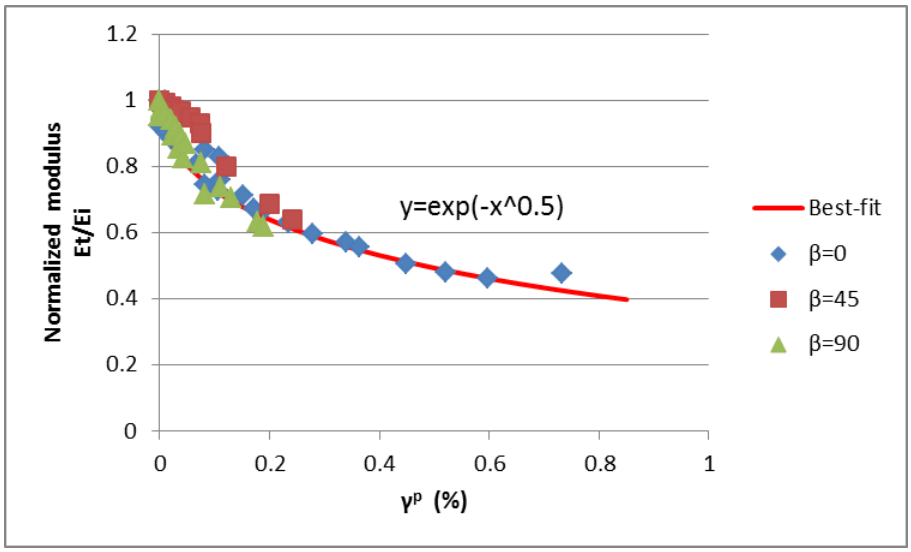

Figure 4.9 Normalized curve of stiffness degradation determined by stress reversal loops

Table 4.1 summarizes the elastic parameters for the Tournemire shale. The in plane Poisson's ratio is found to be independent of the confining pressure. In order to estimate the in plane Poisson's ratio, the bulk modulus K was first calculated by plotting the mean stress ($p = (\sigma_1 + 2\sigma_3)/3$) against the volumetric strain (ε_v). The curve was fitted with linear equations to get the slope which is the required bulk modulus (K). The in-plane Poisson ratio can be computed ($\nu_{\parallel} = 1 - \frac{E}{3K} - \nu_{\perp}$).

Table 4.1 Initial elastic parameters of the Tournemire shale

Variables	Value	Unit
$E_{\perp}$	7.4	GPa
$E_{\parallel}$	13.5	GPa
$\nu_{\perp}$	0.15	
$\nu_{\parallel}$	0.253	
$G_{\perp}/E_{\perp}$	0.21	
$G_{\parallel}$	$E_{\parallel}/2(1+\nu_{\parallel})$	GPa

Note: // is for the in plane stiffness and ⊥ is for the transverse stiffness.

Determination of the viscous component

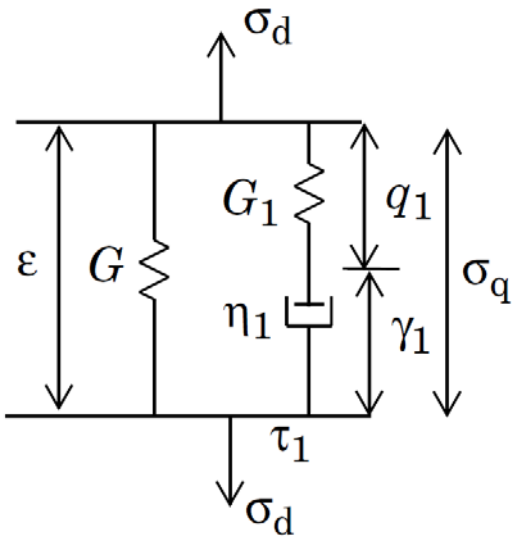

Figure 4.10 Schematic diagram of Maxwell viscoelastic model

The stress tensor and strain tensor can both be decomposed into volumetric and deviatoric parts,

$$\boldsymbol{\sigma} = \boldsymbol{\sigma_d} + \boldsymbol{p} \quad (3)$$

$$\boldsymbol{\varepsilon} = \boldsymbol{\varepsilon_{dev}} + \boldsymbol{\varepsilon_{vol}} \quad (4)$$

where mean stress **p** and volumetric strain $\boldsymbol{\varepsilon_{vol}}$ can be written as

$$\boldsymbol{p} = \frac{\sigma_{11}+\sigma_{22}+\sigma_{33}}{3}\begin{bmatrix}1 & 0 & 0\\ 0 & 1 & 0\\ 0 & 0 & 1\end{bmatrix} \tag{5}$$

$$\boldsymbol{\varepsilon_{vol}} = \frac{\varepsilon_{11}+\varepsilon_{22}+\varepsilon_{33}}{3}\begin{bmatrix}1 & 0 & 0\\ 0 & 1 & 0\\ 0 & 0 & 1\end{bmatrix} \tag{6}$$

For an elastic material, $\boldsymbol{\sigma}$ can be expressed as a function of $\boldsymbol{\varepsilon}$ by the mean and deviatoric components. For example, the isotropic elastic material follows the following relationship

$$\boldsymbol{p} = K\boldsymbol{\varepsilon_{vol}} \tag{7}$$

$$\boldsymbol{\sigma_d} = 2G\boldsymbol{\varepsilon_{dev}} \tag{8}$$

where K and G are respectively the bulk and shear moduli, which are scalar for isotropic material, but are tensors for an anisotropic material.

For a viscoelastic material, the deviatoric stress is not only dependent on the deviatoric strain but also on its time variations. The deviatoric stress is usually written in an integral form as follows (Simo and Hughes, 1998)

$$\boldsymbol{\sigma_d} = 2\int_0^t \Gamma(t-t')\frac{\partial \boldsymbol{\varepsilon_{dev}}}{\partial t'}dt' \tag{9}$$

$\Gamma(t)$ is a relaxation function, which can be approximated by a Prony series

$$\Gamma(t) = G + \sum_{i=1}^{N} G_i \exp(-\frac{t}{\tau_i}) \tag{10}$$

where N is the total number of viscous branches, and τ is relaxation time $\tau = \frac{\eta}{G}$.

A simple rheological model, i.e. the simplified general Maxwell model (also known as the standard linear solid model) that consists of a spring and dashpot in sequence, was implemented in the study of rheological behaviour of Tournemire clay. It is assumed in this study that viscosity only influences the deviatoric components of stress and strain. As only one viscous branch is considered, the integral deviatoric stress can be rewritten as

$$\boldsymbol{\sigma_d} = 2\int_0^t \left(G + G_1\exp(-\frac{t-t'}{\tau_1})\right)\frac{\partial \boldsymbol{\varepsilon_{dev}}}{\partial t'}dt' \tag{11}$$

The above equation reduces to another form in absence of viscosity, i.e. $\tau_1 = 0$,

$$\boldsymbol{\sigma_d} = 2\int_0^t \lim_{\tau_1\to 0}\left(G + G_1\exp(-\frac{t-t'}{\tau_1})\right)\frac{\partial \boldsymbol{\varepsilon_{dev}}}{\partial t'}dt' = 2\int_0^t G\frac{\partial \boldsymbol{\varepsilon_{dev}}}{\partial t'}dt' \tag{12}$$

which suggests that the total stress is imposed solely onto the bulk elastic material when the viscosity diminishes.

As shown in Fig. 4.10, the total deviatoric stress $\boldsymbol{\sigma_d}$ equals in quantity to the sum of both the bulk stress and viscous stress ($\boldsymbol{\sigma_q}$) in the form of

$$\boldsymbol{\sigma_d} = 2G\boldsymbol{\varepsilon_{dev}} + \boldsymbol{\sigma_q} \tag{13}$$

The stress on the spring-dashpot branch takes the following form,

$$\boldsymbol{\sigma_q} = 2G_1\boldsymbol{q_1} = 2\eta_1\dot{\boldsymbol{\gamma}}_\mathbf{1} \tag{14}$$

where G_1 and $\mathbf{q_1}$ are respectively the shear modulus and shear strain tensor of the viscous branch, η and $\boldsymbol{\gamma_1}$ are respectively the viscosity and viscous strain tensor of the dashpot.

The above equation gives rise to the following formula

$$\boldsymbol{q_1} = \frac{\eta_1}{G_1}\dot{\boldsymbol{\gamma}}_\mathbf{1} = \tau_1\dot{\boldsymbol{\gamma}}_\mathbf{1} \tag{15}$$

where τ_1 is the relaxation time.

The total deviatoric elastic strain thus consists of two parts, i.e. 1) the viscous strain γ_1 that is induced by dashpot deformation and 2) the elastic strain q_1 that is attributed to the spring. Then we get

$$\boldsymbol{q_1} + \boldsymbol{\gamma_1} = \boldsymbol{\varepsilon_{dev}} \tag{16}$$

Then the viscous strains are defined by the following equations:

$$\begin{cases} \boldsymbol{\sigma_d} = 2(G + G_1)\boldsymbol{\varepsilon_{dev}} - 2G_1\boldsymbol{\gamma_1} \\ \boldsymbol{\varepsilon_{dev}} = \tau_1\dot{\boldsymbol{\gamma}}_\mathbf{1} + \boldsymbol{\gamma_1} \end{cases} \tag{17}$$

3.2.1 Creep test and the parameterization of viscoelastic model

The time-dependent behaviour of the Tournemire argillite is evident from creep tests. Figure 4.11 shows the variation of axial strain with elapsed time for unconfined creep test on Argillite clay. Loading orientation appears to influence the creep strain significantly. The initial strain of sample with loading angle at β=0 ° is about 3 times of those at β=45 °. When loading in parallel to the bedding plane (β=90 °), the instant strain and long-term creep strain are both the least of all under similar loading conditions. It appears to be anisotropic in creep behaviour, as suggested in previous studies (Rejeb 1999; Pietruszczak, Lydzba, and Shao 2004). Our modelling turns out to show that the rheological model has isotropic creep properties as shown in Table 4.2 while the orientation dependent strain is attributable to the anisotropy in elastoplasticity.

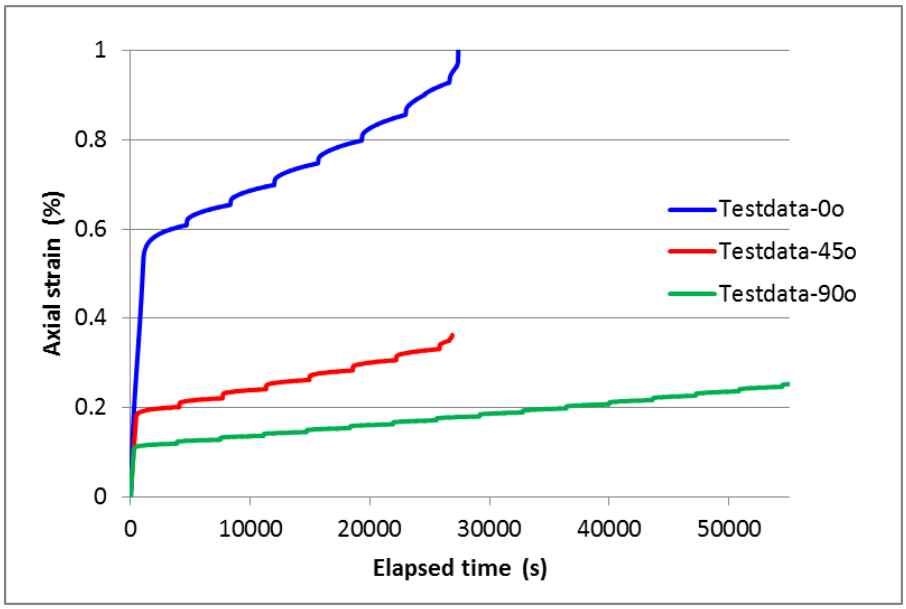

Figure 4.11 Time-dependent behaviour of Argillite clay in creep test

Table 4.2 Viscoelastic model constants best-fitted by Maxwell model for Tournemire clay

Model parameter	Value	Unit
G_1	3.5	GPa
τ_1	500	s

Determination of the plastic strain

The Mohr-Coulomb yield criterion can be written in the following form

$$F = \frac{I_1 sin\phi}{3} + \sqrt{\frac{J_2}{3}}\left((1+sin\phi)cos\theta - (1-sin\phi)cos\left(\theta + \frac{2\pi}{3}\right)\right) - c * cos\phi = 0 \quad (18)$$

where I_1 is the first invariant of stress tensor, J_2 is the second invariant of deviatoric stress tensor, θ is the Lode angle, c is cohesion, and ϕ is frictional angle.

or in a more compact manner,

$$F = \sqrt{J_2}m(\theta) + \alpha I_1 - k = 0 \quad (19)$$

$$m(\theta) = \cos\left(\theta - \frac{\pi}{6}\right) - \sqrt{1/3}\, sin\phi \sin(\theta - \frac{\pi}{6}) \quad (20)$$

$$\alpha = sin\phi/3 \quad (21)$$

$$k = c * cos\phi \quad (22)$$

where θ is Lode angle in the range of (0, π/3).

When the yield criterion is reached, plastic strain occurs. The plastic strain is derived from the plastic potential equation. Here we used a nonassociative flow rule, with the plastic potential taking the form of a Drucker-Prager relation:

$$G = \sqrt{J_2} + \frac{2}{\sqrt{3}}\frac{sin\phi}{3-sin\phi} I_1 - \frac{2\sqrt{3}c*cos\phi}{3-sin\phi} = 0 \quad (23)$$

The above function matches the Mohr-Coulomb yield criterion at compressive meridians.

In this regard, the plastic strain rate takes the form of

$$\dot{\boldsymbol{\varepsilon}}^{\boldsymbol{p}} = \lambda \frac{\partial G}{\partial \boldsymbol{\sigma}} \quad (24)$$

where λ is the consistency parameter that can be determined by classical elasto-plastic theory with appropriate rearrangement of the differentiated form of the yield function (Simo, Hughes, 1998).

The plastic strain can be defined as (e.g. Hashiguchi, 2014)

$$\gamma^p = \int \dot{\gamma}^p dt = \int \sqrt{\frac{2}{3}\dot{\varepsilon}_{ij}^{p\prime}\dot{\varepsilon}_{ij}^{p\prime}}\, dt = \int \sqrt{\frac{2}{3}\left(\dot{\varepsilon}_{ij}^{p} - \frac{1}{3}\varepsilon_v^p \mathbf{I}\right)\left(\dot{\varepsilon}_{ij}^{p} - \frac{1}{3}\varepsilon_v^p \mathbf{I}\right)}\, dt \quad (25)$$

In triaxial conditions, the above formula can be expressed in another form,

$$\gamma^p = \sqrt{\frac{2}{3}\left[\left(\varepsilon_1^p - \frac{1}{3}\varepsilon_v^p\right)^2 + 2\left(\varepsilon_r^p - \frac{1}{3}\varepsilon_v^p\right)^2\right]} \quad (26)$$

where ε_1^p is cumulative axial plastic strain, $\varepsilon_r^p = v\varepsilon_1^p$ is the cumulative radial plastic strain, and ε_v^p is the cumulative volumetric plastic strain.

Development of a mobilized hardening elasto-plastic model

Initial yielding

For brittle rocks, it is usually accepted that there exists a crack initiation threshold that is about 30-60% of the peak strength (see e.g. Martin, 1993). Here we hypothesize that initial yielding starts at the crack initiation threshold, at a certain percent of the peak strength (σ_{1p}), say $\varpi\%$, and the elastic modulus decays gradually throughout the elasto-plastic transition stage due to the crack damage effect. Then we obtain the initial yielding stress

$$\sigma_1^0 = \varpi\sigma_{1p} \quad (27)$$

where σ_1^0 is the initial yielding stress; σ_{1p} is the peak value of major principal stress.

In case of stress level over the crack initiation threshold value, plastic strain in principal stress direction starts to grow with respect to the crack initiation threshold value ϖ

$$\varepsilon_i^p = \begin{cases} 0, & \sigma_1 < \varpi\sigma_{1p} \\ \varepsilon_i - \frac{\sigma_1 - \sigma_3}{E_t}, & \sigma_1 \geq \varpi\sigma_{1p} \end{cases} \quad (28)$$

where ε_i^p is the plastic strain in principal direction; ε_i is the strain in principal direction; ε_i^{ϖ} is the strain corresponding to crack initiation.

Hardening law – A normalized hardening model

A normalized hardening-softening yield surface based on Mohr-Coulomb criterion is proposed here along with the parameterization approaches and selection criterion for the evolution of yield in triaxial test.

Normalized damage

We first define a normalized damage parameter in terms of ω as an important variable contributing to the strain hardening process. It relates the effective plastic strain to the plastic strain at peak strength and gets it transformed into a unified range between (0, 1). Similar processing of plastic strain has been carried out by Martin (1993) in the analysis of strength of Lac du Bonnet granite.

$$\omega = \frac{\gamma^p}{\varepsilon_{epe}}, \quad 0 \leq \omega \leq 1.0 \quad (29)$$

where ε_{epe} is the plastic strain corresponding to the peak strength that marks the end of strain hardening and the starting of softening. For the Tournemire argillite, a linear relationship is found to exist between the plastic strain at the peak axial stress and the confining pressure, as shown in Fig. 4.12.

$$\varepsilon_{epe} = C + D\sigma_3 \quad (30)$$

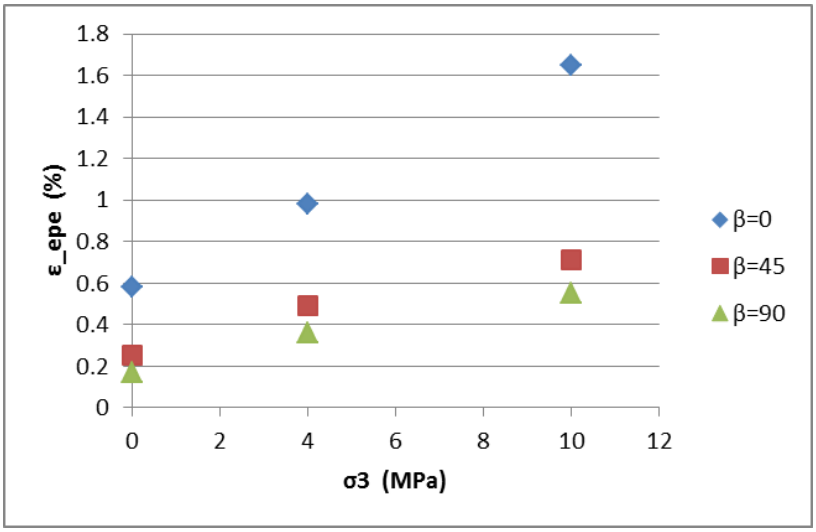

Figure 4.12 Peak plastic strain vs confining pressure for Tournemire Argillite at different orientations

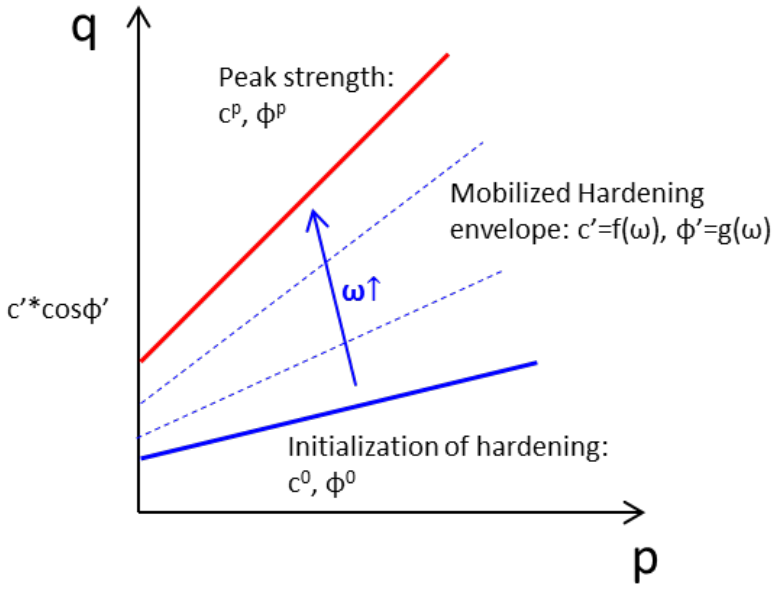

Figure 4.13 Diagram showing the evolution of hardening plastic flow from the initial yielding to the peak failure with varying value of the normalized damage

Mohr-Coulomb parameters in the hardening stage

As shown in Fig. 4.13, between the initial yielding and the peak failure in p-q space, there exists a strain-hardening stage. The development of analytical expression for the hardening law is shown in the appendix. The expressions are as follows:

$$\phi = \mathrm{asin}\left(\frac{m\omega+l-1}{m\omega+l+1}\right) \tag{31}$$

$$cos\phi = \frac{2\sqrt{m\omega+l}}{m\omega+l+1} \tag{32}$$

$$c = \frac{k\omega+h}{m\omega+l+1} cos\phi = \frac{k\omega+h}{2\sqrt{m\omega+l}} \tag{33}$$

The parameters of the above equations, i.e. k, m, h and l, are directionally dependent as shown in Table 4.3 and Figure 4.14. Compared with the conceptual diagram of strength change for brittle granite in Fig. 4.3, it is found that some similarities exist. The frictional angle continuously grows to the peak value with increasing damage, which is in good agreement with Martin's (1993) conceptualization. However, the cohesion of the Tournemire shale does not decrease as compared to brittle rock, but instead increases up to the peak strength. Loss of cohesion in brittle rocks is attributed to crack initiation and propagation. For the Tournemire shale, that phenomenon might be offset by an increase in cohesion due to an increase in the mean stress when the load is increased. The effects of the mean stress on

shear strength parameters are typically more pronounced for softer rocks like shale as compared to harder rocks like granite.

Table 4.3 Orientation dependent hardening parameters determined from curve fitting on test data

	β=0	β=45	β=90	Unit
ϖ	0.3	0.3	0.3	1
C	0.14	0.08	0.015	
D	0.005	0.004	0.004	
k	21.2	12.29	21.85	MPa
m	1.72	1.83	2.58	
h	8.6	4.99	9.04	MPa
l	1.21	1.15	1.27	

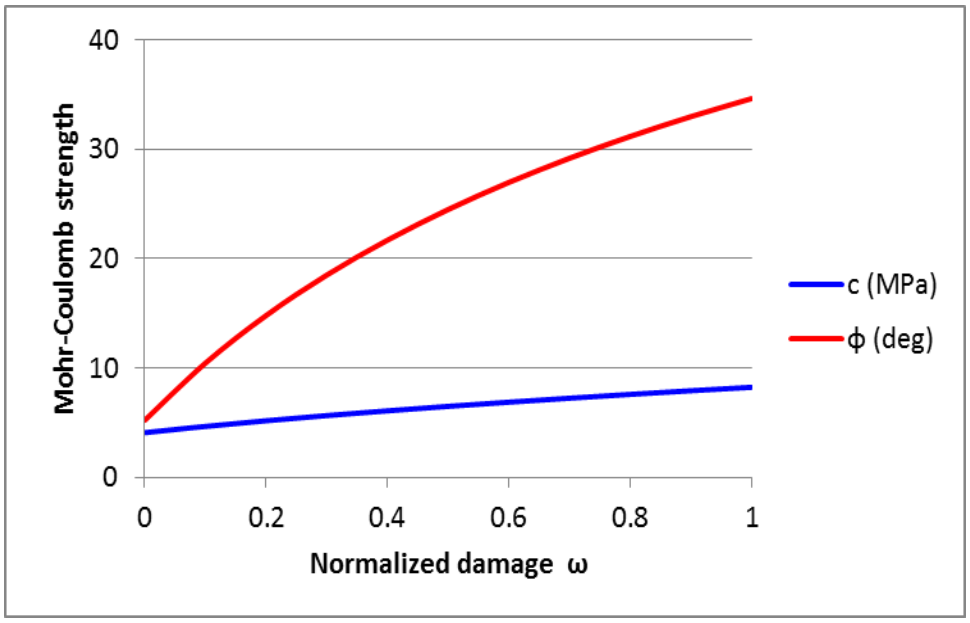

Figure 4.14 Derived Mohr-Coulomb strength parameters of the hardening model for Tournemire shale with bedding orientation at β=90°

Microstructure tensor approach for strengths modelling

The existence of bedding in Tournemire shale results in inherent anisotropy of its yield parameters. Assuming that there is only one orientation of the bedding planes, the anisotropy reduces to a case of transverse isotropy, with two principal directions parallel to bedding, and the third being perpendicular to it. We used the microstructure tensor approach of Pietruszczak and Mroz (2001) in order to take into account the transverse isotropy of the yield parameters as follows.

A generalized loading vector is first defined from the stress tensor as:

$$L_i = L_j e_i^{(j)}; \quad L_j = \sqrt{\sigma_{j1}^2 + \sigma_{j2}^2 + \sigma_{j3}^2}; \quad (i,j = 1,2,3) \tag{34}$$

where $e_i^{(\alpha)}$, α=1,2,3, are the base vectors in the principal directions of the transverse isotropy. The components of L_i represent the magnitudes of traction vectors on the planes normal to the principal material axes. The unit vector along l_i is given by

$$l_i = \frac{L_i}{(L_k L_k)^{1/2}} = \left(\frac{e_k^{(i)} \sigma_{kj} e_l^{(i)} \sigma_{lj}}{\sigma_{ij}\sigma_{ij}} \right)^{1/2} \tag{35}$$

A microstructure tensor a_{ij}, which is a measure of material fabric is introduced. The projection of the microstructure tensor on l_i, becomes

$$\eta = a_{ij} l_i l_j = \frac{a_{ik}\sigma_{ij}\sigma_{kj}}{\sigma_{ij}\sigma_{ij}} \tag{36}$$

The scalar variable η, referred to as anisotropy parameter, specifies the effect of load orientation relative to material axes. The above equation can also be expressed as

$$\eta = \eta_0 \left[1 + A_{ij} l_i l_j \right]; \quad A_{ij} = \frac{a_{ij}}{\eta_0} - \delta_{ij}; \quad \eta_0 = \frac{a_{kk}}{3} \tag{37}$$

where A_{ij} is a symmetric traceless operator. This relation may be generalized by considering higher order tensors, i.e.

$$\eta = \eta_0 \left[1 + A_{ij} l_i l_j + A_{ijkl} l_i l_j l_k l_l + \cdots \right] \tag{38}$$

The above representation is rather complex in terms of implementation and identification. Therefore, it is convenient to use a simplified functional form such as:

$$\eta = \eta_0 \left[1 + \sum b_n \left(A_{ij} l_i l_j \right)^n \right] \tag{39}$$

For triaxial conditions, the above equation reduces to another form as follows. The stress tensor for triaxial test condition can be written as

$$\sigma_{ij} = \begin{bmatrix} \sigma_c & 0 & 0 \\ 0 & \sigma_c & 0 \\ 0 & 0 & \sigma_1 \end{bmatrix} \tag{40}$$

where σ_c is confining stress and σ_1 is the axial stress.

The local coordinate representing the material property, i.e. the rotated orthogonal with respect to z axis, can be defined as

$$[L] = \begin{bmatrix} cos\beta & 0 & sin\beta \\ 0 & 1 & 0 \\ -sin\beta & 0 & cos\beta \end{bmatrix} \tag{41}$$

Then the projected stress tensor in the new local coordinate system becomes

$$\hat{\sigma}_{ij} = [L]\sigma_{ij}[L]^{\mathrm{T}} \tag{42}$$

After matrix operation, we get the following expression,

$$[L]\sigma_{ij}[L]^{\mathrm{T}} = \begin{bmatrix} cos^2\beta\sigma_c + sin^2\beta\sigma_1 & 0 & cos\beta sin\beta(\sigma_1 - \sigma_c) \\ 0 & \sigma_c & 0 \\ cos\beta sin\beta(\sigma_1 - \sigma_c) & 0 & sin^2\beta\sigma_c + cos^2\beta\sigma_1 \end{bmatrix} \tag{43}$$

The above matrix leads to

$$\begin{aligned} {L_1}^2 &= cos^2\beta{\sigma_c}^2 + sin^2\beta{\sigma_1}^2 \\ {L_2}^2 &= {\sigma_c}^2 \\ {L_3}^2 &= cos^2\beta{\sigma_1}^2 + sin^2\beta{\sigma_c}^2 \end{aligned} \tag{44}$$

Then

$$\begin{aligned} l_1^2 &= \frac{{L_1}^2}{{L_1}^2+{L_2}^2+{L_3}^2} = \sqrt{\frac{cos^2\beta{\sigma_c}^2+sin^2\beta{\sigma_1}^2}{{\sigma_1}^2+2{\sigma_c}^2}} \\ l_2^2 &= \frac{{L_2}^2}{{L_1}^2+{L_2}^2+{L_3}^2} = \sqrt{\frac{{\sigma_c}^2}{{\sigma_1}^2+2{\sigma_c}^2}} \\ l_3^2 &= \frac{{L_3}^2}{{L_1}^2+{L_2}^2+{L_3}^2} = \sqrt{\frac{cos^2\beta{\sigma_1}^2+sin^2\beta{\sigma_c}^2}{{\sigma_1}^2+2{\sigma_c}^2}} \end{aligned} \tag{45}$$

In case of unconfined triaxial test, $\sigma_c = 0$, then the above expressions reduce to

$$\begin{aligned} l_1 &= sin\beta \\ l_2 &= 0 \\ l_3 &= cos\beta \end{aligned} \tag{46}$$

The anisotropy in material property can be defined by a microstructure tensor a_{ij}

$$a_{ij} = \begin{bmatrix} a_1 & 0 & 0 \\ 0 & a_1 & 0 \\ 0 & 0 & a_2 \end{bmatrix} \tag{47}$$

Then the deviatoric part of the above tensor becomes

$$\mathrm{dev}(a_{ij}) = \begin{bmatrix} a_1 - \frac{2a_1+a_2}{3} & 0 & 0 \\ 0 & a_1 - \frac{2a_1+a_2}{3} & 0 \\ 0 & 0 & a_2 - \frac{2a_1+a_2}{3} \end{bmatrix} = \frac{a_1-a_2}{3}\begin{bmatrix} 1 & 0 & 0 \\ 0 & 1 & 0 \\ 0 & 0 & -2 \end{bmatrix} \tag{48}$$

After calculation we get

$$A_{ij}l_il_j = A_1(1 - 3l_3^2) \tag{49}$$

Then

$$\eta = \eta_0[1 + \sum b_n(A_1(1 - 3l_3^2))^n] \quad (50)$$

where l_3 is component of the loading unit vector in the direction perpendicular to bedding (Z axis in this case).

Nguyen and Le (2015a) expressed the Mohr-Coulomb strength parameters, e.g. c and ϕ as function of the microstructure tensor and loading orientation using the functional form of equation (50). In this study, c and ϕ are described by the hardening functions in equations 31 and 33. The parameters of those equations are then expressed in the functional form of equation 50, with best fit parameters as shown in Figure 4.15. As a result, the crack initiation threshold, and the peak strength are shown in Figure 4.16.

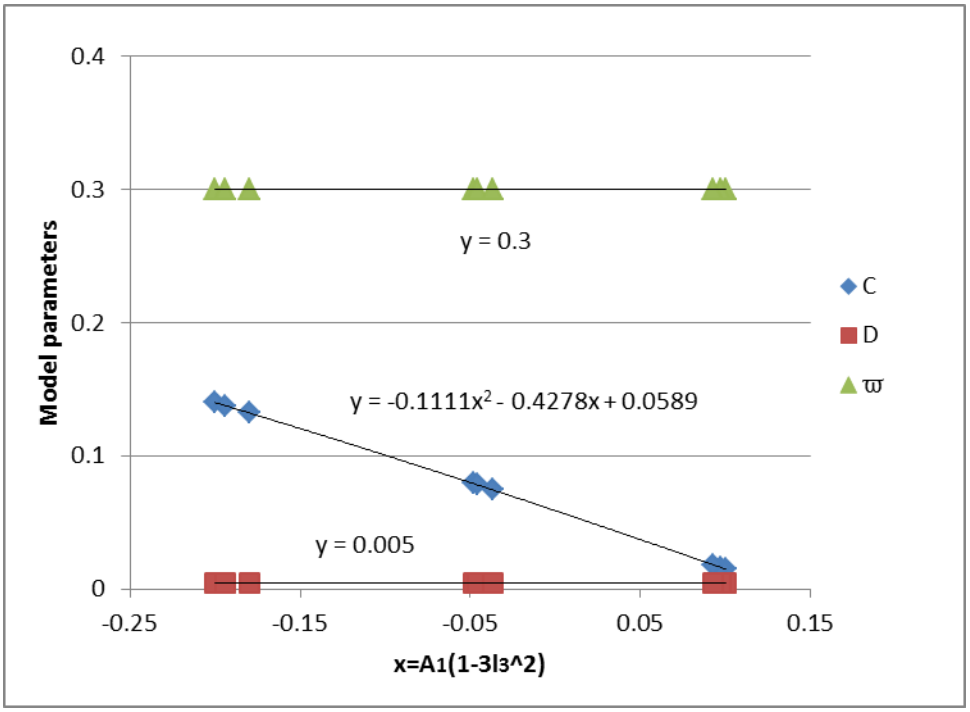

(a)

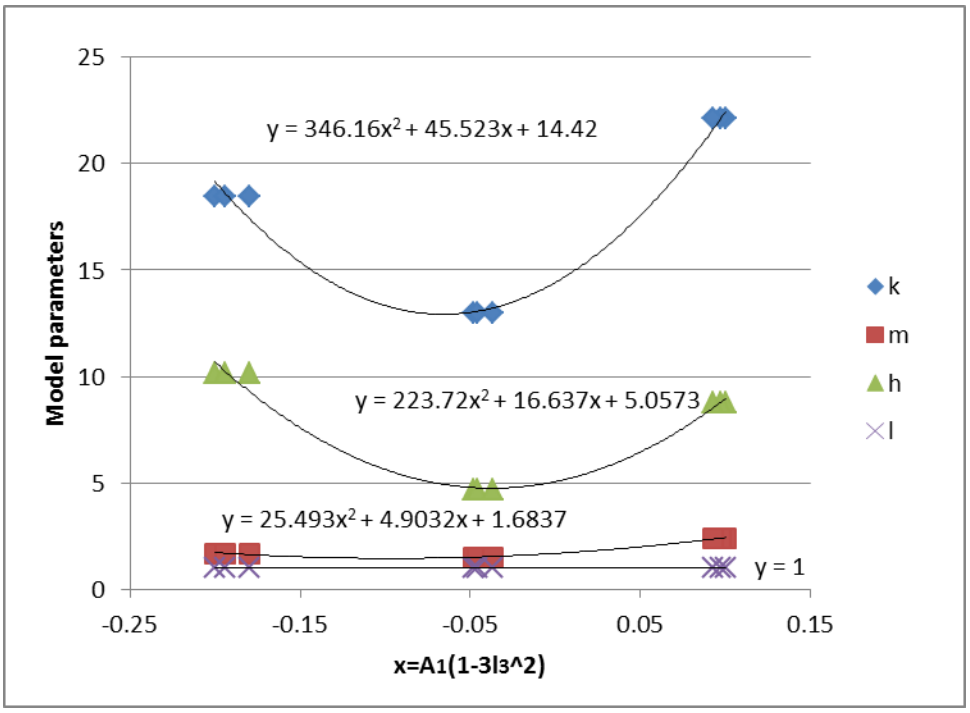

(b)

Figure 4.15 Dependence of hardening model parameters on the microstructural tensor

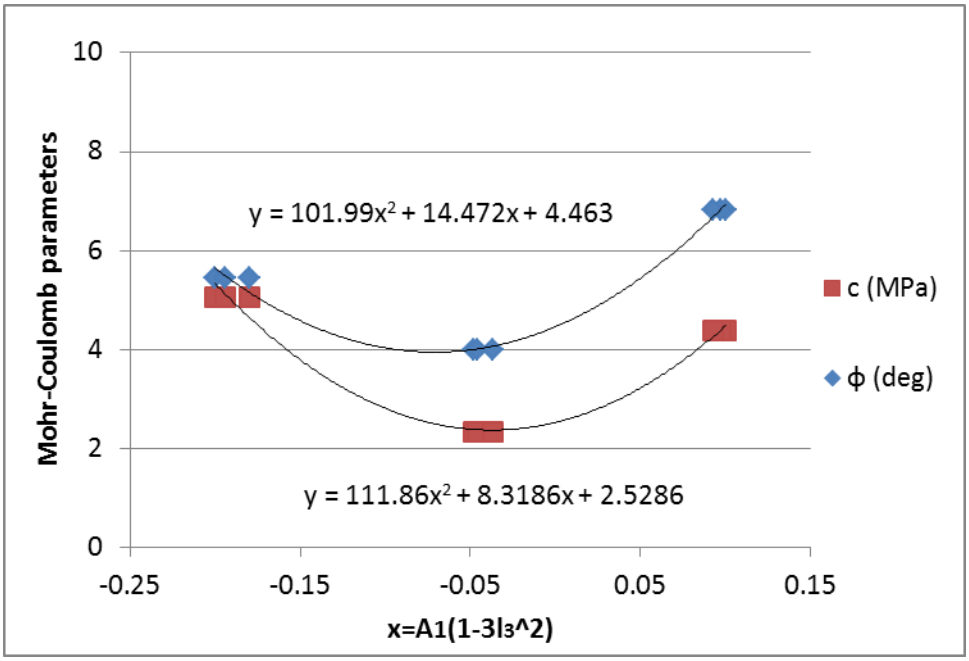

(a)

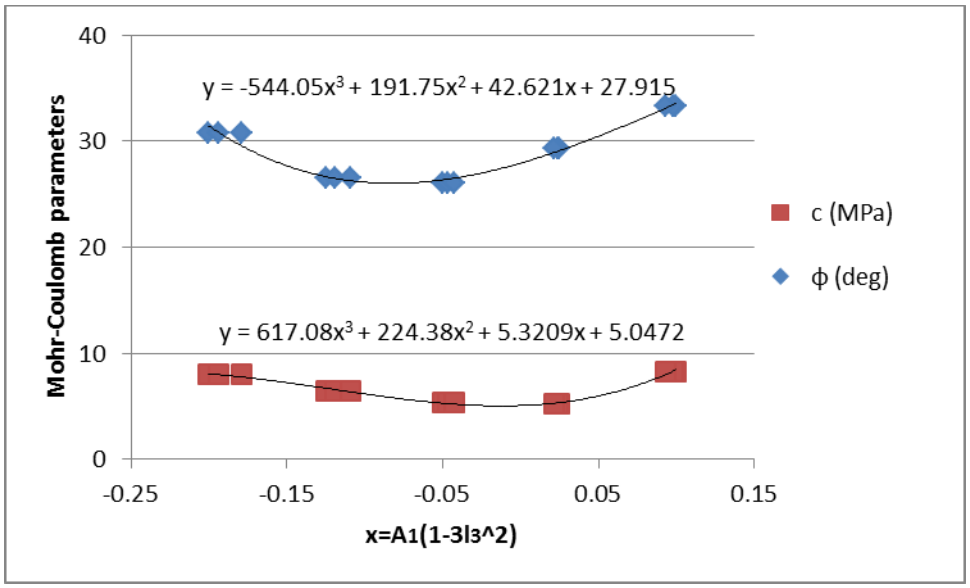

(b)

Figure 4.16 Dependence of Mohr-Coulomb strength parameters on the loading orientation parameter (a) the crack initiation strength and (b) the peak strength

4. FEM model for triaxial test

A 3-D FEM model for the triaxial test was developed with COMSOL Multiphysics (Ver 5.1). The FEM model has a height of 133 mm and a radius of 35 mm in order to exactly represent the dimensions of the test samples. The geometric sketch and FEM mesh of the model are shown in Fig. 4.17. The bottom plane was assigned with fixed displacement in all directions while the side surfaces were subjected to a confining pressure Pc. The upper boundary was prescribed with time-dependent displacement in the vertical direction. The evolution of vertical stress was monitored throughout the simulation for comparison with the test data. Modelling with different confining pressures, e.g. 0, 4 and 10 MPa, and different bedding orientations, e.g. 0, 45 and 90 ^{o}, was performed.

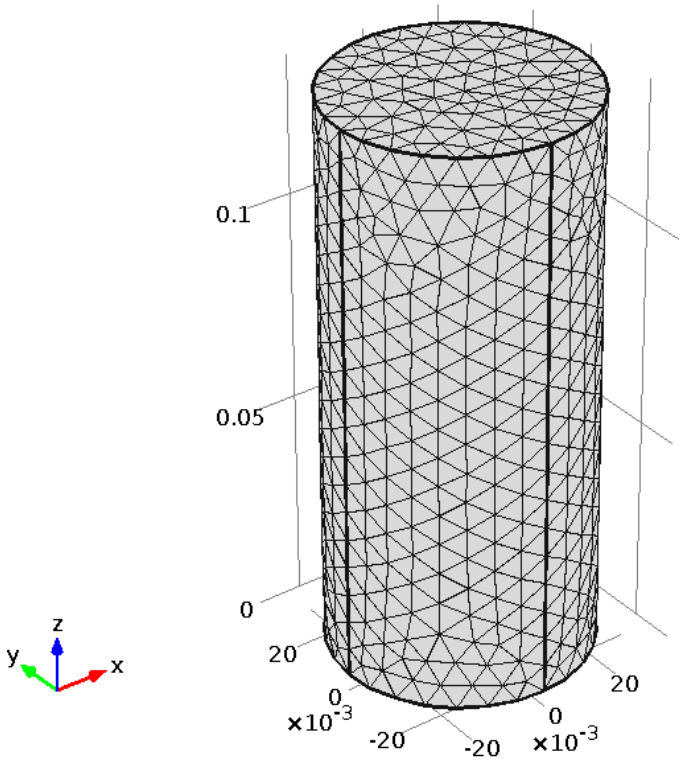

Figure 4.17 The FEM model for triaxial test on Tournemire argillite

5. Results and discussion

Visco-elastoplastic modelling of static triaxial compression test

Stress-strain behaviour

Figure 4.18a-18c shows the modelling results of stress-strain curves in comparison with test data. Good agreement between modelling and test data can be observed. In particular, the model can correctly simulate the influence of confining stress and the direction of loading with respect to the bedding orientation. The linear hardening law with which the model parameters were determined seems sufficient to reflect the gradually curved growth of axial stress with increasing axial strain. The peak strength fits well with the estimated Mohr-Coulomb strength envelope.

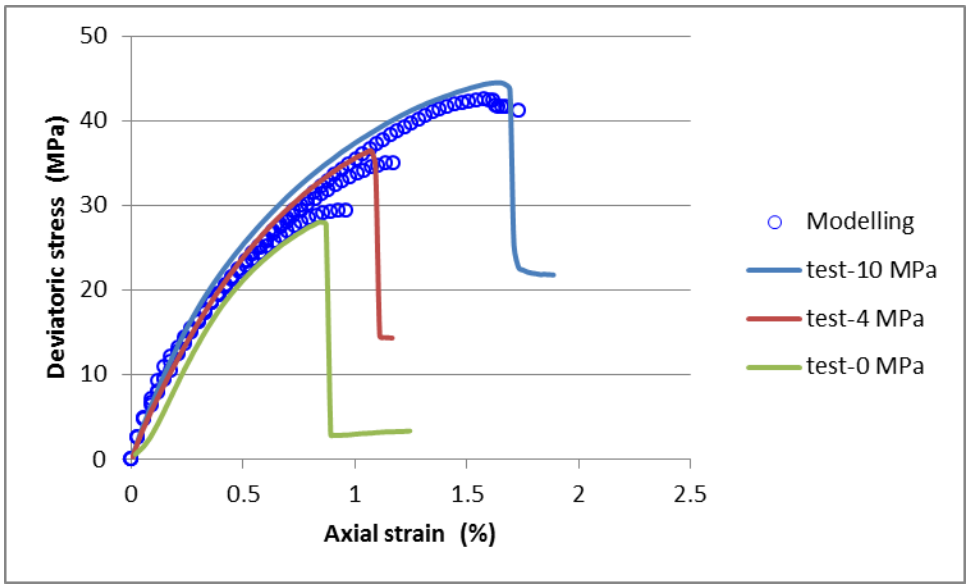
Deviatoric stress (MPa)
50
40
30
20
10
0
0
0.5
1
1.5
2
2.5
Axial strain (%)
Modelling
test-10 MPa
test-4 MPa
test-0 MPa

(a)

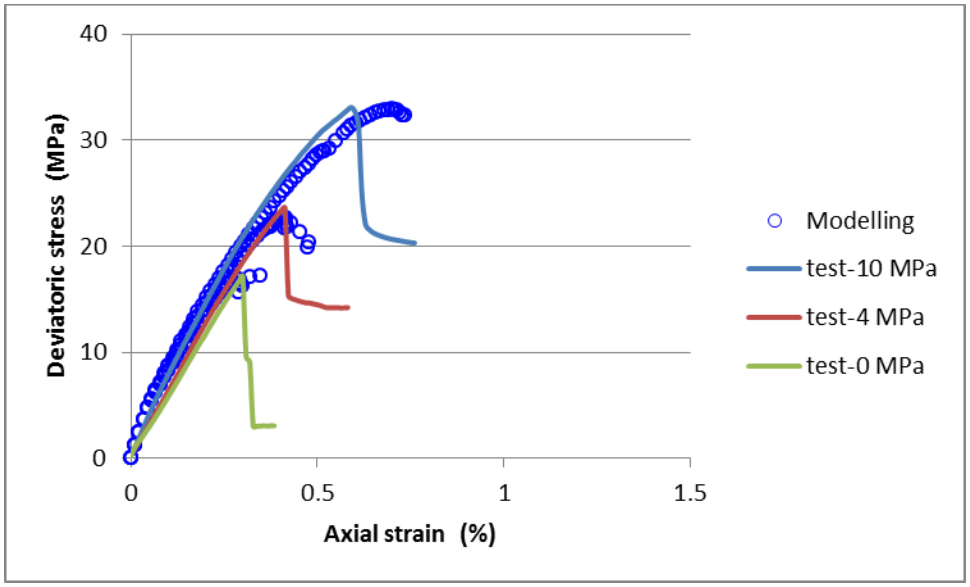
Deviatoric stress (MPa)
40
30
20
10
0
0
0.5
1
1.5
Axial strain (%)
Modelling
test-10 MPa
test-4 MPa
test-0 MPa

(b)

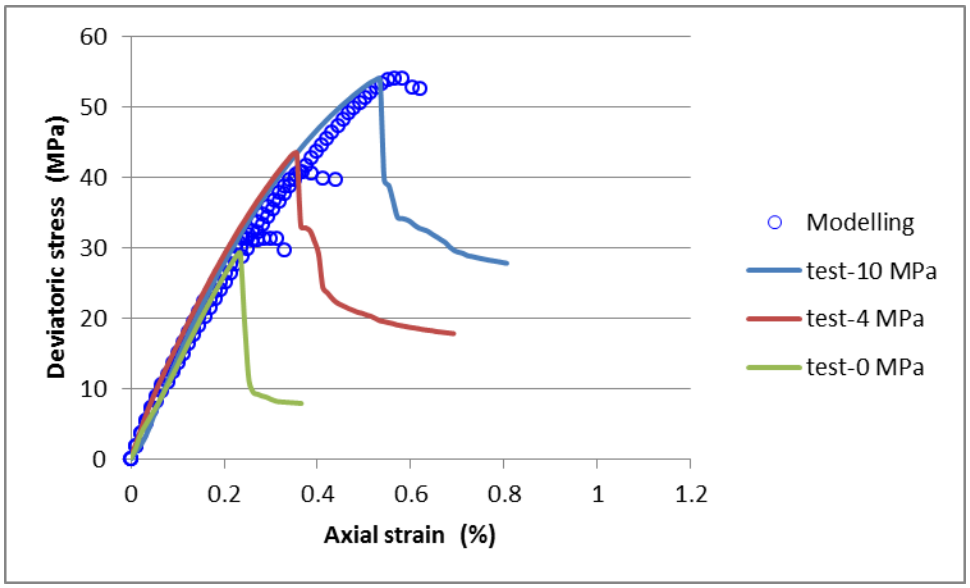

(c)

Figure 4.18(a-c) Stress strain curves for specimens with bedding angle at β=0, 45 and 90° (solid curves are test data and open symbols are simulation results)

Volumetric strain vs axial strain

Figure19a-19c shows the calculated volumetric strain in comparison with the test data. The overall volumetric strain values are well reproduced by our model, particularly for test cases with load angle at 45 and 90 °. In particular, consistently with the experimental data, the modelling results show that:

- The elastic linear portion of the volumetric deformation is restricted to stress level below the crack initiation threshold, which corresponds to approximately 30% of the peak axial load.
- A hardening stage is found up to the point of reversal of the volumetric versus axial strain curve. As discussed previously, that point corresponds to the crack damage threshold, which for the Tournemire shale is very close to the peak axial stress. The calculated values of volumetric deformation is comparable to the experimental values for bedding orientation of β=90 and 45°. The stiffness of the sample at β=0 is much higher as compared to the other two orientations; therefore the model predicts higher compression. However this is not reflected in the experimental data.

The post-failure pattern of stress strain curves was not simulated for the Tournemire argillite. This is because of the lack of information about hydraulic-mechanical coupling that has to be related to effective plastic strain. As for the Tournemire argillite, there were no experiments on the damage induced permeability enhancement available to this study. Therefore it appears to be unnecessary to investigate the post-failure softening behaviour, especially considering the inability of our continuum mechanics-based elasto-plastic model to model the phenomenon with significant strain localization.

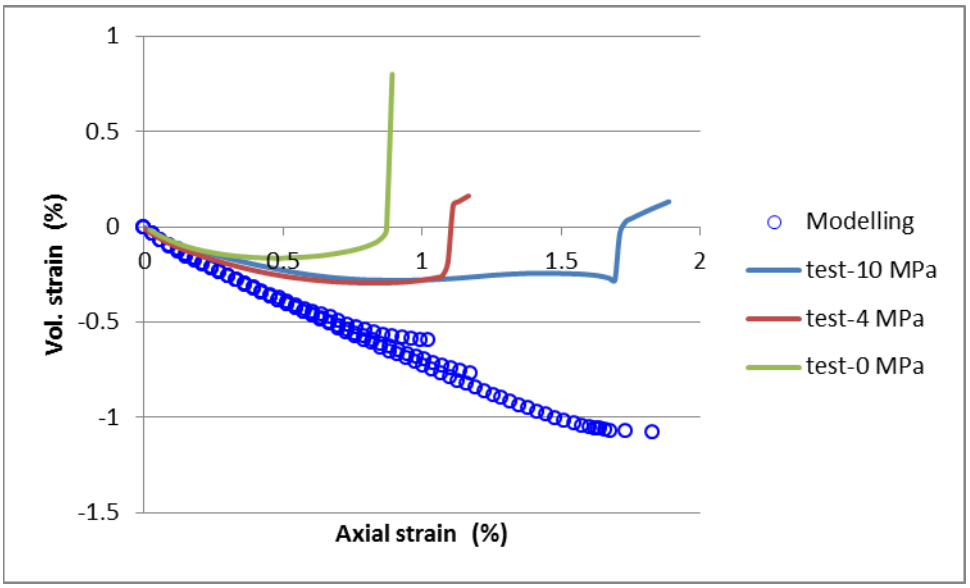
1
0.5
0
-0.5
-1
-1.5
0
0.5
1
1.5
2
Vol. strain (%)
Axial strain (%)
Modelling
test-10 MPa
test-4 MPa
test-0 MPa

(a)

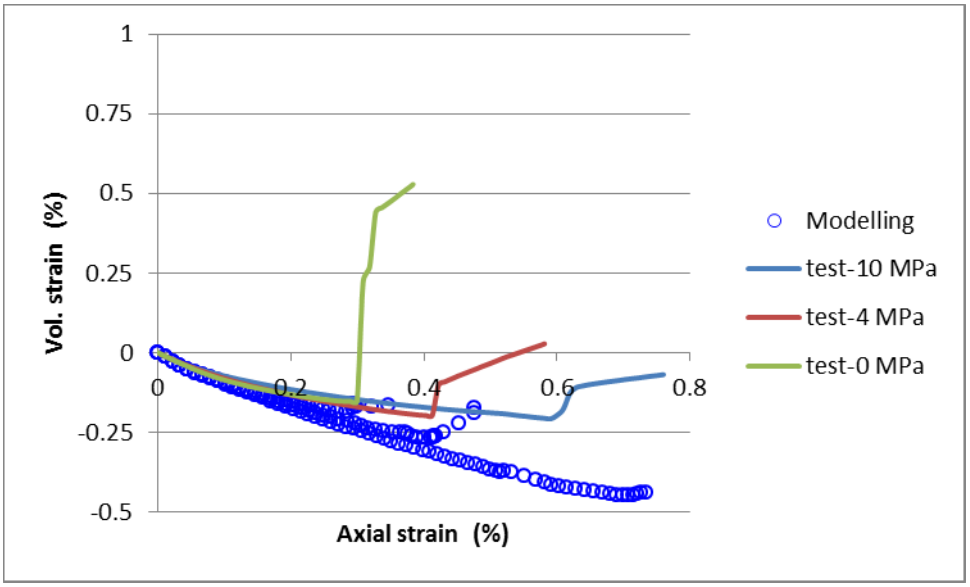
1
0.75
0.5
0.25
0
-0.25
-0.5
0
0.2
0.4
0.6
0.8
Vol. strain (%)
Axial strain (%)
Modelling
test-10 MPa
test-4 MPa
test-0 MPa

(b)

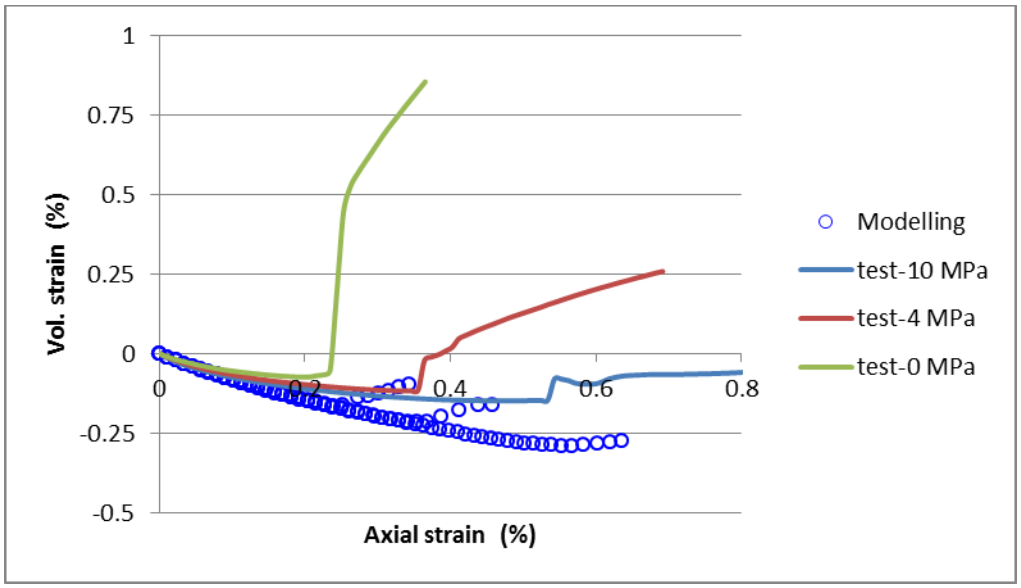

(c)

Figure 4.19(a-c) Volumetric strains for specimens with load angle at β=0, 45 and 90^{o} (solid curves are test data and open symbols are simulation results)

Visco-elastoplastic modelling of creep test

Figure 4.20(a) shows the visco-elastoplastic modelling of the unconfined creep behaviour of Tournemire shale at different loading orientations. The experiment was carried out with unconfined triaxial compression loading cell in stepwise incremental manner as shown in Fig. 4.20(b). It is found that the modelling reproduces the test data with very high consistency. The relaxation time and the Maxwell shear modulus were determined to be 3.5 GPa and 500 s, respectively, for all the three loading orientations. Our results show that a unified set of parameters for the viscoelastic model applies to Tournemire clay, indicating the isotropy in viscoelasticity. This is in agreement with other reports on rheology of anisotropic clay rocks (Zhang et al. 2002). For instance, after extensive experimental investigation of Callovo-Oxfordian argillites, no obvious anisotropy effect on the creep behaviour of the clay rock was found to be comparable to the mineralogical composition and water content factors (Zhang et al. 2002). Rheological heterogeneity is mainly pertinent to hard rocks and related to wave propagation (Carcione and Cavallini, 1994), geological slip systems and fabric frozen in the mantle, and can be used to explain preferential rift propagation and continental break-up (Vauchez et al. 1998). However, rheological anisotropy appears to be rare to soft clay rocks.

It is also worth mentioning that the creep rate at the end of test averages at 8E-9 (s^{-1}) in this study. Fabre and Pellet (2006) reported a smaller creep rate for Tournemire argillite at 4E-10 (s^{-1}), while Zhang et al. (2002) determined the equilibrium creep rate of Oxfordian argillite at 5E-11 (s^{-1}). These experiments were conducted with different duration of time, i.e. the longer the test lasts, the less the creep rate becomes. Zhang et al. (2002)'s creep test was finished over a year, while Fabre and Pellet (2006)'s and ours were done within a day. The creep rate may accelerate if cyclic loading exists and the level of shear stress over passes a certain threshold value (Fabre and Pellet, 2006).

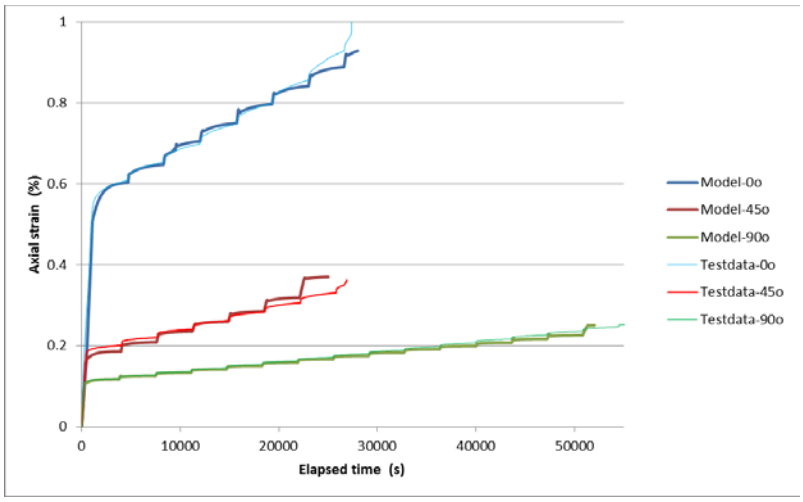

(a)

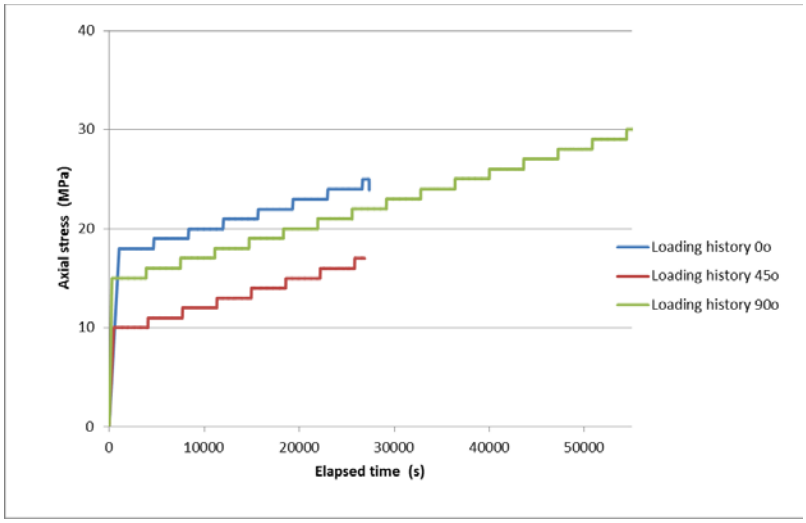

(b)

Figure 4.20 Unconfined creep behaviours of Tournemire clay under various loading orientations (a) modelling results and testdata (b) applied axial stress loading history

Visco-elastoplastic modelling of cyclic triaxial test

Figure 4.21(a-f) shows the stress-strain behaviour of Tournemire shale under cyclic loading conditions. The modelling is able to reproduce the hysteretic cycles as observed in the test data with good agreement. It is noted that the viscoelastic constants that are used for the modelling of the cyclic loading test are identical to those calibrated from the creep test, suggesting that the rheological model is representative of the material property. The modelled stress appears to be higher than the observed value before the first stress reversal. This could be attributed to the closure of cracks under increasing stresses that is not considered in the modelling. When axial stress is reversed, there is always a certain amount of residual strain even at very load stress levels. Abdi et al. (2015) explained such accumulated residual strain as a result of plastic strain, which may not be appropriate according to our analysis. The residual strain should be attributed solely to viscosity when stress is less than the crack initiation

threshold, under which conditions no plastic strain is likely to take place. Compared to previous studies on the mechanical behaviour of Tournemire clay (Niandou et al., 1997), the compressive strength, axial and volumetric strains that were reported by Abdi et al. (2015) are all in the lower end, which has been thought to be scale effect due to the difference in sample sizes. The residual strain after removal of the deviatoric stress is between two-thirds and one-half of the total strain in Abdi et al. (2015), while Niandou et al. (1997) reported a value of one-half. This could be caused by the different loading-unloading rate. According to the viscoelastic model, a higher loading-unloading rate would induce a higher stress increment, and thus a lower strain change under the same range of stress variations. Zhang et al. (2002) reported that the creep behaviour of Argillites clay is not influenced by scale effects even for a factor of two in size difference in the tested specimens. This is in agreement with the inference of our rheological analysis of Tournemire shale.

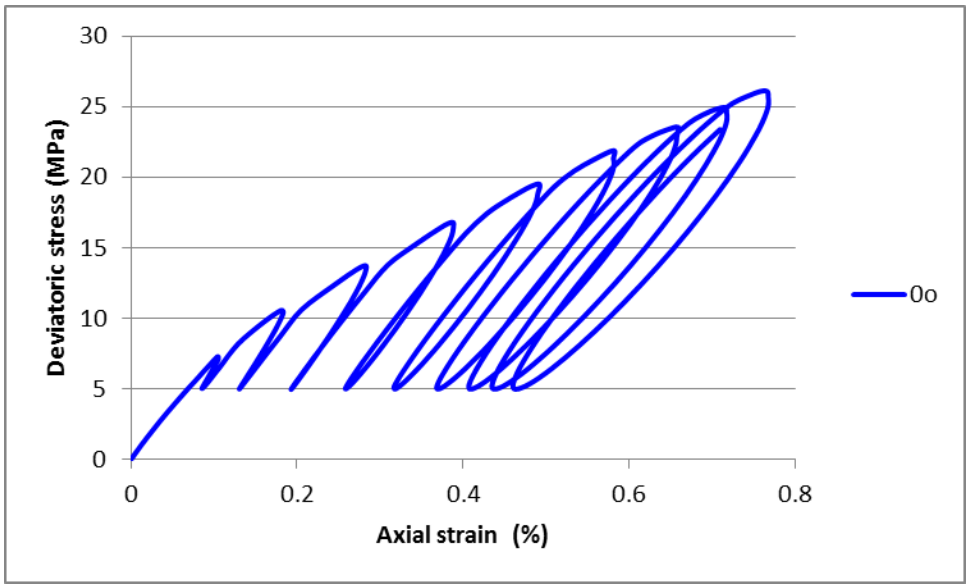

(a)

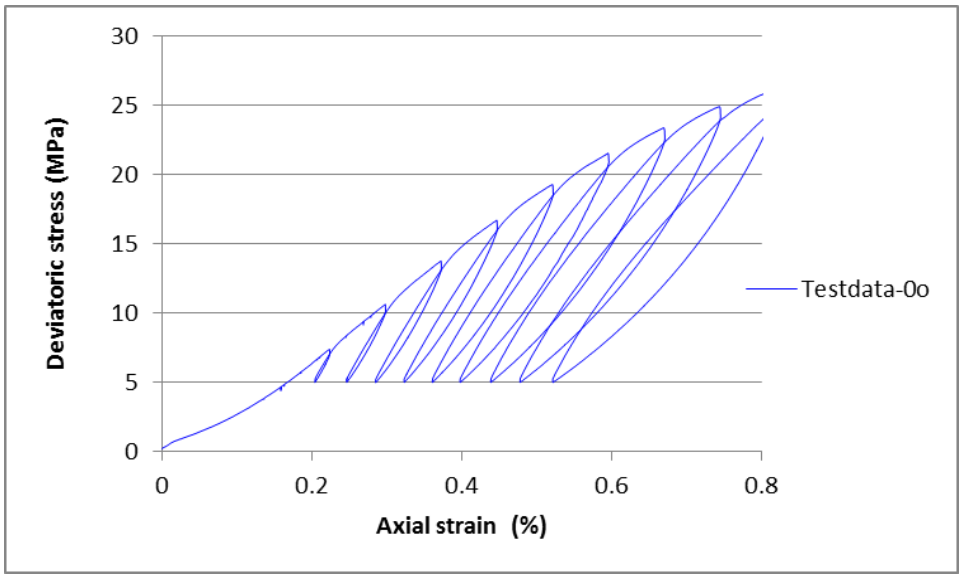

(b)

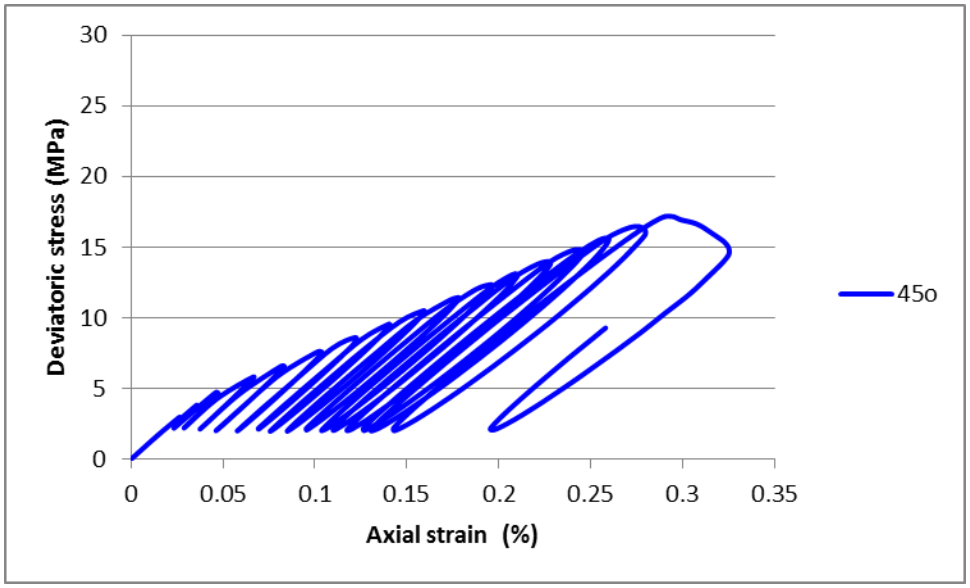
30
25
20
15
10
5
0
Deviatoric stress (MPa)
0
0.05
0.1
0.15
0.2
0.25
0.3
0.35
Axial strain (%)
45o

(c)

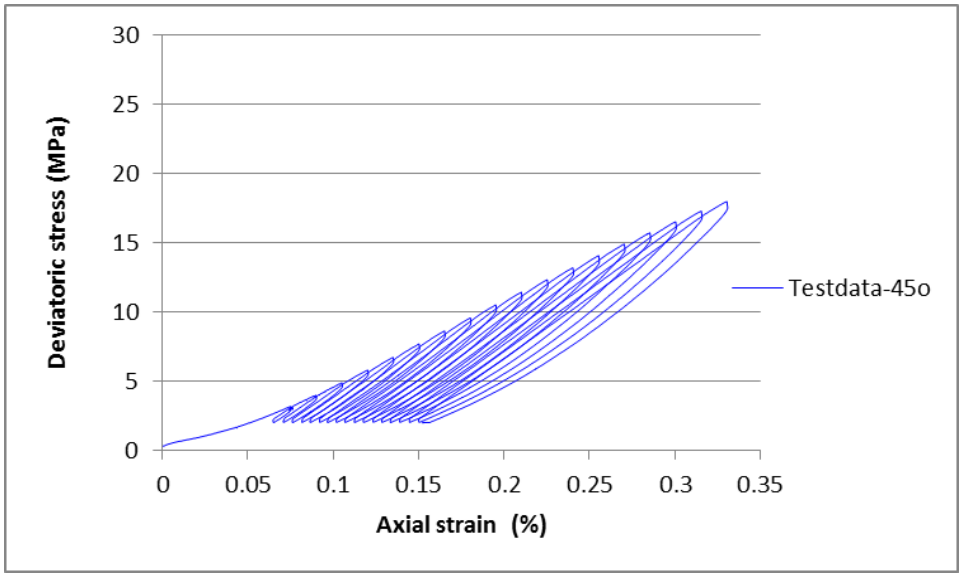
30
25
20
15
10
5
0
Deviatoric stress (MPa)
0
0.05
0.1
0.15
0.2
0.25
0.3
0.35
Axial strain (%)
Testdata-45o

(d)

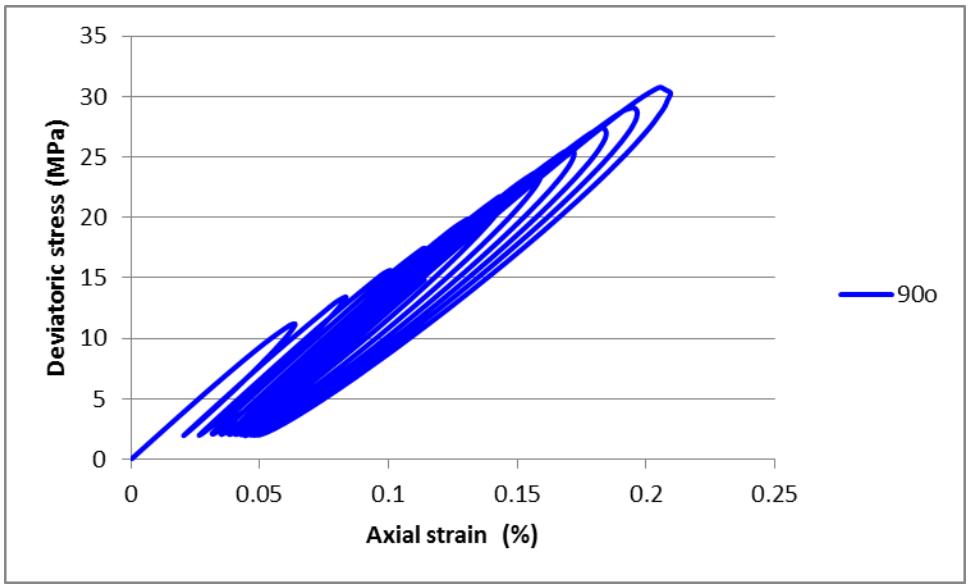

(e)

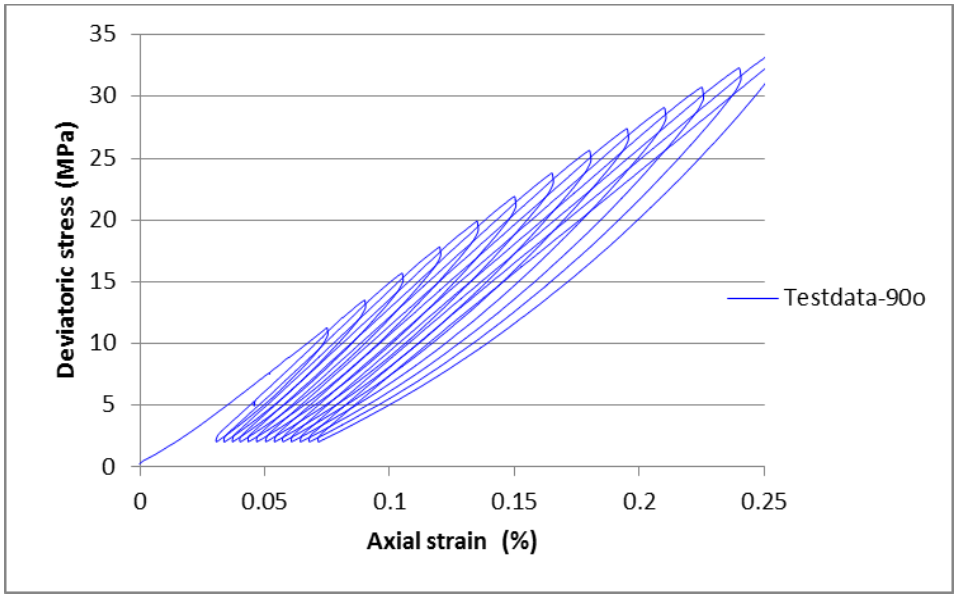

(f)

Figure 4.21 Unconfined stress-strain behaviours of Tournemire clay under cyclic axial loading at different orientations (a) modelling results at β=0 °; (b) test data at β=0 °; (c) modelling results at β=45 °; (d) test data at β=45 °; (e) modelling results at β=90 °; (f) test data at β=90 °

6. Case Study

EDZ in the century old tunnel at the Tournemire URL

The Tournemire site is located in an old railway (100 years old) tunnel that penetrates through the Argillite clay formation. This site became of interest to the IRNS since 1990s due to its suitability to study the confining properties of argillaceous media for deep underground storage of nuclear waste. Two horizontal drifts were excavated in 1996 and 2003 for characterization of excavation damage zones. Radial boreholes were drilled in various locations across the tunnel axis. The retrieved rock logs indicated the thickness of damage zones. Extensive geological investigations and in-situ hydraulic-mechanical coupling experiments have been carried out on site. Seismic imaging and other geophysical method have been implemented to characterize and monitor the evolution of damage over time (Bretaudeau et al., 2014; Okay et al. 2013). Major faults with 0.85-2.4 m thickness were observed to cross the old tunnel. Intensive fractured damage zones with 4-6 m thickness were present in western drift and some boreholes.

The host rock surrounding the old tunnel exhibits a densely fractured, homogeneous EDZ that with an average thickness of 70 cm (Fig. 4.22). In areas close to the major fault, the EDZ thickness reaches 1.3-2.5 m, which suggests the likely interaction between the fault zone and the host rock. The EDZ in the new gallery is much thinner than the old tunnel, approximately 0.30-0.40 m, with desiccation induced cracks distributed parallel to the bedding plane. The EDZ near the new gallery is thought to not be affected by the age of the opening (Millard et al., 2009). Compared to the newly excavated gallery, the old tunnel has much more extensive EDZ in the radial direction. This phenomenon appears to be difficult to explain by HM coupling theories and was the subject of interest of many researchers in the past. Time dependent property change as well as desiccation induced matric suction has been considered as possible reasons for the significant difference in EDZ patterns (Rejeb and Stephansson, 2007).

Previous modelling studies showed that instantaneous equilibration of stress could be achieved in the host rock after excavation when analysed with Mohr-Coulomb elastoplastic theory and without consideration of pore pressure dissipation or material property degradation over time (Millard et al. 2009). HM coupling has to be taken into account because desaturation together with excavation induced stress perturbation and boundary condition changes. Failure of rock mass causes damage to microstructures, leading to growth of microcracks and nucleation of microcracks, which further contribute to the increase permeability. The change in permeability affects the pore pressure distribution pattern and its dissipation rate. The effective stress posed on solid skeleton is then expected to increase much faster relative to the intact rock mass.

Faults characteristics

Faults, which have been absent from previous studies on the same area of interest, might impose significant influence on the evolution of EDZ. The Fault is characterized with intensively fractured, highly permeable, and weakly adhered rock joints. Due to its relatively higher permeability, it acts as permeable draining boundary for the intact rock blocks. Faults introduce incontinuity to the rock mass, facilitate pore pressure dissipation and weaken the overall strength and stiffness. These factors are all included into the mechanistic discussion and numerical simulations in this study.

Fracture analyses from cores drilled through the main fault zone at the Tournemire URL show the existence of weak planes with different types of fillings (mainly calcite) of various sizes (Guglielmi et al. 2015). The fault core contains heterogeneous cataclastic zones where shale clasts are coated by clay layers and highly fractured zones with calcite veins consisting of 10% of the bulk mass (Guglielmi et al.

2015). The fractures appeared to be perfectly sealed and impervious due to these fillings (Boisson et al., 2001).

Fault stiffness is reported to be in the range of 1-100E9 Pa/m. Sealed faults generally have higher stiffness than the open faults. According to the in-situ measurement of the effective elasticity of the fault zone at this site, both the normal and tangential modulus of the interested fault zone can be evaluated to be 2E11 Pa/m and 2.85E11 Pa/m, respectively (Steer et al., 2011). The high value of stiffness of the fault suggests perfect sealing of the fractures, which is in agreement with the field observation of abundant filling materials in fractures. Strength of the fault zone is characterized with peak frictional angle between 22-34 ^{o} and cohesion of 0-0.5 MPa (Guglielmi et al. 2015), corresponding to the reported range of frictional angle between 21-41 ^{o} for carbonate rocks (Cruden and Hu, 1988) and experimentally observed value at 33 ^{o} (atan(0.65)) for clay minerals of illite-kaolinite (Ikari et al., 2011). Although faults have been reported to possess rheological properties that appear to be either hardening or softening and are closely related to strain rate (Ikari et al., 2011), a thin elastic layer is assumed to represent the fault zone in the following numerical studies, with stiffness values being within the range reported in the literature.

Fault permeability has been determined by water injection tests as performed on site (Guglielmi et al. 2015). The permeability of the core of fault zone is in the range of 3-6E-12 m/s when injection pressure is lower than the in-situ ground stress. A significant increase in permeability of the fault zone has been observed in terms of fracture flow once fault got reactivated by over pressured pore fluid. As depressurization is the main process accompanying the excavation and desiccation of the tunnel to be considered in this study, it appears reasonable to adopt a comparatively low level of permeability, which is still more permeable than intact rocks, for the fault zone.

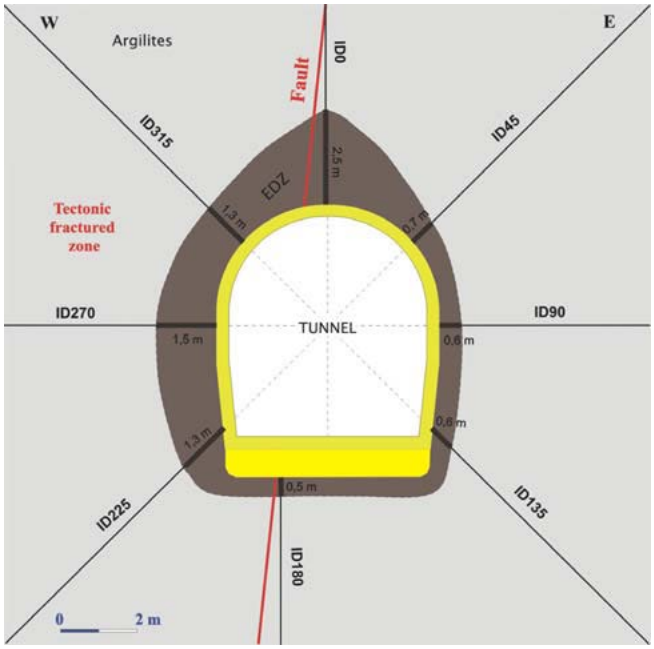

Figure 4.22 The extent of the EDZ around the old tunnel, near the fault (Rejeb and Stephansson, 2007)

Desiccation induced cracks

Due to the desaturation effect of the excavation of tunnel onto the pore pressure distribution and matric suction evolution, cracks that are observable virtually on the younger galleries at Tournemire site have been formed in accordance with change in relative humidity in the air. Previous studies indicated that these cracks are seasonally repetitive and are parallel to the bedding orientation (Rejeb and Stephansson, 2007). Matray, Savoye, and Cabrera (2007) and Genty et al. (2002) both evidenced the important influence of fracturing on the distribution of pore pressure, and inversely the capillary forces on fracturing around the century-old tunnel, and emphasized the necessity of HM coupled simulations. Desiccation induced cracks were considered by those researchers as a possible explanation to the discrepancy in EDZ thickness between the old tunnel and young galleries. The EDZ around the old tunnel has an onion-like layered structure that is aligned with the tangent direction. Several numerical modelling studies of the HM coupled processes associated with the Tournemire tunnel have pointed to the critical role of desaturation in EDZ development (Millard et al., 2009; Rejeb and Stephansson, 2007; Fabre and Pellet, 2006; Pellet et al., 2009). A recent modelling study of EDZ in Callovo-Oxfordian claystone at Andra underground research lab in Bure, France highlighted both mechanical fracturing and desiccation induced enhancement of elasticity and plasticity (Pardoen et al. 2015). However, neither has specifically addressed the strain that resulted from desiccation.

The fact that desiccation creates cracks in clayey and silty soils is well described in the literature, and it is believed that the same phenomenon is applicable to the Tournemire shale. This phenomenon is generally believed to be associated with tensile failure that develops with the interplay between strain constraints and desiccation shrinkage. Matric suction variation and wetting-drying cycles have been systematically investigated. Miller et al. (1998) investigated crack propagation in clay liners and found that cracking takes place in a very intense period of time during desiccation. Cracking was reported to commence when matric suction reaches a threshold value of 0.6 MPa for the clay liner specimen. This observation is consistent with the cracking theory of Peron et al. (2009) which proposes the air entry value (AEV) of soil as the desiccation threshold. Recent image analysis studies by Hedan et al. (2014) and Fauchille et al. (2014) revealed that cracks in Tournemire shale can be quantitatively evaluated under various environmental conditions. In situ monitoring of crack opening and closure for one year suggested the occurrence of subvertical fissures in addition to the prevalent parallel-to-bedding cracks (Hedan et al., 2014). This discovery sheds light on the possibility of explaining the much larger EDZ in the old tunnel as compared to newer galleries by the desiccation cracking mechanism. The shrinkage strain of Argillite clay was observed to be dependent on relative humidity in terms of two separate linear stages, and the inflection was coincident with the measured air entry value.

Based on these previous research findings, we propose herein a model to describe the shrinkage strain of clay rocks as a function of matric suction. Since cracking initiates after the AEV is exceeded in the desiccation process, an elastic shrinkage is considered to be valid before matric suction reaches the AEV, while plastic strains are believed to take place afterwards when matric suction goes beyond AEV. Note that desiccation strain could be dependent on bedding orientation. For simplicity purpose we assume here an isotropic case for desiccation strain.

The empirical relationship between volumetric desiccation strain and matric suction can thus be proposed as,

$$\varepsilon^d = K_1 S_u,\ (0 > S_u > \psi_a) \tag{51}$$

$$\varepsilon^d = K_1 \psi_a + K_2 \ln \frac{S_u}{\psi_a},\ (\psi_a > S_u) \tag{52}$$

where ε^d is desiccation strain, S_u is matric suction, ψ_a is air entry value, K_1 and K_2 are model constants representative of the shrinkage rate at two consecutive stage of desiccating. According to previous tests on desiccation of Tournemire shale as shown in Fig. 4.23, it can be determined that the desiccation parameters K_1=5E-11 (Pa^{-1}), K_2=0.007-0.013 (Pa^{-1}), and the air entry value could be estimated at 30 MPa.

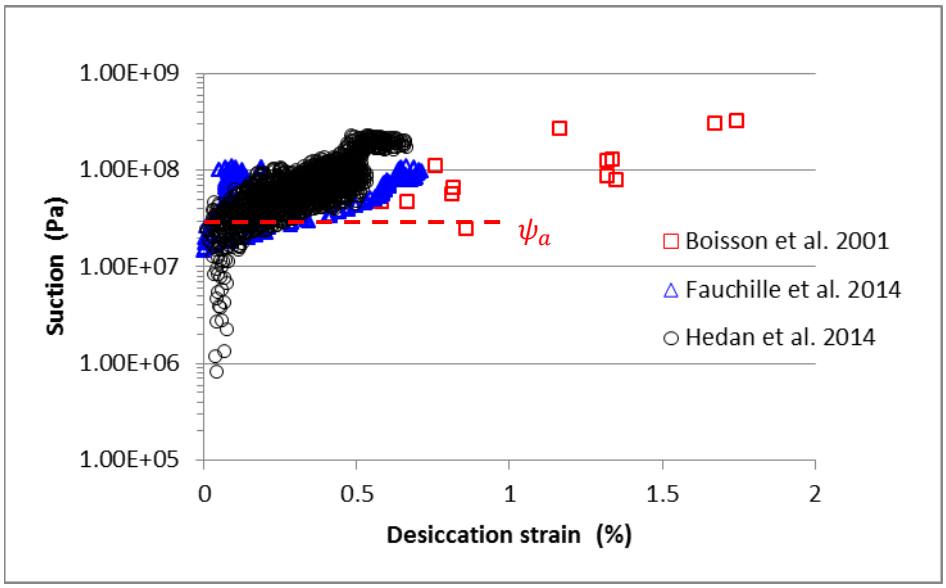

(a)

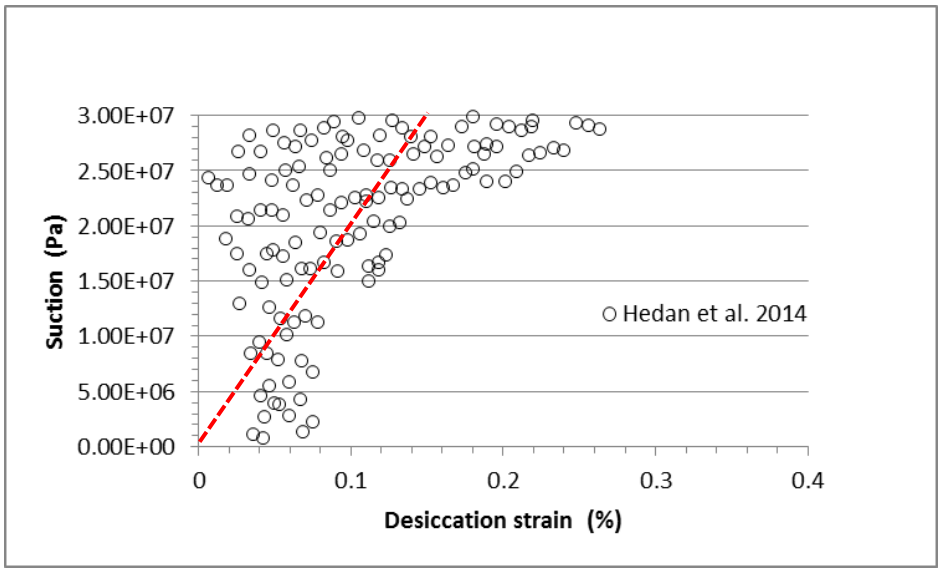

(b)

Figure 4.23 Variation of desiccation strain with suction for Tournemire clay (b) is an excerpt of (a) (Test data are extracted from (Boisson et al. 2001; Fauchille et al. 2014; Hedan et al. 2014))

Numerical modelling of the EDZ around the tunnel

A 3-D FEM model was built with the COMSOL Multiphysics software to simulate the HM coupled processes in the long-term post excavation period. The model is a block with dimension 40m*10m*40m (x*y*z) with the tunnel axis aligned with the Y coordinate as shown in Fig. 4.24. The major fault cutting through the tunnel is modelled as a thin elastic and permeable layer, using zero thickness elements. As hydro-mechanical coupling was taken into account, the outer boundary conditions are confined by rollers and constant pore pressure at 0.5E6 Pa (except for impermeable boundary for the cross sectional boundaries perpendicular to tunnel axis). The inner boundary at the tunnel surface is treated with time-dependent confining loading and pore pressure to simulate the excavation and the following desiccation processes.

The geometric shape of the fault has been evaluated by either logging or seismic reflection methods and has been reported recently (Guglielmi et al. 2015), which intersects the tunnel axis at approximately 28 ^{o}. Normal stiffness and tangential shear modulus have been investigated by in-situ injection tests as reported by Steer et al. (2013), which enables us to estimate the required properties for the fault zone.

Two sets of in-situ ground stress were separately obtained from field tests and showed that the state of stress is approximately hydrostatic with an average value 4.0 MPa. The shale away from the excavation is saturated or nearly saturated with S_e>99%. We assumed an initial uniform distribution of pore pressure of approximately 0.5 MPa in the rock mass around the tunnel. The tunnel wall is covered by masonry on the side and ceiling and ballast and wood on the bottom. These lining materials are omitted in the modelling with the assumption that limited mechanical support would be resulted from. Desaturation of the host rock resulted from drier air inside the tunnel, with annual average relative humidity of 60% and annual average temperature of 10 ^{o}C, corresponding to -70 MPa of matric suction. It is thought that the masonry protects host rock from humidity fluctuation, and the modelling with a hypothetical suction boundary at -33 MPa results in a saturation at 0.90 that is consistent with saturation profile of test data (Matray et al. 2007). As the ballast cover on the bottom would maintain a certain level of moisture compared to the open air, the matric suction at the floor of the tunnel bottom was adjusted to 30% of the value for the side walls. A smooth reducing step function of boundary pressure (lasts for a year and then maintains a constant pressure) was applied to the tunnel surface.

Different mechanical and hydraulic properties are assumed for the rock mass across the fault. Intense fracturing was observed in the western part (e.g. the left block in the model). This implies reduced stiffness and strength for the western block. Isotropic elastoplastic properties were assumed for the left block. In particular, the Mohr-Coulomb yield parameters were assumed to be equal to the ones at 45 ^{o} of bedding orientation as determined from the triaxial tests. For the Eastern (right) block, the mechanical behaviour is defined from the visco-elastoplastic model discussed in the preceding sections, with the required input parameters as calibrated from the laboratory triaxial compression tests. Transverse isotropy of permeability was assumed for the right block, while isotropy of permeability was assumed for the left one. The model parameters are listed in Table 4.4.

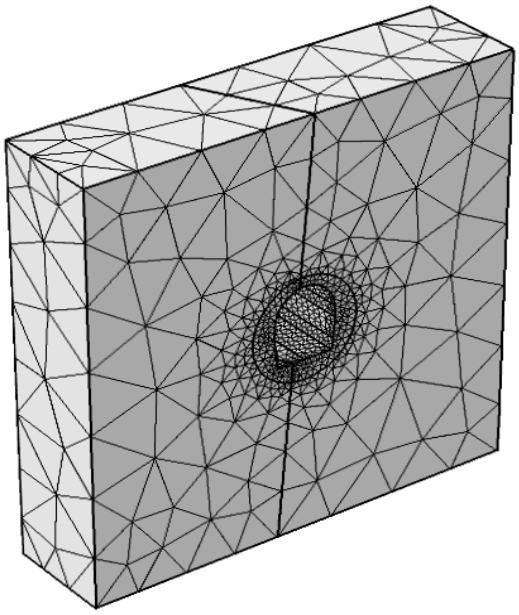

Figure 4.24 Finite element model of the fault zone and rock mass surrounding the old tunnel at Tournemire site

Governing equations for HM coupling

HM coupled processes can be modelled with the same theoretical framework that has been proposed by Nguyen et al. (1995, 2005) and Nguyen and Le (2015a), with some adjustment. The total strain tensor can be decomposed into four parts in our hydraulic-mechanical coupled visco-elastoplastic model, i.e. $\boldsymbol{\varepsilon} = \boldsymbol{\varepsilon}^{\boldsymbol{e}} + \boldsymbol{\varepsilon}^{\boldsymbol{p}} + \boldsymbol{\varepsilon}^{\boldsymbol{d}} + \boldsymbol{\gamma}$, whereas the plastic strain and viscous strain are respectively determined by plastic flow rule and viscoelastic models as above described. The desiccation strain follows Eqs. (51-52).

The equation of static equilibrium is written as follows, with the inclusion of a modified Biot's effective stress principle,

$$\mathbf{D}: \nabla(\boldsymbol{\varepsilon} - \boldsymbol{\varepsilon}^{\boldsymbol{p}} - \boldsymbol{\varepsilon}^{\boldsymbol{d}} - \boldsymbol{\gamma}) + \alpha \nabla p = 0 \tag{53}$$

where $\boldsymbol{\varepsilon}^{\boldsymbol{d}}$ is desiccation strain tensor, $\boldsymbol{\varepsilon}^{\boldsymbol{p}}$ is plastic strain tensor and **γ** is the viscous strain tensor; and **D** is the matrix for material stiffness, α is the Biot's coefficient of consolidation, p is pore pressure.

Following Nguyen and Le (2015-b), the pore pressure is stipulated to be equal to the water pressure for saturated conditions, and equal to the air pressure for unsaturated conditions. Assuming that the air pressure remains constant and equal to atmospheric pressure (p_{atm}), this gives:

$$\begin{cases} p = p_l; & if\ S_e = 1 \\ p = p_{atm}; & if\ S_e < 1 \end{cases} \tag{54}$$

where S_e is effective saturation and p_l is the pore water pressure.

The conservation of pore fluid can be written as

$$\rho_l \left(\frac{C_m}{\rho_l g} + S_e S\right)\frac{\partial p}{\partial t} + \nabla \frac{k\rho_l}{\mu}\nabla p = \alpha \rho_l S_e \frac{\partial \varepsilon_v}{\partial t}, \quad (S_e < 1) \tag{55}$$

$$S\frac{\partial p}{\partial t} + \nabla \frac{k}{\mu}\nabla p = \alpha \frac{\partial \varepsilon_v}{\partial t}, \quad (S_e = 1) \tag{56}$$

where S is a storage term ($S=n\chi_f+(1-n)\chi_s$), χ_f is fluid compressibility, χ_s is solid compressibility, μ is fluid viscosity, ε_v is volumetric strain, k is permeability and C_m is the specific moisture capacity that describes the slope of moisture variation with suction in unsaturated conditions.

The water retention curve is modeled by van Genuchten relationship in the form of

$$S_e = [1 + (\vartheta P_c)^n]^{-m} \tag{57}$$

where P_c is matric suction, ϑ is the reversal of air entry value ($\vartheta = 1/\psi_a$), m and n are van Genuchten model constants that have the relationship of $m = 1 - 1/n$. For saturated case of $P_c \geq 0$, $S_e = 1$.

The permeability takes the form of

$$k = k_0 k_r \tag{58}$$

where k_0 is the intrinsic permeability and k_r is the relative permeability which defines the unsaturated flow by

$$k_r = (S_e)^{0.5}\left[1 - \left(1 - {S_e}^{1/m}\right)^m\right]^2 \tag{59}$$

The fault zone is simplified into a thin elastic layer with isotropic elasticity and fracture flow properties that can be modelled with

$$d\frac{\partial}{\partial t}(\theta \rho_l) + \nabla\left(d\rho_l \frac{k_f}{\mu}\nabla p\right) = 0 \tag{60}$$

where d is the fracture thickness, θ is porosity, k_f is the fracture permeability.

Table 4.4 Parameters for the simulation of the old tunnel at Tournemire site

Variable	Value	Unit
Mechanical parameter		
Right host rock (anisotropic)		
$E_\perp$	7.4	GPa
$E_\parallel$	13.5	GPa
$v_\perp$	0.15	
$v_\parallel$	0.253	
$G_\perp/E_\perp$	0.21	
$G_\parallel$	$E_\parallel/2(1+v_\parallel)$	Pa
ρ	2700	kg/m^3
c	$\frac{k\omega+h}{2\sqrt{m\omega+l}}$	Pa
ϕ	$\mathrm{asin}(\frac{m\omega+l-1}{m\omega+l+1})$	rad
α	0.85	
Left host rock (isotropic)		

E	8.5	GPa
ν	0.15	
ρ	2700	kg/m^3
c	($\beta=45^o$)	Pa
ϕ	($\beta=45^o$)	^{o}
α	0.85	
Fault stiffness		
k_A	20.0	GPa/m
Hydraulic parameter		
Right host rock (anisotropic)		
$k_{//}$	1E-19	m^2
$k_{\perp}$	2E-20	m^2
θ	0.10	
ψ_a	3E7	Pa
n	1/0.6	
χ_p	4E-9	1/Pa
χ_f	4E-10	1/Pa
Left host rock (isotropic)		
k_0	2E-19	m^2
θ	0.15	
ψ_a	3E7	Pa
n	1/0.6	
χ_p	4E-9	1/Pa
χ_f	4E-10	1/Pa
Fault zone		
k_f	3E-19	m^2
d	0.15	m
θ	0.15	

Results

The estimated plastic strain appears to be independent of time even in case of HM coupling, as shown in Fig. 4.25. The shape and scope of the EDZ with consideration of plasticity could not explain the field data which reveals more extensive distribution of the EDZ in the left block of the rock mass and progressive evolution of the EDZ with elapsing time. This phenomenon is consistent with the modelling results of Millard et al. (2009).

Figure 4.26(a-d) shows the simulation results of inelastic strain, which consists of plastic strain and desiccation induced strain, at various time after excavation. The maximum inelastic strain is determined to be 0.38%, which is about 5 times of the maximum plastic strain. The desiccation induced strain accounts for 0.3% under the simulation conditions, which is consistent to Zhang et al. (2002)'s experimental observation of desiccation strain at 0.3% for Callovo-Oxfordian Argillite under 15 MPa of confining pressure. The estimated EDZ thickness is smaller in the right block than the left block; this has been confirmed by field investigations as shown in Fig. 4.22. The arrow-head EDZ above the ceiling is related to the highly permeable fault that drains much faster than the intact rock. The desiccation penetrating along the fault contributes significantly to the inelastic strain, as shown in Fig. 4.27.

Previous modelling studies that have neglected the influence of the fault could not reproduce the peculiar feature of the EDZ on the tunnel ceiling (Millard et al. 2009; Rejeb et al. 2007). Our HM coupled model satisfactorily reproduced the observed EDZ in the old tunnel, suggesting the strong weathering effect onto the Tournemire argillite by the excavation induced desaturation process. On site image monitoring confirmed the strong tendency of cracks along the bedding plane, as well as transverse subvertical microcracks that was not noticeable (Hedan et al. 2014). All these lines of evidences point to the important role of swelling-shrinkage of the Tournemire shale in the formation of cracks and EDZ in the old tunnel.

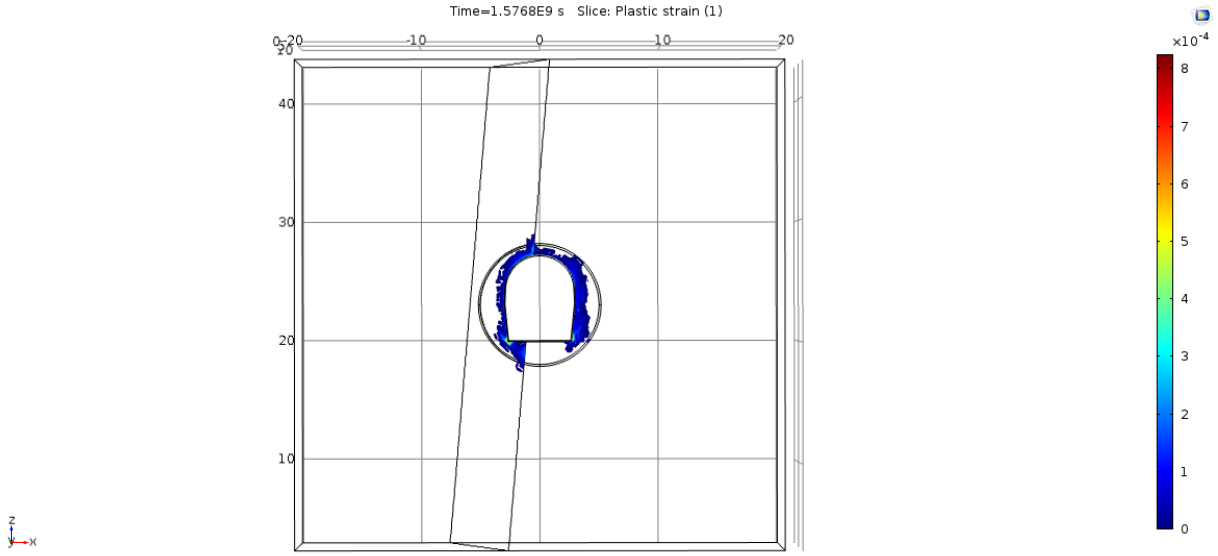

Figure 4.25 Plot of estimated plastic strain in host rocks after excavation

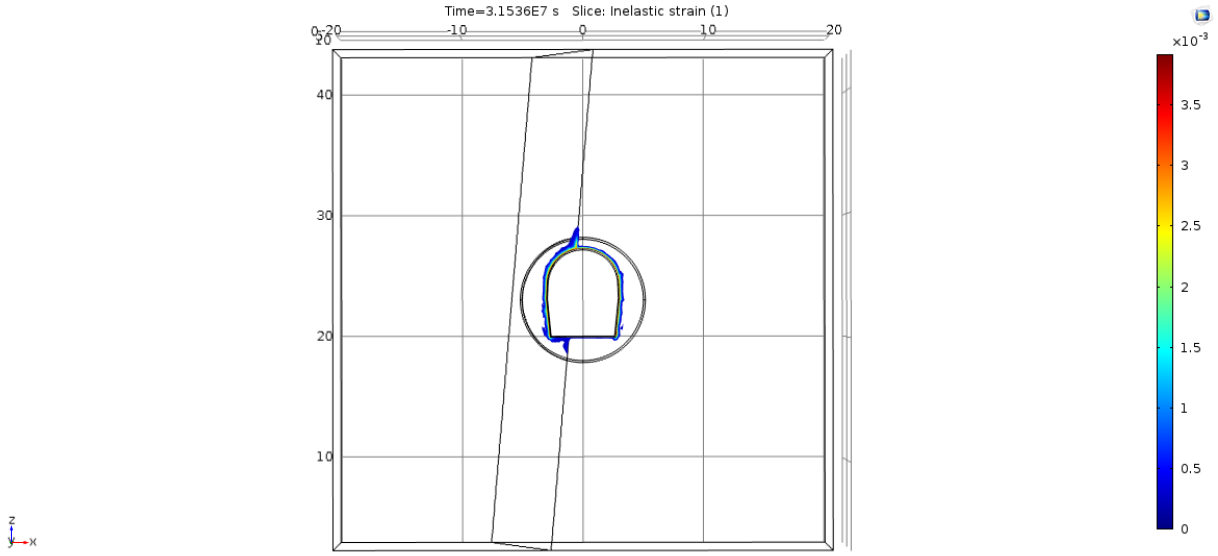

(a)

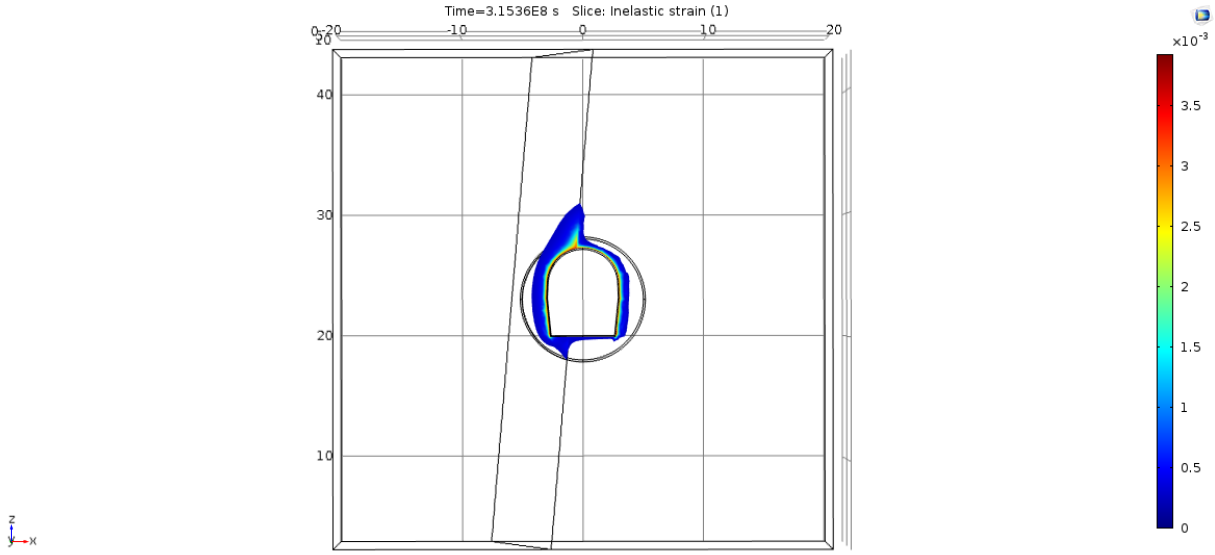
Time=3.1536E8 s Slice: Inelastic strain (1)
-20
-10
0
10
20
40
30
20
10
×10⁻³
3.5
3
2.5
2
1.5
1
0.5
0
z
y
x

(b)

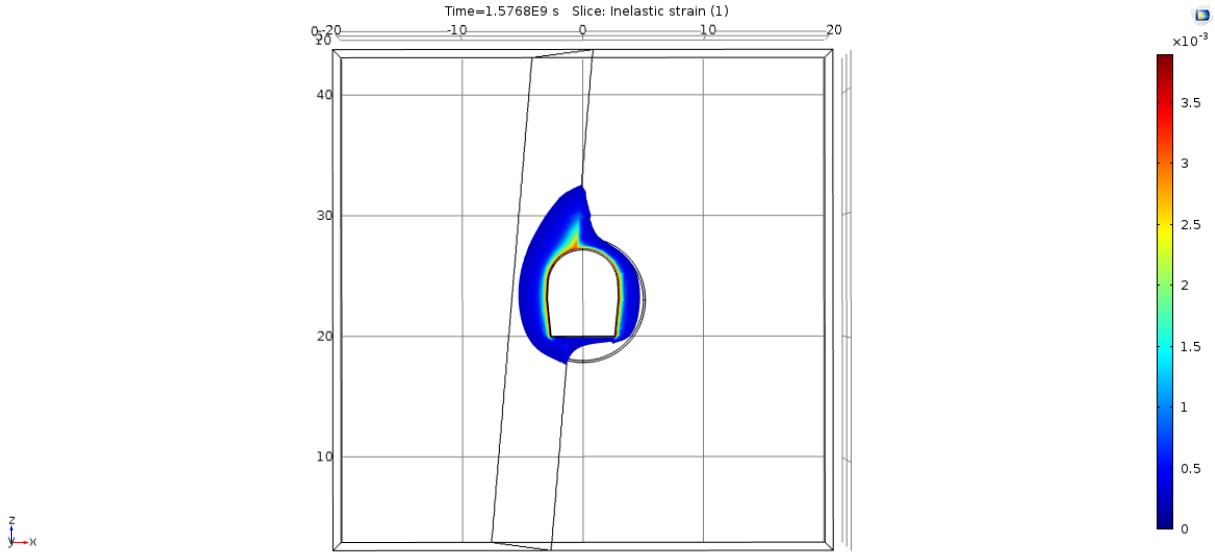
Time=1.5768E9 s Slice: Inelastic strain (1)
-20
-10
0
10
20
40
30
20
10
×10⁻³
3.5
3
2.5
2
1.5
1
0.5
0
z
y
x

(c)

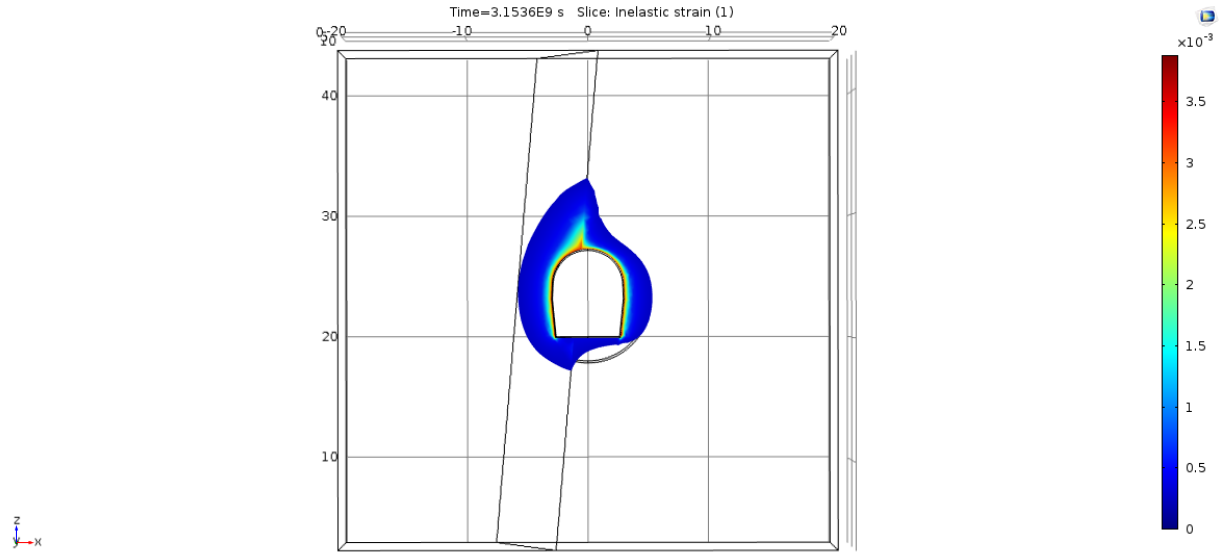

(d)

Figure 4.26 Plot of inelastic strain at various time after excavation (a) 1 year; (b) 10 years; (c) 50 years and (d) 100 years

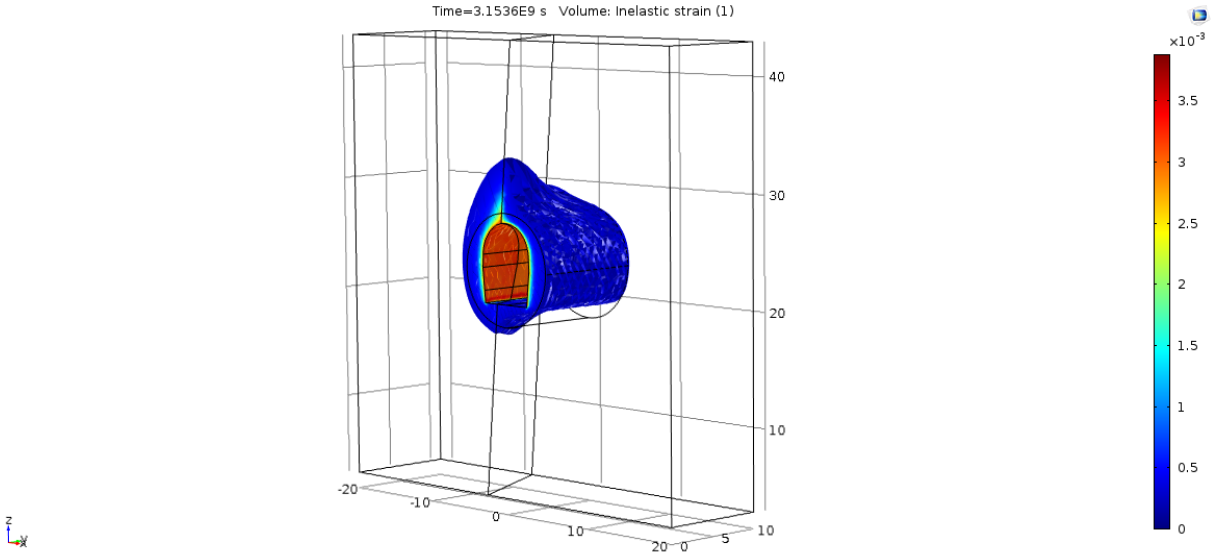

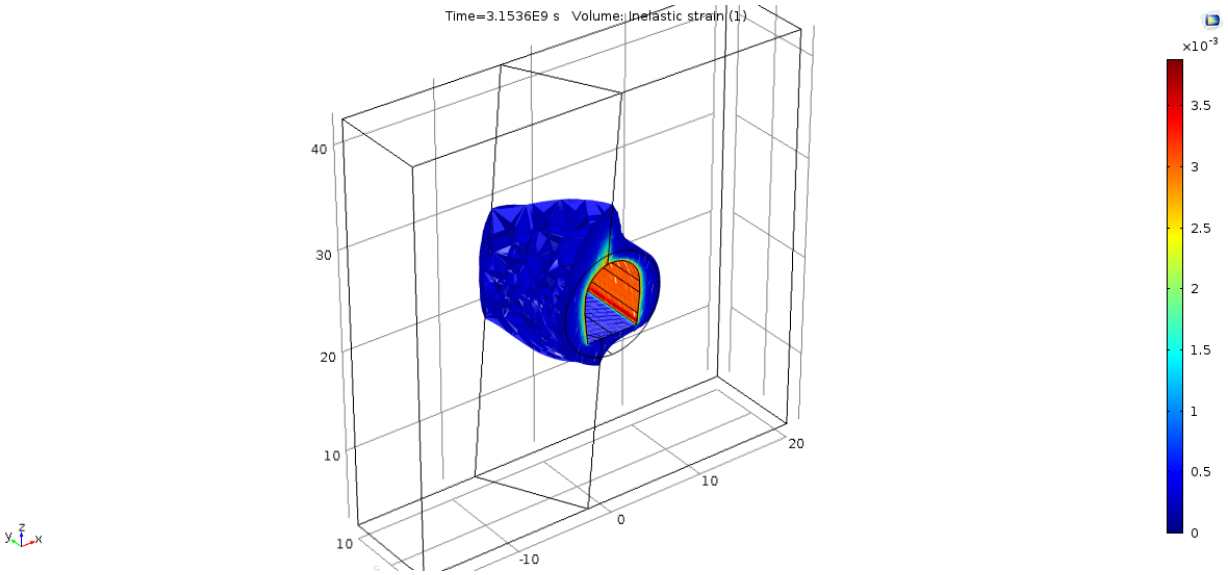

Figure 4.27 Spatial view of the inelastic strain estimated after 100 years of excavation (a) directional view from right side; (b) directional view from left side

7. Conclusions

The understanding and prediction of the mechanical behaviour of argillaceous rocks are important in many areas of industrial activity in this rock type, including fracking for gas and oil exploitation, carbon dioxide sequestration, underground mining or geological disposal of radioactive waste. In this work, the authors took advantage of a comprehensive set of experimental data on the Tournemire shale (Aveyron, France) in order to develop a constitutive model for argillaceous rocks. The experimental data were generated from three sets of triaxial tests: monotonic compression, creep and cyclic loading-unloading tests, using samples with different bedding orientation with respect to the axial loads. The constitutive relationship being proposed is based on the elastoplastic theoretical framework. It includes directional dependence of the elastic and plastic parameters, strain-hardening, and viscosity in order to simulate time-dependent behaviour. A unique set of model parameters were determined from the experimental data. That set of parameters was then used to perform the modelling of the triaxial tests, using the finite element method to solve the equation of static equilibrium. The ability of the model to reproduce the main physics that prevailed in all the tests, using a unified set of experimental data, provides confidence in its robustness.

The proposed constitutive relationship was implemented in a finite element model to simulate the shape and extent of the excavation damage zone (EDZ) around the century-old tunnel at the Tournemire Underground Research Laboratory, from which the laboratory test samples were taken. Hydraulic-mechanical coupling was considered in that model. The same parameters as determined from the laboratory tests were used as input to the model. It is found that mechanical factors alone fail to explain the observed EDZ phenomena. The tunnel was exposed to seasonal fluctuations in temperature and relative humidity, resulting in desaturation and desiccation on the walls, floor and ceiling. Therefore, the authors included in the model the additional effect of desiccation-induced cracking, using an empirical

relationship for suction-desiccation strain. With the above consideration, the model reproduced satisfactorily the observed arrow-head shaped EDZ above the tunnel ceiling and the layered EDZ around the tunnel's walls. The fault zone that intersects the tunnel was also found to contribute to the propagation of desiccation and therefore influenced the shape of the EDZ. Repositories for the disposal of radioactive wastes could be open during the operational period for decades or more and could be exposed to humidity variations, before being sealed and closed. Desaturation and possible desiccation of the rock mass around the openings should be considered in the design and safety assessment of the repositories.

Reference

Abdi, Labrie, H.D., Nguyen, T.S. , Barnichon, J.D., Su, G., Evgin, E., Simon, R. Fall, M. 2015. Laboratory investigation on the mechanical behaviour of Tournemire argillite. Canadian Geotechnical Journal, 52: 268–282

Berry, J.P. 1960. Some kinetic considerations of the Griffith criterion for fracture I: equations of motion at constant force. Journal of the Mechanics and Physics of Solids, 8(3): 194-206

Bieniawski, Z.T. 1967. Mechanisms of brittle fracture of rocks, parts I, II and III. International Journal of Rock Mechanics and Mining Sciences & Geomechanics Abstracts, 4(4):395- 405

Boisson, J.Y., Bertrand, L., Heitz, J.F., Golvan, Y.M.L. 2001. In situ and laboratory investigations of fluid flow through an argillaceous formation at different scales of space and time, Tournemire tunnel, southern France. Hydrogeology Journal, 9: 108–123

Brace, W.F. 1964. Brittle Fracture of rocks, Proc. Int. Conf., State of Stress in the Earth's Crust, W.R. Judd (ed.)

Bretaudeau, F., Gélis, C., Leparoux, D. et al. 2014. High-resolution quantitative seismic imaging of a strike-slip fault with small vertical offset in clay rocks from underground galleries: Experimental platform of Tournemire, France. Geophysics, 79(1): B1–B18

Carcione, J.M., Cavallini, F. 1994. A rheological model for anelastic anisotropic media with applications to seismic wave propagation. Geophysical Journal International, 119(1): 338–348

Chauveau, B., Kaminski, E.2008. Porous compaction in transient creep regime and implications for melt, petroleum, and CO2 circulation. Journal of Geophysical Research, 113: B09406

Chen, L., Shao, J.F., Huang, H.W. 2010. Coupled elastoplastic damage modeling of anisotropic rocks. Computers and Geotechnics, 37(1-2): 187-194

COMSOL user manual. COMSOL Multiphysics (Ver 5.1). COMSOL Inc. 2015.

Cook, N.G.W. 1965. The failure of rock. International Journal of Rock Mechanics and Mining Sciences and Geomechanics Abstracts, 2(4): 389–403

Cruden, D.M., Hu, X.Q. 1988. Basic friction angles of carbonate rocks from Kananaskis country, Canada. Bulletin of the International Association of Engineering Geology, 38(1): 55-59

Duveau, G., Tiantang, Y., Shao, J.F. 2001. Modelling of anisotropy in elastoplastic sedimentary rocks. DC Rocks 2001, The 38th U.S. Symposium on Rock Mechanics (USRMS), 7-10 July, Washington, D.C.

Dvila, C.G., Camanho, P.P., Rose, C. 2005. Failure Criteria for FRP Laminates. Journal of Composite Materials, 39 (4): 323-345.

Eberhardt, E., Stead, D., Stimpson, B., Read, E.S. 1998. Identifying crack initiation and propagation thresholds in brittle rock. Canadian Geotechnical Journal, 35(2): 222-233

Fabre, G., Pellet, F. 2006. Creep and time-dependent damage in argillaceous rocks. International Journal of Rock Mechanics & Mining Sciences, 43: 950–960

Fafard, M., Boudjelal, M.T., Bissonnette, B., Cloutier, A. 2001. Three-dimensional viscoelastic model with nonconstant coefficients. Journal of Engineering Mechanics, 127(8): 808-815

Fauchille, A., Hedan, S., Pret, D., Valle, V., Cabrera, J., Cosenza, P. 2014. Relationships between deformations induced by desiccation, water content and microstructure of Tournemire clay-rock. Journées Nationales de Géotechnique et de Géologie de l'Ingénieur JNGG2014 – Beauvais 8-10 juillet 2014

Genty, A., Wieczorek, K., Richard, F., Le Potier, C., Lamoureux, M., Bruno, G., Cabrera, J. 2002. In-situ desaturation in the Tournemire claystone site: the VENTILOFOR experiment. In S. M. Hassanizadeh, R. J. Schotting, W. G. Gray & G. F. Pinder (Eds.), Computational Methods in Water Resources, Vol. 1 and 2, Proceedings, 47: 81-88

Ghazvinian, E., Perras, M., Langford, C., Diederichs, M. 2013. A comprehensive investigation of crack damage anisotropy in Cobourg limestone and its effect on the failure envelope. GeoMontreal 2013.

Griffith, A.A. 1921. The phenomena of rupture and flow in solids. Phil. Trans. Royal Soc. London, 221 (582-593): 163-197

Guglielmi, Y.G., Henry, P., Nussbaum, C., Dick, P., Gout, C., Amann, F. 2015. Underground Research Laboratories for conducting fault activation experiments in shales. American Rock Mechanics Association. ARMA 15-0480.

Gunzburger, Y., Cornet, F.H. 2007. Rheological characterization of a sedimentary formation from a stress profile inversion. Geophysical Journal International, 168: 402-418

Hashiguchi, K. 2014. Elastoplasticity Theory, Second Edition. Springer-Verlag Berlin Heidelberg.

Haghighat, E., Pietruszczak, S. 2015. Constitutive modelling of Tournemire shale: Final Report. Canadian Nuclear Safety Commission. Technical report.

Hedan, S., Fauchille, A., Valle, V., Cabrera, J., Cosenza, P. 2014. One-year monitoring of desiccation cracks in Tournemire argillite using digital image correlation. International Journal of Rock Mechanics & Mining Sciences, 68: 22–35

Hu, D.W., Zhou, H., Zhang, F., Shao, J.F., Zhang, J.F. 2013. Modeling of inherent anisotropic behavior of partially saturated clayey rocks. Computers and Geotechnics, 48: 29-40

Ikari, M.J., Marone, C., Saffer, D.M. 2011. On the relation between fault strength and frictional stability. Geology, 39(1): 83–86

Martin, C.D. 1993. The Strength of Massive Lac du Bonnet Granite Around Underground Openings. PhD Thesis. University of Manitoba. Winnipeg, Manitoba.

Martin, C.D., Chandler, N.A. 1994. The progressive fracture of Lac du Bonnet granite. International Journal of Rock Mechanics and Mining Sciences & Geomechanics Abstracts, 31(6): 643-659

Matray, J.M., Savoye, S., Cabrera, J. 2007. Desaturation and structure relationships around drifts excavated in the well-compacted Tournemire's argillite (Aveyron, France). Engineering Geology, 90(1-2): 1-16

Millard, A., Maßmann, J., Rejeb, A., Uehara, S. 2009. Study of the initiation and propagation of excavation damaged zones around openings in argillaceous rock. Environmental Geology, 57: 1325–1335

Miller, C.J., Mi, H., Yesiller, N. 1998. Experimental analysis of Desiccation Crack Propagation in Clay liners. Journal of the American Water Resources Association, 34(3): 677–686

Nguyen, T.S., Selvadurai, A.P.S. 1995. Coupled thermal-mechanical-hydrological behaviour of sparsely fractured rock: Implications for nuclear fuel waste disposal. International Journal of Rock Mechanics and Mining Sciences and Geomechanics Abstracts, 32: 465-479.

Nguyen, T.S., Selvadurai, A.P.S., Armand, G. 2005. Modelling the FEBEX THM experiment using a state surface approach. International Journal of Rock Mechanics and Mining Sciences, 42: 639-651.

Nguyen, T.S., Le, A.D. 2015a. Development of a Constitutive Model for a Bedded Argillaceous Rock from Triaxial and True Triaxial Tests. Canadian Geotechnical Journal, 52(8): 1072-1086

Nguyen, T.S., Le, A.D. 2015b. Simultaneous gas and water flow in a damage-susceptible bedded argillaceous rock. Canadian Geotechnical Journal 52(1): 18-32

Niandou, H., Shao, J.F., Henry, J.P., Fourmaintraux, D. 1997. Laboratory investigation of the mechanical behaviour of Tournemire shale. International Journal of Rock Mechanics and Mining Sciences, 34(1): 3-16

Noiret, A., Giot, R., Bemer, E., Giraud, A., Homand, F. 2011. Hydromechanical behavior of Tournemire argillites: Measurement of the poroelastic parameters and estimation of the intrinsic permeability by oedometric tests. International Journal for Numerical and Analytical Methods in Geomechanics, 35(4): 496-518

Okay, G., Cosenza, P., Ghorbani, A. et al. 2013. Localization and characterization of cracks in clay-rocks using frequency and time-domain induced polarization. Geophysical Prospecting, 61: 134–152

Pardoen, A., Levasseur, S., Collin, F. 2015. Using Local Second Gradient Model and Shear Strain Localisation to Model the Excavation Damaged Zone in Unsaturated Claystone. Rock Mechanics and Rock Engineering, 48(2): 691-714

Pellet, F., Roosefid, M., Deleruyelle, F. 2009. On the 3D numerical modelling of the time-dependent development of the damage zone around underground galleries during and after excavation. Tunnelling and Underground Space Technology, 24: 665–674

Peron, H., Hueckel, T., Laloui, L., Hu, L.B. 2009. Fundamentals of desiccation cracking of fine-grained soils: experimental characterisation and mechanisms identification. Canadian Geotechnical Journal, 46(10): 1177-1201

Pietruszczak, S., Mroz, Z. 2001. On failure criteria for anisotropic cohesive-frictional materials. International Journal of Numerical and Analytical Method and Geomechanics, 25: 509-524.

Pietruszczak, S., Lydzba, D., Shao, J.F. 2002. Modelling of inherent anisotropy in sedimentary rocks. International Journal of Solids and Structures, 39(3): 637-648

Pietruszczak, S., Lydzba, D., Shao, J.F. 2004. Description of creep in inherently anisotropic frictional materials. Journal of Engineering Mechanics-ASCE,130(6): 681-690

Popp, T., Kern, H., Schulze, O. 2001. Evolution of dilatancy and permeability in rock salt during hydrostatic compaction and triaxial deformation. Journal of Geophysical Research, 106 (B3): 4061-4078

Rejeb, A. 1999. Mechanical characterisation of the argillaceous Tournemire site (France). Proceedings of the international conference on rock engineering techniques for site characterisation. Oxford and IBH Publishing Co. Ltd. pp. 45-50

Rejeb, A., Stephansson, O. 2007. DECOVALEX-THMC Project- Task C: Excavation damaged zone (EDZ) in argillaceous rock at Tournemire site (France). SKI Report 2007:09. ISSN 1104-1374.

Rouabhi, A., Tijani, M., Rejeb, A. 2007. Triaxial behaviour of transversely isotropic materials: Application to sedimentary rocks. Int. J. Numer. Anal. Meth. Geomech, 31: 1517–1535

Rutenberg, M., Lux, K.H. 2011. Numerical simulation of the time-dependent deformation behaviour of claystone rock mass at the Tournemire site with 2D and 3D models. Physics and Chemistry of the Earth, 36: 1913–1921

Schanz, T., Vermeer, P.A., Bonnier, P.G. 1999. The hardening soil model: Formulation and verification. Beyond 2000 in Computational Geotechnics-10 Years of PLAXIS. Balkema, Rotterdam.

Shen, W.Q., Shao, J.F. 2015. A micromechanical model of inherently anisotropic rocks. Computers and Geotechnics, 65: 73-79

Simo, J.C., Hughes, T.J.R. 1998. Computational Inelasticity. Springer-Verlag New York, Inc.

Simo, J.C. 1987. On a Fully Three-Dimensional Finite-Strain Viscoelastic Damage Model: Formulation and Computational Aspects. Computer Methods in Applied Mechanics and Engineering, 60: 153-173

Steer, P., Bigot, A., Cattin, R., Soliva, R. 2011. In-situ characterization of the effective elasticity of a fault zone, and its relationship to fracture spacing. Journal of Structural Geology, 33: 1541-1553

Sun, C.T., Quinn, B.J., Oplinger, D.W. 1996. Comparative Evaluation of Failure Analysis Methods for Composite Laminates. DOT/FAA/AR-95/109.

Sun, T., Wang, K., Iinuma, T. 2014. Prevalence of viscoelastic relaxation after the 2011 Tohoku-oki earthquake. Nature, 514: 84-87

Vajdova, V., Baud, P., Wong, F. 2004. Compaction, dilatancy, and failure in porous carbonate rocks. Journal of Geophysical Research, 109: B05204-219

Vauchez, A., Tommasi, A., Barruol, G. 1998. Rheological heterogeneity, mechanical anisotropy and deformation of the continental lithosphere. Tectonophysics, 296(1–2): 61–86

Wang, K., Hu, Y., He, J. 2012. Deformation cycles of subduction earthquakes in a viscoelastic Earth. Nature, 484: 327–332

Wang, W., Xie, S.Y., Xu, W.Y. 2013. Experimental study and numerical modelling of thermo-mechanical behaviour of Tournemire argillite. European Journal of Environmental and Civil Engineering, 17: S174-S186

Xiong, Y., Zhang, S., Ye, G., Zhang, F. 2014. Modification of thermo-elasto-viscoplastic model for soft rock and its application to THM analysis of heating tests. Soils and Foundations, 54(2):176–196

Xu, W.J., Shao, H., Hesser, J., Kolditz, O. 2014. Numerical modelling of moisture controlled laboratory swelling/shrinkage experiments on argillaceous rocks. In S. Norris et al. (Eds.), Clays in Natural and Engineered Barriers for Radioactive Waste Confinement, 400: 359-366

Zhang, C., Dittrich, J., Müller, J. , Rothfuchs, T. 2002. Experimental Study of the Hydromechanical Behaviour of the Callovo-Oxfordian Argillites, Part of the MODEX-REP Project. Technical Report. GRS – 187, ISBN 3-931995-55-0

Zhang, C., Rothfuchs, T. 2004. Experimental study of the hydromechanical behaviour of the Callovo-Oxfordian argillite, Applied Clay Science, 26: 325–336.

APPENDIX I

Derivation of the hardening laws

In the hardening stage, the major principal stress can be approximated by the following equation:

$$\sigma_1 = \alpha\omega + \sigma_1^0 \quad \text{(A1)}$$

where ω is a normalized damage parameter, σ_1^0 is the stress level corresponding to the initiation of plastic strain, and the parameter α is a model constant to be determined by experimental data as shown in Fig. 4.A1.

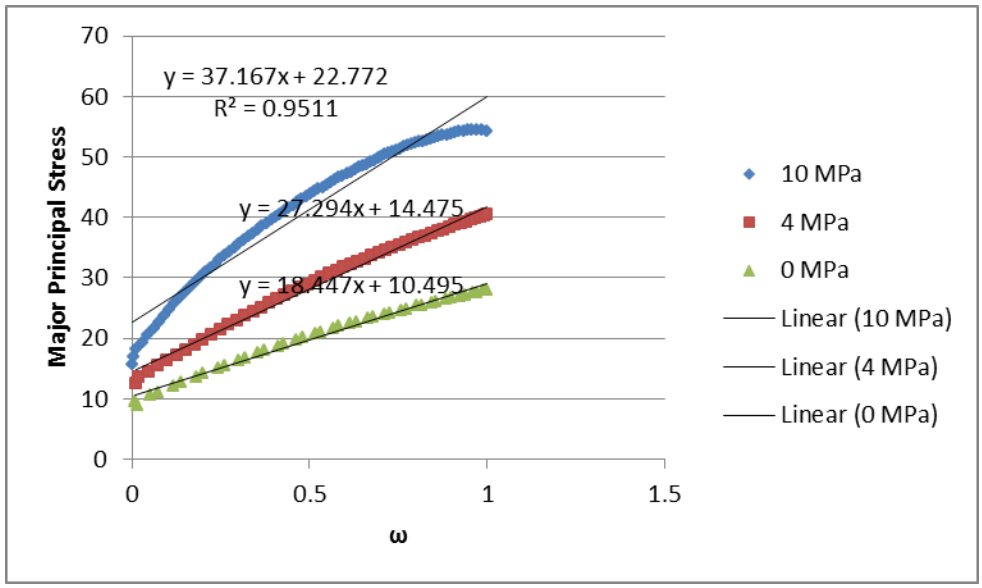

Figure 4.A1 Variation of σ_1 with normalized damage factor ω for various confining pressures (β=0°)

Actually σ_1^0 determines the crack initiation threshold that we assumed represents initial yielding. Instead of focusing on the peak strength, the elasto-plastic transition stress state has to be identified in this study to calculate the strength parameters.

$$\sigma_1^0 = h + l\sigma_3 \quad \text{(A2)}$$

Test with three confining pressures have been conducted on the Tournemire shale. This can lead to the estimation of a set of Mohr-Coulomb parameters that are noted as c^0 and ϕ^0.

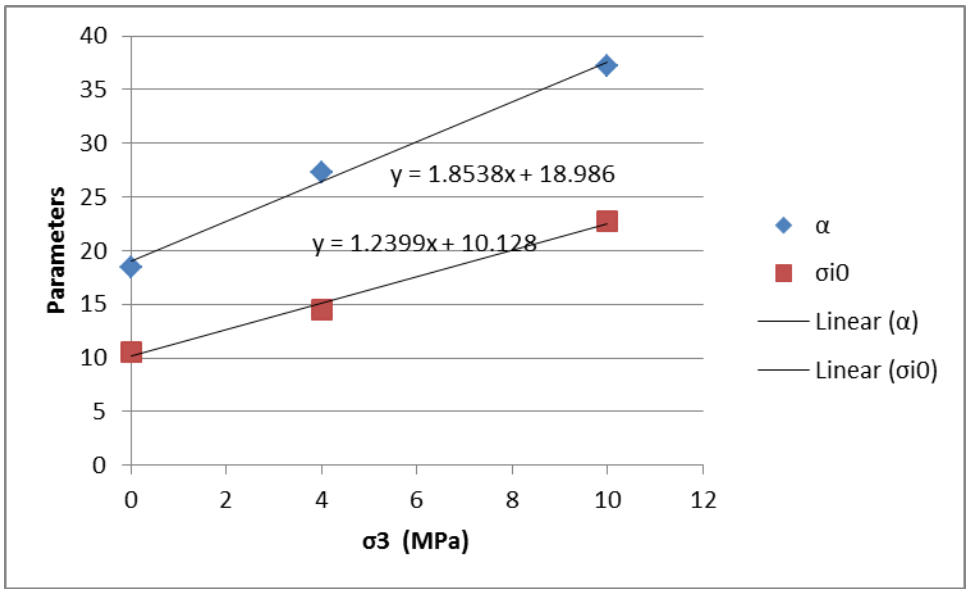

Figure 4.A2 Dependence of hardening parameters α and σ_i^0 on confining pressure (β=0°)

By analyzing the test data, an empirical linear function of confining pressure is found to be valid for the parameter α in such a form as

$$\alpha = k + m\sigma_3 \tag{A3}$$

where model constants of *k* and *m* can be determined by fitting the experimental data for the hardening stage. As shown in Fig. 4.A2, a good linearized form of the test data can be obtained by this equation. The slope and intercept are simultaneously determined. This model takes into account both the initial yielding and the peak failure by a normalized damage parameter ω. Let us look at the two extreme cases with ω=0 and 1 representing the initial yielding and the peak failure, respectively.

$$\sigma_1 = \begin{cases} \sigma_1^0 = h + l\sigma_3, & \omega = 0 \\ \alpha + \sigma_1^0 = (h + k) + (l + m)\sigma_3, & \omega = 1 \end{cases} \tag{A4}$$

The transition between the initial yielding and the peak failure can be modelled smoothly and seamlessly with a series of varying value of ω. The evolution of the Mohr-Coulomb envelope from initial yielding to the peak failure can also be reflected with the proposed hardening model as shown in Fig. 4.13.

This enables the derivation of the following function

$$\sigma_1 = (k\omega + h) + (m\omega + l)\sigma_3 \tag{A5}$$

Then we write the analytical expression for its strength parameters according to Mohr-Coulomb yield criterion,

$$\frac{\sigma_1 - \sigma_3}{2} = c * cos\phi + \frac{\sigma_1 + \sigma_3}{2}\sin\phi \tag{A6}$$

where c and ϕ are Mohr-Coulomb strength parameters for the hardening stage that are dependent on the normalized damage factor ω.

Rearranging the above formula leads to

$$\sigma_1 - \sigma_3 = 2c * cos\phi + (\sigma_1 + \sigma_3)\sin\phi \quad \text{(A7)}$$

$$\sigma_1(1 - sin\phi) = 2c * cos\phi + (1 + sin\phi)\sigma_3 \quad \text{(A8)}$$

$$\sigma_1 = \frac{2c*cos\phi}{1-sin\phi} + \frac{1+sin\phi}{1-sin\phi}\sigma_3 \quad \text{(A9)}$$

Referring back to the hardening law results in

$$k\omega + h = \frac{2c*cos\phi}{1-sin\phi} \quad \text{(A10)}$$

$$m\omega + l = \frac{1+sin\phi}{1-sin\phi} \quad \text{(A11)}$$

Solving the above functions may bring about the required Mohr-Coulomb strength parameters for the hardening model

$$\phi = \text{asin}(\frac{m\omega+l-1}{m\omega+l+1}) \quad \text{(A12)}$$

$$cos\phi = \frac{2\sqrt{m\omega+l}}{m\omega+l+1} \quad \text{(A13)}$$

$$c = \frac{k\omega+h}{m\omega+l+1} cos\phi = \frac{k\omega+h}{2\sqrt{m\omega+l}} \quad \text{(A14)}$$

It is easy to conclude that when ω=0, $c=c^0$, $\phi=\phi^0$; and when ω=1, $c=c^p$, $\phi=\phi^p$.

Table 4.3 shows the derived parameters for the hardening elastoplastic model.

APPENDIX II

Triaxial test results of Cobourg limestone

Figures 4.A3 show the triaxial test results for Cobourg limestone. The rock specimens were sampled from a quarry in Bowmanville, ON. Experiments were carried out at the University of Toronto. So far only part of the proposed tests has been finished. Many important information and parameters about the Cobourg limestone are still missing. Two hydraulic-mechanical coupled compression tests under 5 MPa confining pressure and 3 MPa pore pressure are screened as qualified for the validation against our models. The test data are shown as following.

The first specimen parallel to bedding failed at 103 MPa of axial stress with a maximum axial strain of 0.45% and a radial strain of 0.18%. The triaxial compressional strength of the other specimen tested perpendicular to foliation plane is lower than the ones tested parallel to foliation plane. The specimen perpendicular to bedding plane failed at 47 MPa of axial stress with a maximum axial strain of 0.3% and a radial strain of 0.3%.

Table 4.A1 lists the estimated elasticity and Poisson's ratios for the anisotropic Cobourg limestone. It is noted that the transverse shear modulus is unavailable for the current study, of which the estimation has to address the cases with load angle other than 0 and 90 ^{o}.

Figures 4.A3(c)-A3(d) show the correlation between the volumetric and axial strains. The linear relationship between axial and radial strains suggests a constant value of Poisson's ratio, preceding the peak strength. Dilatancy mainly occurs after the post-failure stage that involves a significant percentage of plastic strain. The peak strength was estimated from the experimental data along with the reported value of friction angle at 31 ^{o} (Damjanac, 2008). Ghazvinian et al. (2013) reported the anisotropic strength properties of Cobourg limestone and showed that its peak strength has a friction angle ranging from 36.9 to 45.6 ^{o} and the crack initiation strength has a friction angle ranging from 23.6 to 30 ^{o}. A medium value (as adopted by ITASCA for mechanical modelling of DGR, $\phi = 31^{o}$) was taken into account in this study. It is also hypothesized that $\phi = 31^{o}$ is valid for both cases with different load angles. Then can we calculate the cohesion as shown in Table 4.3.

The size of the test specimen was measured at L*D=12.5*5.4 cm*cm. According to studies of Ghazvinian et al. (2013) on the same rock, the crack initiation and crack damage values are 30, 60 % of the peak strength, respectively. This suggests potential links between permeability and early stage of plastic hardening, e.g. equivalent to the hypothesis of crack initiation in our mobilized hardening/softening model. In this study, we took 30% as the onset of crack initiation threshold value. This value is also justified by the variation of acoustic velocity as tested on Cobourg limestone by Nasseri and Young (2015).

Note that the objective of this numerical study is not to derive a generalized strength envelope or constitutive model for Cobourg limestone that is valid for all loading conditions (β, σ_3 etc.). Instead, we

are aiming at 1) understanding the hydraulic-mechanical coupling behaviour and the permeability evolution mechanism and formulas, and 2) validating our proposed mobilized hardening/softening model against another set of experimental results. To the end of this study, it seems sufficient to get these objectives fulfilled by the completed numerical simulations.

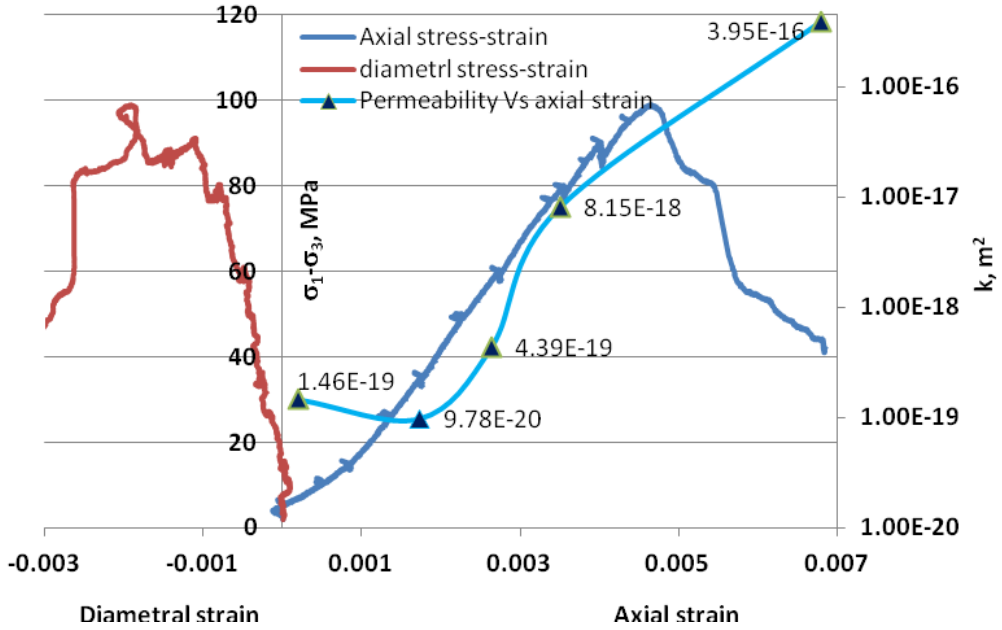

Figure 4.A3(a) Variation of axial and radial strains with differential stresses for specimen CLH-1-U tested at 5 MPa and 3 MPa of confining and pore pressures respectively. β=90°

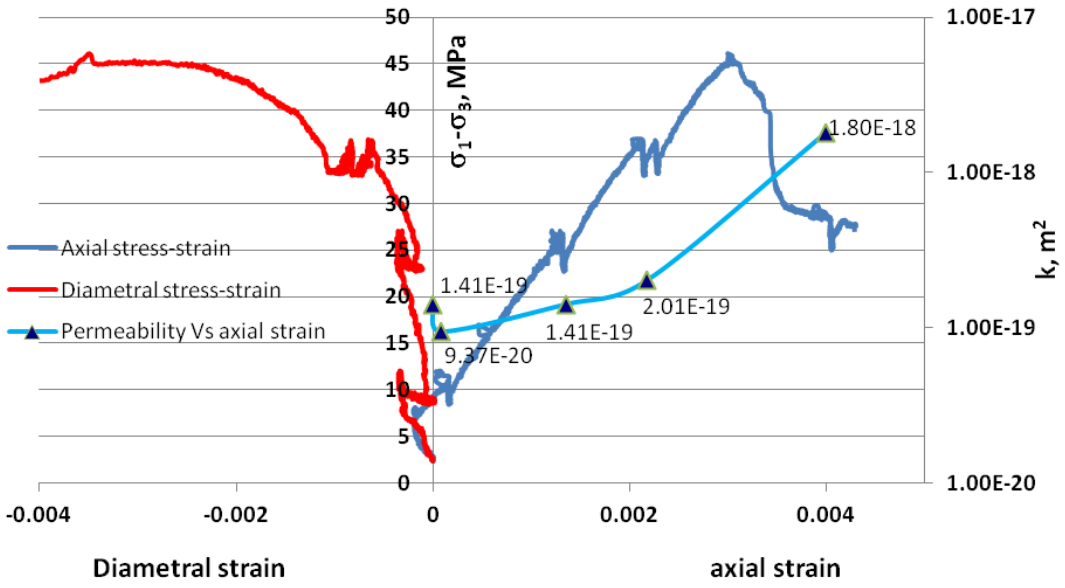

Figure 4.A3(b) Variation of axial and radial strains with differential stresses for specimen CLV-3-T tested at 5 MPa and 3 MPa of confining and pore pressures respectively. β=0°

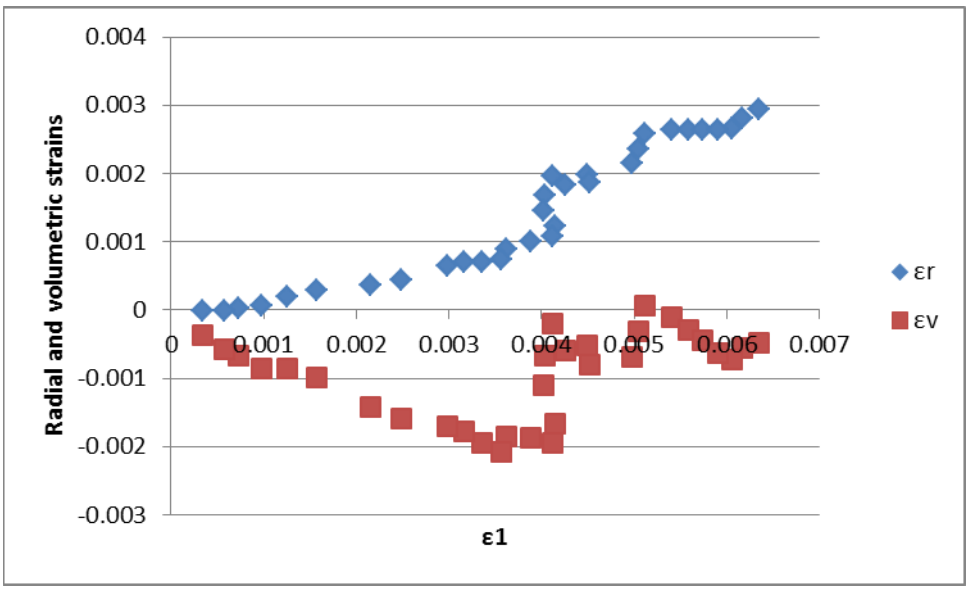

Figure 4.A3(c) Volumetric strain and radial strain vs axial strain for Cobourg limestone. β=90°

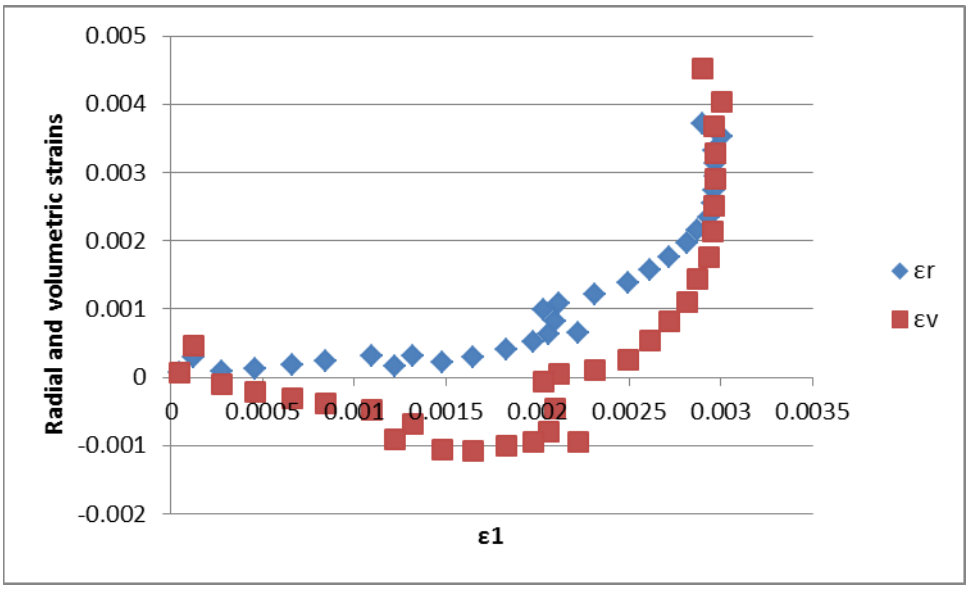

Figure 4.A3(d) Volumetric strain and radial strain vs axial strain for Cobourg limestone. β=0°

Table 4.A1 Stiffness and strength parameters for Cobourg limestone
(Estimated from limited data available at present)

Variables	Value	Unit/note
Stiffness		
$E_{\perp}$	12.3	GPa
$E_{\parallel}$	21.5	GPa
$v_{\perp}$	0.200	
$v_{\parallel}$	0.252	
$G_{\perp}/E_{\perp}$	NA	
$G_{\parallel}$	$E_{\parallel}/2(1+v_{\parallel})$	GPa
Strength		
ϕ	31	deg
$c_{\perp}$	9.73	MPa
$c_{\parallel}$	24.72	MPa
Yielding		
ϖ	0.30	
Post-failure		
E	100	β=0°
E	60	β=90°

FEM modelling for Cobourg limestone

Stress-strain behaviours and volumetric strains

Figure 4.A4 shows the reproduced stress-strain curves for Cobourg limestone using the proposed model. Good agreement with the experimental data is well demonstrated. The modelled stiffness and peak strength are both consistent with the test data.

Figure 4.A5 shows the evolution of volumetric strain. For the first sample at β=0°, the dilatancy after crack initiation is so significant that the volumetric strain heads upward rapidly before reaching the peak strength. The other sample shows moderate dilatancy after the crack initiation strength is exceeded with the volumetric strain remaining in the minus side even at the peak strength. The test data is well reproduced for the perpendicularly loaded sample (β=90°).

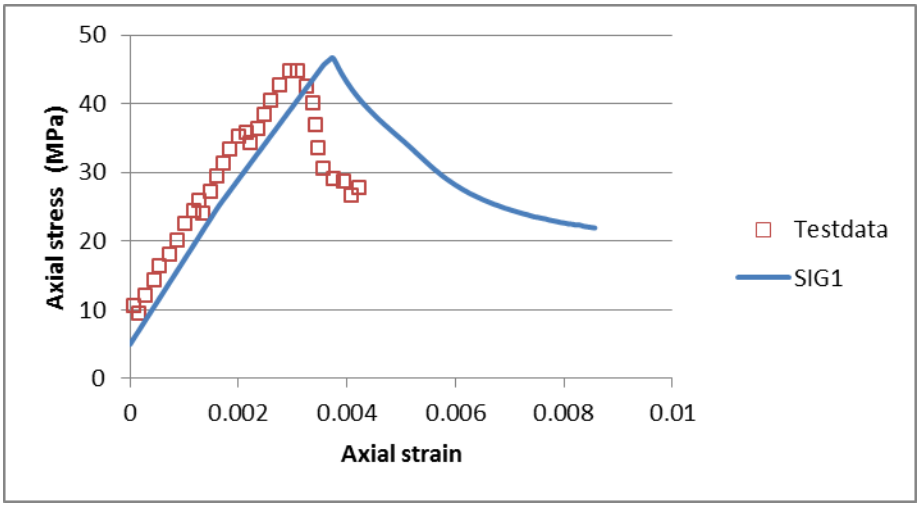

(a)

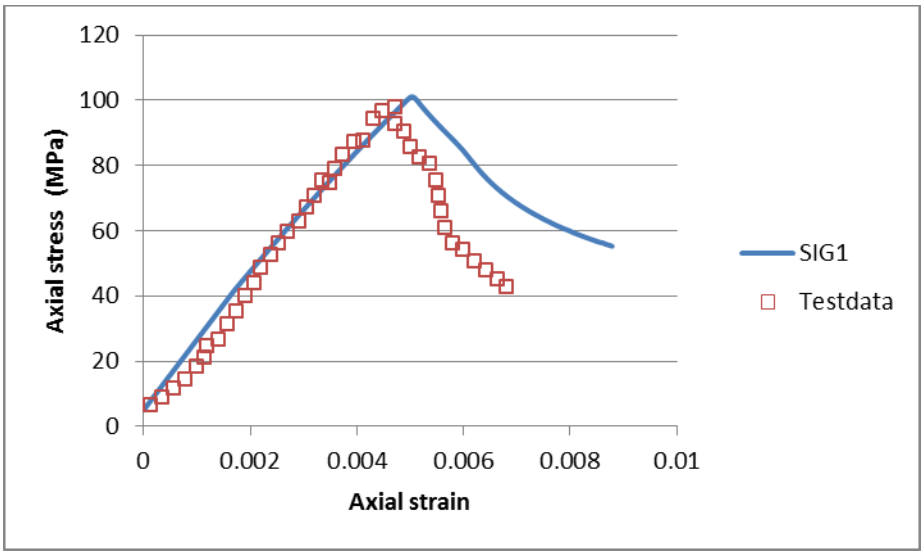

(b)

Figure 4.A4 Modelling results of stress strain curves for Cobourg limestone at two load angles (a) β=0^{o} and (b) β=90^{o}

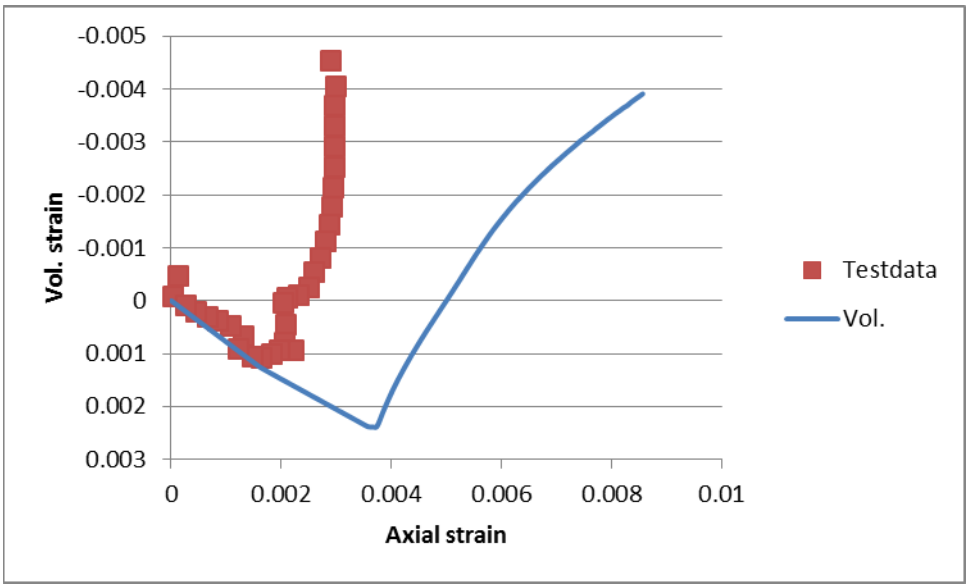

(a)

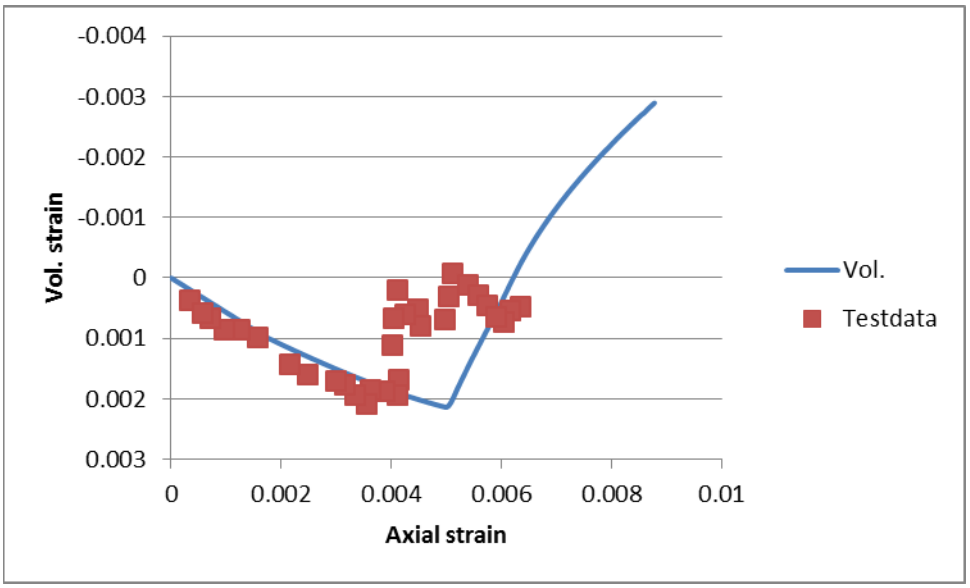

(b)

Figure 4.A5 Modelling results of volumetric strain for Cobourg limestone at two load angles (a) β=0° and (b) β=90°

Permeability versus effective plastic strain

Figure 4.A6 shows the dependence of permeability of Cobourg limestone on plastic strain. A threshold value of plastic strain was observed to dominate the variation of permeability. When Υ^p is less than the threshold value of 5E-5, the rock sample maintains a stable level of permeability at 1E-19 m^2. A rapid increase of permeability takes place when Υ^p>5E-5. Fitting these limited test data results in an expression of the following relationship

$$k = \begin{cases} 6 * 10^{-19} e^{1410 * \gamma^p}, & \gamma^p > 5 * 10^{-5} \\ 10^{-19}, & \gamma^p \leq 5 * 10^{-5} \end{cases} \quad \text{(A15)}$$

where k is permeability, γ^p is plastic strain, the correlation coefficient R^2=0.81.

The above formula resembles the recognized logarithmic relationship for the permeability of damaged geomaterials, which reads (Poulet et al., 2012; Rutqvist et al., 2009)

$$log \frac{k}{k_0} = \kappa' \gamma^p \quad \text{(A16)}$$

where k is the damaged permeability and k_0 is the intact permeability; κ' is the model constant.

This equation can be applied to the modelling of hydraulic-mechanical coupled problems encountered in the Canadian DGR for nuclear waste. Since this is just a preliminary modelling study of Cobourg limestone, we do not have sufficient experimental data to formulate a more reliable and confident

empirical equation for the permeability evolution of the damaged rocks. This issue can only be resolved in future studies when the planned experiments on Cobourg limestone are completed and made available to analysis.

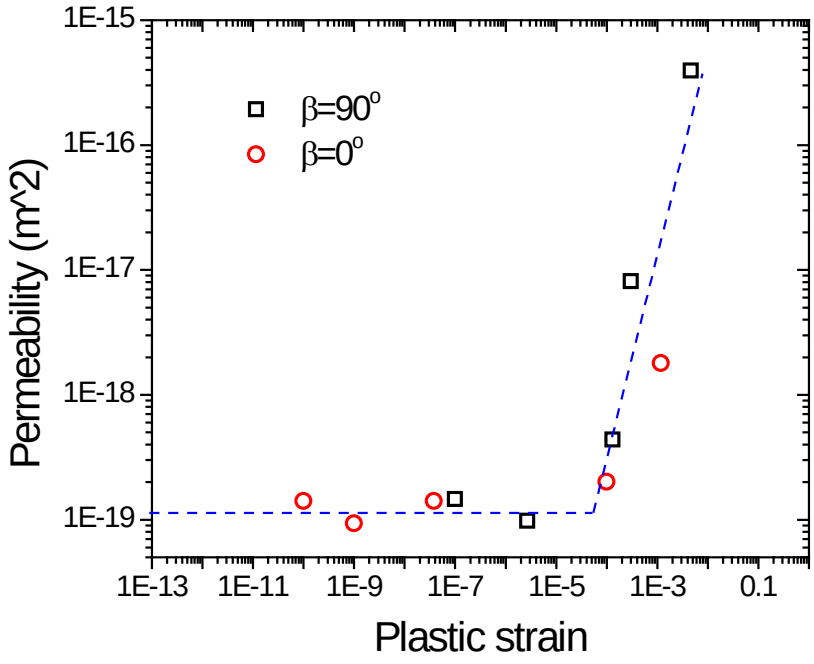

Figure 4.A7 Evolution of permeability with computed plastic strain

Failure mode and experimental proof

Figure 4.A8 shows the plotting of the simulated plastic strain at the end of compression test. It is obvious that shear bands are formed in both cases in the middle portion of the specimen. Figure 4.A8 show the zones of plastic strain calculated with the finite element code COMSOL. The code does not have the capability to model localization, however it is instructive to examine the extent and shape of the calculated plastic zones and compare them to the real failure patterns. The maximum plastic strain is higher in samples with $\beta=90^{o}$ than that with $\beta=0^{o}$. The inclination of the former is also larger than the latter in the slope angle towards the vertical direction. These features are comparable to the experimentally observed pattern of the shear failure planes as shown in Fig. 4.A9. The general shape of the calculated plastic zones is consistent with the factual failure pattern. The simulated plastic zone is concentrated within a limited space, which suggests the nucleation of microcracks resulted from former stage of compression, i.e. the crack initiation stage. This pattern appears near the peak strength and gets intensified in the post-failure stage in our modelling, which is consistent with the concept of crack nucleation and propagation that occurs immediately prior to the peak strength (Martin, 1993).

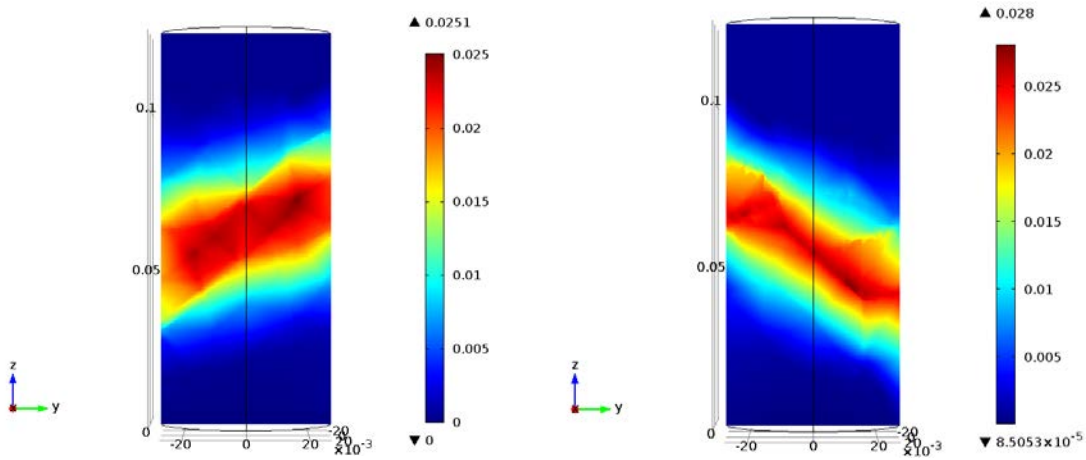

(b) (b)

Figure 4.A8 Simulated failure mode of Cobourg limestone under triaxial compression conditions (a) β=0° and (b) β=90°

(22) (b)

Figure 4.A9 Observed failure mode of Cobourg limestone under triaxial compression conditions (a) β=0° and (b) β=90° (Nasseri and Young, 2015)

Reference for Appendix

M.H.B. Nasseri, R.P. Young (2015). Coupled Hydro-mechanical properties of Cobourg limestone and Tournemire shale with special reference to the Excavation Damage Zone. Canadian Nuclear Safety Commission. Internal Report. Report No. RFDF_CNSC_01.

T. Poulet, A. Karrech, K. Regenauer-Lieb, L. Fisher, and P. Schaubs (2012). Thermal- hydraulic-mechanical- chemical coupling with damage mechanics using ESCRIPTRT and ABAQUS. Tectonophysics 526, 124-132.

J. Rutqvist, L. Borgesson, M. Chijimatsu, J. Hernelind, L.R. Jing, A. Kobayashi, and S. Nguyen (2009). Modelling of damage, permeability changes and pressure responses during excavation of the TSX tunnel in granitic rock at URL, Canada. Environmental Geology 57, 1263-1274.

Chapter 5 Modelling the mechanical and hydraulic behaviour of the Cobourg limestone

Summary

In this chapter, the HM coupled behaviours of Cobourg limestone were studied in detail, including the governing equations, material properties, the damaged permeability, the long-term mechanical and rheological strength as well as the numerical schemes.

Through a systematic review of poroelasticity of sedimentary rocks, the Biot's coefficient is found to vary closely with porosity. We found that low permeable rocks with low porosity always have extremely low Biot's coefficient. The weak HM coupling or poroelastic response of Cobourg limestone is found to pose limited impact to the propagation of the EDZ. This also ensures validity of the pulse decay permeability test method to be applied even under complex stress and loading conditions for granite, shale, marble and argillaceous clay rocks.

Biot's coefficient is recommended to be derived from the experimental data on Skempton's B value, due to the fact that the bulk modulus of the solid skeleton varies with effective mean stress and mineral constituents.

Time dependent failure of rocks under shear stress beyond the crack initiation threshold may involve rheological damage to the overall strength. A visco-elastoplastic model can well reproduce the relaxation test data on an argillite limestone. The progressive time-dependent failure of Cobourg limestone is further implemented in a numerical study of the long-term safety assessment of the waste cavern in repository.

1. Introduction

In Canada, the Cobourg limestone formation of the Michigan Basin is currently being considered as a potential host formation for the deep geological disposal of radioactive waste. The correct understanding of the mechanical and hydraulic behaviour of the Cobourg limestone is thus very important to the safety assessment and design of a potential Deep Geological Repository (DGR) located in this rock type. Typical limestones are characterized by large porosity and high compressibility. However, this is not the case for the Cobourg limestone which shows very little porosity (n=0.01-0.03) and very high elasticity (E=35 GPa) (ITASCA, 2011). Previous studies on Cobourg limestone (Paraskevopoulou et al. 2015; NWMO, 2011) have revealed significant variability in stiffness, strength, crack initiation and crack damage threshold values, and anisotropy, which is attributable to the non-uniform distribution of clay nodules in the limestone. The mechanical behaviour of the Cobourg

limestone has also been investigated experimentally and numerically (ITASCA, 2011). It was shown that this mechanical behaviour could change as a function of time by two mechanisms. There is an effect due to viscosity as shown by unconfined relaxation tests, and secondly there is a degradation of the strength that would lead to delayed failure of a sample when it is loaded above a threshold value. To the best of the authors' knowledge, a complete theoretical analysis of the mechanical behaviour of the Cobourg limestone that integrates all the above factors is still missing at present.

The excavation of a repository and operation of a DGR would induce damage in the rock around the DGR underground openings. The extent and characteristics of that damage zone, usually called the excavation damage zone (EDZ) can be assessed only if robust mathematical models exist. The EDZ might constitute preferential pathways for radionuclides migration since its permeability would be higher compared to the ambient rock. There is however a scarcity of experimental and theoretical studies that establish the relationship between the permeability change and damage. Therefore, the CNSC initiated a collaborative research project with University of Toronto to improve the understanding of the above relationship. Triaxial tests were conducted on Cobourg limestone specimens that were sampled from a quarry in south Ontario. The permeability variation was estimated during the triaxial tests by applying a transient fluid pressure pulse at different loading stages. Acoustic velocity at different directions was also measured to look into the mechanism of the mechanical damage. Microscopic images were taken after the rock specimen was dismantled from the triaxial loading cell after failure. The experimental results have been available to our research team for numerical modelling and interpretation.

The transient pressure pulse test as adopted in the experimental procedure has noticeable difference from the classic approach of Brace et al. (1968), whereas the former took place during the triaxial test and the latter in static stress loading. The loading may inevitably induce the development of a pore pressure that has not fully dissipated at the start of each pressure pulse test. Therefore the determination of the permeability could not be done using the analytical solution in Brace et al. (1968), which assumed a constant and uniform initial pore pressure. For instance, Gutierrez et al. (2015) experimentally investigated the stress-dependent permeability of shale under continuous stress loading by the consolidation test instead of the pulse decay method, which is believed to be viable and interpretable merely under static loading conditions (Gutierrez et al., 2015).

The Cobourg limestone has a permeability of the order of 1×10^{-20} m^2. The samples were immersed in water for a few months in an attempt to saturate them before the triaxial tests. However the low permeability makes it extremely difficult to achieve full saturation, therefore the presence of trace amount of air may affect the pore fluid compressibility significantly.

In this study, we also investigate how narrow failure zones that form after the peak load could influence the stress-strain response and the permeability. In order to simulate the formation of those narrow failure zones, a strain localization model is implemented into the HM coupled numerical model. The results may enable comprehensive understanding of the damage induced permeability enhancement as well as the correct interpretation of pulse decay method.

Another consideration in this study is the time-dependent mechanical behaviour of the limestone. Limestone is reported to have time-dependent, dissipative and viscous behaviour with possible deformation micro-mechanism of pressure-solution creep (Gunzburger, 2010; Robertson, 1960). Brantut

et al. (2014) performed creep experiments on a water-saturated porous limestone and noticed brittle creep with only small strains accumulated before failure, and damage accumulation with increasing strain under effective confining pressure of 10 MPa. The deformation mechanism is reported to include both subcritical crack growth and pressure solution creep processes. The creep rate of limestone was reportedly accelerated by permeation with acidic fluids which induces reactive dissolution of calcite. A much weaker response of the sandstone was also observed compared to the limestones (Le Guen et al., 2007).

A DGR must be shown to provide containment and isolation of the wastes in order to protect humans and the environment for a time frame of up to one million years. The host rock around the repository would be affected by physical and chemical changes due to exposure to the repository environment. Therefore the Cobourg strength would degrade as a function of time. The study on the strength degradation of the Cobourg limestone by unconfined creep test has been reported (Paraskevopoulou et al. 2015). Empirical relationships that were proposed seem agree with the behaviour of other rocks. A rigorous review of creep failure criterion inspires the development of a new relationship in this study as shown in this study.

Objective

This study is aimed to 1) develop a visco-elastoplastic model (VEP) that integrates a creep failure criterion into the model framework; 2) calibrate the model and failure criterion against triaxial compression and unconfined relaxation tests; 3) study the poroelastic effect on pulse decay method for permeability test and explore the damage-permeability relationship for Cobourg limestone; and 4) apply the rheological model and hydraulic properties of the intact and damaged rocks to assess the long-term performance of the DGR shaft under field conditions.

We first compiled the available experimental results on Cobourg limestone from various sources, i.e. UofT and QueensU. We then interpreted the test data in order to predict the mechanical parameters and rheological parameters. It is found that the Maxwell type standard linear solid model reproduced the relaxation test data with very high correlation factor. Moreover, a new creep failure criterion was developed in order to model its long-term strength. Furthermore, the transient pressure pulse technique was discussed and modelled with analytical approximate solution and FEM. The governing equations along with critical poroelastic parameters were characterized for the Cobourg limestone.

Model assumptions

The main assumptions used in developing the model are described as follows:

- The universal laws of mass and momentum conservation are invoked
- The rock mass is conceptualized as an isotropic porous medium. The Cobourg limestone is a sedimentary rock for which bedding can induce inherent anisotropy in both its hydraulic and mechanical behaviour. However, the presence of randomly distributed clay inclusions overwhelms the influence of bedding (Ghazvinian, 2015) and therefore in this paper we adopted the assumption of isotropy for simplification. The effect of inherent anisotropy in sedimentary rocks has been studied and modelled elsewhere (Nguyen and Le, 2015; Pietruszczak and Haghighat, 2015).

- The fluid flow in porous media is assumed to be saturated and is governed by Darcy's law:

$$\boldsymbol{u} = -\frac{\boldsymbol{\kappa}}{\mu}\left(\nabla p + \rho_f \boldsymbol{g}\right)$$

where **u** is the liquid water flux vector, $\boldsymbol{\kappa}$ is the permeability tensor written in matricial form, μ and ρ_f are water viscosity and density, respectively, and $\boldsymbol{g}$ is the acceleration of gravity. Furthermore, the permeability is assumed to vary with volumetric deformation and damage as discussed later in the paper.

- The pore fluid consists of a liquid water phase with dissolved air. Therefore its compressibility is substantially higher than the one of water. The compressibility of the water-air mixture is derived using the methodology by Nguyen and Selvadurai (1995).

- A nonlinear stress-strain relationship based on the classical theory of plasticity is adopted and will be described in more detail in this paper. The onset of irrecoverable deformation is determined by the Mohr Coulomb criterion, with strain hardening up to the peak stress. Strain softening with a non-local plastic deformation (Aifantis, 2011; Antolovich and Armstrong, 2014; Bažant and Pijaudier-Cabot, 1989; Jirásek, 2002; Pijaudier-Cabot and Grégoire, 2014) is assumed for the post-peak behaviour in order to simulate strain localization.

- Biot's effective stress principle is used to account for the effect of pore pressure. Within the framework of poroelasticity, the total stress (σ_{ij}) in a porous media saturated with pore fluid is decomposed into effective stress (σ'_{ij}) and pore pressure (p)

$$\sigma_{ij} = \sigma'_{ij} + \alpha p \boldsymbol{I}$$

where α is the Biot's effective stress coefficient ($\alpha = 1 - \frac{K_D}{K_s}$), K_D is the drained bulk modulus of the porous media and K_s is the bulk modulus of the solid matrix.

Governing equations

Based on the above assumptions, and following the methodology used by Nguyen and Selvadurai (1995), the governing equations of the model are developed as follows.

$$\left(\frac{n}{K_f} + \frac{1-n}{K_s}\right)\frac{\partial p}{\partial t} - \nabla\frac{\boldsymbol{\kappa}}{\mu}\left(\nabla p + \rho_f \boldsymbol{g}\right) - \alpha\frac{\partial \varepsilon_v}{\partial t} = 0$$

$$\nabla\left(\sigma'_{ij} + \alpha p \boldsymbol{I}\right) = 0$$

where n is porosity, K_f and K_s are respectively bulk moduli of fluid and solid, t is time, ε_v is volumetric strain. The above equations respectively express the mass conservation of the pore fluid, and the conservation of momentum of the porous skeleton, in which inertial effects are neglected.

2. Constitutive relationship for the porous skeleton

The governing equations must be complemented by the adoption of a constitutive relationship that relates the stress tensor to the strain tensor. Similarly to (Haghighat and Pietruszczak, 2015; Li et al., 2016; Nguyen and Le, 2015), the model is developed within the framework of elasto-plasticity, using the

Mohr-Coulomb yield criterion that is formulated to include strain-hardening of the yield parameters. Before yielding starts, the material is assumed to be viscoelastic. This results in an equation that relates the effective stress increment to the strain increment:

$$\mathrm{d}\boldsymbol{\sigma}' = \mathbf{D}(\mathrm{d}\boldsymbol{\varepsilon} - \mathrm{d}\boldsymbol{\varepsilon}^{\boldsymbol{p}} - \mathrm{d}\boldsymbol{\gamma})$$

where $\mathrm{d}\boldsymbol{\sigma}'$ is the increment of the effective stress tensor (written as a vector); d**ε** is the increment of total strain tensor (written as a vector); d$\boldsymbol{\varepsilon}^{\mathbf{p}}$ is the increment of the plastic strain tensor (written as a vector); d**γ** is the increment of the viscous strain tensor (written as a vector); and **D** is the elastic stiffness tensor (written as a matrix).

For an isotropic material, the elastic stiffness tensor is defined by two parameters: the Young's modulus E and the Poisson's ratio υ. The viscous and plastic strain components are determined as follows.

Determination of the visco-elastic component

The stress tensor and strain tensor can both be decomposed into volumetric and deviatoric components.

$$\boldsymbol{\sigma} = \boldsymbol{\sigma}_{\boldsymbol{d}} + \boldsymbol{p}$$

$$\boldsymbol{\varepsilon} = \boldsymbol{\varepsilon}_{\boldsymbol{dev}} + \boldsymbol{\varepsilon}_{\boldsymbol{vol}}$$

where the mean stress **p** and the volumetric strain $\boldsymbol{\varepsilon}_{\boldsymbol{vol}}$ can be written as:

$$\boldsymbol{p} = \frac{\sigma_{11} + \sigma_{22} + \sigma_{33}}{3}\begin{bmatrix}1 & 0 & 0\\ 0 & 1 & 0\\ 0 & 0 & 1\end{bmatrix}$$

$$\boldsymbol{\varepsilon}_{\boldsymbol{vol}} = \frac{\varepsilon_{11} + \varepsilon_{22} + \varepsilon_{33}}{3}\begin{bmatrix}1 & 0 & 0\\ 0 & 1 & 0\\ 0 & 0 & 1\end{bmatrix}$$

For an elastic material, $\boldsymbol{\sigma}$ can be expressed as a function of $\boldsymbol{\varepsilon}$ by the mean and deviatoric components. For example, the isotropic elastic material obeys the following relationship

$$\boldsymbol{p} = K\boldsymbol{\varepsilon}_{\boldsymbol{vol}}$$

$$\boldsymbol{\sigma}_{\boldsymbol{d}} = 2G\boldsymbol{\varepsilon}_{\boldsymbol{dev}}$$

where K and G are respectively the bulk and shear moduli, which are scalars for an isotropic material, but tensors for an anisotropic material.

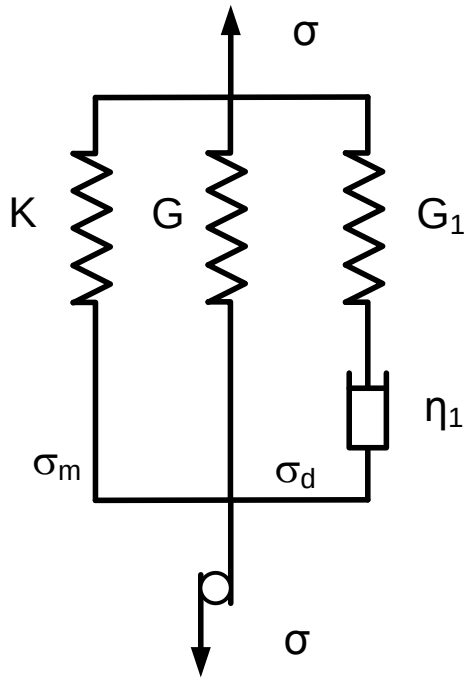

Figure 5.1 Schematic diagram showing the visco-elastoplastic model

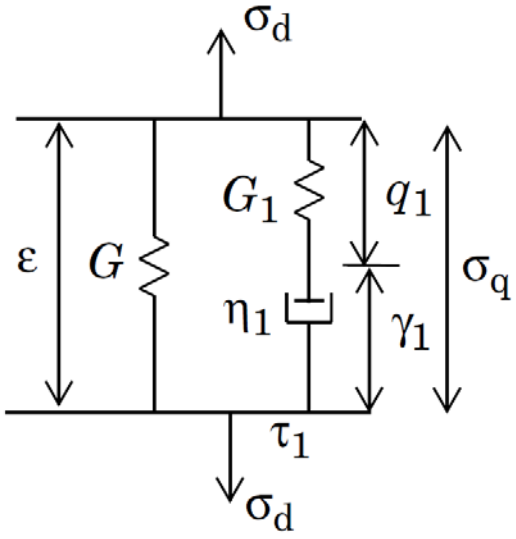

Figure 5.2 Schematic diagram of the SLS model

For a viscoelastic material, the deviatoric stress is not only dependent on the deviatoric strain but also on its time variations. The deviatoric stress is usually written in an integral form as follows (Simo and Hughes, 1998)

$$\boldsymbol{\sigma_d} = 2\int_0^t \Gamma(t-t')\frac{\partial \boldsymbol{\varepsilon_{dev}}}{\partial t'}dt'$$

$\Gamma(t)$ is a relaxation function, which can be approximated by a Prony series

$$\Gamma(t) = G + \sum_{i=1}^{N} G_i \exp(-\frac{t}{\tau_i})$$

where N is the total number of viscous branches, and τ is relaxation time $\tau = \frac{\eta}{G}$.

A simple rheological model, i.e. the simplified general Maxwell model (also known as the standard linear solid model) that consists of a spring and dashpot in sequence as shown in Fig. 5.2, was implemented in the study of the rheological behaviour of the Cobourg limestone. It is assumed that viscosity only influences the deviatoric components of stress and strain, as is the common assumption adapted in geomechanics. Viscosity under hydrostatic loading is rarely measured in the laboratory and is often poorly defined in the literature (Li et al. 2016). For these reasons, the authors adopted the simplifying assumption that viscosity is solely dependent on the deviatoric component of stress.

As only one viscous branch is considered, the integral deviatoric stress can be rewritten as

$$\boldsymbol{\sigma_d} = 2\int_0^t \left(G + G_1 \exp(-\frac{t-t'}{\tau_1})\right) \frac{\partial \boldsymbol{\varepsilon_{dev}}}{\partial t'} dt'$$

The above equation reduces to another form in the absence of viscosity, i.e. $\tau_1 = 0$,

$$\boldsymbol{\sigma_d} = 2\int_0^t \lim_{\tau_1 \to 0} \left(G + G_1 \exp(-\frac{t-t'}{\tau_1})\right) \frac{\partial \boldsymbol{\varepsilon_{dev}}}{\partial t'} dt' = 2\int_0^t G \frac{\partial \boldsymbol{\varepsilon_{dev}}}{\partial t'} dt'$$

which suggests that the total stress is imposed solely onto the bulk elastic material when the viscosity diminishes.

As shown in Figure 5.1, the total deviatoric stress $\boldsymbol{\sigma_d}$ equals the sum of both the bulk stress and the viscous stress ($\boldsymbol{\sigma_q}$) in the form of

$$\boldsymbol{\sigma_d} = 2G\boldsymbol{\varepsilon_{dev}} + \boldsymbol{\sigma_q}$$

The stress on the spring-dashpot branch takes the following form,

$$\boldsymbol{\sigma_q} = 2G_1\boldsymbol{q_1} = 2\eta_1\dot{\boldsymbol{\gamma}}_\mathbf{1}$$

where G_1 and $\mathbf{q_1}$ are respectively the shear modulus and shear strain tensor of the viscous branch: η_1 and $\boldsymbol{\gamma_1}$ are respectively the viscosity and the viscous strain tensor of the dashpot.

The above equation gives rise to the following formula

$$\boldsymbol{q_1} = \frac{\eta_1}{G_1}\dot{\boldsymbol{\gamma}}_\mathbf{1} = \tau_1\dot{\boldsymbol{\gamma}}_\mathbf{1}$$

where τ_1 is the relaxation time.

The total deviatoric elastic strain thus consists of two parts 1) the viscous strain γ_1 that is induced by the dashpot deformation, and 2) the elastic strain q_1 that is attributed to the spring. Then we get

$$\boldsymbol{q_1} + \boldsymbol{\gamma_1} = \boldsymbol{\varepsilon_{dev}}$$

Then the viscous strains are defined by the following equations:

$$\begin{cases} \boldsymbol{\sigma_d} = 2(G + G_1)\boldsymbol{\varepsilon_{dev}} - 2G_1\boldsymbol{\gamma_1} \\ \boldsymbol{\varepsilon_{dev}} = \tau_1\dot{\boldsymbol{\gamma}}_{\boldsymbol{1}} + \boldsymbol{\gamma_1} \end{cases}$$

Determination of the plastic strain

The Mohr-Coulomb yield criterion can be written using the following form:

$$F = \frac{I_1 sin\phi}{3} + \sqrt{\frac{J_2}{3}}\left((1 + sin\phi)cos\theta - (1 - sin\phi)cos\left(\theta + \frac{2\pi}{3}\right)\right) - c \cdot cos\phi = 0$$

where I_1 is the first invariant of the stress tensor; J_2 is the second invariant of the deviatoric stress tensor; θ is the Lode angle; c is the cohesion; and □ is the friction angle.

When the yield criterion is reached, plastic strain occurs. The plastic strain is derived from the plastic potential equation. Here, a nonassociative flow rule is used, with the plastic potential taking the form of a Drucker-Prager relation:

$$Q = \sqrt{J_2} + \frac{2}{\sqrt{3}}\frac{sin\phi}{3 - sin\phi}I_1 - \frac{2\sqrt{3}c * cos\phi}{3 - sin\phi} = 0$$

The above function matches the Mohr-Coulomb yield criterion at compressive meridians.

In this regard, the plastic strain rate is given by:

$$\dot{\boldsymbol{\varepsilon}}^{\boldsymbol{p}} = \lambda\frac{\partial Q}{\partial \boldsymbol{\sigma}}$$

where λ is the consistency parameter determined by the classical elasto-plastic theory with appropriate rearrangement of the differentiated form of the yield function (Simo and Hughes, 1998).

The effective plastic strain can be defined as (Hashiguchi, 2014):

$$\gamma^p = \int \dot{\gamma}^p dt = \int \sqrt{\frac{2}{3}\left(\dot{\varepsilon}_{ij}^p - \frac{1}{3}\varepsilon_v^p\delta_{ij}\right)\left(\dot{\varepsilon}_{ij}^p - \frac{1}{3}\varepsilon_v^p\delta_{ij}\right)}\,dt$$

where δ_{ij} is the Kroenecker delta.

In triaxial conditions, the above formula can be expressed in another form, which is:

$$\gamma^p = \sqrt{\frac{2}{3}\left[\left(\varepsilon_1^p - \frac{1}{3}\varepsilon_v^p\right)^2 + 2\left(\varepsilon_r^p - \frac{1}{3}\varepsilon_v^p\right)^2\right]}$$

where ε_1^p is cumulative axial plastic strain; ε_r^p is the cumulative radial plastic strain; and ε_v^p is the cumulative volumetric plastic strain.

Here we assume that the initial yielding starts at the crack initiation threshold ϖ, at a certain percentage of the peak strength (σ_{1p}), and that the elastic modulus gradually decays with the accumulated damage. Then we obtain the initial yield stress, which is:

$$\sigma_1^0 = \varpi\sigma_{1p}$$

where σ_1^0 is the initial yield stress, and σ_{1p} is the peak value of the major principal stress.

In the case where the stress is higher than the crack initiation threshold value, the plastic strain in the principal stress direction starts to grow with respect to the crack initiation threshold value ϖ:

$$\varepsilon_i^p = \begin{cases} 0, & \sigma_1 < \varpi\sigma_{1p} \\ \varepsilon_i - \dfrac{\sigma_1 - \sigma_3}{E_t}, & \sigma_1 \geq \varpi\sigma_{1p} \end{cases}$$

where ε_i^p is the plastic strain, ε_i is the elastic strain, and ε_i^{ϖ} is the strain corresponding to crack initiation.

A normalized damage parameter is first defined in terms of ω, as an important variable contributing to the strain hardening process. It relates the effective plastic strain to the plastic strain at peak strength, transformed into a normalized range between (0, 1). Similar processing of the effective plastic strain was carried out by Martin (1993) in the analysis of strength of Lac du Bonnet granite.

$$\omega = \frac{\gamma^p}{\varepsilon_{epe}}, \quad 0 \leq \omega \leq 1.0$$

where ω is the normalized damage factor, and ε_{epe} is the plastic strain that corresponds to the peak strength marking the end of strain hardening and the start of softening. For the Cobourg limestone specimen examined in this study, there is only one case of confining pressure considered in the triaxial experiment. Therefore parameter ε_{epe} is not available for us to specifically address its stress-dependence. Instead, a constant value is adopted in the subsequent modelling.

As discussed above, the crack initiation threshold of the Cobourg limestone is assumed to be 30% of the peak strength, which is in agreement with our previous treatment of CI value for Tournemire shale. When the threshold is exceeded, plastic yielding is assumed to occur with hardening taking place until the peak strength is reached.

As indicated by Li et al. (2016), the hardening stage encompasses a gradual change of Mohr-Coulomb strength parameters that can be related to the normalized damage factor ω. The development of analytical expressions defining the hardening law is detail in the paper of Li et al. (2016). These expressions are:

$$\phi = \mathrm{asin}\left(\frac{m\omega + l - 1}{m\omega + l + 1}\right)$$

$$cos\phi = \frac{2\sqrt{m\omega + l}}{m\omega + l + 1}$$

$$c = \frac{k\omega + h}{m\omega + l + 1} cos\phi = \frac{k\omega + h}{2\sqrt{m\omega + l}}$$

It is easy to conclude from above equations that when ω=0, then $c=c^0$, $\phi=\phi^0$; and when ω=1, then $c=c^p$, $\phi=\phi^p$. As for Cobourg limestone, the friction angle is assumed to maintain a constant value throughout the triaxial test. Therefore the parameter ϕ does not vary with the damage factor ω, suggesting

parameter m=0. Hence the internal cohesion becomes $c = \frac{k\omega+h}{2\sqrt{l}}$. Accordingly, there remain three model constants to be determined for the hardening model, i.e. k, h, and l.

Determination of the viscoelastic constants

In absence of plastic strain, the constitutive equation for viscoelastoplasticity can be reduced to the standard linear solid model (SLS). As shown in Fig. 5.2, an elastic spring is placed in parallel with a series of spring and dashpot. Rearranging the constitutive equations for SLS model by eliminating $\boldsymbol{\gamma_1}$ and $\boldsymbol{q_1}$ leads to the following relationship that is merely dependent on total strain and total deviatoric stress,

$$\eta\dot{\boldsymbol{\sigma}}_{\boldsymbol{d}} + G_1\boldsymbol{\sigma}_{\boldsymbol{d}} = \eta(G + G_1)\dot{\boldsymbol{\varepsilon}} + GG_1\boldsymbol{\varepsilon}$$

In order to extract the rheological parameters for the Maxwell model from experimental results, it is important to analyze the above formula using the analytical solutions for the relaxation modulus and creep compliance.

In a stress relaxation test, a constant strain ε_0 is applied upon the material while the time-dependent stress variation is monitored. Using Laplace transform, the relaxation modulus (E_{rel}) is given as (Roylance, 2001)

$$E_{rel} = \frac{\sigma_d}{\varepsilon_0} = G + G_1 e^{-t/\tau}$$

Similarly, the creep compliance (C_M) of the Maxwell model can be derived as

$$C_M = \frac{\varepsilon(t)}{\sigma_0} = \frac{1}{G + G_1} + \left(\frac{1}{G} - \frac{1}{G + G_1}\right)\left[1 - e^{-Gt/[\tau(G+G_1)]}\right]$$

These formulas enable the direct parameterization of the experimental results on relaxation or creep tests, which are both exponential function of time, and can be numerically estimated by optimizing technique, e.g. least-square algorithm etc.

Time-dependent yield criterion

Mechanical damage to intact rock is cumulative in terms of microcracks initiation and acoustic emission. The long-term rheological behaviour and the stability of rock mass are dependent on the extent of the mechanical damage as well as the time history. According to experimental observation of rocks under creep conditions, cumulative damage to rock happens when the deviatoric stress is maintained at a level higher than the crack initiation threshold, which leads to an abrupt failure after a period of time. With respect to the rheological behaviour, the strain rate varies with elapsing time. A typical second phase of creep takes place in terms of steady state strain, and ends with a minimum value in strain rate prior to an accelerated strain rate that is characteristic of the creep failure stage.

Assume that damage is associated with deviatoric stress, then the time required to reach failure (t_F) may be given as a function of stress ratio $\sigma_d/\Im$. By calibrating the test data on Jura limestone as obtained by Queen's University, we get the following empirical relationship:

$$t_F \left(\frac{\sigma_d}{\Im}\right)^{18.9} = 10^{1.54}$$

where $\Im$ is the short-term compressive strength. The above equation means that when a deviatoric stress equals to $\Im$ applied, the sample fails instantaneously. However, if a smaller stress is applied, delayed failure will occur at time t_F. Under unconfined test conditions, $\Im$=UCS and corresponds to time t≈0. Figure 5.3 shows the test data and the best-fitting with the above equation.

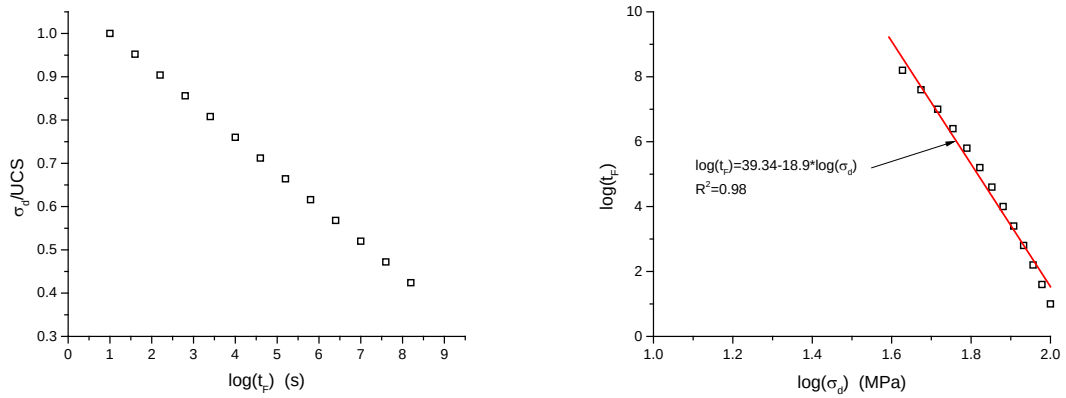

Figure 5.3 Experimental observation of time-to-failure criterion for Jura limestone (left) and the transformed data with best-fitted expression (right) (data are collected from the presentation of Paraskevopoulou et al. (2015))

In the elastoplastic framework, the peak strength can be assumed to be degrading with time. Let $\Im$ be the short-term peak strength, and q_f the temporal peak strength, then the damage factor ω_t can be defined as

$$\omega_t = \frac{q_f}{\Im} = f(t)$$

with t as the time elapsing since beginning of stress loading. It can be easily demonstrated that at the moment when the sample fails under creep loading conditions, i.e. t=t_F, the temporal peak strength q_f equals the applied deviatoric stress σ_d. Therefore the function of time f(t) is written as

$$f(t) = \sqrt[18.9]{\frac{10^{1.54}}{t}}, \qquad t \geq 1\text{s}$$

For Mohr-Coulomb strength, the deviatoric stresses are related to cohesion and friction as shown below,

$$q_f = \sigma_1 - \sigma_3 = 2c * \cos\phi - (\sigma_1 + \sigma_3)\sin\phi$$

$$\Im = \sigma_1^0 - \sigma_3 = 2c^0 * \cos\phi - (\sigma_1^0 + \sigma_3)\sin\phi$$

where superscript 0 indicates the short-term strength parameters (i.e. t≈0). Therefore the internal cohesion takes the form of

$$c = \frac{1}{2\cos\phi}\left[q_f + (\sigma_1 + \sigma_3)\sin\phi\right]$$

Eliminating σ_1 in terms of q_f and σ_3, we get

$$c = \Im f(t)\frac{1+\sin\phi}{2\cos\phi} + \sigma_3\tan\phi$$

Taking into account triaxial test conditions with confining pressure maintained as constant, by inserting $\Im$ into above formula and eliminating σ_1^0 we get

$$c = c^0 f(t) + \sigma_3\tan\phi[1 - f(t) + f(t)\sin\phi]$$

3. Transient pressure pulse decay test for permeability measurement

Transient pressure pulse method, originated in literature from Brace et al. (1968), has been applied to test the permeability of tight rock and concrete with extremely low permeability (Liang et al., 2001; Selvadurai and Carnaffan, 1997). In this technique, rock sample is placed in a confined chamber and is connected to two fluid reservoirs of upstream and downstream. At time t=0 a small pressure pulse (<5%) is introduced to the upstream reservoir and the decay of pressure with time is monitored. The permeability of the test sample can be estimated with an exponential decay function.

The permeability of Cobourg limestone under various stage of triaxial test has been experimentally measured at UofT by the transient pressure pulse method. There remain some unknowns in the test conditions and the incurred poroelastic response of the pore pressure inside the rock specimen, e.g. how and how high the pore pressure develops under loading, how fast the pore pressure responds to the loading, and how the pressure in upstream reservoir evolves. Therefore, a thorough theoretical study may help to unravel the mechanism of the damage-induced permeability change and the dynamic evolution of pore pressure during the triaxial test, as well as to verify the applicability of the pulse decay permeation test method.

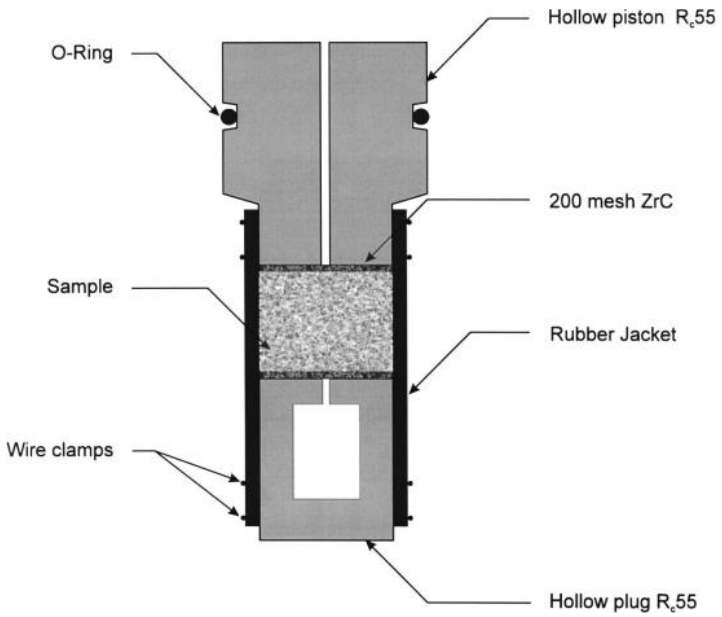

Figure 5.4 The confined sample arrangement used in transient pulse test (Selvadurai and Carnaffan, 1997)

Governing equation and analytical solution by Brace et al. (1968)

According to (Brace et al., 1968), the one-dimensional governing equation of the transient pressure pulse method can be written as

$$\frac{\partial p}{\partial t} = D\frac{\partial^2 p}{\partial x^2}$$

where p is the pore pressure, and D is called the pressure diffusion coefficient that is given as

$$D = \frac{k}{\mu(\phi\chi_f + \chi_V)}$$

with ϕ is the porosity, χ_f is the fluid compressibility, χ_V is the effective compressibility of the solid skeleton, k is permeability, μ is the dynamic viscosity. It was shown that $\chi_V = \chi_{eff} - \chi_s(1+\phi)$ with χ_s the mineral compressibility. Due to the fact that the compressibility of rock minerals is less than 1/40 of fluid compressibility, later studies generally adopted a slightly modified version of the effective compressibility ($\chi_V = \chi_{eff}$), e.g. (Selvadurai and Carnaffan, 1997; Selvadurai and Ichikawa, 2013). The equation of (Brace et al., 1968) could be derived from the hydraulic governing equations as outlined at the beginning.

Both upper and lower boundaries need to address the mass conservation in the fluid reservoirs. Then we have

$$\begin{cases} \dfrac{dp_1}{dt} = -\dfrac{DA\phi}{V_1}\dfrac{\partial p}{\partial x}\Big|_{x=0} \\ \dfrac{dp_2}{dt} = \dfrac{DA\phi}{V_2}\dfrac{\partial p}{\partial x}\Big|_{x=L} \end{cases}$$

where p_1 and p_2 are respectively source and exit reservoir pressure, A is the cross section area of the porous media, V_1 and V_2 are respectively the source and exit reservoir volume, and L is the length of the porous media.

The initial conditions are shown as

$$\begin{cases} p(x,0) = p_i \\ p_1(0) = p_{10} \\ p_2(0) = p_{20} \end{cases}$$

Sometimes the initial value of the exit reservoir pressure is maintained equal to the pore pressure inside the rock, then $p_2(0) = p_i$.

The analytical solution was given by (Brace et al., 1968), in terms of the pressure pulse in the source reservoir that decreases exponentially in terms of

$$p = p_f - \Delta p \left(\frac{V_2}{V_1 + V_2}\right) e^{-\varsigma t}$$

where Δp is the step change of pressure in source reservoir, V_1 and V_2 are respectively the volume of the source and exit reservoirs, and L is the length of sample, with exponent given as

$$\varsigma = \frac{DA\phi}{L}\left(\frac{1}{V_1} + \frac{1}{V_2}\right)$$

By determining the exponent of pulse pressure decay with time (ς), we can estimate the permeability as

$$k = \mu L \chi_f \varsigma \frac{V_1 V_2}{A(V_1 + V_2)}$$

For the experimental conditions of this study, the downstream reservoir is maintained as a constant fluid pressure boundary, suggesting an infinite volume V_2. Then the permeability of the matrix can be estimated by

$$k = \mu L \chi_f \varsigma \frac{V_1}{A}$$

Inserting all model parameters into above formula leads to a simplified expression as

$$k = 1.38 \times 10^{-15} \varsigma$$

where ς is the exponential index of the pulse decay curve with respect to time (s) by fitting the curve with equation of $y = y_0 + A_1 e^{-\varsigma t}$.

Let V_1=V_2, V_1/A=0.1, L=0.02 m, r=0.005 m, k=10^{-19} m^2 and $\chi_f = 4 \times 10^{-10} \mathrm{Pa}^{-1}$, we can run the HM coupled FEM model for the Cobourg limestone to test the numerical results against the analytical solution. Figure 5.5 clearly demonstrates the consistence between the FEM and the analytical solutions. It is noted that the analytical solution of the pulse decay problem by Brace et al. (1968) has several simplified assumptions, i.e. the pore pressure distribution in rock specimen follows a linear pattern, which may contribute to the slight discrepancy at later stage of the pulse decay test.

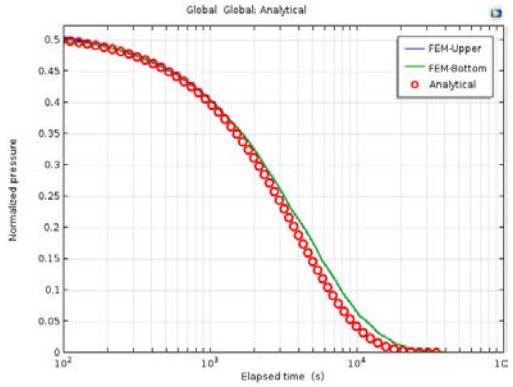

(a)

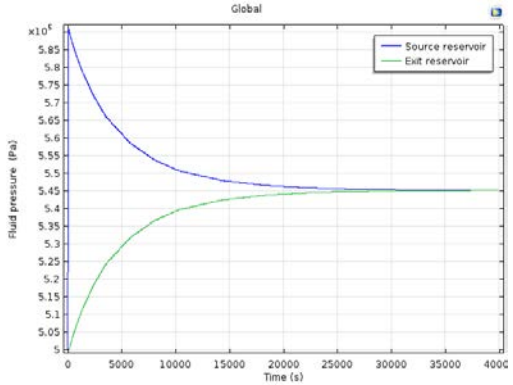

(b)

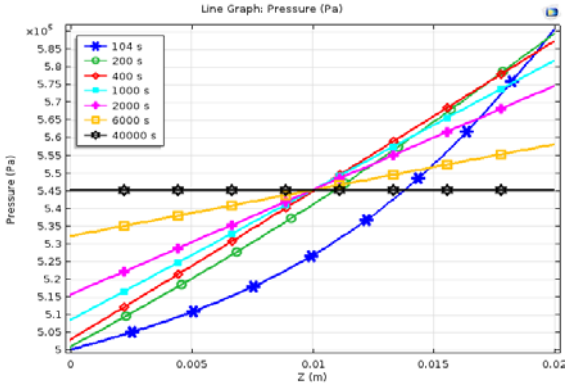

(c)

Figure 5.5 FEM vs analytical solution of pulse decay permeation test (a) normalized pressure versus time (b) reservoir pressures versus time (c) pressure profile in rock at various stage of permeation (Let V_1=V_2, V_1/A=0.1, L=0.02, r=0.005, k=1×10^{-19} and $\chi_f = 4 \times e^{-10}$)

Permeability of damage zone

The permeability of damaged rock is found to depend on various factors, including the resultant porosity, the size of the crack openings, the confining pressure, the volumetric change in post-peak stage, and the moisture content. In the current VEP framework as developed in this study, the adopted plastic flow function contributes to the dilatancy in volumetric strain. The confining pressure was maintained constant during the triaxial test, and samples were saturated with water. Therefore the damage factor becomes the most obvious factor pertinent to the permeability evolution of a damaged sample. An exponential relationship, as discussed previously (Maleki and Pouya, 2010), is applicable to this study and is given as

$$k = k_0 e^{A_p \bar{\varepsilon}_p} e^{A_v \varepsilon_{vol}} e^{A_t \Theta}$$

where k_0 is the intrinsic permeability of the rock at the initial state; A_p, A_v, and A_t are model constants; and Θ is an indicator of tensile failure and is given as

$$\Theta = \begin{cases} 1, & \sigma_3 \geq f_t \\ 0, & \sigma_3 < f_t \end{cases}$$

where f_t is the tensile strength with f_t=1 and 8 MPa for β=90 and 0 °, respectively.

It is clear that the permeability is a function of the mechanical damage that depends on the effective plastic strain $\bar{\varepsilon}_p$, volumetric variation, and extent of tensile cracking. Permeability can also be empirically correlated to stress level to reflect the initial crack closure stage.

The above relationship has been calibrated by numerical simulation against triaxial test data on Cobourg limestone, resulting in a set of parameters given as A_t=4.34, A_v=200, and a power-type step function for parameter A_p given as

$$A_p \bar{\varepsilon}_p = \begin{cases} 300\sqrt{\bar{\varepsilon}_p}, & \bar{\varepsilon}_p < \varepsilon_0 \\ 300\sqrt{\varepsilon_0} + 100\left(\bar{\varepsilon}_p - \varepsilon_0\right), & \bar{\varepsilon}_p \geq \varepsilon_0 \end{cases}$$

where threshold value for permeability evolution is determined from backward analysis by best-fitting the pulse decay test data, $\varepsilon_0 = \frac{\varepsilon_i}{2}$, with ε_i the plastic strain corresponding to the crack damage threshold value.

Compressibility of pore fluid

The fluid compressibility χ_f, as a key component to the storage term, is important for computation of hydraulic flow, especially for transient pulse decay test in estimation of the permeability. Under isothermal and brine free conditions, χ_f strongly depends on fluid phase and its saturation in the porous media. The compressibility of an air/water mixture has been theoretically studied by (Bishop and Eldin, 1950; Fredlund et al., 2012; Schuurman, 1966; Yang, 2005). The classic Bishop's formulation takes the form of

$$C_m = C_a[1 - S_l + hS_l] + C_f S_l$$

where C_m is the effective compressibility of air/water mixture with the liquid water saturated with air dissolution, S_l is water saturation degree, h is Henry's coefficient ($h = 0.0178$).

Nguyen and Selvadurai (1995) defined in the context of rock mass the effective compressibility of the air-water mixture as

$$C_m = C_a * S_a + C_f(1 - S_a)$$

where S_a is the air saturation degree ($S_a = 1 - S_l$ by neglecting the Henry's effect), p_{atm} is the atmospheric pressure, and p is pore water pressure, and the air compressibility $C_a = \frac{1}{p+p_{atm}}$ following Boyle's law of ideal gas. Selvadurai & Ichikawa (2014) studied the influence of air solubility on compressibility of water and proposed such a form of expression by modifying the expression of Nguyen (1995) with a Henry's coefficient, which resembles the Bishop's equation.

Effect of initial saturation degree

As for unsaturated porous media, the capillary pressure associated with initial saturation degree may play an important role in the calculation of air/water mixture compressibility (Fredlund et al., 2012). Schuurman (1966) proposed a theoretical relationship of the mixture's compressibility by taking into account the surface tension effect of microbubble on the enhanced air pressure compared with pore water pressure. At an elevated pore pressure condition, the bubble may collapse and dissolve in liquid phase completely. The disappearance of air bubble leads to sharp change in the compressibility of pore fluid. It is clearly demonstrated that a mass conservation for air phase has to be implemented in the derivation of effective compressibility for mixture of air/water pore fluid. The following will be devoted to the development of a mass conservation formula for the entrapped air in pore space.

Assumptions

Let us assume a porous media at total volume V, with initial air volume at V_0 and air pressure at p_0. The following assumptions define the state of the problem:

- Assume the air-water system is in thermodynamic equilibrium state.
- The constrained air is not permitted to escape from the representative element volume.
- The infiltrated water has been deaerated and is free of air dissolution.

After a certain period of infiltration, the air volume becomes V_1 and air pressure at p_1, with liquid saturation degree at S_1. Then we can write the saturation degree of the initial condition as

$$\frac{V_0}{V} = 1 - S_0$$

And at the end state

$$\frac{V_1}{V} = 1 - S_1$$

where S_0 and S_1 are respectively the initial and the end water saturation degree.

Volume of dissolved air irrespective of pressure

The volume of the dissolved air is defined as V_s. According to Boyle's and Henry's laws, this volume V_{sa} will be constant and thus independent from the pressure (Schuurman, 1966). V_{sa} is only dependent on

the volume of water and can be calculated by multiplying the relative liquid volume V_w by the coefficient of solubility (h) in terms of

$$V_{sa} = hV_w = hS_l V$$

The above argument can be proven by referring to the definition of Henry's law and is shown as follows.

The dissolved air mass (c) in unit weight of liquid water (m_w) is given as

$$c = hp_a = \frac{m_a}{m_w}$$

Let the volume of dissolved air as V_{sa}, then the total dissolved mass of air (m_a) is written as

$$m_a = M\frac{p_a V_{sa}}{RT}$$

Eliminating m_a leads to the expression of V_{sa} as

$$V_{sa} = \frac{hRT}{M}m_w$$

where R is ideal gas constant, T is temperature, and M is the molecular mass of air. So far the direct dependence of dissolved air volume on liquid water mass or volume is proven.

Mass conservation for air in pore space

Therefore the mass conservation of air in porous media can be given as

$$p_a^0(V_0 + V_{s0}) = p_a^1(V_1 + V_{s1})$$

Then the pore air pressure at the end of the infiltration becomes

$$p_a^1 = p_a^0\frac{V_0 + V_{s0}}{V_1 + V_{s1}} = p_a^0\frac{1 - S_0 + hS_0}{1 - S_1 + hS_1}$$

For an unsaturated soil at S_0=0.5, and end saturation S_1=1.0, then the end air pressure equals to $p_a^1 \cong 25p_a^0$. Another case according to Schuurman (1966) with S_0=0.94, and the critical air pressure $p_a^1 \cong 3p_a^0$ when air bubbles are believed to collapse and Skempton pore pressure coefficient becomes unity, the end water saturation is satisfyingly estimated to be $S_s^l = 0.97$. This suggests the presence of residual gas saturation $S_r^a = 0.03$, which contributes to the effective saturation degree in the form of

$$S_e = \frac{S_l - S_r^l}{S_s^l - S_r^l}$$

with the constraint of

$$S_r^a + S_s^l = 1$$

where S_s^l is the saturated water saturation, S_r^l is the residual water saturation, and S_r^a is the residual air saturation.

The pore water pressure (p_w) is governed by the capillary pressure (S_u) that is dependent on saturation degree.

$$p_w = p_a - S_u$$

The above relationship places a constraint on the maximum value of the pore air pressure, which is presumably expected to happen to full saturation when S_e=1.0, under which condition the suction reduces to zero, i.e. $p_a = p_w$. For a typical test specimen that is saturated by backpressure method, the backpressure defines the upper limit of the pore water pressure. Therefore pore air pressure may under no circumstance goes beyond the applied backpressure. However, it is also unconservative to believe that pore air pressure will quickly reach the equivalent level of the backpressure. The permeability of the porous media to a large extent controls the rate of saturation.

Effective compressibility of air-water mixture

Then the effective compressibility of air-water mixture can be written as

$$C_m = \frac{(1 - S_l + hS_l)^2}{p_a^0(1 - S_l^0 + hS_l^0)} + C_f S_l, \qquad S_l < 1$$

where S_l is the end water saturation, and S_l^0 is the initial water saturation.

Note that if full saturation is achieved (physically rather than the effective saturation), then the term representing air compressibility should disappear simultaneously (Fredlund et al., 2012; Schuurman, 1966). Because air bubble always take place in companion with residual air saturation, even in case of full saturation achievable for the effective saturation Se, the compressibility may remain at a substantially high level.

Let the residual water saturation as 0, rewriting the above equation in terms of effective saturation degree (S_e) leads to the following equation,

$$C_m = \frac{\left(1 - S_e S_s^l + hS_e S_s^l\right)^2}{p_a^0(1 - S_l^0 + hS_l^0)} + C_f S_e S_s^l$$

Effect of acoustic wave velocities

Acoustic wave velocities were measured during triaxial test on Cobourg limestone by UofT. From the seismic parameters we can not only assess the dynamic moduli, but can also calculate the fluid compressibility. The following parts will be devoted to illustrate the theories on the dynamic elasticity based acoustic wave velocities.

The dynamic shear modulus G_d is related to shear wave velocity V_s as follows (Gassmann, 1951)

$$V_s = \sqrt{\frac{G_d}{\rho}}$$

The shear wave velocity is found in various experiments to be insensitive to water saturation, and is treated in wave propagation theories as a constant for both dry and saturated porous media. Therefore the dynamic shear modulus G_d is independent of water saturation.

The compressional wave velocity V_p is associated with both bulk and shear modulus in the form of

$$V_p = \sqrt{\frac{K_{sat} + \frac{4}{3}G_d}{\rho}}$$

The dynamic Young's modulus E_d is given as

$$E_d = \rho {V_s}^2 \frac{3{V_p}^2 - 4{V_s}^2}{{V_p}^2 - {V_s}^2}$$

The dynamic Poisson's ratio is thus obtained

$$\nu_d = \frac{E_d}{2G_d} - 1$$

Then the dynamic bulk modulus K_d becomes

$$K_d = \frac{E_d}{3(1 - 2\nu_d)}$$

By calibrating the P-wave velocity with dry rock specimen will lead to the dynamic dry bulk modulus K_{dry}. Gassmann's formulation of saturated bulk modulus of porous media is given as

$$K_{sat} = K_{dry} + \alpha^2 M$$

$$\alpha = 1 - \frac{K_{dry}}{K_s}$$

$$\frac{1}{M} = \frac{\alpha - n}{K_s} + \frac{n}{K_f}$$

where K_f is pore fluid bulk modulus of interest to us, K_{sat} is the saturated dynamic bulk modulus, K_{dry} is the dynamic bulk modulus of dry rock which is believed to be air-dried rock with moderate water content to moisturize the mineral grain contacts, K_s is the bulk modulus of the mineral component, α is the Biot coefficient, M is model constant, n is porosity. Rearranging the above equation results in the formula for pore fluid bulk modulus

$$K_f = \frac{n}{\frac{\alpha^2}{K_{sat} - K_{dry}} - \frac{\alpha - n}{K_{sat}}}$$

The compressibility of pore fluid is easy to derive as

$$C_m = \frac{1}{K_f}$$

The compression wave velocity of dry Cobourg limestone is missing from UofT studies. Therefore we can only estimate K_{dry} from reported studies in the literature. Since the porosity of Cobourg limestone is very small, the difference between V_p of dry and saturated rocks would not be significant. Pore fluid saturation is found to influence V_p for more porous stones, e.g. sandstone, and for shale that is sensitive to fluid-rock interaction at grain contacts (Assefa et al., 2003). The difference in V_p between dry and saturated limestones is reported to be limited ($3<\Delta V_p<60$ m/s) for those with porosity less than 6%

(Assefa et al., 2003). Another seismic study on calcarenite rocks indicates V_p variation in less than 30 m/s for high porosity samples (n=30%) (Ahmouni et al. 2013).

It is noted that the bulk modulus of pore fluid depends on the difference between dry and saturated bulk modulus of the specimen. A highly compressible pore fluid entails a small difference between K_{sat} and K_{dry}. From the table below the dynamic bulk modulus of saturated Cobourg limestone is calculated to be 38.8 GPa, which is about 3 times of the static bulk modulus (10.7 GPa). The Biot coefficient for dynamic analysis is 0.035. Assuming a dry V_p=4.99 km/s, the estimated pore fluid compressibility is $4.60\text{x}10^{-10}$ Pa^{-1}, which is exactly equal to that for deaerated water, and is about 50% of the experimentally calibrated $\chi_m=1.1\times10^{-9}$ for the source water reservoir. It is thus implied that the rock specimen might have been completely saturated.

It should be pointed out that structural heterogeneity, cracks, foliation and layers were not considered in the analysis of acoustic velocity. V_p is representative of axial direction, which is found to be higher than that of the transverse direction.

Table 5.1 Dynamic properties of Cobourg limestone

Parameter	Value	Unit	Note
E_d	3.88×10^4	MPa	Dynamic Young's modulus
G_d	1.46×10^4	MPa	Dynamic shear modulus
ν_d	0.33		Dynamic Poisson's ratio
K_{d_sat}	3.88×10^4	MPa	Saturated dynamic bulk modulus
K_{dry}	3.86×10^4	MPa	Estimated from literature
K_S*	4.00×10^4	MPa	Dynamic solid compressibility
V_p	5	km/s	
V_s	2.5	km/s	
ρ	2330	kg/m^3	
α	0.035		Biot coefficient by dynamic moduli
M	1.90×10^5	MPa	
K_f	2.17×10^3	MPa	
χ_m	4.60×10^{-10}	Pa^{-1}	Equivalent to compressibility of de-aired water

Note:

*: K_s is less than that for mineral constituents (60 GPa) considering the presence of clay contents in Cobourg limestone. Cosenza et al. (2002) reported K_s=35 GPa for marble at porosity of 2%.

Calibrated reservoir water compressibility

UofT report provided experimental data on volumetric change of the pressurized upstream reservoir where the pressure pulse was applied, as well as its pressure evolution with time. This enables us to calibrate the compressibility of the fluid and the reservoir container as a whole system. According to the definition of compressibility in the following equation (Selvadurai and Najari, 2016)

$$C_{res} = -\frac{1}{V_t}\frac{dV_t}{dp} = -\frac{1}{V_t}\frac{dV/dt}{dp/dt}$$

where C_{res} is the combined compressibility of fluid-container system in upstream reservoir, V_t is the total volume of the reservoir, and p is the recorded pressure, dV is the recorded change of water volume.

It is noted that for pressure less than 15 MPa, the measured water volume change is -0.25 mL with the total dead-end reservoir volume at 15 mL. Therefore the compressibility of fluid-container system of the test analyzed in this study is estimated to be

$$C_{res} = \frac{0.25}{15 \times 15 \times 10^6} = 1.11 \times 10^{-9}$$

Determination of poroelastic parameters

Poroelastic response of porous rock involves comparative compressibility of the solid skeleton and the pore fluid under both drained and undrained boundary conditions. Numerous poroelastic theories have been developed to correlate several property factors, e.g. C_s, C_f, C_u, n, C_b, B and α. Meanwhile, pore pressure coefficient B and effective stress coefficient α have been extensively investigated by experiments on various rocks. It is worthwhile to perform a thorough analysis of the poroelastic properties for Cobourg limestone with these well-established theories and experimental evidences.

On nonlinear Skempton's B value

According to Bishop (1973), the B parameter is written as (Brown and Korringa, 1975)

$$B = \frac{\Delta p}{\Delta \sigma} = \frac{1}{1 + n\dfrac{C_m - C_s}{C_b - C_s}}$$

where n is porosity, σ is confining pressure, C_m is fluid compressibility (for either air, water or the mixture), C_b and C_s are respectively the drained bulk compressibility and the compressibility of the solid grains.

(Wang, 1993) derived a form similar to the above equation but distinguished as

$$B = \frac{1}{1 + n\dfrac{C_m - C_\phi}{C_b - C_s}}$$

where C_φ is the compressibility of pore space, and is said to be close to C_f at lower effective stress and approximate to C_s at elevated effective stress.

Zimmerman et al. (1986) has a formula of B based on pore compressibility (C_{pp}) that can be rewritten as

$$B = \frac{1}{1 + n\dfrac{C_f}{C_{bc} - (1+\phi)C_s}}$$

with C_{bc}=C_b, and the pore fluid compressibility C_f=C_m.

Evidence shows nonlinear B value with effective stress. Mesri et al. (1976) experimentally measured Skempton's B value for different type of rocks, and found 0.33<B<0.6 for marble, granite, sandstone and limestone under high level of effective stress. They noted rapid decrease in B value with increasing effective mean stress, which is attributed to crack closure and decrease in compressibility of solid skeleton. It was further emphasized that there is a major problem of calculating the B value because of its sensitivity to C_s. Green and Wang (1986) found the same trend in B value for sandstones, which is close to 1 at zero effective stress, but decreases to 0.6 at 13 MPa of effective stress.

The declining trend is consistent with other studies. Hart (2000) measured the induced pore pressure of Indiana limestone (porosity at 15-21%) and found the Skemptons's B value varies from 0.4-0.25 under effective confining pressure varying from 2-32 MPa. A declining trend of B value with increasing confining pressure has been observed in laboratory experiments on various rock and soils. For example, Lockner and Stanchits (2002) studied poroelastic properties of Berea sandstone, Navajo sandstone and Ottawa sand, and found a unique relationship for all tested sandstones between B value and effective confining pressure, which decreases nonlinearly from 0.8 to 0.4 with increasing P_c from 5 to 35 MPa. Lion et al. (2004) reported B value of porous limestone (n=20%) as low as 0.17. Ramos da Silva et al. (2010) reported poroelastic parameters for limestone as B=0.37. Lockner and Stanchits (2002) also investigated the nonlinear change of B value with effective mean stress, as shown in Fig. 5.6.

Nonlinear B value is attributed to the nonlinear variation bulk modulus or pore compressibility with increasing confining pressure (Mesri et al., 1976; Wang, 1993; Zimmerman et al., 1986). Crack closure is the predominant mechanism for the initial rapid change in B value. Biot (1973) proposed a nonlinear rheological theoretical framework to address the semilinear poroelastic behaviour of rocks. Nonlinear term for stress and fluid mass content in quadratic order was developed with variational principle and consideration of free energy. This may shed lights on the nonlinear behaviour in pore pressure response. However, it is outside the topic of this study and will not be further discussed.

In spite of the variability in rock types, the pore pressure coefficient shows a unique trend. From the reported test data we derived the following best-fitting empirical relationship:

$$B = 0.39 + 0.48 * 0.86^{\sigma'}$$

This relationship has very important implication for the assessment of the poroelastic behaviour of Cobourg limestone. Considering that the compressibility of solid skeleton of argillaceous rock is difficult to determine, a theoretical calculation of B value appears impractical. We have to rely on experimentally determined B value for further studies on HM coupled behaviour of the host rock for DGR. More importantly, the effective stress analysis requires Biot's coefficient to be accurately determined. For the same reason, the theoretical Biot's coefficient is ill-defined as K_s is indistinctive. However, the above formula allows us to derive the Biot's coefficient from the Skempton's B value that has profound physics.

An alternative approach to calculating compressibility for air-water mixture involves B pore pressure parameters by relating the effective compressibility with confining pressure σ_3 (Fredlund et al., 2012),

$$C_m = C_f S_l B_w + \frac{B_a}{p_a}(1 - S_l + hS_l)$$

where B_a and B_w are respectively pore air and pore water pressure coefficient. Experimental data showed very low value in B value for induced air pressure ($B < 0.1$) for most of the saturation range (Fredlund et al., 2012), which is consistent with the theoretical analysis on the effect of air phase on significant reduction of B value by (Yang, 2005).

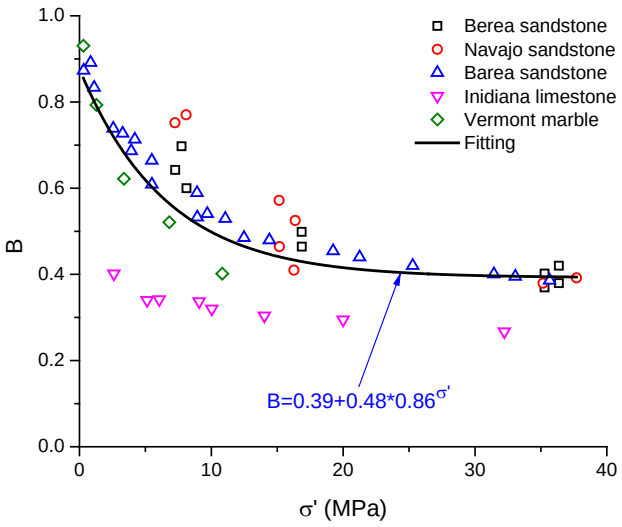

Figure 5.6a Dependence of B value on effective stress (data cited from Lockner and Stanchits 2009; Hart 2000; Mesri et al. 1976)

Biot's coefficient

Since Skempton's B value has been extensively measured and a wealth of data is available in literature, it may unravel some important perspectives on the poroelastic properties of different types of rocks, including Cobourg limestone.

The Skempton's B value is related to the Biot's coefficient α as follows:

$$B = \frac{1}{(1+n) + \frac{n}{\alpha}\left(\frac{C_m}{C_b} - 1\right)}$$

which leads to

$$\alpha = \frac{n\left(\frac{C_m}{C_b} - 1\right)}{\frac{1}{B} - (1+n)}$$

As indicated in the above equations, Biot's coefficient is closely related to porosity and Skempton's B value. For highly porous media, e.g. sandstone and limestone, comparatively high Biot's coefficient as α=0.75-0.8 has been experimentally observed (Lion et al., 2004; Ramos da Silva et al., 2010). For less porous rocks, i.e. marble and granite at porosity of about 2%, Cosenza et al. (2002) reported low Biot's coefficient as low as α=0.2 in the hydrogeological modelling of limestone aquifer.

Here we conducted a parametric analysis of Biot's coefficient for Cobourg limestone. It is surprising to find that Biot's coefficient is not that high as commonly believed (α=0.7-0.8 by (Selvadurai and Najari, 2016)). Let B=0.5, n=0.01, $C_m=\chi_f=1\times10^{-9}$, and $C_b=1\times10^{-10}$. Then we get α=0.09. If B=0.3, then α=0.04. Only in case of highly compressible pore fluid, i.e. $C_m=100*\chi_f=1\times10^{-7}$, then Biot's coefficient could reach the level of 0.9 (when B=0.5). For impermeable rocks like marble and argillaceous limestone, a trace proportion of porosity significantly affects the Biot's coefficient. This significantly constrains the poroelastic behaviour of such rocks. It will be explained in more details in the subsequent HM coupled modelling of the pulse decay test.

From the pulse decay curves of UofT's tests on Cobourg limestone, we speculated that it is unlikely to have underpressure, or overpressure in the tested rock sample during triaxial test, which has been observed in the numerical modelling due to strong poroelastic effect. Several factors simplified the analysis. Firstly, as indicated by the simulations, underpressure due to insufficient backpressure saturation leads to steep pressure gradient at reservoir/rock interface, and subsequently a fluid flux in 1-2 orders of magnitude higher than the observation. Secondly, overpressure causes backward flux toward the upstream reservoir, turns to increase the pulse pressure, which has not been observed in the experiment. Thirdly, if maintaining the compressibility of solid matrix (C_s) as constant, then both α and B are constant by definition, which deviates from the experimental observations of changing B value with effective stress, as reported widely in literature.

Therefore, the following viewpoints hold well according to comprehensive questioning and analysis of poroelastic theories:

1. The poroelastic response of Cobourg limestone is not as significant as expected. The Biot's effective stress coefficient α=0.05-0.1.
2. By setting α as high as 0.4-0.8 we overestimate the poroelastic behaviour, and thus overestimate the compressibility of pore fluid, which was speculated to be 100 times of that for de-aired water.
3. Skempton's B value varies with effective stress, and has been extensively tested in literature. This enables the derivation of a formulation for Biot's coefficient α based on the best-fitted B value equation by least-square regression method.

Effect of porosity on Biot's coefficient

We further the discussion on Biot's coefficient by taking into account the porosity effect. Hashin-Shtrikman (HS) bounds provide narrower and more reliable bounds on elastic properties of composite material (Hashin and Shtrikman, 1963). It assumes spherical inclusion of one material in another, and correlates the bulk and shear moduli of both pure materials with volume fraction, or porosity. We assume here an ideal composite porous media made up of solid matrix and liquid-filled pore space that

is isolated from each other and not interconnected. This applies to rocks with extremely low permeability and low porosity, for example clay rocks, marble and granite. The original formulas on the lower and upper bounds of the effective elasticity are modified here in order to address the two-phase porous media consisting of pore fluid and solid matrix, and are given as

$$K_D^{min} = K_f + \frac{1-\phi}{\frac{1}{K_s - K_f} + \frac{\phi}{K_f}}$$

$$K_D^{max} = K_s + \frac{\phi}{\frac{1}{K_f - K_s} + \frac{3(1-\phi)}{3K_s + 4G_s}}$$

where K_D^{min} and K_D^{max} are respectively the lower and upper bounds of the drained bulk modulus (K_D), K_f and K_s are respectively the bulk moduli of fluid and mineral matrix, G_f and G_s are respectively the shear moduli of fluid and mineral matrix.

Seismic properties of rocks are amongst the most extensively investigated parameters. It is thus convenient to use if the acoustic velocity is applied. The p-wave modulus M is given as

$$M = \frac{3K_s + 4G_s}{3} = \rho V_p^2$$

Therefore and upper bound for drained bulk modulus is derived as

$$K_D^{max} = K_s + \frac{\phi}{\frac{1}{K_f - K_s} + \frac{1-\phi}{\rho V_p^2}}$$

Therefore the Biot's coefficient has the bounds as

$$1 - \frac{K_D^{max}}{K_s} \leq \alpha \leq 1 - \frac{K_D^{min}}{K_s}$$

Zimmerman et al. (1986) considered the bulk modulus of dry rock, and rewrote the upper HS bounds on the bulk moduli using the Poisson's ratio of the mineral matrix, with the assumption of isotropy and monomineral,

$$\frac{K_D}{K_s} \leq \frac{1-\phi}{1 + \frac{\phi(1+\upsilon)}{2(1-2\upsilon)}}$$

where ϕ is the rock's interconnected porosity and ν is the effective Poisson's ratio of the rock's mineral matrix. According definition of Biot's coefficient, rearranging the above formula results in a lower Hashin-Shtrikman bound for the Biot's coefficient as (Zimmerman et al. 1986)

$$\alpha \geq \frac{3\phi(1-\upsilon)}{\phi(1+\upsilon) + 2(1-2\upsilon)}$$

However, the above bound by Zimmerman et al. (1986) only addresses dry rocks with interconnected air-filled pore space. In drained conditions, the pore fluid may not maintain a constant bulk modulus.

Therefore no lower bound for drained bulk modulus K_D is available to Zimmerman et al. (1986)'s method (Hasanov et al., 2015).

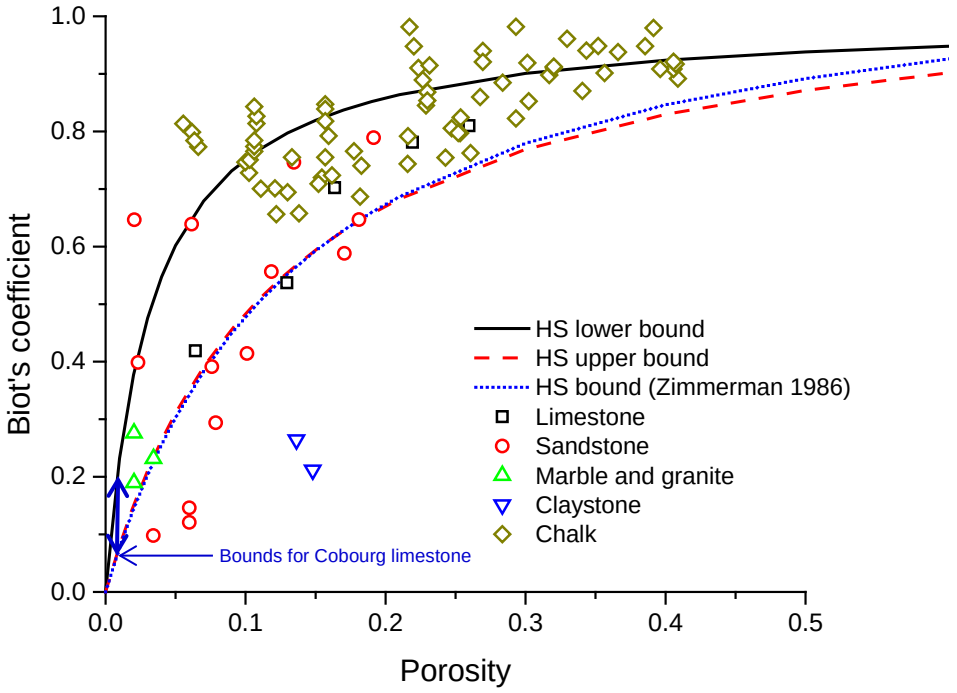

Figure 5.6b. Biot's coefficient as a function of porosity for various rock types and comparison with HS bounds (Calculation involves K_f=2.4 GPa, K_s=75 GPa, V_P=5.5 km/s, ρ_s=2700 kg/m3, v=0.45. Data cited form (Alam et al., 2012; Cosenza et al., 2002; Hasanov et al., 2015))

Figure 5.6b shows the reported Biot's coefficients for various rocks and the comparison with HS bounds. It is clearly demonstrated that the Biot's coefficients of rocks depend strongly on its porosity especially when porosity becomes very small. The common sense of Biot's coefficient around 0.7-0.95 is only valid for highly porous rocks with porosity ranging from 0.1-0.4. But for argillaceous rocks, the porosity is always less than 1%, which implies a much lower value in Biot's coefficient in the range of 0.05-0.2.

Note that the upper bound of Biot's coefficient involving the lower bound of K_D is only applicable to porous media with predominantly isolated and fully saturated micropores. From the comparison with test data, this upper bound for α seems reasonable for porosity ranges ϕ<0.2. Besides, it is reported that cementation of solid grains affects the Biot's coefficient as well (Alam et al. 2012). After studying the poroelastic behaviour of poorly cemented chalk, Alam et al. (2012) found that α does not change significantly with porosity and remains close to unity, whereas for strongly cemented rocks, α decreases rapidly with decreasing porosity. Therefore, for intact rocks there apparently exists a general dependence of Biot's coefficient on porosity, while for soils, gravels or highly fractured rocks there might not be such a significant relationship with porosity.

Volumetric averaged bulk modulus for argillaceous limestone

Moreover, we can rationalize the low Biot's coefficient for Cobourg limestone in an alternative way. Take a representative unit volume of Cobourg limestone matrix for analysis, the clay content in volume is defined as S_c, and the rest is regarded as pure calcite 1-S_c. Following the definition of bulk modulus (K_s) for solid matrix in poroelastic theory, the volume change ΔV under hydrostatic pressure variation Δp can be written as

$$\Delta V = \frac{\Delta p}{K_s}$$

By decomposing the volumetric change into those of mineral components, respectively, we obtain the following expression

$$\Delta V = \Delta V_c + \Delta V_r = \Delta p \left(\frac{S_c}{K_{sc}} + \frac{1 - S_c}{K_{sr}} \right)$$

where K_{sc} and K_{sr} are bulk modulus of clay mineral and calcite, respectively, V_c and V_r are volume change for clay and rock, respectively.

Therefore the averaged bulk modulus K_s of the argillaceous limestone is given as

$$K_s = \frac{1}{\frac{S_c}{K_{sc}} + \frac{1 - S_c}{K_{sr}}}$$

Let K_{sr}=50 GPa, K_{sc} varies from 1 to 5 GPa, the volumetric averaged bulk modulus is calculated as a function of clay content, which is plotted in Fig. 5.6c. It is clearly shown that trace amount of clay in the rock significantly reduces the bulk modulus in the whole. Cobourg limestone has been reported to have considerable level of clay composition, which varies from 10 to 20% according to OPG's study of the rock specimen (NWMO, 2011). The calculated Biot's coefficient is plotted in Fig. 5.6c(right) by using the experimental results of K_D=10 GPa. By comparison with the upper and lower bounds for Biot's coefficient from Fig. 5.6b, the bulk modulus of argillaceous content in Cobourg limestone is estimated to be 1.5<K_{sc}<3 GPa. This is consistent with the reported range of K_s for Toarcian Claystone and Domerian Claystone in Paris basin (Cosenza et al., 2002).

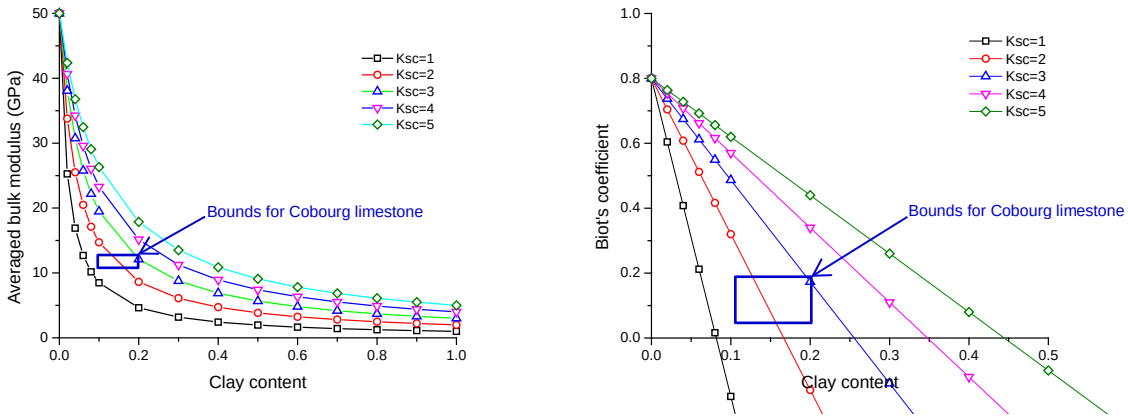

Figure 5.6c Modelled averaged bulk modulus (left) and the Biot's coefficient (right) of argillaceous limestone with increasing clay content (The drained bulk modulus of Cobourg limestone is experimentally measured as 10 GPa.)

Regularized strain gradient localization theory

Various plasticity phenomena, strength properties, shear band, and crack tip propagation have been found to display size effect (Bažant and Pijaudier-Cabot, 1989; Fleck et al., 1994; Jirásek, 2002). Stronger response is always associated with small size. The mechanical properties of crystalline materials are found to be related to grain sizes, including the constitutive behaviour and physical mechanism of strength, plasticity, shear localization, fatigue and creep (Meyers et al., 2006). It is generally believed that microscale crystallization contributes to the overall strengthening of materials, which can be interpreted with theories involving a characteristic length.

Local continuum model with strain-softening constitutive law would cause loss of ellipticity of the governing differential equations, ill-posedness and localization of damage into a zero volume zone, and the mesh-dependence for FEM simulations (Jirásek, 2002). The fracture may appear to be localized in a narrow crack, however, the determining factors underlying the initiation, coalescence and interconnection of fracturing involves nonlocal homogenization and energy release from a finite volume surrounding the microcrack. Some causes of nonlocality have been illustrated by Bažant and Jirásek (2002) as a result of heterogeneity of microstructure, interaction between microcracks, and the intrinsic statistical distribution.

The softening behaviour still imposes convergence difficulty when implemented in COMSOL. We apply a well-known regularized procedure to accommodate the singularity problem for localization (Bažant and Jirásek, 2002; Forest, 2008; Jirásek, 2002). The basic idea is to let the sharp contrast of deformation upon shear bands to diffuse into the surrounding domain, with the consideration of a certain influence range that has sound physical meaning. This allows the singularity problem to be circumvented in numerical simulations.

Similar to other authors (Bažant and Jirásek, 2002; Jirásek, 2002; Pijaudier-Cabot and Grégoire, 2014), a nonlocal plastic strain is defined, and is determined from the solution of the Helmholtz equation:

$$\bar{\gamma} - l_c^2 \nabla^2 \bar{\gamma} = \varepsilon^p$$

where l is the characteristic length indicating the influence zone, $\bar{\gamma}$ is the nonlocal equivalent plastic strain and ε^p is the local effective plastic strain.

The boundary condition of the above differential equation is taken as a homogeneous Neumann boundary

$$\frac{\partial \bar{\gamma}}{\partial n} = 0$$

It is easy to get the above equation implemented in COMSOL, simply by adding a separate physics interface in addition to the governing equations shown in the beginning. The integrated value for the nonlocal plastic strain $\bar{\gamma}$ is then used in the strain-gradient softening model.

There are alternative ways of defining the nonlocal plastic strain, mainly by assuming explicit functions of the nonlocal strain versus the local one. A few of examples follows,

$$\bar{\gamma} = \int_V \alpha(x,\xi)\varepsilon^p \mathrm{d}\xi$$

where $\alpha(x,\xi)$ is the nonlocal weight function, and is always rescaled to unity as follows

$$\alpha(x,\xi) = \frac{\alpha_0(|x-\xi|)}{\int_V \alpha_0(|x-\zeta|)\,\mathrm{d}\zeta}$$

The form of α_0 can be chosen from a number of options, e.g. Gaussian function, truncated bell-shaped function, amongst others (Jirásek, 2002). The Gaussian function is given as

$$\alpha_0(r) = \exp\left(-\frac{r^2}{2l_c^2}\right)$$

where r is distance from the source point.

A linear weighting function is used to harmonize the integrated effect of both plastic strain and its gradient, which is given as (Jirásek, 2002)

$$\gamma = m'\varepsilon^p + (1-m')\bar{\gamma}$$

where γ is the plastic strain measure that is proposed in this study to consist of two components, i.e. the effective plastic strain, ε^p, and the regularized plastic strain measure, $\bar{\gamma}$, and m' is a weighting factor to evaluate the combined influence of effective plastic strain and the effective elastic strain gradient.

Damage model

The softening behaviour in the post-peak stage of compressive loading involves the coalescence and propagation of microcracks that can be described with damage theory. In the Drucker-Prager or Mohr-Coulomb criterion, a simplified softening model is proposed to take into account the cumulative damage induced by both plastic strain and the strain gradient,

$$D = D_r + (1-D_r)e^{-l_p\gamma}$$

where D is a weighted damage factor in the post-peak stage, which differs from the hardening damage factor ω, and D_r is the residual damage factor (an input parameter).

Therefore the cohesion can be written as a function of damage factor

$$c = c_0(1-D)$$

where c_0 is the cohesion for intact specimen.

4. Experimental results and calibration of models for Cobourg limestone

Triaxial test

The mathematical model previously described was implemented in a commercial finite element code, COMSOL Multiphysics, in order to simulate the triaxial tests and the pointwise pressure tests as described in more details in the companion paper. COMSOL Multiphysics is a high-level programming language that numerically solves the governing equations, along with all auxiliary equations that come from the assumed constitutive relationships, and the appropriate boundary conditions. The COMSOL finite element model with the mechanical and hydraulic boundary conditions is shown in Fig. 5.7a. The boundary conditions include a confining pressure P_c applied on the sidewall, fixed constraint for the bottom boundary, and a prescribed displacement on the top end. The sample was originally saturated with fluid before axial loading was applied. Other loading conditions include the vertical loading strain rate at 1.6×10^{-6} s^{-1}, with the target stress achieved within 2s. The mobilized hardening/softening elastoplastic model was integrated in the simulation. Table 3 lists the model parameters that have been obtained from either experiments or calibration with numerical modelling. For instance, the elasticity parameters were calculated by analysis of triaxial test data, and were found to be comparable with the reported data. The confining pressure P_c was maintained at 5 MPa, and initial pore pressure P_i at 3 MPa throughout the experiment, which resulted in an effective initial stress of σ_i=2 MPa. Both ends of the test sample were applied with controlled fluid pressure at p_b=3 MPa during triaxial test, except when the pulse pressure decay test was conducted as the upper boundary was then supplied with a pulse of elevated fluid pressure to 4 MPa and then allowed to decrease with time (p_1=f(t)). Hydraulic-mechanical coupling was considered in order to reflect the experimental conditions. The permeability of the damage zone was updated on the basis of the stepwise function relating permeability with damage indicator of plastic strain.

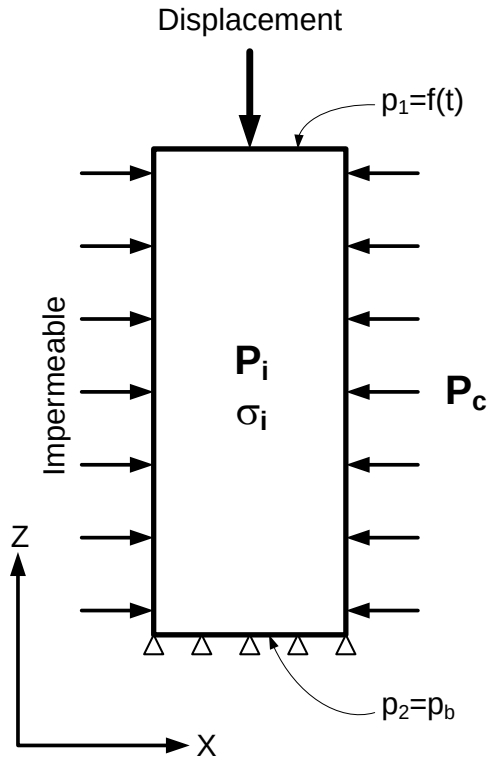

Figure 5.7a Boundary conditions for the triaxial test along with pulse decay permeability measurement

Figure 5.7b shows the stress-strain relationship of Cobourg limestone under triaxial test conditions when foliation is in line with the direction of the loading axis. The peak strength is determined as 100 MPa. The post-failure strength declines quickly to about 1/3 of the peak. No obvious plastic flow is observed. Figure 5.7b also shows the triaxial tests of the same sample with foliation perpendicular to the loading axis. The peak strength is at about 50 MPa, showing strong orientation dependence, at least for the number of samples being tested.

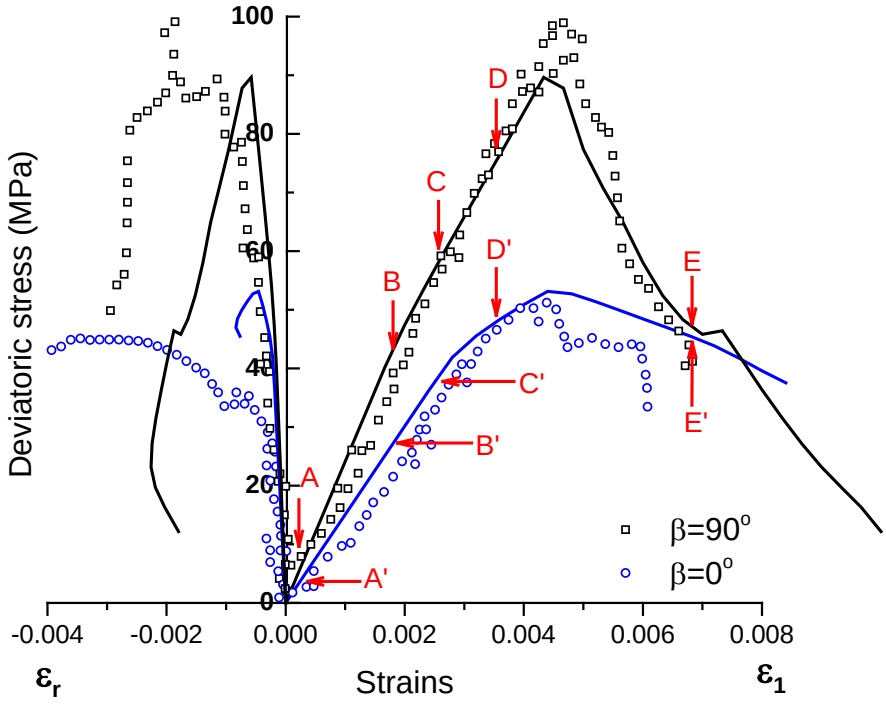

Figure 5.7b Variation of deviatoric stress of Cobourg limestone with axial and radial strains (confining pressure P_c=5 MPa, pore pressure p=3 MPa. Solid lines are modelling results. Foliation of the specimen is oriented at angle β with respect to the horizontal direction). Points A, A', B, B' etc. are where pulse tests were performed.

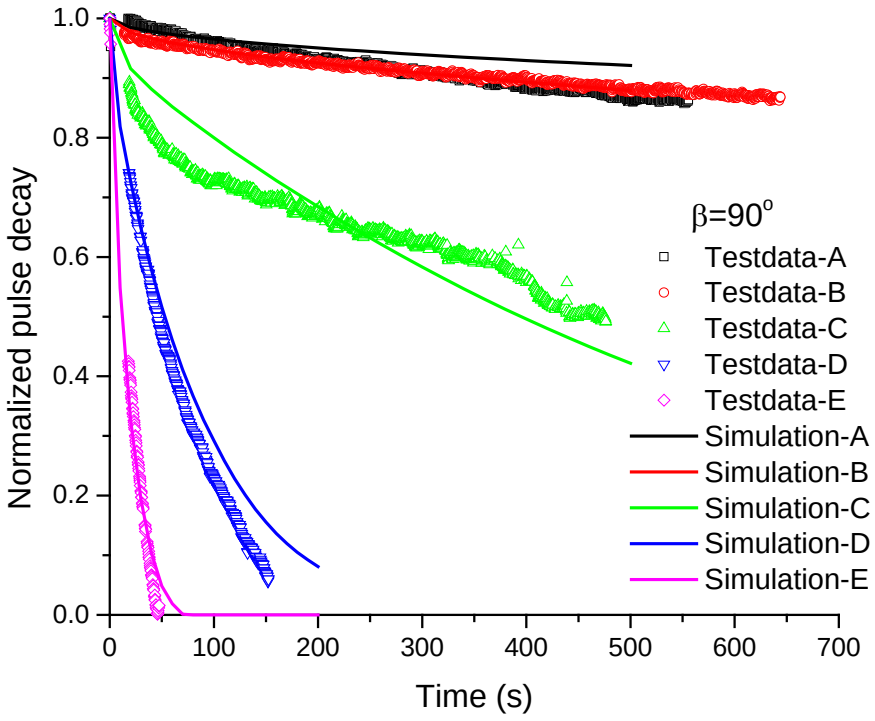
Normalized pulse decay
Time (s)
β=90°
Testdata-A
Testdata-B
Testdata-C
Testdata-D
Testdata-E
Simulation-A
Simulation-B
Simulation-C
Simulation-D
Simulation-E

(a)

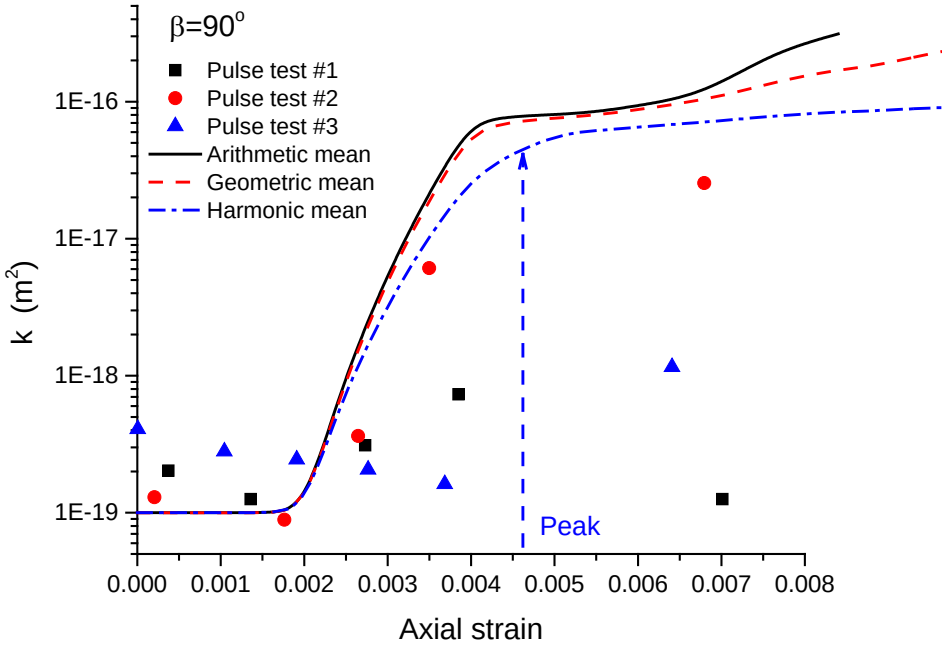
β=90°
Pulse test #1
Pulse test #2
Pulse test #3
Arithmetic mean
Geometric mean
Harmonic mean
Peak
k (m²)
Axial strain

(b)

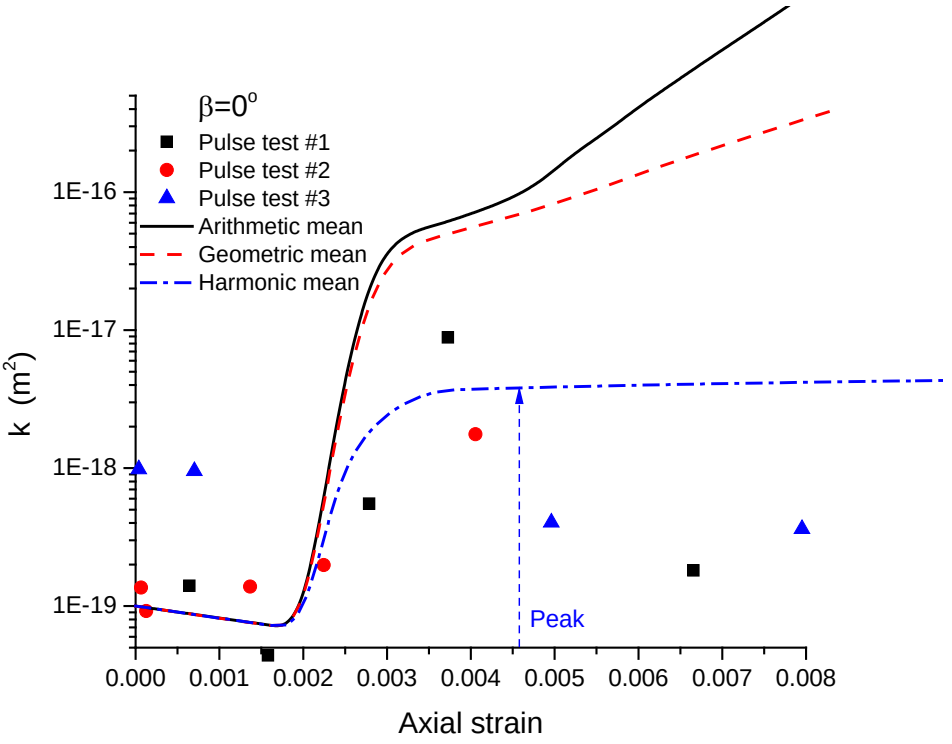

(c)

Figure 5.8 Simulated and measured pulse decay curves for rock under different stage of triaxial test (a) temporal variation (β=90°), (b) the permeability evolution with axial strain (β=90°), and (c) the permeability evolution with axial strain (β=0°) (Scattered dots are experimental data and the lines are simulated results)

Transient pressure pulse decay test has been conducted for measurement of permeability under the triaxial test conditions. Figure 5.8a shows the recorded temporal evolution of the pulse pressure in the source reservoir after normalized to unity. The test data were analyzed using the analytical solution by Brace et al. (1968) with satisfyingly high degree of correlation. The determined permeability was shown in Fig. 5.8b-c, which remains low and stable for σ_d lower than the CI threshold. Further increase in deviatoric stress caused cumulative damage and enhanced permeability. This is in agreement with some previous results on the permeability variation of damaged rock samples, which typically has 2-3 orders of magnitude increase due to connected fractures (Green and Wang, 1986; Zhang, 2014).

Rheological tests on Jura limestone

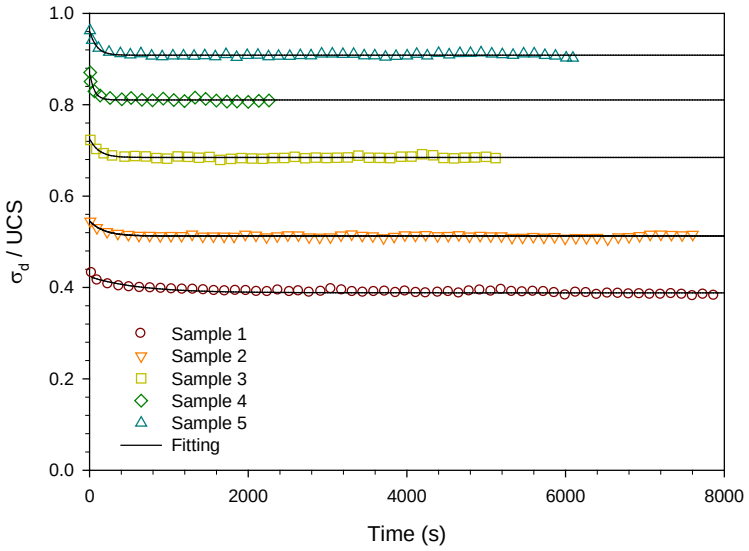

Figure 5.9 Stress relaxation of Jura limestone with time under various deviatoric loadings

Stress decay of Jura limestone during the uniaxial unconfined relaxation test is shown in Fig. 5.9. The measured stress was normalized against the peak strength, and plotted with elapsed time. The stress relaxation compliance formula for SLS model was applied to best-fit the test data. The obtained parameters as shown in Fig. 5.10 include the elastic shear modulus (G_1) and relaxation time (τ) of the Maxwell viscoelastic branch. The best-fitted empirical relationship for the SLS model parameters can be written as

$$G_1 = 0.07G$$

$$\frac{1}{\tau} = -0.007 + 0.024\frac{\sigma_d}{UCS}$$

It is noted that the relaxation time, which represents the viscosity of the rock sample, depends uniquely on the stress level. In order to simplify the application in modelling, the damage factor ω was adopted to represent the stress ratio. Therefore the above equation turns into another expression,

$$\frac{1}{\tau} = -0.007 + 0.024\left[\left(1 - \frac{CI}{\Im}\right)\omega + \frac{CI}{\Im}\right]$$

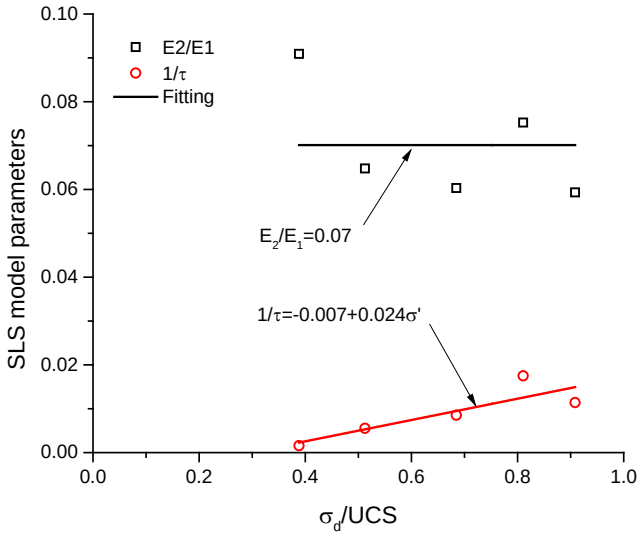

Figure 5.10 SLS model parameters versus normalized stress ratio and the regression formula

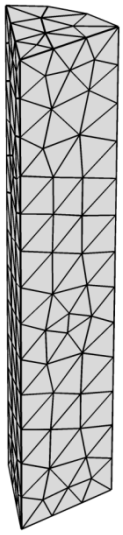

Figure 5.11 FEM model for simulation of the relaxation and creep tests

Verification with numerical models

Triaxial test

Using the above derived model parameters, the triaxial tests, including the stress relaxation test, were reproduced numerically by applying appropriate boundary conditions to the FEM model as shown in Fig. 5.11 that we have developed with COMSOL. This includes rollers on two vertical axisymmetric planes, confining pressure applied on the sidewall, and spring foundations for both top and bottom boundaries (elasticity K=1E10 N/m^2). Other loading conditions include the vertical loading rate at 1×10^{-7} m/s, with

the target stress achieved within 2s. The mobilized hardening elastoplastic model and the SLS viscoelastic model were integrated in the simulation.

Hydraulic-mechanical coupling was considered in order to reflect the experimental conditions. Isotropy is assumed valid for the studied regional Cobourg limestone due to the fact that variability of strength and stiffness parameters is predominantly dependent on clay content than on the bedding orientation. The permeability of the damage zone was updated on the basis of the stepwise function relating permeability with damage factor ω. Pulse decay was not simulated in this case, instead, included in the subsequent modelling case.

Figure 5.7a-c and Figure 5.8a-b show the modelling results on triaxial tests and the pulse decay permeability tests. The modelling results are found to reproduce the stress-strain behaviour prior to the peak with very good agreement. The decrease in shear strength at post-failure stage compares well with the experimental results. The permeability evolution is also reproduced with high consistency. Figure 5.12 shows the modelling results of stress relaxation as compared to the experimental data, suggesting very good agreement with each other.

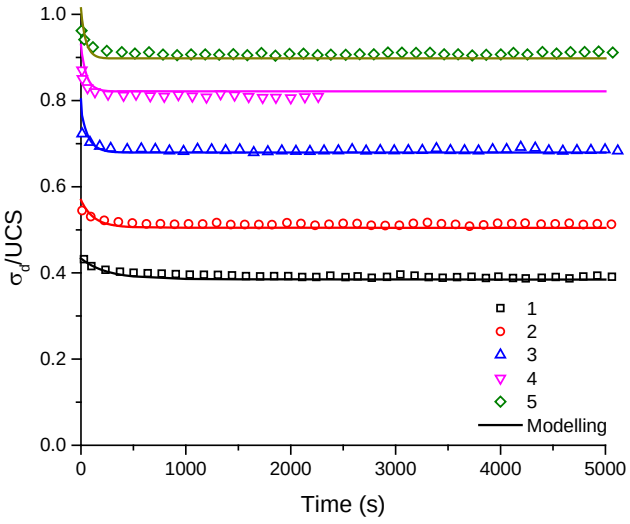

Figure 5.12 Modelled stress decay curves (solid lines) versus experimental measurement (scattered dots) (Vertical loading rate: 1×10^{-7} m/s; target stress achieved within 2s; T=2450, 3220, 4340, 4900, 5250, and 5740 s.)

The time-to-failure behaviour for Jura limestone has been reported by (Paraskevopoulou et al., 2015). As shown in Fig. 5.3, our new failure criterion gives good fit to the test data. The obtained parameters for the creep failure criterion were implemented in COMSOL to analyze the sudden failure due to cumulative damage under constant loading. Unconfined uniaxial compressive loading was applied to the specimen. Figure 5.13 shows the temporal evolution of strain rate under various deviatoric stress loadings. The rheological model is based on SLS, therefore the strain rate keeps declining with elapsed time. The sharp increase in strain rate to the end indicates the occurrence of creep failure. The modelling results of time-to-failure parameter t_F are plotted in Fig. 5.14 against the fitting curve for the

test data. It is found that the modelling results agree well with the fitting curve, suggesting that the creep failure criterion has been correctly applied in the numerical scheme.

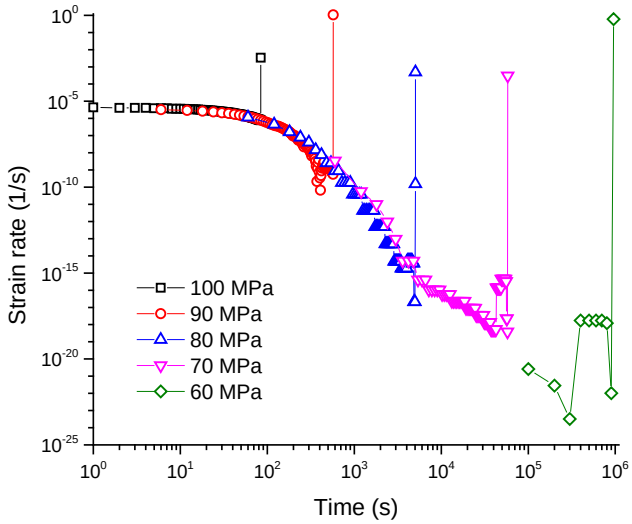

Figure 5.13 FEM results on temporal strain rates under different deviatoric stress until creep failure

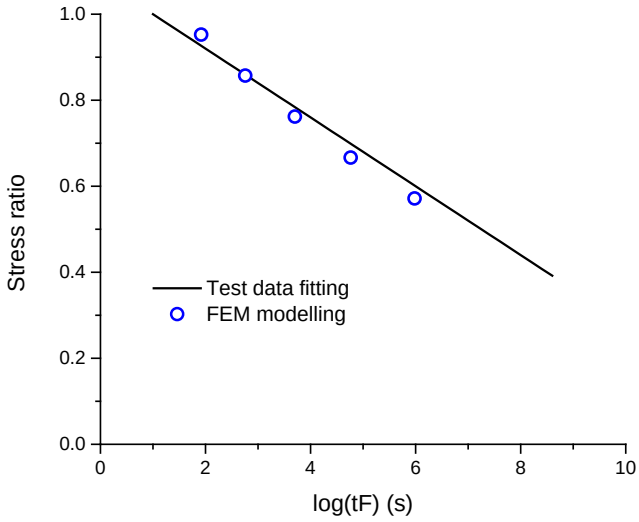

Figure 5.14 The modelled failure time versus the fitting curve from experimental results

Table 5.2 lists the model parameters that have been obtained from either experiments or calibration with numerical modelling. For instance, the elasticity parameters were calculated by analysis of triaxial test data, and were found to be comparable with the reported data. The rheological model parameters were derived with analytical solution. The peak plastic strain and parameters for the mobilized hardening law were estimated by backward analysis of the test data. The hydraulic properties for the

water retention curve of Cobourg limestone were cited from NWMO technical report and modified to reflect the influence of ground stress level.

Table 5.2 Model constants for HM coupled modelling of permeation and triaxial test on Cobourg limestone

Parameters	β=0°	β=90°	Unit
Mechanical properties			
E	21	15	GPa
ν	0.175	0.175	
c_0	8.8	-	MPa
σ_τ	4.4	-	MPa
CI	25-30	15	Mpa
CD	80	-	Mpa
UCS	100	50	Mpa
ρ	2300	2300	kg/m^3
ϕ	32	32	deg
ϖ	0.3	0.3	initial yielding
α	0.05	0.05	Biot's coefficient
Rheological properties			
G_1	0.068*E	0.068*E	GPa
τ	41/ω	41/ω	s
Hydraulic properties			
porosity	0.01	0.01	
Λ	Stepwise function	2/3*Λ	Damage-permeability relationship
k_0	1×10^{-19}	1×10^{-19}	m^2
X_f	1.1×10^{-9}	1.1×10^{-9}	1/Pa

X_s	1×10^{-11}	1×10^{-11}	1/Pa
van Genuchten parameters			
α*	0.001	0.001	1/m
n	1.67	1.67	
l	0.5	0.5	
Mobilized hardening law			
ε_{epe}	5×10^{-4}	5×10^{-4}	Threshold plastic strain at peak strength
k	54.7	24.6	MPa
m	0	0	
h	30	13.5	MPa
l	3.124	3.124	
Strain gradient parameters			
l_c	1	1	mm
l_p	100	100	
m'	0.7	0.7	Weighting factor
D_r	0.2	0.2	

Note:

The van Genuchten parameter is modified from Geosynthesis report (α=0.0005 by NWMO).

Pulse decay test

As for the modelling of pulse decay test, the boundary condition at the reservoir-rock interface differs from the classical Dirichlet or Neumann types. Therefore an add-on module representative of an ordinary differential equation boundary was assigned to both the upper and lower boundaries to accommodate the time and spatial derivatives of the fluid pressure. The signs of boundary conditions are reversed compared to those shown in literature (Brace et al., 1968; Liang et al., 2001; Selvadurai and Carnaffan, 1997). This modification is adopted because of the sign convention of the numerical simulator.

Figures 5.8a-5.8c show the simulated pulse decay curve at different times during the triaxial test on Cobourg limestone. The curves were previously analyzed with analytical solution from Brace and al. (1968) to estimate the permeability. This estimated value is compared here against the averaged permeability on the boundary calculated by the finite element model using the damage-permeability

relationship. It is found to coincide with each other very well. It is also noted that boundary conditions affects the damage extent and thus the permeability distribution. A less permeable boundary layer is observed when horizontal deformation is constrained at the top-end boundary. The friction between load pedestal and rock specimen may act as a horizontal constraints. Therefore the measured permeability by pulse decay method applied on the top boundary may somewhat underestimate the volumetrically averaged value.

Figure 8a shows the comparison between the test data and the simulated pulse decay curves at different points during the triaxial test on Cobourg limestone. The simulation gives good agreement with the experimental observation, suggesting the validity of the proposed permeability function. Figures 5.8b-c shows the variation of the effective permeability estimated from the analytical solution from with increasing axial strain. The figures also show the arithmetic, geometric and harmonic means of the permeability derived from the finite element model. The initial decrease in permeability is attributable to the crack closure under increasing confining pressure. The subsequent permeability increase results from the development of micro-cracks when shear stress goes beyond the crack initiation threshold value. This rapid increase continues until the peak strength is reached. In the post-failure stage, the evolution of permeability is found to be complicated by either decreasing or increasing trends with further axial strain. As discussed in the companion paper, the observed permeability reduction can be attributed to grain crushing and pore collapse, which is not included in the current modelling.

Various permeability means are evaluated to assess the stress-induced heterogeneity. The arithmetic mean, and harmonic mean of the permeability are respectively given as

$$k_a = \frac{\sum V_i k_i}{\sum V_i}$$

$$k_h = \frac{\sum V_i}{\sum \frac{V_i}{k_i}}$$

while the geometric mean of the permeability is

$$k_g = \sqrt[n]{k_1 k_2 k_3 \dots k_n}$$

or

$$k_g = \exp\left(\frac{\sum V_i \log(k_i)}{\sum V_i}\right)$$

According to a previous study, the effective permeability is believed to be equivalent to kg, and ranges between ka and kh as

$$k_h < k_{eff} < k_a$$

It has been reported that for Indiana limestone with natural heterogeneity in permeability, the geometric mean value appears to be representative of the effective permeability. The above authors successfully verified that the geometric mean is a good proxy as a homogeneous material property to the experimentally measured heterogeneous distribution of permeability. It is noted that no evidence of hydraulic anisotropy or fractures is considered in that study. Therefore we computed both the

arithmetic and geometric means of the simulated permeability to assess the impact of nonlocal deformation on overall variation in permeability.

Figures 5.8b-5.8c show the comparison between these two variables against the experimental data and the estimated effective permeability from the simulated pulse decay curve by Brace equation. It is found that the harmonic mean can well reproduce the results of pulse decay test when deformation is comparatively uniform, and all three means of permeability are consistent with each other. Once nonlocal deformation is formed, both the arithmetic and geometric means cannot represent the rapidly evolving heterogeneity anymore. The harmonic mean of permeability is the closest proxy to the estimated permeability by pulse decay method. Therefore, the pulse decay test, either in the form of experimental or numerical simulation, is highly recommended to assess the resulting permeability variation in the post-failure stage.

Long-term stability of room excavation in Cobourg formation

The Cobourg limestone at depth is generally stronger and stiffer than the one analyzed in the laboratory triaxial tests, since the samples came from a quarry. The calibrated material properties and creep failure criterion as previously discussed are used, with the values of cohesion modified by a correction factor of 1.5 in order to adjust for this difference. The final values shown in Table 5.2 were then implemented into the modelling of the long-term stability of a single room excavated in the Cobourg limestone. Figure 5.15 shows the FE model representative of the in-situ conditions, with the room center line as the symmetric plane. The Cobourg formation of interest to this study is 30 m high and at 688 m depth. The righter most boundary, at 12.9 m, corresponds to the centre line of the pillar between two adjacent rooms. The room floor is located 4 m above the underlying Sherman Fall formation. The strength parameters cited in Table 5.3 are in the conservative end, indicating the long-term strength behaviours i.e. the crack initiation values.

In-situ stress as measured in the region consists of vertical hydrostatic stress, σ_z and horizontal stresses as followings (ITASCA, 2011): $\sigma_x = 36.7$ MPa; $\sigma_y = 28.3$ MPa; $\sigma_z = 22.5$ MPa. However, a conservative scenario was considered by assuming vertical initial stress equivalent to the overlain hydrostatic stress and isotropic horizontal stress $\sigma_x = 1.5\sigma_z$, which was consistent with the parametric settings of the FE modelling by ITASCA (2011). Roller boundary is assigned to symmetric plane, far-end side wall, and the bottom and cross-section surfaces. Initial condition for pore pressure is set equivalent to the hydrostatic pressure. The evolution of damage, pore pressure, and the displacement are investigated and analysed as shown in Figs. 5.16-5.18.

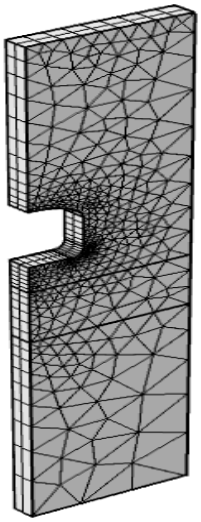

Figure 5.15 FEM model for excavated emplacement room in Cobourg formation

Table 5.3 Model constants for HM coupled modelling of repository for DGR

Unit	E (GPa)	v	c (MPa)	ϕ (^{o})	α (m^{-1})	χ_f (Pa^{-1})
Cobourg limestone	35	0.31	time-dependent	32	0.05	1×10^{-9}
Weak Sherman Fall	10.74	0.1	3	32	0.1	1×10^{-9}
Sherman Fall	16.8	0.31	4.27	34.7	0.1	1×10^{-9}

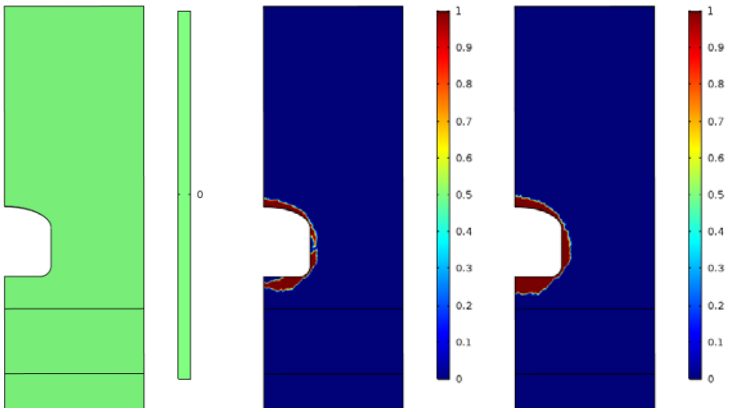

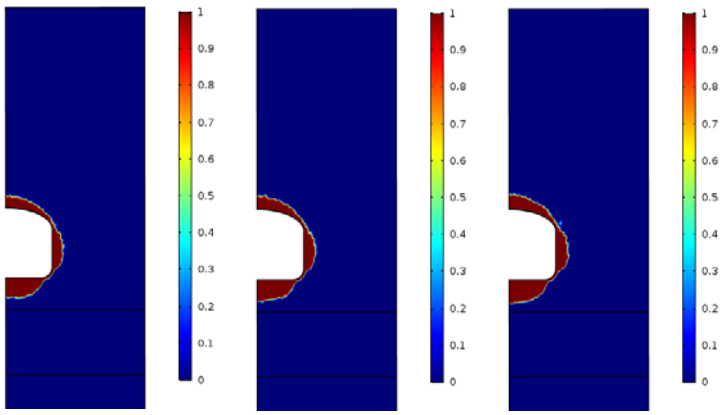

Figure 5.16 Distribution of plastic damage zone (T=0, 1 month, 1, 10, 100, 1000 years)

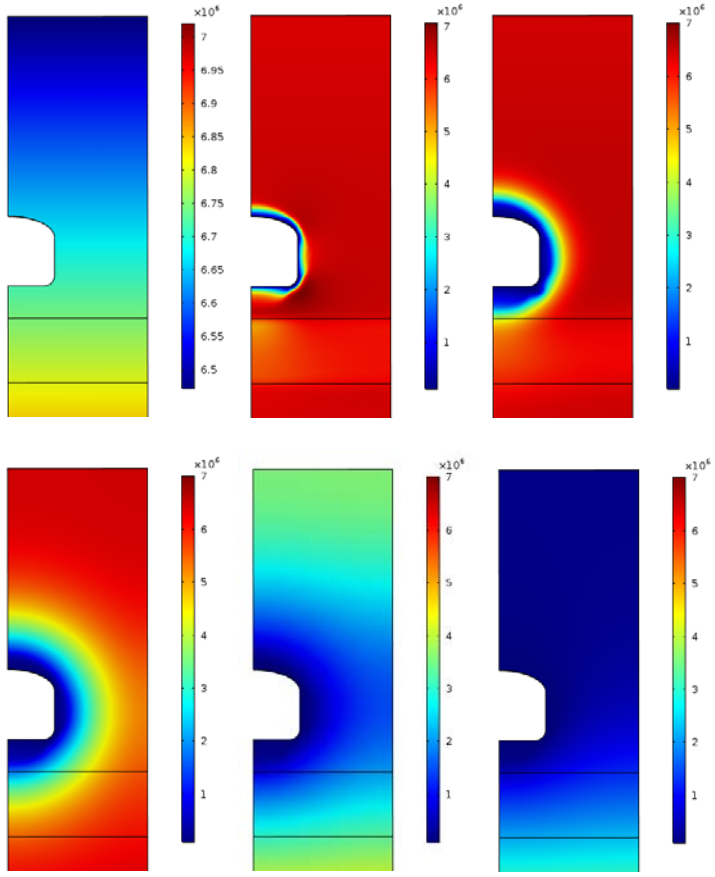

Figure 5.17 Contour of pore pressure distribution (T=0, 1 month, 1, 10, 100, 1000 years)

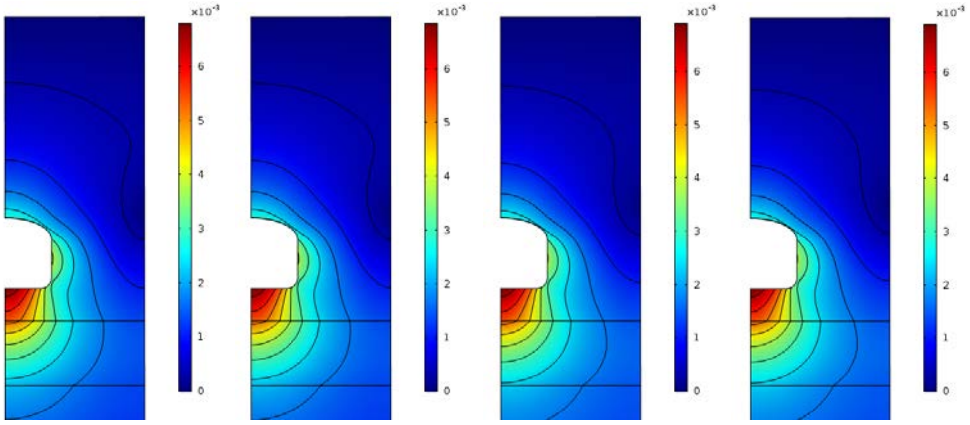

Figure 5.18 Contour of displacement (T=1 month, 1, 100, 1000 years)

The modelling leads to the following findings:

- HM coupling is weak for Cobourg limestone.
- Damage is mainly caused by time-dependent creep failure under conditions above the CI threshold.
- Failure mainly occurs in the room floor and almost penetrates through the Cobourg formation. Damage also happens on the ceiling. This phenomenon agrees with our previous HM coupled modelling study on the same site.
- The upper layer of Weak Sherman Fall is not found to be mechanically damaged as a result of poroelastic impact by dissipation of pore pressure. The disturbance mainly takes the form of deformation/displacement.
- Displacement is mainly observed in vertical direction, in Cobourg limestone formation, and at the zones beneath the repository floor.

5. Conclusions

- In this study, we successfully verified the HM coupled models, the material properties, the damaged permeability, the long-term mechanical and rheological strength as well as the numerical schemes.
- The weak HM coupling or poroelastic response of Cobourg limestone is found to pose limited threat to the propagation of the EDZ.
- EDZ is densely concentrated on the room floor, distributed at the ceiling in a thin layer, but does not exist in the side wall. This finding may be helpful to the structural engineers to better design and maintain the long-term stability of the emplacement room.
- We found that low permeable rocks with low porosity always have extremely low Biot's coefficient. This ensures validity of the pulse decay permeability test method to be applied even under complex stress and loading conditions for granite, shale, marble and argillaceous clay rocks.

- Biot's coefficient is recommended to be derived from the experimental data on Skempton's B value, due to the fact that the bulk modulus of the solid skeleton varies with effective mean stress and mineral constituents.
- It remains unknown to us if the mechanical and rheological properties obtained under compressive loading conditions are applicable to an extensile unloading circumstance. Therefore, it is recommended for future research projects on DGR related topics to consider the experimental studies on mechanical, hydraulic and rheological properties of the host rock under extensile unloading conditions.

Appendix: Discussion on level of compressibility of the pore fluid

Problem of $\chi_f > b_f$ in modelling of the pulse decay behaviours

Why $\chi_f > b_f$

The simulation of Fig. 5.A1 shows strong poroelastic effect induced by compressive loading. The magnitude of X_f affects the pulse decay curve significantly. In case $\chi_f <= 4\times10^{-9}$, the pulse on upper boundary increases with time due to outward fluid flux from the core of rock sample. Only when $\chi_f >= 4\times10^{-8}$, a declining trend is observed, suggesting a lower pore pressure in rock than the boundary pressure. It is thus believed that pore fluid might not be fully saturated because of its speculated high compressibility.

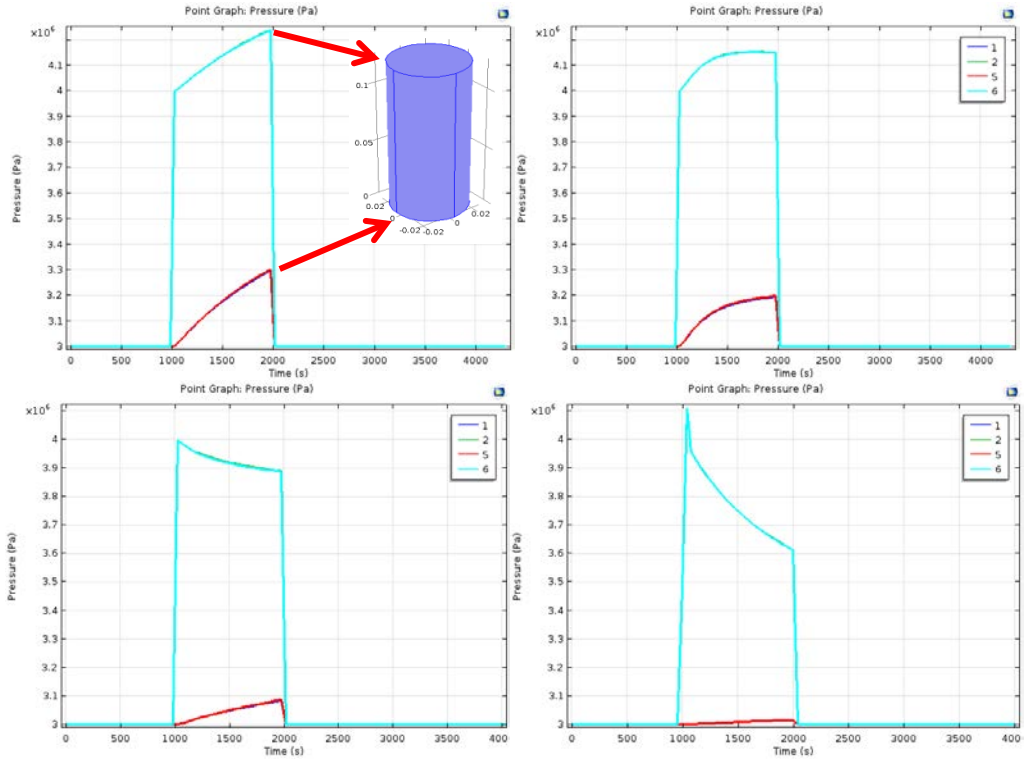

Figure 5.A1 Development of pulse pressure at source and exit reservoirs for cases with various pore fluid compressibilities ($\chi_f = 4\times10^{-10}$, 4×10^{-9}, 4×10^{-8} and 4×10^{-7}, respectively; $\alpha = 0.8$; $b_f = 1\times10^{-9}$)

Effect of reservoir compressibility

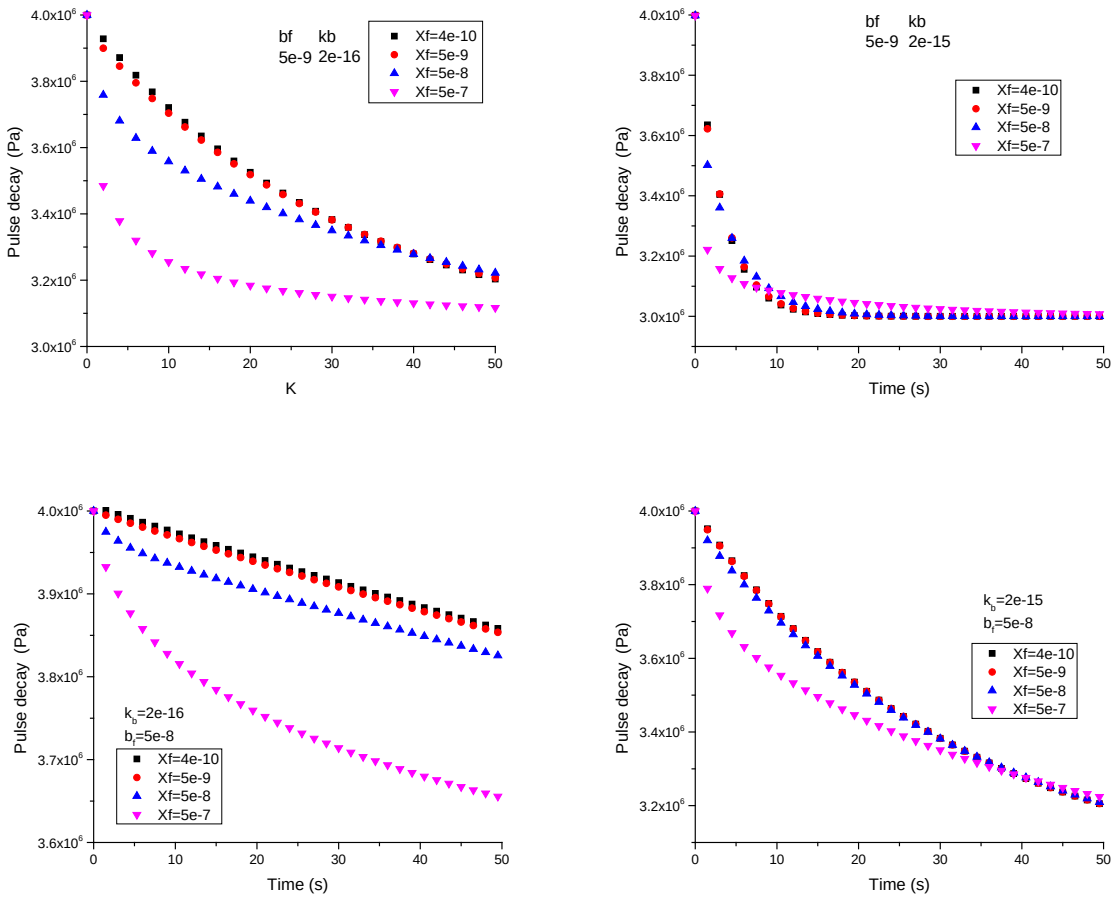

Figure 5.A2 Variation of pulse decay curves with elapsed time for different parametric settings

As shown in Fig. 5.A2, when $\chi_f <= b_f$, the pulse decay curves agree with each other very well. When $\chi_f > b_f$, and t<10s, obvious discrepancy is observed. The pulse decay curve at later stage seems to underestimate the permeability. b_f is critical to the overall estimation of permeability.

The compressibility of pore fluid χ_f is expected to be at the magnitude of 1×10^{-7} Pa^{-1}, according to the hydraulic-mechanical coupled modelling of the triaxial test, which would otherwise lead to extremely high pore water pressure in the process of compression failure under poroelastic effect.

Note the experimental results of UofT associated with large axial strain has much lower value in peak pulse pressure, which suggests the rapid dissipation of pulse pressure in the reservoir due to either high permeability in rock sample or high compressibility in pore fluid. The author believes that there is high connectivity between reservoir and the macrocracks in proximity of the top end of the rock specimen, which is consistent with the morphology of the microscopic photo of the sample. Therefore it is viable to treat the compressibility of the reservoir fluid as equivalent in quantity to that of the pore fluid.

But, it is very likely that at later stage of the triaxial test, bubbles originally trapped inside the rock sample due to insufficient efforts in sample saturation, can be released out and contribute to increase of

compressibility of the source reservoir fluid. Then the bf value after CD threshold is reached should theoretically increase substantially in amount.

Effect of initial pore pressure

In this case, the intrinsic permeability k_s is homogeneous in rock mass, and is equal to the boundary permeability kb. We only examine the effect of initial pore pressure on the pulse decay behaviour as shown in Fig. 5.A3. As for the pore fluid compressibility, we set initial saturation degree S_0=0.5, and residual liquid saturation degree S_{sl}=0.9. This yields to an effective compressibility $\chi_f=2.7\times10^{-7}$ when effective saturation degree S_e=1.0.

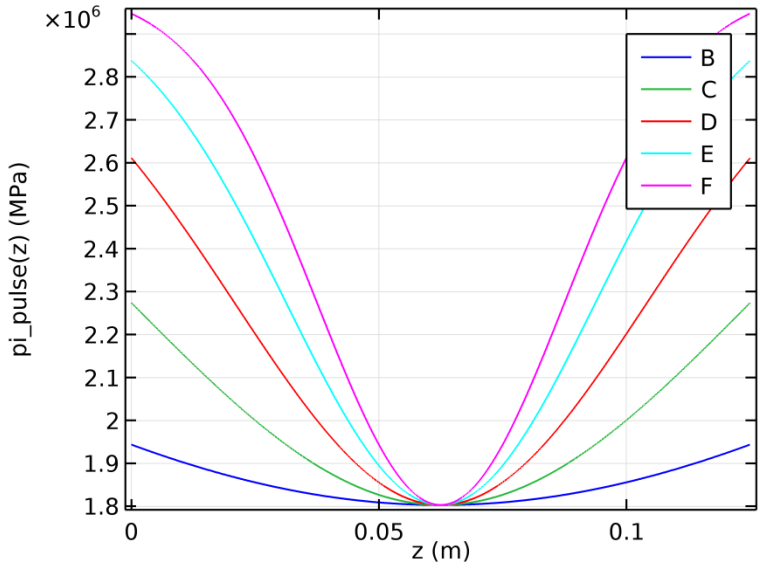

Figure 5.A3 Initial pore pressure distribution with depth z for various simulation cases (#B-#F)

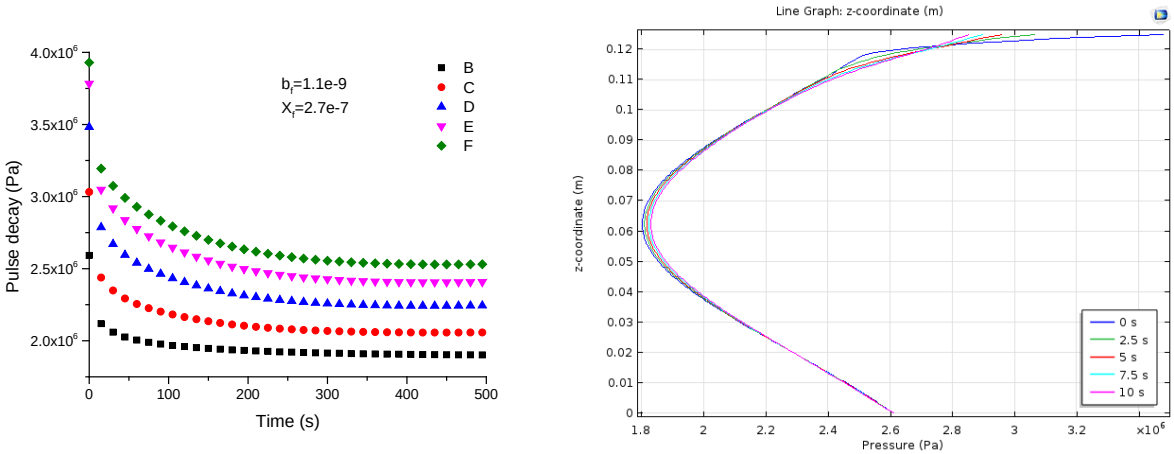

Figure 5.A4 Modelled pulse decay curves and vertical pore pressure distribution in rock ($\chi_f = C_m$; $b_f=1.11\times10^{-9}$; $k_s=k_b=1\times10^{-17}$)

It is shown in Fig. 5.A4 that, the less compressible pore fluid ($\chi_f = b_f$) equilibrates the pore pressure quickly with the outside boundary condition, while the highly compressible pore fluid ($\chi_f = C_m = 200 * b_f$) needs much longer time to equilibrate the pore pressure with the boundary condition. Using the analytical solution to estimate the permeability at reservoir-rock boundary yields very good agreement with input parameter, with discrepancy less than 60 %. It is noted that the data of pulse pressure within the beginning 10 s were not included in the regression analysis. Detailed discussion on this methodology will be given below.

Underpressure inside rock specimen will not significantly induce large discrepancy in permeability estimation, only in case of higher value in compressibility of pore fluid. But even pore pressure distribution turns out to cause several times of magnitude in the estimated permeability, which is mainly caused by the difference in pore fluid compressibility. This discrepancy would become much more significant in quantity if a rigorous boundary condition for the outlet reservoir pressure is applied in the curve fitting.

The underpressure in rock as initial condition for pulse decay test makes it extremely difficult to estimate the permeability by regression method using the analytical solution. Generally speaking, the pore fluid compressibility (not the reservoir fluid compressibility) has to be used in the analytical solution to estimate permeability when outlet boundary pressure is constrained in curve fitting by regression method. Instead, if only the reservoir fluid compressibility is available, a free regression method is recommended for the curve fitting, without constraint on the outlet reservoir pressure. This approach although will cause error in the results, the difference can be controlled to be less than one order of magnitude.

Advantages of $X_f = b_f$

UofT has calibrated the reservoir fluid compressibility as 1.11×10^{-9} Pa^{-1}. Assume this parameter maintains this level without any perturbation from the triaxial test (i.e. no air bubble was released or migrated into the source reservoir). We have the following simulation results. Figure 5.A5 shows the effect of permeability on the trend of pulse decay curves. More permeable boundary and less compressible pore fluid are found to dissipate reservoir fluid pressure more rapidly. The estimated permeability is also found to be very close to the modelling input parameter.

Figure 5.A6 shows the influence of initial pore pressure. Underpressure seems to get equilibrated with the boundary condition quickly after 10 seconds since the pulse was applied. The pulse decay curves in the source reservoir were found to be consistent in shape, regardless of the magnitude of both the initial pore pressure and the boundary fluid pressure.

After comprehensive simulation attempts with various combination of parametric settings, it is concluded that it is only possible to reproduce the experimental results on pulse decay curves by setting equivalent or less compressible pore fluid, i.e. $\chi_f <= b_f$.

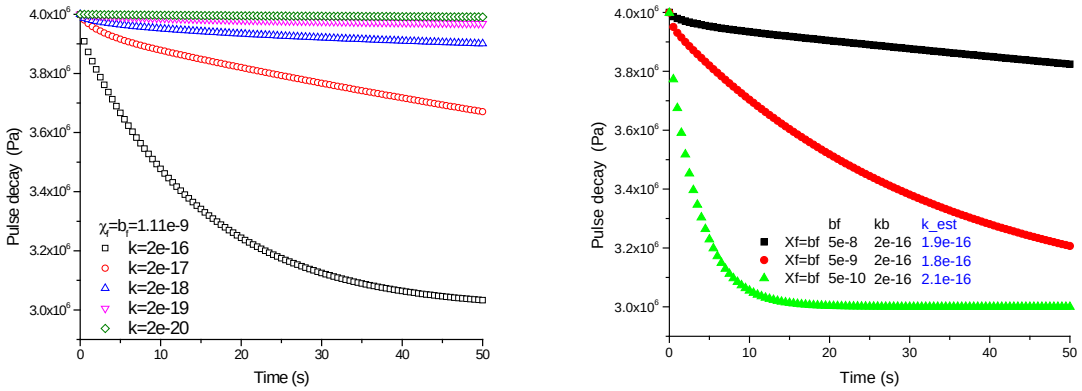

Figure 5.A5 Modelled pulse decay curves with equivalent compressibility between pore fluid and reservoir fluid (left, effect of permeability; right, effect of reservoir compressibility)

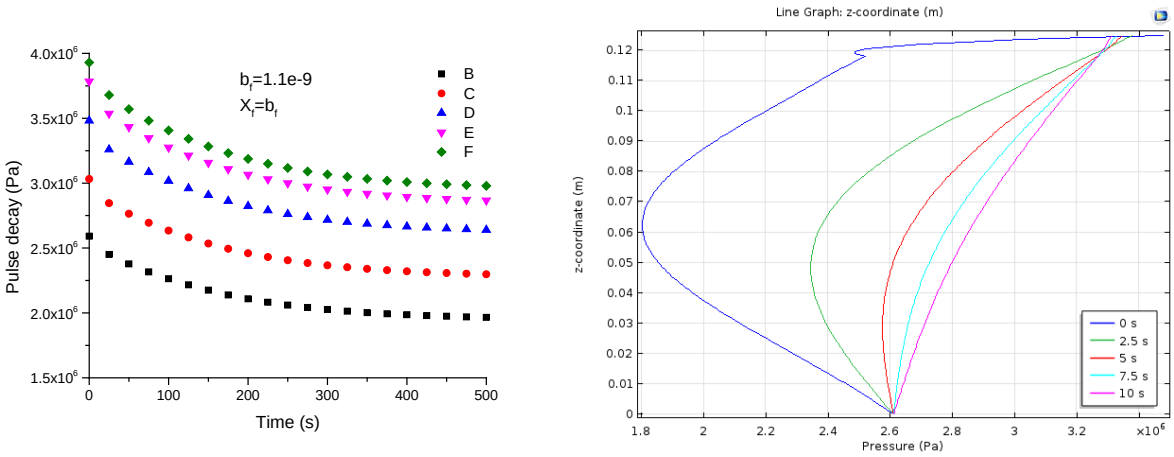

Figure 5.A6 Modelling results with underpressure initial conditions (left, pulse decay curves; right, transient pore pressure response at beginning of test) ($\chi_f = b_f = 1.11\times10^{-9}$; $k_s = k_b = 1\times10^{-17}$, initial pore pressure as shown in Fig. A3)

References

Aifantis, E.C., 2011. On the gradient approach – Relation to Eringen's nonlocal theory. International Journal of Engineering Science, 49(12): 1367-1377.

Alam, M.M., Fabricius, I.L. and Christensen, H.F., 2012. Static and dynamic effective stress coefficient of chalk. GEOPHYSICS, 77(2): L1-L11.

Antolovich, S.D. and Armstrong, R.W., 2014. Plastic strain localization in metals: origins and consequences. Progress in Materials Science, 59: 1-160.

Assefa, S., McCann, C. and Sothcott, J., 2003. Velocities of compressional and shear waves in limestones.

Geophysical Prospecting, 51(1): 1-13.
Bažant, Z.P. and Jirásek, M., 2002. Nonlocal Integral Formulations of Plasticity and Damage: Survey of Progress. Journal of Engineering Mechanics, 128(11): 1119-1149.
Bažant, Z.P. and Pijaudier-Cabot, G., 1989. Measurement of Characteristic Length of Nonlocal Continuum. J. Eng. Mech., 115(4): 755-767.
Biot, M.A., 1973. Nonlinear and semilinear rheology of porous solids. Journal of Geophysical Research, 78(23): 4924-4937.
Bishop, A.W. and Eldin, G., 1950. Undrained Triaxial Tests on Saturated Sands and Their Significance in the General Theory of Shear Strength. Géotechnique, 2(1): 13-32.
Brace, W.F., Walsh, J.B. and Frangos, W.T., 1968. Permeability of granite under high pressure. J. Geophys. Res., 73(6): 2225-2236.
Brantut, N., Heap, M.J., Baud, P. and Meredith, P.G., 2014. Mechanisms of time-dependent deformation in porous limestone. J. Geophys. Res. Solid Earth, 119(7): 5444-5463.
Brown, R.J.S. and Korringa, J., 1975. ON THE DEPENDENCE OF THE ELASTIC PROPERTIES OF A POROUS ROCK ON THE COMPRESSIBILITY OF THE PORE FLUID. Geophysics, 40(4): 608-616.
Cosenza, P., Ghoreychi, M., de Marsily, G., Vasseur, G. and Violette, S., 2002. Theoretical prediction of poroelastic properties of argillaceous rocks from in situ specific storage coefficient. Water Resources Research, 38(10): 25-1-25-12.
Fleck, N.A., Muller, G.M., Ashby, M.F. and Hutchinson, J.W., 1994. Strain gradient plasticity: Theory and experiment. Acta Metallurgica Et Materialia, 42(2): 475-487.
Forest, S., 2008. Some links between Cosserat, strain gradient crystal plasticity and the statistical theory of dislocations. Philosophical Magazine, 88(30-32): 3549-3563.
Fredlund, D.G., Rahardjo, H. and Fredlund, M.D., 2012. Unsaturated Soil Mechanics in Engineering Practice. Wiley.
Gassmann, F., 1951. Elastic waves through a packing of spheres. Geophysics, 16(4): 673.
Ghazvinian, E., 2015. Fracture initiation and propagation in low porosity Crystalline rocks: implications for excavation damage Zone mechanics, Queen's University, Kingston, ON, Canada.
Green, D.H. and Wang, H.F., 1986. Fluid pressure response to undrained compression in saturated sedimentary rock. Geophysics, 51(4): 948-956.
Gunzburger, Y., 2010. Stress state interpretation in light of pressure-solution creep: Numerical modelling of limestone in the Eastern Paris Basin, France. Tectonophysics, 483(3-4): 377-389.
Gutierrez, M., Katsuki, D. and Tutuncu, A., 2015. Determination of the continuous stress-dependent permeability, compressibility and poroelasticity of shale. Marine and Petroleum Geology, 68: 614-628.
Haghighat, E. and Pietruszczak, S., 2015. Constitutive modelling of Tournemire shale.
Hart, D., 2000. Laboratory measurement of poroelastic constants and flow parameters and some associated phenomena, University of Wisconsin-Madison.
Hasanov, A., Batzle†, M. and Prasad, M., 2015. The determination of reservoir poroelastic properties from oscillating pore pressure method, SEG Technical Program Expanded Abstracts 2015. Society of Exploration Geophysicists.
Hashin, Z. and Shtrikman, S., 1963. A variational approach to the theory of the elastic behaviour of multiphase materials. Journal of the Mechanics and Physics of Solids, 11(2): 127-140.
Jirásek, M., 2002. Objective modeling of strain localization. Revue Française de Génie Civil, 6(6): 1119-1132.
Le Guen, Y., Renard, F., Hellmann, R., Brosse, E., Collombet, M., Tisserand, D. and Gratier, J.P., 2007. Enhanced deformation of limestone and sandstone in the presence of high P co 2 fluids. J. Geophys. Res., 112(B5).
Li, Z., Nguyen, S., Su, G., Labrie, D. and Barnichon, J.D., 2016. Development of a viscoelastoplastic model

for a bedded argillaceous rock from laboratory triaxial test. Canadian Geotechnical Journal, In press.
Liang, Y., Price, J.D., Wark, D.A. and Watson, E.B., 2001. Nonlinear pressure diffusion in a porous medium: Approximate solutions with applications to permeability measurements using transient pulse decay method. J. Geophys. Res., 106(B1): 529-535.
Lion, M., Skoczylas, F. and Ledésert, B., 2004. Determination of the main hydraulic and poro-elastic properties of a limestone from Bourgogne, France. International Journal of Rock Mechanics and Mining Sciences, 41(6): 915-925.
Lockner, D.A. and Stanchits, S.A., 2002. Undrained poroelastic response of sandstones to deviatoric stress change. J. Geophys. Res., 107(B12): ETG 13-1-ETG 13-14.
Maleki, K. and Pouya, A., 2010. Numerical simulation of damage–Permeability relationship in brittle geomaterials. Computers and Geotechnics, 37(5): 619-628.
Mesri, G., Adachi, K. and Ullrich, C.R., 1976. PORE-PRESSURE RESPONSE IN ROCK TO UNDRAINED CHANGE IN ALL-ROUND STRESS. Geotechnique, 26(2): 317-330.
Meyers, M.A., Mishra, A. and Benson, D.J., 2006. Mechanical properties of nanocrystalline materials. Progress in Materials Science, 51(4): 427-556.
Nguyen, T.S. and Le, A.D., 2015. Development of a constitutive model for a bedded argillaceous rock from triaxial and true triaxial tests 1. Canadian Geotechnical Journal, 52(8): 1072-1086.
Nguyen, T.S. and Selvadurai, A.P.S., 1995. Coupled thermal-mechanical-hydrological behaviour of sparsely fractured rock: Implications for nuclear fuel waste disposal. International Journal of Rock Mechanics and Mining Sciences & Geomechanics Abstracts, 32(5): 465-479.
NWMO, 2011. Descriptive Geosphere Site Model, Intera Engineering Ltd.
Paraskevopoulou, C., Perras, M., Diederichs, M., Amann, F., Low, S., Lam, T. and Jensen, M., 2015. Observations for the long-term behavior of rocks based on laboratory testing, EUROCK15 64th Geomechanics Colloquium.
Pietruszczak, S. and Haghighat, E., 2015. Modeling of Fracture Propagation in Concrete Structures Using a Constitutive Relation with Embedded Discontinuity. Studia Geotechnica et Mechanica, 36(4).
Pijaudier-Cabot, G. and Grégoire, D., 2014. A review of non local continuum damage: Modelling of failure? Networks and Heterogeneous Media, 9(4): 575-597.
Ramos da Silva, M., Schroeder, C. and Verbrugge, J.C., 2010. Poroelastic behaviour of a water-saturated limestone. International Journal of Rock Mechanics and Mining Sciences, 47(5): 797-807.
Robertson, E.C., 1960. Chapter 8: Creep of Solenhofen Limestone Under Moderate Hydrostatic Pressure, Geological Society of America Memoirs. Geological Society of America, pp. 227-244.
Roylance, D., 2001. Engineering Viscoelasticity. In: M.I.o. Technology (Editor).
Schuurman, I.E., 1966. The Compressibility of an Air/Water Mixture and a Theoretical Relation Between the Air and Water Pressures. Géotechnique, 16(4): 269-281.
Selvadurai, A.P.S. and Carnaffan, P., 1997. A transient pressure pulse method for the mesurement of permeability of a cement grout. Canadian Journal of Civil Engineering, 24(3): 489-502.
Selvadurai, A.P.S. and Ichikawa, Y., 2013. Some aspects of air-entrainment on decay rates in hydraulic pulse tests. Engineering Geology, 165: 38-45.
Selvadurai, A.P.S. and Najari, M., 2016. Isothermal Permeability of the Argillaceous Cobourg Limestone. Oil & Gas Science and Technology – Revue d'IFP Energies nouvelles, 71(4): 53.
Simo, J.C. and Hughes, T.J.R., 1998. Computational Inelasticity. Springer.
Wang, H.F., 1993. Quasi-static poroelastic parameters in rock and their geophysical applications. Pure and Applied Geophysics PAGEOPH, 141(2-4): 269-286.
Yang, J., 2005. Pore pressure coefficient for soil and rock and its relation to compressional wave velocity. Geotechnique, 55(3): 251-256.
Zhang, C.L., 2014. Investigation of gas migration in damaged and resealed claystone. Geological Society,

London, Special Publications, 415(1): 75-93.
Zimmerman, R.W., Somerton, W.H. and King, M.S., 1986. Compressibility of porous rocks. J. Geophys. Res., 91(B12): 12765-12777.
ITASCA, 2011. Long-term geomechanical stability analysis. Technical report. NWMO DGR-TR-2011-17.

Chapter 6 Application of the Diffuse Double Layer theory to the characterization of the fundamental properties of bentonite sealing materials

Summary

Characterization of the fundamental properties of expansive soil always involves different experimental strategies and methods. In this study, a unified theoretical framework was developed to address the uniqueness of various fundamental parameters behind the discrepancy in characterizing techniques. The classical Poisson-Boltzmann (PB) equation for diffuse double layer (DDL) was modified by taking into account the mass balance principle in order to reproduce the experimental results. The swelling pressure, suction and permeability of expansive soil (i.e. MX-80) were separately analyzed, discussed and calibrated against test data with the PB equation based models. Influences of dry density of soil and salinity of pore fluid on the swelling pressure, water retention curve, compression curve and permeability of bentonite clay were all successfully modelled. For unsaturated expansive soil, the air/water interface (meniscus) which was discovered to possess positive electric potential is believed in this study to be attracted by the negatively charged clay surface. This electrostatic attractive pressure in unsaturated porous media, which was discussed for the first time, was comparable to the experimentally observed matric suction. Using analytical approximate solution of the attractive pressure between asymmetrically charged planes, the water retention curve of bentonite was linearized and modelled with excellent agreement. On the other hand, flow in DDL predominated pore space of saturated bentonite was found to be governed by both viscosity and electro-osmosis, coupling of which results in electro-viscous retardation to the pressure driven flow. Using PB equation and the governing equation for electrokinetic flow, the permeability of compacted bentonite at various dry densities and salinities were numerically evaluated and compared against the reported test data with satisfying agreement. It is shown that DDL greatly determines almost every aspect of the bentonite's hydraulic-mechanical behaviour and the versatile DDL theories are sufficient to model these behaviours.

1. Introduction

Bentonite is a water-sensitive clay material that can experience large volumetric change at different water content. The most active component is the montmorillonite mineral, which hydrates into colloid of dispersive nature in contact with water. Bentonite finds important applications in various fields, e.g. as adsorbent in wastewater treatment, as a major mixing component in materials used for waste containment liners, and for the sealing of emplacement rooms, tunnels and shaft in deep geological repositories for the disposal of radioactive waste. The abundant surface charges and strong colloidal properties of bentonite are believed to be responsible for their swelling and shrinkage behaviour. The

diffuse double layer theory (DDL) has been found suitable for the explanation of this behaviour. In particular, the use of the DDL theory in order to predict the maximum swelling pressure and maximum swelling strain proves to be very successful (Komine and Ogata 2003; Tripathy et al. 2004).

Properties that are critical to the assessment of the hydraulic behaviour of bentonite are in most cases empirically determined and there is a need for theoretical interpretation of the empirical relations. For instance, the water retention curve of bentonite is usually estimated by empirical relationships e.g. van Genuchten, Brooks and Corey etc. The swelling pressure of bentonite under unsaturated condition cannot be analyzed by the classical DDL theory because saturation is the condition for its validity. The saturated permeability is another parameter that is usually estimated using empirical relations. New perspectives that were obtained from recent progress in physical chemistry on the properties of the air-water interface and electrokinetic flow in DDL dominant pore space enable us to address the above questions from a more fundamental perspective.

Matric suction is ubiquitous in porous media. This suction is widely believed to result from the capillary effect of various micro/macropores. Water meniscuses are formed when soil is partially saturated. The curved meniscus retains water from draining out due to surface tension forces. As for clay minerals, there are additional chemo-osmotic effects that can largely enhance the water retention capacity. Some clay minerals show a strong tendency to absorb thick layers of water upon the particle surface and even in between crystal lattices. In such cases, DDL theory has been widely applied to explain the swelling behaviours. Fundamentally, DDL is formed upon the surface of colloids with intrinsic electric charges (see Figure 6.1) in the presence of water. Because of the intrinsic electric charge on the surface (negative for most of clay minerals), the cations in water will be attracted to the vicinity of the solid surface while the anions will be expelled away towards the bulk solution. Accompanied with the strong solvation energy of these ions, water molecules will be bounded closely to the solid surface through the formed diffuse double layer.

DDL theory is based on Boltzmann's thermodynamic assumption (Mitchell and Soga, 1976). It also involves fundamental properties, e.g. temperature and salt concentration that can be determined by experiments. However, some other parameters, e.g. electric potential of the solid surface or the midplane between clay plates, are difficult to determine experimentally (Tripathy et al. 2004). Besides, diffuse layer theory ignores the influence of the Stern layer (it accounts for counter ions' closest approach to the charged surface in the magnitude of the ionic radius) on surface electric potential distribution, and thus may overestimate the repulsive force between clay particles. Some recent studies have taken the Stern layer into account (Tripathy et al. 2014). Because of these shortcomings, some researchers have thus criticized the applicability of diffuse layer theories in the prediction of swelling pressure of highly compacted bentonite due to the discrepancy between modelling and experimental results (SKI report 1998). After careful examination of the available literature, we found that a significant principle of mass conservation for dissolvable ions in expansive soil was missing from these previous studies on DDL theory. By taking into account of the mass conservation principle, we successfully demonstrated the versatile applicability of DDL theory for the modelling of swelling of bentonite soil.

This study aims to apply the classical DDL theory to the analysis of swelling pressure of saturated bentonite, water retention curve of unsaturated bentonite, and the hydraulic conductivity of saturated bentonite in presence of pore fluid with various degrees of salinity. Either analytical solution, semi-analytical solution or numerical solution is used to study the variation of these fundamental properties of bentonite with density or pore ratio. The modelling is further calibrated with a large collection of experimental results on a typical bentonite of MX-80 that are currently considered for application in nuclear waste disposal in several countries in the world. Finally, a unified theoretical framework is developed for the characterization of different fundamental properties of bentonite. Based on the derived models, the water retention curve, compressibility, permeability and swelling pressure of MX-80 bentonite are predicted for subsequent hydraulic-mechanical coupled modelling of infiltration and mock tests that are ongoing at Queen's University.

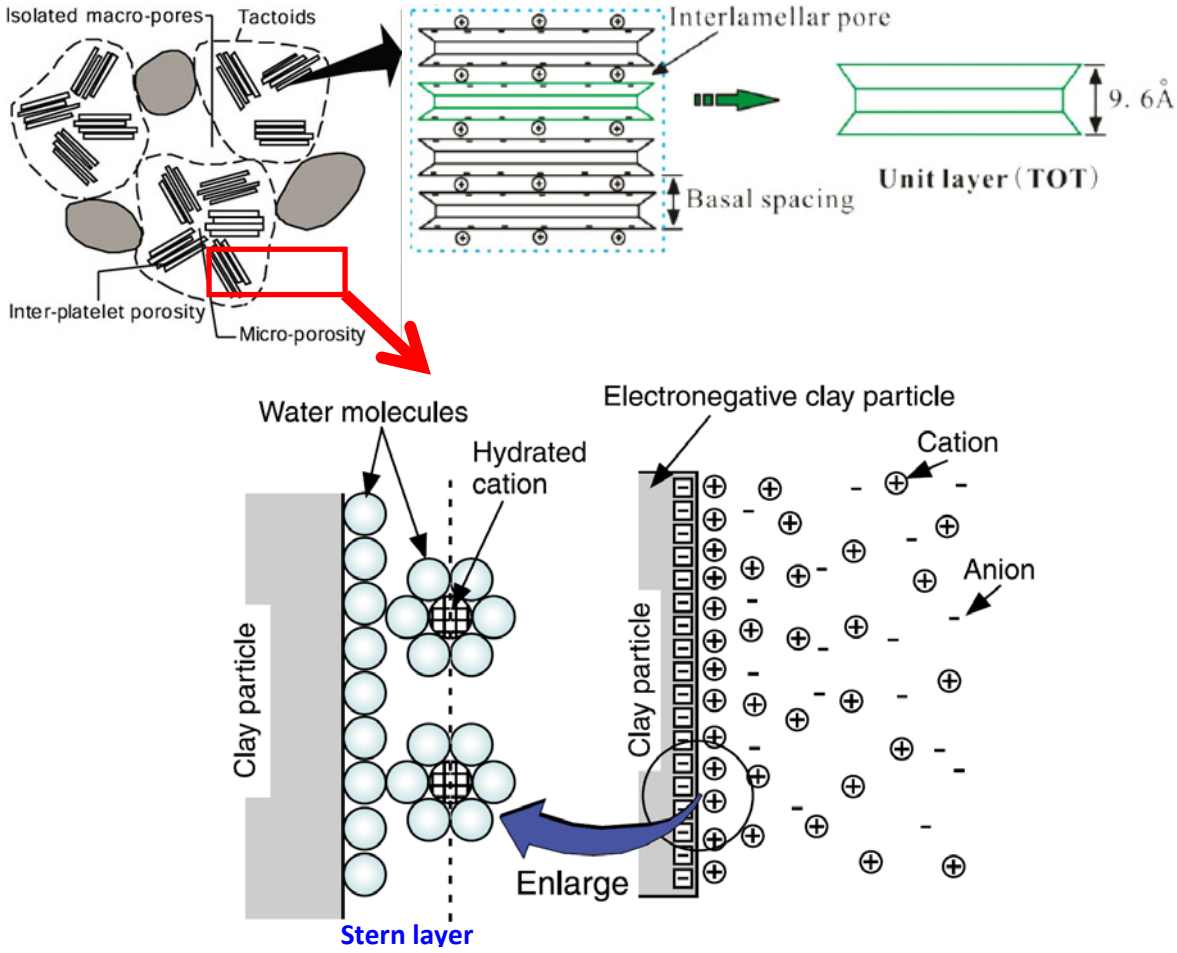

Figure 6.1 Schematic illustration of the diffuse double layer problem for hydrated bentonite. (Komine and Ogata 2003; Ye et al. 2013)

2. Swelling of bentonite

Compacted expansive clays swell due to two mechanisms: the crystalline swelling and the diffuse double-layer swelling (Rao et al. 2013; Ye et al. 2013) as shown in Fig. 6.1. Crystalline swelling is driven

by adsorption of water molecules between montmorillonite unit layers with separations of 10–22 Å which is regarded as the basal spacing of crystal lattice. Diffuse double layer swelling occurs as surface hydration at larger separations [>22 Å]. After the adsorption of maximum number of hydrates, surface hydration becomes less significant and diffuse double-layer repulsion becomes the governing swelling mechanism (Ye et al. 2013).

The swelling of compacted clay always develops in sequence of time and reduces with increase in solute concentration in bulk solution. The nanopores and micropores are believed to have much larger osmotic suction and matric suction than the macropores. In case of hydrating with low concentration solutions, crystalline swelling takes place first with the swelling pressure reaching its first peak. Followed by the swelling of aggregates, this induces the collapse of the soil skeleton under confined conditions, which is characterized by the thick quasicrystals splitting into thinner ones and filling into the macro-pores (inter-aggregate pores), resulting in the dropping of the swelling pressure. The following delamination of clay stacks contribute to the growth of diffuse double layer in quantity, and thus give rise to a subsequent gradual increase of swelling pressure (Ye et al. 2013). This softening behaviour of swelling pressure has been well explained by the extended BBM theory using the same concept of duality in pore structures (Alonso et al. 2011).

Also of importance, is the way water will be distributed amongst different level of pore spaces, i.e. the micropore, the macropore or the basal space. The sizes of macropore and micropore of compacted MX-80 bentonite pellets are reported to be in a range of 0.6-300 μm and 4-100 nm, respectively. The peak of the bimodal pore size distribution is found at 1.5 μm and 12-20 nm, respectively (Seiphoori et al. 2014). Sand-bentonite mixture is reported to have much larger pore size than MX-80, with the bimodal peaks of the former respectively at 200 μm and 300 nm (Romero, 2013). The bimodal pattern of pore structure can be turned into a mono-pattern by simple saturation in a wetting-drying cycle (Seiphoori et al. 2014), while the fraction of macropore (>1 μm) reduces significantly from 15% to less than 1%.

Kaufhold et al. (2010) experimentally investigated the specific surface area (SSA) of various bentonite soils by N_2BET test and found that bentonites with a low SSA (e.g., <20 m^2/g) consist of low-microporous quasi-crystals with almost 100 layer per stack or more when soil is in dry condition. This is in very good agreement with the reported stacking number of MX-80 when suction surpasses the air entry value (Seiphoori et al. 2014). Taking all the above information into account enables us to calculate the contribution of macropores to the total porosity. Assume a simple packing of solid sphere (radius of r) to be representative of the clay, then the specific surface area of the packing can be calculated as ($\mathrm{SSA} = \frac{4\pi r^2}{G_S \frac{4}{3}\pi r^3}$): SSA=0.02, 20 and 200 m^2/g for particles with diameter of 100 μm, 100 nm and 10 nm. Therefore the observed SSA of bentonite at 20 m^2/g is equivalent to the packing of clay particles in diameter of 100 nm, which is equivalent to 100 stacks of montmorillonite unit layers, corresponding exactly to the reported speculation (Seiphoori et al. 2014; Kaufhold et al. 2010). Using the experimental results of pore size distribution of as-compacted bentonite pellets, we may be able to predict the SSA value specifically at various saturations, which may help to explain the discrepancy in permeability modelling results from the test data to the end of this study.

Komine and Ogata (1999) observed that the voids in the material were completely filled by swelling deformations of hydrated bentonite using a scanning electron microscope. By isolating the expansive mineral, i.e. montmorillonite, from the rest of soil components, Komine and Ogata (2003) proposed the formula of the so called "effective montomorillonite dry density" to characterize the swelling pressure and swelling strain of bentonite with various proportion of sand/bentonite mixture. This relationship was identical to that adopted by Man and Martino (2009) in analysis and normalization of swelling behaviours of bentonites.

3. Modelling of swelling pressure

Poisson-Boltzmann equation

In the classical DDL theory, the Poisson's equation of electrostatic is combined with Boltzman's law in order to describe the electric field in the DDL (Mitchell and Soga 1976). The Poisson's equation in SI units is:

$$\nabla^2\psi = -\frac{\rho}{\varepsilon_0\varepsilon_r} \quad (1)$$

where ψ is the electric potential (V), ρ is the charge density (C/m^3), ε_0 is the vacuum dielectric permittivity (F/m) and ε_r is the relative dielectric constant of the medium (ε_r=80 for water).

The concentration of charged ions in an electrolyte is related to the electric potential by the Boltzmann law, which states that the density of a charged particle is proportional to the exponential of the potential. By Boltzmann law we can write the concentration as

$$c = c_0 e^{-ze\psi/k_B T} \quad (2)$$

where c is the transient solute number concentration (1/m^3) which reads as

$$c = N_A * C \quad (3)$$

where N_A is the Avogadro constant (6.02214086 × 10^{23} mol^{-1}) and C is the molar concentration (mole/m^3); c_0 is the bulk solute concentration in infinite distance from colloidal surface, e is the elementary charge (e= 1.60217662 × 10^{-19} coulombs), k_B is the Boltzmann constant (1.38 × 10^{-23} m^2 kg s^{-2} K^{-1}), z is ionic valence (either plus or minus) and T is the absolute temperature (K). Assume a solution of balanced 1:1 chemical species, the total density consists of two components, i.e. the cationic part and the anionic part. Therefore the charge density is given by:

$$\rho = \sum ez_i c_i = \sum ez_i c_{i0} e^{-z_i e\psi/k_B T} \quad (4)$$

Assuming a one dimensional model, the Poisson-Boltzmann (PB) equation reduces to

$$\frac{\mathrm{d}^2}{\mathrm{d}y^2}\psi = -\frac{e}{\varepsilon_0\varepsilon_r}\sum z_i c_{i0} e^{-z_i e\psi/k_B T} \quad (5)$$

Using the following dimensionless potential ϕ,

$$\phi = \frac{ze\psi}{k_B T} \tag{6}$$

and assuming a 1:1 electrolyte with valence of 1, the PB equation can be rewritten in 1-D form as

$$\frac{\mathrm{d}^2}{\mathrm{d}y^2}\phi = -\frac{e^2 c_0}{\varepsilon_0 \varepsilon_r k_B T}\left(e^{-\phi} - e^{\phi}\right) = \frac{2e^2 c_0}{\varepsilon_0 \varepsilon_r k_B T}\sinh(\phi) \tag{7}$$

Or

$$\frac{\mathrm{d}^2}{\mathrm{d}y^2}\phi = 2 l_B c_0 \sinh(\phi) \tag{8}$$

where l_B is the Bjerrum length that can be written as

$$l_B = \frac{e^2}{\varepsilon_0 \varepsilon_r k_B T} \tag{9}$$

The Bjerrum length gives the distance between two electron charges where the interaction energy equals to $k_B T$. For salt water at room temperature (T=300 K), the Bjerrum length is l_B=0.7 and 1.4 nm, respectively for c_0=0 and 5.86 M NaCl.

Or

$$\frac{\mathrm{d}^2}{\mathrm{d}(\kappa y)^2}\phi = \sinh(\phi) \tag{10}$$

where Debye length is

$$\lambda_D = \frac{1}{\sqrt{2 l_B c_0}} \tag{11}$$

And its reciprocal κ (m^{-1}) is written as

$$\kappa = 1/\lambda_D = \sqrt{2 l_B c_0} \tag{12}$$

The boundary condition for the above equation of the DDL problem at the charged surface is:

$$\phi = \phi_0|_{y=0} \tag{13}$$

For two charged surfaces separated by a distance 2d, the second boundary condition is:

$$\frac{\mathrm{d}\phi}{\mathrm{d}y} = 0\Big|_{y=d} \tag{14}$$

When the distance between charged surfaces are very large, the second boundary condition could be approximated as:

$$\phi = 0|_{\,y=\infty} \tag{15}$$

The analytical solution to the above equation with associated boundary conditions originated from Derjaguin and Landau (1941) and subsequently revisited by Burgreen and Nakache (1964) and Levine et al. (1975). There are also a number of approximate solutions which will not be included here. Instead,

we will demonstrate a numerical solution using the finite element method (FEM) later in the discussion of the electrokinetic flow problems.

Electrostatic pressure

The repulsive pressure (or disjoining pressure according to (Derjaguin and Kusakov 1936)) due to the electrostatic interaction of charged particles can be derived from the Gibbs–Duhem relation for a two-component ideal gas system that is in equilibrium (Schuhmann, 1955)

$$V\mathrm{d}\Pi - S\mathrm{d}T - \sum N\mathrm{d}\mu = 0 \tag{16}$$

where V is the total volume (m^3), S is the entropy (J/K), T is the absolute temperature (K), N is the number of ions and μ is the chemical potential (J/kg). At constant temperature the entropy term vanishes, then we get

$$\mathrm{d}\Pi = \sum \frac{N}{V}\mathrm{d}\mu = \sum c\mathrm{d}\mu \tag{17}$$

Considering the expression for the electro-chemical potential in the form of

$$\mu = \mu^0 + k_B T\ln c + ze\psi \tag{18}$$

we can write the disjoining pressure as

$$\mathrm{d}\Pi = \sum(k_B T\mathrm{d}c + zec\mathrm{d}\psi) = \sum k_B T\mathrm{d}c + \rho\mathrm{d}\psi \tag{19}$$

where μ^0 is the reference chemical potential. The charge density ρ (C/m^3) is obtained by rearranging Poisson's equation as:

$$\rho = -\varepsilon_0\varepsilon_r\nabla^2\psi \tag{20}$$

And the ionic concentration can be differentiated from Boltzmann's law as

$$\mathrm{d}c = -\frac{c_0 ze\psi}{k_B T}e^{-ze\psi/k_B T}\mathrm{d}\psi \tag{21}$$

Note that

$$\nabla^2\psi\mathrm{d}\psi = \frac{1}{2}\mathrm{d}(\nabla\psi)^2 \tag{22}$$

Integrating the above differential equation from the infinite distance to distance d (with electric potential at ψ) towards the plane surface leads to

$$\Pi = k_B T c_0\left(e^{-\frac{ze\psi}{k_B T}} + e^{\frac{ze\psi}{k_B T}} - 2\right) - \frac{\varepsilon_0\varepsilon_r}{2}(\nabla\psi)^2 \tag{23}$$

$$\Pi = 2k_B T c_0(\cosh\frac{ze\psi}{k_B T} - 1) - \frac{\varepsilon_0\varepsilon_r}{2}(\nabla\psi)^2 \tag{24}$$

The disjoining pressure can be further written with the dimensionless potential ϕ

$$\Pi = 2k_B T c_0(\cosh\phi - 1) - \frac{\varepsilon_0\varepsilon_r}{2}\left(\frac{k_B T}{ze}\right)^2 (\nabla\phi)^2 \quad (25)$$

or

$$\Pi = 2k_B T c_0(\cosh\phi - 1) - \frac{k_B T}{2l_B}(\nabla\phi)^2 \quad (26)$$

Repulsive pressure for saturated clay

When dilute salt solution saturates the clay soil of diffuse double layer, the dimensionless electric potential at the mid-plane (ϕ_c) between adjacent clay plates will maintains the validity of the following condition

$$\nabla\phi_c = 0|_{y=d} \quad (27)$$

According to force equilibrium, the pressure Π does not vary with location in any interplanar space. Then the disjoining pressure can be reduced to the classical double layer repulsive force that is expressed as

$$\Pi = 2k_B T c_0(\cosh\phi_c - 1) \quad (28)$$

For dilute electrolyte solutions (C_0<0.1 M), it can be further written as

$$\Pi = 2RTC_0(\cosh\phi_c - 1) \quad (29)$$

where R is the ideal gas constant (R=8.314 L kPa K^{-1} mol^{-1}) and ϕ_c is the dimensionless midplane potential.

Gregory (1975) developed a "compression" approximation to the above equation and proved that it gives the closest results to the exact solution of PB equation than other approximation methods such as linear superposition approximation (LSA) and linear P-B expression. There are also significant differences in pressure-distance relationship under constant potential and constant charge conditions (Gregory 1975).

For symmetric constant charge case, the compression approximation of the exact solution of the repulsive pressure takes the form of (Gregory 1975)

$$\Pi = 2c_0 k_B T\left(\sqrt{1 + \phi_0^2\mathrm{csch}^2(\kappa d)} - 1\right) \quad (30)$$

where κ is the reciprocal of the Debye-Huckel length, d is the half distance between the charged solid surface and ϕ_0 is the dimensionless potential on the solid surface,

$$\phi_0 = \frac{ze\xi}{k_B T} \quad (31)$$

where ξ is the surface electric potential (V), namely the zeta potential that can be experimentally measured by electro-osmosis and $\xi = \psi_0$. The above equation gives the following brief relationship

$$\phi_0 = 40\xi \quad (32)$$

This method is based on the clay surface property and solute concentration in the pore fluid. The surface electric potential can be directly measured as zeta potential by various techniques, and has been intensively studied in the literature due to its significance. It differs from some previous double layer theories of Tripathy et al. (2004) and Sridharan and Jayadeva (1982) that rely on an empirical relationship between the midplane potential and the interplanar distance. Although the latter method avoids the integration of electrical potential, it introduces uncertainty in determining the midplane potential, which can only be estimated by an empirical approach as detailed in Tripathy et al. (2004).

Modified DDL theory for repulsive pressure of saturated clay

Some variations of the "compression" approximation of repulsive pressure of diffuse double layer theory by Gregory (1975) can be obtained by applying the mass balance principle for the dissolvable ions.

Mass balance

Bentonite has abundant intrinsic charges and a considerable amount of cation exchange capacity (CEC) which can be as high as 0.8 mol/kg (800 meq/kg). This large quantity of cations exists between the crystal lattices as well as the planar surfaces. CEC basically indicates the reference solute concentration, and indirectly reflects the level of swelling potential. The principle of mass balance is expected to be pertinent to bentonite soil that is soaked in DI water as its extremely low permeability ensures unlikelihood of mass leakage during transient lab tests like swelling pressure tests and water retention tests. And thus the mass balance equation of the following form is derived

$$c_b w = c_0 w_0 \quad (33)$$

where c_0 and w_0 are respectively the reference solute concentration in pore fluid and the reference gravimetric water content, and w is the transient gravimetric water content and c_b is the transient solute concentration in bulk solution. Parameter w_0 is suggested to be taken as the free swell index since this is soil-specific and is a well-recognized reference property.

Note that the above relationship is not valid for solute transport problems and needs delicate treatment in models.

Interplanar half distance

Dual level of microstructure, i.e. the macropores and micropores, has been long accepted for compacted bentonite soil (Masin and Khalili, 2015). The macropores exist between aggregates of clay particles while the micropore is present inside the clay aggregates. The extensive pore size distribution studies revealed the range of macropores as 1-100 μm for macropores and as 20-200 nm for micropores (Romero, 2013; Seiphoori et al. 2014). In contrast, the basal spacing of smectite, the major constituent of bentonite, is just less than 2 nm.

The basal spacing of bentonite is governed by both chemo-osmotic pressure and matric suction. Herbert et al. (2008) discusses the evolution of basal spacing of bentonite that generally varies between 2 and 4 layers of water molecules in spite of various concentration of salt solution from 0.5 – 3 M NaCl. X-ray diffraction analysis and neutron diffraction analysis of MX-80 bentonite shown by Seiphoori et al. (2014) suggested basal spacing of 1 – 3 layers (<2 nm) of water molecules under matric suctions from 7 MPa up to 50 MPa.

Although DDL theory proves successful in the modelling of expansive soils, it has been pointed out that at extremely small interplanar distances (d<1.5 nm, in equivalence of 2 water layers), the DDL theory will fail to predict the experimental observation because of quantum mechanics effects (Mašín and Khalili, 2016). We believe that such small interplanar distance in nanometer scale can only exist between crystal layers, namely the interlayer spacing or basal spacing. It is thus clarified here that DDL theory applies only to the voids larger than 10 nm in size exclusive of crystal basal spaces less than 2 nm.

The average interplanar half distance (d) is calculated as follows by assuming that expansive clay mineral lattices are (1) stacked in layered structure ideally, and (2) soaked in pore fluid in a homogeneous pattern

$$d * S * \gamma_w = w \tag{34}$$

where S is the specific surface area of the clay mineral (m^2/g), w is the gravimetric water content and γ_w is the unit weight of water (1000 kg/m^3). The thickness of DDLs of adjacent clay plates is no more than the interplanar half distance d. Note that *w* is the saturated water content for the analysis of swelling pressure. Later in this paper the above relationship is further applied to calculating the effective DDL thickness of unsaturated soils, where w turns to be the transient gravimetric water content. The above equation is similar in form to those applied to the modelling of swelling pressure by Tripathy et al. (2004) and Mašín and Khalili (2016).

For bentonite saturated with dilute solution, citing the Debye length

$$\kappa^{-1} = 10^{-9}\frac{0.304}{\sqrt{c_b}} \tag{35}$$

then we get

$$\kappa d = \frac{\sqrt{2 l_B c_0 w_0 w}}{\gamma_w S} = 10^9 \frac{\sqrt{c_0 w_0 w}}{0.304 \gamma_w S} \tag{36}$$

$$\Pi = 2 k_B T \frac{c_0 w_0}{w}\left(\sqrt{1 + \phi_0^2 \mathrm{csch}^2(\kappa d)} - 1\right) \tag{37}$$

For bentonite saturated with concentrated brine or saline solution, the mass balance relationship is not valid any more. The salt concentration maintains the level of the saturated value (c_0). Then

$$\kappa d = \frac{w}{\gamma_w S}\sqrt{2 l_B c_0} = 10^9 \frac{w\sqrt{c_0}}{0.304 \gamma_w S} \tag{38}$$

$$\Pi = 2k_B T c_0 \left(\sqrt{1 + \phi_0^2 \mathrm{csch}^2(\kappa d)} - 1\right) \quad (39)$$

Calibration of the model with swelling pressure and compression curve

Figure 6.2 shows the modelled results for the ρ_d-log(Π) relationship and the reported experimental data. The used model constants are shown in Table 6.1. The DDL theory can reproduce the test data with very good agreement only when the mass balance equation is taken into account. It is noted that only two parameters need to be determined, i.e. the surface electric potential ϕ_0 and the reference salt concentration c_0. The salt concentration can be regarded as experimental conditions as a known parameter. However, fitting of the test data on MX-80 bentonite with DI water reveals two distinct patterns, both of which are consistent with the observed results. The initial salt concentration is found to be either 0.001 M or 0.1 M, as shown in Table 6.1. This discrepancy might be attributed to the variation of data sources, test methods and soil types. Under similar conditions (e.g. equal surface electric potential and water content), bentonite in concentrated salt solution shows higher swelling pressure when the soil is more compact (with less w). But above a threshold value of water content, this pattern becomes reversed. This phenomenon will be discussed in detail later in the modelling of compression curve.

The dimensionless surface electric potential ϕ_0 corresponds to the real surface potential (ξ) that can be determined by electrophoresis method. It is clear that the best-fitted ϕ_0 for saline solution reduces to half of the original value for DI water, which is consistent with various experimental observations. The zeta potential of bentonite colloid varies with ionic strength and pH of the solution. The predicted zeta potential of MX-80 lies in the normal distribution range of the experimental results (-50 — -200 mV).

Table 6.1 DDL model constants for the swelling pressure calculation

Parameter	DI-1	DI-2	Saline	Unit
ϕ_0	8	8	5	
c_0	0.001	0.1	3	M
w_0*	13	13	--	
ξ**	-0.200	-0.200	-0.150	V

*: This is the free swell index of bentonite determined in deionized water.

**: This is the detectible surface electric potential of the colloids.

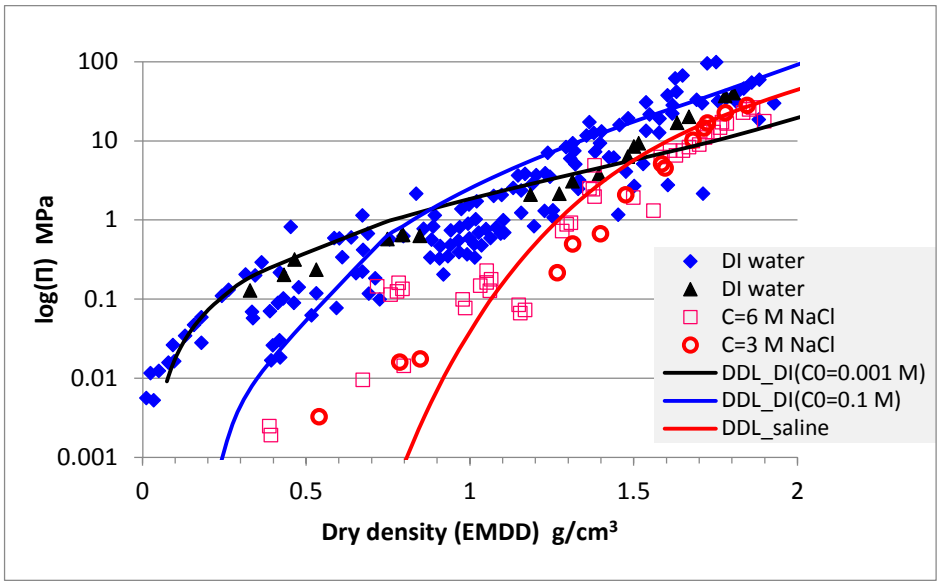

Figure 6.2 Swelling pressure vs effective montmorillonite dry density for MX-80 bentonite (dots are data from Man and Martino 2009 while curves are modelling results with DDL theory)

Void ratio can be easily determined for saturated soil

$$e = G_s w \tag{40}$$

where G_s is the specific density of clay mineral.

This enables us to investigate the void ratio-swelling pressure relationship. Considering soil as saturated and equilibrated in stress, the swelling pressure should be equal to the overburden loading. Thus the compression curve as obtained by oedometer consolidation test can be modelled with the modified DDL theory. Figure 6.3 shows the modelling of swelling pressure for MX-80 in DI water at various void ratios. Some reference modelling results are also compared against the experimental data. It is clear that our modelling gives the best fit. Note that the modelling of Schanz and Tripathy (2009) relies on an empirical fitting of midplane potential ϕ_c that requires several parameters. Instead, our model only fits one variable parameter, i.e. the surface potential ϕ_0 (comparable to zeta potential ξ=75 mV). The remaining parameters are all pertinent to MX-80 bentonite as material properties, e.g. $c_0 \approx$CEC, S=750 m^2/g, w_0=13.

Salt concentration in pore fluid significantly changes the swelling pressure of bentonite. The exchangeable cations originally confined in mineral lattices contribute to the reference salt concentration (c_0) in addition to the externally supplied pore fluid. Thus it is easy to understand that higher swelling pressure is pertinent to more CEC values. Figure 6.4a shows that the best-fitted reference solute concentration of MX-80 bentonite is c_0= 0.1 M, which is in the same order of magnitude with its CEC value. Besides, c_0=0.1 M is consistent with the estimated value of the initial salt concentration at 0.169 M by analyzing the water retention curves with DDL theory. Further, leaching test of Na-Montmorillonite based GCL (similar to MX-80) revealed Na^+ concentration at the level of 0.1

M (Jo et al. 2005). Previous study on the chemical composition of porewater of MX-80 in equilibration with fresh water for a year suggested a level of 0.15 M NaCl at dry density of 1.5 g/cm^3 (Muurinen and Lehikoinen 1998). Therefore, the modified DDL model seems adequate to describe the deformation of bentonite. For c_0=0.1 M and ϕ_0=3, DDL model reproduced well the compression curve of MX-80 bentonite (Wang 2013). For c_0=6 M and ϕ_0=1, the swelling pressure and compression curve of MX-80 in contact with model brine solution can be predicted, which is shown in Figs. 4a-4b. Experimental results are in good agreement with the modelling. Preliminary results of MX-80 from Queens University suggest Π=0.2 MPa when e=1.0. This is again within the modelled range of distribution.

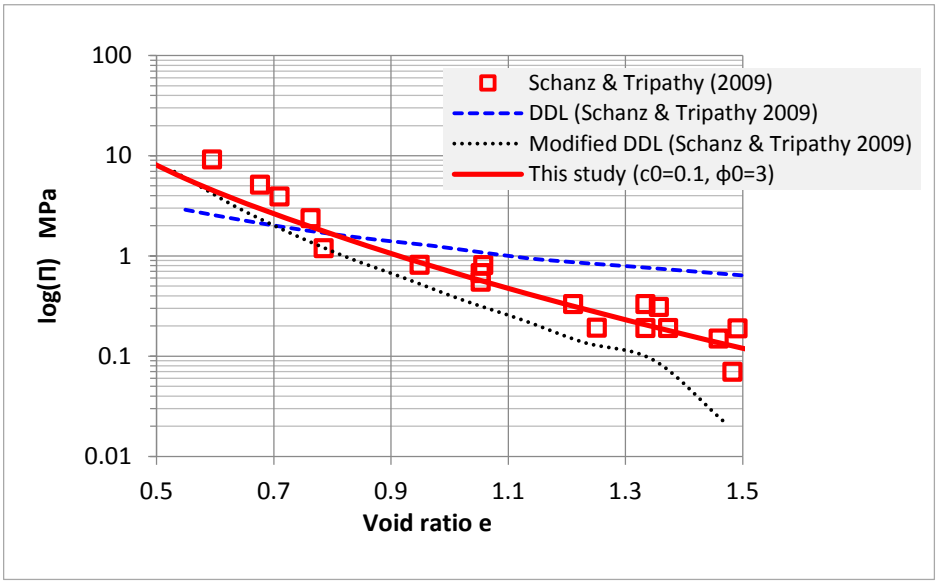

Figure 6.3 Swelling pressure of versus void ratio for MX-80 in deionized water (data from Schanz and Tripathy. 2009)

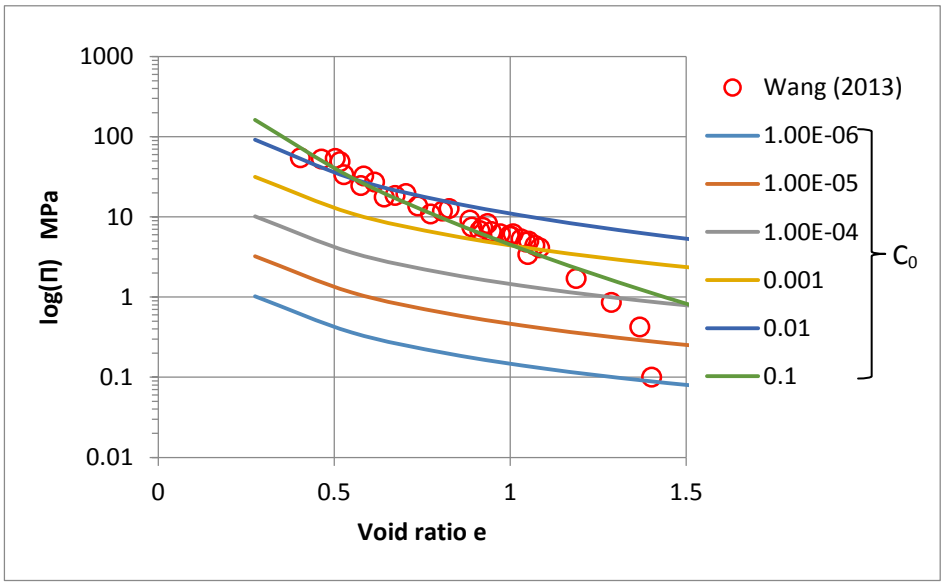

(a) ϕ_0=8

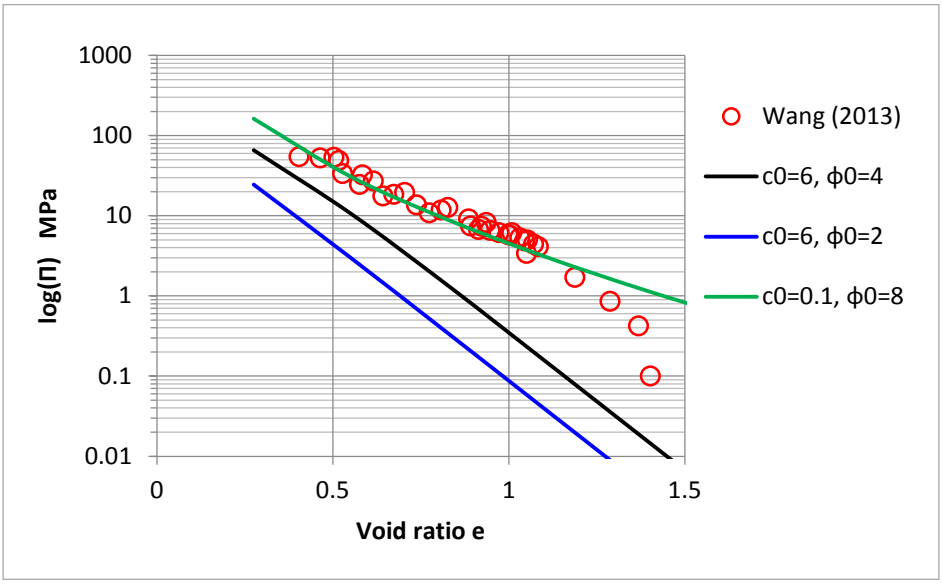

(b) ϕ_0=2-8

Figure 6.4 Modelled and tested compression curve of MX-80 bentonite (Modelling results are in solid line and are obtained by the modified DDL theory at various salt concentrations and surface electric potentials. The test data was from consolidation tests on S/B mixture. The void ratio is normalized onto bentonite by excluding sand from consideration)

4. Physics of suction in porous media

Suction is thought to cause compressive stress on soil skeleton in terms of Bishop's equation $\sigma' = (\sigma - u_a) + \chi(u_a - u_w)$. Some recent studies have been devoted to developing and verifying the relationship between suction and effective stress for various clay soils (Lu et al. 2010; Agus et al. 2013; Baille et al. 2013). Experimental data evidence the strong correlation between externally applied stress and suction induced stress, which appear to be equivalent to each other in a wide range of stress levels (Agus et al. 2013). For expansive soils, the equivalence of suction and external stress maintains validity up until and beyond the air entry value. This phenomenon has been theoretically discussed in the closed-form effective stress formula of Lu et al. (2010). Capillary pressure is generally believed to be responsible for the suction in cohesionless soils, while osmosis and chemical potential are related to clayey soils. As far as the writer knows, there is still no mechanistic theory to explain the nature of suction and suction induced compaction of expansive soils from the DDL point of view. The following is dedicated to this attempt by proposing a concept of clay-meniscus interaction model.

Surface electric potential of air-water interface

The density, dielectric permittivity and polarization of interfacial water change from their bulk water values to those of the gas over a distance of nanometer. Ions behave differently at the surface to their

behaviour in the bulk liquid (Jungwirth and Tobias 2006; Chaplin 2015). The interfacial water structure of the water/air interface is deemed hydrophobic. The lack of hydrogen bonding between water molecules and a substance often defines a hydrophobic interface. It is supported by the existence of the dangling OH bonds at the interface (Tian and Shen 2009). As shown in Fig. 6.5, the sign convention for the surface electric potential at air-water interface is generally taken as measured from the air into the solution. Therefore a negative potential means the bulk is negatively charged and the surface is positively charged, which is consistent with results of most water models (Chaplin 2015). Highly polarizable ions e.g. Cl^-, Br^- and O^{2-} favour the air-water interface as they only interact weakly with water (Jungwirth and Tobias 2006; Leung 2010), which may result in negatively charged water film due to charge transfer from the anions locating close to the surface (Chaplin 2015). For more information on the physical chemistry of air-water interface please refer to the review of Jungwirth and Tobias (2006) and Chaplin (2015).

This thin layer of negatively charged water film mimics exactly the diffuse double layer in the vicinity of a positively charged plate, which is similar in mechanism to the Stern layer (positive charge) on the surface of clay minerals (negative charge). This surface polarization can further cause perturbation to water structure (cluster of water) within about 250 nm of the interface (Teschke and Souza). In the microscale pore space of compacted bentonite, this perturbation range (250 nm) is large enough to call for the consideration of air-water interface for the analysis of the electrostatic interaction with the charged plane of the clay minerals.

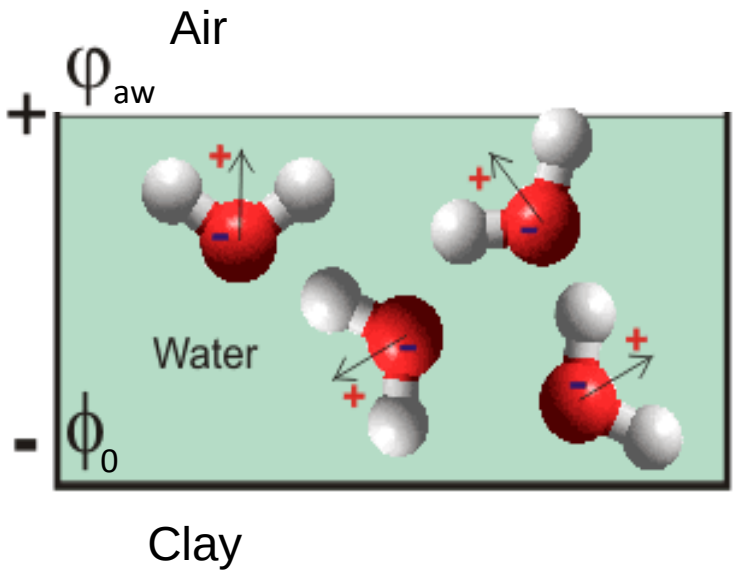

Figure 6.5 Schematic diagram of the surface electric potential at air-water interface (Chaplin 2015)

Attractive pressure for unsaturated clay

According to the latest physicochemistry research finding of air-water interface properties, it is generally believed that a certain amount of positive electrostatic potential persists at the air-water interface

(Jungwirth and Tobias 2006; Leung 2010). This electrostatic potential is defined in this study as ψ_{aw}. It is reported in the range of 0-1 V and to be dependent on dissolved electrolyte type and concentration (Jungwirth and Tobias 2006). In view of the composition of the brine solution considered in this study, it is reported to be $\psi_{aw} = 0.065\ V$ corresponding to distilled water and $\psi_{aw} = 0.046\ V$ for 0.1 mM NaCl (Chaplin 2015). Note that surface electric potential diminishes in quantity with increasing salt concentration. However, the same trend applies to the surface electric potential of clay minerals due to the specific adsorption of cations. Using Gouy-Chapman theory to calculate the surface electric potential of a typical montmorillonite mineral plate results in an equivalent value at $\psi_0 = -0.05\ V$ (Nextnano tutorial). Generally speaking, it is reasonable to assume a pair of symmetric reversely charged plates for clay-meniscus system. As such, the meniscus-clay plate system can be conceptualized into an asymmetrically charged plane interaction problem.

For such a system, it is shown that either repulsive or attractive pressure can exist at different scaling regimes (dependent on distance and charge density). According to Ben-Yaakov et al. (2007), the attractive electrostatic pressure Π, can be written as the sum of electrical interaction between the interplanar space and the osmotic pressure in the bulk solution.

$$\Pi' = -\frac{1}{2l_B}\left(\frac{d\phi}{dz}\right)^2 + 2c_b(\cosh\phi - 1) \tag{41}$$

where c_b is the bulk salt concentration and $\Pi = k_B T \Pi'$.

The Gouy-Chapman length is in the form of (Andelman 2006)

$$\lambda_{GC} = \frac{e}{2\pi l_B \sigma} \tag{42}$$

where σ is the surface charge density (C/m^2). In case of Bentonite plate in distilled water (σ=0.3 C/m^2), the Gouy-Chapman length becomes $\lambda_{GC} = 1.2\text{Å}$.

And the Debye-Huckel length is written as a function of electrolyte density c_b (bulk 1:1 salt concentration)

$$\lambda_D = \frac{1}{\sqrt{2l_B c_b}} \tag{43}$$

For SI units of c_b measured in molar concentration, the Debye-Huckel length becomes

$$\lambda_D = \frac{1}{\sqrt{2l_B N_A I(\text{M})}} = \frac{0.304}{\sqrt{c_b(\text{M})}} nm \tag{44}$$

where N_A is the Avogadro number and I(M) is the ionic strength in molar/m^3. It varies from 0.3 nm for 1 M NaCl to about 1 μm for DI water. Note that for $d<\lambda_D$, the electrostatic Coulombic interaction is only slightly screened, while for $d>\lambda_D$, the screening is strong and takes the form of an exponential relationship.

In case of concentrated brine solution at room temperature, let c_b=6 M then

$$\frac{\lambda_D}{\lambda_{GC}} = \frac{0.122}{0.24} = 0.51 \tag{45}$$

Even when bentonite is permeated with distilled water, the naturally contained exchangeable ions can still be released out in a large quantity (Jo et al. 2005). It is reported to be as high as 100 mM. NaCl has been observed to leach out from bentonite based geosynthetic clay liners. In such, the length ratio becomes

$$\frac{\lambda_D}{\lambda_{GC}} = \frac{0.929}{0.12} = 7.7 \tag{46}$$

Under such circumstances as described above that corresponds to low potentials where Poisson-Boltzmann equation can be linearized, the attractive force is approximated by (Ben-Yaakov et al. 2007)

$$\Pi' = \begin{cases} -\frac{2}{\pi l_B \lambda_{GC}^2} e^{-\frac{d}{\lambda_D}}, \ \lambda_D \ll \lambda_{GC} \\ -\frac{2}{\pi l_B \lambda_D^2} e^{-\frac{d}{\lambda_D}}, \ \lambda_D \gg \lambda_{GC} \end{cases} \tag{47}$$

where d is the distance between two charged surfaces. The minus sign indicates the nature of attractive force.

Rearranging the above equation leads to

$$\ln(-\Pi') = -\frac{d}{\lambda_D} + \ln\left(\frac{2}{\pi l_B \lambda_{GC}^2}\right) = -d\sqrt{2 l_B c_b} + \ln\left(\frac{2}{\pi l_B \lambda_{GC}^2}\right) \tag{48}$$

Then the attractive force can be regulated by assigning the dimensional terms and can be rewritten as the following

$$\Pi = k_B T \Pi' = -\frac{2 k_B T l_B \sigma^2}{e^2} e^{-d/\lambda_D} \tag{49}$$

where Π is the attractive force in [Pa]. It is noted that the maximum attractive force could be as high as 100-1000 MPa, which can be approximated by extrapolating the water retention curve as shown in Fig. 6.6. Fredlund et al. (2012) repeatedly asserted that an upper limit of matric suction can be treated as high as 1E9 Pa for clayey soils. Although no reason has ever been given on how this value is obtained, it gets verified by our mechanistic model that treats air-water interface or meniscus as positively charged plane.

Influence of desiccation on attractive pressure

As for sand/bentonite mixed soil, the water content w is transformed into the effective montmorillonite water content (EMWC), which assumes that all of the liquid water is absorbed by montmorillonite rather than sand grains, and EMDC is written as

$$EMWC = \frac{g_w}{g_m} \tag{50}$$

where g_w is water mass and g_m is bentonite clay mass.

For unsaturated soil, the average distance d between mineral plane and air-water interface can always be quantified by

$$d * S * \gamma_w = w \tag{51}$$

where S is the specific surface area, w is the gravimetric water content and γ_w is the unit weight of water.

Then we can write out the attractive force in its full expression,

$$\ln(-\Pi) = -\frac{1}{S\gamma_w}\sqrt{2l_B c_0 w_0 w} + \ln(2l_B\sigma^2) \tag{52}$$

In case of dilute salt solution, e.g. the test of Bentonite with distilled water (I<0.001 M), the Bjerrum length maintains a constant value. The above equation reduces to another form

$$\ln(-\Pi) \propto \sqrt{w} \tag{53}$$

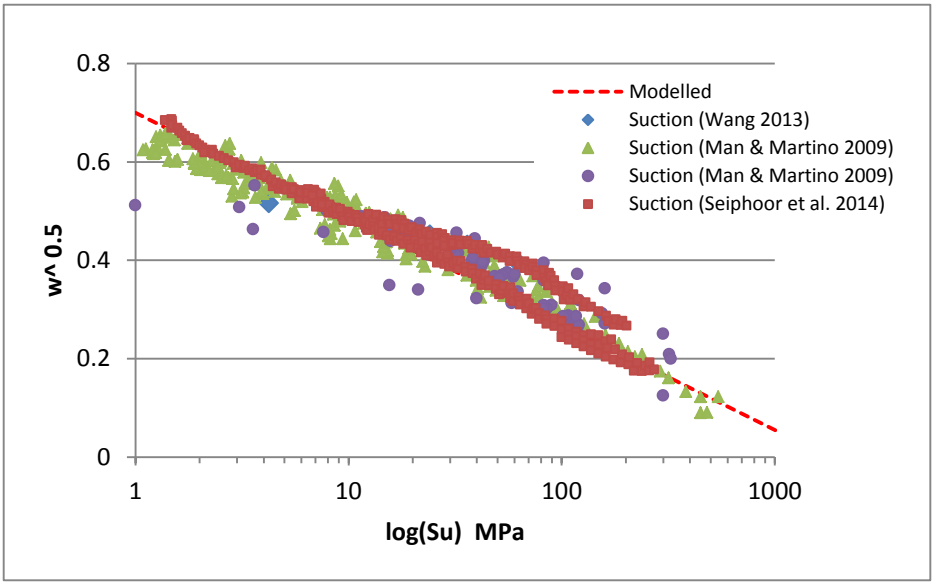

(a)

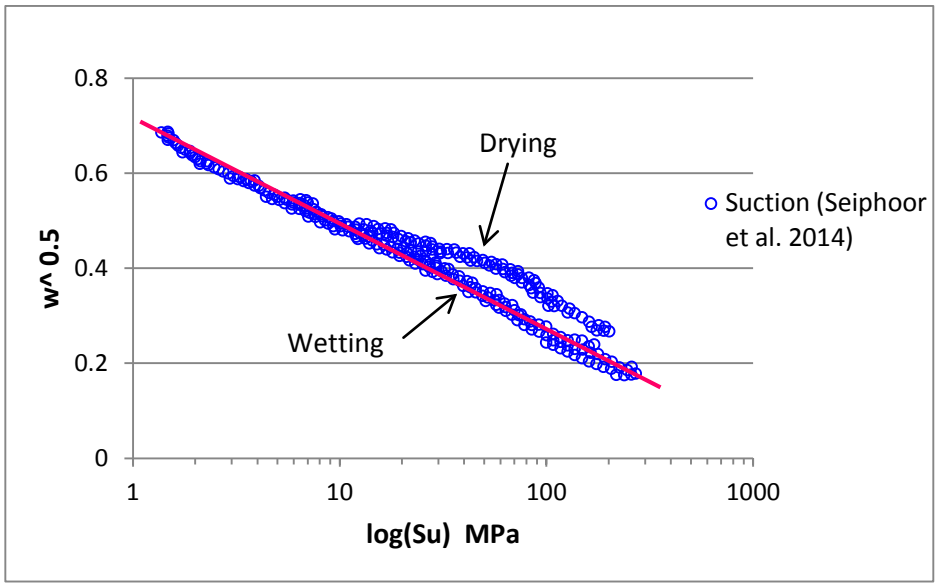

(b)

Figure 6.6 Linearized water retention curves for MX-80 bentonite from various sources (This hysteresis can be attributed to the transition of attractive force between applicable domains, i.e. from the Dybe-Huckel regime to the Intermediate regime. The two regions follow the same variation pattern in terms of exponential decay, but differ for the maximum interaction force.)

As shown in Fig. 6.6, the water retention curve of MX-80 for DI water can be modelled by

$$\sqrt{w} = -0.215 * \log\frac{S_u}{1800} \tag{54}$$

where

$$-\Pi = S_u \tag{55}$$

According to the above equation, the naturally contained salt concentration in MX-80 can be estimated as

$$\frac{\sqrt{c_0 w_0}}{S\gamma_w 3.04\times10^{-10}} = \frac{\ln 10}{0.215} \tag{56}$$

where specific surface area of S=700 m^2/g, liquid density of γ_w=10^6 g/m^3, free swell index of w_0=13. Then

$$c_0 = 0.399\ \mathrm{M} \tag{57}$$

This amount of salt concentration may be attributed to the naturally contained exchangeable ions. According to Lee and Shackelford (2005) the molar Na concentration of the permeant with DI water

from Na-bentonite based geosynthetic clay liner reaches as high as 0.10 M (Jo et al. 2005). This initial salt concentration c_0 is equivalent to half of the CEC of bentonite at 0.8 eq/kg.

As a result the surface charge density of the clay mineral can also be calculated by

$$\sigma = \sqrt{\frac{\Pi_m e^2}{2k_B T l_B}} \tag{58}$$

where Π_m is the experimentally estimated maximum suction (1800 MPa for MX-80 bentonite). It is shown that the calculated surface charge density of the bentonite equals to 0.68 C/m^2, which is approximately two times of the reported value of 0.3 C/m^2.

Influence of brine on attractive pressure

It is noted that the Bjerrum length l_B is dependent on dielectric constant of the bulk medium. It is reported that permittivity of salt water is not a constant, but reduces in quantity with growing salinity, as shown in Fig. 6.7, following the following relationship (Gavish and Promislow, 2012):

$$\varepsilon_c = \varepsilon_w - \beta L\left(\frac{3\alpha}{\beta} c_b\right) \tag{59}$$

where L is the Langevin function

$$L(v) = \coth(v) - \frac{1}{v} \tag{60}$$

ε_w is the dielectric of the pure solvent, α is the total excess polarization of the ions and β is the relative difference between an effective ion-pair dipole moment and the water dipole moment. As for concentrated NaCl solution at T=20 °C, the empirical parameters are α=12 and β=52.94 (Gavish and Promislow, 2012).

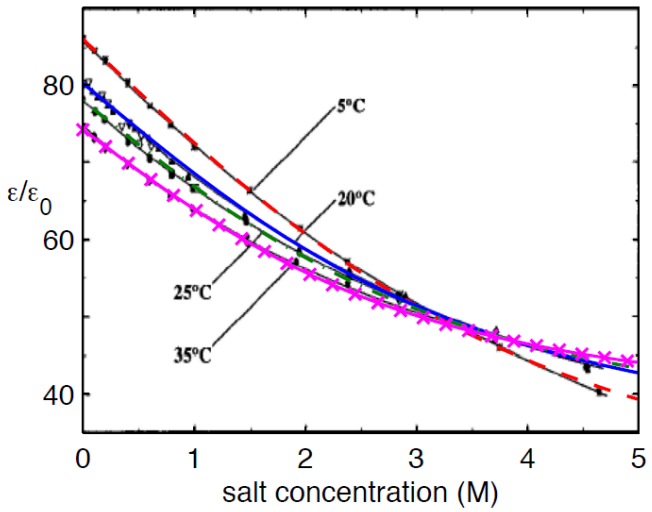

Figure 6.7 Comparison of the predicted dielectric constant with experimental data as a function of ionic concentration c for NaCl at various temperatures (Gavish and Promislow, 2012)

For simplification purpose, the nonlinear relationship between relative permittivity of salt water with salt concentration can be linearized for c_b>5 M by

$$\varepsilon_c = 58 - 3c_b \tag{61}$$

Then

$$\ln(-\Pi) = -\frac{1}{s\gamma_w}\sqrt{\frac{2c_0 w_0 e^2}{k_B T}\frac{w^2}{58w-3c_0 w_0}} + \ln\left(\frac{2\sigma^2 e^2}{k_B T}\frac{w}{58w-3c_0 w_0}\right) \tag{62}$$

This equation is highly nonlinear and thus is hard to be normalized by the square-root-log relationship.

Considering the saturation molarity of NaCl at c_b=5.86 M, in which case the salt concentration remains constant and will not grow with further evaporation, the mass equilibrium will not be valid since crystallization of salt will occur. The above equation can be approximated by

$$\ln(-\Pi) = -\frac{w}{s\gamma_w}\sqrt{2l_B c_{bs}} + \ln(2l_B\sigma^2) \tag{63}$$

where c_{bs} is the saturated salt concentration (c_{bs}=5.86 M). In such conditions, the Bjerrum length corresponds to saturated solution, i.e. l_B=1.4 nm due to the reduced permittivity of the salt water.

It can be further derived from Eq. (63) that

$$\ln(-\Pi) \propto w \tag{64}$$

The above relationship is easy to verify if brine water retention curve is experimentally determined. So far the writer could not find relevant information from the literature. Besides, similar experiments that have already been planned in a joint research project remain to be implemented. Therefore an alternative approach is taken to verify the proposed suction-water content relationship.

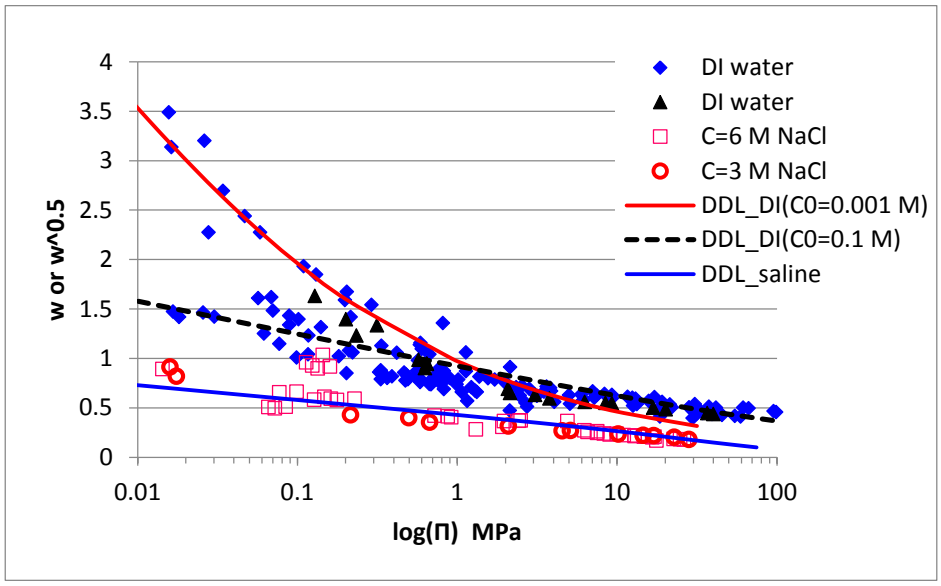

Figure 6.8 Gravimetric water content vs repulsive pressure for MX-80 bentonite

Water retention curve for brine solution

According to the equivalence of effective stress for unsaturated soils, the relationship between water content and suction can be extracted from the equivalent relationship between w and Π as shown in Fig. 6.8. Note that this relationship is not shown here, but can be derived in a different manner, as demonstrated by Dr. Nguyen in a personal discussion. As shown above, because the saline water retention experimental data is lacking, we can only rely on the swelling test to validate the theoretically derived suction-water content relationship with the assistance of the equivalence principle.

The linear relationship for the brine water retention curve can be expressed as

$$w = -0.2018 * \log \frac{S_u}{150} \tag{65}$$

where S_u is the suction in MPa and w is the gravimetric water content with respect to bentonite**.** Compared to DI water, the maximum suction in MX-80 towards brine solution is estimated to be 150 MPa, which is approximately 1/10 of that towards DI water (1800 MPa).

It is noted that the parametric analysis may verify the proposed model from another perspective. Comparing the theoretical formula with the above fitted empirical equation leads to

$$\frac{\sqrt{c_{bs}}}{S\gamma_w 3.04\times10^{-10}} = \frac{\ln 10}{0.2018} \tag{66}$$

Then the salt concentration can be estimated

$$c_{bs} = 5.78 \text{ M} \tag{67}$$

This is exactly the saturated salt concentration of NaCl in room temperature.

With respect to the extremely dry case where water content is 0 and suction $\widetilde{\Pi}_m$=150 MPa, we get the surface charge density for the clay plates as

$$\sigma = 0.14\ \mathrm{C/m^2} \tag{68}$$

It is shown that surface charge density of MX-80 reduces to 20 % of the original value when immersed in saturated brine solution. This behaviour can be explained by specific adsorption of counter ions onto the negative sites of bentonite mineral plates, which causes the reduction of the amount of the overall surface charges.

Effective stress

According to the Bishop's effective stress in expression, suction is taken into account by a coefficient χ that ranges from 0 to 1.0 as

$$\sigma' = \sigma + \chi S_u \tag{69}$$

The consolidation behaviour of sand/bentonite mixture as reported by Wang (2013) can be normalized into a consistent compression curve as shown in Figs. 8-9. The original test data are from a number of different types of test, including suction-controlled oedometer test, free swell test, fixed-loading swell test and swell test with technical void (Wang 2013). The results of these different tests are shown in Fig. 6.9. Discrepancy persists amongst each other.

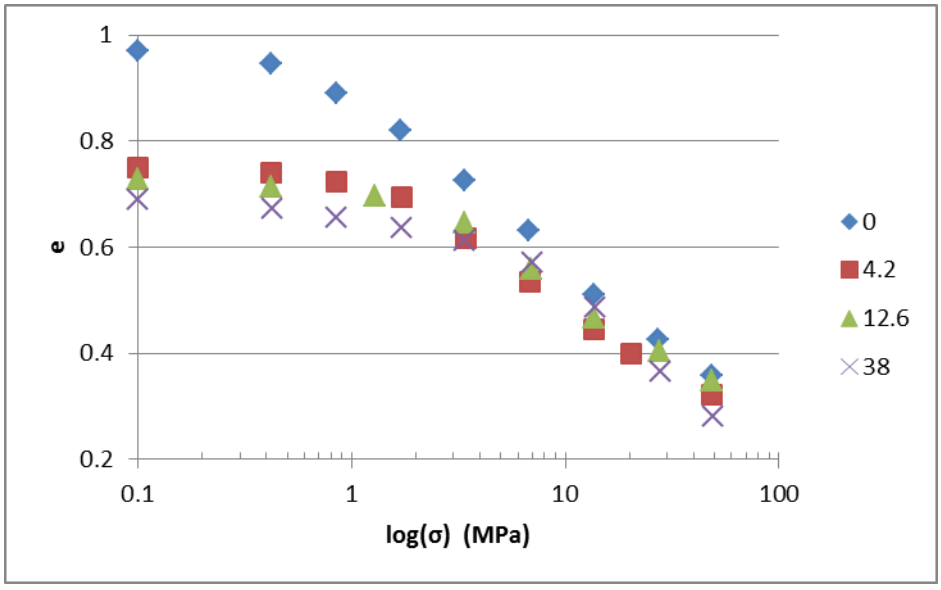

(a)

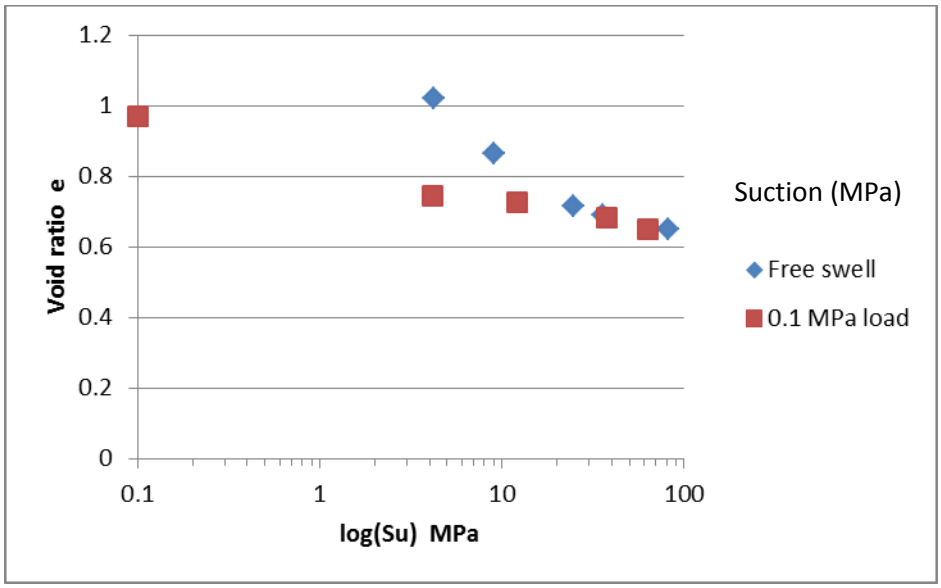

(b)

Figure 6.9 Compression curve (a) and swelling curve (b) of MX-80 bentonite/sand mixture under various suctions (Data from Wang (2013))

With the effective stress in consideration, matric suction and external loading are both responsible for the observed compression. Numerous experiments on volumetric change of bentonite indicate the equivalence of suction with loading when suction is less than the air entry value. When suction is beyond the AEV, this equivalence diminishes in a much weaker form. Accordingly, a multilinear form of Bishop's equation can be derived. As for the aforementioned sand/bentonite mixed soil (30/70), the normalization takes the Bishop coefficient in the value of the following form

$$\chi = \begin{cases} 1, & S_u/AEV \leq 1 \\ 0.1, & 1 < S_u/AEV < 3 \\ 0.05, & S_u/AEV \geq 3 \end{cases} \quad (70)$$

The oedometer compression test data of sand/bentonite mixture under various suction conditions (see Fig. 6.9) can be normalized into a unique curve as shown in Fig. 6.10.

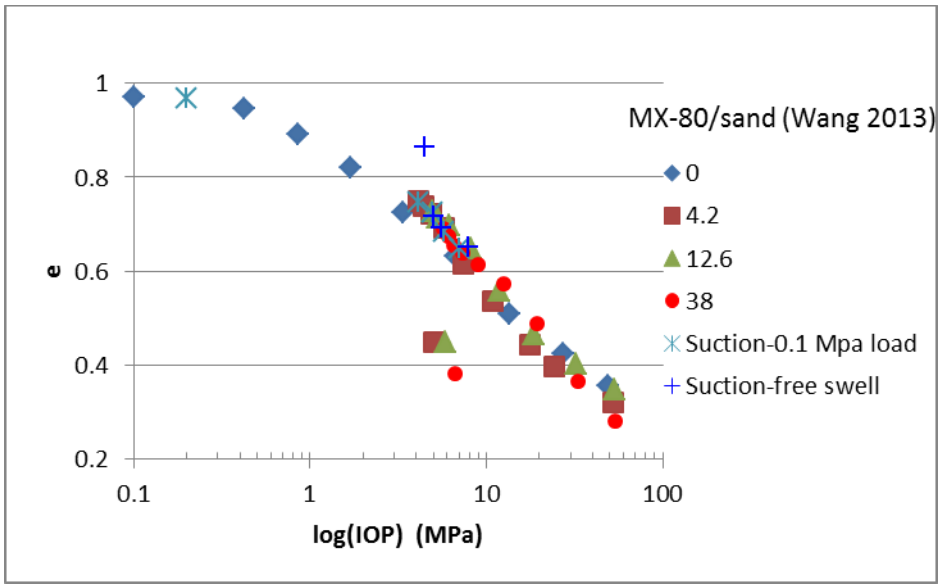

Figure 6.10 Normalized e-log(IOP) relationship for S/B mixture in DI water

5. Modelling of electric-hydraulic coupled flow in diffuse-double-layer dominant porous medium

Empirical relationship of permeability

Hydraulic conductivity of compacted bentonite is critical to the evaluation of infiltration and mechanical response of engineered barrier system for hazardous waste containment. A number of infiltration experiments have been previously conducted under various salinity conditions as shown in Fig. 6.11.

Hydraulic conductivity of brine (350 g/L) in compacted bentonite is reported to take the form of

$$k = 2.5 \times 10^{-10} \left(\frac{2.78}{1+e}\right)^{-15.8} \tag{71}$$

where k is the hydraulic conductivity (m/s). This equation can be turned into the permeability as

$$\kappa = \frac{k\mu}{\rho g} = 3.75 \times 10^{-17} \left(\frac{2.78}{1+e}\right)^{-15.8} \tag{72}$$

where viscosity of brine at room temperature is 2.0 mPa s (Ozbek 1971) and the density is 1360 g/mL.

The unsaturated hydraulic conductivity has been reported to take the form of (Fredlund et al. 2012)

$$\frac{k_u}{k_0} = \begin{cases} \left(\frac{S_u}{AEV}\right)^{-2.18}, & S_u > AEV \\ 1, & S_u \leq AEV \end{cases} \tag{73}$$

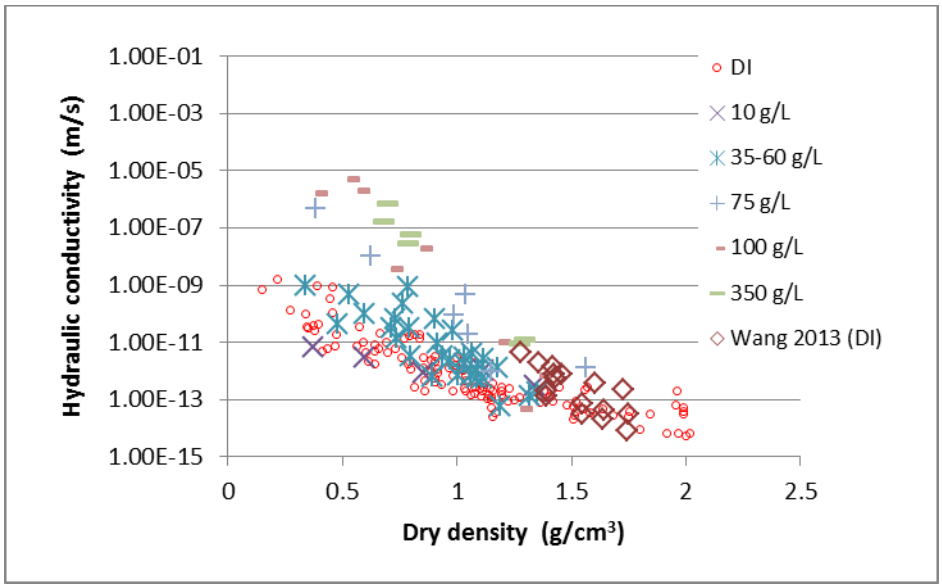

Figure 6.11 Variation of hydraulic conductivity of MX-80 bentonite with dry density (Wang 2013; NWMO 2009)

Coupled electrokinetic flow

Pressure driven flow in porous media is governed by both fluid viscosity and the electrokinetic properties of the porous media. In cases with larger pore radius and less significant diffuse double layer effect, viscous flow dominates the flow phenomenon. Using the Navier-Stokes theory and homogenization approach, Cheng and Tang (2010) successfully explained the Darcy's law for compacted sand. However, for clayey soils where DDL plays an important role, the electrokinetic influence, which is introduced by the surface electric potential and the redistribution of charged ions in pore fluid, has to be taken into account. Freundlich (1909) observed equivalent proportionality of volumetric flow to electric current between pressure driven streaming potential and electro-osmotic flow. Burgreen and Nakache (1964) reported the first theoretical study on the coupled electrokinetic flow in capillary slit. However, the deduction of the semi-analytical solution for the governing equation needs to be rectified due to some minor errors in expression, as pointed out by (Levine et al. 1975). Li et al. (2014) studied the electric-hydraulic-chemical coupled flow in clay liners of GCL. The retarding electro-osmotic flow imposed by the streaming potential was modelled with an empirical linear approximation, which proves to be a variable rather than a constant, valid under limited conditions and thus needs further extensive studies. As discussed earlier in this report, the saturated bentonite appears to have only on mode of pore size distribution with the modal peak at 10 nm (Seiphoori et al. 2014), which is in the nanometer scale and is regarded as representative of the micropores between clay stacks. Therefore DDL predominates in this situation. The following part will be devoted to reproducing the semi-analytical solution of the electrokinetic flow problem.

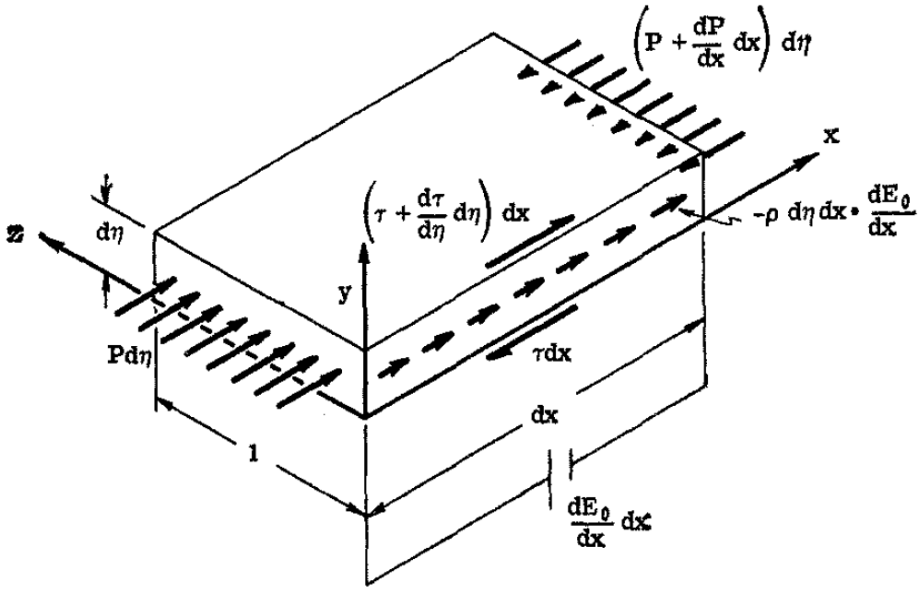

Figure 6.12 Schematic diagram showing the force balance on fluid in interplanar space (Burgreen and Nakache 1964)

Note that this model assumes a steady state is quickly reached under boundary conditions. If we apply a solute front at boundary, it will cause an osmosis flow, which may interpret Dominijanni's phenomenological theory on HMC couplings (Geotechnique, 2013).

For a representative element of fluid in pore space as shown in Fig. 6.12, the axial electric field ($Y = \frac{dE}{dx}$) can cause a body load on the charged ions. And thus the governing equation of the viscous flow can be written as

$$-\frac{dP}{dx} + \mu \frac{d^2u}{dy^2} - \rho Y = 0 \tag{74}$$

where P is pore pressure (Pa), u is fluid velocity (m/s), Y is electric field (C/m), x is in fluid flow direction and y is perpendicular to the flow direction.

Boundary conditions include the following, with h being the half distance between parallel plates

$$u(0) = 0,\ \left.\frac{du}{dy}\right|_{y=h} = 0 \tag{75}$$

$$\psi(0) = \psi_0,\ \left.\frac{d\psi}{dy}\right|_{y=h} = 0 \tag{76}$$

The solution of the above equation is always of the form

$$u = u_p + u_e \tag{77}$$

where u_p is pressure drive fluid velocity and u_e is the electroosmotic velocity.

or

$$u = -\frac{1}{2\mu}[y^2 - 2yh]\frac{\mathrm{d}P}{\mathrm{dx}} + MY\left(1 - \frac{\psi}{\psi_0}\right) \tag{78}$$

with

$$u_p = -\frac{1}{2\mu}[y^2 - 2yh]\frac{\mathrm{d}P}{\mathrm{dx}} \tag{79}$$

$$u_e = MY\left(1 - \frac{\psi}{\psi_0}\right) \tag{80}$$

where μ is the fluid viscosity, y is the distance from solid surface, and the mobility $M = \xi\varepsilon_0\varepsilon_r/\mu$ with zeta potential of the clay mineral as ξ.

The mean velocity in the pore space can be expressed as

$$\bar{u} = -\frac{h^2}{3\mu}\frac{\mathrm{d}P}{\mathrm{dx}} + \frac{MY}{h}\int_0^h \left(1 - \frac{\psi}{\psi_0}\right)\mathrm{dy} \tag{81}$$

Different from the disjoining pressure which only requires the differential of the electric potential ψ, the flow rate requires the integration of surface potential ψ. Burgreen and Nakache (1964) gave a solution that can be numerically integrated in terms of

$$\bar{u} = -\frac{h^2}{3\mu}\frac{\mathrm{d}P}{\mathrm{dx}} + MY[1 - G] \tag{82}$$

$$G = G(\alpha, \omega h) = \frac{1}{\omega h}\int_0^h \frac{\psi}{\psi_0}\mathrm{d}(\omega y) \tag{83}$$

where the inverse of Debye length reads $\omega = \frac{1}{\lambda_D}$, and $\alpha = \phi_0$ is the ionic energy parameter.

Then we have to determine the axial electric field induced by either the external electric potential or the retardation potential, i.e. streaming potential. Assume a voltage source E_0 placed across the capillary. Then the net electric current is comprised of two components, i.e. the conduction current Ic and the transport current It

$$I = I_c + I_t \tag{84}$$

where

$$I_t = -\int_A \rho u \mathrm{d}A \tag{85}$$

$$I_c = KAY \tag{86}$$

where K is specific electric conductance, and A is cross section area. Miller et al. (1988) reported various factors affecting the specific conductance of dilute salt solutions. It is noted that a linear relationship between conductivity and salt concentration pertains to a constant temperature.

$$K = 10.12c_b + 8.74 \times 10^{-2} \quad [\mathrm{S/m}] \tag{87}$$

In case of no external electric potential, the total current diminishes as

$$I = 0 \tag{88}$$

Then

$$\int_A \rho u \mathrm{d}A = KAY \tag{89}$$

Substitution of u into the above equation yields

$$\int_A \rho \left[u_p + MY\left(1 - \frac{\psi}{\psi_0}\right)\right] \mathrm{d}A = KAY \tag{90}$$

After rearranged we get the electric potential gradient

$$Y = \frac{\int_A \rho u_p \mathrm{d}A}{KA - M\int_A \rho\left(1 - \frac{\psi}{\psi_0}\right)\mathrm{d}A} \tag{91}$$

Using the charge density function (Boltzmann equation) results in

$$\int_A \rho u_p \mathrm{d}A = -\varepsilon_r \varepsilon_0 \int_0^h \frac{\mathrm{d}^2\psi}{\mathrm{d}y^2} u_p \mathrm{d}y \tag{92}$$

Setting pressure-driven velocity up into the above equation and integrate by parts twice, we get

$$\frac{-\int_0^h \frac{\mathrm{d}^2\psi}{\mathrm{d}y^2} u_p \mathrm{d}y}{\frac{1}{2\mu}\frac{\mathrm{d}P}{\mathrm{d}x}} = \int_0^h (y^2 - 2yh)\mathrm{d}\left(\frac{\mathrm{d}\psi}{\mathrm{d}y}\right) = (y^2 - 2yh)\left(\frac{\mathrm{d}\psi}{\mathrm{d}y}\right)\Big|_{y=0}^{h} - \int_0^h \left(\frac{\mathrm{d}\psi}{\mathrm{d}y}\right)\mathrm{d}(y^2 - 2yh) = 0 - \int_0^h \frac{\mathrm{d}\psi}{\mathrm{d}y}(2y - 2h)\mathrm{d}(y) = 2\int_0^h (h - y)\mathrm{d}(\psi) = 2(h - y)\psi|_{y=0}^{h} - 2\int_0^h \psi \mathrm{d}(h - y) = 2h\psi_0 + 2\int_0^h \psi \mathrm{d}y \tag{93}$$

Then

$$\int_A \rho u_p \mathrm{d}A = \frac{\varepsilon_r \varepsilon_0}{\mu}\frac{\mathrm{d}P}{\mathrm{d}x} h\psi_0 \left(1 + \frac{1}{h}\int_0^h \frac{\psi}{\psi_0}\mathrm{d}y\right) = Mh\frac{\mathrm{d}P}{\mathrm{d}x}(1 - G) \tag{94}$$

There fore the electric potential gradient turns into

$$Y = \frac{Mh\frac{\mathrm{d}P}{\mathrm{d}x}(1 - G)}{Kh - M\int_0^h \rho\left(1 - \frac{\psi}{\psi_0}\right)\mathrm{d}y} \tag{95}$$

Substitution of above equation into the electro-osmotic velocity yields

$$u_e = M\left(1-\frac{\psi}{\psi_0}\right)\frac{Mh\frac{\mathrm{d}P}{\mathrm{d}x}(1-G)}{Kh-M\int_0^h \rho\left(1-\frac{\psi}{\psi_0}\right)\mathrm{d}y} \tag{96}$$

Finally the average fluid velocity becomes

$$\bar{u} = -\frac{h^2}{3\mu}\frac{\mathrm{d}P}{\mathrm{d}x} + \frac{M^2}{K}\frac{\mathrm{d}P}{\mathrm{d}x}\frac{(1-G)^2}{1-\frac{M}{Kh}\int_0^h \rho\left(1-\frac{\psi}{\psi_0}\right)\mathrm{d}y} \tag{97}$$

or in another form involving with the ratio of the transport current over the conduction current (It/Ic) (Burgreen and Nakache 1964)

$$\bar{u} = \left[-\frac{h^2}{3\mu} + \frac{M^2}{K}\frac{(1-G)^2}{1+{}^{I_t}/_{I_c}}\right]\frac{\mathrm{d}P}{\mathrm{d}x} \tag{98}$$

with

$$\frac{I_t}{I_c} = -\frac{M}{Kh}\int_0^h \rho\left(1-\frac{\psi}{\psi_0}\right)\mathrm{d}y \tag{99}$$

The above equation can also be expressed by elliptic integral of second kind as followings (Burgreen and Nakache 1964)

$$\frac{I_t}{I_c} = -\frac{M^2\omega^2\mu}{K}\frac{1}{\omega h(\alpha/2)^2\kappa}\left[\tanh\left(\frac{\alpha}{2}\right)\cot(\theta_0) + E(\theta_0,\kappa) - E\left(\frac{\pi}{2},\kappa\right)\right] \tag{100}$$

Both G and It/Ic can be approximated by analytical solutions, which have been discussed previously (Burgreen and Nakache 1964; Levine et al. 1975). However, the integrals of the average velocity can be numerically computed by solving the Poisson-Boltzmann equation and the governing equation of the electrokinetic flow. In this study, a FEM model was built with COMSOL Multiphysics (ver 5.1). The average velocity was numerically investigated, which enables easy and convenient calculation of the integrals.

Citing the Darcy's law leads to the apparent hydraulic conductivity

$$k = k_p - k_e = \frac{h^2}{3\mu} - \frac{M^2}{K}\frac{(1-G)^2}{1+{}^{I_t}/_{I_c}} \tag{101}$$

With hydraulic conductivities of the pressure driven flow and the electroviscous retardation flow, respectively, as

$$k_p = \frac{h^2}{3\mu} \tag{102}$$

$$k_e = \frac{M^2}{K}\frac{(1-G)^2}{1+{}^{I_t}/_{I_c}} \tag{103}$$

Note that the former term k_p is exactly the form of the empirical expression for hydraulic conductivity of sandy soil except that the numerator is the grain size in the empirical formula (Cheng and Tang, 2010).

Numerical simulation and discussion

The electrical potential and charge density distribution of a typical DDL representative of Montmorillonite as shown in Eq. (5) together with boundary conditions of Eqs. (13-14) were numerically simulated with COMSOL Multiphysics (ver 5.1). For the modelling of the hydraulic conductivity, Eq. (83) and Eq. (99) were obtained by integral computation with COMSOL. The rest of model parameters were shown in Table 6.2. Figure 6.13 shows the FEM model of DDL with the left boundary as the solid surface and the right boundary as the midplane in pore space.

The calculated potential and charge density are shown in Figs. 14-15. The integrated model parameters G and It/Ic are shown in Fig. 6.16, based on which the hydraulic conductivity of bentonite can be calculated as shown in Figs. 6.17-6.18. It is obvious that more salinity leads to less electroviscous retardation effect. The hydraulic conductivity increases gradually with increasing salinity until the retardation factor becomes negligible. Comparison with experimental data reveals very good agreement. Note that for both dense and loose bentonites, the electroviscous effect is less significant to the pressure driven flow. In such circumstances, other mechanisms like flocculation of colloidal particles and overlapping of DDL may be too significant in magnitude to be neglected in analysis. However, the normally compacted bentonite basically is well described by the electrokinetic flow model.

Table 6.2 Model constants for the electrokinetic flow problem

Parameter	Value	Unit
c_b	10-6000	mol/m^3
z	1	
e	1.6e-19	C
T	298.15	K
K_B	1.38e-23	$m^2*kg/(s^2*K^1)$
ε_0	8.854e-12	F/m
ε_r	78	
μ	1E-7	Pa*m/kg ($\mu=\eta/\gamma_w g$)
ψ_0	25	mV
S	700	m^2/g

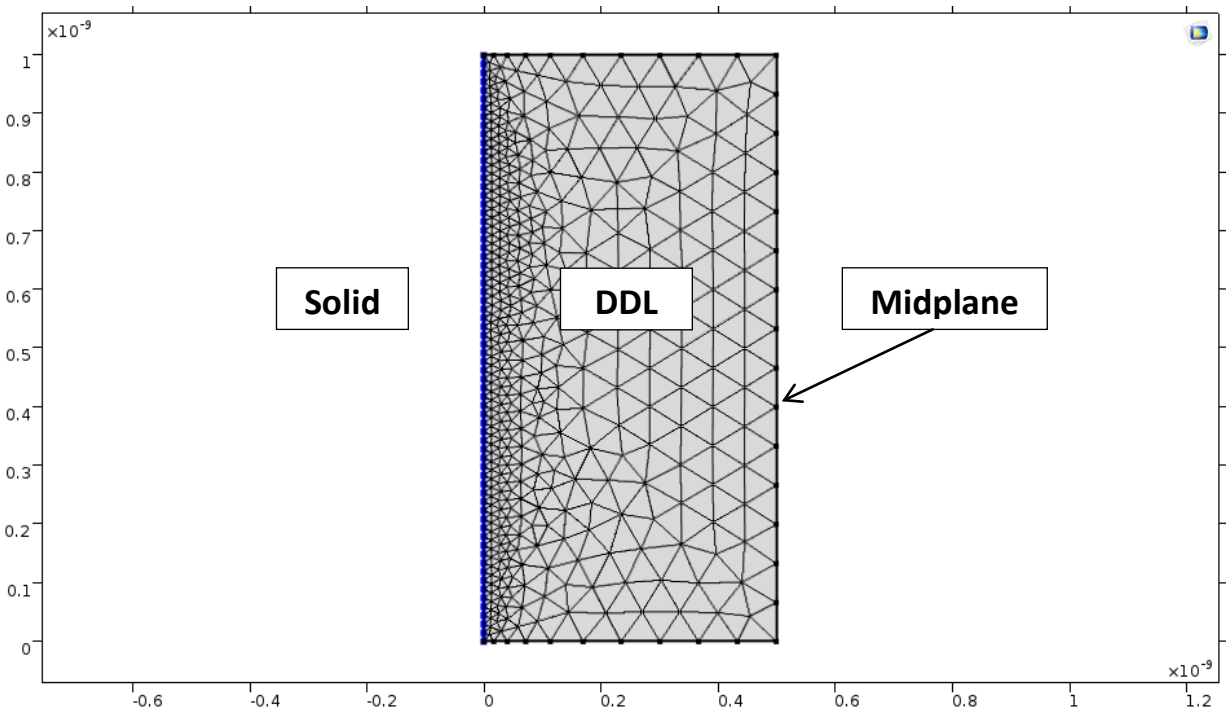

Figure 6.13 FEM model of diffuse double layer for hydrated bentonite clay

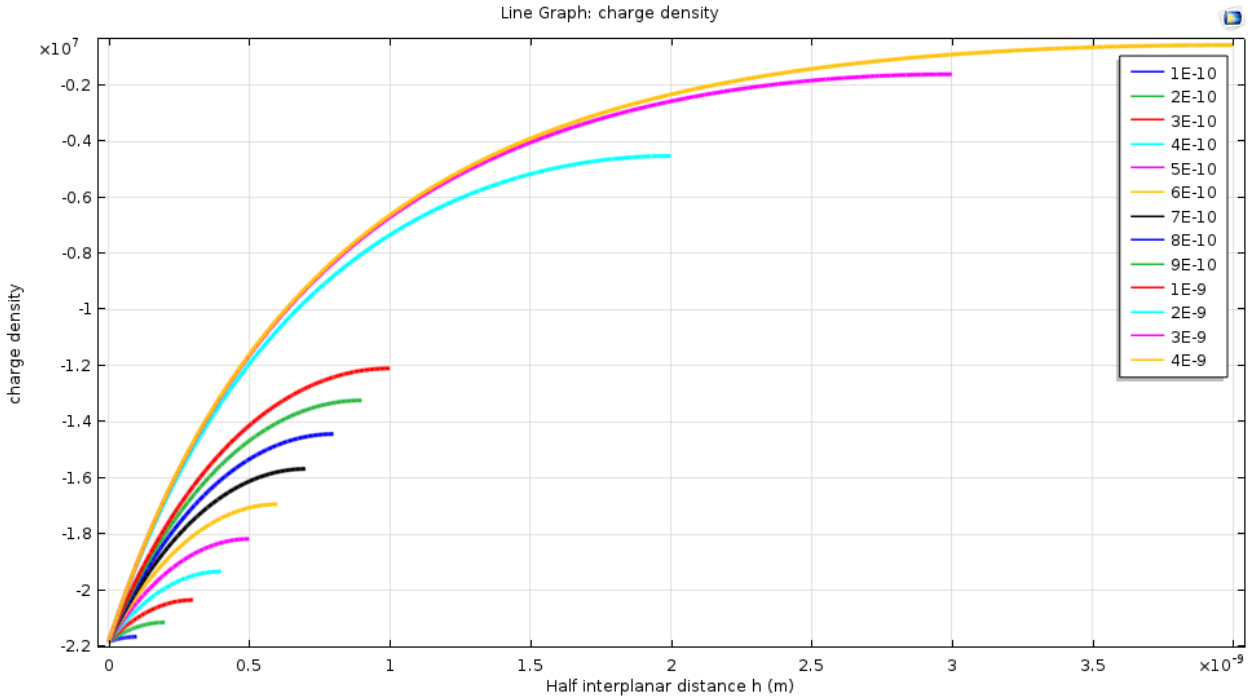

Figure 6.14 Variation of charge density with half interplanar distance h from 1 to 40 nm

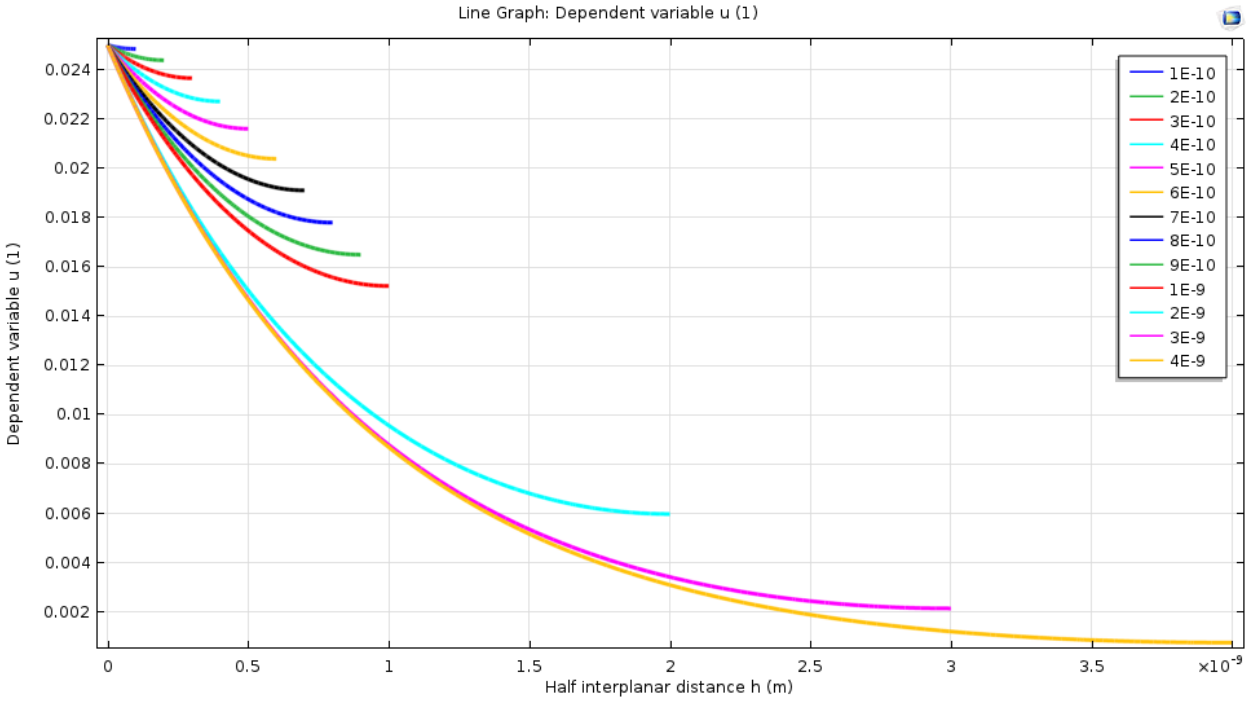

Figure 6.15 Electric potential (u) distribution in the diffuse double layer (1 nm < h < 40 nm; c0=0.1 M)

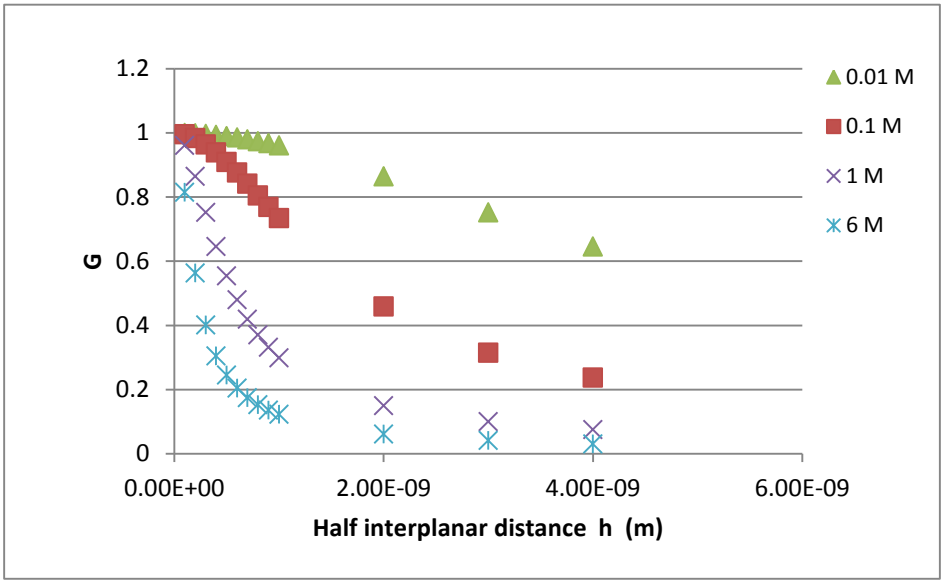

(a)

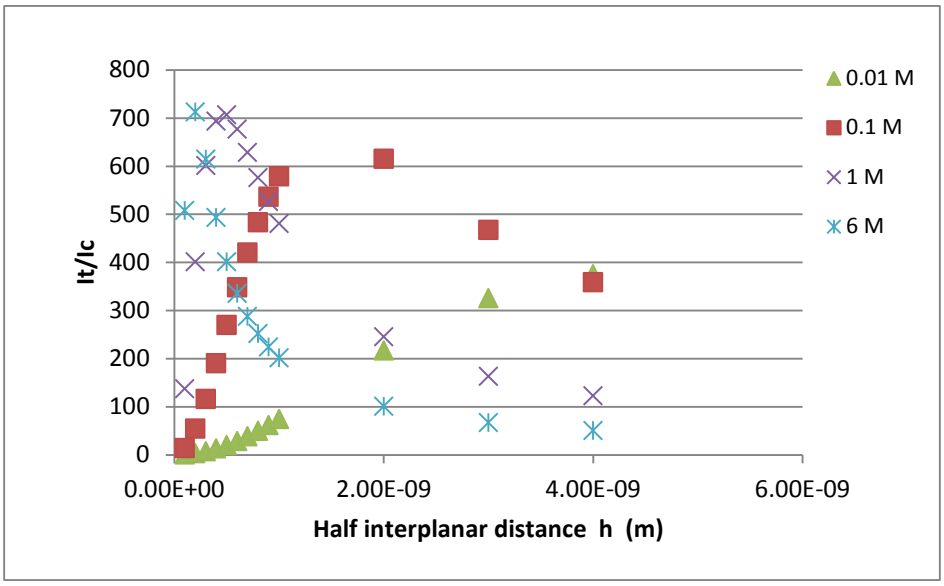

(b)

Figure 6.16 Numerically computed parameters of G (a) and It/Ic (b) with increasing h

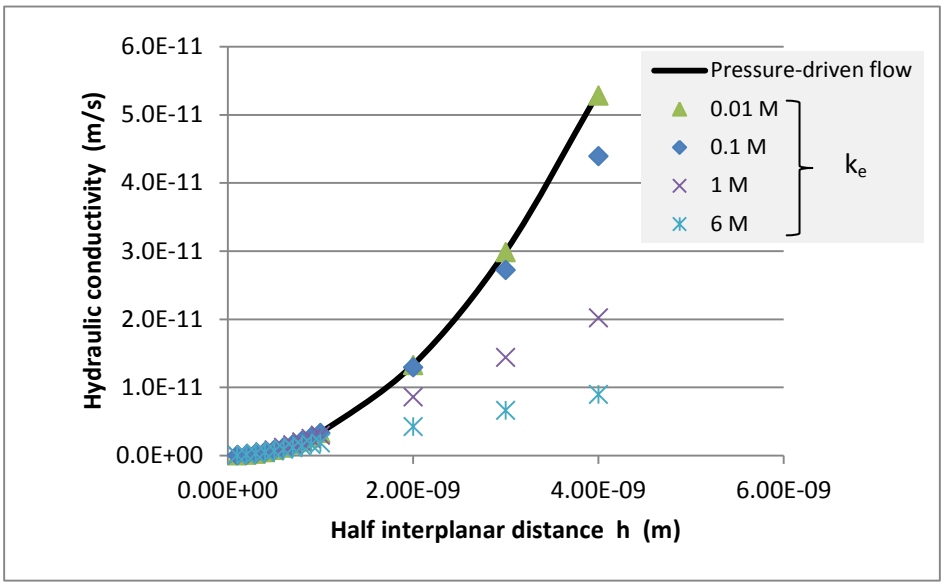

Figure 6.17 Variation of modelled hydraulic conductivities (kp and ke) with half interplanar distance

Note that the following relationship has to be cited for calculating the dry density of soil on the basis of half interplanar distance d:

$$\rho_d = \frac{G_s}{1+e} = \frac{G_s}{1+G_s w} = \frac{G_s}{1+G_s S \gamma_w d} \quad (104)$$

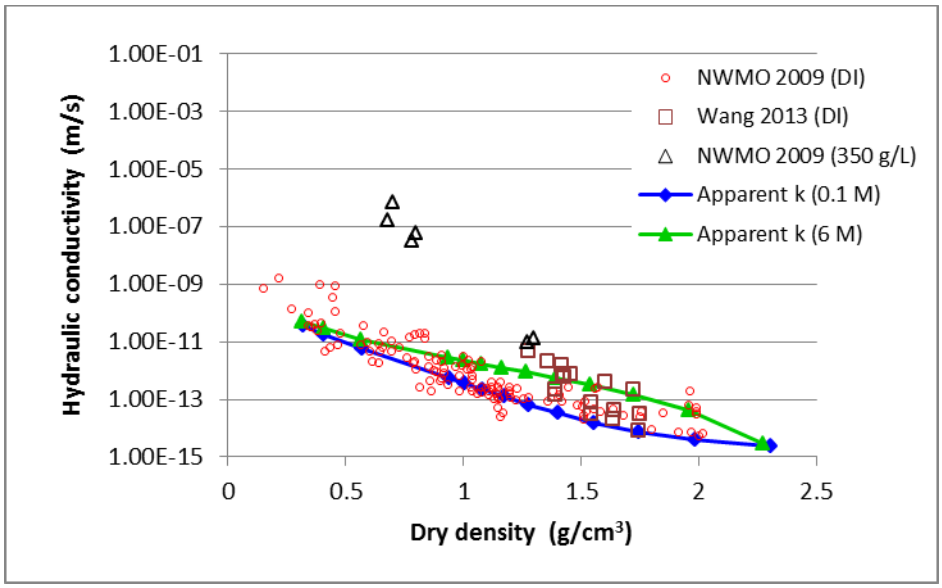

Figure 6.18 Modelled apparent hydraulic conductivity of bentonite clay and its comparison with reported experimental results

6. Conclusion

So far, a unified theoretical framework was developed to address the uniqueness of various fundamental parameters behind the differences in characterization techniques, i.e. the swelling pressure, compression, suction and permeability of expansive soil (i.e. MX-80) that were all successfully modelled with the PB equation based models.

Attempts were made to investigate the possibility of explaining the matric suction with assumption of positively charged meniscus film and its asymmetric electrostatic interaction with clay minerals. Various aspects of the water retention curve of expansive soil were well illustrated by the new model.

Using the same set of PB equation and the governing equation for electrokinetic flow, the permeability of compacted bentonite at various dry densities and salinities were numerically evaluated and compared against the reported test data with satisfying agreement.

It is shown that DDL greatly determines almost every aspect of bentonite's hydraulic-mechanical behaviours and the versatile DDL theories are sufficient to model these behaviours.

References

Agus, S.S., Arifin, Y.F., Tripathy, S., Schanz, T. (2013) Swelling pressure–suction relationship of heavily compacted bentonite–sand mixtures. Acta Geotechnica. 8:155–165

Andelman, D. (2006) Introduction to Electrostatics in Soft and Biological Matter. Chapter 6 in Soft Condensed Matter Physics in Molecular and Cell Biology. Edited by W.C.K. Poon and D. Andelman. Taylor & Francis 2006. Pages 97–122

Baille, W., Tripathy, S. and Schanz, T. (2013) Effective Stress in Clays of Various Mineralogy. Vadose Zone J. doi:10.2136/vzj2013.06.0112

Ben-Yaakov, D., Burak, Y., Andelman, D. and Safran, S. A. (2007) Electrostatic interactions of asymmetrically charged membranes. E.P.L. 79: 48002

Burgreen, D., Nakache, F. R. (1964) Electrokinetic Flow in Ultrafine Capillary Slits. J. Phys. Chem. 68 (5), 1084-1091

Chaplin, M.F. (2015). Water Structure and Science. London South Bank University. Published online at http://www1.lsbu.ac.uk/water/water_structure_science.html

Cheng, G.C., Tang, X.W. (2010) An easy-to-implement multi-scale computation of permeability coefficient for porous materials, Microporous & Mesoporous Material, 130(1-3):274-279

Derjaguin, B. V. and Kusakov, M. M. (1936) The properties of thin layers of liquids. Proceedings of the Academy of Sciences of the USSR, Chemistry series. **5** : 741-753.

Derjaguin, B. and Landau, L. (1941) A theory of interaction of particles in presence of electric double lovers md the stability of Iyophobe colloids and disperse systems. Acta Physicochim (USSR) 14:633–662

Gregory, J. (1975) Interaction of unequal double layers at constant charge. Journal of Colloid and Interface Science. 51(1): 44-51

Gavish, N., Promislow, K. (2012) Dependence of the dielectric constant of electrolyte solutions on ionic concentration. PACS numbers: 61.20.Qg,77.22.Gm,77.22.Ch

Herbert, H.J., Kasbohm, J., Sprenger, H., Fernández, A.M., Reichelt, C. (2008). Swelling pressures of MX-80 bentonite in solutions of different ionic strength, Physics and Chemistry of the Earth, Parts A/B/C, 33(S1): S327-S342

Huang, H., Ruckenstein, E. (2004) Interaction force between two charged plates immersed in a solution of charged particles. Coupling between double layer and depletion forces. Langmuir. 20(13):5412-7

Jo, H.Y., Benson, C.H., Shackelford, C.D. et al. (2005) Long-Term Hydraulic Conductivity of a Geosynthetic Clay Liner Permeated with Inorganic Salt Solutions. Journal of Geotechnical and Geoenvironmental Engineering. 131(4): 405-417

Jungwirth, P. and Tobias, D. J. (2006) Specific ion effects at the Air-Water interface. Chem. Rev. 106: 1259-1281

Kaufhold, S., Dohrmann, R., Klinkenberg, M., Siegesmund, S., Ufer, K. (2010) N2-BET specific surface area of bentonites. Journal of Colloid and Interface Science 349:275–282

Komine, H., and Ogata, N. (1999). Experimental study on swelling characteristics of sand–bentonite mixture for nuclear waste disposal. Soils and Foundations, 39(2): 83–97.

Komine, H., and Ogata, N. (2003) New equations for swelling characteristics of bentonite-based buffer materials. Can. Geotech. J. 40: 460–475

Levine, S., Marriott, J.R. and Robinson, K. (1975) Theory of electrokinetic flow in a narrow parallel-plate channel. J. Chem. Soc., Faraday Trans. 2,71, 1-11

Lee, J.M. and Shackelford, C.D. (2005) Solution Retention Capacity as an Alternative to the Swell Index Test for Sodium Bentonite. Geotechnical Testing Journal. 28(1): 61-70

Leung, K. (2010) Surface potential at the air-water interface computed using density functional theory. The Journal of Physical Chemistry Letters. 1: 496-499

Li, Z., Xue, Q., Katsumi, T., Inui, T. (2014) Electric–hydraulic–chemical coupled modeling of solute transport through landfill clay liners. Applied Clay Science 101: 541–552

Lu, N., Godt, J.W. and Wu, D.T. (2010) A closed‐form equation for effective stress in unsaturated soil. Water Resources Research. 46: W05515

Mašín, D., Khalili, N. (2016) Swelling phenomena and effective stress in compacted expansive clays. Canadian Geotechnical Journal. 53(1): 134-147

Miller, R. L., Bradford, W. L., Peters, N. E. (1988) Specific Conductance: Theoretical Considerations and Application to Analytical Quality Control. U.S. Geological Survey Water-Supply Paper 2311

Mitchell, J. and Soga, K. (1976) Fundamentals of soil behaviors. Wiley.

Muurinen, A., Lehikoinen, J. (1998) Evolution of the porewater chemistry in compacted bentonite. Mat. Res. Soc. Symp. Proc. Vol. 506: 415-422.

Nextnano tutorial. http://www.nextnano.com/nextnano3/tutorial/1Dtutorial_GouyChapman.htm

Ozbek, H. (1971) Viscosity of aqueous sodium chloride solutions from 0 - 150^{o}C. American Chemical Society 29th Southeast Regional Meeting, Tampa, FL, November 9-11

Rao, S.M., Thyagaraj, T., Rao. P. R. (2013) Crystalline and Osmotic Swelling of an Expansive Clay Inundated with Sodium Chloride Solutions. Geotech Geol Eng. 31:1399–1404

Romero, E. (2013) A microstructural insight into compacted clayey soils and their hydraulic properties. Engineering Geology. 165: 3-19.

Seiphoori, A., Ferrari, A., Laloui, L. (2014) Water retention behaviour and microstructural evolution of MX-80 bentonite during wetting and drying cycles. 64: 9, 721-734

Schuhmann, Jr. R. (1955) Application of Gibbs-Duhem equations to ternary systems. Acta Metallurgica. 3(3): 219-226

Teschke, O. and de Souza, E. F. (2005) Water molecular arrangement at air/water interfaces probed by atomic force microscopy, Chem. Phys. Lett. 403: 95-101

Tian, C. S. and Shen, Y. R. (2009) Structure and charging of hydrophobic material/water interfaces studied by phase-sensitive sum-frequency vibrational spectroscopy. PNAS. 106 (36) 15148-15153

Ye, W.M., Zhu, C. M., Chen, Y.G. et al. (2013) Influence of salt solutions on the swelling behavior of the compacted GMZ01 bentonite. Engineering Geology. 166:74-80.

Chapter 7 A model for the coupled hydraulic-mechanical behaviour of sand-bentonite mixture inundated with brine

Summary

Based on diffuse double layer (DDL) theory of expansive clay, the swelling behaviour of MX-80 bentonite was predicted before relevant experimental results were available. A new constitutive model for unsaturated expansive soil was proposed in this study. The new model considers the well-known Bishop's effective stress principle, and assumes a unique equilibrium state line coincident with the virgin compression curve. The rebound strain due to unloading in terms of effective stress is assumed to be elastic. Wetting of unsaturated soil induces reduction in effective stress and the corresponding rebound swelling strain. However, this is not sufficient to represent the overall swelling when the soil is subject to wetting, as intensely discussed in the literature. Therefore an additional component of the total swelling strain that is designated to the DDL expansion due to suction variation is defined in the classical e-log(σ') graph by invoking an equilibrium state line for the final swollen state. The suction-relevant swelling strain addresses the concerns on the limit of Bishop's effective stress from the advocators for bimodal stress state variables.

Besides, for expansive soils the saturation-degree-based water retention curve is insufficient to address the large strain induced saturation degree change. An alternative relationship based on gravimetric water content is adopted to model the WRC of highly expansive soil. The governing equation for the unsaturated hydraulic flow is derived in accordance with the w-log(S_u) relationship.

Based on the new constitutive model, a series of hydraulic-mechanical coupled modelling was undertaken to predict the variation over time of the swelling pressure of a gradually saturated sand-bentonite mixture at designated initial density and left with technical void and fixed total volume. The modelling predicts the wetting-induced softening in swelling pressure and a subsequent hardening behaviour. A number of factors that influence the swelling performance were also examined. The modeling results indicate that the mock-up test could be equilibrated within days of brine infiltration.

1. Introduction

In many countries, including Canada, geological disposal is being proposed for the long term management of radioactive wastes. Geological disposal relies on a multiple barrier system, including the rock formations, the containers and the engineered seal materials, in order to provide long term containment and isolation of the wastes. Bentonite-based sealing materials are being considered in many countries as the primary candidates as buffer around the waste containers, as backfill for the emplacement rooms, and as sealing materials for access shafts and galleries. Therefore, theoretical and experimental research has been conducted actively in order to confirm the long term performance of

bentonite-based material in the presence of heat loading from the wastes and water re-infiltration from the host rock (Huertas and Santiago 1998, Martin and Barcala 2005, Villar et al. 2012, Millard et al. 2014, Saba et al. 2014, Chen et al. 2014). Most of these studies focused on the effects of thermal loading, and infiltration and the resulted swelling pressure of groundwater with relatively low salinity. In the Canadian context, sedimentary rock formations of the Michigan Basin are being considered as potential candidates for the disposal of radioactive wastes (NWMO 2011).

The groundwater at the depths being considered to host a potential repository is brine, with salinity on the order of 200-300 g/L (NWMO 2011). At the present time, the impact of such a high salinity on the mechanical and hydraulic behaviour of bentonite has not been extensively researched. The CNSC is currently conducting a collaborative research project with Queen's University (Kingston, Ontario, Canada) to experimentally investigate the swelling behavior of MX-80 bentonite permeated with highly concentrated saline solution that represents the field conditions of groundwater.

In this report, we developed a mathematical model in order to simulate the swelling pressure developed during infiltration tests performed at Queen's University. The model simulations were performed at the time when no experimental results were available. In this report we will therefore present the model description, and the simulation results without reconciliation with the experimental data. The latter will be performed at a later stage, when the experimental data will be available. The mathematical model coupled the equation of pseudo-static equilibrium with a modified Richard's equation for porewater flow in unsaturated media. A Bishop's type of effective stress principle is proposed, and an effective stress-strain constitutive relationship based on the Basic Barcelona Model (Alonso et al. 1999) is formulated.

2. A modified effective stress principle

Effective stress is an important principle in soil mechanics. Terzaghi (2010) first proposed that the deformation of soil matrix can be attributed to the difference between the total stress and pore pressure

$$\sigma' = \sigma - p$$

where σ is total stress, σ' is the effective stress, and p is pore pressure.

Biot (1941) further modifies the effective stress principle by proposing a rigorous expression for the consistence in volumetric strains of both pore fluid and solid matrix under hydrostatic stress increment, which defines the effective stress as

$$\sigma' = \sigma - \alpha p$$

The effective stress in unsaturated expansive soil usually takes the Bishop's formula of

$$\sigma' = (\sigma - u_a) + \chi(u_a - u_w)$$

where u_a is air pressure, u_w is water pressure, χ is the Bishop coefficient, $(\sigma - u_a)$ is defined as the net stress (Fredlund et al., 2012) and (u_a-u_w) is the matric suction.

In the recent text book of Fredlund et al. (2012), it is argued that Bishop's effective stress principle is merely constitutive and not physically sound ("violates the basic assumption inherent to classical continuum mechanics") to account for the effect of matric suction on both wetting/drying volumetric strain and shear strength, and "places serious constraints on subsequent formulations". However, some recent studies better rationalized the physical significance of the Bishop's effective stress principle by compiling a volume of experimental results and analysis of thermodynamics (Lu et al. 2010). Effective stress exerts influence on the soil behaviour in two ways, i.e. the volumetric deformation and the shear strength. The following part will be devoted to the elaboration of these viewpoints.

Volumetric-strain-based effective suction stress

Suction is known to induce shrinkage of soils, and has been correlated to the net stress in order to calculate the so-called "matric suction equivalent" (MSE) (Fredlund et al. 2012). The MSE is determined in oedometer test by soaking soil to allow swelling until full saturation and then compress the swollen specimen to its initial volume. It can be viewed as the effective stress exerted on the soil skeleton to prevent the soil from expanding to its full saturation state. The MSE serves the purpose of measuring the magnitude of the effective stress. Fredlund (2012) later compared this MSE with the swelling pressure determined by constant volume swelling test. But due to the energy dissipation during the deformation process, it always lies in the lower end of the measured value for specific soils compared to the swelling pressure by constant volume approach.

Vu (2004) assumes that the matric suction equivalent and matric suction are related to one another through a factor that varies from 0 to 1, which is approximated as the degree of saturation when the matric suction is less than the air-entry value (AEV) (Vu and Fredlund 2004). However, no experimental data has been provided to support this assumption. This ratio factor for some expansive soils sampled at field conditions was recently studied by Singhal et al. (2015). It mainly addressed the suction ranges much higher than the AEV, as shown in Fig. 7.1. The transition of the ratio factor from S_e at AEV to about 0.1-0.2 at higher suctions indicates that the contribution of matric suction to the equivalent net normal stress state vanishes to 0 when the soil is completely dry (Vu and Fredlund 2004).

A recent study by Baille et al. (2014) applied the concept of "the suction stress characteristic curves" developed by Lu et al. (2010) to volumetric compression of different clay minerals subject to a suction range of 0.03 to about 219.0 MPa. The effective stress– void ratio responses of the clays prove to be comparable to the oedometric compression behavior of initially saturated clays. For applied suctions smaller than the air-entry value of any clay, effective suction stress produced a similar volume change of the clay (χ=1) as the net stress on the same order of magnitude. It is also clearly demonstrated that suction changes beyond the AEV cannot produce equivalent volume changes in unsaturated soils, suggesting a weakening influence of matric suction on build-up of effective suction stress (χ<1) in unsaturated soils, which is consistent with the observation of Singhal et al. (2015).

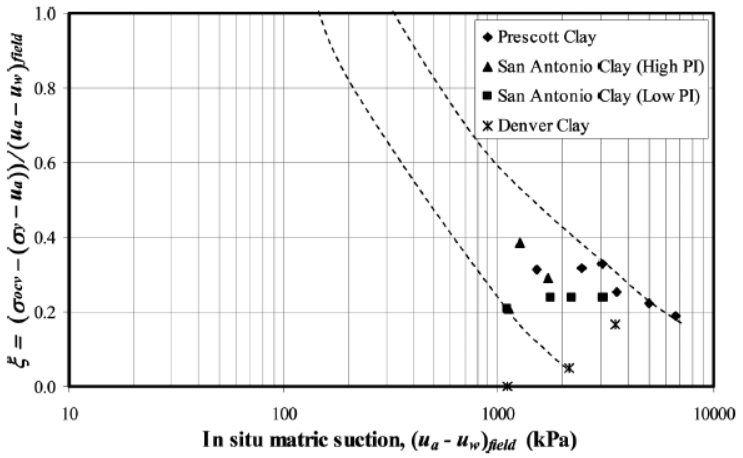

Figure 7.1 Bishop coefficient varies with suction in a logarithmic scale for expansive soils investigated in field conditions (σ_{ocv} is the MSE determined by oedometer test (Singhal et al. 2015))

Shear-strength-based effective suction stress

For unsaturated soils, the shear strength grows nonlinearly with the increase of matric suction. Fredlund et al. (2012) has reviewed a number of formulas for shear strength of unsaturated soils based on independent state variables. Basically three parameters are needed to fully address the unsaturated shear strength, i.e. the effective cohesion c', effective friction angle ϕ' and friction angle ϕ^b with respect to matric suction:

$$\tau = c' + (\sigma - u_a) * \tan\phi' + (u_a - u_w)\tan\phi^b$$

The Bishop's coefficient χ can be derived from Fredlund (2012) on the basis of shear strength equation and Bishop equation as

$$\chi = \frac{\tan\phi^b}{\tan\phi'}$$

This formula was later normalized into a unique equation of suction (Khalili and Khabbaz 1998). After analyzing a large collection of shear strength experimental results, a new Bishop effective stress coefficient χ was correlated with a suction $S_u=u_a-u_w$ normalized to the AEV through an expression as follows

$$\chi = \left(\frac{S_u}{AEV}\right)^{-0.55}$$

The above equation has important implication. It greatly simplifies laboratory testing to determine the shear strength of unsaturated soils; that is to say, no additional parameters are required other than the air entry value (Khalili and Khabbaz 1998).

Lu et al. (2010) proposed a power law suction stress characteristic curve that represents the effective stress for the shear strength behavior of unsaturated soil. The proposed closed-form equation is

intrinsically related to the soil water characteristic curve. Both semi-quantitative and quantitative validations show that the proposed closed-form equation well represents effective stress for a variety of soils ranging from sands to clays. It is claimed that the closed form expression provides a new shear strength criterion for unsaturated soil, which implicitly integrates the Bishop's effective stress principle. A comprehensive literature review on recent advances in effective stress principle can be found in Lu et al. (2014).

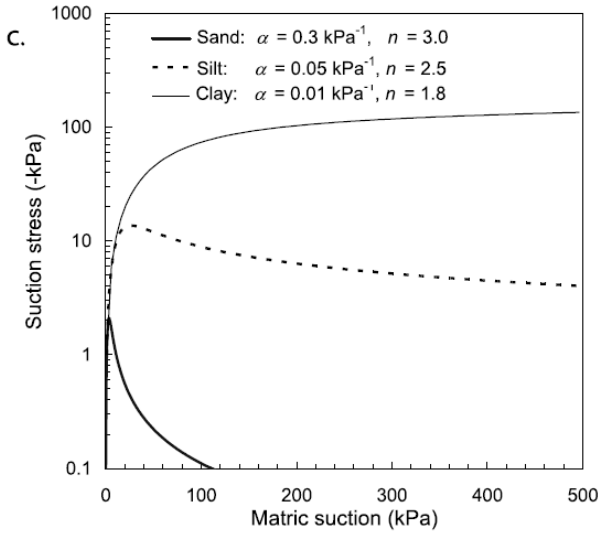

Figure 7.2 Estimated effective suction stress by Lu et al. (2010) for the typical soils in terms of matric suction

Incremental form of Bishop's effective stress

The classical Bishop equation in an incremental form is expressed as:

$$\mathrm{d}\sigma' = \mathrm{d}\sigma + \chi \mathrm{d}(u_a - u_w)$$

The effective stress that develops when a sample is fully resaturated starting from an initial suction S_u is:

$$\sigma' = \sigma + \int_0^{S_u} \chi \mathrm{d}(S_u)$$

According to the above literature review, a nonlinear Bishop's coefficient is proposed as

$$\chi = \begin{cases} 1, & (u_a - u_w) \le AEV \\ \gamma e^{-k(u_a - u_w + AEV)}, & (u_a - u_w) > AEV \end{cases}$$

where γ and k are two model constants. Integrating the differential Bishop's effective stress from full saturation to any suction value S_u leads to the following expression:

$$\sigma_B = \sigma' - \sigma = \begin{cases} S_u, & S_u \le AEV \\ AEV + \frac{\gamma}{k}\left(1 - e^{-k(S_u - AEV)}\right), & S_u > AEV \end{cases}$$

where σ_B is the MSE (Fredlund 2012) or suction stress (Lu et al. 2010).

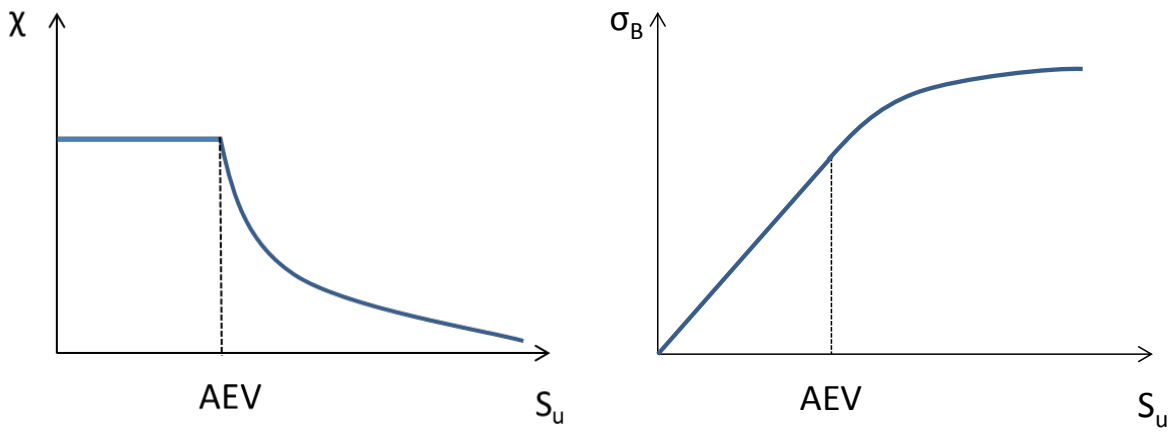

Figure 7.3 Diagram showing the nonlinear Bishop's coefficient and suction stress (the integral of χ with respect to increasing suction (γ=1))

The following graph shows the versatility and flexibility of the proposed exponential form of Bishop's effective stress. The above formula can also be proven numerically to be consistent with the normalized form of Bishop's effective stress parameter as proposed by Khalili and Khabbaz (1998).

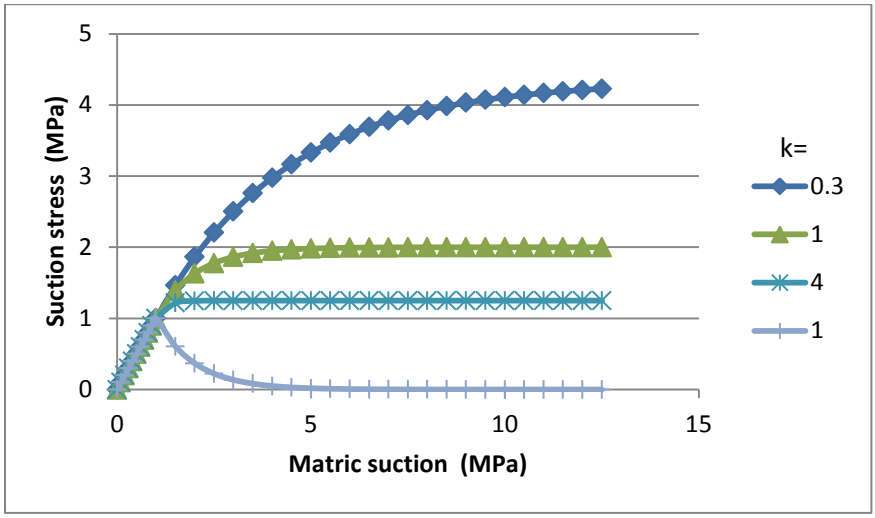

Figure 7.4 Parametric influence of k on shape of suction stress vs matric suction (Note the softening curve is obtained by setting $\chi = -e^{k(S_u - AEV)}, S_u > AEV$ in order to compare with the suction effective stress curve for sand soil as defined by Lu et al. (2010))

Agus et al. (2013) tested the relationship between suction and swelling pressure of S/B mixture, and noticed a threshold in suction that makes difference in swelling behavior for most of the compacted soils. They assume that the observed swelling pressure is due to net stress variation, and formulating a similar "swelling pressure increment ratio" to the above function. The determined swelling pressure against suction is depicted in Fig. 7.5, which clearly resembles the trend of Fig. 7.4, partly suggesting the validity of our proposed Bishop's coefficient. Similar to Lu et al. (2010), our proposed Bishop's coefficient has two parameters, i.e. the air entry value and the exponential index k. Figure 7.4 shows the computed suction stress with various values of parameter k. It is clearly demonstrated that our model resembles the general trend of the suction stress estimated by Lu's model as shown in Fig. 7.2 (Lu et al. 2010).

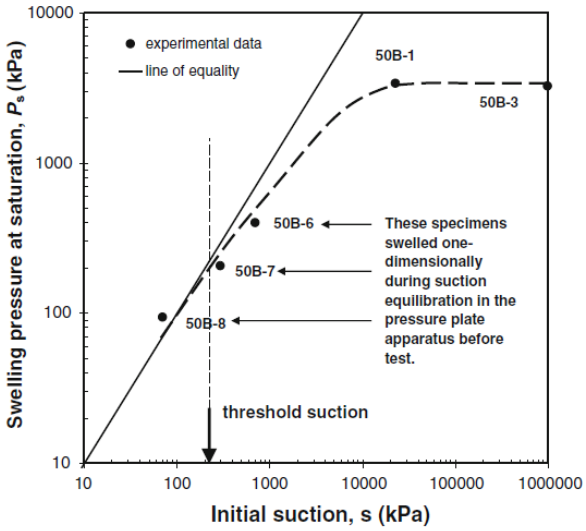

Figure 7.5 Experimentally determined swelling pressure (constant volume approach) of S/B versus initial suction (Agus et al. 2013)

3. Constitutive model for unsaturated expansive soil

Cam-Clay model for saturated soils

Cam-clay assumes the validity and presence of a critical state in typical clays, the slope of which can be related to Mohr-Coulomb strength parameter ϕ through

$$M = \frac{6\sin\phi}{3-\sin\phi}$$

and a logarithmic relationship between void ratio and mean stress:

$$e = e_0 - \lambda \ln \frac{p_c}{p_{c0}}$$

The yield function for modified Cam-Clay model is expressed as

$$F = q^2 + M^2 p(p - p_c) = 0$$

The critical state line together with the yield locus determines the elasto-plastic constitutive behaviour of the soil. When the stress level surpasses the preconsolidation pressure, strain-hardening happens in the form of

$$p_c = p_{c0} e^{-\frac{1+e_0}{\lambda-\kappa}\varepsilon_p}$$

where e_0 is the initial void ratio, ε_p is the effective plastic strain, and p_{c0} is the initial preconsolidation pressure.

Cam-Clay-based Basic Barcelona Model (BBM) for unsaturated soils

BBM is based on Cam-Clay model and extends it to consider the effect of matric suction on the constitutive behavior of an unsaturated soil. The BBM can be depicted in the p-q-s stress space as in Fig. 7.6. Load collapse line LC is an exponential function of suction that determines the maximum swelling pressure in wetting path. Suction also contributes to the internal cohesion (p_s) which follows a linear relationship in p-s plane (p_s=k*S_u).

The yield function for BBM is expressed as:

$$F_{BBM} = q^2 + M^2(p + p_s)(p - p_c) = 0$$

For constant volume swelling test, the stress is hypothesized to follow the neutral line (NL) in p-s plane as shown in the Fig. 7.6b. When NL hits the LC curve, stress turns to follow the yield curve LC and thus leads to decreasing swelling pressure with further wetting. Further extension of the BBM to Barcelona Extended Model (BexM) considers the bimodal porosity pattern and assumes elastic and plastic strains happen to microscale and macroscale porosities, respectively, in response to suction variation. It is shown that pore size transition from macro to micro pores indeed happens to the swelling of expansive soils. The transition leads to secondary hardening behavior in swelling pressure under constant volume conditions, after the primary softening stage.

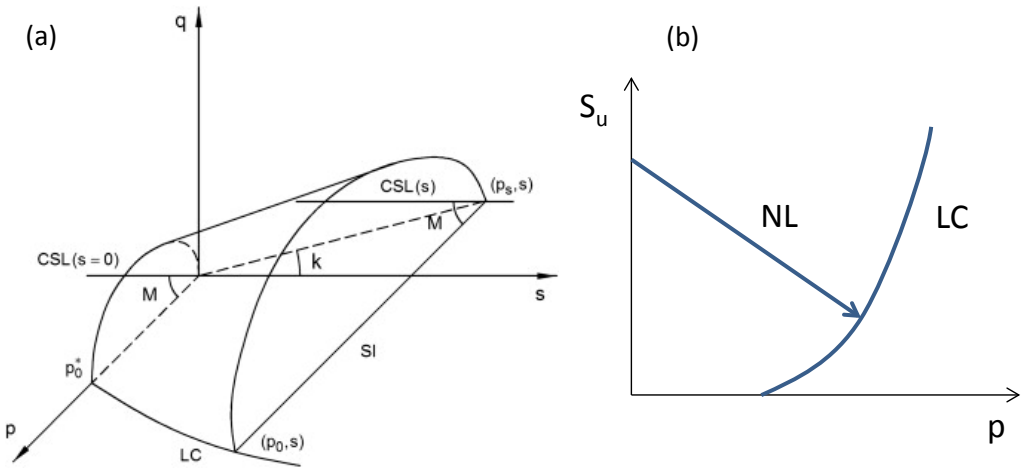

Figure 7.6 BBM yield loci in (a) p-q-s space and (b) p-s plane (Alonso et al. 1999)

Effective stress-integrated model (ESIM) for unsaturated expansive soils

Yield function

Following the Bishop's effective stress concept, the suction can be incorporated into the mean effective stress and thus being removed from the model, which greatly simplifies the BBM theory in expression, e.g. the load collapse yield surface can be represented by a single effective pre-consolidation stress Pc' as shown in Fig. 7.7.

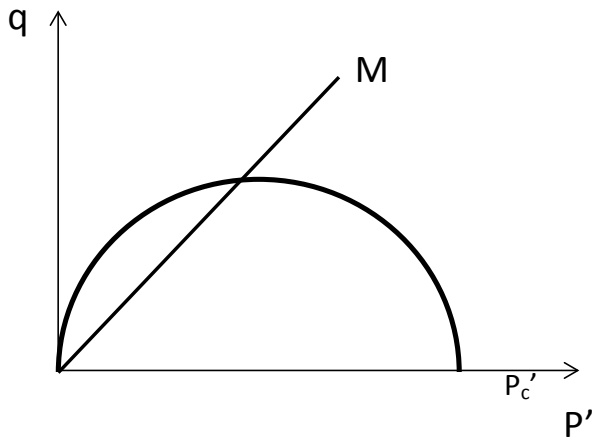

Figure 7.7 Yield locus and critical state line of ESIM

The effective-stress-based yield function takes the form of

$$F_e = q^2 + M^2 P'(P' - P_c') = 0$$

$$P_c' = P_{c0} + \sigma_B$$

$$P' = P + \sigma_B$$

where P is the net total mean pressure, P' is the Bishop's effective mean pressure, P_c' is the effective preconsolidation pressure, P_{c0} is the net preconsolidation pressure and σ_B is the Bishop's effective stress imposed by matric suction.

It is clear from the above yield function that the effective preconsolidation stress P_c' remains to be a variable as long as suction is present in the matrix, and keeps decreasing in magnitude in wetting path. Furthermore, the enhanced internal cohesion of bentonite due to suction effect is implicitly included in the yield function by the parameter P'. From the above description of the new ESIM model, you may find the great advantage of avoiding the determination of a number of extra model parameters that are necessary for classical models with double stress state variables.

The plastic strain in yield is computed from

$$\varepsilon_p = \lambda_p \frac{\partial F_e}{\partial \sigma}$$

where λ_p is the plastic multiplier.

Volumetric strain

It is assumed that the volumetric change of the unsaturated soil follows the compression and rebounding of the curves as shown in Fig. 7.8. Similar to the Cam-Clay model, void ratio varies linearly with logarithm of the effective stress. Suppose a stress path of the two red lines in Fig. 7.8, it is clear that elastic strain occurs to the rebounding line while both elastic and plastic strain occurs to the compression curve. During the re-saturation of an initially unsaturated soil, effective stress would decline according to the Bishop effective stress equation.

In the meantime, swelling strain other than the elastic rebounding deformation would be induced. This leads to the shift of e-log(σ') relationship from the rebound curve upward, as demonstrated in Fig. 7.8. This upward shift would not be infinite. Instead, it would stop and equilibrate somewhere near the virgin compression curve. This equilibrium state is critical to the development of the constitutive relationship for the swollen unsaturated soils. It has solid physical meanings and has to be addressed separately as below.

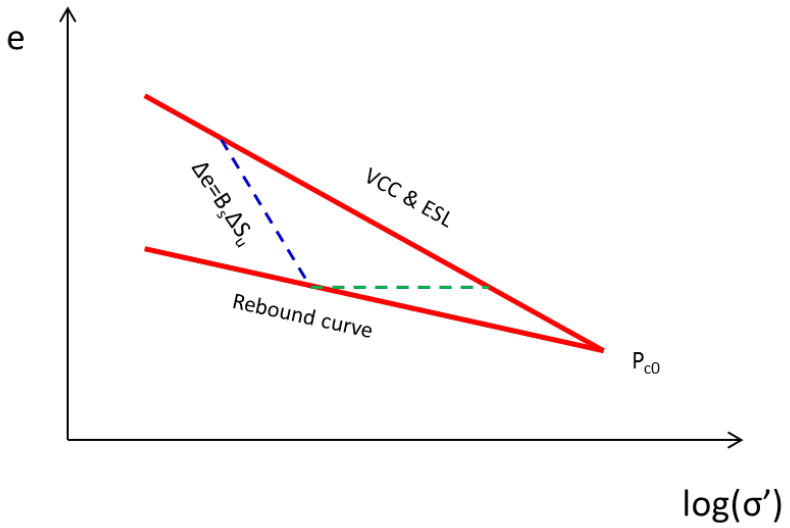

Note:
VCC: Virgin compression curve;
ESL: Equilibrium state line in full saturation;
P_{c0}: Pre-consolidation pressure.

Figure 7.8 Sketch diagram of compression and swelling of bentonite soil with the effective stress principle and the equilibrium state taken into account

Equilibrium state line

Numerous experimental studies have verified the existence of an equilibrium state or residual state for various type of soil when subjected to shear loading, which forms the foundation of the critical state constitutive models for clay soils. As for unsaturated expansive soil, such equilibrium can usually be achieved through wetting the soil to its full saturation. For instance, Sun et al. (2015) reported that

saturated pure bentonite shows a unique linear relationship between montmorillonite void ratio and mean stress in a logarithmic plot. It is also shown that the volumetric strain under a given vertical stress, and swelling pressure at a constant volume can be predicted based on this line.

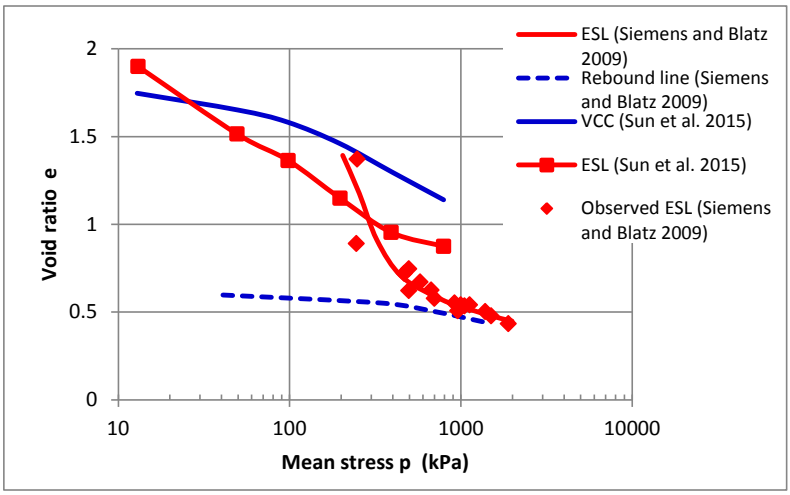

Figure 7.9 Void ratio vs. mean net stress relationship of two bentonites before and after fully saturated with water (GMZ Ca–bentonite from Sun et al. (2015) and S/B mixture from Siemens and Blatz (2009))

Siemens and Blatz (2009) studied the influence of various stress path and boundary conditions on the development of final swelling equilibrium of sand/bentonite (50:50 mixture). It was shown that the specific volume of the sample dominate the development of swelling pressure, which lies upon a unique swell equilibrium line between void ratio and swelling pressure. They went on arguing that this equilibrium state could be used to predict the final soil state under wetting conditions for different boundary and loading conditions as shown in Fig. 7.9. Their test data again verified the unique correlation between maximum swelling pressure and void ratio for any given initial specimen conditions (including void ratio and water content). Liu et al. (2014) studied the influence of stress-volume paths on the equilibrium swelling behavior of a local Australian expansive soil. Different stress-volume paths and initial conditions (including void ratio and water content) were applied to the test sample. The test results suggest that the stress-volume path does not influence the final swollen state significantly.

It is assumed in this study that there exists an equilibrium state of fully disturbed bentonite soil at full saturation besides the virgin compression curve. We also assume that that the two curves ESL and VCC are coincident with each other. Siemens and Blatz (2009)'s data demonstrated that the swollen ESL lies above the elastic rebound line. This is different from the observation of compacted bentonite possessing structured characteristics, e.g. with high porosity or granularity, under extremely dry condition, in which case the VCC lie above the ESL (Sun et al. 2015). For uniformly compacted sand/bentonite, it may not fall in the category of structured soils.

With regard to the relationship between ESL and VCC, we have to examine the source of the swelling, i.e. the DDL force amongst adjacent clay layers. When compacted bentonite becomes fully hydrated, the

surface of the montmorillonite clay is covered with thick layer of bounded DDL of water, exerting repulsive pressure to resist further compression of the soil matrix. More importantly, this force is reversible to a large extent. Assuming that friction is negligible between hydrated clay particles, the only force counteracting the external pressure would be the DDL repulsive pressure. Theoretical and experimental studies unambiguously revealed the unique e-σ relationship, i.e., for a given compacted bentonite at certain void ratio, the maximum swelling pressure σ is certain. That is to say, at a given stress loading, there will be a unique and predictable void ratio developed to the end of equilibrium, regardless of the stress path (i.e., whether it is compressive (VCC) or expansive conditions (ESL)). With such logic in mind, it is expected that VCC coincides with ESL for the normally compacted expansive soil with high clay mass ratio.

Extra swelling strain

We rely on the ESL for the description of the swelling strain of unsaturated expansive soils. The wetting-induced swelling strain can be estimated by the expansive coefficient B_s as indicated in Fig. 7.10. Although the stress path from P_i to P_s cannot be determined directly, the wetting induced strain can be decomposed into two parts: the one following the rebound curve and the other filling the rest portion. This extra swelling strain Δe_1 blocks the route to entry of air into soil matrix, which can be regarded as the plastic strain in macropore that is adopted in BexM. In the meanwhile, the elastic strain Δe_2 is mainly attributable to the loading/unloading effect, similar to the strain in micropore as that in BexM. The introduction of the equilibrium state line together with VCC and RC determine the upper and lower boundaries of the unsaturated soils' swelling and shrinkage deformation.

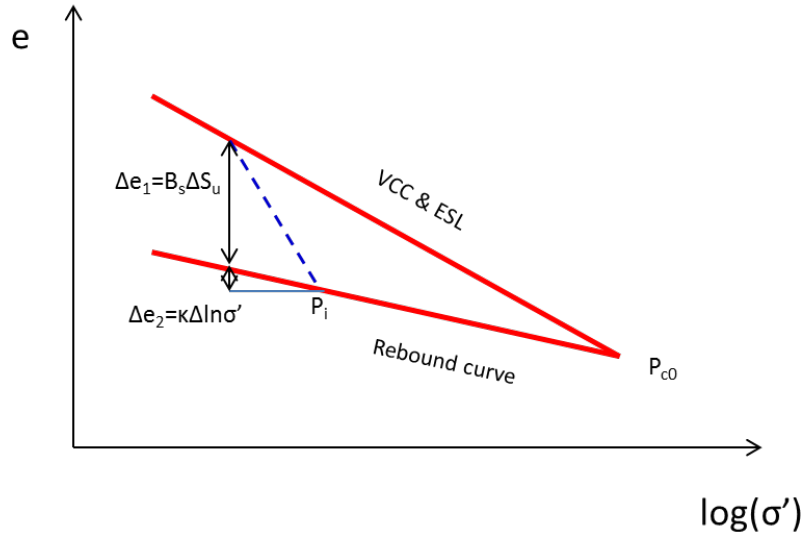

Figure 7.10 Decomposition of swelling strain into elastic rebound strain and plastic extra swelling strain

The following assumptions are adopted for the constitutive model for unsaturated expansive soil:

1. Elastic deformation occurs during unloading;
2. Plastic strain occurs to the virgin compression curve and to the compression beyond preconsolidation stress;

3. Wetting causes volumetric strain other than the elastic rebound strain when a certain threshold matric suction is overpassed, which is usually the air entry value (AEV);
4. The final equilibrium state in e-log(σ') space always falls below or upon the virgin compression curve, in no circumstance above the VCC;
5. The final equilibrium state stands for the fully saturated situation, and is assumed to be identical to the VCC for highly expansive bentonite in this study.

The swelling strain coefficient can be written as

$$B_s = \begin{cases} \dfrac{\lambda - \kappa}{AEV} \ln\left(\dfrac{\sigma'}{P_c'}\right), & 0 < S_u \leq AEV \\ 0, & S_u > AEV \end{cases}$$

The swelling strain is determined by

$$\varepsilon_s = \frac{\Delta e_1}{1 + e_0} = \frac{B_s \Delta S_u}{1 + e_0}$$

The overall constitutive function reads

$$\boldsymbol{\sigma}' = \mathbf{C} \cdot \left(\boldsymbol{\varepsilon} - \boldsymbol{\varepsilon_p} - \boldsymbol{\varepsilon_s}\right)$$

4. Hydraulic modelling

Water retention curve

The linear relationship for the brine water retention curve can be predicted by diffuse double layer (DDL) theory as evidenced in Chapter 6.

The water content-suction correlation takes the form of

$$w = -0.2018 * \log\frac{S_u}{150}$$

Or simply reads

$$w = A + B\log S_u$$

where S_u is the suction in MPa and w is the gravimetric water content with respect to bentonite**.** Compared to DI water, the maximum suction in MX-80 with brine solution is estimated to be 150 MPa, which is approximately 1/10 of that with DI water (1800 MPa).

According to the experimental observation of water retention curve for MX-80 bentonite, a linear relationship exists between gravimetric water content and matric suction (Millard et al. 2014). Therefore, the above formula is applied to the modelling of the hydraulic behavior of unsaturated bentonite.

The following will be devoted to the derivation of the w-log(S_u) based mass balance equation.

The effective water saturation (S_e) is

$$S_e = \begin{cases} \frac{G_s w}{e}, w < w_s \; and \; p < AEV \\ 1, \qquad w \geq w_s \; or \; p \geq AEV \end{cases}$$

where w_s is the saturated water content.

Water mass balance equation with w-log(S_u) form of WRC

By neglecting the atmospheric pressure perturbation, the classical water mass balance equation describes unsaturated flow through porous media:

$$\frac{\partial}{\partial t}(\rho_l n S_e) - \nabla \frac{k_s k_r}{\mu} \rho_l \nabla p = Q_m$$

where p is the pore fluid pressure, k_s is the saturated permeability, k_r is the relative permeability, Q_m is the source term due to external infiltration.

In this study, the above equation will be modified with the new WRC that correlates suction with gravimetric water content. The porosity (n) is related to void ratio (e) in the form of

$$n = \frac{e}{1+e}$$

The equivalence of water mass in the pore space with respect to porosity and dry solid mass is given as

$$n S_e = (1-n)\frac{\rho_s}{\gamma} w = (1-n) G_s w$$

Therefore

$$\rho_l n S_e = \rho_l (1-n) G_s w$$

and

$$e S_e = G_s w$$

Note that the porosity of a porous media is dependent on two stress states, i.e. 1) the pore pressure (or suction) that causes grain compression and 2) the effective stress that induces grain sliding and reorientation, which can be expressed in the form of

$$\frac{\partial n}{\partial t} = \frac{\partial n}{\partial p}\frac{\partial p}{\partial t} + \frac{\partial n}{\partial \sigma'}\frac{\partial \sigma'}{\partial t}$$

The second term of the above equation can be related to the overall volumetric strain (ε_v) due to effective stress variation,

$$\frac{\partial n}{\partial \sigma'}\frac{\partial \sigma'}{\partial t} = -\frac{\partial \varepsilon_v}{\partial t}$$

In a representative elemental volume of porous media, the liquid flux is thus described as

$$\begin{aligned}\frac{\partial}{\partial t}(\rho_l n S_e) &= \frac{\partial}{\partial t}[\rho_l(1-n)G_s w] = G_s\frac{\partial}{\partial t}[\rho_l(1-n)w] \\ &= G_s\left[(1-n)w\frac{\partial\rho_l}{\partial p}\frac{\partial p}{\partial t} - \rho_l w\left(\frac{\partial n}{\partial p}\frac{\partial p}{\partial t} + \frac{\partial n}{\partial \sigma'}\frac{\partial \sigma'}{\partial t}\right) + \rho_l(1-n)\frac{\partial w}{\partial p}\frac{\partial p}{\partial t}\right] \\ &= G_s\left[(1-n)w\frac{\partial\rho_l}{\partial p} - \rho_l w\frac{\partial n}{\partial p} + \rho_l(1-n)\frac{\partial w}{\partial p}\right]\frac{\partial p}{\partial t} - G_s\rho_l w\frac{\partial n}{\partial \sigma'}\frac{\partial \sigma'}{\partial t}\end{aligned}$$

If we let

$$\frac{\partial}{\partial t}(\rho_l n S_e) = S\frac{\partial p}{\partial t} + Q$$

where S is the storage term and Q is part of the source term attributable to the volumetric strain. Then we get the storage term

$$S = G_s w\left[(1-n)\frac{\partial\rho_l}{\partial p} - \rho_l\frac{\partial n}{\partial p}\right] + G_s\rho_l(1-n)\frac{\partial w}{\partial p}$$

and the partial source term

$$Q = G_s\rho_l w\frac{\partial \varepsilon_v}{\partial t}$$

The compressibility of fluid takes the form of

$$\frac{\partial\rho_l}{\partial p} = \chi_f\rho_l$$

And the compressibility of the matrix consists of two parts, the compression of solid skeleton and the compression of the pore void. Following the sign convention of soil mechanics (positive for compression), the compression of the solid mass due to suction variation is written as

$$\frac{\partial n}{\partial p} = \chi_s n$$

where ε_v is the volumetric strain under mechanical loading.

The specific moisture capacity of the water retention curve is given by

$$C_m = \frac{\partial w}{\partial p} = \frac{B}{S_u}$$

Accordingly the storage term turns into

$$S = G_s w\rho_l\left[(1-n)\chi_f - n\chi_s\right] + G_s\rho_l(1-n)C_m = \rho_l S_e e\left[(1-n)\chi_f - n\chi_s\right] + G_s\rho_l(1-n)C_m$$

Inserting the above expression into the mass balance equation leads to

$$\left[\rho_l S_e e\left((1-n)\chi_f - n\chi_s\right) + G_s\rho_l(1-n)C_m\right]\frac{\partial p}{\partial t} - \nabla\frac{k_s k_r}{\mu}\rho_l\nabla p = -\rho_l S_e e\frac{\partial \varepsilon_v}{\partial t} + Q_m$$

When implemented in COMSOL Multiphysics (Version 5.1) (COMSOL, 2016), the above formula turns into the target equation in the form of

$$\frac{\partial}{\partial t}(\rho_l n S_e) = \rho_l\left(S_e\overline{S} + \frac{\overline{C_m}}{\rho_l g}\right)\frac{\partial p}{\partial t} = \overline{Q_m}$$

where

$$\overline{S} = e\left[(1-n)\chi_f - n\chi_s\right]$$

$$\overline{C_m} = G_s\rho_l g(1-n)C_m$$

And the mass source

$$\overline{Q_m} = -\rho_l S_e e\frac{\partial \varepsilon_v}{\partial t} + Q_m$$

The relative permeability is assumed to follow a power law of the effective saturation, similar to the Brooks-Corey model, as follows

$$k_r = (S_e)^l$$

5. Swelling experiment

Oedometer swelling experiments on sand/bentonite mixture is being investigated at Queen's University. The specimen is sized at R×H=19 mm×20 mm. Constant volume swelling test, free swelling index test, mineralogical test, permeability test were systematically investigated in laboratory experiments. In one type of experiment, called mock-up test, a 1 mm radius gap would be left for limited free swelling. Both the top and bottom layers of the specimen are in contact with porous stones that are later subjected to the circulation of highly concentrated synthetic saline solution from the bottom. The swelling pressure of the sample is monitored throughout the test duration.

The initial dry density is at 1.65 Mg/m^3. The effective bentonite dry density (ρ_{EBDD}) equals to

$$\rho_{EBDD} = \frac{0.7G_s}{0.7+e}$$

The calculated effective bentonite dry density is 1.40 Mg/m^3, which corresponds to effective void ratio (e/0.7) of 0.978. Figure 7.11 shows the experimental results of the maximum swelling pressure of MX-80 bentonite against various initial dry density as well as the modelling results based on diffuse double layer theory (Li 2016). It is estimated from this graph, that the maximum swelling pressure of the above mentioned specimen is approximately 2 MPa.

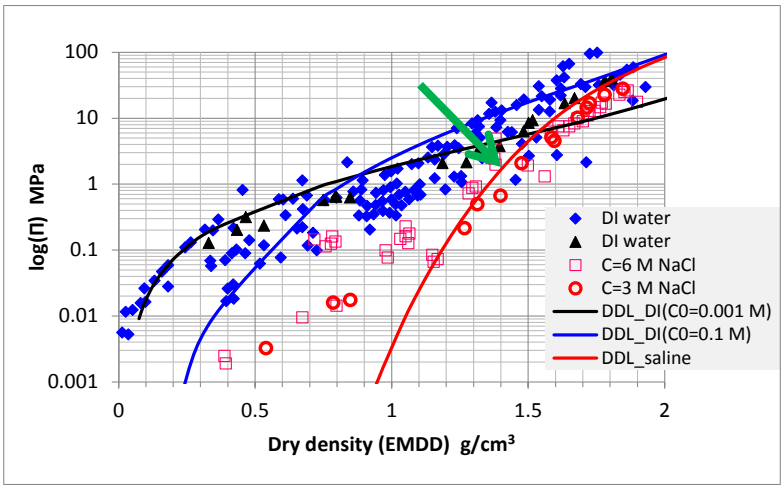

Figure 7.11 Experimental and modelling results of swelling pressure for bentonite at various effective densities (DDL_Saline corresponds to 6 M NaCl salinity)

Table 7.1 Parameters for the modelling of the mock-up test with prefabricated void

Cam-Clay model parameters	Value	Unit
P_{0e}	0.93	MPa
P_{c0}/P_0	2.5	
λ^*	0.137	
κ	0.046	
e_0	0.985	
N	1.048	
ν	0.15	
M	0.8-1.0	
Bishop coefficient parameters		
γ	0.1	
k	0.4	
Hydraulic properties		
p_0	-28	MPa
k_s	1.00E-19	m^2
ρ_l	1135	Mg/m^3
μ	0.0016	Pa*s
Gravimetric water content vs suction		
AEV	0.5	MPa
B	-0.2018	
l	5	

Note: * The compression index is estimated by DDL theory taking into account the chemical influence on swelling of bentonite clay. The swelling index is taken as 1/3 of the compression index.

Mohtar (2013) studied shear strength of sand-bentonite mixture at 0-5 % clay content and reported that the critical state friction angle remains at 31° and yield strength friction angle reduces from 23 ° to 17°.

Friction angle of sand-bentonite mixture varies from 44 ^{o} to 22^{o} when clay content increases from 0 to 9 %. Others (Fredlund 2012) also reported an average friction angle of 20^{o}, which corresponds to M=0.80 for the slope of the critical state line.

6. Conceptual model

Figure 7.12 shows the 2-D axisymmetric model for the oedometric swelling test. Both the top and bottom boundaries are assigned with roller boundaries, while the side wall is treated as a spring foundation, which has nonlinear strain-dependent stiffness with maximum allowable deformation of 1 mm in radial direction. The hydraulic boundary includes permeable top and bottom layers and a temporary pervious side boundary that seals up and becomes impermeable when the radial deformation of the soil gets in touch with the sidewall of the oedometer chamber.

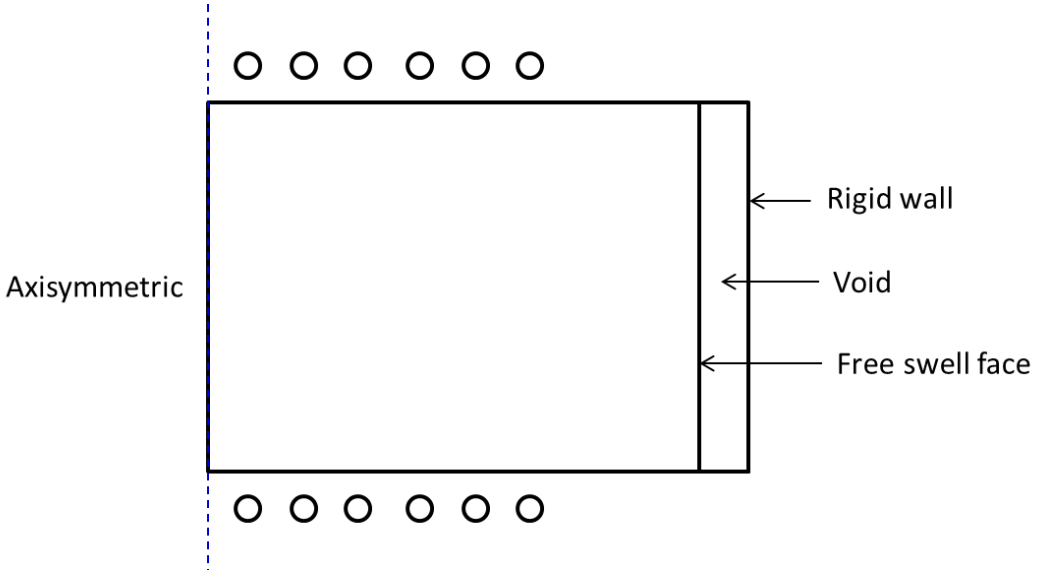

Figure 7.12 Schematic diagram of the mock-up test cell (R=18-19 mm, H=20 mm)

7. Numerical simulation

The numerical solution of the hydraulic-mechanical coupling equations is implemented using COMSOL. An exponential Bishop effective stress model and w-log(S_u) type water retention curve were both implemented in the coupled model.

The following equations address the required hydraulic-mechanical coupling and are solved numerically using COMSOL:

$$\left(S_e\overline{S} + \frac{\overline{C_m}}{\rho_l g}\right)\frac{\partial p}{\partial t} - \nabla\frac{k_s k_r}{\mu}\nabla p + eS_e\frac{\partial \varepsilon_v}{\partial t} = 0$$

$$\nabla \boldsymbol{\sigma}' + \chi \nabla \boldsymbol{p} = \nabla\left[\mathbf{C} \cdot \left(\boldsymbol{\varepsilon} - \boldsymbol{\varepsilon_p} - \boldsymbol{\varepsilon_s}\right)\right] + \chi \nabla \boldsymbol{p} = 0$$

Initial conditions include

$$p_i = -28 \text{ MPa}$$

$$\sigma_{0i} = -100 \text{ kPa}$$

$$\sigma_i = \sigma_{0i} + \chi p$$

where p_i is the initial pore pressure, σ_{0i} is the initial total stress and σ_i is the initial effective stress.

The model solution infiltrates from the bottom and side boundaries, except for the top boundary, as designed in the mock-up test.

Measures (weak form) were implemented in order to keep track of mean effective stress for the whole domain and all boundaries, which was later used for computation of the swelling coefficient for the next time step. Therefore the stress-dependent swelling coefficient can be sequentially updated on the basis of the results on the previous time step.

Cases with various combinations of model parameters are investigated numerically with COMSOL in order to understand the relevant significance to the overall swelling behaviors. Constant volume (CV) swelling test and limited free swelling (LFS) test were both studied. The most representative results are described in the following section of this report.

8. Results and discussion

Swelling pressure of sample under CV and LFS

Figure 7.13 shows the computed swelling pressure under CV and LFS conditions. When infiltrated from the bottom boundary only, the swelling pressure increases gradually for both CV and LFS conditions. The swelling pressure reaches its peak value after 250 hrs of infiltration for CV test, while it takes about 120 hrs for LFS test. Similar pattern in swelling pressure occurs to tests with infiltration from both side and bottom boundaries, where a much faster swelling develops up to 0.5 MPa within 30 hrs for both CV and LFS tests. The following stage of infiltration causes little difference in swelling pressure, which is usually less than 0.05 MPa, for different boundary conditions.

When infiltrated from all boundaries, a peak in swelling pressure shows up immediately after the soaking. A softening stage takes place afterwards and prior to reaching the equilibrium state. This behavior can be attributed to the wetting induced shrinkage of the yield surface in p-q-s space. The LFS sample always has less swelling pressure compared to the CV case. The general trend of softening and then hardening behavior is clearly demonstrated by the modelling results. Martin et al. (2014) reported the long-term performance of the FEBEX mock-up test and found that the more saturated materials showed a lower pressure peak than the less saturated ones (i.e. the softening pattern), but the absolute decrease with respect to the previous values is higher. It seems that the pressure loss is more intense for wetter clays, and longer for drier clays.

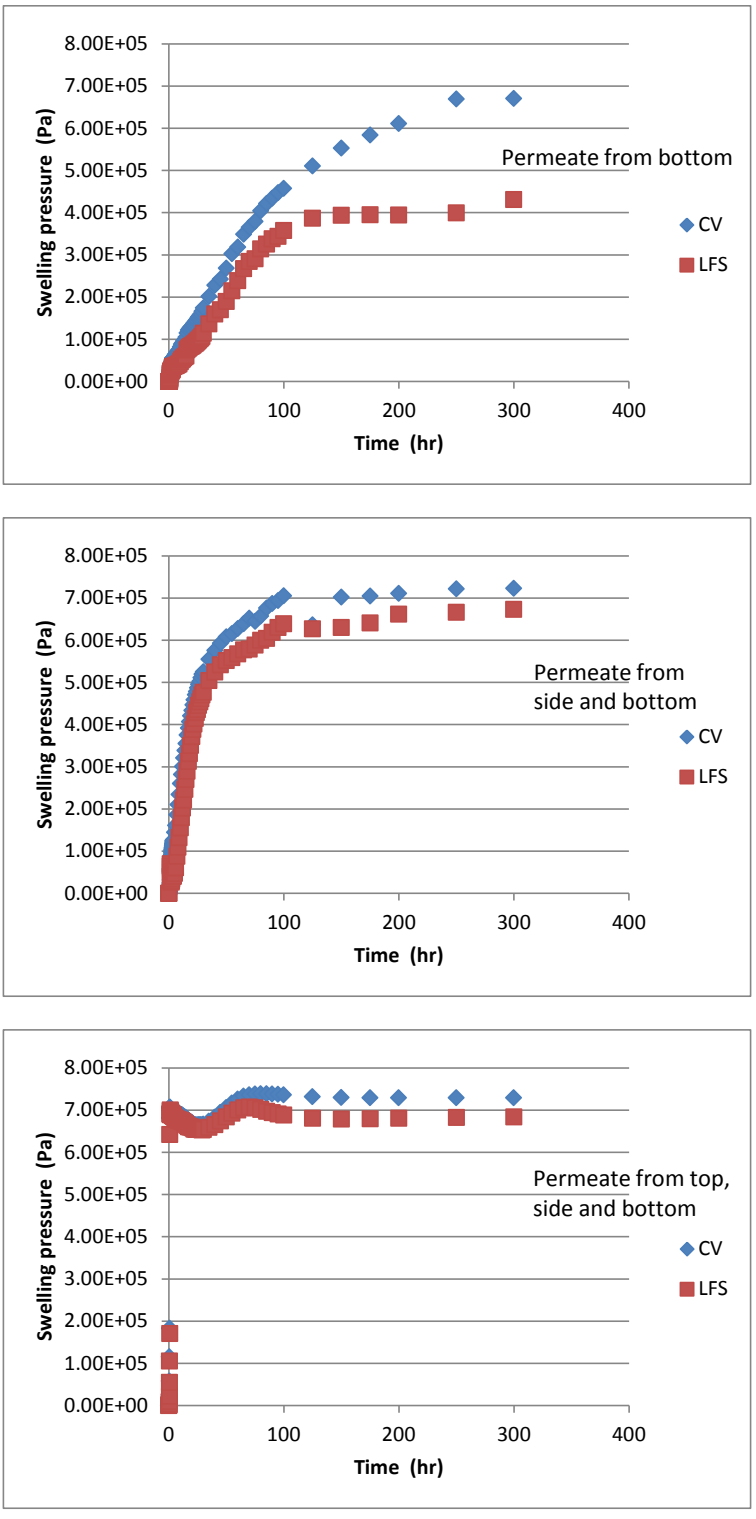

Figure 7.13 Computed average swelling pressure at the top boundary with elapsed time of infiltration under various boundary conditions

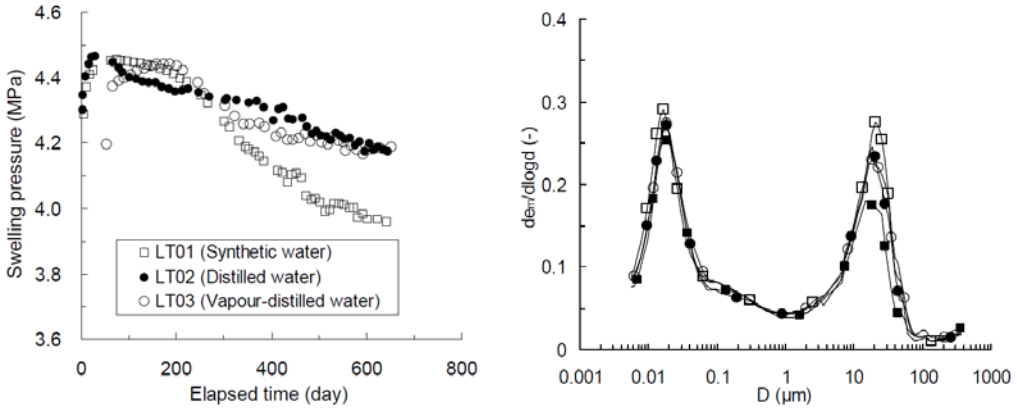

(a) (b)

Figure 7.14 Evolution of swelling pressure of S/B (70/30, 1.70 Mg/m^3) with infiltration period of time (Wang 2012)

Wang (2012) observed from small scale swelling test that bimodal pore size distribution (micropore at 0.02 μm and macropore at 20 μm) still exist in sand/bentonite mixed soil even after saturated with water for over 700 days. The pore size distribution curves of S/B inundated for 700 days are shown in Fig. 14b. No significant change in the pore size distribution is observed for the entire test samples despite minor variation in macropore of the one saturated with synthetic salt solution. According to Seiphoori et al. (2014), the microstructural evolutions of compacted granular bentonite in the fully saturated condition indicate a significant reduction of the macropores due to further hydration, rearrangement, swelling and filling and homogenization of the bentonite assemblages. Therefore it is believed that the soil specimen in Wang (2012)'s study has not reached full saturation yet, since the macropore (r>1 μm) is still present in the system. A major conclusion of Seiphoori et al. (2014) is that macropore will disappear in full saturation. The modelling results in this work suggest a gradual increase of swelling pressure is expected to entail the first stage of reduction. The absence of the second stage of swelling pressure increase may indicate the yet-to-reach final equilibrium state.

Contours of swelling pressure at various times

Figure 7.15 shows the contour plotting of the vertical total stress (equivalent to measured swelling pressure) at various elapsed times. It is noticed that the swelling pressure is non-uniform in the specimen and develops gradually with continuous infiltration of water. Stress concentration is observed at the saturation front, where the majority of the swelling strain takes place.

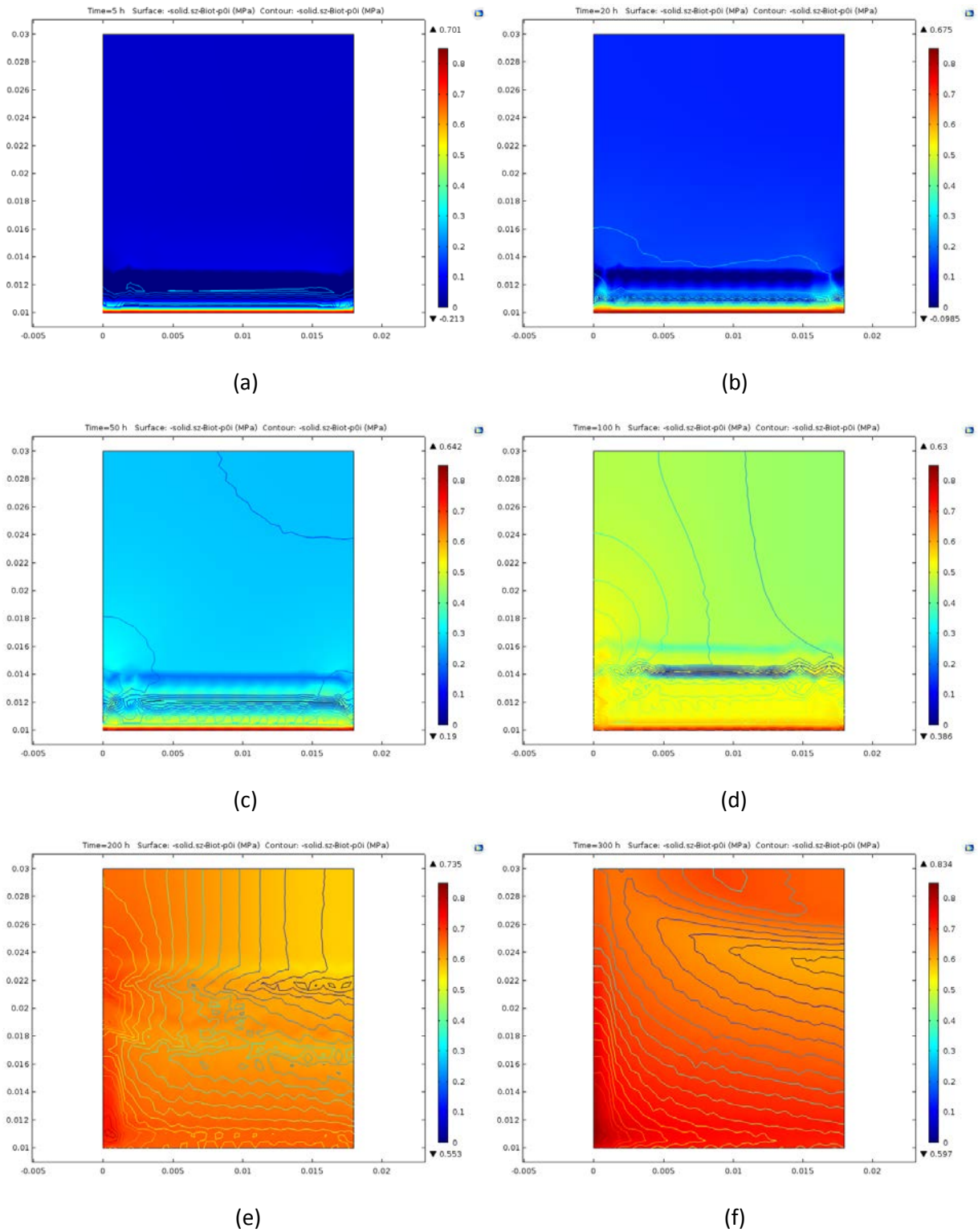

Figure 7.15 Contour plotting of vertical total stress (equivalent to measured swelling pressure) at various elapsed times (a-f: 5, 20, 50, 100, 200, and 300 hours) under CV conditions and permeation from bottom only

9. Conclusions

This study numerically simulated the mock-up swelling test of S/B mixture inundated with brine solution. The Bishop's effective stress principle is reviewed and adopted in the constitutive model for unsaturated expansive soil. An equilibrium state line is proposed to define the final state of the expansive soil at its full saturation. Together a new ESIM model is developed in the framework of Cam-clay model. A w-log(S_u) relationship-based WRC is implemented into the mass balance equation for unsaturated flow in large strain problems. The new constitutive model and the new HM coupled model are then applied to predict the variation of the swelling pressure of a gradually saturated sand-bentonite mixture at designated initial density and left with prefabricated void and fixed total volume.

References

Huertas, F. and Santiago, J.L. (1998) Scientific Basis for Nuclear Waste Management Xxi. McKinley, I.G. and McCombie, C. (eds), pp. 343-349.

Martin, P.L. and Barcala, J.M. (2005) Large scale buffer material test: Mock-up experiment at CIEMAT. Engineering Geology 81(3), 298-316.

Villar, M.V., Martin, P.L., Barcena, I., Garcia-Sineriz, J.L., Gomez-Espina, R. and Lloret, A. (2012) Long-term experimental evidences of saturation of compacted bentonite under repository conditions. Engineering Geology 149, 57-69.

Millard, A., Barnichon, J.D., Mokni, N., Thatcher, K.E., Bond, A. and Blaheta, R. (2014) Modelling benchmark of a laboratory test on hydro-mechanical behavior of bentonite.

Saba, S., Cui, Y.J., Tang, A.M. and Barnichon, J.D. (2014) Investigation of the swelling behaviour of compacted bentonite-sand mixture by mock-up tests. Canadian Geotechnical Journal 51(12), 1399-1412.

Chen, L., Liu, Y.M., Wang, J., Cao, S.F., Xie, J.L., Ma, L.K., Zhao, X.G., Li, Y.W. and Liu, J. (2014) Investigation of the thermal-hydro-mechanical (THM) behavior of GMZ bentonite in the China-Mock-up test. Engineering Geology 172, 57-68.

NWMO (2011) Geosynthesis, Nuclear Waste Management Organization.

Alonso, E.E., Vaunat, J. and Gens, A. (1999) Modelling the mechanical behaviour of expansive clays. Engineering Geology 54(1–2), 173-183.

Fredlund, D.G., Rahardjo, H. and Fredlund, M.D. (2012) Unsaturated soil mechanics in engineering practice, John Wiley & Sons, Inc., Canada.

Lu, N., Godt, J.W. and Wu, D.T. (2010) A closed-form equation for effective stress in unsaturated soil. Water Resources Research 46.

Vu, H.Q. and Fredlund, D.G. (2004) The prediction of one-, two-, and three-dimensional heave in expansive soils. Canadian Geotechnical Journal 41(4), 713-737.

Singhal, S., Houston, S.L. and Houston, W.N. (2015) Swell pressure, matric suction, and matric suction equivalent for undisturbed expansive clays. Canadian Geotechnical Journal 52(3), 356-366.

Baille, W., Tripathy, S. and Schanz, T. (2014) Effective Stress in Clays of Various Mineralogy. Vadose Zone Journal 13(5).

Khalili, N. and Khabbaz, M.H. (1998) A unique relationship for chi for the determination of the shear strength of unsaturated soils. Geotechnique 48(5), 681-687.

Lu, N., Khalili, N., Nikooee, E. and Hassanizadeh, S.M. (2014) Principle of Effective Stress in Variably Saturated Porous Media. Vadose Zone Journal 13(5).

Agus, S.S., Arifin, Y.F., Tripathy, S. and Schanz, T. (2013) Swelling pressure-suction relationship of heavily compacted bentonite-sand mixtures. Acta Geotechnica 8(2), 155-165.
Sun, W.J., Wei, Z.F., Sun, D.A., Liu, S.Q., Fatahi, B. and Wang, X.Q. (2015) Evaluation of the swelling characteristics of bentonite-sand mixtures. Engineering Geology 199, 1-11.
Siemens, G. and Blatz, J.A. (2009) Evaluation of the influence of boundary confinement on the behaviour of unsaturated swelling clay soils. Canadian Geotechnical Journal 46(3), 339-356.
Liu, X.F., Buzzi, O.P. and Vaunat, J. (2014) Influence of stress-volume path on swelling behavior of an expansive clay.
Li, Z. (2016) Application of the Diffuse Double Layer theory to the characterization of the fundamental properties of bentonite sealing materials, Canadian Nuclear Safety Commission.
Mohtar, E.I.e.a. (2013) Liquefaction Mitigation Using Bentonite Suspensions. Journal of Geotechnical and Geoenvironmental Engineering 139(8), 1369-1380.
Martin, P.L., Barcala, J.M. and Villar, M.V. (2014) Behaviour of a bentonite barrier under thermal and hydraulic gradients: FEBEX mock-up test, 16 years of operation.
Wang, Q. (2012). Hydro-mechanical behaviour of bentonite-based materials used for high-level radioactive waste disposal, Universitie Paris-Est; Tongji University Shanghai, Paris, Fance.
Seiphoori, A., Ferrari, A. and Laloui, L. (2014) Water retention behaviour and microstructural evolution of MX-80 bentonite during wetting and drying cycles. Geotechnique 64(9), 721-734.

K. Terzaghi. 2010. Soil Mechanics in Engineering Practice. Warren Press.
M.A. Biot. 1941. General theory of three-dimensional consolidation. J. Appl. Phys., 12: 155-164.

Chapter 8 Hydro-Mechanical-Chemical Coupled Modelling of MX-80 Bentonite Flooded with Brine

Summary

The DGRs for nuclear wastes are commonly faced with potential risks on the long-term behaviors of engineered barrier system (EBS) imposed by the interaction with moderate to highly concentrated brine water present in the geological formations on site. The bentonite-based EBS is expected to be compacted to a target density at optimum water content that is adjusted with non-saline water. When this expansive soil is exposed to the in-situ saline groundwater, transient mass transport (hydraulic flow and solute transport) will take place right after. This process will involve time-dependent Hydraulic-Mechanical-Chemical (HMC) couplings and appear to be different from our previous predictions based on the equilibrium state principle. The laboratory experiments conducted at Queens' University have already indicated some "odds", e.g. the swelling pressure of MX-80 bentonite inundated with brine shows a big and instant pulse at early stage of flooding but diminishes gradually afterwards. In order to fully understand the underlying mechanism for these experimental observations, a comprehensive HMC coupled model has to be developed.

A dual-porosity conceptual model was proposed in this study to reflect the transient variation of swelling pressure observed in MX-80 bentonite, when flooded with highly concentrated brine water representative of the geological groundwater at Bruce DGR site. In order to describe the fully coupled HMC influences on expansive soils, governing equations for HMC processes were developed by adopting a dual-porosity framework and some hypothesis of microstructure-water content dependence and WRC-chemistry correlation. The dependence of hydraulic and mechanical properties on factors including porosity, salinity, and water content was discussed in detail. The proposed models were successfully implemented into a general-purpose mutiphysics-coupled FEM software COMSOL (Ver 5.2a), and were further calibrated with experimental results on the swelling pressure of compacted MX-80 bentonite flooded with brine model water (from Queens'U), and infiltration of bentonite column with clean water (from POSIVA). The observed temporal evolution of water content, suction and swelling pressure of compacted MX-80 can be well reproduced by our model.

The elastic moduli, permeability, WRC parameters were predetermined experimentally, while the chemo-osmosis semipermeable coefficient, suction toe, fluid exchange rate, mass exchange rate were optimized by best-fitting the swelling pressure evolution curves through numerical simulation. A number of unique relationships are developed for MX-80, i.e. permeability of micropore at various void ratios, WRC of micro- and macro-pores, constitutive relations of micropore dependence on water content, and the diffusion coefficients at various porosities. These constitutive relations are physically sound, verifiable by experiments, and unique to MX-80. It can thus be applied to analyzing complicated HMC couplings of the engineered barrier system for waste disposal in both short-term and long-term risk assessments.

1. Review of hydro-chemo-mechanical coupled behaviors of bentonite

Chemo-mechanical behaviours

Oedometric test

Chemical solutions have long been recognized to influence the swelling and shrinkage behaviours of expansive soils. Lime has been widely used to stabilize problematic expansive soil in foundation engineering, road construction and trenching excavations. Chemical solutions of various dielectric constants have been found to significantly affect the swelling behaviour of expansive soils. This study focused on chemical solutions with dissolvable electrolyte in water. Literature review has been conducted to understand chemical-induced consolidation of bentonite-based soil, the recent porosimetric studies on the pore structures, and the effect of chemical solutions on fundamental properties of compacted bentonite.

Di Maio (1996) reported chemical consolidation of a Na-bentonite in contact with saturated chemical solutions of NaCl, KCl and $CaCl_2$. The prepared oedometric soil specimens have very high void ratio (e_0=8). Increased vertical loading subsequently applied on the soil specimens led to volumetric contraction. Replacement of pore fluid with saturated saline caused additional volumetric contraction, which was termed as osmotic consolidation. Saline water containing certain amount of dissolved chemicals is able to draw water from the clay aggregate under osmotic suction. The contraction of clay aggregate directly contributes to the overall volumetric shrinkage. This osmotic effect seems additive to the overburden loading, as shown in Figure 8.1.

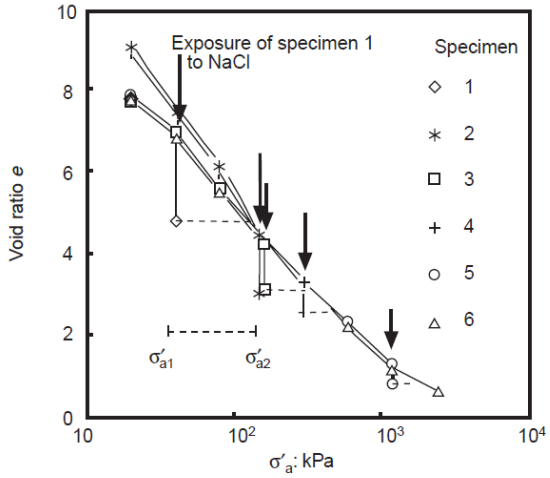

Figure 8.1 Virgin compression curves for bentonite with replacement of pore fluid (Di Maio, 1996)

Figure 8.2 shows the experimental results on consolidation of bentonite soils from different sources (Di Maio, 1996; Schanz and Tripathy, 2009; Wang 2013). . It is observed that the rebounding curve of the highly porous bentonite of Di Maio (1996) soaked with DI water overlaps with the compression curves of dense MX-80 bentonite or sand/MX-80 mixture. The rebounding curve of saline soaked bentonite maintains a constant slope lying beneath the ESI of the DI water.

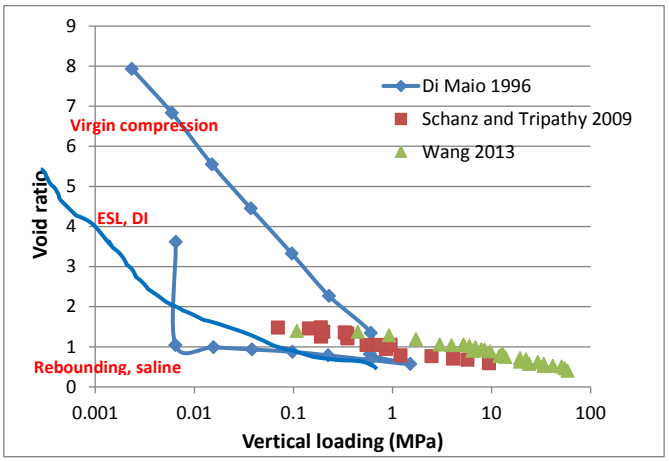

Figure 8.2 Comparison of compression curves of various bentonites

According to (Montañez, 2002) a limit state with negligible volume change exists for expansive soils when fully saturated with DI water. This limit state appears to be void of influence from stress path and suction path, as shown in Figure 8.3. Similar phenomenon has been reported by Siemens and Blatz (2009), in which a critical state was verified by experiments on swelling of bentonite under various wetting paths.

From the results of (Di Maio, 1996), an equilibrium state line (ESL) is speculated to exist for bentonite soaked with saline of a certain chemical concentration. Due to the osmotic suction effect, this ESL for saline would lie below the ESL for DI water, and would be smaller in the slope of compression or rebound curves. This hypothesis is partly supported by the data of (Di Maio, 1996), and is further supported by the results of Ye et al. (2015). Basically it constitutes the foundation of some chemo-mechanical constitutive models (Do Guimarães et al., 2013; Jussila, 2006; Murad and Moyne, 2008).

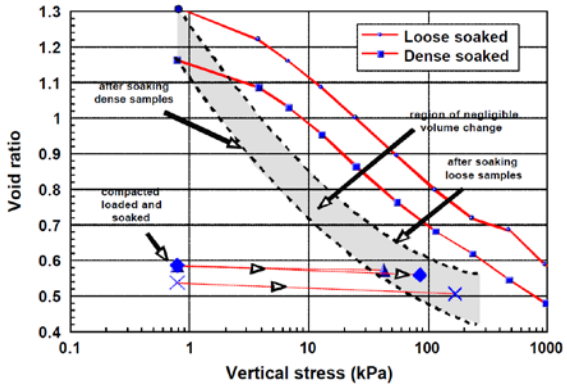

Figure 8.3 Void ratio versus vertical stress for bentonite under compression and wetting conditions (Montañez, 2002)

The effect of osmotic suction from NaCl solution upon bentonite was found to be reversible, i.e. if the concentrated salinity was replaced by DI water, the void ratio increases quickly to the rebounding curve of bentonite for DI water. For instance, Musso et al. (2003) studied the role played by the soil structure in the evolution of chemo-mechanical-coupled processes in bentonite. Soils was either compacted or

consolidated to target dry density and then subject to permeation cycles of 5.5 M NaCl solution and DI water in sequence. The observed volumetric deformations are shown in Fig. 8.4. The first stage of volumetric decrease is due to osmotic suction of saline and the later reflection is because of DI leaching of salt solution that removes the osmotic suction. Chemical cycling of compacted bentonite was also investigated by Di Maio (1996), and the results are shown in Fig. 8.5. The rebounding curve of the sample, which was originally exposed to saline solution and subsequently leached with DI water, was found to shift back to the rebounding curve of DI water (Do Guimarães et al., 2013).

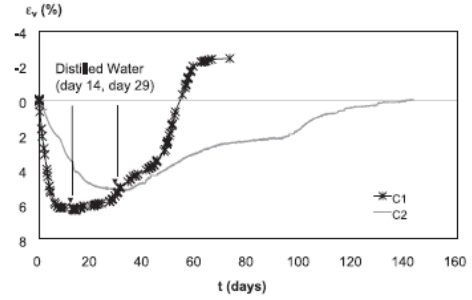

Figure 8.4 Deformations during the chemical cycle of compacted bentonite (Musso et al. 2003)

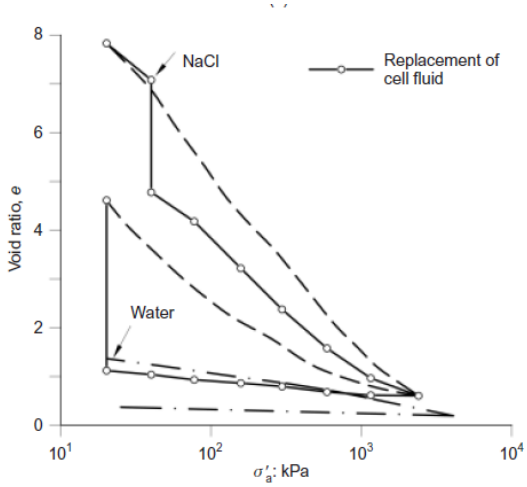

Figure 8.5 Volume change of sodium bentonite subjected to consolidation and swelling with and without fluid replacement (after Di Maio, 1996). In this figure, the volume change curves with and without fluid replacement are respectively indicated by symbol-solid line and dotted line.

Porosimetric study

Microstructure of bentonite has been the focus of many porosimetric studies. Double porosity is a state feature that is common to most compacted bentonite specimen. Figure 8.6 shows the pore size distributions of bentonite under chemical cycling. The macropores in the size of 10-300 µm reduces significantly in quantity to mesopores in the size of 0.1-10 µm after a loop of chemical cycling. Concentrated salt solution causes flocculation of fine minerals and contraction of aggregates, and thus contributes to the formation of macropores even when fully saturated, as evidenced by (Manca et al., 2016) in their studies on sand-bentonite mixture shown in Figure 8.7. Leaching of salinity from porous

media has been reported to cause enhanced dispersion and deflocculation in compacted Kaolin, i.e. larger void ratio under similar settling conditions in soil slurry (Li et al., 2013), which is in good agreement with the observation of (Musso et al., 2013; Musso et al., 2003).

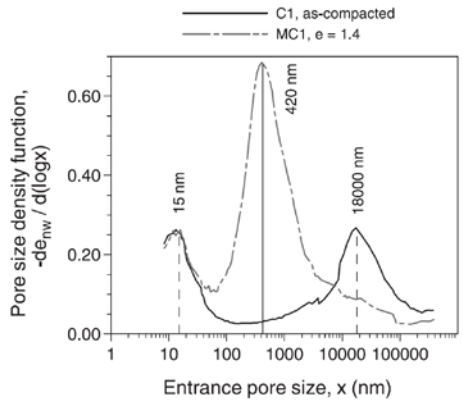

Figure 8.6 Pore size distribution of bentonite saturated with saline water and subsequently leaching with water

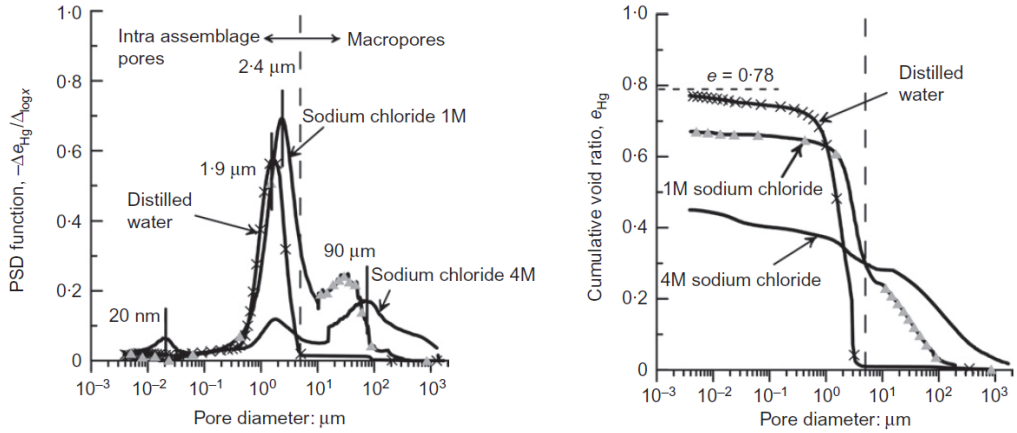

Figure 8.7 MIP test results of the S/B mixture prepared using different types of water. Comparison between distilled water and sodium chloride solutions (Manca et al., 2016)

Manca et al. (2016) reported microfabric studies on sand-bentonite mixture under desiccation and chemical immersion as shown in Fig. 8.7. The pore size distribution of the test specimen show some similarity in pattern due to the increase of suction, either matric suction or osmotic suction. Suction increase leads to growth in macropores and decrease in size of micropores, e.g. compaction of clay stacks and expansion of interaggregate voids. However, concentrated saline could not cause as much of compaction of clay stacks as desiccation does (average clay stack radius around 2 µm for saline versus 0.3 µm for desiccation), but results in occurrence of micropores in the size of 20 nm, which is absent from the specimens subject to desiccation. This trait may suggest intercalation of Na^+ into interlayers of montmorillonite, which may increase the CEC value of bentonite and then a higher affinity towards water. Further studies on water retention curve of bentonite in contact with saline water should be conducted to investigate this assumption.

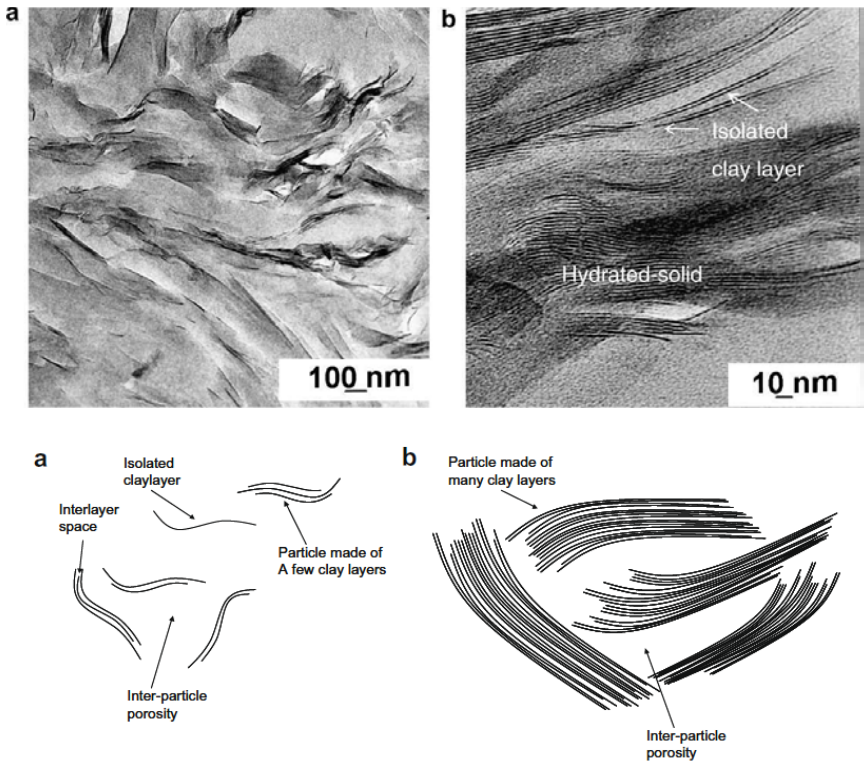

Figure 8.8 Microstructure of swollen bentonite (top) and schematic diagram (bottom) (after Melkior et al. 2009)

Melkior et al. (2009) studied the microstructure of various types of bentonite, which emphasized the role of a gel phase in the material in governing the pore structure and ionic diffusion behaviours. A homogeneous gel structure occurs in pure Na-smectite and in low salinity (typically NaCl, 10^{-3} M). Under such conditions, an isotropic network of ‘‘lens-like” pores, with homogeneous size, is developed. The pores are limited by walls constituted by stacks of only 5–10 TOT layers. In pure Na-smectite and in concentrated solution (NaCl, 10^{-1} M), or with Ca- or Mg-smectite, an isotropic network of lens-like pores is observed, delineated by ‘‘walls” made of 40– 60 TOT layers. This kind of microstructure is referred to as aggregate in this study. It is shown that increased salinity results in thick stacks of mineral layers and closer, denser pack of clay aggregates. In turn this observation agrees well with the chemo-mechanical behaviour of bentonite.

While porosimetry test of hydrated bentonite has repeatedly demonstrated a micropore size around 10 nm, and sometimes around 100 nm, it would be appropriate to assume the presence of dual-porosity and develop corresponding governing equations for such pore structures.

Water retention test

Water retention curve of MX-80 saturated with saline was reported by (Kuusela-Lahtinen et al., 2016) and shown in Figure 8.9. The curve appears to move upward from the common case of saturation with DI water when saturation degree is larger than 40 %. Similar trend has been recently observed in the Chinese GMZ bentonite by (He et al., 2016). They measured the water retention curve under four different salinity conditions, and found an enhancement in water retention capacity for bentonite.

When osmotic suction is subtracted from the measured total suction, the water retention curve still lies above the one for DI water, as shown in Figure 8.10. This suggests that the elevated salinity in pore fluid indeed enhances the clay's capacity to retain water. This change in water retention capacity for swelling soil due to chemical influence may be explained in two ways: 1) strengthened cation exchange capacity (CEC); and 2) increase of macropore volume and structuredness.

The factor of CEC has been discussed in the literature. For instance, the porosimetry test on MX-80 observed abnormal appearance of micropores at 20 nm (Manca et al., 2016), which was speculated to be related to strengthened CEC. This is also in agreement with the change in water retention capacity. Besides, according to the chemo-hydro-mechanical theory of (Guimarães et al., 2013), CEC greatly determines the ability of bentonite to deform reversibly under chemo-mechanical loadings. Therefore, the volumetric contraction due to chemical loading might be somewhat offset by the increased CEC under elevated salinity. This implication remains to be carefully explored in the future.

In the meanwhile, the increase of macropore volume has also been well documented in the literature. MIP studies on MX-80 have consistently found chemical-induced increase of macropore volume in size larger than 2 μm. Chemo-mechanical coupled studies have observed decreasing compressibility and swell index for expansive soils permeated with saline at elevated chemical concentrations. The growth in macropore volume implies the shrinkage of micropore under constant volume condition, which may turn to increase the capillary pressure of the sample under the same level of saturation degree. Therefore, the WRC for salt water may appear to be shifted upward with respect to DI water.

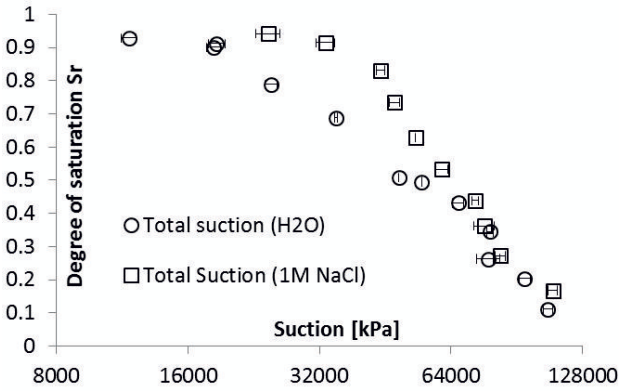

Figure 8.9 Estimation of water retention behaviour of MX-80 bentonite partially saturated with saline solution (Kuusela-Lahtinen et al., 2016)

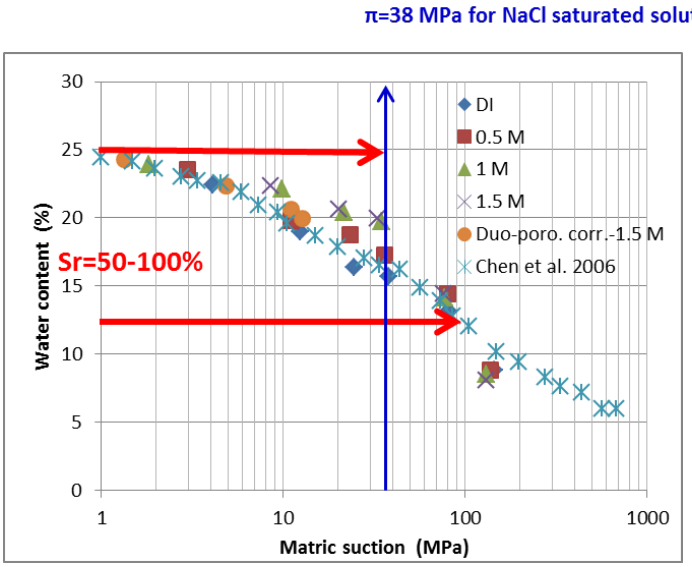

Figure 8.10 Water retention curve of GMZ bentonite under pure matric suction effect with osmotic suction subtracted from the total suction (after (He et al., 2016))

Hydraulic properties of bentonite

Tortuosity of bentonite from diffusion test

The solute transport equation takes the form of

$$(\phi + \rho K_d)\frac{\partial C}{\partial t} = D_e \frac{\partial^2 C}{\partial x^2}$$

Or

$$\frac{\partial C}{\partial t} = \frac{D_e}{\phi + \rho K_d}\frac{\partial^2 C}{\partial x^2} = D_a \frac{\partial^2 C}{\partial x^2}$$

For latent chemicals like Cl^-, ClO^{4-} and I^-, the sorption affinity K_d can be regarded as small and negligible as 0. Then we rewrite the above formula into

$$\frac{\partial C}{\partial t} = \frac{D_e}{\phi}\frac{\partial^2 C}{\partial x^2} = D_a \frac{\partial^2 C}{\partial x^2}$$

With

$$D_e = D_a \phi$$

A lot of test data (Nakashima, 2006; Tachi and Yotsuji 2014; Bourg et al. 2007) show an exponential decay or power law relationship between apparent diffusion coefficient D_a and porosity for swollen bentonite (see Fig. 8.11) in DI water or slightly salt solution in the form as follows:

$$\frac{D_a}{D_0} = \exp^{-6(1-\phi)}$$

Therefore

$$D_e = D_0 \phi \exp^{-6(1-\phi)}$$

According to Tachi and Yotsuji (2014), the effective diffusion coefficient can be given as

$$D_e = D_0 \frac{\phi \delta_g}{\tau^2}$$

where δ_g is the factor for constricted effect of the pore geometry. Other forms of the effective diffusion coefficient include $D_e = D_0 \frac{\phi}{\tau}$, and $D_e = D_0 \frac{\phi}{1+0.5(1-\phi)}$. But they can all be generalized into the above formula by varying the constrictivity factor δ_g.

Accordingly the tortuosity factor can be given as

$$\tau = \delta_g^{\frac{1}{2}} \exp^{3(1-\phi)}$$

By regression analysis, this equation can be correlated to a power function of pore ratio in the form of

$$\tau = 4.5 \delta_g^{\frac{1}{2}} e^{-0.66}$$

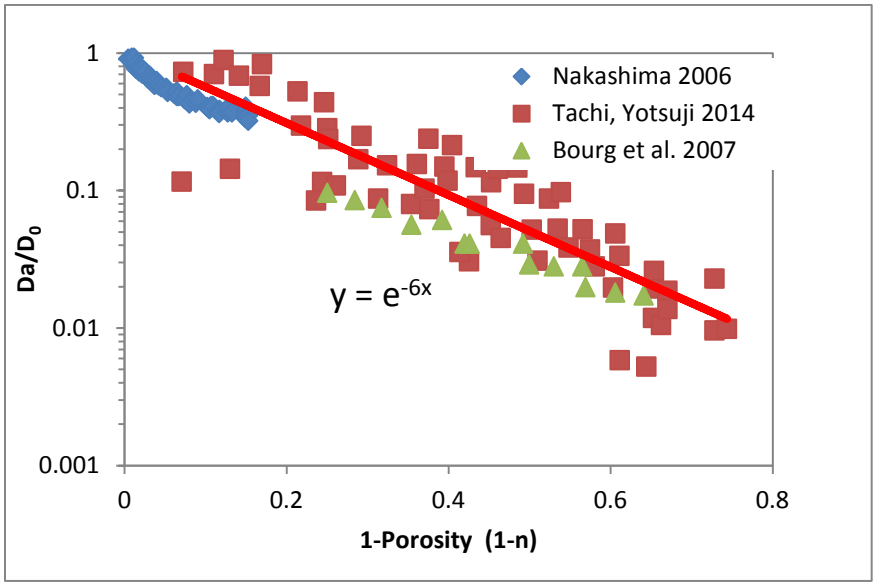

Figure 8.11 Diffusion coefficients of non-sorptive species in compacted bentonite

Kozeny-Carman permeability

Kozeny (1927) and Carman (1938, 1956) developed the following semiempirical, semitheoretical formula for predicting the permeability of porous media:

$$k = \frac{\gamma}{\mu C_{kc} S^2} \frac{e^3}{1+e}$$

where k is permeability, γ is specific gravity, μ is pore fluid viscosity, S is specific surface area in unit volume of solid phase, C_{kc} is the Kozeny-Carmen empirical coefficient, e is void ratio. The above equation can be rewritten as

$$C_{kc} = \frac{\gamma}{\mu S^2} \frac{e^3}{k(1+e)}$$

For bentonite swollen in DI water (Fig. 8.12), the permeability (m/s) can be described in an empirical formula of

$$k(1+e) = 10^{-13} e^{3.74}$$

We have $\frac{\gamma}{\mu} = 7.6 \times 10^6$ 1/m s. The specific surface area in unit volume S of typical MX-80 can be calculated from SSA value of 500 m^2/g, which leads to $S = SSA * \gamma_s \times 10^6 = 1.35 \times 10^9$ 1/m.

Therefore C_{kc} can be calculated as

$$C_{kc} = \frac{\gamma}{\mu S^2} 10^{13} e^{-0.74} = 41.7 * e^{-0.74}$$

From the shape of the above function we can see it is very close in form to the tortuosity. Assuming this Kozeny-Carmen coefficient C_{kc} is equivalent to the tortuosity factor, we can get a formula for the geometric constrictivity factor δ_g

$$\frac{1}{\sqrt{\delta_g}} = 0.108 * e^{-0.08}$$

This parameter is calculated to be in a very narrow range of $68 < \delta_g < 106$ when pore ratio distributes amongst 4>e>0.25. Also note that C_{kc} is way much larger than the well-recognized value of 5 for packed sandy soils as indicated by Carrier (2003). This is likely due to the thick electric double layer of clay particles, that greatly hinders the transitivity of compacted clay, through electric-hydraulic coupled effects (Li et al., 2014), and thus increases the C_{kc} factor.

From the above discussion on Kozeny-Carman permeability theory and compared against the test data on tortuosity, permeability for bentonite swollen in DI water, we can see that the Kozeny-Carmen theory basically applies to the specific case of MX-80 bentonite permeated with DI water. The rest of permeability data under chemical influences will be discussed later by porosity-effective pore diameter correlation using the fractal dimension analyses.

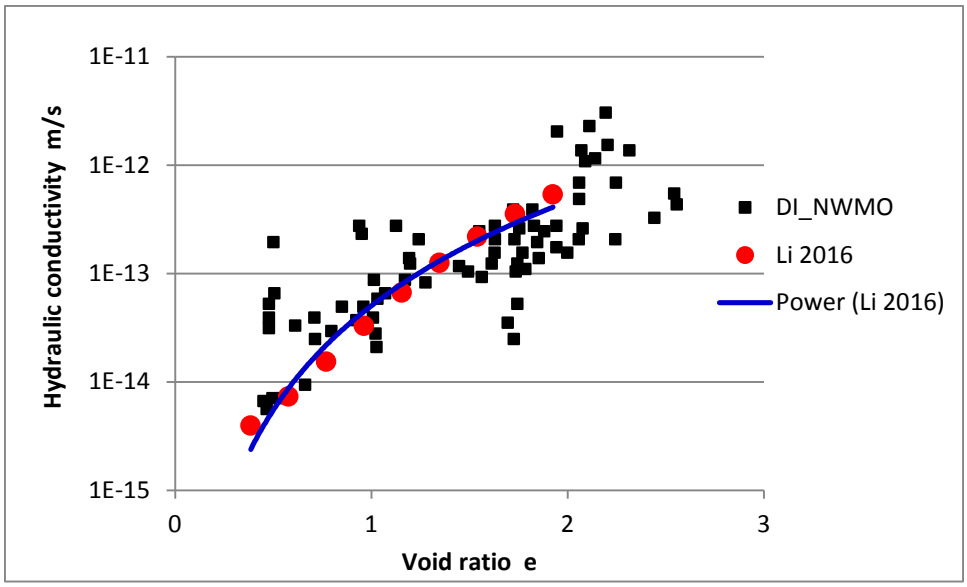

Figure 8.12 Variation of hydraulic conductivity of bentonite with permeant of DI water

Hydraulic-chemistry coupled behaviours

Chemical solution has intrinsic osmotic suction. When chemical solution is in contact with expansive soil, this osmotic suction has been commonly observed to induce contraction of clay aggregates, and the overall volumetric reduction in macroscopic level. Many efforts have been devoted to clarify the relationship between this osmotic suction and the matric suction due to capillary effect. So far it seems safe to establish equivalence for both suctions (matric suction and osmotic suction) regarding the micropore. This equivalence is critically important for this study to develop a conceptual model for micropore void ratio, which is believed to vary linearly with the gravimetric water content as widely observed in the shrinkage curve of expansive soils.

Electro-viscous analysis

Using electric-hydraulic coupled theories, we have investigated the permeability of bentonite under various salinities and void ratios. The hydraulic conductivities of the pressure driven flow and the electro-viscous retardation flow, respectively, are given as

$$k_p = \frac{h^2}{3\mu}$$

$$k_e = \frac{M^2}{K}\frac{(1-G)^2}{1+{I_t}/{I_c}}$$

$$k = k_p - k_e$$

where k is the apparent permeability, kp and ke are respectively the pressure driven and electro-osmotic permeability, h is interplanar distance, μ is fluid viscosity, K, M G, It and Ic are model parameters seen in section 5, Chapter 6.

Note that the former term k_p is exactly the form of the empirical expression for hydraulic conductivity of sandy soil except that the numerator is the grain size in the empirical formula (Tang et al., 2002). Figure 8.13 shows a comparison of hydraulic conductivities between the modelling and experimental results. It is found that EH coupled modelling generally underestimates the permeability in loosely compacted bentonite, i.e. when dry density is less than 1.5. This is attributable to the development of macropores by formation of aggregates due to osmotic suction of concentrated saline. This dual structure of porosity then greatly affects the hydraulic properties of bentonite. Therefore, a homogeneous single porosity model as adopted in Chapter 6 cannot fully describe the nature of the bentonite-saline system.

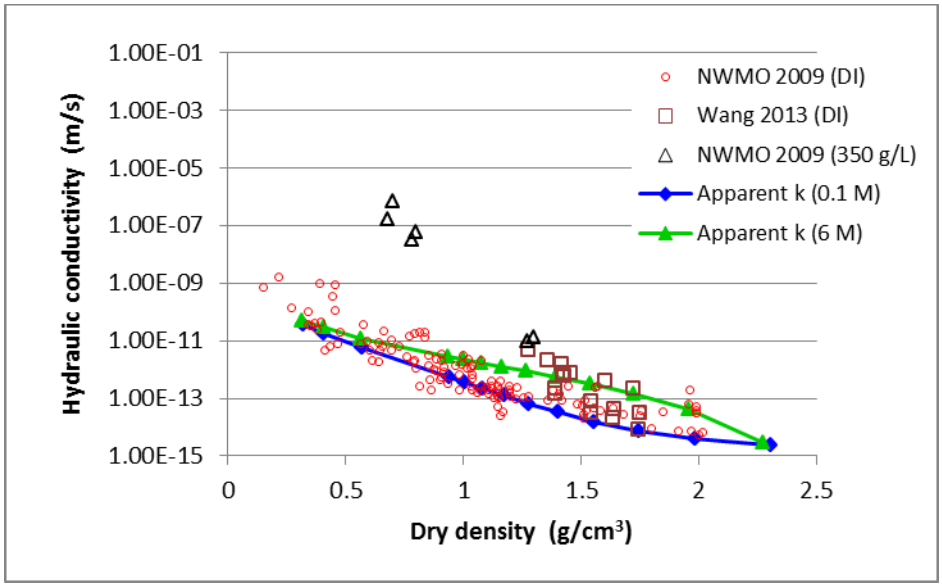

Figure 8.13 A comparison of modelled apparent hydraulic conductivity of bentonite clay with reported experimental results

Figure 8.14 shows the effect of chemical concentration on the variation of permeability of compacted bentonite with increasing pore void ratio. The test data are fitted to power function with regression approach. Highly concentrated chemical solution is found to significantly increase the permeability of compacted bentonite.

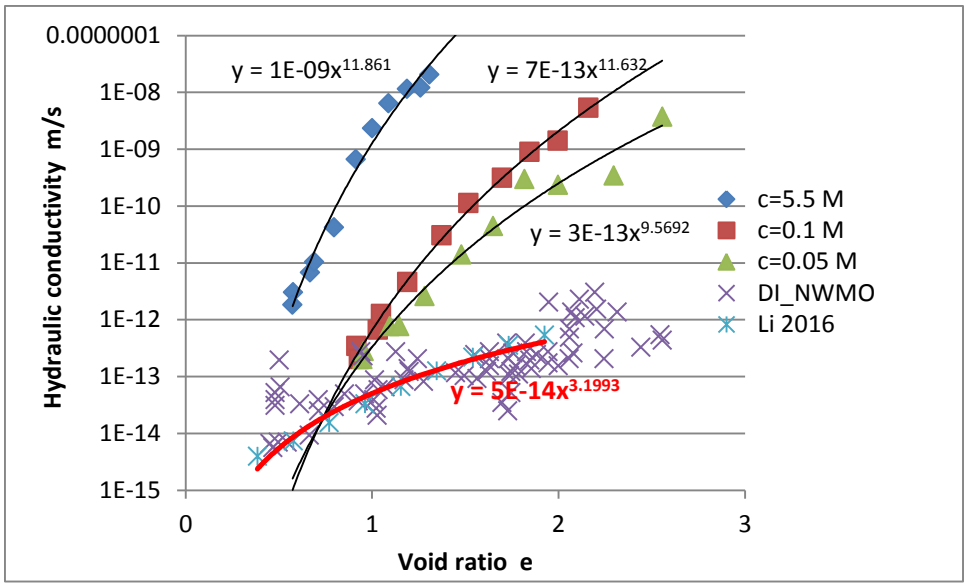

Figure 8.14 Variation of hydraulic conductivity of bentonite with permeant of various salinity (upper three series of data are cited from Musso et al. (2013) on FEBEX bentonite)

Fractional dimension theory analysis

Kozeny-Carman equation on permeability of porous media can be applied to analyzing the porosity-pore size correlation.

$$k = c\phi d_{eff}^2$$

This leads to the empirical relationship of the following form

$$d_{eff} = \delta\phi^{\varsigma}$$

where d_{eff} is the effective pore diameter, δ is a model constant, and ς is the power index, which can be related to fractal dimension of the pore geometry. For bentonite immersed in highly concentrated saline water, this parameter ς is found to be around 10.5. The effective pore size is found to depend on porosity in a power law, which can be further supported by the limited amount of existing studies on the fractal dimension of the desiccation induced cracks (SAND2016-10311R; Goehring et al. (2015)).

Geometry of pore space has fractal dimensions between 3 and 4 according to previous studies into the self-similarity of pore features by fractal theory. According to the box-counting method for determination of fractal dimension,

$$N = N_0 r^{-n}$$

where N is the total number of boxes with side length r, and n is the fractal dimension that may not necessarily be an integer. Divide the total box information by the overall area, or volume of the representative element leads to the 2D, or 3D porosity, respectively as

$$\phi_{2D} = \frac{Nr^2}{A_0} \propto r^{2-n}$$

$$\phi_{3D} = \frac{Nr^3}{V_0} \propto r^{3-n}$$

where A_0 and V_0 are the area and volume of the representative element, respectively. Take 3D case for example, the pore size can be related to the accumulated porosity in the form of

$$r \propto (\phi_{3D})^{\frac{1}{3-n}}$$

If we assume the macroporosity ϕ_M is in proportion to the total porosity ϕ, the above formula can be transplanted into the case of bentonite by replacing r with d_{eff}, which results in

$$d_{eff} \propto \phi^{\varsigma} = \phi^{\frac{1}{3-n}}$$

Therefore the power index of ς is associated with the geometric fractal dimension factor of n as

$$\varsigma = \frac{1}{3-n}$$

From these discussions on the relationship between effective pore size and fractional dimension it is suggested that the permeability of expansive soil under desiccation from either matric suction of osmotic suction can be somewhat qualitatively estimated by the fractional factor that is measurable for the specimen. However, for precise quantification, there are some uncertainties in the determination of model parameters like c and N, which appears to hinder its applicability and convenience to use.

Geometric mean analysis

For natural heterogeneous porous media, effective permeability can be estimated by the mean of permeability values, including the arithmetic mean, geometric mean, and harmonic mean. Amongst them the geometric mean was demonstrated by (Selvadurai and Selvadurai, 2014) to be representative of the effective permeability by investigating typical sandstone possessing medium heterogeneity. The geometric mean is used in this work to interpret the permeability change of bentonite under chemical influences. The geometric mean of the permeability is given as

$$k_g = \sqrt[n]{k_1 k_2 k_3 \dots k_n}$$

or

$$k_g = \exp\left(\frac{\sum V_i \log(k_i)}{\sum V_i}\right)$$

By dividing the pore space into two regimes of micropore and macropore, we can rewrite the geometric mean of the effective permeability in the form of

$$\log(k) = \phi_m \log(k_m) + \phi_M \log(k_M)$$

where k_m and k_M are respectively the micropore permeability and the macropore permeability. For micropores inside the clay aggregate, the strong electric interaction and prominent semi-permeable membrane property together ensure a very slow chemical intrusion. With this speculation in mind, regardless of the salinity in pore fluid (which is largely distributed in the macropores), the micropore permeability is believed to follow the Kozeny-Carman equation of bentonite with DI permeation. Therefore

$$k_m = 10^{-13} \frac{{e_m}^{3.74}}{(1 + e_m)} \sim 5 \times 10^{-14} {e_m}^{3.2}$$

In the meantime, the micropore void ratio can be determined by the gravimetric water content as

$$e_m = w_m G_s$$

Note that w_m has to be distinguished from the total water content w, and is governed by the osmotic suction of chemical solution. The relationship between w_m and osmotic suction can be determined by the soil water characteristic curve of bentonite for DI water.

Therefore the macropore permeability can be derived as

$$\log(k_M) = \frac{\log(k) - \frac{w_m G_s}{1 + e} \log(k_m)}{1 - \frac{w_m G_s}{1 + e}}$$

It is shown that the parameter k_M is a constant of $10^{-4.5}$ m/s for the available dataset on permeability of bentonite. Using this regressed empirical value of macropore permeability, we can estimate the effective permeability of bentonite at various void ratios and pore fluid salinities, as shown in Fig. 8.15. The existing data are well reproduced by the conceptual model of permeability based on geometric mean of permeabilities for both micro- and macropores.

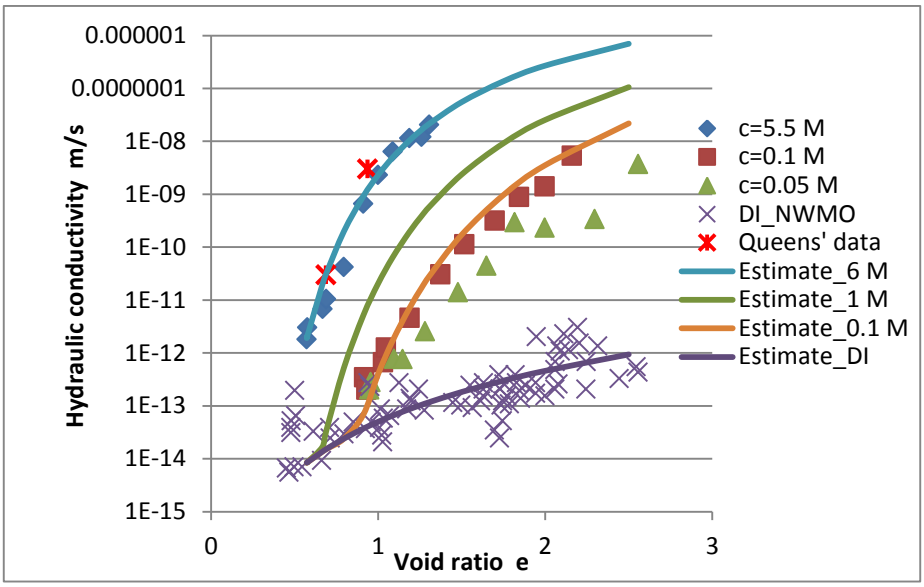

Figure 8.15 Dependence of permeability on void ratio for FEBEX bentonite (Musso et al. 2003)

Debye length and macropore threshold value

The Debye length (κ^{-1}) of expansive soil typical of MX-80 is generally in the range of 1000 to 1 nm when 10^{-7} < I < 0.1 M, and is less than 1 nm when solution ionic strength I≥0.1 M (Bharat and Sridharan, 2015). This suggests that for pore sizes larger than this range, the electric-hydraulic coupling of electric double layer would greatly diminished. And thus the permeability of pore space with $d \gg \kappa^{-1}$ would be predominantly governed by the viscosity effect, namely the power law of various forms, including the known Kozeny-Carmen relationship (Carrier Iii, 2003).

The macropore is typically classified due to a threshold pore diameter of d=1μm, according to a number of microstructural investigations into the dual porosity of expansive soils by mercury intrusion porometry studies (Seiphoor et al. 2014). This threshold value of d=1 μm can be justified by the dependence of Debye length on salinity of pore fluid. Pore fluid salinity of Na-bentonite has been experimentally determined to be about 0.1 M in several studies (Shackelford et al. 2005). Then a reasonably small value of Debye length would be expected for nanopores, which generally is sized between 1-2 nm, specifically for interlayer spaces. But for macropore space, a comparatively dilute salinity would be expected when Na-bentonite is saturated with DI water, due to the strong tendency of electrolyte to concentrate upon vicinity of electric double layers. Therefore, a larger Debye length would be expected for macropres, e.g. 1 μm as generally accepted (Manca et al., 2016).

2. HMC coupled model for expansive soil

The conceptual model

A dual-porosity type conceptual model for compacted bentonite is believed to consist of two levels of pore structures, i.e. the micropore at about 1 μm and macropore at about 100 μm in pore diameters.

Various studies (Manca et al., 2016) have confirmed the existence of dual-porosity for unsaturated compacted bentonite, and saline-saturated bentonite, by using mercury intrusion porosimetry or TEM test. Both of the conditions resulting in dual-porosity share the similarity in suction effect which is induced either by matric suction or osmotic suction. Microstructural morphological study on bentonite under wetting paths indicates gradual loss of the macropores of about 100 µm in diameter, and steady cumulative growth in the abundance of micropores of about 1 µm in diameter (Manca et al., 2016). However, this is not the case for bentonite when saturated with brine, whereas the macropores mostly remain to exist and appear to increase in abundance with increasing salinity in the pore fluid. Therefore, it seems appropriate to assume a prevalent dual-porosity structure for compacted bentonite under flooding of saline water.

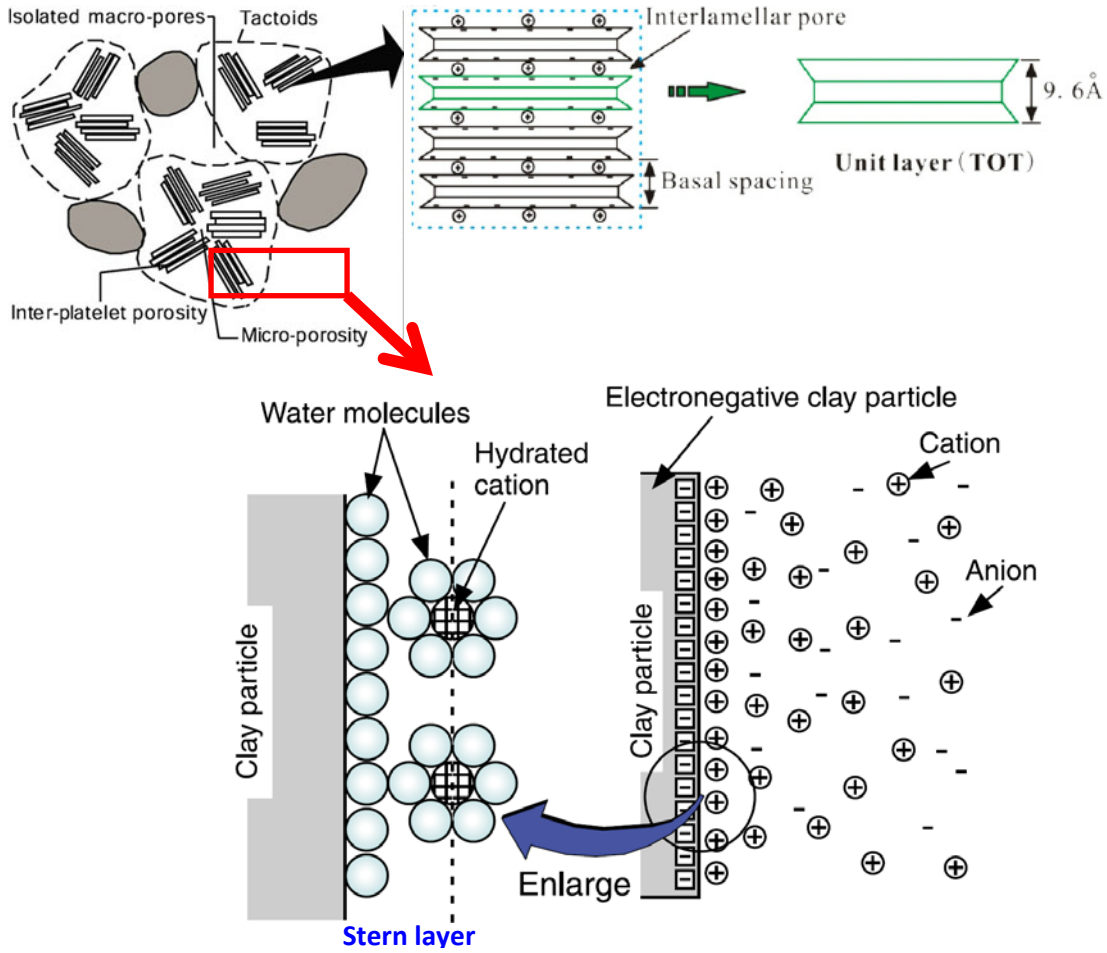

Figure 8.16 Schematic illustration of the diffuse double layer problem for hydrated bentonite. (Komine and Ogata 2003; Ye et al. 2013)

Another question that has to be addressed is the variation and conversion between the micro- and macropores, e.g. the n^m and n^M. The extended BBM model considers a harmonized variation between both porosities, in order to reflect the gradual softening in swelling pressure when bentonite is saturated and the suction is close to its air entry value. They assume that swelling pressure mainly

comes from the micro-porosity (n^m), and the collapse of macro-porosity n^M and its transformation to micro-porosity n^m causes growth of effective porosity and thus a reduction in the thickness of diffuse double layer, which contributes to the decrease in swelling pressure. However, porosimetric characterization of soil specimen at different stage of the swelling test may be insufficient to develop such an empirical relationship. When bentonite is saturated with saline water in constant volume condition, as encountered in this study, the macroporosity n^M would be expected to maintain at a substantial level. Therefore we assume here that the dual-porosities do not convert interchangeably. Instead, the micro-porosity, as a determinant factor, varies with suction and exerts swelling pressure under confinement, while the macro-porosity fills the rest of the total porosity.

The effect of externally applied net stress on void ratio can be characterized by oedometer compression test, which clearly shows non-reversible plastic deformation for saturated expansive soils regardless of pore fluid chemistry (Di Maio, 1996). This unrecoverable deformation is believed to be largely attributed to the collapse of macropores. When the applied external loading is unloaded, part of the compressive deformation can be recovered gradually, particularly significant for expansive soils saturated with nonsaline water. Taking the diffuse double layer effect into account, this reversible deformation is linked to the expansion of hydrated DDL which mainly happens in the micropores. The rebound curve is treated as typical of elastic deformation in classical Cam-Clay model, and is adopted in this study as well.

Hydraulic flow

Flow equations for a homogeneous unsaturated expansive soil is given as follows taking the chemical couplings into account,

$$G_s\rho_l w\left[(1-n)\left(\chi_f+\frac{B}{P_m w}\right)-n\chi_s\right]\frac{\partial P_m}{\partial t}-\nabla\frac{k_s k_r}{\mu}\rho_l\nabla P_m + G_s\rho_l w\left[-n\chi_s k_c+(1-n)\left(\frac{k_2}{\rho_l}+\frac{k_1}{w}\right)\right]\frac{\partial C}{\partial t}-\nabla\frac{k_s k_r}{\mu}\rho_l k_c\nabla C=-G_s\rho_l w\frac{\partial\varepsilon_v}{\partial t}+Q_m$$

By neglecting the chemical perturbation, the above equation can be reduced to the following expression for unsaturated flow problem, which has been shown in Chapter 6

$$\left[\rho_l S_e e\left((1-n)\chi_f-n\chi_s\right)+G_s\rho_l(1-n)C_m\right]\frac{\partial p}{\partial t}-\nabla\frac{k_s k_r}{\mu}\rho_l\nabla p=-\rho_l S_e e\frac{\partial\varepsilon_v}{\partial t}+Q_m$$

Detailed derivation of the above equation

Take a representative element of porous media for analysis, and let n is porosity, S_e is the saturation degree, ρ_l is fluid density, G_s is the specific gravity of solid, and w is water content in mass ratio. By assuming G_s stays constant over time, i.e. no dissolution or precipitation reactions take place, then we can write the following equation

$$\frac{\partial}{\partial t}(\rho_l n S_e)=\frac{\partial}{\partial t}[\rho_l(1-n)G_s w]=(1-n)G_s\frac{\partial}{\partial t}(\rho_l w)+\rho_l G_s w\frac{\partial}{\partial t}(1-n)$$

$$=(1)+(2)$$

Further differentiate the above equation gives

$$(1) = (1-n)G_s\left[\frac{\partial}{\partial P_m}(\rho_l w)\frac{\partial P_m}{\partial t} + \frac{\partial}{\partial P_{os}}(\rho_l w)\frac{\partial P_{os}}{\partial t}\right]$$
$$= (1-n)G_s\left[\left(\chi_f \rho_l w + \frac{B}{P_m}\rho_l\right)\frac{\partial P_m}{\partial t} + \frac{\partial}{\partial C}(\rho_l w)\frac{\partial C}{\partial t}\right]$$

where B is the slope of w-log(S_u) relationship for bentonite, P_{ms} is matric suction (S_u), and P_{os} is osmotic suction. Note that fluid density varies with chemical concentration.

Since

$$\frac{\partial}{\partial C}(\rho_l w) = w\frac{\partial \rho_l}{\partial C} + \rho_l\frac{\partial w}{\partial C} = k_2 w + k_1 \rho_l$$

Therefore

$$(1) = (1-n)G_s\left[\left(\chi_f \rho_l w + \frac{B}{S_u}\rho_l\right)\frac{\partial P_m}{\partial t} + (k_2 w + k_1\rho_l)\frac{\partial C}{\partial t}\right]$$

where k_1 and k_2 are material properties that are given as $k_2 = \frac{\partial \rho_l}{\partial C}$, and $k_1 = \frac{\partial w}{\partial C} = \mathbf{0}$.

Meanwhile,

$$(2) = \rho_l G_s w\frac{\partial}{\partial t}(1-n) = -\rho_l G_s w\frac{\partial n}{\partial t} = -\rho_l G_s w\left(\frac{\partial n}{\partial \sigma'}\frac{\partial \sigma'}{\partial t} + \frac{\partial n}{\partial P}\frac{\partial P}{\partial t}\right)$$

Note that the total suction pressure consists of matric suction and osmotic suction, we have

$$P = P_m + P_{os}$$

And osmotic suction is dependent on solute concentration C in the form of

$$P_{os} = k_c C$$

where k_c=RT for dilute salt solutions (I<0.1 M), in which case k_c=8.314 kPa/K M * 300 K≈2.5 MPa L/mol. This formula has to be modified for highly concentrated saline water, i.e. the osmotic suction of the model saline water (C≈6.6 mol/L in terms of monovalent electrolyte) used in this study was measured to be 40.6 MPa with the Chilled Mirror device, suggesting a constant k_c=6.15 MPa L/mol. In addition, 1 M NaCl solution has osmotic suction of 4.8 MPa.

Then

$$(2) = -\rho_l G_s w\left[-\frac{\partial \varepsilon_v}{\partial t} + \chi_s n\left(\frac{\partial P_m}{\partial t} + \frac{\partial P_{os}}{\partial t}\right)\right] = -\rho_l G_s w\left[-\frac{\partial \varepsilon_v}{\partial t} + \chi_s n k_c\frac{\partial C}{\partial t} + \chi_s n\frac{\partial P_m}{\partial t}\right]$$

Inserting the above components (1) and (2) into the flow function of the following form

$$\frac{\partial}{\partial t}(\rho_l n S_e) - \nabla\frac{k_s k_r}{\mu}\rho_l \nabla P = Q_m$$

will lead to a general expression

$$G_s\rho_l w\left[(1-n)\left(\chi_f+\frac{B}{S_u w}\right)-n\chi_s\right]\frac{\partial P_m}{\partial t}-\nabla\frac{k_s k_r}{\mu}\rho_l\nabla P_m+G_s\rho_l w\left[-n\chi_s k_c+(1-n)\left(\frac{k_2}{\rho_l}+\frac{k_1}{w}\right)\right]\frac{\partial C}{\partial t}$$
$$-\nabla\frac{k_s k_r}{\mu}\rho_l k_c\nabla C=-G_s\rho_l w\frac{\partial\varepsilon_v}{\partial t}+Q_m$$

Dual-porosity flow equations

Based on the above shown governing equation for homogeneous media, we can derive the flow equations for the assumed dual-porosity media as follows.

In micropore,

$$G_s\rho_l w^m\left[(1-n^m)\left(\chi_f+\frac{B}{P_m w^m}\right)-n^m\chi_s\right]\frac{\partial P_m}{\partial t}-\nabla\frac{k_s^m k_r}{\mu}\rho_l\nabla P_m$$
$$+G_s\rho_l w^m\left[-n^m\chi_s k_c+(1-n^m)\frac{k_2}{\rho_l}\right]\frac{\partial C^m}{\partial t}-\nabla\frac{k_s^m k_r}{\mu}\rho_l k_c\nabla C^m=-G_s\rho_l w\frac{\partial\varepsilon_v^m}{\partial t}+Q_m$$

Taking into account the constitutive relationship for the microporosity, it is inferred that the micropores are mostly saturated or are close to full saturation ($S_e^m=w^m G_s/e^m=w^m G_s/w^m G_s$ $=1$). Then the flow function for the micropores can be greatly simplified into the Darcy's flow form

$$\frac{\partial}{\partial t}(\rho_l n^m)-\nabla\frac{k_s^m}{\mu}\rho_l(\nabla P_m+k_c\nabla C^m)=Q_m$$

In macropore,

$$G_s\rho_l w^M\left[(1-n^M)\left(\chi_f+\frac{B}{P_M w^M}\right)-n^M\chi_s\right]\frac{\partial P_M}{\partial t}-\nabla\frac{k_s^M k_r}{\mu}\rho_l\nabla P_M$$
$$+G_s\rho_l w^M\left[-n^M\chi_s k_c+(1-n^M)\frac{k_2}{\rho_l}\right]\frac{\partial C^M}{\partial t}-\nabla\frac{k_s^M k_r}{\mu}\rho_l k_c\nabla C^M=-G_s\rho_l w\frac{\partial\varepsilon_v^M}{\partial t}+Q_M$$

The permeability of micropore follows that of bentonite with DI permeation, while the permeability of macropore follows the effective permeability, the upper bound of permeability for various salinity situations, as determined from the geometric mean.

The volumetric strain can be linked to the porosity variation in the following form

$$\frac{\partial\varepsilon_v^m}{\partial t}=-\frac{\partial n^m}{\partial t}$$
$$\frac{\partial\varepsilon_v^M}{\partial t}=-\frac{\partial n^M}{\partial t}$$

The mass flux takes the following form

$$Q_M=-a^M$$
$$Q_m=a^M$$
$$a^M=\bar{\alpha}(P_m-P_M+\Pi^m-\Pi^M)$$

where $\bar{\alpha}$ is the fluid exchange rate that is dependent on micropore permeability, and the osmotic suction $\Pi = -k_c\Delta$.

Here we neglect the difference of B parameter for the water retention curves between micro- and macro-pores. Note also that the intrinsic permeability k_s can be determined by the corresponding porosities.

Solute transport

For solute transport in unsaturated porous media,

$$\frac{\partial(\theta C)}{\partial t} = \nabla(D\nabla C) - \nabla(vC) + Q_c$$

where θ is the volumetric water content, D is diffusion coefficient, v is flux of the pore fluid, and Q_c is the source flux of chemicals.

Since

$$\theta = nS_e$$

Then we have

$$\frac{\partial\theta C}{\partial t} = Cn\frac{\partial S_e}{\partial t} + CS_e\frac{\partial n}{\partial t} + S_e n\frac{\partial C}{\partial t}$$

By neglecting the compressibility of solid matrix and pore fluid, the variation of porosity is assumed to be dependent on volumetric strain only in the solute transport equation.

Therefore we have

$$S_e n\frac{\partial C}{\partial t} = \nabla D\nabla C - \nabla(vC) + Q_c - C\left(n\frac{\partial S_e}{\partial t} + S_e\frac{\partial \varepsilon_v}{\partial t}\right)$$

By taking into account of the chemo-osmosis effect, or the so-called semipermeable membrane effect of expansive soils (Li et al. 2014), and the adsorption effect, the solute transport equation can be given as

$$S_e n\frac{\partial C}{\partial t} = (1-\omega)[\nabla D\nabla C - \nabla(vC)] + \frac{\partial}{\partial t}Q_c - C\left(n\frac{\partial S_e}{\partial t} + S_e\frac{\partial \varepsilon_v}{\partial t}\right) - \rho_b K_s\frac{\partial C}{\partial t}$$

where ω is membrane coefficient, K_s is partition coefficient between pore fluid and solid mass.

In macropore, a simplified version is obtained as follows by neglecting the semi-permeable membrane effect,

$$n^M S_e^M\frac{\partial C^M}{\partial t} = D\nabla^2 C^M - \nabla(v^M C^M) + \frac{\partial}{\partial t}Q_c^M - C^M n^M\frac{\partial S_e^M}{\partial t}$$

In micropore, the full equation has to be implemented

$$n^m S_e^m\frac{\partial C^m}{\partial t} = (1-\omega)[\nabla D\nabla C^m - \nabla(v^m C^m)] + \frac{\partial}{\partial t}Q_c^m - C^m\left(n^m\frac{\partial S_e^m}{\partial t} + S_e^m\frac{\partial \varepsilon_v}{\partial t}\right)$$

Note that it is hypothesized here the micropore is always nearly saturated, which guarantees the validity of constitutive relationship of microporosity n^m with gravimetric water content w^m. Therefore, the solute transport equation for micropore can be reduced to

$$n^m \frac{\partial C^m}{\partial t} = (1-\omega)[\nabla D \nabla C^m - \nabla(v^m C^m)] + \frac{\partial}{\partial t} Q_c^m - C^m \frac{\partial \varepsilon_v}{\partial t}$$

The mass exchange flux Q_c is given as a function of fluid exchange rate a^M and mass transfer coefficient $\overline{D}$,

$$Q_c^M = (1-\omega)\left[-a^M C^{\overline{M}} + \overline{D}(C^m - C^M)\right]$$

And

$$Q_c^m + Q_c^M = 0$$

The convective mass flux is directional with respect to which concentration (i.e. Cm or CM) is carried by the fluid flow. We define

$$C^{\overline{M}} = \begin{cases} C^m, & if\ a^M \geq 0 \\ C^M, & if\ a^M < 0 \end{cases}$$

Fluid exchange rate a^M is governed by pore pressure and osmotic suction differences. The mass transfer coefficient can be approximated to be

$$\overline{D} = \frac{D_0}{l_c}$$

where l_c is the characteristic length of the clay aggregate. Musso et al. (2013) proposed a similar concept of mass exchange between dual porosities, and developed a mathematical equation in exponential form for the transfer coefficient

$$\overline{D} = \alpha e^{-HC^M}$$

where α and H are two parameters to be calibrated by experiments, which were reported to be 0.8 and 8, respectively for MX-80 in contact with NaCl solution (Musso et al. 2013).

It is believed in this study that salinity in micropore dominates the mass exchange rate. As inside clay aggregate, DDL is dominating and the void ratio is greatly dependent on the DDL interactions. Opening of micropore makes way for infiltration of pore fluid, and migration of chemicals. And thus opening of micropore is resulted from DDL shrinkage by the change of micropore salinity, namely the C^m. We modify the above expression to correlate the transfer coefficient with chemical concentration in micropore to accommodate the special case of brine infiltration in this work, shown as

$$\overline{D} = \frac{D_0}{l_c} e^{-HC^m}$$

Our numerical simulation of brine-bentonite interaction leads to the following set of parameters, i.e. l_c=10 μm, H=0.004 (B_1.6 sample) and H=0.005 (SB_1.8 sample) for salinity C^m in the unit of molar/m^3.

Intraparticle diffusion

Besides, the partition factor $\overline{D}$ is a nonlinear function of average grain size and chemical concentration difference between inside and outside the micropore. Detailed derivation needs to be supplemented here to elaborate such a relationship. An alternative approach is adopted here to work around the unknown relationship for chemical partitioning, by invoking an intraparticle diffusion flux q_{in} to account for the exchange of chemical species between the dual porosities. Therefore,

$$Q_c^M = (1-\omega)\left[-a^M C^{\overline{M}} + q_{in}\right]$$

In order to obtain the expression for the intraparticle diffusion flux, we assume a simple 1-D stack of clay aggregate of characteristic length of $2l_c$, and micropore channel through which the chemicals migrate from the macropore inwards the clay aggregate is in the planar direction.

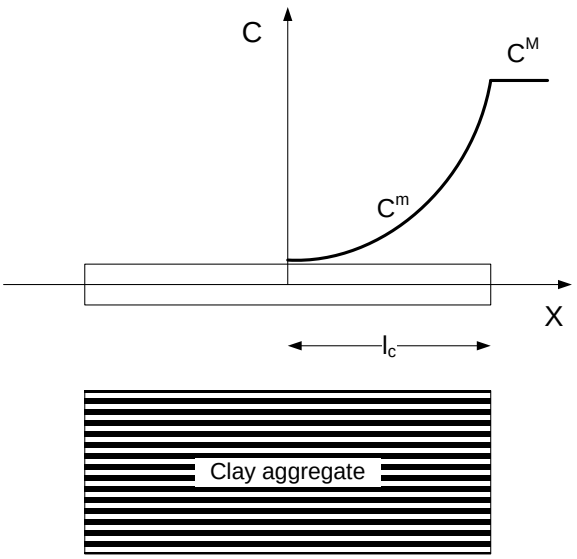

Figure 8.17 Schematic diagram for the intraparticle diffusion model

Let diffusion prevail, then the governing equation turns out to be

$$\frac{\partial C}{\partial t} = D\frac{\partial^2 C}{\partial x^2}$$

The boundary and initial conditions can be given as

$$\begin{cases} C(x,0) = 0 \\ C(x,t) = C^M|_{x=l_c} \\ \dfrac{\partial C(x,t)}{\partial x} = 0\Big|_{x=0} \end{cases}$$

The analytical solution for the above diffusion function takes the form of

$$C = C^M\left\{\left[1 - erf\frac{x-l_c}{\sqrt{4Dt}}\right] + \left[1 - erf\frac{x+l_c}{\sqrt{4Dt}}\right]\right\}$$

The intraparticle solute flux at the inlet boundary can be derived as

$$q_{in} = -D\frac{\partial C}{\partial x}\Big|_{x=l_c} = DC^M \frac{1}{\sqrt{D\pi t}}\left[e^{-\left(\frac{x-l_c}{\sqrt{4Dt}}\right)^2} + e^{-\left(\frac{x+l_c}{\sqrt{4Dt}}\right)^2}\right]\Bigg|_{x=l_c} = DC^M \frac{1}{\sqrt{D\pi t}}\left[1 + e^{-\frac{(l_c)^2}{Dt}}\right]$$

This chemical flux can further be implemented in the solute transport governing equations for the dual-porosity model.

3. Constitutive model for unsaturated expansive soil

The overall constitutive function for unsaturated expansive soil reads

$$\boldsymbol{\sigma}' = \mathbf{C} \cdot \left(\boldsymbol{\varepsilon} - \boldsymbol{\varepsilon_p} - \boldsymbol{\varepsilon_s}\right)$$

where C is the compliance matrix, $\boldsymbol{\varepsilon_p}$ is plastic strain and $\boldsymbol{\varepsilon_s}$ is the extra swelling/shrinkage strain due to suction variation below the air entry value.

Fundamental assumptions

Effective stress principle

The Bishop's effective stress principle is assumed to hold true, we have the following nonlinear expressions,

$$\mathrm{d}\sigma' = \mathrm{d}\sigma + \chi \mathrm{d}(S_u)$$

$$\chi = \begin{cases} 1, & (u_a - u_w) \le AEV \\ \gamma e^{-k(u_a - u_w + AEV)}, & (u_a - u_w) > AEV \end{cases}$$

where AEV is the air entry value, k and γ are model constants that can obtained by regression analysis of data on shrinkage test.

The AEV can be determined as the following by considering chemical effect on matric suction ($w_{sat} = A_0 + k_1 C + B\ln(AEV)$)

$$AEV = e^{\frac{\frac{e\gamma_w}{G_s} - (A_0 + k_1 C)}{B}}$$

Dual mode of volumetric expansion by wetting

When expansive soil gets wetted from the dry end far beyond its air entry value under constant net stress, the stress path would experience a decrease in effective stress due to the change in matric suction, during which process the deformation would be elastic and can be described by

$$\varepsilon^e = \frac{\Delta e_1}{1 + e_0} = \frac{\kappa}{1 + e_0}\ln\left(\frac{\sigma'}{P_c'}\right) = \frac{\kappa}{1 + e_0}\ln\left(\frac{P_c' - \int_{S_{u0}}^{S_{u1}} \chi \mathrm{d}x}{P_c'}\right)$$

where P_c' is the effective pre-consolidation pressure. The pre-consolidation pressure P_c' is an experimental parameter, and can thus be determined from compression curves.

When soil approaches its full saturation and matric suction is less than the air entry value, deviation of the deformation from the rebound curve of the oedometer test would be expected, which can be termed as the extra swelling strain. The swelling strain is determined by

$$\varepsilon_s = \frac{B_s \Delta S_u}{1 + e_0}$$

In this situation the coefficient for the extra swelling strain can be written as

$$B_s = \begin{cases} \dfrac{\lambda^e - \kappa}{AEV} \ln\left(\dfrac{\sigma'}{P_c'}\right), 0 < S_u \le AEV \\ 0, \qquad\qquad S_u > AEV \end{cases}$$

where λ^e and κ are respectively the compression and swelling indexes of the equilibrium state line of expansive soil at its full saturation. Note that the swelling coefficient B_s may not be a constant during wetting of unsaturated specimen, which changes the effective stress σ' and the B_s value simultaneously.

Cam-Clay model for saturated soils

Cam-clay assumes the validity and presence of a critical state in typical clays, the slope of which can be related to Mohr-Coulomb strength parameter ϕ through

$$M = \frac{6 \sin \phi}{3 - \sin \phi}$$

and a logarithmic relationship between void ratio and mean stress:

$$e = e_0 - \lambda \ln \frac{p_c}{p_{c0}}$$

The yield function for modified Cam-Clay model is shown as

$$F = q^2 + M^2 p(p - p_c) = 0$$

The critical state line together with the yield locus determines the elasto-plastic constitutive behaviour of the soil. When the stress level surpasses the preconsolidation pressure, strain-hardening happens in the form of

$$p_c = p_{c0} e^{-\frac{1+e_0}{\lambda - \kappa}\varepsilon_p}$$

where e_0 is the initial void ratio, ε_p is the effective plastic strain, p_{c0} is the initial preconsolidation pressure.

Cam-Clay-based Basic Barcelona Model (BBM) for unsaturated soils

BBM is based on Cam-Clay model and extends it to consider the effect of matric suction on the constitutive behavior of an unsaturated soil. The BBM can be depicted in the p-q-s stress space as in Fig.

8.18. Load collapse line LC is an exponential function of suction that determines the maximum swelling pressure in wetting path. Suction also contributes to the internal cohesion (p_s) which follows a linear relationship in p-s space (p_s=k*S_u).

The yield function for BBM is written as:

$$F_{BBM} = q^2 + M^2(p + p_s)(p - p_c) = 0$$

For constant volume swelling test, the stress is hypothesized to follow the neutral line (NL) in p-s plane as shown in the Fig. 8.6b. When NL hits the LC curve, stress turns to follow the yield curve LC and thus leads to decreasing swelling pressure with further wetting. Further extension of the BBM to Barcelona Extended Model (BExM) considers the bimodal porosity pattern and assumes elastic and plastic strains happen to microscale and macroscale porosities, respectively, in response to suction variation, citing empirical parameters of f_a and f_b that appears to be complicated to determine. It is shown that pore size transition from macro to micro pores indeed happens to the swelling of expansive soils. The transition leads to secondary hardening behavior in swelling pressure under constant volume conditions, after the primary softening stage.

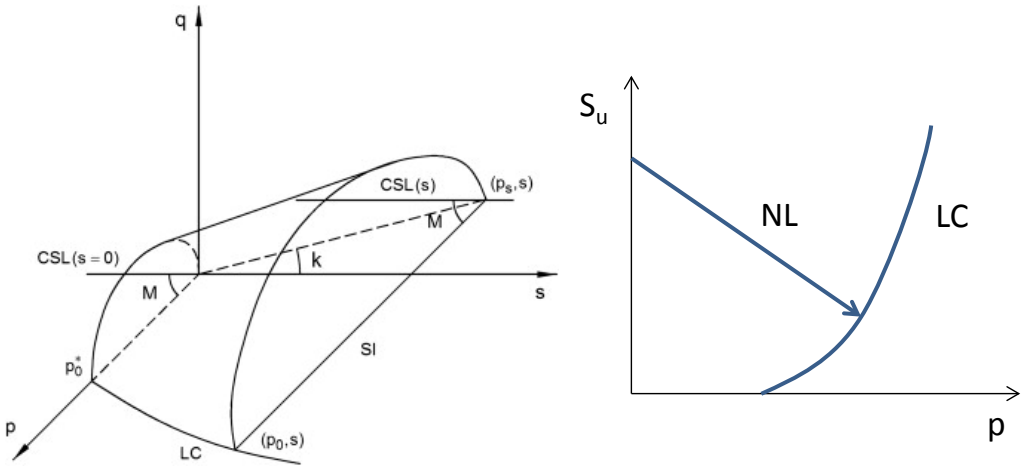

Figure 8.18 BBM yield loci in (a) p–q-s space and (b) p-s plane (Alonso et al., 1999)

Effective stress-integrated model (ESIM) for unsaturated expansive soils

Yield function

By the Bishop effective stress concept, the suction can be incorporated into the mean effective stress and thus being removed from the model, which greatly simplifies the BBM theory in expression, e.g. the load collapse yield surface can be represented by a single effective pre-consolidation stress Pc' as shown in Fig. 8.19.

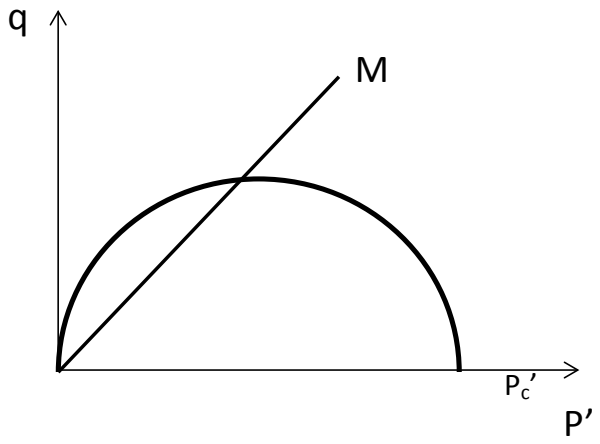

Figure 8.19 Yield locus and critical state line of ESIM

The effective-stress-based yield function takes the form of

$$F_e = q^2 + M^2 P'(P' - P_c') = 0$$

$$P_c' = P_{c0} + \sigma_B$$

$$P' = P + \sigma_B$$

where P is the net total mean pressure, P' is the Bishop's effective mean pressure, P_c' is the effective preconsolidation pressure, P_{c0} is the net preconsolidation pressure and σ_B is the Bishop's effective stress imposed by matric suction.

It is clear from the above yield function that the effective preconsolidation stress P_c' remains to be a variable as long as suction is present in the matrix, and keeps decreasing in magnitude in wetting path. Furthermore, the enhanced internal cohesion of bentonite due to suction effect is implicitly included in the yield function by the parameter P'. From the above description of the new model, you may find the great advantage of integrating and avoiding determination of a number of extra model parameters that are necessary for classical models with dual stress state variables.

Macroscopic level of strain

It is assumed that the volumetric change of the unsaturated soil follows the compression and rebounding of the curves as shown in Fig. 8.20. Similar to the Cam-Clay model, void ratio varies linearly with logarithm of the effective stress. Elastic strain occurs to the rebounding line while both elastic and plastic strain occurs to the compression curve. During the re-saturation of an initially unsaturated soil, effective stress would decline according to the Bishop effective stress equation.

In the meantime, swelling strain other than the elastic rebounding deformation would be induced. This leads to the upward shift of e-log(σ') relationship from the rebound curve, as demonstrated in Fig. 8.20. This upward shift would not be infinite, instead, it would stop and equilibrate somewhere near the equilibrium state line. This equilibrium state is critical to the development of the constitutive

relationship for the swollen unsaturated soils. It has solid physical meanings and has to be addressed separately as discussed above.

The overall volumetric elastic strain increment is governed by the effective stress

$$d\varepsilon_v^e = \frac{dp'}{K}$$

with bulk modulus of $K = \frac{1+e}{\kappa} p'$. The deviatoric elastic strain increment is defined as

$$d\varepsilon_q^e = \frac{dp'}{3G}$$

where G is the shear modulus and is given as a function of Poisson's ratio v,

$$G = \frac{3K}{2}\frac{1-2\nu}{1+\nu}$$

The plastic strain in yield is computed from

$$\mathrm{d}\varepsilon_p = \mathrm{d}\lambda_p \frac{\partial F_e}{\partial \sigma}$$

where λ_p is the plastic multiplier that can be determined from the consistency condition of $\mathrm{d}F_e = 0$.

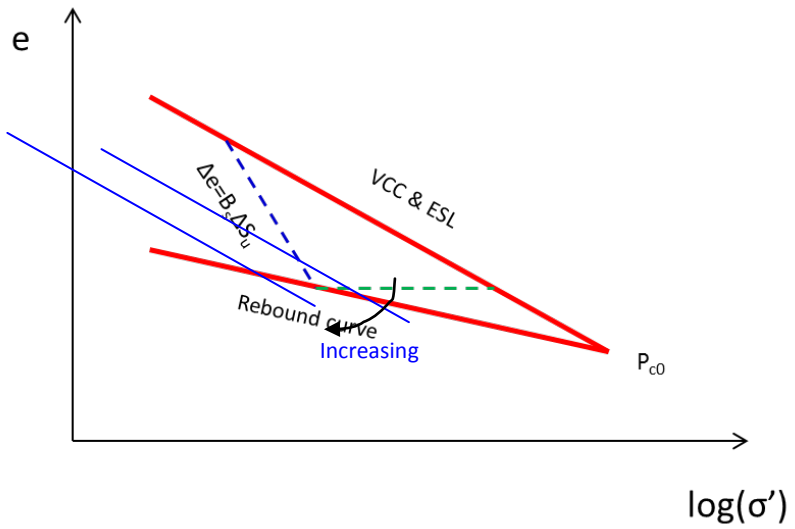

Note:
VCC: Virgin compression curve;
ESL: Equilibrium state line in full saturation;
P_{c0}: Pre-consolidation pressure.

Figure 8.20 Sketch diagram of compression and swelling of bentonite soil with the effective stress principle and the equilibrium state taken into account

ESL is physically equivalent to the experimentally measured swelling pressure versus void ratio. The structuredness induced by salinity variation can be represented by the shift of VCL.

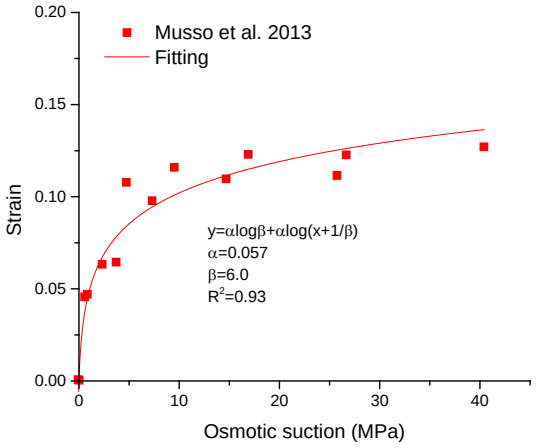

Figure 8.21 Dependence of volumetric strain of FEBEX bentonite on osmotic suction

Under net overburden loading of σ, matric suction S_u=0, and osmotic suction of Π, the total volume strain due to osmotic suction is given as

$$\varepsilon_v = \frac{\lambda}{1+e_0}\log\frac{\sigma+\chi\Pi}{\sigma'} = \frac{\lambda}{1+e_0}\log\frac{\chi}{\sigma'} + \frac{\lambda}{1+e_0}\log\left(\Pi+\frac{\sigma'}{\chi}\right)$$

Or written as

$$\varepsilon_v = \alpha\log\beta + \alpha\log(\Pi+\frac{1}{\beta})$$

where $\alpha = \frac{\lambda}{1+e_0}$, and $\beta = \frac{\chi}{\sigma'}$. Note $\sigma = [\mathrm{MPa}]$.

As shown in Figure 8.21, the volumetric strain due to chemo-consolidation observed in Musso et al. (2013) can be well reproduced by the above equation, resulting in high coefficient of correlation (R^2=0.93). The test conditions include dry density of 1.65, total vertical loading of 500 kPa. The fitting parameters are also found to be reasonable as λ≈0.1, σ'= 167 kPa if let χ=1, which are all consistent with the experimental conditions. The effective stress is generally less than the total overburden loading, which is expected for the model. The virgin compression index λ of FEBEX bentonite was reported elsewhere as 0.25 for DI water (Alonso et al., 2005), therefore λ=0.1 is reasonable for brine.

Microscopic level of strain

The void ratio is decomposed into two parts, according to the assumption of dual-porosity,

$$e = e^m + e^M$$

The microscopic deformation is assumed to be elastic under all circumstances, while the macroscopic deformation is mostly regarded as plastic. The void ratio correlates to porosity by

$$n^i = \frac{e^i}{1 + e^i}$$

$$\mathrm{d}\varepsilon = \mathrm{d}n = \frac{\mathrm{d}e}{1 + e_0}$$

where the superscript ^{i} indicates either the total porosity, the micro-porosity or the macro-porosity.

Determination of microporosity

The microscopic elastic strain has to involve two modes of deformation as well, depending on the suction level with respect to the air entry value, at which the macropore development is expected to happen. In BExM, the double structure of pore ratio is correlated by a transformation factor that varies with suction. The inherent hypothesis of the transformation function is that the micropore is linearly related to suction and the macropore is a nonlinear function of suction. In this study, we invoke the concept of single stress variable principle, which involves a decay function of Bishop's coefficient with suction. As such, the hypothesis of BExM for micropore ratio can be modified to correlate with gravimetric water content (w). This linear correlation can be manifested by the fundamental test of the shrinkage curve. Therefore

$$w = \frac{e^m X \rho_l}{\rho_s}$$

where X is mass ratio of water over total mass of saline water, and ρ_l is the density of saline water, which is larger than that of pure water.

In this study, the mass of 1 L model water was measured as 1223.1 g. The total dissolved salt (TDS) of the MW2-supernatant was 328.9 g/L. In this case, the mass of DI water (894.2 g) was calculates as 73% of the mass of 1 L of MW2-supernatant. Therefore X=0.73 is justifiable for saline water of ρ_l=1223 kg/m^3.

Then

$$e^m = \frac{w\rho_s}{X\rho_l} = \frac{2.75}{0.73 * 1.223} w = 3.08w$$

And thus the macropore void ratio can be determined by subtracting micropore void ratio from the total pore ratio. Therefore the elastic strain associated with micropore is given as

$$\mathrm{d}\varepsilon_m^e = \frac{\rho_s}{\rho_l} \frac{\mathrm{d}w}{1 + e_0}$$

where w is gravimetric water content in macroscopic scale. This relationship turns out to be very convenient to determine the initial conditions of the dual structure porosities from this formula, which only depends on an easily measurable parameter of water content.

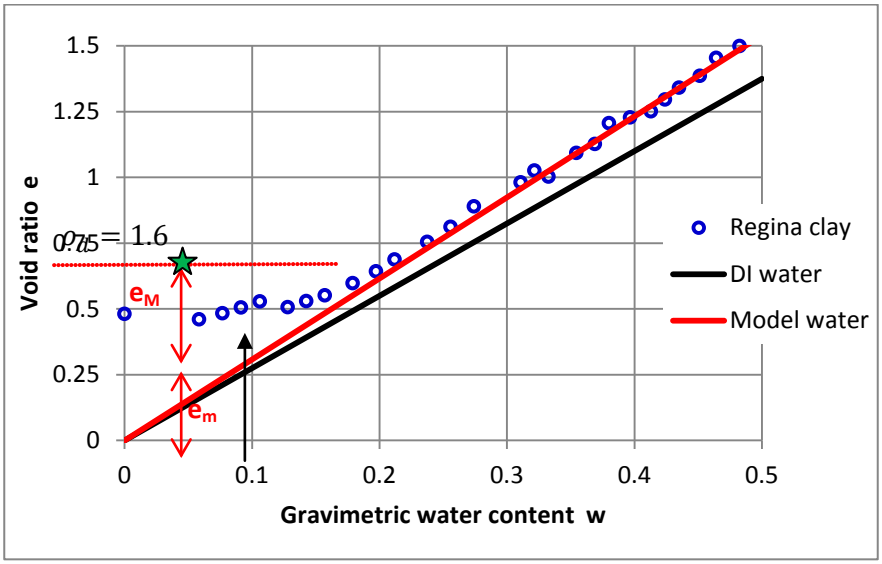

Figure 8.22 The shrinkage curve for Regina clay paste and theoretical line (data from Fredlund et al. (2012))

Using the above relationship, we can predict the ratio of micropore to total pore void ratios, defined as

$$f_m = \frac{e_m}{e_0}$$

For instance, the osmotic suction level of 40 MPa for C=6.6 M model water corresponds to gravimetric water content of 0.15 for bentonite with pore fluid of DI water. If dry density of sample is 1.6 g/cm^3, this results in micropore void ratio $e_m = 3.08w$ and the percentage of microporosity $f_m = 0.643$ after brine saturation. The initial condition of the as-compacted specimen is w_0=0.10, ρ_d=1.6, which indicates $e_m = 0.3$ and $f_m = 0.42$ without brine infiltration.

Manca et al. (2016) conducted MIP test to determine the macropore (r>1μm) void ratio for bentonite under permeation of 4 M saline at 0.35 for e_0=0.78, corresponding to a percentage of microporosity $f_m = 0.55$. This can be illustrated in Figure 8.22 as well. First we calculate the osmotic suction of 4 M NaCl solution as $\Pi = 4.8 * 4 = 19.2$ MPa. Then the water content of bentonite inundated with DI water under this level of matric suction is calculated as 0.185 from soil water characteristic curve (SWCC) plot. Then find the micropore void ratio as e_m=0.48 from Figure 8.22 corresponding to w=0.185 by interpolating between the two bound curves. This corresponds to $f_m = 0.6$ and is close to the experimental results of f_m=0.55. Therefore, the proposed model can be used to correlate the microporosity with water content.

This method for macropore void ratio calculation can be conceptualized as follows.

- The micropores inside the aggregate are generally responsive, in terms of swelling and contraction, to both matric suction and osmotic suction of the macropore fluid.

- The osmotic suction of macropore fluid can be comparable to that of matric suction in view of its ability to extract water from the micropores.
- Solute transport into micropores may introduce some sort of perturbation to the microstructure, and the swelling pressure.
- Diffusion of chemical species into the micropore is mediated by the semi-permeable membrane properties of the aggregate, and thus takes longer time to complete or reach equilibrium than the macropores.

It can be seen that for transient analysis, the above mentioned calibration method (gravimetric water content based method) for determination of dual porosity is sufficient to fulfill the purpose, and is generally in good agreement with the MIP results. But for long term studies, the slow processes of solute transport inward the aggregate has to be addressed appropriately. Chemo-mechanical response of micropore is thought to be critical to integrate reactive solute transport and geomechanical models (Yustres et al. 2017). Time dependent evolution of micropores has to be interpreted and described by appropriate constitutive relationships, which enables prediction of porosity, microporosity, overall solute transport and hydraulic flow, etc. (Yustres et al. 2017).

The micropore under chemical effect may not remain elastic all the time. It also may involve chemo-plasticity, as it cannot rebound to the initial void ratio after unloading the overburden mechanical stress. Basically two mechanisms are invoked here:

- Transient loading of osmotic suction onto aggregate, causing instant shrinkage;
- Time-dependent migration of chemicals into micropore, causing long term slow shift in ESL, and thus volumetric shrinkage under overburden net stress.

Constitutive model for micropores

Therefore, we have to adopt additional hypotheses that (1) inside aggregate matric suction plays a predominant influence on its constitutive behaviour (Terzaghi 2010), (2) air entry into aggregate may not happen except under extreme desiccated situations, and (3) no shear strain is expected to happen to micropore. In another word, suctions (matric or osmotic suction) contribute to contraction of micropore in an equivalent manner to that of net stress. As a result,

$$\mathrm{d}\varepsilon_m^e = \frac{1}{K_m}\mathrm{d}\hat{p} = \frac{\kappa_m}{(1+e_0)\hat{p}}\mathrm{d}\hat{p}$$

where $\hat{p}$ is an additive sum of all stress components and shown as

$$\hat{p} = p + \widehat{S_u} + \widehat{\Pi}$$

where $\widehat{S_u}$ and $\widehat{\Pi}$ are respectively the matric suction and osmotic suction inside micropores (or within aggregates). The suction has to equilibrate with that of macropore. Thus

$$\widehat{S_u} + \widehat{\Pi} = S_u^M + \Pi^M$$

When macropore is in full saturation of saline, $S_u^M = 0$. And thus $\widehat{S_u} + \widehat{\Pi} = \Pi^M$. Therefore

$$\mathrm{d}\varepsilon_m^e = \frac{\kappa_m}{(1+e_0)(p+\Pi^M)}\mathrm{d}(p+\Pi^M)$$

These parameters are computable by the above derived hydraulic equation; as such the mechanical component is well coupled into the hydraulic problem. Under constant overburden net stress, the microstructural strain can be given as

$$\mathrm{d}\varepsilon_m^e = \frac{\kappa_m}{(1+e_0)(p+\Pi^M)}\mathrm{d}(\Pi^M)$$

By integrating the above formula in the range of osmotic suction from a to b, it leads to

$$\varepsilon_m^e = \frac{\kappa_m}{(1+e_0)}\log(p+\Pi^M)|_a^b$$

An alternative to the above equation is to correlate directly to the osmotic suction by an exponential function (Musso et al., 2013) below:

$$\mathrm{d}\varepsilon_m^e = \beta e^{-\alpha\Pi} d\Pi^M$$

where α and β are model constants.

The integral form of the above formula results in the elastic strain of micropore given as

$$\varepsilon_m^e = -\frac{\beta}{\alpha}\left(e^{-\alpha\Pi^M}\right)\Big|_a^b$$

Despite the difference in expression, the above two formulas for the micropore strain can be demonstrated to be equivalent to reproduce the experimental observations, as shown in Figure 8.23 by best-fitting the test data reported by Musso et al. (2013).

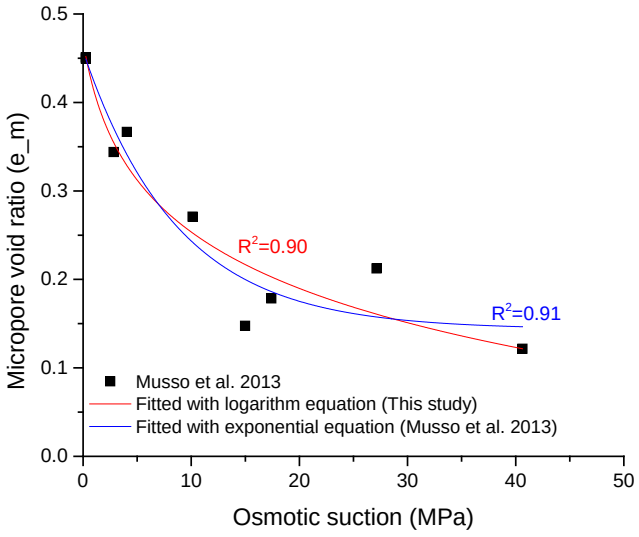

Figure 8.23 Effect of osmotic suction on the micropore void ratio, experimental observation and modellings

In BExM theory, the double structure is useful for explanation of swelling pressure collapse under certain range of suction variations for the highly compacted bentonite soil. Later on, double structure is regarded as a fundamental property of bentonite for the modelling of coupled hydraulic and solute

transport processes. But the link between hydraulic-mechanical-chemical couplings is still missing at present. A comprehensive theoretical framework for the wetting of unsaturated bentonite with saline is proposed in this study.

Characteristics of constant volume swelling pressure test

In case of constant volume swelling, the above mentioned framework has to be adjusted to match the following features:

- No plastic deformation is expected.
- Swelling pressure mainly originates from micropore swelling.
- Elastic correlation is assumed for the swelling pressure as $\Delta\sigma = K\Delta\varepsilon_m^e$.
- Chemical effect on swelling pressure is due to micropore shrinkage, i.e. $\Delta\varepsilon_m^e \propto f(C)$.

The numerical simulation examples in section 5 will elaborate these points in further details.

4. Chemical-dependent fundamental parameters

WRC for MX-80 bentonite

The gravimetric water content for MX-80 has been experimentally determined and is plotted against the measured suction that is determined by chilled mirror technique (Figure 8.24). The chilled mirror technique gives the total suction of the soil specimen. The total suction can be decomposed into matric suction and osmotic suction; the two suction components can be added up for characterization purpose. By subtracting the osmotic suction of the model brine water, the matric suction of compacted MX-80 bentonite with respect to brine was found to vary in a logarithmic form with the gravimetric water content, which is consistent with our mechanistic modelling with DDL theory as reported in Chapter 6. The water retention curve of brine solution is generally less than that of DI water. The extrapolated limit value for matric suction in full desiccation is determined from Fig. 8.24 to be 270 MPa, which is close to the regressed limit value of 150 MPa by DDL theory.

In case of wetting with DI water, MX-80 seems to follow a different pattern to correlate with suction, i.e. a w^0.5-log(S_u) relationship. The measurement of the water retention curve for MX-80 in permeation of DI appears to be consistent with the results of Seiphoor et al. (2014).

Empirical relationships can be derived by best-fitting the test data,

$\sqrt{w} = -0.215 * \log\left(\frac{S_u}{1800}\right)$, DI water

$w = -0.124 * \log\left(\frac{S_u}{270}\right)$, Brine

Based on the conceptualization of clay-brine interaction in this work, the pore space is divided into two categories, i.e. the macropore and micropore. The micropore basically replicates the clay-wet-with-DI situation. Therefore, the presence of brine can be regarded as an introduction of an extra osmotic suction for the micropore system, which implies that the WRC for the micropore can be treated as the

WRC for MX-80 subtracting the osmotic suction π of brine solution. From the graph we find that the WRC for MX-80 in brine is above the WRC for micropore in brine, suggesting extra water retained besides the micropore. The rest of the water retained in the brine-saturated MX-80 soil would be attributed to the macropore system. Therefore, the water retention capacity for the macropore can be derived as the difference between the WRC for micropore in brine and the WRC for MX-80 in brine. The data analysis gives the following relationship,

$$w = -0.045 + \frac{0.3}{\sqrt[2.36]{1+S_u}}, \qquad \text{macropore, brine}$$

The above equations are plotted in Fig. 8.24 for comparison. If plotted as a function of saturation degree, the Brooks-Corey relationship can best-fit the WRC for the macropore, as shown in Fig. 8.25.

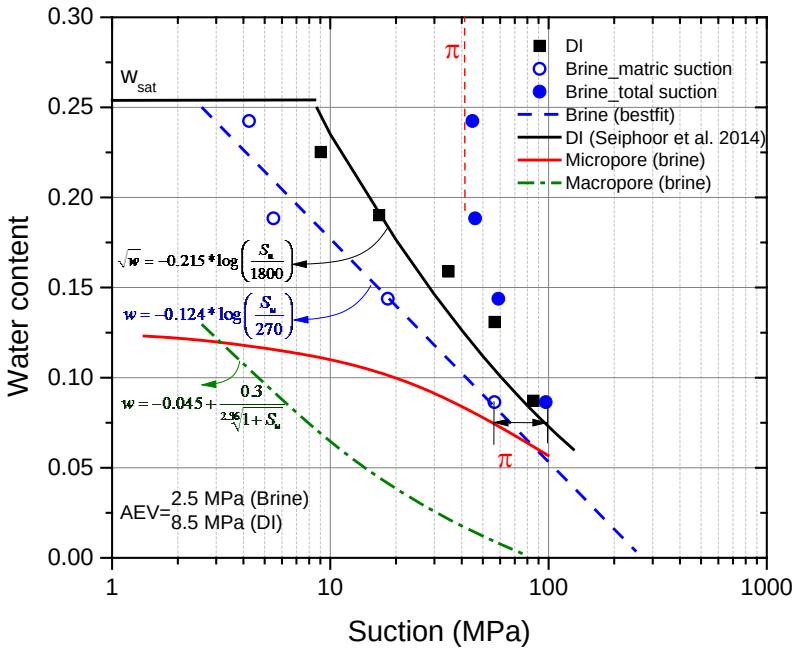

Figure 8.24 WRC of MX-80 for various pores and pore fluid scenarios (The air entry values for DI and model brine water are determined by the intersection with the level line corresponding to the saturated water content (w_{sat}). Osmotic suction of model water was determined as 40.6 MPa by Queens' University.)

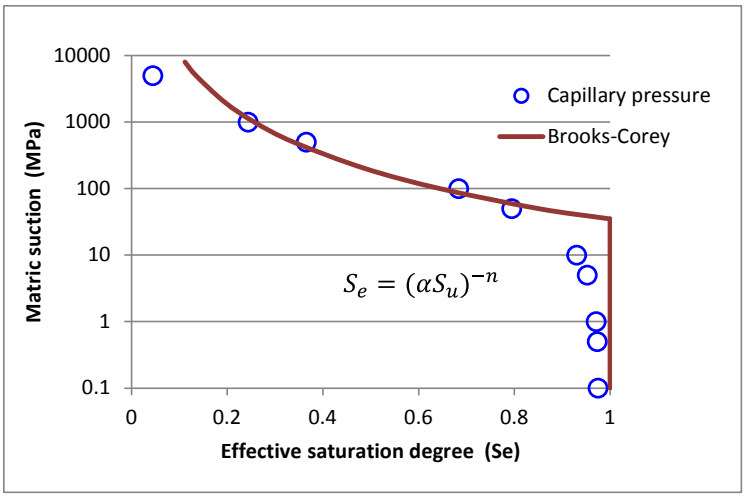

Figure 8.25 Macropore water retention curve versus Brooks-Corey model (α=0.03, n=0.4)

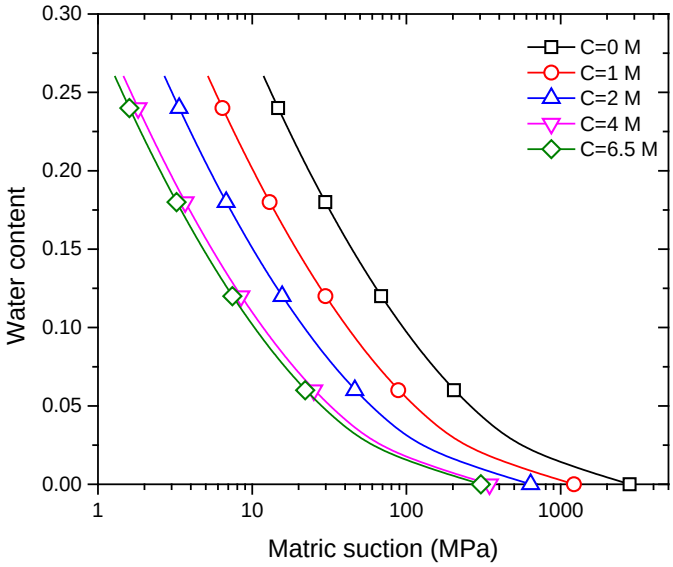

Figure 8.26 WRC for micropore varies with salinity

WRC of the micropore as shown in Fig. 8.24 is not in its equilibrium state when bentonite is permeated with brine solution. With the migration of chemicals into the micropore space, its WRC will vary accordingly. In this study we address this chemical-dependent variation of WRC by proposing an empirical formula as below.

Suction toe (S_{ut}) represents the interception of WRC with time axis at w=0, and is hypothesized to be dependent on chemical concentration inside the micropore as shown in Figure 8.26. An exponential function is proposed for this relationship as below.

$$S_{ut} = S_{ur} + \vartheta e^{-A*C}$$

where S_{ur}=300 MPa; ϑ=2500 MPa; A=0.001. Applying the above relationship results in a set of WRCs for MX-80 under different salinities as shown in Fig. 8.26. It is clearly shown that the water retention capacity of bentonite is gradually decreased by elevated salinity.

Swelling pressure at various dry densities

Figure 8.27 shows the variation of swelling pressure of MX-80 bentonite with EMDD at various salinity conditions. Brine generally leads to decrease in swelling pressure for bentonite. The logarithm of swelling pressure is found to change linearly with EMDD. The test data in this work on SP of MX-80 follows the general trend as reported in existing studies. The remaining uncertainty here is the long-term reduction in swelling pressure, which is likely attributed to the chemistry of model water, i.e. the high concentration of Ca, Mg, K etc. Herbert et al. (2008) observed a similar trend in swelling pressure decrease under chemical influences. Their geochemical and XRF investigations revealed significant reduction in interlayer charge density over time, which is speculated to take place either by cation exchange with clay mineral or dissolution of Al from tetrahedral crystals. Mineral alteration is a possible mechanism for this behaviour.

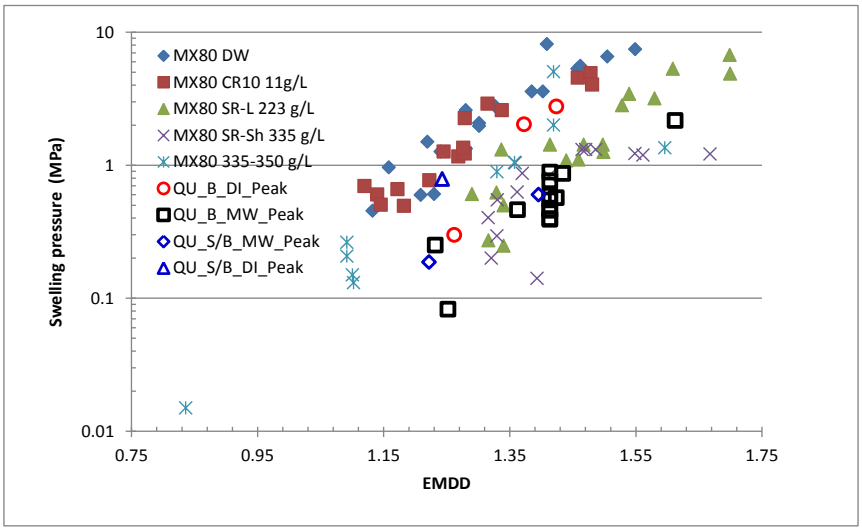

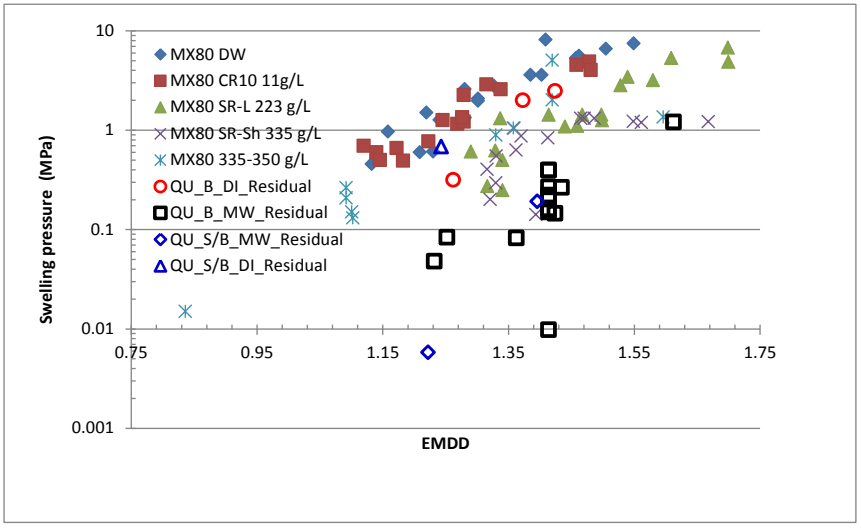

Figure 8.27 Variation of swelling pressure of MX-80 bentonite with EMDD at various salinity conditions (Data points of solid symbols are collected from Dixon et al. (2017); QU stands for Queens' University.)

Temporal variation of swelling pressure

Softening of swelling pressure is always associated with dual-porosity structures, and has different underlying mechanisms, i.e. mechanical response, and chemical influence. Pore fluid chemistry has significant impact on the swelling of bentonite as shown in Fig. 8.28. With the same dry density, DI water has several times higher (5X) swelling pressure than MW. Within 500 hrs, no obvious variation in swelling pressure can be noticed from the test data. However, after 8000 hrs of continuous permeation, swelling pressure of DI stabilizes most of the time, whereas MW causes 80-90 % of swelling pressure loss. Our modeling efforts will focus on reproduction of the gradual weakening in swelling under permeation of brine water.

Imbert and Villar (2006) reported an observation of a unique softening behaviour (40-50 % of reduction) in swelling pressure developed as a result of 100 hrs of water infiltration. However, the swelling pressure was subsequently increased to a higher level than the initial peak pressure after 200 – 1000 hrs of continuous infiltration of water. This phenomenon is attributed to the strong structuredness of macropores, which is induced by mechanical processing in preparation of bentonite pellets and is able to resist the volume expansion of the micropores within a certain suction range, and lower initial water content (5%) that helps to retain the structuredness. When initial water content is increased to over 10 %, the double peak and initial softening behaviour in development of swelling pressure disappears (Imbert and Villar 2006).

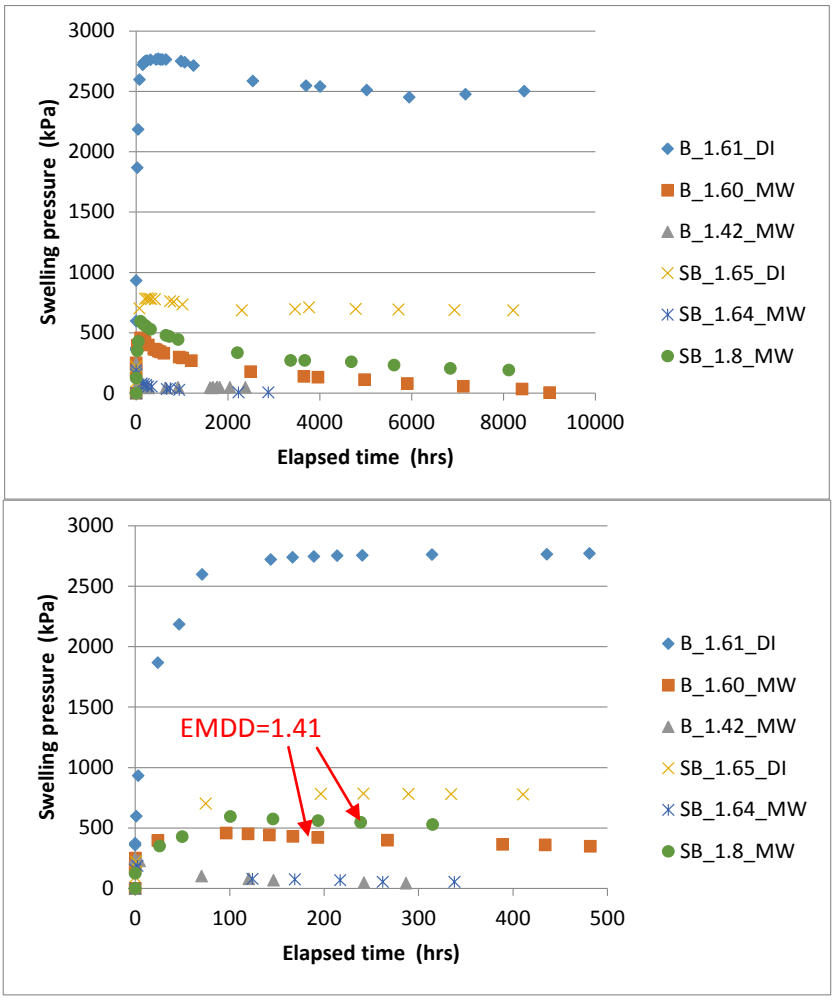

Figure 8.28 Variation of swelling pressure with elapsed time for MX-80 at different dry densities and pore fluid scenarios (a) long-term behvaiour and (b) short-term behavior (Queens' University progress report #3, 2017)

Effect of chemistry on oedometric properties

Compression index λ and swelling index κ are dependent on matric suction, as well as salt concentration. According to the previous discussion in this chapter on compression behavior of unsaturated bentonite, these indexes are found to be unique to stress (i.e. independent of the effective stress) when a single stress variable is employed. Then it can be reduced to

$$\lambda = \mathrm{f}(C)$$

$$\kappa = \mathrm{g}(C)$$

Both swelling index and compression index of bentonite have been shown to be a function of salinity of pore fluid in a number of studies (see Fig. 8.30). There obviously exist range limits for both indexes, corresponding to extreme conditions of distilled water and saturated saline water. A special case holds for bentonite saturated with distilled water with respect to the equilibrium state line, i.e.

$$\lambda = \lambda^e = \kappa, \qquad C = 0$$

Besides, a saturated bentonite with distilled water (when C=0) may not ensure the coincidence of its virgin compression index (λ) to that of the ESL (λ^e), which only happens under special circumstances, i.e. ideal homogeneity, therefore

$$\lambda > \lambda^e = \kappa, \qquad C > 0$$

Additionally, the VCL and the virgin compression index λ of saline-saturated bentonite are found to depend on initial dry density ρ_{d0}. This may be attributed to the dual porosity structure due to contraction of clay lattices in contact with saline. Contraction of clay lattices not only contributes to the decrease in thickness of diffuse double layer, but also the bonds between clay aggregates, which was shown to increase the cohesion and frictions of clay. The increase in macroporosity contributes to the upward shift of the VCL when comparing the VCLs of MX-80 with model water at different initial dry densities. This is a sign of increased structuredness and a transition of a homogeneous clay soil to a structured soil.

The intercept of VCL with semi-horizontal elastic re-compression line reflects the preconsolidation pressure (Pc') for sample preparation. Existing consolidation data on MX-80 from Queen's University (Rowe and Brachman 2016) suggests a unique value of P_c' at about 1.0 MPa for two sets of specimens with different initial dry density of 1.43 and 1.61 g/cm3. The slopes of the VCLs are also found to be independent of salinity or initial dry density. So we have

$$\lambda = \lambda_0 = \text{const.}$$

So far there is still a lack of comprehensive study on virgin compression index of MX-80 bentonite in various chemical concentrations of pore fluid and initial dry density. An empirical relationship can be developed from the laboratory experiments available in this work.

$$\lambda = \begin{cases} \kappa, & \sigma' < P_c' \\ \lambda_0, & C \geq 0, \sigma' \geq P_c' \end{cases}$$

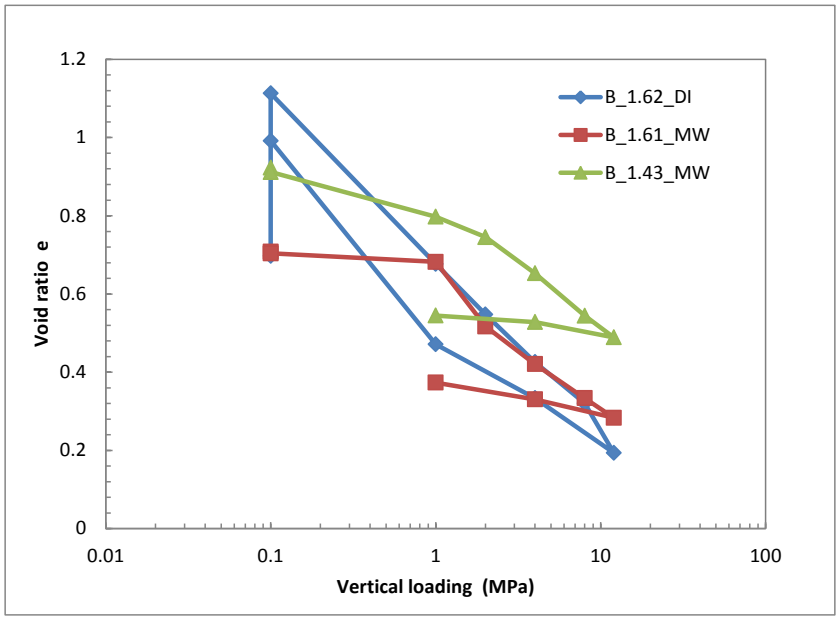

(a)

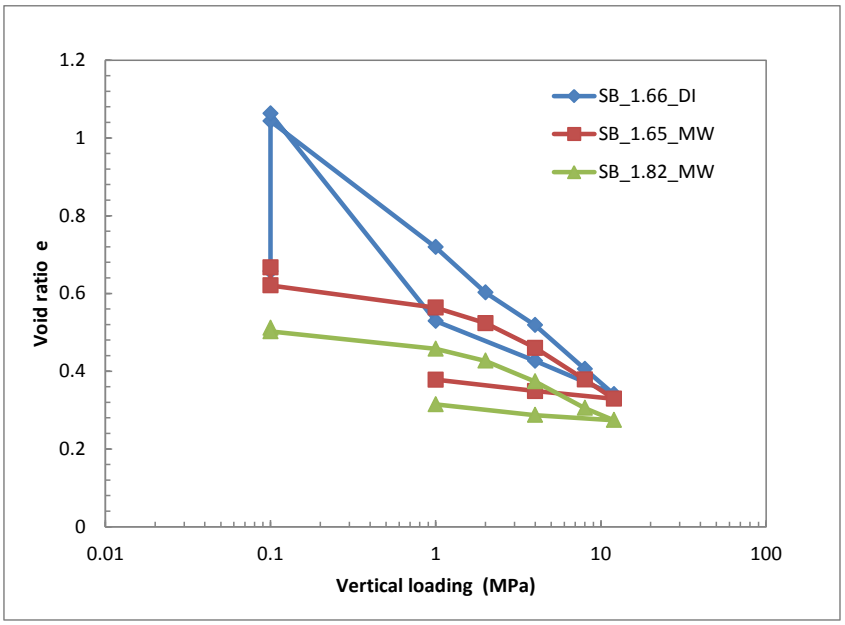

(b)

Figure 8.29 Compression curves of (a) compacted MX-80 bentonite and (b) sand-bentonite mixture flooded with DI water, model saline water under various initial dry densities

Figures 8.29 (a-b) show oedometer test data on MX-80 and S/B mixed soil. Model water permeation decreases the swelling index κ. But the compression indexes are not significantly affected by salinity. Table 8.1 shows the calculated parameters. S/B generally shows less tendency to deform. These observations are in good consistence with the reported compression indexes by Siddiqua et al. (2011) as shown in Fig. 8.30.

Table 8.1 Compressibility of MX-80 determined by oedometer test

	B_1.62	B_1.61	SB_1.8
	DI	MW	MW
λ	0.43	0.358	0.199
κ	0.256	0.083	0.038

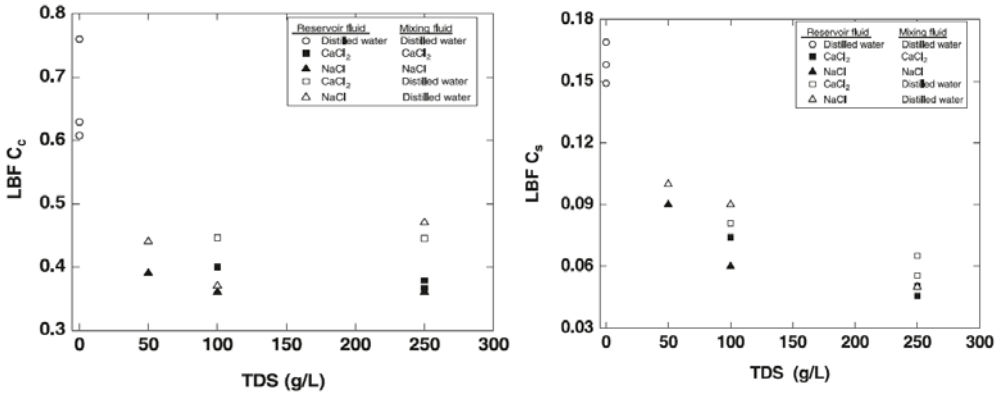

Figure 8.30 Compression indices of S/B mixture (50/50) by Siddiqua et al. (2011)

Note: The unit of vertical loading in Siddiqua et al. (2011) study is at kPa, which is different from the unit of MPa used in this study.

Relative viscosity of brine

Phillips et al. (1980) reviewed and experimentally measured the viscosity of sodium chloride, potassium chloride and calcium chloride to generate tables of smoothed values over the ranges 20-350 °C, 0-5 molar/L, and pressures up to 50 MPa. Their dataset covers the range of experimental conditions encountered in this study, i.e. the room temperature and the brine (model water) mainly composed of NaCl at its full saturation, which allows us to develop a formula for the relative viscosity of pore fluid. Figure 8.31 shows the viscosity of saline of various concentrations and chemical compositions. It can be seen that for NaCl and KCl mixture, the viscosity is expected to stay stable at a level approximate to that of DI water. Therefore chemical effect on dynamic viscosity of the pore fluid is ignored in the numerical studies in this work.

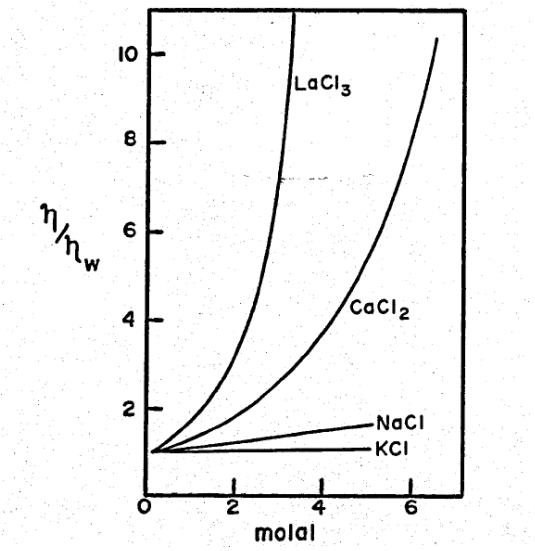

Figure 8.31 Relative viscosity of various chemical solutions at 20 °C (Phillips et al., 1980)

5. Numerical simulation of Queens' University experiment

FE model for constant volume swelling test

Figure 8.32 shows the finite element model mesh of the compacted bentonite specimen, at the size of (radius*height=19mm*12 mm). The bottom boundary is connected to supply of permeant at constant pressure of 0.1 MPa, while the top boundary is left open to ambient atmospheric pressure prior to flow through. Once pore fluid breaks through the specimen, the top boundary is maintained at a constant pressure at 0 MPa. This is a mixed Robin type boundary condition given as

$$\frac{\partial p}{\partial z} = \begin{cases} 0, & p \leq 0 \\ \mathbb{L}(p - p_{ext}), & p > 0 \end{cases}$$

where $\mathbb{L}$ is a random large number taken as shown in Table 8.2, p_{ext} is the target pressure (0 MPa in this work).

The side wall is maintained as impermeable boundary. Chemical concentration is kept constant (6.5 M in this work) as inflow at bottom boundary. The top end is Neumann type boundary for solute transport.

Table 8.2 shows the rest of model input parameters. Extensive simulation trials have been carried out to determine an appropriate range for these model parameters. These shown parameters are all tested and able to best reproduce the experimental data.

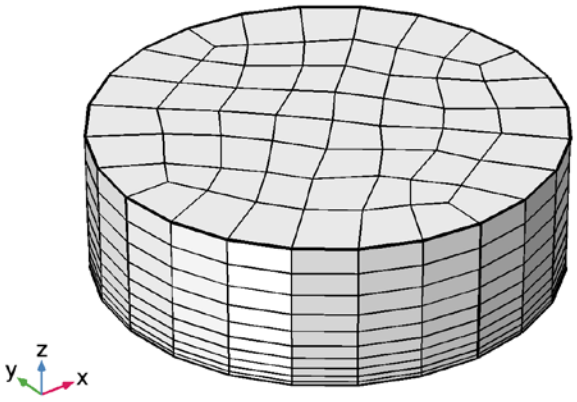

Figure 8.32 FEM model and the meshing for the constant volume swelling test

Table 8.2 Model input parameters

Variable	Unit	Expression
Initial conditions		
G_s		2.75
e_0		G_s/1.6-1

m_0		0.11
e^m		$m*G_s$
Permeability		
k^M	m/s	$1E-9*(e_0)^{11.86}$
k^m	m/s	$(1E-13*e_0^{3.74})/(1+e_0)$
Chemo-osmosis		
ω		0.97-0.98
k_c	Pa m^3/mol	40*1E3/6.5
Mass exchange		
$\bar{\alpha}$	m/Pa s	$2* k^m$
D_0	m^2/s	$1E-9/(45*e^m{}^{(-0.66)})$
l_c	m	10E-6
$\overline{D}$	m/s	$D_0/lc*\exp(-H*C^m)$
H	m^3/mol	0.004 - 0.005
Q^M	m/s	$\bar{\alpha}*(S_u^m+p^M-p^m+k_c*(C^m-C^M))$
Water retention curve		
S_u^m	Pa	$1E6*S_{ut}*10^{((-m^{0.5})/0.215)}$
S_{ut}	Pa	$300+2500*\exp(-0.001*C^m)$
S_u^M	Pa	$1E4*(1/0.03)*(S_e)^{(-2.5)}$ [Pa]
Boundary condition		
$\mathbb{L}$	m/s	$0.5E7*k^M$

Note: m is micropore water content; C is [mol/m^3].

Temporal variation of swelling pressure for MX-80 specimen

A series of constant volume swelling tests with several different combinations of test conditions have been conducted at Queens' university (Rowe and Brachman 2016). The effect of chemistry on swelling pressure has been well documented, is shown to be astonishingly significant, and takes place slowly but continuously even after 1 year of permeation with brine water (Rowe and Brachman 2016). This chemical-induced long-term change in swelling pressure has been interpreted by Herbert et al. (2008) as a result of chemical reaction in the octahedral layer of smectite: (1) decrease of interlayer charge via Mg-Al replacement; (2) replacement of interlayer cation of Na with Mg, K or Ca; and (3) mineral alteration from montmorillonite to illite and eventually to kaolinite in the long run (i.e. kaolinitization/pyrophyllitization). The high salinity pore fluid used in Herbert et al. (2008) covers a wide range of geochemical conditions, including Portland cement pore water, degradation fluid from salt-concrete interaction, groundwater, saturated NaCl etc. Some of the fluid samples contain high concentration of cations like Na, Mg, K and Ca. The chemistry of pore fluid is very similar to the model water in this study. Therefore the mechanism discussion for the drop in swelling pressure is applicable to the situation in this work.

Figure 8.33 shows the modeling results and the comparison against the measurements. It is shown that the model reflects the pulse of swelling pressure very well. The effect of salinity can also be well achieved by changing the inflow chemical concentration. The observed swelling pressures of compacted MX-80 bentonite are well predicted by the model, using bulk moduli K comparable to the experimentally determined value.

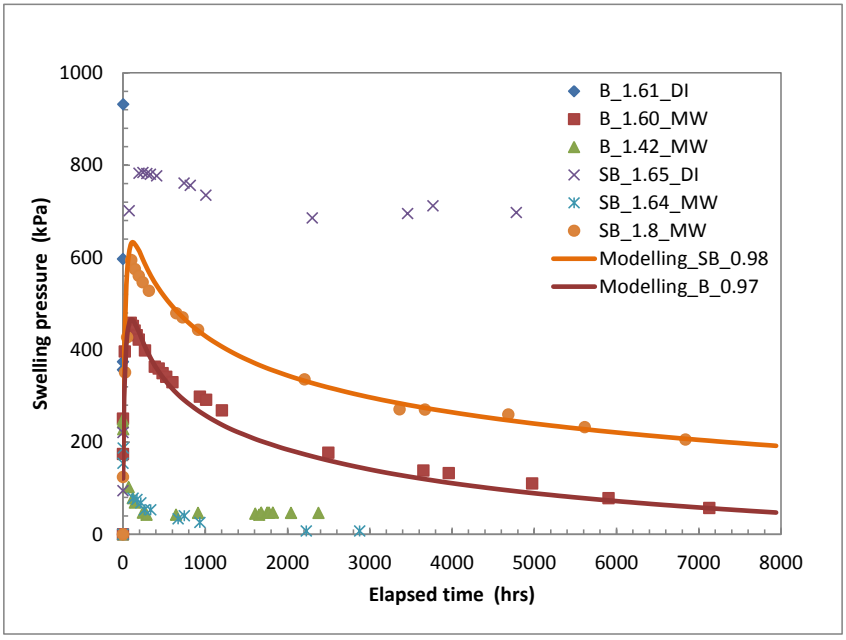

(a)

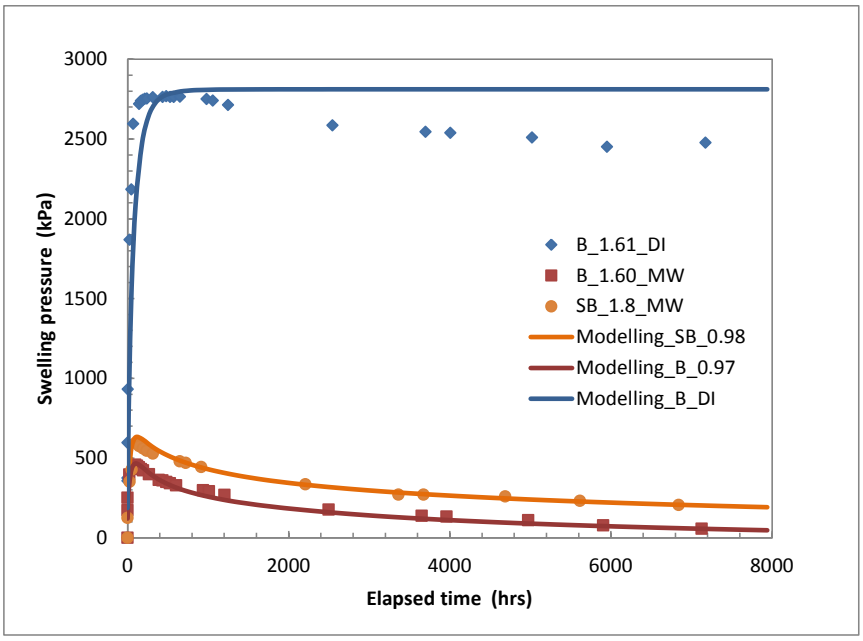

(b)

Figure 8.33 Temporal variation of swelling pressure of MX-80 bentonite under permeation of brine (a) and DI water (b)

(Bulk moduli are shown in Table 8.3. Semi-permeable membrane efficiency ω=0.97-0.99. Fluid exchange rate $\alpha=2k_0$, with k_0=intrinsic permeability of bentontie with DI permeation.)

Table 8.3 Bulk moduli (K) of MX-80 specimen flooded with brine and DI water

	B_1.62 (MPa)	SB_1.80 (MPa)	B_1.61 (MPa)
	MW	MW	DI
Oedometer test	4.75*	8.59*	10.8**
Modelling estimation	6.87	8.75	10.6

*: Reference effective stress for modulus calculation is taken as 1 MPa.

**: Reference effective stress for modulus calculation is 2.7 MPa.

Effect of initial water content

The initial water content is found not to affect the trend of volume-average water content in micropore with prolonged permeation time. The presence of peak in water content appears at 0.145 quickly after infiltration was initiated, and declines in a very smoothly curved manner. Lab test on a number of compacted MX-80 under different initial water content showed the same trend. In our model, the micropore water content is linear to both microporosity, and the swelling pressure. Therefore, a unique value in peak water content suggests a unique value of swelling pressure that is not subject to impact from initial water content. This finding is in good agreement with the laboratory observations.

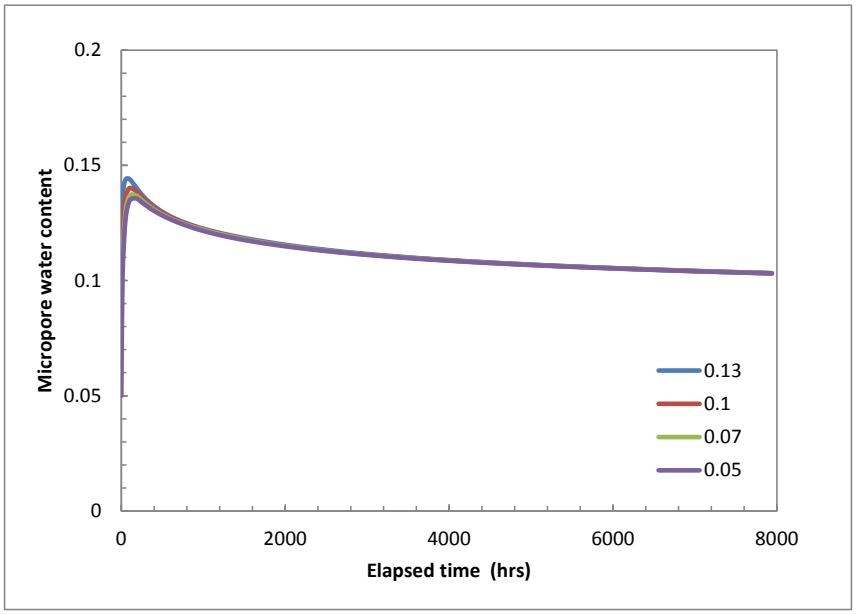

Figure 8.34 Effect of initial water content on evolution of water content in micropore (m_0=0.05, 0.1, 0.11 and 0.15, respectively)

Effect of macropre permeability

The effect of macropore permeability is investigated by numerical simulation and the results of micropore water content are shown in Fig. 8.35. When permeability of macopore is larger than or comparable to that of the micropore, the micropore water content appears to approach an asymptote with peak around 0.14. A less permeable macropore, which is unlikely because macropre is always more permeable than micropore, results in decreased peak and delayed presence of peak in micropre water content. This simulation scenario shows that the permeability of macropore is not the governing factor for swelling of bentonite. Mass transfer coefficient between dual-porosities contributes significantly to the overall swelling behaviour of brine-infiltrated bentonite.

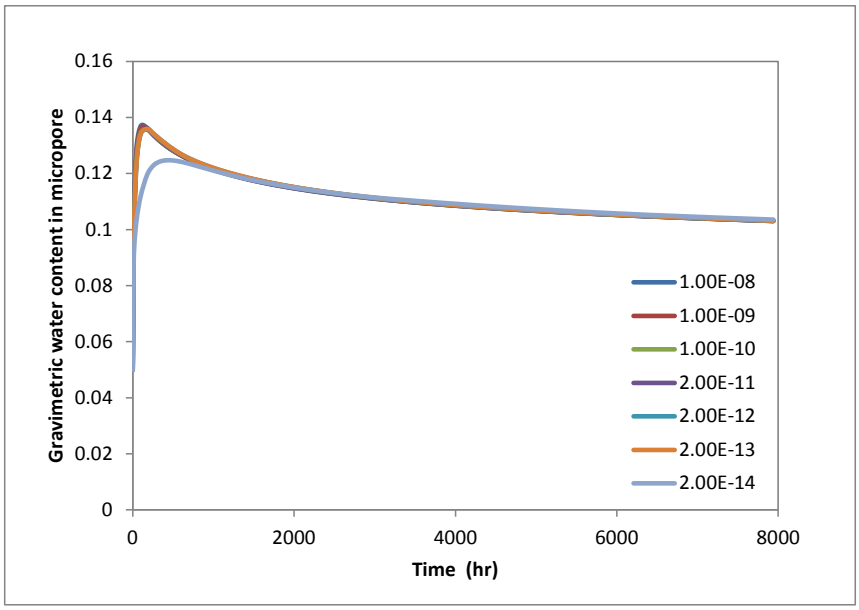

Figure 8.35 Effect of macropore permeability (D_0=1e-9 for macropore)

Effect of salinity

Our model shows that high salinity suppresses the swelling potential of bentonite by decreasing the maximum amount of water retained in micropore, as shown in Fig. 8.36. The micropore water content is decreasing with increasing salinity. At C<3 M, swelling will reach equilibrium quickly and maintains at a stable level. At C≥3 M, swelling appears to be softening with elapsed time.

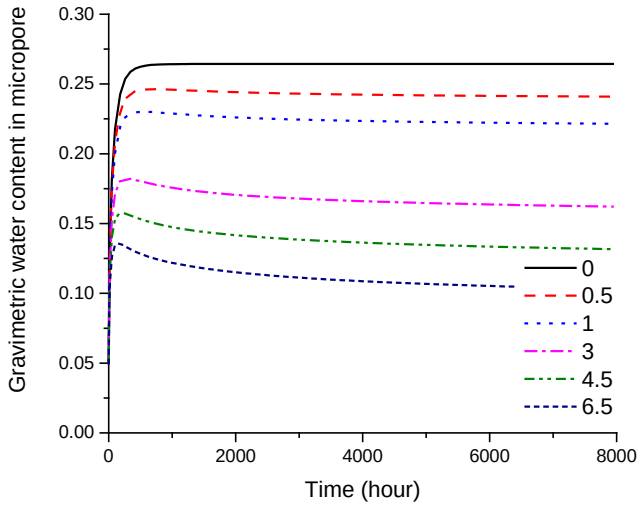

Figure 8.36 Effect of salinity on water content in micropore (initial water content m_0=0.05)

Effect of specimen thickness

Figure 8.37 shows effect of specimen thickness on evolution of micropore swelling under infiltration of model brine solution (C^M=6.5 M). Thinner specimen is found to reach higher pulse peak than thicker specimen. The peak of pulse in micropore water content is also reached in a shorter period of infiltration for thinner specimen. This behaviour has not been identified in our ongoing laboratory experiments since a lack of test on different specimen size. However, field mock-up test on MX-80 does show a slow increase of swelling pressure and blunt shape of peak pressure, which is in contrast to the sharp pulse and rapid change in swelling pressure pertinent to our test on thin bentonite specimens (Millard et al. 2009). It is clear that this is attributable to the size effect.

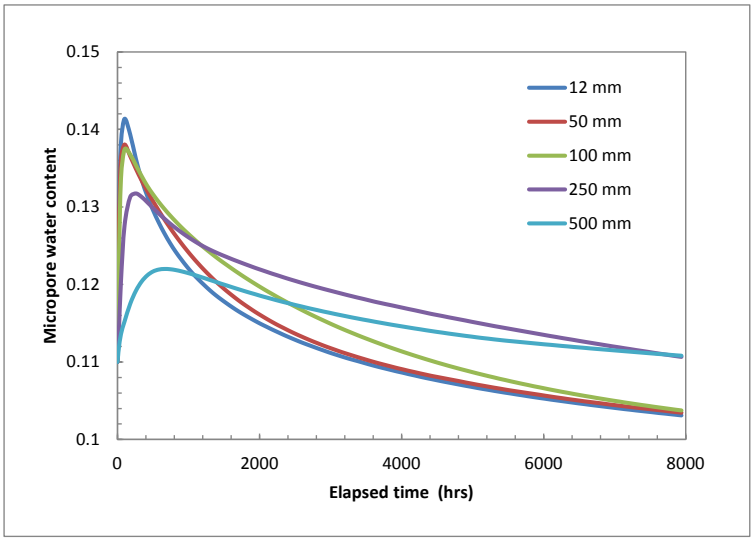

Figure 8.37 Temporal variation of micropore water content at different specimen thicknesses

Profile of variables at different permeation time

Figure 8.38 shows the profile of several variables at different permeation period. The macropore reaches full saturation within a few days. In the meanwhile, micropore water content and matric suction is still changing. Mass exchange between the dual-porosities leads to gradual increase of micropore salinity, which in most of the time remains less than that of the macropore. The Fig. 8.38 gives a brief description of the overall HMC coupled processes happening to MX-80 under permeation of brine water.

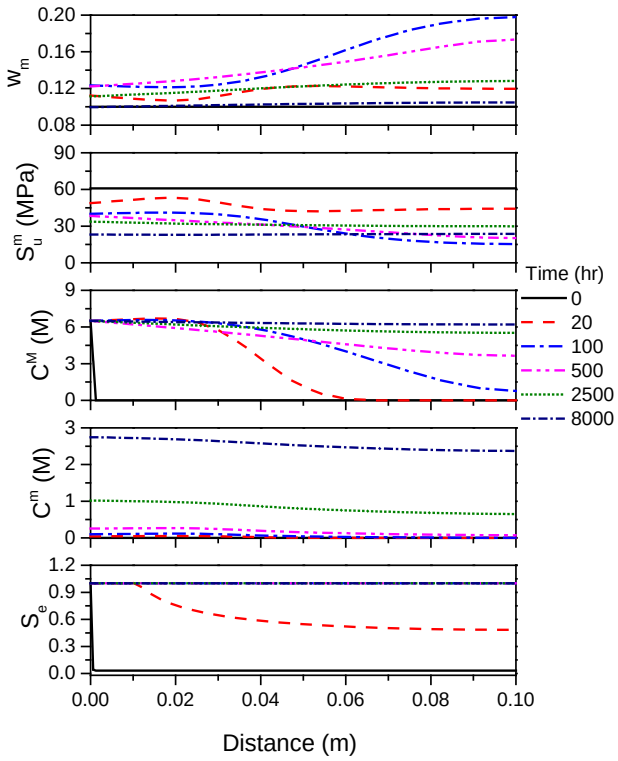

Figure 8.38 Evolutions of water content, suction salinity and saturation degree in dual-pores

6. Calibration with POSIVA data on MX-80

Infiltration of clean water (salinity 0.87 g/L) through compacted MX-80 bentonite column has been carried out with dry density at 1.7 g/cm^3, with initial water content of about 5 %. The pressure head is maintained at 2 MPa for the inlet by GDS pressure adjustment system, while the outlet is open to ambient atmospheric pressure. The specimen has diameter of 5 cm and height of 6.3 cm. Figure 8.39 shows the sketch of the instrumentation. Detailed description of the comprehensive experimental program can be referenced in Pintado et al. (2013). This study only interprets a single series of test data for #100416.

The numerical model and its application in COMSOL are kept the same as the above calibration example about data from Queens'U. Due to the very low salinity of permeant, we ignore the effect of pore fluid chemistry and considered mainly the interaction between macro- and micro-pores. Figures 8.40-8.43 show the modelling results and the comparison with experimental data in terms of inflow volume, water content profile, suction profile, and swelling pressure measured as the axial load.

It can be seen from these figures that the water infiltration volume, the suction profile are both well reproduced. The modeled swelling pressure follows the right trend and retains the same end value as the measurement. The discrepancy relies on the water content profile, which is likely due to the

inconsistence of water retention curve between the model and the test specimen, as the water content is computed on the basis of water retention curve.

As shown in Table 8.4, most of the model parameters are the same as what we derived theoretically for MX-80 bentonite. Only minor adjustments were made with respect to the permeabilities and unsaturated state variables. Other than that, it is all in good consistence with our modelling results. It can also be seen that the total volume of water injection at the end of test after 2 months remains very small compared to the total volume of the soil specimen (32 mL versus 124 mL).

For the swelling pressure calculation, a linear function of the following form is adopted,

$$\sigma_{sp} = K(e^m - e_r)$$

where K is the bulk modulus and e_r is the reference void ratio. It is determined to be K=36.4 MPa by modelling and K=43.5 MPa by oedometer measurement.

It is indicated that the assumptions in the model are consistent with the mechanism underlying the swelling process and the development of swelling pressure. Using a bulk modulus similar to the oedometer measurement is found to result in a satisfying prediction of swelling pressure.

Table 8.4 Critical parameters used in the modelling

Variable	Expression	Note
alfa	(1e-13*e0^3.74)/(1+e0)*2	2 times of theoretical formula
k^m	alfa	
k^M	4*alfa	Much less than the theoretical value for macropore
k_r_M	Se^3	Relative permeability in macropore
k_r_m	0.8^6	Fitted parameter: relative permeability in micropore
k_intra	k_r_m*alfa	Inter-pore permeability
C_{Cm}	1e4*Gs*(1-em/(1+em))*2*SOS*0.215/(-p3)*(p3<-AEV)+1e4*Gs*(1-em/(1+em))*0.215*mA_sqrt*(-p3)/(AEV^2)*(p3>=-AEV&&p3<0)+0*(p3>=0)	Specific moisture capacity by theory following w-log(Su) relationship
C_m	C_{Cm}/4	Fitted parameter: specific moisture capacity
K	36.4 MPa	K=43.5 MPa by oedometer (rebounding elasticity)

The rest parameters are kept the same as we derived for MX-80 bentontie.

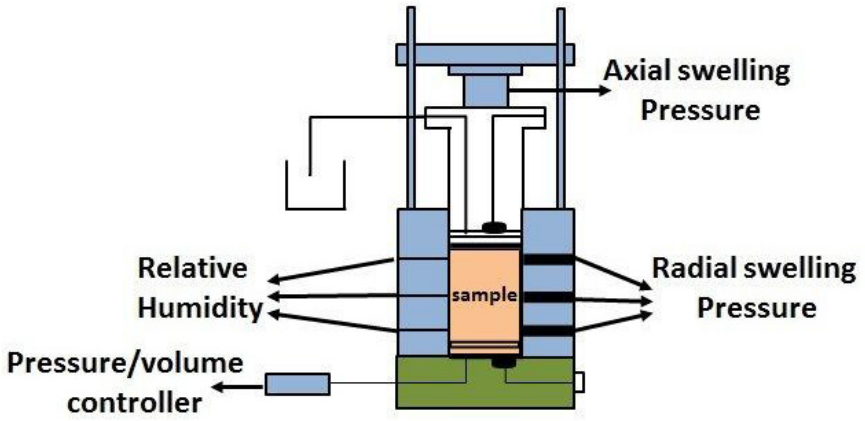

Figure 8.39 Schematic diagram of the infiltration test setup (Pintado et al. 2013)

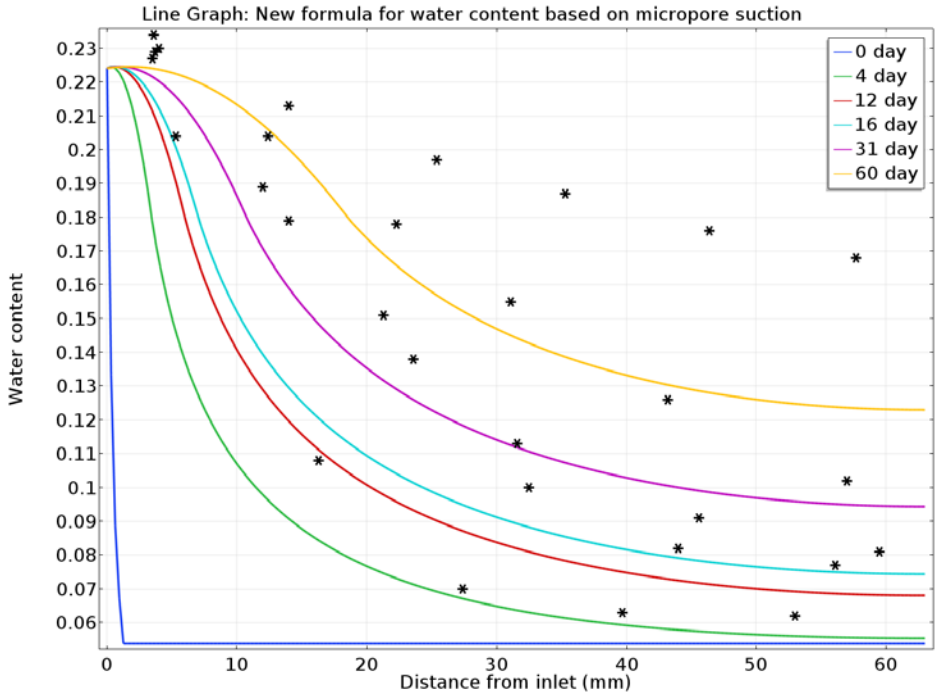

Figure 8.40 Dependence of water content on distance at various permeation time

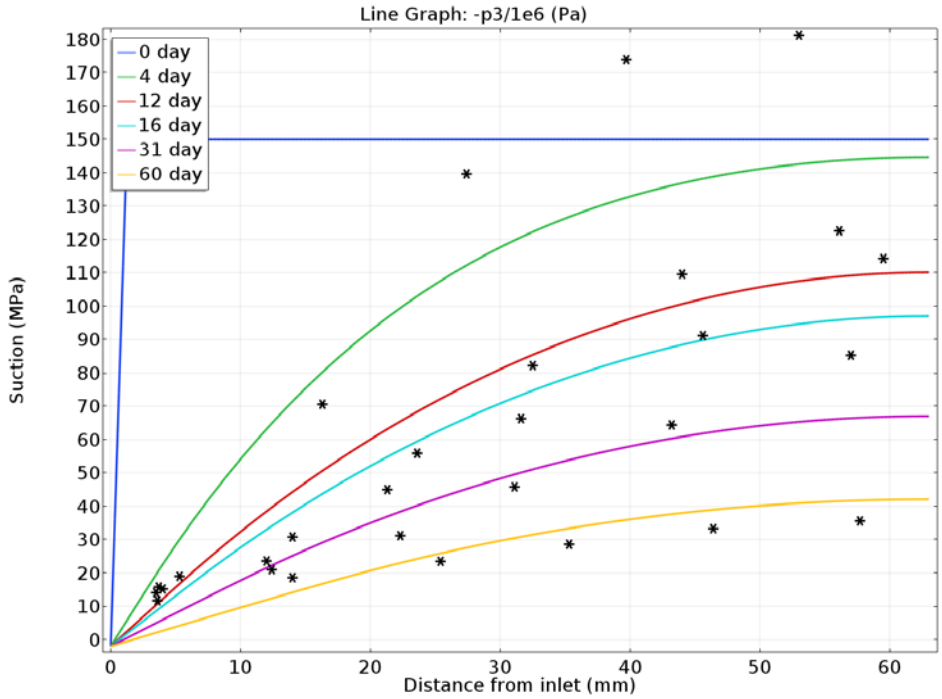

Figure 8.41 Dependence of matric suction on distance at various permeation time

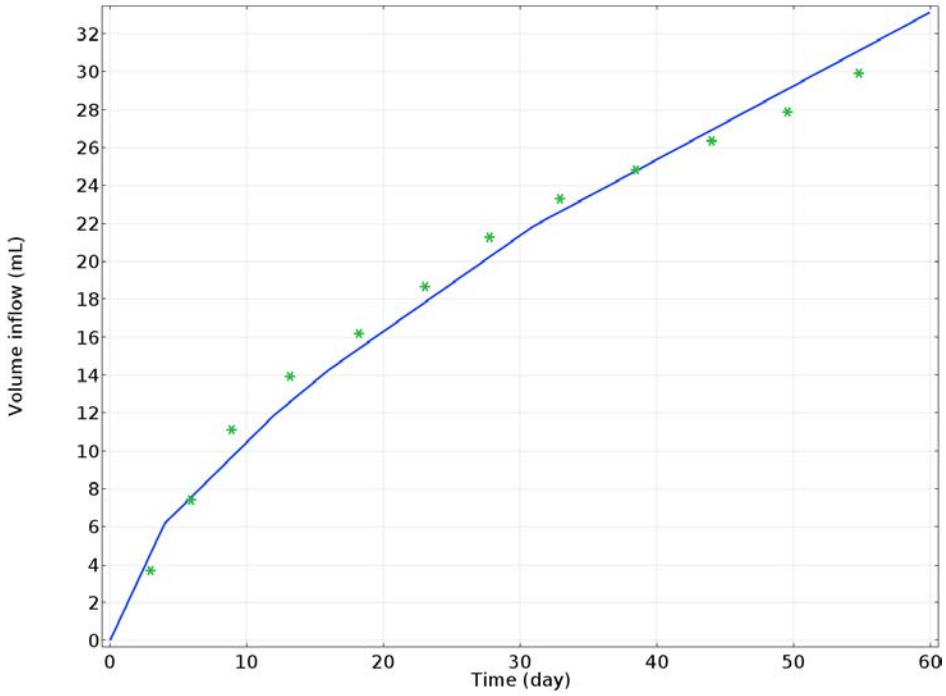

Figure 8.42 Variation of inflow volume with elapsed permeation period of time

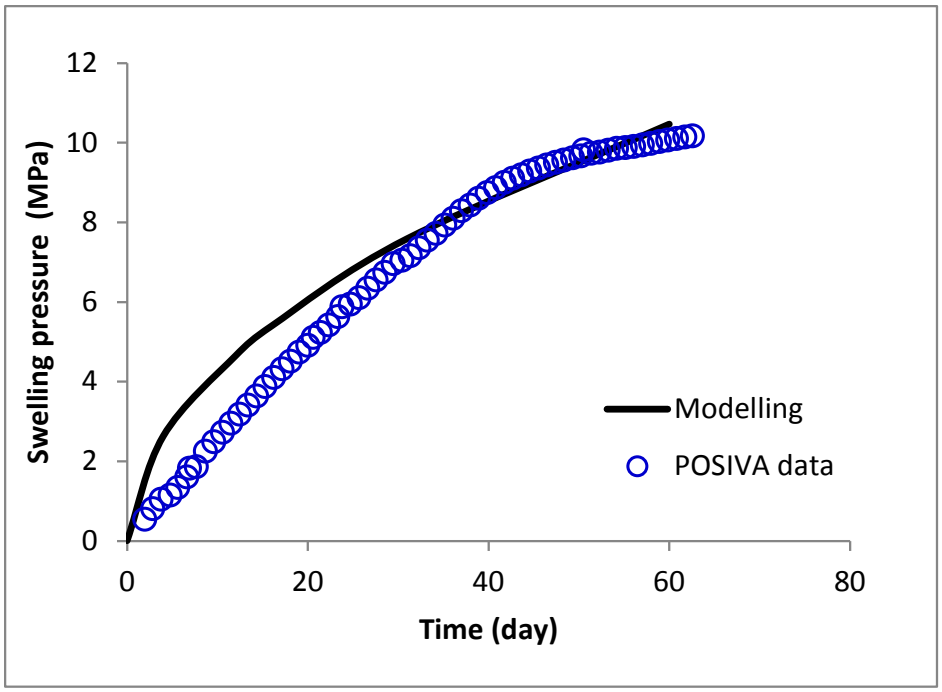

Figure 8.43 The measured and modelled temporal variation of swelling pressure

7. Conclusion

In this study, a HMC coupled model was developed for compacted unsaturated expansive soil. The model is based on a dual-porosity framework, and considers effect of chemical on various hydraulic and mechanical properties. A series of unique relationships has been obtained for MX-80 bentonite. The model was further implemented and calibrated with laboratory experiments from different sources. The pulse of swelling pressure can be well predicted by the model. The calibration with infiltration test suggests very well agreement between the modelling and the experiment. The dataset of model parameters as well as the proposed HMC coupled model can be implemented in the future long-term performance studies of DGRs for nuclear waste.

Despite the success in reproducing laboratory test data by the proposed HMC coupled model, it should be emphasized that the micropore constitutive model has to be calibrated with further in-depth microporosimetric studies under similar HMC coupled effects. Ongoing experimental program in Queens' University has taken into account the chemical effect of micropore evolution. It is thus expected to extend the current modeling capacity for future verification and correlation with upcoming test data.

Appendix

In this appendix, we demonstrate how to derive a smoothened water retention curve for bentonite that is kept under a certain dry density and is confined to a certain dry density during drying-wetting cycles of stress path.

Water retention curve transitions across air entry value

WRC can be expressed in terms of water content versus suction, under free swelling conditions. When confinement is applied, e.g. under constant volume conditions, the WRC turns out to be curved towards the saturated water content. Such a curved behaviour can be expressed by a smooth transition function given as below.

Assume a polynomial function of second order for regions with suction less than AEV. The slope of the polynomial function should be equal to the slope of the WRC under free swelling conditions in the intersection point, besides the equivalence in water content.

Let x be suction, then the free swelling WRC is written as

$$\alpha = \frac{\partial w}{\partial \log x} = x\frac{\partial w}{\partial x}$$

Near the air entry value region (x=A), we get

$$\frac{\partial w}{\partial x} = \frac{\alpha}{A}$$

Define a linear function for variable $\frac{\partial w}{\partial x}$, we have

$$\frac{\partial w}{\partial x} = \frac{\alpha}{A^2}x, \;\; 0 \leq \; x \leq A$$

We have the following expression for WRC below AEV

$$w = \frac{\alpha}{2A^2}x^2 + C$$

where C is a constant.

For bentonite permeated with DI water, we have the following WRC functions,

$$\sqrt{w} = a + b\log x, \quad x > A$$

Then

$$\frac{\partial w}{\partial x} = \frac{2b\sqrt{w}}{x}$$

And

$$\alpha = 2b\sqrt{w}$$

And the water content at air entry value can be determined as

$$w_0 = (a + b\log A)^2$$

Therefore the WRC for the curved portion is given as

$$w = \frac{b\sqrt{w_0}}{2A^2}x^2 + w_{sat},\ \ 0 \leq\ x \leq A$$

Or

$$x = \sqrt{\frac{2(w - w_{sat})}{b\sqrt{w_0}}}A$$

Air entry value

In full saturation of a specimen at certain dry density, the corresponding suction under free swelling condition can be determined as

$$\sqrt{w_{sat}} = a + b\log S_u$$

Or

$$\overline{S_u} = 10^{\left(\frac{\sqrt{w_{sat}} - a}{b}\right)}$$

The AEV must be larger than this value to ensure smooth transition in the curved portion of WRC. Therefore

$$A = N\overline{S_u}$$

where N is in the range of N∈(1,2).

In the meanwhile, the polynomial WRC below AEV has to maintain equivalency at AEV to ensure continuity. This means the following equation

$$w_0 = \frac{b}{2}\sqrt{w_0} + w_{sat} = (a + b\log A)^2, x = A$$

Solving the above equation gives the air entry value as

$$A = 10^{\left(\frac{1}{4}+\frac{\sqrt{w_{sat}+\left(\frac{b}{4}\right)^2}-a}{b}\right)}$$

The WRC of MX-80 can thus be determined to be a smooth curve as shown in the following graph by considering the curved plateau near the air entry value region. For this case the parameter N=1.78.

Simulation case

As shown in Fig. 8.A1, the WRC of MX-80 can be expressed in a very smooth form by spanning both the regions below and above the air entry value. This study case considers a soil sample with dry density of 1.61 and WRC function of MX-80 interacting with DI water. No salinity is discussed in this case. It appears that the above mentioned approach serves the purpose of smoothing the WRC very well.

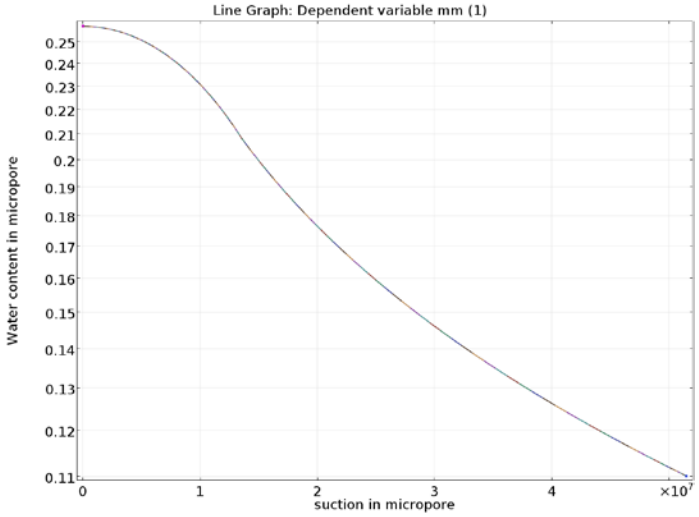

Figure 8.A1 WRC of MX-80 for CSV swelling pressure test at ρ_d=1.61

References

Alonso, E.E., Romero, E., Hoffmann, C. and García-Escudero, E., 2005. Expansive bentonite-sand mixtures in cyclic controlled-suction drying and wetting. Engineering Geology, 81(3): 213-226.

Alonso, E.E., Vaunat, J. and Gens, A., 1999. Modelling the mechanical behaviour of expansive clays. Engineering Geology, 54(1–2): 173-183.

Bharat, T.V. and Sridharan, A., 2015. A critical appraisal of debye length in clay-electrolyte systems. Clays and Clay Minerals, 63(1): 43-50.

Carrier Iii, W.D., 2003. Goodbye, Hazen; hello, Kozeny-Carman. Journal of Geotechnical and Geoenvironmental Engineering, 129(11): 1054-1056.

Di Maio, C., 1996. Exposure of bentonite to salt solution: osmotic and mechanical effects. Géotechnique, 46(4): 695-707.

Do Guimarães, L.N., Gens, A., Sánchez, M. and Olivella, S., 2013. A chemo-mechanical constitutive model accounting for cation exchange in expansive clays, Bio- and Chemo- Mechanical Processes in Geotechnical Engineering - Geotechnique Symposium in Print 2013, pp. 18-31.

Fredlund, D.G., Rahardjo, H. and Fredlund, M.D., 2012. Unsaturated Soil Mechanics in Engineering Practice. Wiley.
Goehring, L., Nakahara, A., Dutta, T., Kitsunezaki, S. and Tarafdar, S., 2015. Desiccation Cracks and their Patterns: Formation and Modelling in Science and Nature. Desiccation Cracks and their Patterns: Formation and Modelling in Science and Nature, 1-349 pp.
Guimarães, L.D.N., Gens, A., Sánchez, M. and Olivella, S., 2013. A chemo-mechanical constitutive model accounting for cation exchange in expansive clays. Geotechnique, 63(3): 221-234.
He, Y., Chen, Y.-G., Ye, W.-M., Chen, B. and Cui, Y.-J., 2016. Influence of salt concentration on volume shrinkage and water retention characteristics of compacted GMZ bentonite. Environmental Earth Sciences, 75(6): 535.
Herbert, H.J., Kasbohm, J., Sprenger, H., Fernández, A.M. and Reichelt, C., 2008. Swelling pressures of MX-80 bentonite in solutions of different ionic strength. Physics and Chemistry of the Earth, 33(SUPPL. 1): S327-S342.
Jussila, P., 2006. Thermomechanics of porous media - I: Thermohydraulic model for compacted bentonite. Transport in Porous Media, 62(1): 81-107.
Kuusela-Lahtinen, A., Sinnathamby, G., Mendez, J., Sołowski, W.T., Gallipoli, D., Pintado, X. and Korkiala-Tanttu, L.K., 2016. Estimation of water retention behaviour of MX-80 bentonite partially saturated with saline solution, E-UNSAT-2016.
Li, Z., Katsumi, T., Inui, T. and Takai, A., 2013. Fabric effect on hydraulic conductivity of kaolin under different chemical and biochemical conditions. Soils and Foundations, 53(5): 680-691.
Li, Z., Xue, Q., Katsumi, T. and Inui, T., 2014. Electric-hydraulic-chemical coupled modeling of solute transport through landfill clay liners. Applied Clay Science, 101: 541-552.
Manca, D., Ferrari, A. and Laloui, L., 2016. Fabric evolution and the related swelling behaviour of a sand/bentonite mixture upon hydro-chemo-mechanical loadings. Geotechnique, 66: 41-57.
Montañez, J.E.C., 2002. Suction and Volume Changes of Compacted Sand-Bentonite Mixtures, Imperial College London.
Murad, M.A. and Moyne, C., 2008. A dual-porosity model for ionic solute transport in expansive clays. Computational Geosciences, 12(1): 47-82.
Musso, G., Romero, E. and della Vecchia, G., 2013. Double-structure effects on the chemo-hydro-mechanical behaviour of a compacted active clay. Geotechnique, 63(3): 206-220.
Musso, G., Romero Morales, E., Gens, A. and Castellanos, E., 2003. The role of structure in the chemically induced deformations of FEBEX bentonite. Applied Clay Science, 23(1-4): 229-237.
Phillips, S.L., Ozbek, H., Igbene, A. and Litton, G., 1980. Viscosity of Nacl and Other Solutions up to 350 °C and 50 Mpa Pressures. LBL-11586, UC-66, University of California, Lawrence Berkeley Laboratory.
Selvadurai, P.A. and Selvadurai, A.P.S., 2014. On the effective permeability of a heterogeneous porous medium: The role of the geometric mean. Philosophical Magazine, 94(20): 2318-2338.
Siddiqua, S., Blatz, J. and Siemens, G., 2011. Evaluation of the impact of pore fluid chemistry on the hydromechanical behaviour of clay-based sealing materials. Canadian Geotechnical Journal, 48(2): 199-213.
Siemens, G. and Blatz, J.A., 2009. Evaluation of the influence of boundary confinement on the behaviour of unsaturated swelling clay soils. Canadian Geotechnical Journal, 46(3): 339-356.
Tang, C.A., Tham, L.G., Lee, P.K.K., Yang, T.H. and Li, L.C., 2002. Coupled analysis of flow, stress and damage (FSD) in rock failure. International Journal of Rock Mechanics and Mining Sciences, 39(4): 477-489.
Imbert, C., Villar, M.V. 2006. Hydro-mechanical response of a bentonite pellets/powder mixture upon infiltration. Applied Clay Science 32: 197–209.

Yustres, A., Jenni, A., Asensio, L., et al. 2017. Comparison of the hydrogeochemical and mechanical behaviours of compacted bentonite using different conceptual approaches. Applied Clay Science. 141: 280–291.
X. Pintado, H.M. Mamunul, J. Martikainen. 2013. Thermo-hydro-mechanical tests of buffer materials. Technical Report: POSIVA 2012-49
R.K. Rowe, R.W.I. Brachman. 2016. Progress report for R613.4: Laboratory determination of sealing material performance. Queen's University.

Chapter 9 An integrative HM coupled model for long-term behaviours of deep geological disposal

Summary

This chapter reports a second round of scoping study on the repository host rock and bentonite seals, by incorporating the recently acquired knowledge from the previous phases of the project. Assumptions were reviewed, parameters were updated, and the scenarios were reassessed. We basically confirm most of the assumptions and parameters adopted in the original model. No major discrepancy in conclusions and findings is noticed in this study compared to the preliminary scoping analyses. The conservative scenario is confirmed to be justifiable. Around a typical emplacement room, the excavation induced damage zone (EDZ) penetrates the Cobourg formation into the underlying Sherman Fall formation. The EDZ appears to be limited within 1-2 diameters into the sidewall of the shaft, preferential in perpendicular to the major principal stress. The tunnel pressure resulting from gases causes perturbation to the regions around the vertical shaft which is more permeable to other rocks. Glacial cycle would not impact the mechanical stability of all formations under consideration.

1. Introduction

The author under contract to Canadian Nuclear Safety Commission (CNSC), has undertaken a second round of numerical simulation work for the hydraulic-mechanical (HM) behaviour of a Deep Geological Repository (DGR) for Low and Intermediate Wastes proposed by Ontario Popwer Genweration (OPG) at the Bruce nuclear site located in Kincardine, Ontario, Canada. The purpose of this repetitive numerical study is to reassess the short-term and long-term performance of the DGR, focusing on the application of the newly acquired knowledge and perspectives regarding the geological formations and constitutive models in the analysis of coupled behaviour of the vertical shafts and waste caverns that are viewed as the potential route for the upward migration of waste gases and pollutants.

This report summarizes the results of the HM coupled modeling study which was initially completed as part of the first research task in the period November 2014 to December 2014, and was later revisited and updated on April 2017. Conceptual models were constructed in accordance with the preliminary design parameters as proposed by OPG. Geoscientific data used in this study were collected from various available technical reports published by the Nuclear Waste management Organization, Geofirma and Quintessa (Itasca, 2011; Intera, 2011; NWMO, 2011; Quintessa, 2011).

This report provides a summary description, assessment and interpretation of numerical simulations carried out in terms of a series of modeling efforts which cover the theoretical background, conceptual

model, model parameters, modeling scenarios, evolution of pore pressure and effective stress after excavation and postclosure, change in the factor of safety, displacement and strain etc. The modeling is completed with the COMSOL (ver 5.3) multiphysics simulation platform.

2. Theoretical framework for HM coupled modeling

2.1 Mathematical model

Following Nguyen (1995), the following reduced form of the hydraulic-mechanical coupled model can be obtained:

$$G\frac{\partial^2 u}{\partial {x_i}^2} + (G+\lambda)\frac{\partial^2 u}{\partial x_i \partial x_j} + \alpha\frac{\partial p}{\partial x_i} + F_i = 0$$

$$\alpha\frac{\partial}{\partial t}\left(\frac{\partial u}{\partial x_i}\right) - C_e\frac{\partial p}{\partial t} + \frac{\partial}{\partial x_i}\left(\frac{k_{ij}}{\mu}\left(\frac{\partial p}{\partial x_j} + \rho_f g_j\right)\right) = 0$$

where the shear modulus G=E/2(1+v); $\lambda = \nu E/(1+\nu)(1-2\nu)$; Biot's coefficient $\alpha = 1 - K_D/K_S$; body force F_i; fluid density ρ_f; parameter $C_e = \frac{n}{K_f} - \frac{n}{K_S} + \frac{\alpha}{K_S}$; k is permeability and μ is viscosity of pore fluid; n is porosity; u is strain and p is pore pressure.

2.2 Implementation of models in COMSOL

With the HM coupled models in consideration, COMSOL provides the option to solve the above partial differential equations. In this study, the Solid Mechanics and Darcy's Flow modules were used to accomplish the coupling purpose.

The COMSOL software solves the following equation of equilibrium of the porous medium

$$-\nabla\sigma = F_V$$

While the equations for Darcy's flow is

$$\mathbf{u} = -\frac{k}{\mu}(\nabla p + \rho g \nabla D)$$

The water mass conservation equation is written as

$$\frac{\partial}{\partial t}(\rho\varepsilon_p) + \nabla(\rho\mathbf{u}) = Q_m$$

Accordingly the body load F_V is actually the coupling term from the pore pressure. As pore pressure represents a countering balance toward the overall total stress, the sign of this variable should be minus in the equation. It can thus be written as

$$F_V = -\alpha \frac{\partial p}{\partial x} - \rho g$$

The mass source for the flow equation reads

$$Q_m = -\rho \alpha \frac{\partial \varepsilon_V}{\partial t} + \rho C_e \frac{\partial p}{\partial t}$$

where ε_V is the volumetric strain.

In COMSOL we can turn to the storage equation to represent the second term in the above equation that addresses the compressibility of both pore fluid and solid particles.

$$C_e = n\chi_f + (1-n)\chi_p$$

where χ_f is compressibility of fluid and χ_p is compressibility of solid particles. This equation equals to the definition of C_e if $\alpha = 1$.

Along with appropriate boundary conditions, the HM coupled excavation problems both in the Cobourg Lower formation and across multilayers along the vertical shaft can be numerically analyzed.

Table 9.1 Geophysical parameters of interested formations for the room and shaft modeling scenarios

Top vertical depth	Formation	Hydraulic Conductivity		Porosity	Mechanical parameters			Rock density			Formation pressure		α**
		kh	kh:kv	%	E	v	σ_{1C} *	wet bulk	dry bulk	grain	Top	Bottom	
m		m/s			GPa		MPa	g/cm^3	g/cm^3	g/cm^3	MPa	MPa	
447.7	Queenston	3.00E-14	10	7.05	15	0.31	48	2.65	2.59	2.76	4.76	3.24	0.34
518	Gorgian Bay	3.00E-14	10	7.1	12	0.23	32	2.65	2.59	2.76	3.24	3.31	0.34
608.9	Blue Moutain	3.00E-14	10	7.35	5	0.1	21	2.65	2.59	2.76	3.31	3.95	0.34
651.6	Collingwood Member	2.00E-14	10	2.1	30	0.27	107	2.69	2.66	2.71	5.54	5.54	0.22
659.5	Cobourg Lower member	1.00E-14	10	1.8	39	0.3	113	2.69	2.66	2.71	5.54	6.36	0.22
688.1	Sherman Fall	9.00E-15	10	1.72	23	0.22	49	2.69	2.66	2.71	6.36	6.11	0.22
716.1	kirkfield	4.00E-15	10	1.95	26	0.2	64	2.69	2.66	2.71	6.11	7.54	0.22
762	Coboconk	2.00E-11	10-1000	0.75	68	0.33	118	2.69	2.66	2.71	7.54	8.71	0.22
785	Gull River	2.00E-12	10-1000	1.95	56	0.27	132	2.69	2.66	2.71	8.71	10.64	0.22
838.6	Shadow Lake	1.00E-09	10	1.95	23	0.33	72	2.6	2.54	2.72	10.64	10.64	0.408
843.8	Cambrian	3.00E-06	1	8.9	23	0.33	72	2.6	2.54	2.72	10.64	10.64	0.408
860.7	Precambrian	1.00E-10	1	3.8	68	0.33	118	2.6	2.54	2.72	10.64	10.64	0.408
Reference	Table 3.1 in DGSM	Table 4.19 in DGSM		Fig. 4.2 in DGSM	Table 3.14 in Geosynthesis			Table 4.1 in DGSM			Fig. 5.2 in Geosynthesis		

Note:

*: The uniaxial compressive strength is obtained from lab test within limited time duration and thus represents the peak strength of intact rock. To account for long-term degradation in host rocks, σ_{1C} needs to be reduced to 65% for the calculation of FS (Note that σ_{1C} is taken as the crack initialization value of 30% of peak strength for the well-investigated Cobourg limestone formation).

**: The Biot's coefficient is determined as a function of porosity, according to detailed discussion in a previous report. It is given as $\alpha = \frac{1.13n}{0.135+n}$.

2.3 Mechanical and hydrological parameters

Table 9.1 lists the complete dataset showing the stratigraphic, mechanical and hydrological information that are required for the numerical simulations. The anisotropy in permeability is not considered in this study. Instead, an isotropic permeability is assumed for the whole analysis domain. The formation pressure that is regarded as the initial state is interpolated with depth and is assigned onto the whole domain. Parameter α is calculated from the relative stiffness, whereas the negative value is taken as 0.0 in the simulation to indicate that the HM coupling could be negligible due to the extremely high value in Young's modulus of the host rock.

Mobilized elastoplastic model for Cobourg limestone

The model is developed within the framework of elasto-plasticity, using the Mohr-Coulomb yield criterion that is formulated to include strain-hardening of the yield parameters. The effective stress increment is given as:

$$\mathrm{d}\boldsymbol{\sigma}' = \mathbf{D}(\mathrm{d}\boldsymbol{\varepsilon} - \mathrm{d}\boldsymbol{\varepsilon}^{\boldsymbol{p}})$$

where $\mathrm{d}\boldsymbol{\sigma}'$ is the increment of the effective stress tensor (written as a vector); $\mathrm{d}\boldsymbol{\varepsilon}$ is the increment of total strain tensor (written as a vector); $\mathrm{d}\boldsymbol{\varepsilon}^{\boldsymbol{p}}$ is the increment of the plastic strain tensor (written as a vector); $\mathrm{d}\boldsymbol{\gamma}$ is the increment of the viscous strain tensor (written as a vector); and **D** is the elastic stiffness tensor (written as a matrix).

The plastic strain component is determined as follows. The Mohr-Coulomb yield criterion can be written using the following form:

$$F = \frac{I_1 sin\phi}{3} + \sqrt{\frac{J_2}{3}}\left((1+sin\phi)cos\theta - (1-sin\phi)cos\left(\theta + \frac{2\pi}{3}\right)\right) - c \cdot cos\phi = 0$$

where I_1 is the first invariant of the stress tensor; J_2 is the second invariant of the deviatoric stress tensor; θ is the Lode angle; c is the cohesion; and □ is the friction angle.

When the yield criterion is reached, plastic strain occurs. The plastic strain is derived from the plastic potential equation. Here, a nonassociative flow rule is used, with the plastic potential taking the form of a Drucker-Prager relation:

$$Q = \sqrt{J_2} + \frac{2}{\sqrt{3}}\frac{sin\phi}{3 - sin\phi} I_1 - \frac{2\sqrt{3}c\ cos\phi}{3 - sin\phi} = 0$$

The above function matches the Mohr-Coulomb yield criterion at compressive meridians.

In this regard, the plastic strain rate is given by:

$$\dot{\boldsymbol{\varepsilon}}^{\boldsymbol{p}} = \lambda \frac{\partial Q}{\partial \boldsymbol{\sigma}}$$

where λ is the consistency parameter.

The effective plastic strain can be defined as:

$$\bar{\varepsilon}_p = \sqrt{\frac{2}{3}(\varepsilon^p)^T \varepsilon^p}$$

Using the effective plastic strain and dilatational volumetric strain as a measure of damage, the Young's moduli are assumed to degrade as follows:

$$E = E_i e^{-30\bar{\varepsilon}_p} e^{-20\varepsilon_{vol}}$$

where E_i is the initial tangent modulus. The two parameters are best-fit from analysis of the experimental results.

The model selects the effective plastic strain as an internal variable; therefore, the cohesion and friction angle can be produced as a function of plastic strain

$$c = c(\bar{\varepsilon}_p)$$

$$\phi = \phi(\bar{\phi}_p)$$

Based on this observation, the fitting of $c(\varepsilon_p)$ and $\varphi(\varepsilon_p)$ will be determined based on the initial yield, interlocking, and residual points. For all specimens used in the triaxial compression test, the change of $c(\varepsilon_p)$ is assumed to follow an exponential law

$$c(\bar{\varepsilon}_p) = c_0 + (c_0 - c_r)\exp(-A_c\bar{\varepsilon}_p)$$

and the change of $\bar{\varepsilon}_p$ is assumed to be a square root function from 0 to the interlocking point and an exponential function after interlocking

$$\phi(\bar{\varepsilon}_p) = \begin{cases} \phi_0 + \phi_i\sqrt{\bar{\varepsilon}_p/\varepsilon_i}, & \varepsilon \le \varepsilon_i \\ \phi_r + (\phi_i - \phi_r)\exp(-A_\phi\bar{\varepsilon}_p), & \varepsilon > \varepsilon_i \end{cases}$$

3. Conceptual model

On the basis of our recent modelling developments for both the host rock, i.e. the Cobourg limestone, and the MX-80 bentonite based engineered barrier system, we are able to simulate the short-term evolution of HMC couplings with the consideration of the following engineering factors:

- Excavation induced damage in the host rock
- HM coupled response of the host rock

3.1 Geometry of the conceptual models for waste cavern and shaft excavation

HM coupling behaviours in the host rock is computed for 20 yrs after quick excavation. The constitutive model for Cobourg limestone follows the one we recently developed, i.e. the anisotropic mobilized-elastoplastic model. The strength parameters are assumed to be time-dependent and take the form of creep failure in the long run.

Figures 9.1a-9.1b shows the geometry of conceptual models for both emplacement room and shaft in the comprehensively investigated formations, i.e. the Cobourg, Weak Sherman Fall and Sherman Fall. A

typical room is considered as a plane strain problem while the shaft is axisymmetric. The size of the room is 7 m high and 4.3 m in half width. The corners are rounded to avoid stress localization. The left boundary at x=0 indicates a symmetric center in width. The right boundary indicates the centerline between two adjacent rooms (distant from each other with an interval of 17.2 m).

For the shaft model, the radius of the excavated shaft is at 6.5 m. The preliminary design of the DGR considers the excavation of two shafts, one for room access and one for ventilation purposes, with a system of access galleries and rooms around the shafts. The main shaft has a finished diameter of 6.5 m in the design of NWMO. A 3-D model is developed to study the extent of the excavation induced damage zone surrounding the vertical shaft. For computational economy, the cubic length extends to 5 times of the shaft radius.

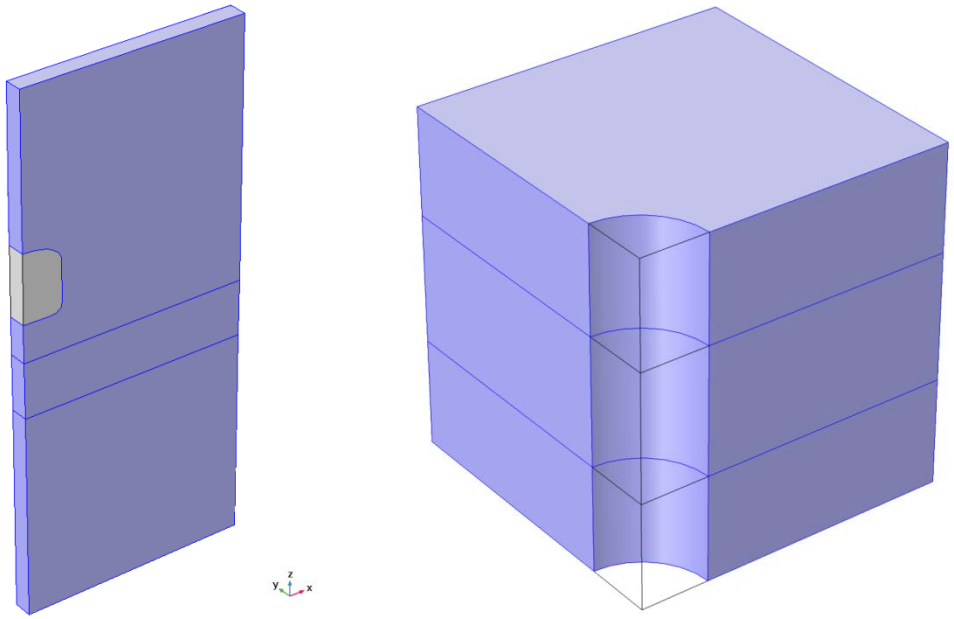

(a) (b)

Figure 9.1 Geometry of the conceptual models for (a) a typical room and (b) the vertical shaft

Figure 9.2 shows the geological stratigraphy of each formation considered in this study. The upper boundary is at the top layer of the Cobourg, while the bottom boundary is fixed into the Sherman Fall layer. The depth as adopted in the simulation is referenced from the ground surface. The repository rooms are located in the lower Cobourg formation.

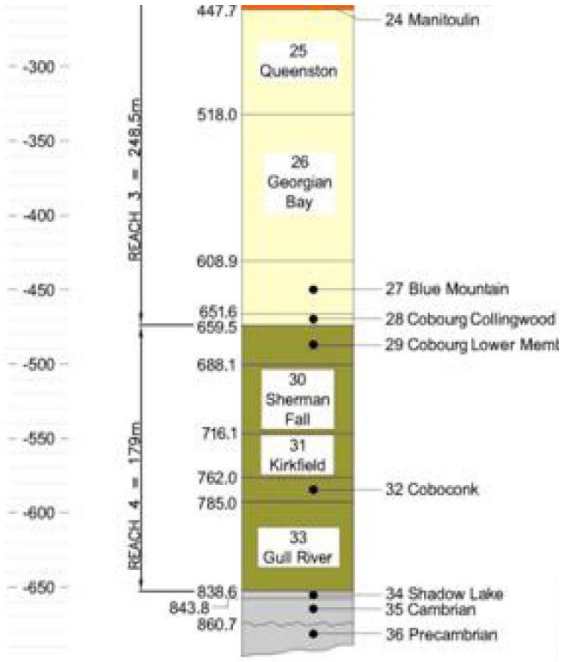

Figure 9.2 The stratigraphic sequence of the geological profile

3.2 Porosity profile

Figure 9.3 shows the distribution of porosity with depth as determined from well loggings. The solid line indicates the average value of test data and is adopted as the input parameter in this study.

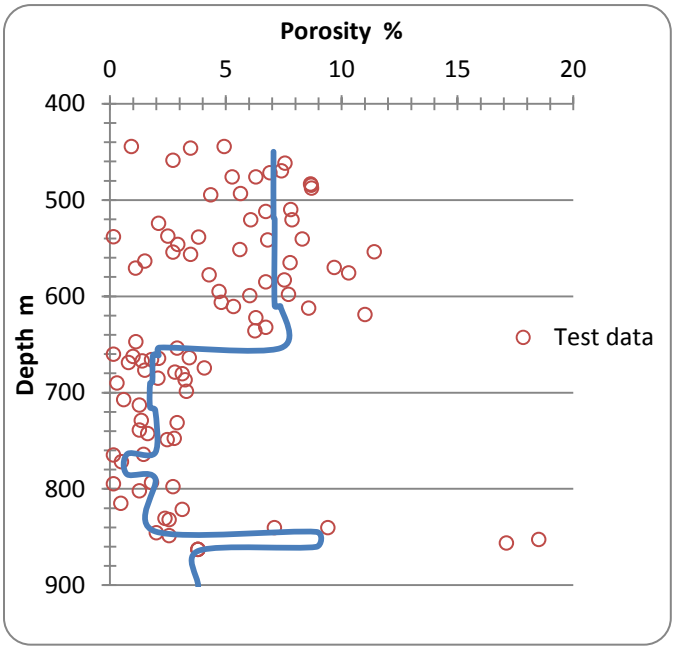

Figure 9.3 Porosity profile vs depth as determined from DGR core

3.3 Boundary conditions

The room excavation model is assumed symmetric across the center of adjacent rooms. Therefore the left and right boundaries are treated as rollers, allowing only vertical displacement. The bottom boundary is fixed, and the top boundary is constrained by vertical stress loading.

The room boundary is prescribed with initial ground stress for the initialization computation. Pore pressure and stress loading at the room boundary are gradually removed to mimic the time-dependent excavation stage.

Subsequent simulation is also carried out after the excavation is finished, in order to evaluate the long-term HM evolution of the surrounding rocks.

Roller boundary is applied to left, top, right and bottom boundaries, except for the excavation front which is treated as a boundary load in terms of the following expression,

$$F_{ij} = \left(\sigma_{ij} + \alpha p \delta_{ij}\right) * \mathrm{exc}(t)$$

where σ_{ij} is the in-situ total stress; α is Biot's coefficient; exc(t) is a stepwise reducing function ranging from 1.0 to 0.0 with increasing time that models the excavation stage.

3.4 Excavation duration

The excavation is supposed to finish within a limited time span. It can be achieved within days to dig through the room front. For this purpose, we may need to consider a conceptualized room model with a certain length, for instance 50 m. Then a somewhat extended period may be reasonable to attain a complete excavation. We consider here an excavation period of 30 days during which the boundary loading upon the surrounding rock is gradually removed in a smoothly declining manner. Figure 9.4 shows the time-dependent excavation function exc(t).

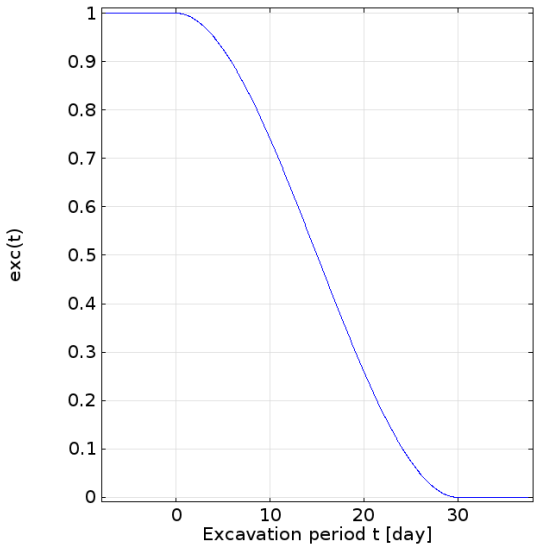

Figure 9.4 Excavation time-dependent function exc(t)

3.5 Initial conditions

Regional data for in-situ stress indicate that horizontal stresses are larger than the vertical stress, with a maximum ratio of 2.0. To be on the conservative side, it is assumed in this study that the initial horizontal stress is twice the vertical static stress. The initial pore pressure is taken from the Geosynthesis report as well as the DGSM report. Underpressure in the target formations is commonly observed. Averaged value in pore pressure is adopted in this study. The depth profile of pressure is shown as following.

The horizontal stress reads:

$$\sigma_x = 2\rho g h$$

And the vertical stress is written as:

$$\sigma_z = \rho g h$$

The pore pressure distribution follows the observed pattern of the field data. Underpressure in a number of formation layers, in particular in the host and overlying cap rocks, is considered. Overpressure is present in deeper regions such as the Gull River, Cambrian and Precambrian formations. The pore pressure and environmental head distribution with depth are shown in the following graphs (Figure 9.5).

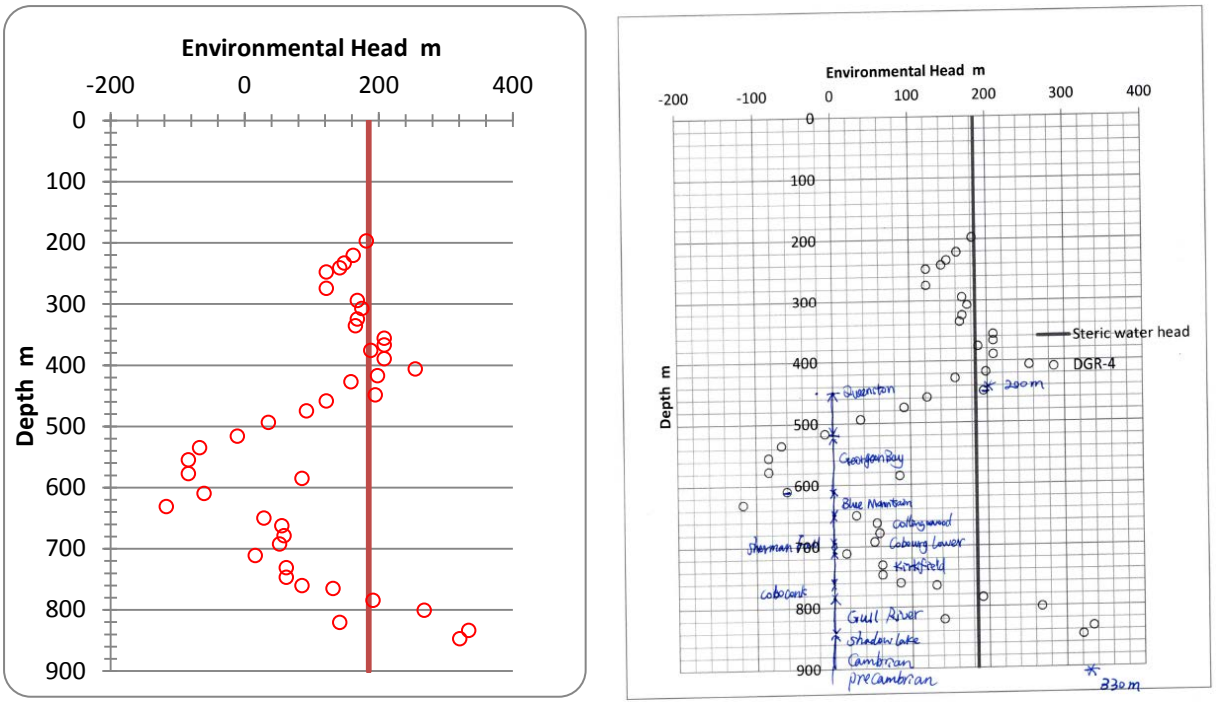

Figure 9.5 Stratigraphy vs formation pore pressure expressed in environmental head (m) (solid vertical line is hydrostatic pressure head)

4. Results and discussion

Summary of findings

- Mechanical response of the host rock is not significantly dependent on time effect in short term, because of the very weak hydraulic-mechanical coupling indicated by very low Biot's coefficient (0.05).
- The mobilized elastoplastic model predicts that the excavation induced damage to host rock mainly happens to the ceiling and floor of the room, and the damage extends through the Cobourg formation downward into the underlying Sherman Fall layer. This result is consistent with the design expectation that the waste cavern will collapse and eventually fill up to about double size of the excavated space.
- Excavation induced unloading causes volumetric expansion of the Cobourg limestone covering most of the inter-room rock pillars, and displacement of host rock towards the open space.
- Displacement mainly happens to the vertical plane aligned along the maximum principal stress (X-axis in this case).
- The underlying weak formation of Weak Sherman Fall may be severely disturbed by excavation as the EDZ is found to be very intense compared to the rest formations.

EDZ after excavation

Figure 9.6 shows the distribution of EDZ after the cavern or shaft is excavated and left open for 20 years. It is clearly shown that the damage develops in a direction perpendicular to the maximum principal stress (σ_x). For the waste cavern, the ceiling and floor are both moderately damaged. The size of the EDZ approximate the size of the cross sectional area of the cavern. The side wall appears to be damaged at toe and shoulder corners, but remains intact on the side. For the vertical shaft, damage is more severe in the underlying formations, i.e. the Weak Sherman Fall and Sherman Fall layers. The EDZ extends to as much as 5.8 m in Y-direction.

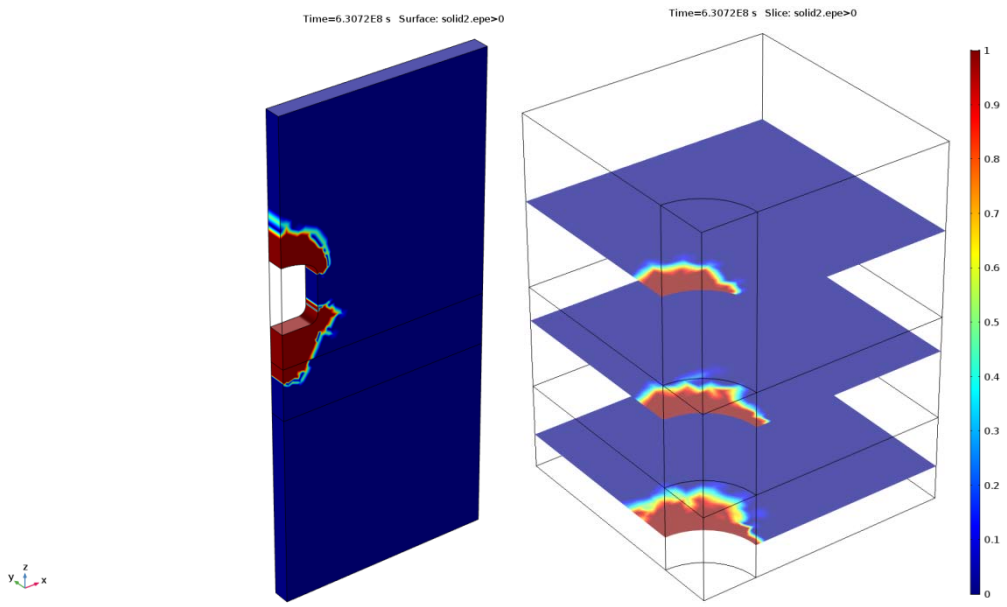

Figure 9.6 Contour plots of the EDZ after 20 yrs of excavation

Pore pressure evolution

Figure 9.7 shows the distribution of pore pressure after excavated for 20 years. Despite the consideration of damage-induced permeability enhancement, the pore pressure fluctuation (both reduction and increase) is restrained within a limited region, and is much less in size than the predicted EDZ. Fluctuation in pore pressure is closely related to the overall volumetric strain. Therefore an increase in pore pressure suggests a contractive volumetric strain, which is found to locate above the cavern ceiling and around the shaft side wall in all three formations. At the same time, the extra pore water head shows a ring-shape, and always circumvents the underpressurized zones. This phenomenon may be explained as a result of arch effect in the comparatively intact host rock that supports the extra loadings that are unloaded by excavation.

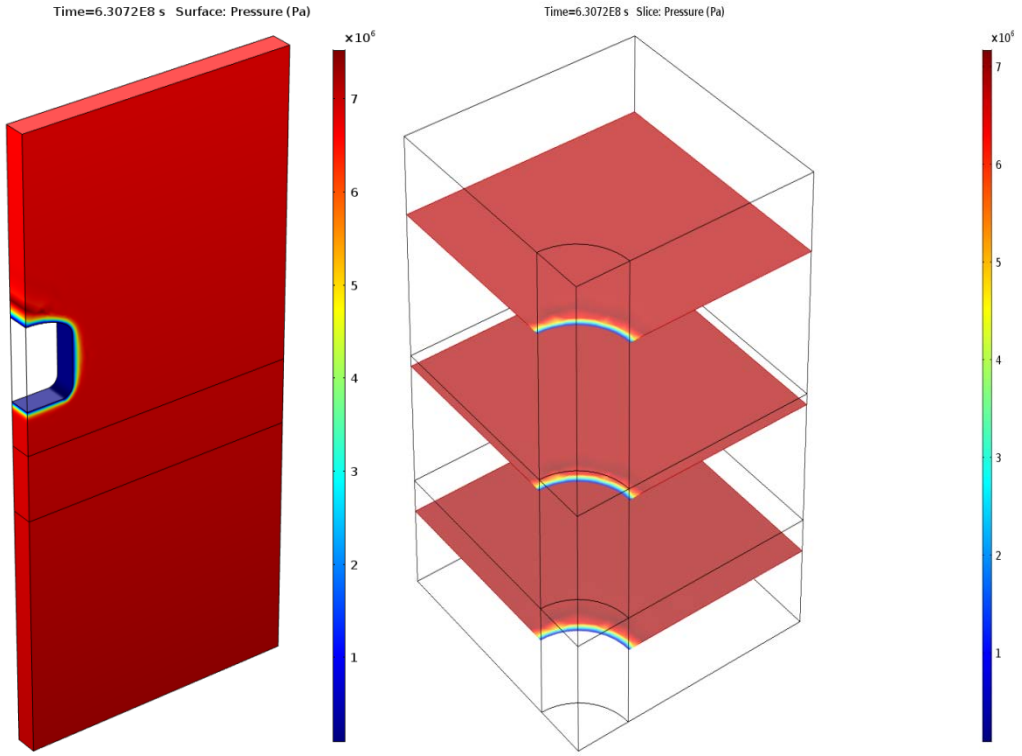

Figure 9.7 Contour plots of the pore pressure after 20 years of excavation

Total displacement

Figure 9.8 shows the contour plotting of total displacement. In case of cavern, maximum displacement is found on the surface of side wall. As for the vertical shaft, the trend is different in separate formations. For Cobourg formation, the displacement in X-direction is larger than in Y-direction, which is consistent with the cavern case. But for the underlying Sherman Fall, the displacement, which is found to be generally more than the Cobourg, is larger in Y-direction than that in X-direction. This may be due to the different constitutive relations as implemented in the numerical model. Since the underlying Sherman Fall composed of interbedded limestone and shale is comparatively softer than the Cobourg argillite limestone, its displacement and volume strain is expected to be larger than the latter. Displacement arrow diagrams are shown in Figure 9.9. The opening is found to distort the orientation of the displacement, which is generally found to align with the major principal stress orientation.

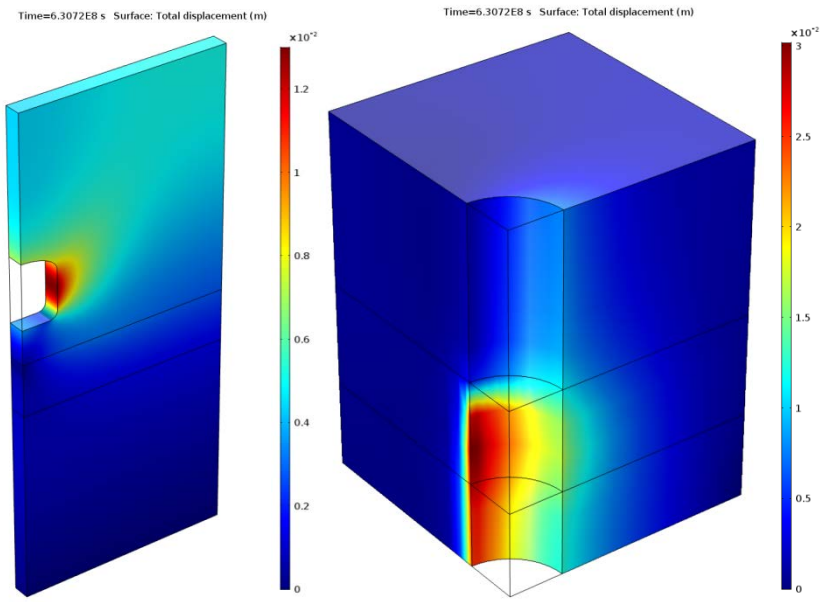

Figure 9.8 Displacement contour after 20 years of excavation

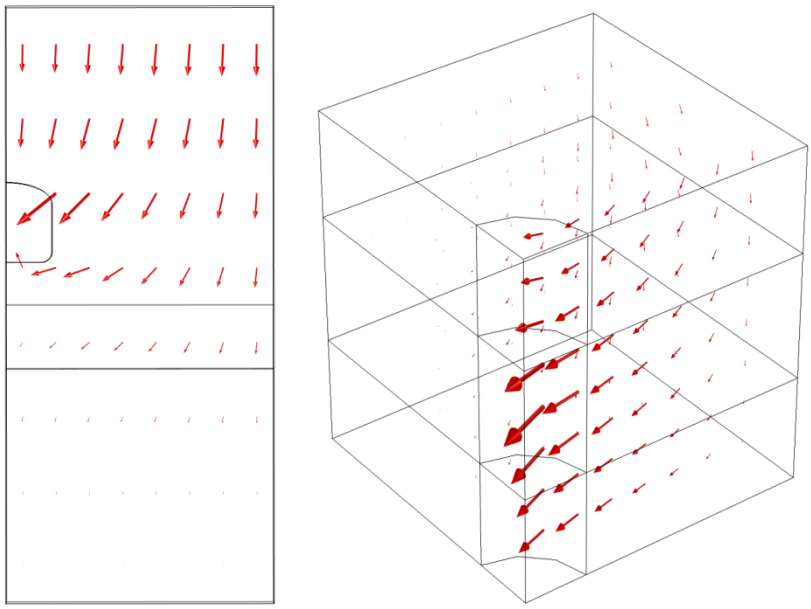

Figure 9.9 Displacement arrow diagrams after 20 years of excavation

Volumetric strain

Compressive deformation occurs to the ceiling, shoulder and toe corners of the cavern, while dilation happens to the side wall. With regard to the vertical shaft, dilation deformation in Sherman Fall prevails over the one in the Cobourg. Expansive volumetric strain is found to form a hedge shape in the Cobourg for the cavern case. In the case of shaft, expansion occurs in all formations, most of the underlying Sherman Fall and majority of Cobourg except for the shaded zone in Y-direction at an approximately equivalent thickness of the shaft radius. It is shown in this example that the construction of vertical shaft

seems to introduce much stronger disturbance to the host rock. In particular the Weak Sherman Fall may expand in volume to a larger extent than the adjacent layers, causing inter-formation interactions that may affect the stability of the target repository formation. The shaft is designed to be drilled into a deeper host rock than the repository formation. Whether or not we really need to disturb the weak formation remains to be an open question in the writer's viewpoint. Further detailed study on the interaction between weak formation and intact formation may help to clarify concerns and justify engineering designs.

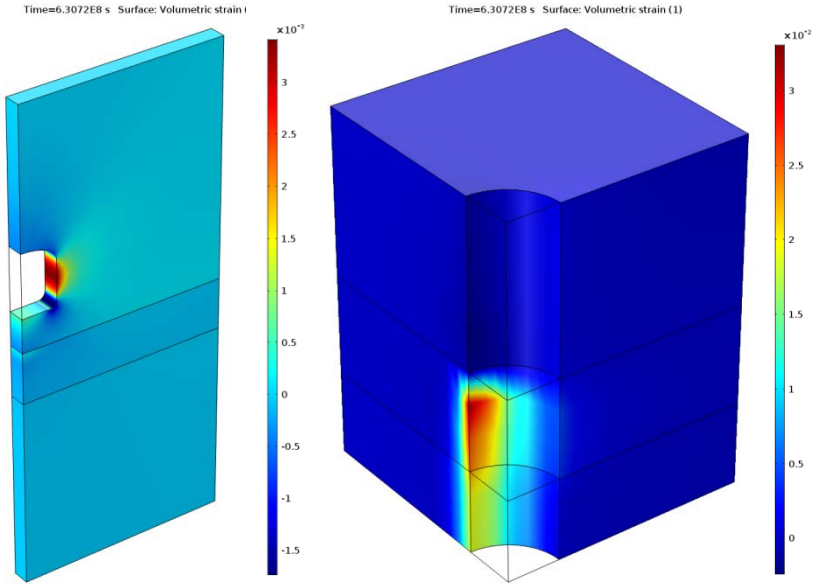

Figure 9.10 Volumetric strain contour after 20 years of excavation

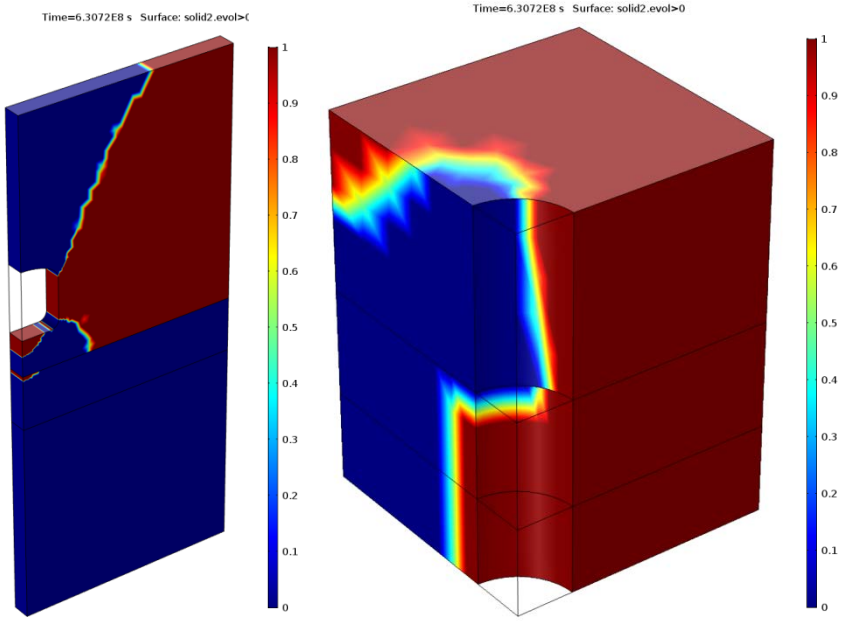

Figure 9.11 Volumetric strain in expansion mode after 20 years of excavation

5. Large scale long-term evolution scenarios

5.1 Large scale repository model

In this simulation case, the shallow geological formations are included in the FEM analysis zones. Figure 9.12 shows the plan view of the designed repository rooms, monolith, and the vertical shafts. The repository is located in Cobourg formation at 680 m underneath the ground surface. There are two panels of emplacement rooms, 8.6m wide and 7 m high, with total volume at 420,000 m^3. The emplacement rooms are separated by 17.2 m wide pillars to support roof loading. There are two shafts, one is the main shaft (r=6.5 m) and the other acts as ventilation (r=5.0 m). Access tunnels with various lengths are also included in the design.

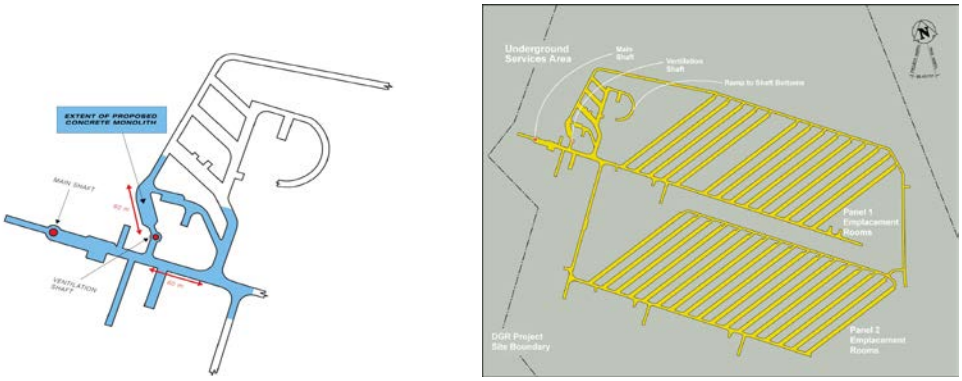

Figure 9.12 The design sketch for the extent of the proposed monolith (left) and base case layout showing the access tunnel length measured at 250 m from the main shaft (OPG letter, 2012)

5.1.1 Conceptual model

Figure 9.13 shows the conceptual model for the field conditions. The vertical shafts are simplified into a single shaft with equivalent radius at 5.9 m, and acts as the axis of the axisymmetric model. The access tunnel is omitted here to conceptualize the most important feature of the repository. The length and volume of the repository are calculated to reflect the total equivalence of the designed volume. The damage zone around the repository rooms is shown to be approximately 2 times the room height in the previous simulation case. For the long term analysis, we assume that the damaged zone would fall into the rooms in the form of rock debris that would swell and fill the rooms. The total volume of the enlarged rooms filled with debris is then assumed to be two times of the volume of the original rooms.

The initial conditions include both the mechanical and hydrogeological conditions. The initial pore pressure of the rock mass follows the distribution shown in Figure 9.5 and 14. As for the shaft and repository, the initial pore pressure is assumed to be at atmospheric pressure. In order to avoid the potential difficulty in numerical computations for the weak sediments near the ground surface, the upper boundary of our analysis domain is confined at z=100 m depth.

The above modeling of the EDZ in shaft suggests a maximum of damaged radius of 5.8 m in Weak Sherman Fall. An even smaller EDZ is obtained for Cobourg formation in the model. Therefore the previous assumption of shaft radius at 5.9 m was maintained without any change as a conservative scenario in this study.

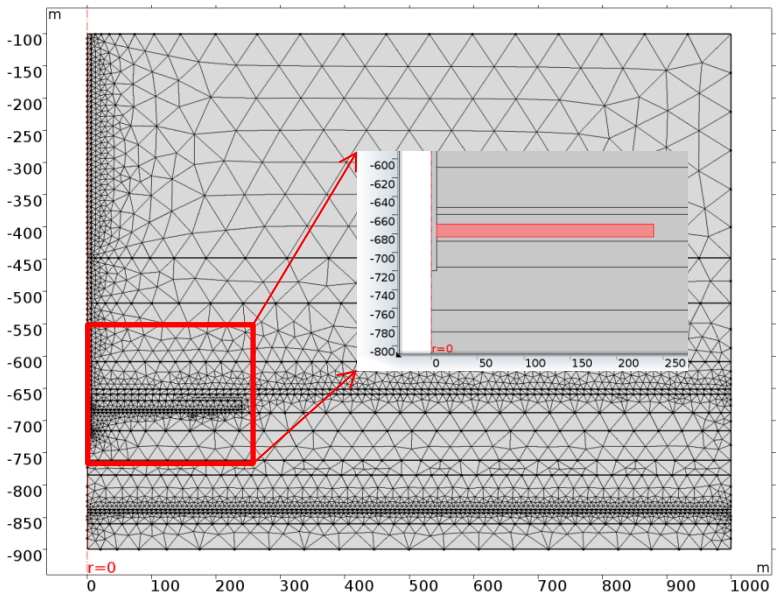

Figure 9.13 Conceptual model and meshing of the large scale HM analysis

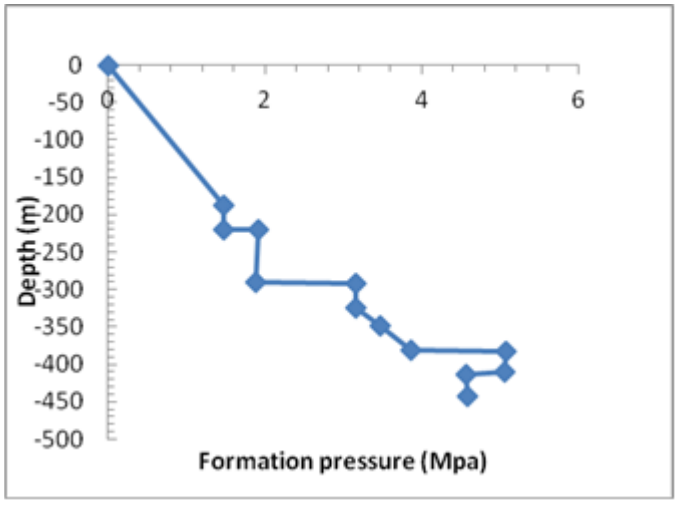

Figure 9.14 Formation pressure in shallow sedimentary rocks

5.1.2 Properties of the shallow formations

Shallow formations above the Queenston formation include several aquifers and interlayered stiff and soft rocks. The fundamental properties of these rock masses are obtained from the DGSM report and shown in Table 9.2. The porosity and permeability profiles are plotted in Figure 9.15.

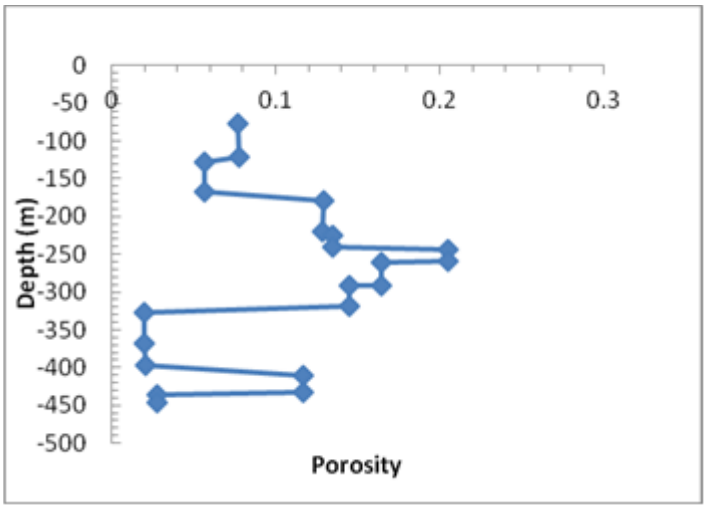

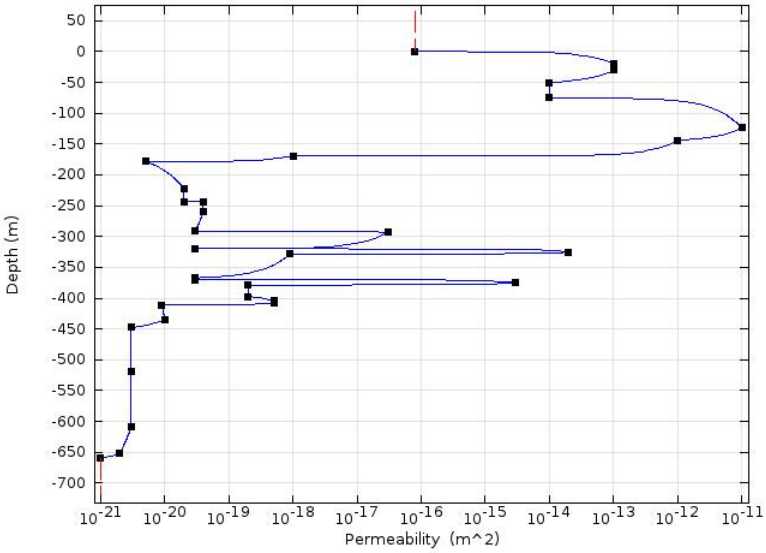

Figure 9.15 Porosity profile (upper) and permeability profile (bottom) with depth for shallow sedimentary rocks

Table 9.2 Properties of shallow formations above the Queenston formation

Top depth (m)	Formation	E	v	σ_1	C_e
		Gpa		Mpa	
20	Lucas	-	-	-	-
30.4	Amherstburg	43	0.21	98	2.80E-12
75	Bois Blanc	37	0.18	94	5.20E-12
124	Bass Islands	19	0.23	43	1.24E-11
178.6	Salina F	12	0.21	31	1.52E-11
244.6	Slina C	9	0.17	20	1.64E-11

260.3	Slina B	3	0.4	8	1.88E-11
293.1	Salina A2	19	0.11	48	1.24E-11
325.5	Salina A1	41	0.23	143.1	3.60E-12
370.5	Salina A0	63	0.43	197.6	0
374.5	Guelph	28	0.32	60	8.80E-12
378.6	Goat Island	37	0.37	148	5.20E-12
411	Cabot Head	4	0.38	13	1.84E-11
434.8	Manitoulin	23	0.24	66	1.08E-11
-	Shaft seals	Varies with depth	0.34	10	1.00E-6
Reference	Table 3.1 in DGSM	Table 3.14 in Geosynthesis			

5.1.3 Equivalent repository material

The repository rooms are spaced from each other and separated with pillars. In this 2D-axisymmetric model, the repository is treated as an equivalent homogeneous domain with equivalent properties. For example, the equivalent elastic modulus is calculated by force balance equation that considers the relative cross section area of the rooms and pillars,

$$E_{eq} = \frac{2}{3} E_0$$

$$\sigma_{1C\_eq} = \frac{2}{3} \sigma_{1C}$$

The permeability of the repository is assumed to be very high, with a value of 1.7E-10 m^2.

5.1.4 Properties of the shaft seals

The shaft seals are conceptually designed to consist of asphalt, cement plugs and 30/70 sand/bentonite mixture. Our emphasis in this study is mainly about the S/B mixture compacted to the target dry density of 1.75.

Elasticity of porous medium depends on porosity, confining pressure and volumetric compressivity. The constrained elastic modulus (E_k) of solid skeleton of a porous medium is reported to have the following relationship with compression coefficient C_c (Jorgensen, 1980):

$$E_k = \frac{(1 + e_0)\sigma_c}{0.434 C_c}$$

where e_0 is the initial pore ratio and σ_c is the confining pressure.

Blatz et al. (2003) reported the modulus of a different sand-bentonite mixture at 50/50 ratio as 0.14 (wetter) and 0.09 (drier) with dry density at 1.7 g/cm3 and saturation of about 85% (the matric suction ranges from 3.7-4.5 MPa). Using the above shown equation for elastic modulus, E_k can be obtained for the results of Rueedi (2013) and Blatz (2003) respectively as 9.3 MPa and 102 MPa. Putting the estimated E_k for Blatz (2003) in the following graph gives a good agreement with the experimental results of Tang (1999).

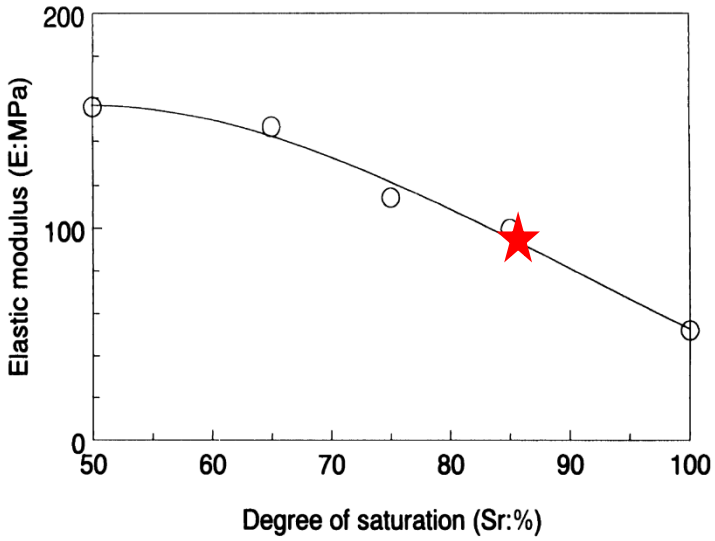

Figure 9.16 Elastic modulus vs saturation as reported by Tang (1999) (ρ_d=1.75 g/cm^3, Sr=85%, mass ratio at 50/50. Star shows the estimated Ek based on the result of Blatz (2003).)

As a convenient treatment, the elastic modulus of buffer material is hypothesised to vary linearly with depth with a scaling parameter *R*:

$$E = (1 + Rz)E_0$$

where E_0 is the laboratory result of sand-bentonite mixture on elasticity (100 MPa), z is depth (m). In this study it is taken as R=0.0125. At 700 m depth the elasticity of the buffer material is assumed to be 0.975 GPa, which is still much softer than the surrounding rock (E>5 GPa).

5.1.5 Glacial stress loading

During the last million years, it is estimated that the Northern Hemisphere was subjected to 9 glacial cycles, each one lasting approximately 120,000 years. It is estimated that in another 60,000 years another glacial cycle similar to past ones will occur. Figure 9.17 shows the calculated vertical stress resulting from the glacial impact that is used for the “dry case” where at the base of the glacier, free draining conditions are assumed, and the water is assumed to be at atmospheric pressure. In the wet case situation, the phreatic table is assumed to be at the top surface of the glacier. The dry case is studied and discussed in detail in the following sections. The wet case, although likely to happen in certain circumstances, is not included in the current study.

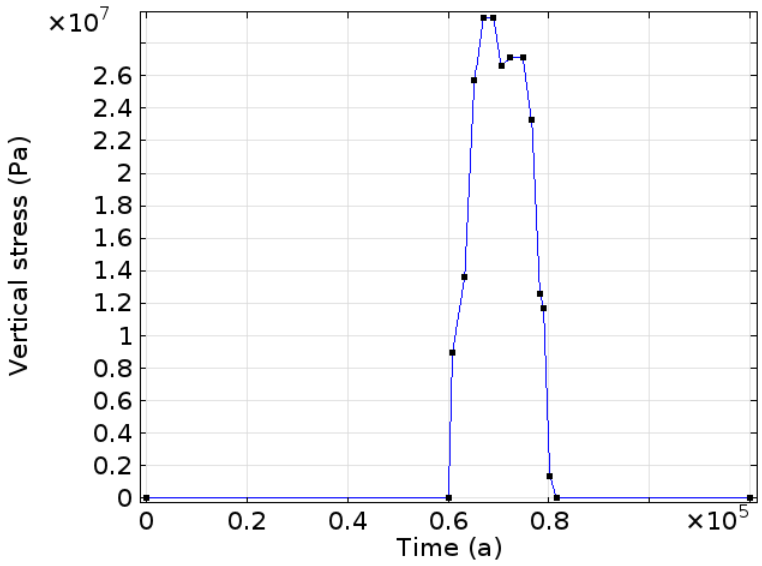

Figure 9.17 Simulated evolution of ice sheet load during single glacial event as assumed in the longterm scoping analysis

5.1.6 Gas pressure in the rooms

The repository rooms would become gradually filled with gases produced by corrosion and biological degradation of the waste. Figure 9.18 shows the evolution of room gas pressure with increasing elapsed time in the postclosure period up to 1Ma. These data are from the gas modeling results of NWMO report (AECOM, 2011) and were further adopted in the long-term geomechanical stability analysis of DGR as conducted by Itasca Consulting Group Inc. It contains both an extreme scenario and a base scenario that represent different probability of potential risk posed on the room safety. This study considers both cases in the numerical simulation, however, in this report only the results corresponding to the extreme scenario are shown in the following section.

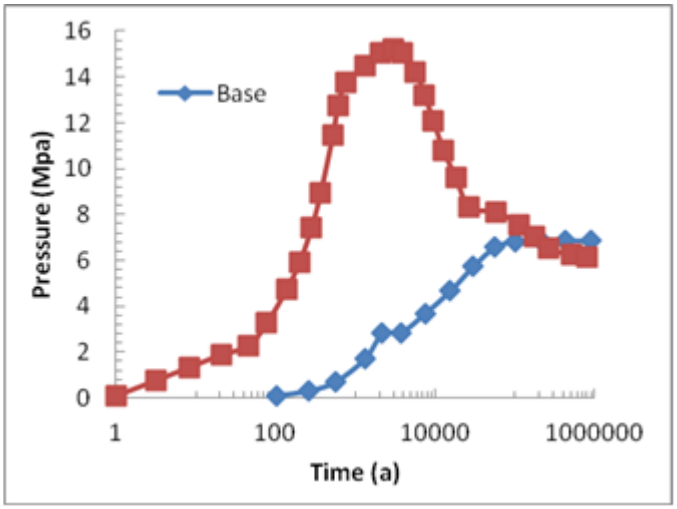

Figure 9.18 Pressure inside the room vs postclosure time

5.1.7 Monitoring points and cut lines for data postprocessing

Figure 9.19 shows the selected points for results visualization and analysis. They are all located in regions of interest for the stability and pore pressure change when exposed to glacial stress loading. Figure 9.20 shows the sampling time for contour plotting of key variables like *p*, mean stress and factor of safety.

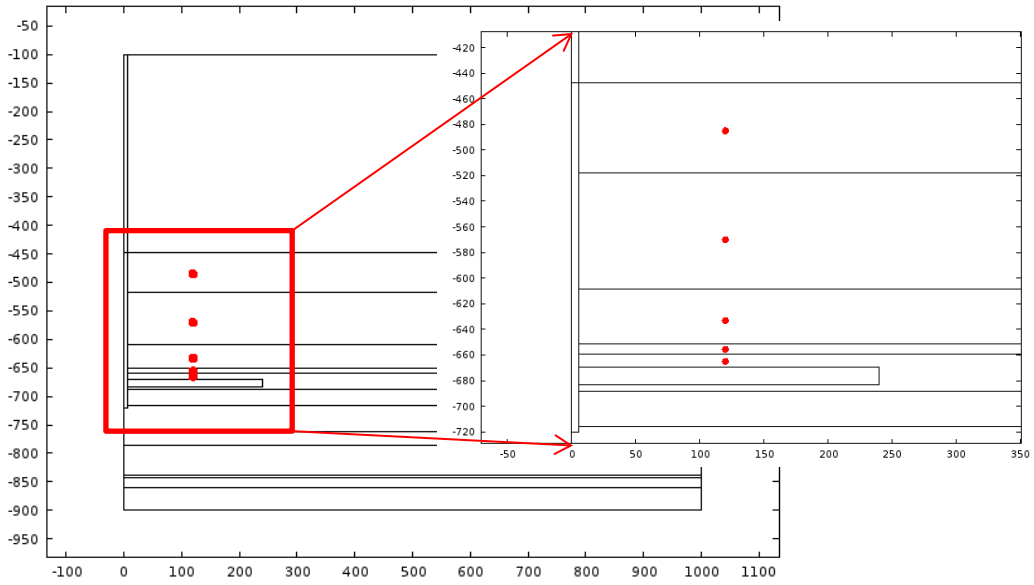

Figure 9.19 Monitoring points (P1-P5) along the vertical center line above the tunnel

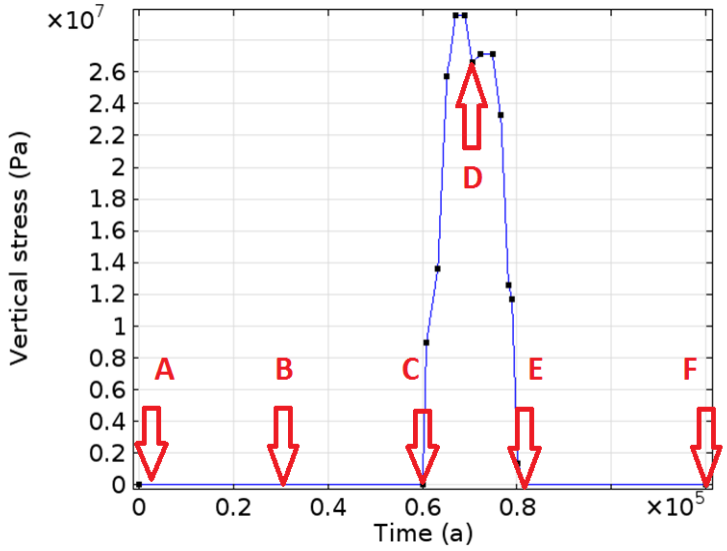

Figure 9.20 Sampling time for the plotting of contours

5.1.8 Factor of safety

The classic Hoek-Brown failure criterion is used for the calculation of the safety factor. The Hoek-Brown criterion is written as

$$\sigma'_{1f} = \sigma'_3 + \sigma_{1C}(m_b \frac{\sigma'_3}{\sigma_{1C}} + S)^a$$

where σ'_{1f} is the major effective principal stress at failure; σ'_3 is the minor effective principal stress; σ_{1C} is the uniaxial compressive strength (UCS) of the intact rock material; m_b is a reduced value (for the rock mass) of the material constant for the intact rock; S and a are constants which depend upon the characteristics of the rock mass.

Then the factor of safety is defined as:

$$\mathrm{FS} = \frac{\sigma'_{1f}}{\sigma'_1}$$

where σ'_1 is the actual major principal stress.

It is noteworthy that the strength of intact rock needs to be reduced to a certain percentage in order to be representative of the rock-mass mechanical behavior that associates with the scale effect and the effect of rock mass jointing (Long term Geomechanical Stability Analysis Report, 2011, P 13). According to the Itasca Consulting Group's parametric input, the Hoek-Brown strength criterion for the Sherman Fall limestone includes the following three values,

mb=3.438, S=0.0205, a=0.502.

And the shale formations, e.g. Blue Mountain formation etc., have the following Hoek-Brown criterion:

mb=2.740, S=0.0357, a=0.501.

These parameters were obtained by using GSI=75, mi=8 and damage factor D=0 as a starting point to develop properties for mechanical analysis. The choice of the above set of parameters has been detailed in the Long-term Geomechanical Stability Analysis report (Page 26, NWMO DGR-TR-2011-17).

Furthermore, the value of σ'_{1C} obtained from laboratory uniaxial compressive stress are reduced to 65%, in order to account for long term strength degradation for most of the host rock formations except for the Cobourg limestone, for which the CI value of 30 % is adopted.

It may not be justifiable to apply the above set of parameters on the whole domains, however, this can be regarded as a conservative case study especially in view of the comparative strengths of various types of rock mass. Rocscience has compiled a collection of Hoek-Brown strength criteria for different rocks. According to literature (Rocscience), a massive weak rock has the following model constants: m_b=6.675, s=0.062, a=0.501. It is also noted that shale typically has a constant m_b=6$\pm$2. Therefore, the choice of the model constants for Hoek-Brown criterion can be representative of the needed conservative scenario.

Rocscience. Rock mass properties. See link at:
http://www.rocscience.com/hoek/corner/11_Rock_mass_properties.pdf

5.1.9 Key Simulation Parameters

Table 9.3 shows the simulation case—dry-extreme—undertaken in the long term HM assessment. Critical parameters e.g. shaft permeability and upper boundary loading types are also given in this table. Since the permeability of the shaft material may significantly influence the pore pressure evolution in the shaft and surrounding regions, a conservatively high permeability is used to investigate the long-term impact. The design permeability of the engineered barrier material in the shaft is 10^{-18} m^2. The permeability of S/B mixture is affected by brine saturation, as widely observed in HMC coupled studies.

Our data showed that this may cause 100 times of increase in hydraulic conductivity from 10^{-14} to 10^{-12} m/s. This is consistent with the design criterion of less than 10^{-19} m^2 in permeability. For the dry case, we assumed that the permeability increases by a factor of 10. This treatment in simulation is in agreement with the previous report. Therefore no change was made with respect to the shaft seal properties.

Compared to the original model, this study updates the Biot's coefficient of various formations according to the regressed relationship with porosity.

Table 9.3 Simulation cases and the key parameters used in the analysis

Case type	Dry
Room pressure type	Extreme
Room permeability (m^2)	1.7E-10
Shaft permeability (m^2)	1.2E-18
Upper boundary loading	Stress

5.2 Results and discussion

The calculated FS indicates that the whole domain is mechanically stable throughout the 120,000 years of simulation period. The mechanical stress seems to be responsive to both tunnel pressure and overburden loading. The tunnel pressure reaches peak within 10,000 years, causing perturbations to the regions around the vertical shaft which is more permeable than other rocks. The distribution of pore pressure changes in pattern with elapsed time. The shaft acts as a permeable interlayer connection that facilitates the flow of pore water in regions near the shaft between 400 to 650 m in depth. Glacial loading induces extra pore pressure uprising especially for the thick layers between 40 and 750 m in depth. This perturbation rapidly disappears once the vertical glacial loading is removed.

Factor of safety

At Z=630 m, FS turns to be near 1.0 for most of the postclosure period. This domain represents the Blue Mountain formation, which is a weak shale layer and has been found to be damaged due to excavation in the shaft simulation case. This stage of damage corresponds to the peak in tunnel pressure as shown in Figure 9.22. Therefore the damage is thought to be caused by the overpressure of the gases generated in the repository tunnel. Other parameters appear to be normal with respect to the overburden glacial stress. For the whole analysis domain, FS turns to be increased by the glacial loading. This phenomenon will be discussed in detail by the stress patch approach in the following section.

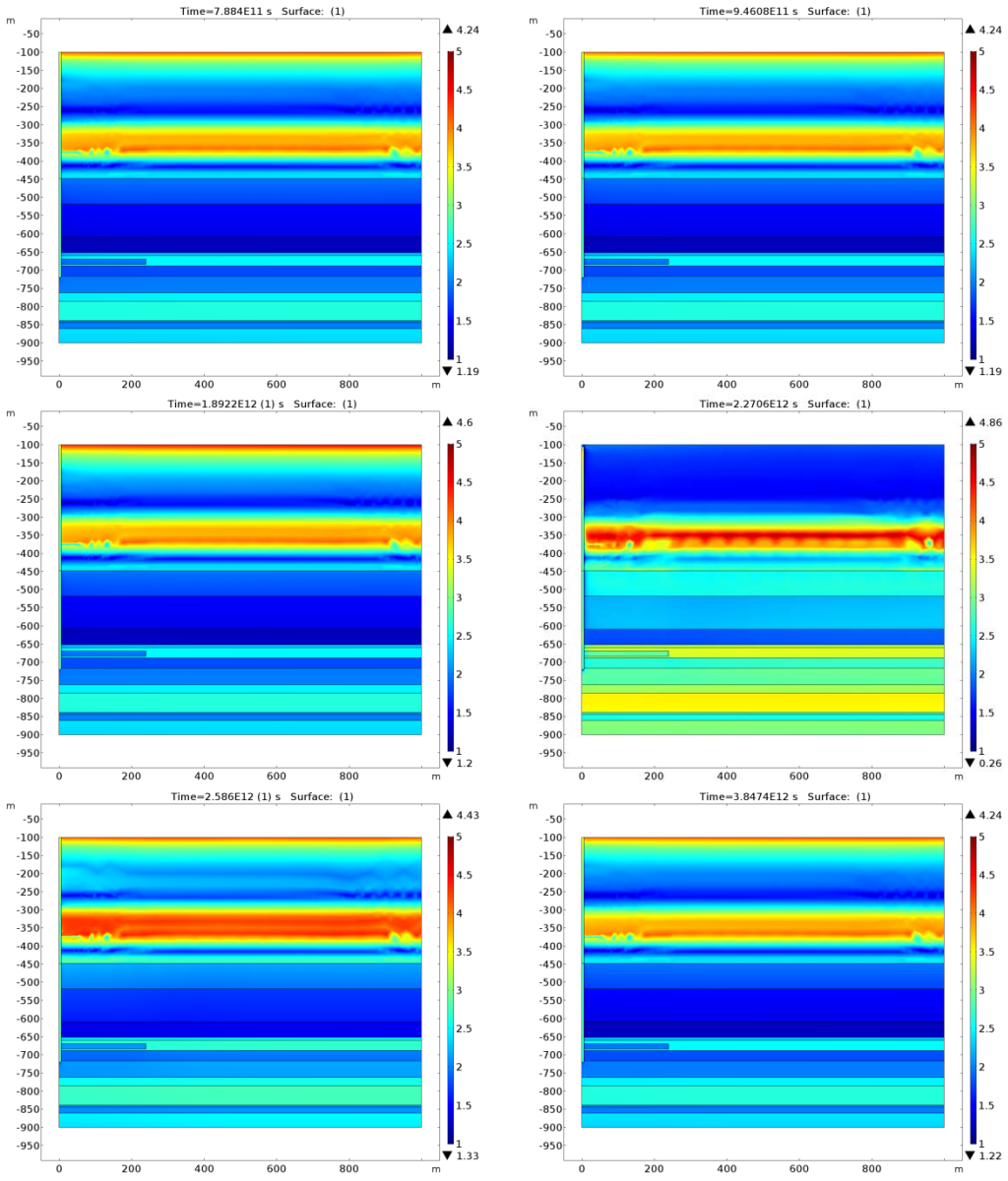

Figure 9.21 Spatial distribution of the factor of safety at different postclosure time corresponding to sampling points A-F

Pore pressure

The pore pressure evolution is shown in Figure 9.22. The tunnel pressure follows the assigned boundary condition. In Figure 9.22b-22c, regions near the vertical shaft in Queenston and Gorgian Bay seem to have smaller pore pressure than the normal level of the formation pressure. This phenomenon results from the higher permeability of the shaft that contributes to the pore pressure dissipation in these two formations with limited influence from the repository tunnel. Corresponding to the peak of glacial loading in Figure 9.22d, the pore pressure increases within formations between Queenston and Sherman Fall with a maximum pressure of 26 MPa. It is indicated that almost all the extra loading from

the glacier is reflected and transmitted to the formations ranging from -600 to -700 m underneath the ground level. At this moment, the cavern and shaft are conductive to hydraulic flow and potential release of contaminants from the repository. At the end of glacial loading, the pressure in this region sharply decreases to levels lower than the ones prior to glacial loading (Figure 9.22e) due to the HM coupling effect, and gradually regains the equilibrium state (Figure 9.22f).

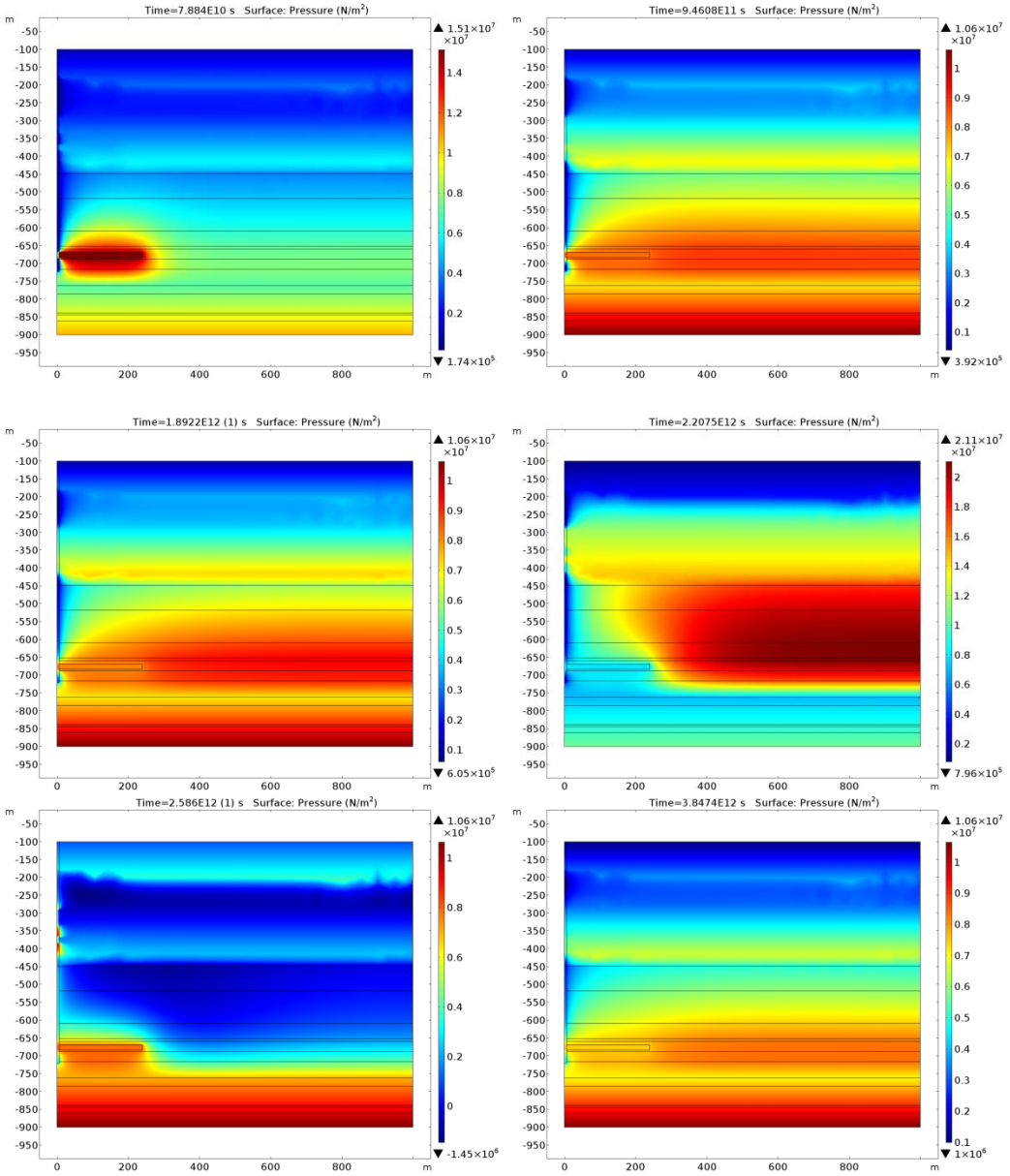

Figure 9.22 Spatial distribution of the pore pressure at different postclosure time corresponding to sampling points A-F

Monitoring results on cut points P1-P5

Figure 9.23 shows the time-dependent results of FS, pore pressure and principal stresses on interested monitoring points P1-P5. It is clearly demonstrated that the FS increases by 60-70 % during the glacial loading period, during which time the pore pressure also increases. For the peak of pore pressure as observed before t=10 ka, it is believed to be the result of gas pressure accumulation inside the repository tunnel. The principal stresses show more vertical stress increase compared to the horizontal stress variation as caused by the overlying glacial loading. In the post-glaciation stage, the major principal stress at different depths all temporarily drop to a level lower than the equilibrium state, suggesting a compensation and temporal delay in dissipation of pore pressure.

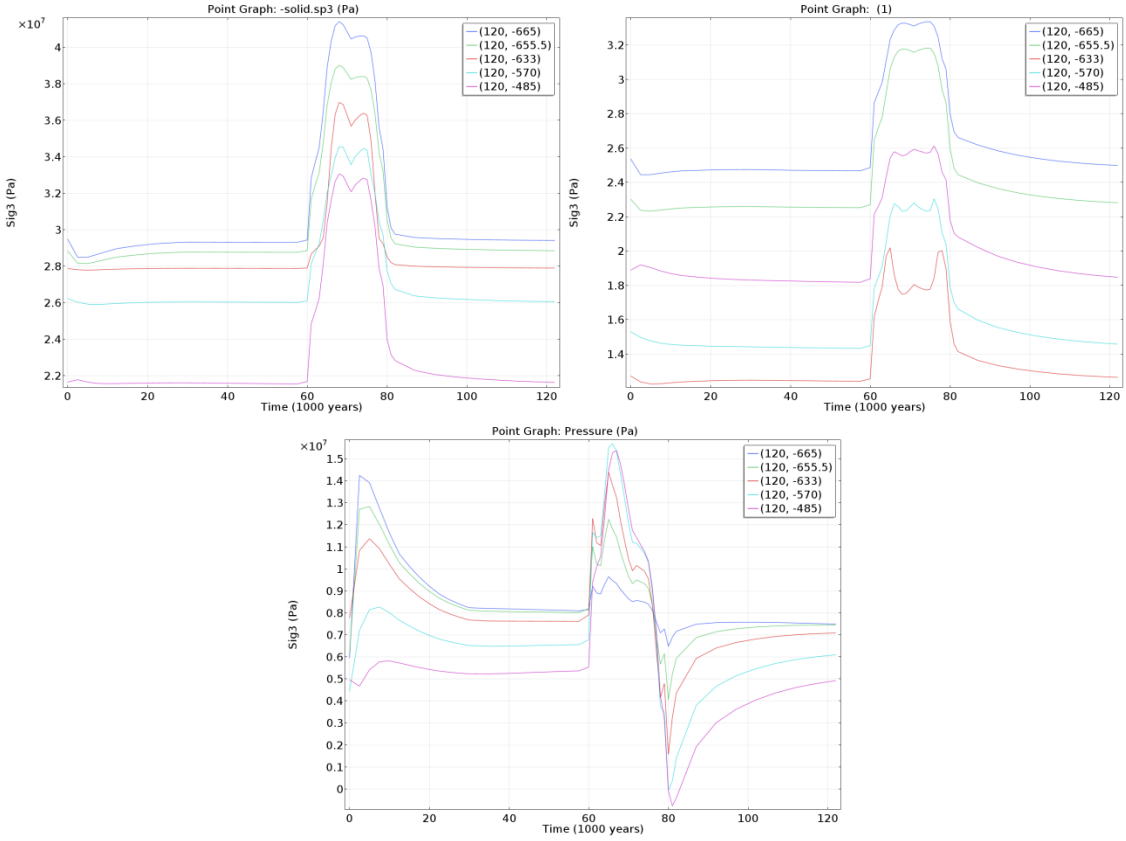

Figure 9.23 Variation of parameters at cut points with elapsed time in postclosure period

Tracer migration modelling

Figure 9.24 illustrates the solute transport modelling results under the glacial cycle impacts. The tracer is found to migrate from the emplacement room towards the vertical shaft at the beginning and moves upward until 600 m below the ground surface. Further prolonged duration and the glaciation seem not to affect the vertical migration of the tracer. Diffusion is identified as the predominant transport mechanism for the tracer.

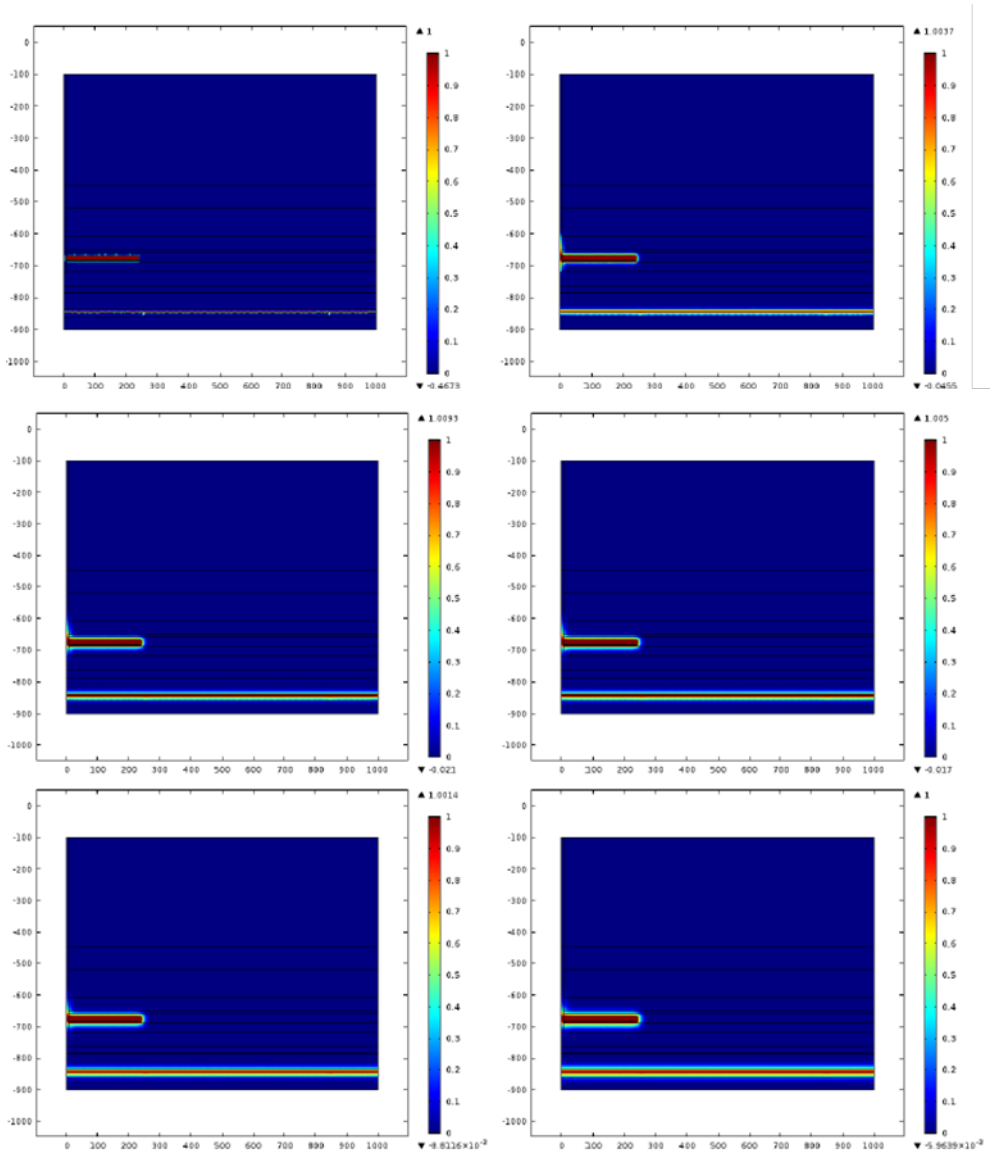

Figure 9.24 Contour plotting of tracer concentration at various post-closure times corresponding to sampling points A-F

6. Conclusions

The numerical analyses reported here incorporate the recently acquired knowledge on the repository host rock and bentonite seals. We update the original conservative scenarios in order to assess the potential HM changes to the surrounding rock mass as well as the long-term evolution of the whole geological formations in view of the glacial cycles. The new study basically confirms most of the assumptions and parameters adopted in the original model. The excavation damage zone (EDZ) is investigated for the tunnel and shaft. The long-term hydraulic-mechanical coupled modeling study for the large scale repository system takes into consideration the ice load on the surface due to a future glacial cycle and gas pressure generated in the repository.

The model parameters are carefully selected from published technical reports previously carried out on the Bruce nuclear site. For the calculation of factor of safety (FS), special attention was given to long term strength degradation behavior of the rock mass under in situ stress conditions. We assume a 65 % of the peak UCS to represent the long term strength parameter. Internal boundary conditions for the emplacement tunnel are also considered in the simulations. For the present scoping analysis, only 1 cycle of glacial influence is included in the analysis. The conclusions from this study are summarized as below.

- The new study confirms most of the assumptions and parameters adopted in the original model. No major discrepancy in conclusions and findings is noticed in this study. The conservative scenario is confirmed to be justifiable.
- The excavation induced damage zone (EDZ) from the floor of the emplacement room extends through the Cobourg formation into the underlying Sherman Fall formation. The overall scope of the damage zone is approximately 2 times of the tunnel height and penetrates marginally over 1 m into the 13 m thick pillars at shoulder and toe corners.
- The EDZ appears to be limited within 1-2 diameters into the sidewall of the shaft, preferentially in the direction perpendicular to the major principal stress. The maximum EDZ extent is found to be approximately 5.9 m in radius in the Weak Sherman Fall layer underneath the waste repository formation.
- The tunnel pressure resulting from gases causes perturbation to the regions, which is more permeable to other host rocks, around the vertical shaft.
- Glacial cycle would not impact the mechanical stability of all formations under consideration. However, disturbance to pore pressure and hydraulic flow is indeed observable in the model. The effective stress in some formations is found to interact with the dissipation of pore pressure, and thus appears to be time-dependent and delayed with respect to the glacial loading.

Reference

Blatz, J. A. & Graham, J. (2003) Elastic-plastic modelling of unsaturated soil using results from a new triaxial test with controlled suction. Geotechnique 53, No. 1, 113–122.

Geofirma Engineering Ltd. And Quintessa Ltd. (2011) Postclosure Safety Assessment: Gas Modelling. NWMO DGR-TR-2011-31

Itasca Consulting Group Inc. (2011) Long-Term Geomechanical Stability Analysis. NWMO DGR-TR-2011-17.

Intera Engineering Ltd. (2011) Descriptive Geosphere Site Model. NWMO DGR-TR-2011-24.

Jorgensen, Donald G. Relationships between Basic Soils-Engineering Equations and Basic Ground-Water Flow Equations. Geological Survey Water-Supply Paper 2064. United States Government Printing Office, Washington: 1980.

Nguyen, Son (1995) Computational modeling of thermal-hydrological-mechanical processes in geological media. PhD Thesis. McGill University, Montreal, Quebec, Canada.

NWMO: Nuclear Waste Management Organization (2011) Geosynthesis. NWMO DGR-TR-2011-11

OPG letter (2012) Albert Sweetnam to JRP Chair, “Updated Information in Support of OPG’s Licence Application for a Deep Geologic Repository for Low and Intermediate Level Waste”. CD# 00216-00531-00101.

Quintessa Ltd. (2011) Postclosure Safety Assessment: Analysis of the Normal Evolution Scenario. NWMO DGR-TR-2011-26

Tang, Gary Xiangmin (1999) Suction Characteristics and Elastic-Plastic Modeling of Unsaturated Sand-Bentonite Mixture. Thesis. Department of Civil and Geological Engineering, University of Manitoba, Winnipeg, Manitoba.

Acknowledgement

This study is sponsored by the Canadian Nuclear Safety Commission. The broad and extensive explorations into the various unknowns about the THMC coupled processes happening to the deep geological repositories may not be possible without the great, inspiring, creative, constructive and in-depth discussions with my supervisor Dr. Son Nguyen, and with Dr. Grant Xueqing Su, amongst other team members including Dr. Julie Brown, Dr. Karina Lange, Dr. Matthew Herod, Qinghuai Zheng, and Dr. Shizhong Lei, as well as substantial support from Director Andrew McAllister, Mr. Peter Button, Mr. Zhao Chang Zeng, and many others in the CNSC that I cannot name all in this place. Many of the contents investigated in this study come from our valuable collaborators, including CANMET Mining, IRSN, Queens' University and the University of Toronto. I would like to express my sincere appreciation to all of those who have helped out at a certain point of this project.

The project lasts for almost three years and has become one of my most memorable endeavours in the engineering consultations. I would also like to thank my family for their love and support.

Zhenze Li

May 23, 2017